Flow Processes in Composite Materials

Edited by

Suresh G. Advani

Professor of Mechanical Engineering

Associate Director, Center for Composite Materials
University of Delaware
Newark, DE 19716
USA

Foreword

The Flow Processes in Composite Materials (FPCM) Conference is devoted to manufacturing and processing of polymer matrix composites. The first Conference was held at Brunel University in 1988 with the mission of attracting high quality papers and providing a forum for discussion among academics and industrialists. The intent was to meet every two to three years. The next four meetings were held at University of Limerick (1991), University of Galway (1994), University College of Wales (1996) and University of Plymouth (1999). The sixth meeting was held at University of Auckland (2001) in New Zealand. These proceedings contain all the manuscripts presented at the seventh meeting. This was the first meeting in United States and was held on July 7th- 9th 2004 at the University of Delaware, Newark, DE 19716.

I have organized the manuscripts according to the subject area. The topics that are addressed in this volume span various issues from process modeling to material characterization for composite manufacturing processes. The new emerging topics of nano-composites and reactive thermoplastic processing have been introduced for the first time. The fabric permeability topic continues to interest many researchers as they search for an answer that goes beyond characterization. New processes that can enhance flow and impregnation focus on the theme of manufacturing large-scale composite structures as they move away from the traditional autoclave processing which usually limited the size of the part to be fabricated. The research direction in manufacturing has also embarked on addressing flow control as the material and process variability uncertainties continue to be a major reason for the low yield. This approach naturally lends itself to development of a platform to introduce automation in composite manufacturing processes. Flow and cure simulations continue to be one of the accepted tools to design the process, optimize the parameters and also develop control strategies. Micro level understanding of flow and cure phenomena in composites manufacturing has played a pivotal role in improving composite properties and many of the manuscripts in this volume address modeling and characterization at the micro level.

I want to thank the Director of Center for Composite Materials, John W. Gillespie, for his support for this conference. I am grateful to the scientific advisory board and the local organizing committee for reviewing the abstracts of these manuscripts. I would also like to acknowledge The Boeing Company for publishing these proceedings. A Big Thank You goes to Corinne Hamed for collecting and organizing the manuscripts with the help of Valentin Neacsu in a form suitable for publication and it would not look so attractive without Dawn Fiore's design of the cover. This bound volume of manuscripts would not be possible without the contribution of the authors and I hope that these well presented papers enhance your understanding of the manufacturing science in composite materials and are useful in your quest for further improvements and discoveries in composites.

<div align="right">

Suresh Advani
June 16th, 2004

</div>

TABLE OF CONTENTS

Section 2.
THERMOPLASTIC PROCESSING

55

Section 3.
RESIN TRANSFER MOLDING

143

Section 4.
VACUUM INFUSION PROCESSES

Section 5.
PROCESS CONTROL

Section 6.
MODELING AND SIMULATION: I NUMERICAL METHODS

Section 8.
MODELING AND SIMULATION: III FLOW AND CURE

Section 11.
PREFORM MODELING AND EFFECTS: III. COMPRESSIBILITY

Section 13.
POST-PROCESS PROPERTIES AND CHARACTERIZATION

Section 14.
NANOCOMPOSITES

SHORT FIBER COMPOSITES

AFM Investigation of Microscopic Flow of Matrix Leading to Interphase Formation in Short Melamine Fiber Reinforced Rubber Composites

R.S. Rajeev[1], S. Bandyopadhyay[2], S.K. De[3] and A.K. Bhowmick[4*]

[1]*Dep of Chemical Eng, U South Carolina, Columbia, SC-29208, USA: RAJEEV@engr.sc.edu*
[2]*School of Materials Sci & Eng, UNSW, Sydney 2052, Australia: S.Bandyopadhyay@unsw.edu.au*
[3]*College of Leather Technology, Salt Lake City, Kolkata, India: sadhan41de@yahoo.co.in*
[4]*Rubber Technology Center, IIT Kharagpur-721302, India : anilkb@rtc.iitkgp.ernet.in*
Corresponding author: anilkb@rtc.iitkgp.ernet.in

SUMMARY: Melamine fiber reinforced elastomer composites are potential candidates as insulators for launch vehicles by virtue of their low density and excellent ablative properties. In this paper atomic force microscopy (AFM) study of the interphase formation in short melamine fiber reinforced rubber composites with ethylene propylene diene (EPDM), maleated EPDM and acrylonitrile co-butadiene rubbers (NBR) as matrices is reported. A dry bonding system comprising of resorcinol, hexamine and hydrated silica was used for enhancing wetting and aiding microscopic matrix flow onto the fiber. Mechanical testing of the composites proved the reinforcing capability of the melamine fiber; particularly containing the bonding agent. Further, thermal aging of the fibers increased the tensile strength and modulus. A probe using AFM revealed the presence of a thick, well-defined fiber-matrix interphase in the composites with the bonding system. For the thermally aged fibers, AFM studies revealed an increase in the surface roughness providing a greater interfacial surface area enabling the matrix to flow into the crevices of the roughened fiber. The improved tensile strength and modulus of the aged composites can thus be attributed to the excellent mechanical interlock, as was evident from the AFM images. All the three matrices portrayed similar behavior. The studies reveal that melamine fiber is a suitable reinforcing fiber for EPDM, mEPDM or NBR matrices, and that AFM is a powerful novel technique to investigate the microscopic flow of the matrix onto the fibers and obtain wetting and interface formation..

KEY WORDS: atomic force microscopy; interphase; melamine fiber; rubber matrix, microscopic flow, wetting.

INTRODUCTION

Though short fiber-rubber composites (SFRCs) find application in hose, belt, tires, and automotives [1], one of the most important recent applications of these composites is as thermal insulators [2] where the material will protect the metallic casing by undergoing a process called ablation i.e. sacrificial removal of material to protect structures subjected to high rates of heat transfer [3]. FRP composites and SFRCs are potential ablative materials because of high specific heat, low thermal conductivity and the ability of the fiber to retain the char formed during ablation [4]. Originally, asbestos-filled phenolic resins and elastomers were used for this purpose

[2]. Because of the health hazards, replacement of asbestos fibers in high temperature applications is a must. Melamine fiber, a recent generation high performance fiber offering i) high operating temperature, ii) high limiting oxygen index, iii) combined fire protection & heat stability properties along with iv) good chemical, hydrolysis and UV resistance and v) superior thermal and ablative properties is an extremely good candidate for replacing asbestos [5]. Like aramid fiber, melamine fiber has no specific melting point - an important prerequisite as an ablative material.

Although the lifetime of rubber compound as insulator is short, its mechanical as well as aging properties are important [6]. The density of the rubber should be as low as possible. The choice of rubber matrix for insulator development is based on these criteria. Nitirle rubber based compositions are widely used in solid rocket motor insulators because of the better rubber-metal adhesion. Since EPDM rubber combines low density with high specific heat, good thermal stability, good resistance to chemicals, low thermal conductivity compared to all other general-purpose synthetic elastomers, it has potential application in the area of thermal insulators such as solid rocket motor insulators [7]. Achieving proper fiber – matrix adhesion is one of the most important challenges in the development of SFRCs for high performance applications. The use of external bonding agent is important, especially in the case of a non-polar matrix like EPDM rubber. A dry bonding system consisting of resorcinol (or a resorcinol derivative), hexamethylene tetramine (hexamine) and hydrated silica [RHH], is useful in such cases [8]. The objective of the present study is to analyze, using AFM and SEM, the effect of incorporation of melamine fiber and dry bonding system on the microscopic flow of matrices of EPDM, maleated EPDM and nitrile rubber based vulcanizates. Special attention has been made to analyze the role of the dry bonding system in improving the wetting of the fiber surface by the matrix and providing smooth extrudate, as are important in the development of high performance SFRCs.

EXPERIMENTAL

Matrices used: EPDM rubber (Royalene 535, supplied by M/s Uniroyal Chemical Co. USA), maleated EPDM rubber (Royaltuf 490, supplied by M/s Uniroyal Chemical Co. USA) and nitrile rubber (supplied by Japan Synthetic Rubber, Japan). The respective masterbatches were prepared by mixing the rubber, melamine fiber (supplied by M/s BASF Corporation, Singapore) and other compounding ingredients in a Brabender Plasticorder at 80°C at a rotor speed of 30 rpm. The curatives were added in a two roll rubber mixing mill. The RHH system is used as the dry bonding system. Typical formulation (in phr) contains rubber, 100; ZnO, 5; strearic acid, 1; antioxidant TQ, 1; melamine fiber, 30; MBT, 1.5; TMTD, 1 and sulfur 1.5 apart from resorcinol, hexamine and silica, whose concentration varied in the order 0/0/0, 5/3/15 and 10/6/15, to optimize the level of the bonding system. Vulcanization of the compositions was carried out in a hydraulic press. EPDM and nitrile rubber based compositions are cured by using sulfur-accelerator system only. Since maleated EPDM rubber contains maleic anhydride groups as well as double bonds, it can be cured by conventional covalent crosslinking system based on sulfur/accelerator or ionic crosslinking system using metal oxides or mixed crosslinking system consisting of both covalent and ionic bonds. The ionic crosslinking system contained no sulfur/accelerator but 10 phr ZnO and 20 phr zinc stearate. In order to study the suitability of the composites as solid rocket motor insulators, the ablative properties were determined by

subjecting the cylindrically shaped composites to plasma arc jet facility to simulate the high temperature environment of the insulators. The specimen was exposed to plasma arc jet of know heat flux for 20 seconds. The length of the specimen before and after exposure is used to calculate the thermal erosion rate.

Stress-strain properties of the cured samples were measured according to ASTM D 412-98a specification. Aging studies were performed by determining the mechanical properties after aging of the composite test specimens at 150°C for 48 hours in a circulating air oven. The tensile fractured samples and the extrudate surfaces, obtained after extruding through the Monsanto processability tester were studied by using a JEOL scanning electron microscope (model, JSM 5800). Extrudate surfaces were obtained by extruding the compounds through a capillary rheometer at 120°C and at a shear rate of $64.1s^{-1}$. For AFM investigations, a relatively flat surface structure is necessary to avoid damaging of the tip. AFM specimens were prepared by cryomicrotoming in a Reichert-Jung Ultracut Ultramicrotome, using glass knives after freezing the specimens to below the T_g of the matrix using liquid nitrogen. Average sample thickness was 20 microns. AFM study was carried out in air at ambient conditions (25°C) using a Dimension 3000 Atomic Force Microscope made by Digital Instruments, Santa Barbara, CA, USA. Topographic images were scanned and recorded in the tapping mode. Images were subsequently analyzed using Nanoscope IIIa software. Details of AFM technique/application/analysis for fiber composites [5, 8, 9-11], filler-composites [12, 13], polymer recycling [14-16] and polymer blends [17, 18] by the authors and the co-researchers are available in the literature.

RESULTS AND DISCUSSION

Mechanical Properties of the Composites: As is evident from Table 1, the interfacial adhesion between melamine fiber and the rubber matrix is significantly improved in presence of the dry bonding system. Without bonding system, the composite $EB_0Si_0F_{30}$ is weak; having tensile strength only 1.6 MPa and the value is comparable to that of the gum compound $EB_0Si_0F_0$. Addition of resorcinol, hexamine and silica in the ratio 5:3:15 increases the tensile strength and modulus more than 3 times (composite $EB_1Si_{15}F_{30}$). When the concentration of the constituents of the dry bonding system is optimized (resorcinol, hexamine and silica concentration 10/6/15, composite $EB_2Si_{15}F_{30}$), there is further improvement in the mechanical properties (17% increase in tensile strength and 25% increase in tensile modulus). Similar results were obtained in the case of composites based on both maleated EPDM rubber and nitrile rubber, as shown in Table 1. Apparently, a multilayer adhesion, involving fiber, bonding system and the elastomeric matrix takes place here [19]. The methylol group in the melamine fiber forms hydrogen bonding with the hydroxyl groups in the dry bonding system. The binding force between the adhesive and the elastomer comes from the vulcanization of the elastomer. The dry bonding system, upon heating, produces resorcinol-formaldehyde resin through crosslinking between the unsaturated bonds in the elastomer and the bonding system, assisted by the heat of vulcanization in the presence of sulfur/accelerator. This hypothesis is confirmed by the improvement in properties of the aged composites containing the dry bonding system.

Aging at 150°C for 48 hours causes a distinct change in the mechanical behavior of the composites. Again Table 1 shows that the composites display an increase in tensile strength and modulus after aging, particularly in the presence of the bonding system. At the same time in the

absence of fiber, aging causes a drop in tensile strength ($EB_2Si_{15}F_0$). Even in the absence of bonding system, there is an increase in tensile strength and modulus of the composite $EB_0Si_0F_{30}$ due to aging, however, when bonding system is present, the strength and modulus are further increased (composite $EB_2Si_{15}F_{30}$). This illustrates the contribution of dry bonding system in improving the fiber-matrix adhesion.

Table 1. Mechanical properties of the composites based on EPDM rubber.
(Values in the brackets indicate properties obtained after aging the vulcanizates at 150°C for 48 hours)

Compositions[a]	EB_0Si_0 F_0	EB_0Si_0 F_{30}	EB_1Si_{15} F_{30}	EB_2Si_{15} F_0	EB_2Si_{15} F_{30}	SB_0Si_0 F_{30}	SB_2Si_{15} F_{30}	NB_0Si_0 F_{10}	NB_2Si_5 F_{10}
Rubber	EPDM	EPDM	EPDM	EPDM	EPDM	Maleated EPDM	Maleated EPDM	Nitrile	Nitrile
Resorcinol/hexa/ silica (phr)	0/0/0	0/0/0	5/3/15	10/6/15	10/6/15	0/0/0	10/6/15	0/0/0	10/6/5
Fiber (phr)	0	30	30	0	30	30	30	10	10
Stress at 100% elongation (MPa)	1.2 (1.5)	1.5 (--)	4.8 (--)	1.7 (2.8)	6.0 (--)	2.5 (--)	6.8 (--)	1.2 (1.4)	3.6 (3.3)
Tensile strength (MPa)	1.5 (1.5)	1.6 (2.2)	5.9 (8.5)	5.5 (5.2)	6.9 (9.8)	3.7 (4.3)	9.3 (11.0)	2.4 (2.5)	10.6 (10.7)
Elongation at break (%)	141 (109)	124 (60)	197 (79)	362 (183)	154 (81)	137 (66)	214 (72)	388 (222)	416 (300)
Hardness (Shore A)	47 (50)	61 (68)	66 (74)	53 (61)	67 (73)	67	76 (79)	51(52)	62 (64)

a, all compositions contain common ingredients, EPDM-100, ZnO-5, stearic acid-1, antioxidant-1, MBT-1.5, TMTD-1, sulfur-1.5

In the case of maleated EPDM rubber based composites, though fiber in presence of the dry bonding system improves the mechanical properties of those cured by using sulfur/accelerator crosslinking system (Table 1), presence of fiber and/or dry bonding system significantly reduces the tensile strength of the composites cured by using ionic crosslinking system (Table 2). This is possibly due to the fact that the presence of fibers and other compounding ingredients partially hinder the aggregation of ionic groups to form multifunctional crosslinking sites. The higher elongation at break of the gum compound ($IB_0Si_0F_0$) is due to the occurrence of the stress induced ion exchange, lowering stress concentration resulting in high elongation. The lowering of strength of the fiber filled composites even in the presence of the bonding system (composite $IB_2Si_{15}F_{30}$) confirms that the RHH dry bonding system is more effective if sulfur and accelerator are also present in the matrix.

Table 2. Mechanical properties of the maleated EPDM rubber-melamine fiber composites (ionic crosslinking system**)**

Compositions	$IB_0Si_0F_0$	$IB_0Si_0F_{30}$	$IB_2Si_{15}F_0$	$IB_2Si_{15}F_{30}$
Resorcinol/hexamine/silica (phr)	0/0/0	0/0/0	10/6/15	10/6/15
Fiber (phr)	0	30	0	30
Stress at 100% strain (MPa)	1.2	1.3	2.1	3.4
Tensile strength (MPa)	12.3	7.1	7.5	6.4
Elongation at break (%)	1001	850	637	466

Ablative Properties of the Composites: The thermal erosion rate of the unfilled and fiber filled composites based on the EPDM rubber matrix are given in Table 3.

Table 3. Thermal erosion rate of the composites

Composite	Thermal erosion rate (mm/sec)
$EB_0Si_0F_0$	0.40 ± 0.01
$EB_0Si_0F_{30}$	0.22 ± 0.03
$EB_2Si_{15}F_0$	0.38 ± 0.02
$EB_2Si_{15}F_{30}$	0.20 ± 0.01

Incorporation of 30 phr melamine fiber even in the absence of the bonding system causes around 45% reduction in the erosion rate ($EB_0Si_0F_{30}$). However, when the fiber-rubber adhesion is improved through the dry bonding system, there is a significant reduction in thermal erosion rate (composite $EB_2Si_{15}F_{30}$ vis-à-vis $EB_0Si_0F_{30}$). The presence of silica alone does not help in improving the ablative properties, as is evident from the high erosion rate of the compound $EB_2Si_{15}F_0$. The fiber, when properly bonded to the matrix, adds strength to the char until they reach their own decomposition temperature.

AFM and SEM Analysis of the Composites: The AFM images shown in Figs. 1(a) to 1(c) are the section analyses of the EPDM-melamine fiber composites with resorcinol/hexamine concentration of 0/0, 5/3 and 10/6 phr respectively. The improved wetting of the matrix on the fiber due to the presence of the bonding system is evident here. It is seen that in the absence of the dry bonding system, the width of the interphase is only 0.59 μm (Fig. 1(a)). The fiber matrix interphase is very smooth, indicating insignificant interaction [poor wetting] between the fiber and the matrix. When resorcinol and hexamine are added in the ratio 5:3, the width of the interphase is increased to 1.79 μm (Fig. 1(b)). When the concentration of resorcinol and hexamine is increased to 10 and 6 phr respectively, the width of the interphase is further increased to 5.39 μm (Fig. 1(c)). So, as the ratio of the constituents of the dry bonding system is raised, the interphase thickness is increased. The mechanical properties described earlier are in line with the increase in interphase thickness. SEM photomicrographs of the tensile fracture surfaces also show that in the absence of the bonding system, the fibers are loosely held to the matrix and the fracture mode is fiber pullout (Fig 1(d)) However, better fiber-matrix adhesion is observed in presence of the bonding system, as shown in Fig. 1(e).

Table 1 shows that aging improves the tensile strength and modulus of the composites. AFM images in Fig. 1(b) also reveal that though an interphase is formed with the addition of the dry bonding system, the bonding between the fiber and the matrix is not achieved to the maximum in the case of the unaged composites. There is debonding between the fiber and the matrix before aging. In some areas, the gap between the fiber and the matrix is in the range of 0.74 to 0.93 μm. This distance is proportional to the extent of debonding. The fiber surface is also smooth, which shows inadequate mechanical interlocking.
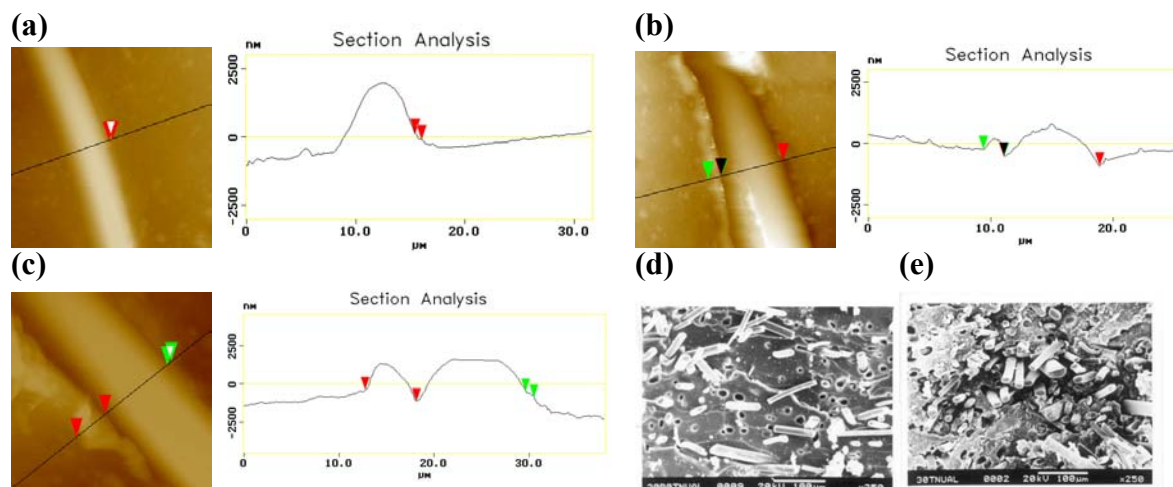
Fig.1. (a)-(c) AFM section analysis of the unaged EPDM-melamine fiber composites with resorcinol/hexa/silica concentration 0/0/0, 5/3/15 and 10/6/15 respectively; (d) and (e), SEM photomicrographs of the tensile fracture surfaces of the unaged EPDM-melamine fiber composite- (d) without and (e) with dry bonding system

The improved wetting of the matrix on the fiber surface, in the presence of the bonding system is evident in the SEM and AFM images of the aged EPDM-melamine fiber composites, given in Fig.2. In the SEM image of the tensile fracture surface of the aged composite (Fig. 2 (a)), the failure mode is mainly fiber breakage because of the improved fiber-matrix adhesion. AFM section analysis also shows that before aging the fiber surface is smooth (Figs. 1(b) and 1(c)); however, after aging, due to the greater mechanical interlocking between the fiber and the matrix, the undulations are more (Fig. 2 (b)). Comparison of the surface profile generated by the AFM tip over the fiber surface of the composite $EB_2Si_{15}F_{30}$ before and after aging, given in Fig. 2 (c), reveals the changes induced on the fiber surface by aging. The surface roughness of the fiber itself is changed upon aging. The AFM phase images of a single melamine fiber filament before and after aging are given in Fig. 3 along with corresponding AFM section analysis of the height images. The changes in the surface morphology of the filament due to aging are visible here.
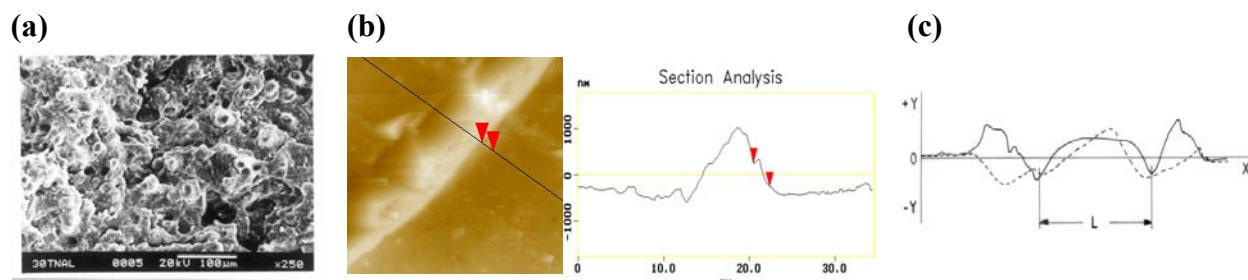
Fig. 2. (a) SEM fractograph and (b) AFM section analysis of the aged composite $EB_2Si_{15}F_{30}$ containing the dry bonding system; (c) surface profile generated by the AFM tip over the fiber surface on the composite before aging (_____) and after aging (---------)

AFM roughness analysis of the melamine fiber filaments show that the average filament surface roughness is increased from 5.66 nm to 12.61 nm due to aging at 150°C for 48 hours. This presents a greater interfacial surface area [typically 4 times] enabling the matrix to flow into the

crevices of the roughened fiber, causing improved wetting. Dry bonding system assists the matrix flow. The better tensile strength and modulus of the aged composites are considered as the consequence of this excellent mechanical interlock, as evident from the AFM images. The enhanced roughness of filament surface upon aging are probably due to surface oxidation as well as removal of adsorbed water layer [5].
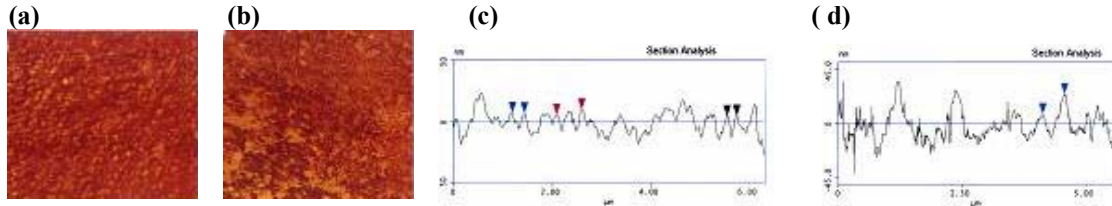
Fig. 3. (a) and (b) AFM phase image of the unaged and aged single melamine fiber filament; (c) and (d), section analysis of the AFM height image of the unaged and aged single melamine fiber filament.

The improved wetting due to aging is only observed in the presence of the dry bonding system, by comparing SEM and AFM images of the aged composites containing no bonding agent (Fig. 4 (a) and (b)) with those containing the bonding system (Figs. 2(a) and 2(b)). This observation is further confirmed in the three dimensional AFM topographic image of the aged matrix of the composite $EB_0Si_0F_{30}$ (Fig. 4 (c)), which contains no bonding system. The figure shows a bed in the matrix, which is actually the position where the fiber was laid on. In the absence of the bonding system, the fiber is easily removed leaving the matrix unreinforced.
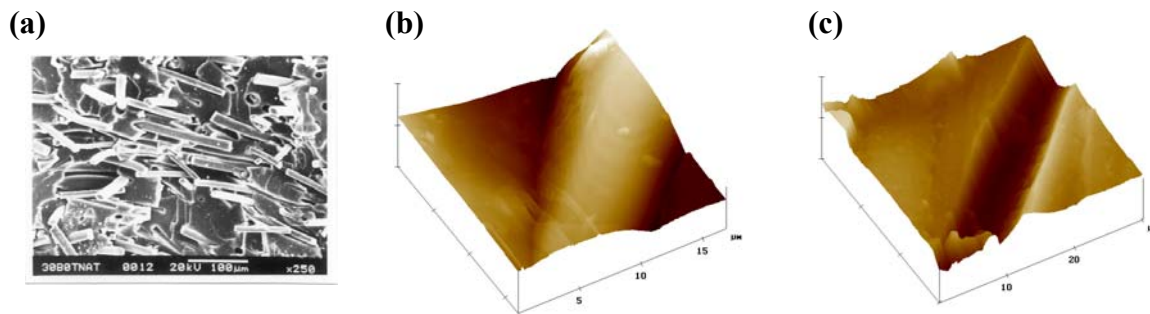
Fig. 4. (a) SEM fractograph and (b) AFM surface plot image of the aged composite $EB_0Si_0F_{30}$, containing no bonding system; (c) AFM surface plot image of the matrix showing the bed where fiber was laid on, for the composite $EB_0Si_0F_{30}$, aged at 150°C for 48 hours.

AFM images of composites based on maleated EPDM rubber and nitrile rubber also display similar trend – shown in Figs. 5(a) and 5(b) for maleated EPDM rubber based composite without and with bonding agent; similarly in Figs. 5(c) and 5(d) for nitrile rubber composites.

(a)   **(b)**   **(c)**   **(d)**
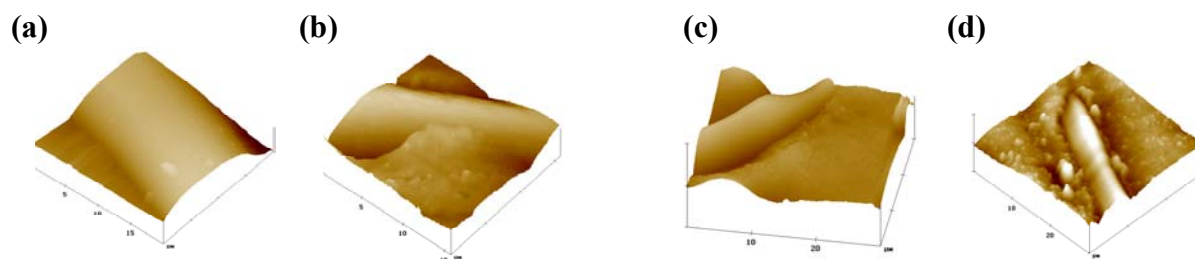
Fig.5. AFM surface plot images of the composites: (a) and (b), maleated EPDM rubber –melamine fiber composites without and with dry bonding system; (c) and (d), nitrile rubber-melamine fiber composites without and with dry bonding system.

Dry bonding system helps to achieving a smooth extrudate surface, which is important in the development of high performance composites. Figs. 6 (a) and 6 (b) present SEM micrographs of the extrudate surfaces of EPDM-melamine fiber compounds without and with dry bonding system. Melting of resorcinol at the extrusion temperature and the presence of silica helps in obtaining a smooth extrudate. Also, the fiber prevents melt fracture and reduce die swell.

(a)   **(b)**
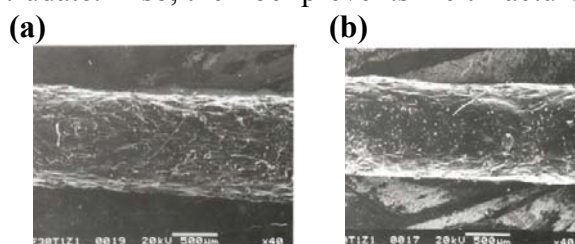
Fig. 6. SEM photomicrograph of the extrudate surface of the compounds based on EPDM and melamine fiber; (a) without dry bonding system and (b) with dry bonding system

CONCLUSIONS

The present study shows that high performance fiber-rubber composites can be prepared using melamine fiber. It is found that reinforcement of EPDM, maleated EPDM and nitrile rubbers using melamine fiber takes place through RHH dry bonding system. Tensile strength and stress at 100% strain of the composites increase when both fiber and bonding system are simultaneously present. Fiber-rubber composites in presence of the bonding system show higher retention of strength and modulus even after prolonged aging at 150°C due to better matrix flow and wetting. Without fiber, the mixes show lowering of properties due to aging, which explains the role of melamine fiber in retaining the properties on aging. Using AFM and SEM, the role of the bonding system in improving the fiber-matrix interaction and the reasons for the improved strength and modulus of the composite after aging are quantitatively analyzed. As the ratio of the bonding system is increased from 5:3:15 to 10:6:15, the width of the interphase is increased from 1.79 μm to 5.39 μm. SEM fractographs of the aged composites show that after aging there is no debonding of the fiber from the matrix and failure occurs mainly due to the breakage of fibers, which are well bonded to the matrix due to better wetting. AFM studies also confirm, quantitatively, change in surface morphology of the fiber as well as the composites due to thermal aging. Comparison of mechanical properties and analysis of SEM and AFM images of

unaged and aged composites suggest that presence of both fiber and bonding system are necessary for improvement in strength and modulus of the composites by thermal aging. There is a significant improvement in the ablative properties of the composites in the presence of melamine fiber especially if there is proper adhesion between the fiber and the matrix through the dry bonding system. Determination of the interphase modulus using an ultramicro/nano-indentor [20] should be a useful future work.

ACKNOWLEDGEMENT

REFERENCES

1. V.M. Murty and S.K. De, "Short Fiber Rubber Composites", *Polymer Engineering Review*, Vol. 4(4), 1984, pp.313.
2. A.P. Foldi in *Short Fiber-Polymer Composites*, Eds. S.K De and J.R White, Woodhead Publishing Limited, Cambridge, England, 1996, pp.242.
3. N.S. Vojvodich in *Ablative Plastics*, G.F. D'Alelio and J.A. Partker, Eds., Marcel Dekker Inc., New York, 1971, pp.41.
4. V. Fitch and N. Eddy, *33rd AIAA/ASME/SAE/ASEE Joint Propulsion Conference,* Seattle, June 6-9, 1997 (in AIAA-97, No. 2992).
5. R.S. Rajeev, Anil K Bhowmick, S.K De, Bill Gong and S. Bandyopadhyay, "Atomic Force Microscopy, X-ray Diffraction, Electron Spectroscopy and Thermal Studies of New melamine Fiber", *Journal of Adhesion Science and Technology,* Vol. 16(14), 2002, pp.1957.
6. A Saha Deuri and Anil K Bhowmick, "Aging of rocket insulator compound based on EPDM", *Polymer Degradation and Stability*, Vol. 16(3), 1986, pp.221.
7. R.S. Rajeev, S.K. De, Anil K. Bhowmick and Baby John, ""Studies on thermal degradation of short melamine fiber reinforced EPDM, maleated EPDM and nitrile rubber composites", *Polymer Degradation and Stability,* Vol. 79(3), 2003, pp. 449.
8. R.S. Rajeev, Anil K Bhowmick, S.K De, G.J.P. Kao and S. Bandyopadhyay, "New composites based on short melamine fiber reinforced EPDM rubber", *Polymer Composites* Vol. 23(4), 2002, pp.574.
9. Rajeev, R S, S K De, A K Bhowmick, GJP Kao and S Bandyopadhyay, "Atomic force microscopic studies of short melamine rubber reinforced EPDM rubber", *Journal of Materials Science*, Vol. 36(11), 2001, pp.2621.
10. Rajeev R.S, Anil K. Bhowmick and S.K De, S. Bandyopadhyay, "Effect of crosslinking system on the properties of short melamine fiber filled maleated EPDM rubber composites with special reference to atomic force microscopic and scanning electron microscopic studies", *Journal of Applied Polymer Science*, Vol. 89(5), 2003, pp. 1211.

11. Rajeev R.S, Anil K. Bhowmick, S.K De and S. Bandyopadhyay, "Short melamine fiber filled nitrile rubber composites", *Journal of Applied Polymer Science*, Vol. 90(2), 2003, pp. 544.

12. A. M. Shanmugharaj, Sudip Ray, S. Bandyopadhyay and A. K. Bhowmick, "Surface morphology of styrene-butadiene rubber vulcanizate filled with novel electron beam modified dual phase filler by atomic force microscopy", *Journal of Adhesion Science & Technology,* Vol. 17(9), 2003. pp.1167.

13. Sudip Ray, Anil K. Bhowmick and S. Bandyopadhyay, "Atomic force microscopy studies on morphology and distribution of surface modified silica and clay fillers in an ethylene-octene copolymer rubber", *Rubber Chemistry and Technology,* Vol. 76(5), 2003, pp. 1091.

14. S. Anandhan, P. P. De, S. K. De, S. Bandyopadhyay and Anil K. Bhowmick, "Mapping of thermoplastic elastomeric nitrile rubber/poly(styrene-co-acrylonitrile) blends using tapping mode atomic force microscopy and transmission electron microscopy", *Journal of Materials Science*, Vol. 38(13), 2003, pp.2793.

15. S. Anandhan, P. P. De, A. K. Bhowmick, S. K. De and S. Bandyopadhyay, "Thermoplastic elastomeric blends of nitrile rubber and poly [styrene-co-acrylonitrile]. II. Replacement of nitrile rubber by its vulcinizate powder", *Journal of Applied Polymer Science*, Vol. 90(9), 2003, pp. 2348.

16. S.Anandhan, S. K. De, P. P. De, S. Bandyopadhyay and Anil K. Bhowmick, "Novel thermoplastic elastomers based on acrylonitrile-butadiene-styrene (ABS) terpolymer and nitrile rubber", *Rubber Chemistry and Technology,* Vol. 76(5), 2003, pp. 1146.

17. S. Ghosh, D. Khastagir, A. K. Bhowmick, S..Bandyopadhyay, G.J.P. Kao and L. Kok, "Atomic force microscopy studies of molded thin films of segmented polyamides", *Journal of Materials Science Letters*, Vol. 19(23), 2000, pp. 2161.

18. A. Ghosh, Rajeev R. S, A.K. Bhattacharya, A.K. Bhowmick, S K De, B.Wolpensinger and S. Bandyopadhyay, "Atomic force microscopy studies on microheterogeneity of blends of silicone rubber and tetrafluoroethylene/propylene/vinylidene fluoride terpolymer", *Rubber Chemistry and Technology,* Vol. 76(1), 2003, pp. 220.

19. Y. Kubo in *Elastomer Technology Handbook*, Ed. Nicholas P. Cheremisinoff, CRC Press, Boca Raton, USA, 1993, pp. 857.

20. T. Das, P.R. Munroe, S.Bandyopadhyay, T. Bell and M.V. Swain, "Interfacial behavior of $6061/Al_2O_3$ metal matrix composites", *Materials Science and Technology,* Vol. 13(9), 1997, pp. 778.

Fiber Dynamics in Concentrated Suspensions of Short Glass Fibers in Polymers

Maryam Sepehr [1] [1], Pierre J. Carreau [1], and Gilles Ausias [2]

[1] CRASP, Chemical Engineering Department, Ecole Polytechnique, PO Box 6079, Stn Center-Ville, Montreal, QC, H3C 3A7, Canada: pierre.carreau@polymtl.ca
[2] LG2M, Université de Bretagne Sud, Rue de St Maudé, BP 92116, 56321 Lorient Cedex, France: gilles.ausias@univ-ubs.fr

SUMMARY: Rheological experiments have been conducted on concentrated suspensions of short glass fibers in a polypropylene and a polybutene under simple shear transient flows. A stress and a rate-controlled rheometer with plate-plate geometry have been used. The viscosity and the normal stress differences have been shown to depict overshoots in stress growth experiments, as well as when the flow was reversed. However, for the reverse flow experiments negative normal stress differences have been observed for the initial part of the experiments. The filled polybutene exhibited a similar behavior compared to that of the filled polypropylene. A Folgar-Tucker model for the fiber dynamics combined with the Lipscomb stress equation has been used to predict the steady-state and transient data. This model developed for dilute or semi-dilute suspensions is able to qualitatively predict the transient observations. However, important differences are observed between the experimental overshoots and the predictions. This implies that experimental fiber dynamics is markedly slower than predicted by the model. Fiber-fiber interactions are discussed and a slip factor introduced in the Folgar-Tucker model is shown to improve the fits.

KEYWORDS: short fiber, concentrated suspension, rheological properties, viscosity overshoot.

INTRODUCTION

Main advantages of thermoplastic materials are their low density and their low production cost. But these materials have weak mechanical properties and they are often filled with short fibers. Reinforced thermoplastics could be processed with conventional machines and tools. However, to be efficient short fibers must be oriented in the stress direction. The final orientation in a part is induced by the composite flow in the processing tool and is hard to control. Moreover, the content of fibers in industrial reinforced thermoplastics is large and, generally, concentrated suspensions with a complex rheological behavior have to be considered. In this work typical experimental results obtained for a commercial glass fiber filled polypropylene and suspensions of fibers in a polybutene will be presented. Simulation results based on a modified Folgar-Tucker model will be discussed and compared with experimental data.

---

[1] Present address: IMI, National Research Council Canada, Government of Canada, 75 de Mortagne, Boucherville, QC, J4B 6Y4, Canada (maryam.sepehr@cnrc-nrc.gc.ca)

MODEL

Fiber motion

A fiber orientation can be described with an orientation vector p, a unit vector parallel to the main axis of the fiber. For a population of fibers, a statistical orientation distribution function $\psi(\mathbf{p})$ can be used to describe the average state of orientation in a fluid element. A second- and a fourth-order orientation tensors have been defined by Advani and Tucker [1]:

$$\mathbf{a_2} \Leftrightarrow a_{ij} = \int_{\mathbf{p}} p_i p_j \psi(\mathbf{p}) d\mathbf{p}, \tag{1}$$

$$\mathbf{a_4} \Leftrightarrow a_{ijkl} = \int_{\mathbf{p}} p_i p_j p_k p_l \psi(\mathbf{p}) d\mathbf{p}, \tag{2}$$

where $\mathbf{a_2}$ is a symmetric tensor with trace equal to one. A closure approximation is necessary to evaluate the fourth-order orientation tensor. The time derivative of $\mathbf{a_2}$ can be derived from that of $\mathbf{p}$ established by Jeffery [2] for dilute suspensions of ellipsoids in a Newtonian fluid under simple shear and at low Reynolds numbers. It has been improved by Folgar and Tucker [3] for semi-dilute suspensions of fibers and can be written as:

$$\dot{\mathbf{a}}_2 = \frac{D\mathbf{a}_2}{Dt} = \frac{1}{2}(\mathbf{\Omega}\mathbf{a}_2 - \mathbf{a}_2\mathbf{\Omega}) + \frac{\lambda}{2}(\dot{\gamma}\mathbf{a}_2 + \mathbf{a}_2\dot{\gamma} - 2\dot{\gamma}:\mathbf{a}_4) + 2C_I\overline{\dot{\gamma}}(\mathbf{I} - 3\mathbf{a}_2), \tag{3}$$

where $\lambda = (r^2 - 1)/(r^2 + 1)$ and r is the ellipsoid aspect ratio. $\dot{\gamma}$ and $\mathbf{\Omega}$ are respectively the rate of strain and the vorticity tensor defined by $\dot{\gamma} = (\mathbf{\kappa} + \mathbf{\kappa}^t)$ and $\mathbf{\Omega} = (\mathbf{\kappa} - \mathbf{\kappa}^t)$ where $\mathbf{\kappa}^t$ is the velocity gradient tensor. $\overline{\dot{\gamma}}$ is the effective deformation rate (square root of half of the second invariant of the rate of strain tensor) and C_I a phenomenological coefficient. For large ellipsoid aspect ratios, λ tends toward 1. Fibers in filled polymer composites are considered to be ellipsoids having an aspect ratio of r.

Constitutive equation

Following Jeffery [2], Hand [4] and Giesekus [5], Lipscomb *et al.* [6] have proposed a constitutive equation for dilute particles suspensions, which can be written for ellipsoids with high aspect ratio, as:

$$\mathbf{\sigma} = -P\mathbf{I} + \eta_m\dot{\gamma} + \eta_m\phi\{2\dot{\gamma} + \mu_2\dot{\gamma}:\mathbf{a}_4\}, \tag{4}$$

where η_m is the matrix viscosity, P the hydrostatic pressure, ϕ the fiber volume fraction and μ_2 is rheological coefficient. The last term of Eqn. 4 describes the coupling between hydrodynamic forces and fiber orientation; hence we call μ_2 the coupling coefficient.

Closure approximations

To complete the model the fourth-order orientation tensor is evaluated knowing the second-order orientation tensor. Many closure approximations have been proposed. Among the most recent, the orthotropic [7, 8] and the natural [9] closure approximations are similar in philosophy. Invariants of the second-order tensor are used to calculate the fourth-order tensor. Different closure approximations have been tested in forward and reverse flows. The orthotropic has been chosen as the more accurate to fit our experimental results.

EXPERIMENTS

A commercial unfilled polypropylene (PP, Targor PPN 0160D1) and a filled polypropylene containing 30 wt.% short glass fibers (PP30, Targor Hostacom G3 N01L) have been used. Targor also prepared other fiber suspensions with different fiber contents in experimental batches under the same conditions as PP30. The fiber average length measured after blending using an internal mixer was 260 μm for PP30. They have a diameter of 14 μm. Filled polypropylene has been pyrolyzed, the fibers recovered and blended in a Newtonian polybutene (PB, Stanchem Indopol H100) with a molecular mass of 920 g/mol, a density of 0.89 g/mL and a viscosity of 24 Pa.s at 25°C. Experiments have been conducted with a rate-controlled rheometer, ARES (Rheometric Scientific). Parallel plate fixtures were used with the gap between the two plates *H* varying between 1.4 and 1.5 mm for all experiments. For the polypropylene fiber composites, the plate radius *R* was equal to 12.5 mm, the temperature was set at 200°C and experiments conducted under a nitrogen blanket. For polybutene fiber suspensions, the plate radius was 25 mm and experiments carried out at room temperature. Stress growth experiments have been conducted in forward and reverse flow directions. The viscosity and the normal stress differences have been shown to depict overshoots in the forward stress growth experiments as well as when the flow was reversed. However, for the reverse flow experiments negative normal stress differences have been observed for the initial part of the experiments. The filled polybutene exhibited a similar behavior compared to that of the filled polypropylene.

DISCUSSION

The model presented above is able to qualitatively predict the transient observations. However, important differences were observed between the experimental and the predicted overshoots. This implies that the experimental fiber dynamics is much slower than predicted by the model, due to fiber-fiber interactions. A slip factor is introduced in the Folgar-Tucker model as:

$$\gamma_e = \alpha \dot{\gamma} t \qquad (5)$$

where γ_e is the modified experimental deformation and α is the slip factor. It improves the fits of the data, but this empirical approach is valid only for simple shear flows as the model will no longer be objective. The modified model contains three adjustable parameters, μ_2, C_I and α. The model predictions for reverse overshoot viscosity data of PB05, PB10 and PB30 and results are presented in Fig. 1. The model parameters are reported in Table 1. Using the same values of the model parameters the predictions for the normal stress data are compared in Fig. 2. For both figures, the fits are quite reasonable.

Table 1 Model parameters for the filled PB at different fiber mass fractions.

	PB05	PB10	PB20
μ_2	280	210	195
C_I	0.0003	0.0008	0.0010
α	0.7	0.6	0.5
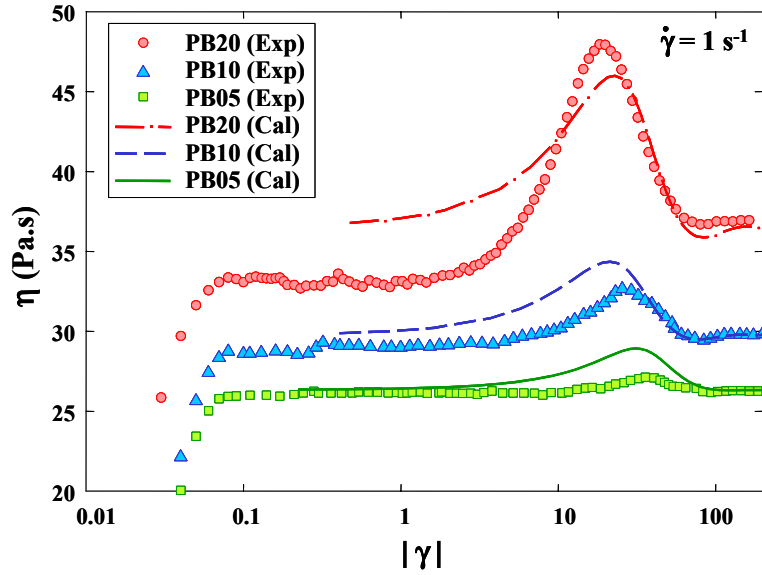
Fig. 1. Comparison of the model predictions and the experimental viscosity data of PB suspensions obtained for reverse stress growth experiments.
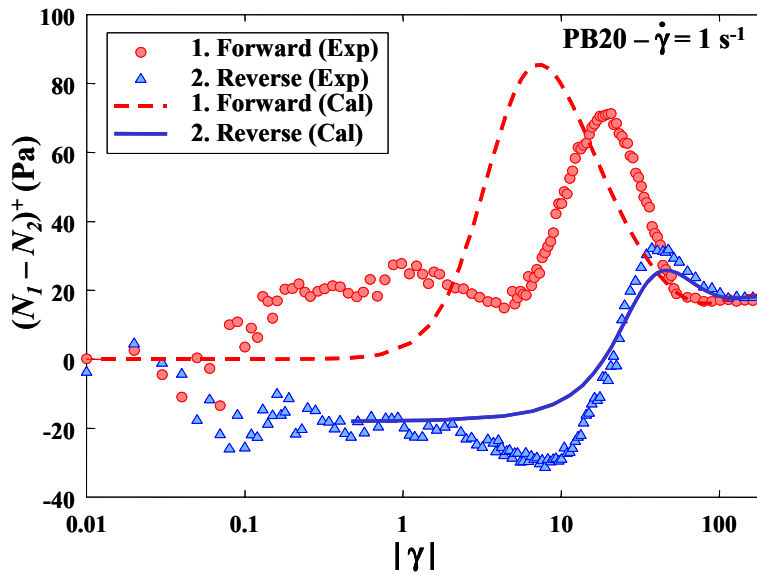
Fig. 2. Comparison of the model predictions and the experimental normal stress data of PB20 obtained for forward and reverse stress growth experiments.

CONCLUSION

The rheological properties of glass short fiber filled polypropylene has been studied and compared to data of suspensions of the same fibers in a polybutene, obtained under transient shear flows. Viscosity and normal stress overshoots were observed each time the flow direction was reversed. When the flow was reversed, the normal stress differences took initially negative values before depicting a positive overshoot and reaching a steady-state value. A model based on the Lipscomb and Folgar-Tucker equations can qualitatively describe the rheological behavior. The simulations carried out with this model predicted viscosity overshoots of smaller width than those measured. A slip parameter has been empirically introduced in the model to reduce the fiber rotation motion and the modified model is shown to describe fairly well the stress growth overshoots for the viscosity as well as for the normal stress differences.

ACKNOWLEDGEMENTS

REFERENCES

1. S.G. Advani, C.L. Tucker, "The use of tensors to describe and predict fiber orientation in short fiber composites", *Journal of Rheology*, Vol.31, 1987, pp. 751.
2. G.B. Jeffery, "The motion of ellipsoidal particles immersed in a viscous fluid", *Proc. Roy. Soc. London, Ser.,* A102, 1922, pp 161.
3. F.P. Folgar and C.L. Tucker, "Orientation behavior of fibers in concentrated suspensions", *Journal of Reinforced Plastics and Composites*, Vol.3, 1984, pp. 99.
4. G.L. Hand, "A theory of dilute suspensions", *Archive for Rational Mechanics and Analysis*, Vol.7, 1961, pp. 81.
5. H. Giesekus, " Elastico-viscous fluids displaying a large normal stress component in steady flow ", *Rheologica Acta*, Vol.2, 1962, pp. 50.
6. G.G. Lipscomb, "Analysis of suspension rheology in complex flows", Ph. D dissertation, University of California, Berkeley, 1987.
7. J.S. Cintra and C.L. Tucker, "Orthotropic closure approximations for flow-induced fiber orientation", *Journal of Rheology*, Vol.39, n°6, 1995, pp. 1095.
8. E.D. Wetzel and C.L. Tucker, "Area tensors for modeling microstructure during laminar liquid-liquid mixing", *International Journal of Multiphase Flow*, Vol.25, 1999, pp. 35.
9. V. Verleye and F. Dupret, "Numerical prediction of fiber orientation in complex injection molded parts", *Proceedings of the ASME Winter Annual Meeting*, MD, Vol.49, HTD-Vol. 283, 1994, pp. 264.

A Fitted Closure of the Sixth-Order Orientation Tensor for Short-Fiber Reinforced Polymer Composite Modeling

Jack, D.A.[1] and Smith, D.E.[2]

[1] *Department of Mechanical and Aerospace Engineering, University of Missouri - Columbia*
E2411 Engineering Building East; Columbia, MO 65211: dajfd5@mizzou.edu
[2] *Department of Mechanical and Aerospace Engineering, University of Missouri - Columbia*
E2411 Engineering Building East; Columbia, MO 65211: smithdoug@missouri.edu
Corresponding Author's e-mail: dajfd5@mizzou.edu

SUMMARY: Orientation tensors are commonly used in short-fiber reinforced injection molding simulations of industrial polymer composite products. Unfortunately, the evolution equation for each even-order orientation tensor is written in terms of the next higher even-order orientation tensor. It has been shown that current fourth-order closures approach the fourth-order truncation limit when representing the fiber orientation distribution function so that an increase in accuracy necessitates the development of a sixth-order closure. A sixth-order fitted closure is presented which assumes that the orthotropic planes of material symmetry of the sixth-order orientation tensor correspond to the principal directions of the second-order orientation tensor. The sixth-order closure is computed using a fitting procedure which minimizes differences between the exact and the fitted sixth-order orientation tensors over a range of orientations encompassing much of the eigenspace of the second-order orientation tensor. The sixth-order closure is demonstrated to approach the sixth-order truncation limit in representing the fiber orientation distribution function over a range of flow fields.

MODELING THE DISTRIBUTION OF FIBERS

Short-fiber polymer composites are used extensively in industrial applications due in large part to their high strength to weight ratio. The orientation state of the short-fibers is critical since it dictates the material properties of the composite structure. Therefore understanding and predicting the fiber orientation is necessary for practical structural design purposes. Most polymer composite fiber orientation simulations begin with the model presented by Folgar and Tucker [1] which superimposes the motion of a single rigid particle in a dilute suspension with that of interacting particles through the use of an interaction coefficient C_I to account for interactions between fibers. The Folgar-Tucker model, which solves the orientation distribution function of fibers $\psi(\theta,\phi)$, is constrained to simple flow simulations due to excessive computation time and memory usage, but is considered to be the benchmark for fiber orientation simulations [2-8]. The solution of the Folgar Tucker model will be referred to as the 'exact' solution throughout the remainder of the paper recognizing that the fiber orientation distribution $\psi(\theta,\phi)$ is solved numerically.

For industrial injection molding applications, Advani and Tucker [2] defined orientation tensors using moments of the fiber orientation distribution function to represent the fiber orientation state. The orientation tensors, a_{ij}, a_{ijkl}, a_{ijklmn}, *etc.* capture the stochastic nature of the fiber orientation distribution in a compact form [2] and are defined through the dyadic products of the unit vector p_i which lies along the fiber axis and the distribution function $\psi(\theta,\phi)$ over the unit sphere

$$a_{ij} = \int_{S^2} p_i p_j \psi(\theta,\phi) dS \qquad a_{ijkl} = \int_{S^2} p_i p_j p_k p_l \psi(\theta,\phi) dS \qquad \cdots \qquad (1)$$

By the application of Eqn. (1) the orientation tensors can be shown to be completely symmetric with respect to any pair of indices. Higher order orientation tensors completely describe the lower order orientation tensors using the normalization condition for the distribution function $\psi(\theta,\phi)$ along with Eqn. (1) [2]

$$1 = a_{ii} \qquad a_{ij} = a_{ijpp} \qquad a_{ijkl} = a_{ijklqq} \qquad (2)$$

where repeated indices indicate summation, *i.e.* $a_{ii} = a_{11} + a_{22} + a_{33}$. Advani [2] combined Eqn. (1) with the Folgar-Tucker model for the distribution function $\psi(\theta,\phi)$ to obtain the evolution of the even order orientation tensors a_{ij}, a_{ijkl}, etc. The time required to compute the evolution of the second-order orientation tensor is significantly less than the computation time required to evolve the distribution function $\psi(\theta,\phi)$. Unfortunately, the evolution of the second-order orientation tensor a_{ij} is a function of the fourth-order orientation tensor a_{ijkl}, and the evolution equation of the fourth-order tensor a_{ijkl} contains the sixth-order tensor a_{ijklmn} [2]

$$\frac{Da_{ijkl}}{Dt} = -(\omega_{im} a_{mjkl} - a_{ijkm}\omega_{ml}) + \lambda(\dot{\gamma}_{im} a_{mjkl} + a_{ijkm}\dot{\gamma}_{ml} - 2\dot{\gamma}_{mn} a_{ijklmn}) +$$
$$C_I \dot{\gamma}[-20 a_{ijkl} + 2(a_{ij}\delta_{kl} + a_{ik}\delta_{jl} + a_{il}\delta_{jk} + a_{jk}\delta_{il} + a_{jl}\delta_{ik} + a_{kl}\delta_{ij})] \qquad (3)$$

where ω_{ij} is the vorticity tensor, λ is the fiber aspect ratio, and $\dot{\gamma}$ is the scalar magnitude of the rate of deformation tensor $\dot{\gamma}_{ij}$. Indeed, the evolution equation of any even-ordered orientation tensor requires information from the next higher even-ordered orientation tensor which necessitates the use of a closure which approximates an orientation tensor in terms of the components of the lower ordered orientation tensors. There exist many closures of the fourth-order orientation tensor as a function of the second-order tensor [2,4-7], along with several closures of the sixth-order orientation tensor [2,8].

A FITTED SIXTH-ORDER CLOSURE

In the literature there exists only a brief investigation into sixth-order closures. Altan *et al.* [8] presented a sixth-order quadratic closure for dilute suspensions of fibers. Their closure is only accurate for highly aligned distributions and has been stated to provide little improvement over fourth-order closure results for the additional computational expenses [5]. Advani and Tucker [2] present a sixth-order hybrid closure, but for most industrial applications the sixth-order hybrid closure overestimates the actual alignment of the fibers [9,10].

This paper presents a sixth-order fitted closure similar in construction to the fourth-order fitted closures of Cintra and Tucker [5], VerWeyst *et al.* [7] and Chung and Kwon [6]. Our sixth-order fitted closure is computed from the components of a_{ijkl} and assumes that the planes of

orthogonal symmetry of the sixth-order orientation tensor correspond to the principal directions of the second-order orientation tensor. In this formulation each principal component of the sixth-order orientation tensor is represented as a function of the independent principal components of the second-order orientation tensor.

A general sixth-order orientation tensor has 729 components of which 28 are independent by symmetry arguments for orientation tensors. If we assume that the principal frame of the second-order tensor a_{ij} forms the orthotropic planes of material symmetry for the sixth-order tensor a_{ijklmn}, only 10 independent nonzero components of a_{ijklmn} remain

$$\bar{a}_{111111}, \ \bar{a}_{111122}, \ \bar{a}_{111133}, \ \bar{a}_{112222}, \ \bar{a}_{112233}, \ \bar{a}_{113333}, \ \bar{a}_{222222}, \ \bar{a}_{222233}, \ \bar{a}_{223333}, \ \bar{a}_{333333} \tag{4}$$

where the overbar indicates that components of the sixth-order orientation tensor are given with respect to the principal frame of the second-order orientation tensor. Using Eqn. (2) for the relation between the fourth- and sixth-order orientation tensors, it can easily be shown that only four unknown components of $\bar{a}_{ijklmn}$ remain from those shown in Eqn. (4) (see *e.g.* [9]). The newly created Eigenvalue Based Fitted sixth-order closure (EBF$_6$) is formed by arbitrarily selecting the four components $\bar{a}_{111111}$, $\bar{a}_{111122}$, $\bar{a}_{222222}$, and $\bar{a}_{333333}$ to be unknown.

A second-order orientation tensor a_{ij} has three eigenvalues $a_{(i)}$, two of which are independent from Eqn. (2). The two independent principal values of the second-order tensor are selected to be $a_{(1)}$ and $a_{(2)}$ when setting $a_{(1)} \geq a_{(2)} \geq a_{(3)}$. The four unknowns of the EBF$_6$ are formed by fitting the four remaining independent components of the sixth-order tensor to a second-order polynomial of the eigenvalues of the second-order orientation tensor as

$$\begin{Bmatrix} \bar{a}_{111111} \\ \bar{a}_{111122} \\ \bar{a}_{222222} \\ \bar{a}_{333333} \end{Bmatrix} = \begin{bmatrix} C_{11} & C_{12} & C_{13} & C_{14} & C_{15} & C_{16} \\ C_{21} & C_{22} & C_{23} & C_{24} & C_{25} & C_{26} \\ C_{31} & C_{32} & C_{33} & C_{34} & C_{35} & C_{36} \\ C_{41} & C_{42} & C_{43} & C_{44} & C_{45} & C_{46} \end{bmatrix} \begin{Bmatrix} 1 & a_{(1)} & a_{(2)} & a_{(1)}a_{(2)} & a_{(1)}^2 & a_{(2)}^2 \end{Bmatrix}^T \tag{5}$$

The new sixth-order closure is computed from the fourth-order orientation tensor a_{ijkl}. First the second-order orientation tensor a_{ij} is formed from a_{ijkl} using Eqn. (2). Then the eigenvalues $a_{(1)}$ and $a_{(2)}$ are computed and the rotation tensor is formed from the eigenvectors of a_{ij}. Next, the principal components of the sixth-order orientation tensor $\bar{a}_{ijklmn}$ are computed using the EBF$_6$ closure from Eqn. (5). Finally, the sixth-order orientation tensor in the principal frame is rotated into the material frame yielding a_{ijklmn} for the given a_{ijkl}.

DISTRIBUTION FUNCTION RECONSTRUCTION

Reconstruction of the fiber orientation distribution function provides a quantitative means of assessing the effect of introducing closure approximations on representing $\psi(\theta,\phi)$ [9,10]. Onat and Leckie [11] demonstrated that an approximate distribution function $\hat{\psi}_N$ of Nth order can be reconstructed based upon the deviatroic form of the orientation tensors as

$$\hat{\psi}_N(\theta,\phi) = f_o V_o + f_{ij} V_{ij} + f_{ijkl} V_{ijkl} + f_{ijklmn} V_{ijklmn} + \cdots \tag{6}$$

where $f_o, f_{ij}, f_{ijkl}, f_{ijklmn}$ are the basis functions and $V_o, V_{ij}, V_{ijkl}, V_{ijklmn}$ are the corresponding Fourier coefficients which can be written entirely in terms of the orientation tensors (see *e.g.* [2,9] for a full discussion). This method is identical to expanding the orientation distribution function $\psi(\theta,\phi)$ in terms of orthogonal functions of p_i [11].

To asses the error between the exact distribution function $\psi(\theta,\phi)$ and the Nth order reconstruction of the distribution function, $\hat{\psi}_N(\theta,\phi)$ we use the following error metric [9,10]

$$ERR_N = \sqrt{\int_{S^2} (\psi(\theta,\phi,t_o) - \hat{\psi}_N(\theta,\phi,t_o))^2 \, dS} \tag{7}$$

where the integration is performed over the unit sphere at the time t_o. Equation (7) may be used to form an Nth order truncation limit from the exact N^{th} order orientation tensors in Eqn. (1) which is used to assess the accuracy of a given closure. To form the truncation limit for a particular flow field it is necessary to first evolve the exact distribution function $\psi(\theta,\phi)$. The orientation tensors are computed from $\psi(\theta,\phi)$ by Eqn. (1) and the distribution function is reconstructed to the desired order with Eqn. (6). This reconstructed distribution function is then used with the exact distribution function $\psi(\theta,\phi)$ in Eqn. (7) to quantify the error when representing $\psi(\theta,\phi)$. When the exact orientation tensors a_{ij}, a_{ijkl}, a_{ijklmn}, etc. are used in Eqn. (7), the truncation limit of the reconstruction is obtained. Alternatively, when a closure is employed to compute any of the orientation tensors, Eqn. (7) indicates the additional error introduced by the closure. Note that any N^{th} order closure of an orientation tensor can only be as accurate in representing the distribution function as the exact N^{th} order reconstruction. As discussed in Jack and Smith [10] the existing fourth-order closures approach the fourth-order reconstruction limit, therefore any substantial increase in accuracy in the representation of the distribution function will need to come from a higher-order closure.

COMPUTING THE EIGENVALUE BASED SIXTH-ORDER CLOSURE

In this study, the finite difference technique of Bay [3] is used to evaluate the distribution function $\psi(\theta,\phi)$ for the five representative flows used in the fitted closure of Cintra and Tucker [5]. All flows have a large interaction coefficient, $C_I = 10^{-2}$, representing the upper range of fiber interactions for industrial applications of injection molding processes. The unknown coefficients C_{ij} in Eqn. (5) are determined by minimizing the difference between the components of the actual a_{ijklmn} in Eqn. (1) and those computed with the closure approximation in Eqn. (5) using the optimization package VisualDOC 4.0 [12]. The cost function is minimized in less than 40 iterations using the BFGS method for unconstrained optimization with the resulting fitted components given as

$$[C_{ij}] = \begin{bmatrix} 0.07492 & 0.10439 & -0.42312 & 0.27277 & 0.79524 & 0.49666 \\ 0.05126 & -0.13977 & -0.10376 & 0.48791 & 0.09708 & -0.05669 \\ 0.14046 & -0.37744 & -0.26722 & 0.64968 & 0.23585 & 1.07191 \\ 0.97708 & -1.72435 & -1.86763 & 1.60122 & 0.74654 & 0.91396 \end{bmatrix} \tag{8}$$

To demonstrate the increased accuracy that may be gained through a sixth-order closure; the error metric presented in Eqn. (7) is shown for two flows, Simple Shear and Shear Stretch B (see *e.g.* [5]). These two flows are used in the fitting procedure for most fitted closures [4-7], and are indicative of flow behavior occurring in injection molding processes. The approximate sixth-order orientation tensor is computed from the exact fourth-order orientation tensor a_{ijkl} from Eqn. (5) and is used to compute the error metric ERR_6EBF_6 from Eqn. (7). The values for the error metric for the transient solution are given in Fig. 1 for both flows. For reference purposes, the error metric for an exact second-order truncation ERR_2, fourth-order truncation ERR_4, and sixth-order truncation ERR_6 are also shown (see *e.g.* [9,10]). Note that any closure of the fourth-order

orientation tensor will only approach the fourth-order truncation line ERR_4, whereas throughout the flow history the EBF_6 closure is able to attain a level of error below the fourth-order truncation limit ERR_4 and approaches the sixth-order limit ERR_6.
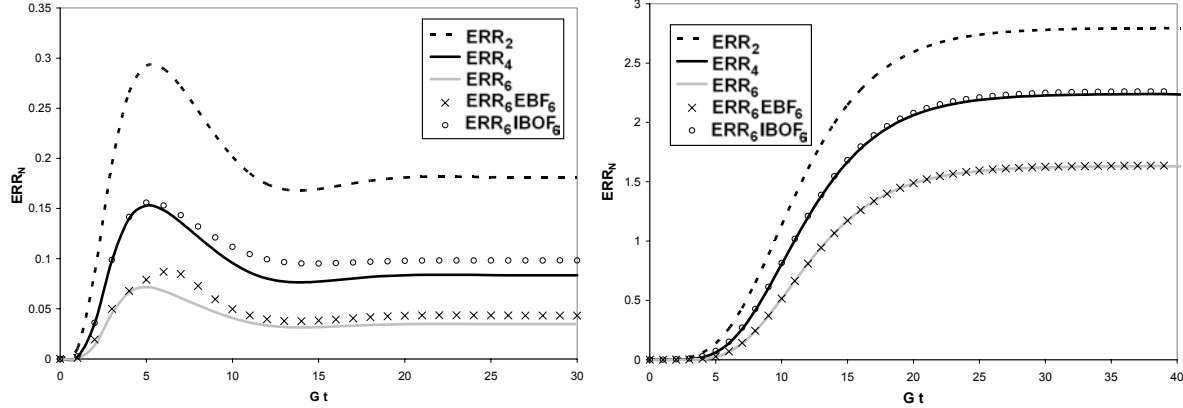
Fig. 1. Transient Error for Simple Shear (left) and Shear-Stretch B (right) for $C_I = 10^{-2}$

CONCLUSIONS

To obtain accuracy greater than the fourth-order truncation limit in representing fiber distributions in short-fiber injection molding simulations, a sixth-order closure becomes necessary. We present a fitted sixth-order closure that is computed from the components of the fourth-order orientation tensor and assumes that the principal directions of the second-order orientation tensor define the orthotropic planes of material symmetry of the sixth-order orientation tensor. The newly formed sixth-order fitted closure is demonstrated to more accurately represent the distribution function under certain flow situations than the fourth- order truncation limit when representing the fiber orientation distribution function. To fully utilize a closure of the sixth-order orientation tensor, it will be necessary to demonstrate the applicability of the higher order closure by evolving the fourth-order orientation tensor for actual injection molding processes.

ACKNOWLEDGEMENTS

REFERENCES

1.   F.P. Folgar and C.L. Tucker.   "Orientation Behavior of Fibers in Concentrated Suspensions", *Jn. of Reinforced Plastics and Composites*, Volume 3, Pages 98-119, (1984).

2.   S.G. Advani and C.L. Tucker.   "The Use of Tensors to describe and Predict Fiber Orientation in Short Fiber Composites", *Jn. of Rheology*, Volume 31, Issue 8, Pages 751-784, (1987).

3.   R.S. Bay and C.L Tucker.   "Fiber Orientation in Simple Injection Moldings: Part 1 - Theory and Numerical Methods", *Plastics and Plastic Composites: Material Properties, Part Performance, and Process Simulation, ASME 1991*, Volume 29, Pages 445-471, (1991).

4.   V. Verleye and F. Dupret, "Prediction of Fiber Orientation in Complex Injection Molded Parts", *Developments of Non-Newtonian Flows*, Pages 139-163, (1993).

5.   J.S. Cintra and C.L. Tucker. Orthotropic Closure Approximations for Flow-Induced Fiber Orientation", *Jn. of Rheology*, Volume 39, Issue 6, Pages 109-1122, (1995).

6.   D.H. Chung and T.H. Kwon.   "Invariant-Based Optimal Fitting Closure Approximation for the Numerical Prediction of Flow-Induced Fiber Orientation", *Jn. of Rheology*, Volume 46, Issue 1, Pages 169-194, (2002).

7.   B.E. Verweyst, C.L. Tucker, P.H. Foss, and J.F. O'Gara.   "Fiber Orientation in 3-D Injection Molded Features: Prediction and Experiment", *International Polymer Processing*, Volume 14, pages 409-420, (1999).

8.   M.C. Altan, S. Subbiah, S.I. Guceri, and R.B. Pipes.   "Numerical Prediction of Three-Dimensional Fiber Orientation in Hele-Shaw Flows", *Polymer Engineering and Science*, Volume 30, Pages 848-859, (1990).

9.   D.A. Jack, "Investigating the Use of Tensors in Numerical Predictions for Short-Fiber Reinforced Polymer Composites", Master's thesis, University of Missouri - Columbia, (2003)

10.   D.A. Jack and D.E. Smith, "Assessing the Use of Tensor Closure Methods With Orientation Distribution Reconstruction Functions", *Jn. of Composite Materials, Submitted for Publication*, (2004).

11.   E.T. Onat and F.A. Leckie.   "Representation of Mechanical Behavior in the Presence of Changing Internal Structure", *Jn. of Applied Mechanics*, Volume 55, Pages 1-10, (1998).

12.   VisualDOC 4.0.   Vanderplaats Research and Development, Inc. Colorado Springs, Colorado, (2004).

In-Line Compounding of Long Fiber Thermoplastics for Injection Molding

Ronald C. Hawley[1] and Roger F. Jones[2]

[1]Woodshed Technologies Inc., Winona, MN 55987;
E-Mail: ron@compositeproducts.com
[2]PlastiComp, Inc., Winona, MN/Franklin International LLC, Broomall, PA 19008;
E-Mail: jones@plasticomp.com

SUMMARY: A new process has been developed for in-line compounding and injection molding in a single operation. Selected short to long fiber reinforced thermoplastic mixtures are created and fed directly into the injection-molding barrel while still hot. Compositions containing glass fibers of 3 to 12mm in length have been molded successfully on a 230 ton injection press. The new processing system is adaptable to existing injection molding machines. This novel technology permits molded parts to be produced with longer fiber lengths than heretofore possible, thereby improving finished product performance. In-line compounding also permits molded articles to be produced at cost levels competitive with those incurred when molding parts from conventional long and short fiber reinforced thermoplastic compounded pellets.

Key Words: Long fiber, injection molding, in-line compounding, Pushtrusion™, viscous entrainment, hot fiber chopping

Introduction

Investigation and development of the new process began in 1999 in the laboratories of Woodshed Technologies, Inc., which had been founded for the purpose of developing and commercializing in-line compounding of long fiber thermoplastics for injection molding. The new process utilizes the same formulation ingredients typically found in pultruded "long fiber" injection molded pellets [1].   The long fiber composites industry understands that impregnation/wet-out of the glass fiber filaments must take place prior to extensive mixing in order to preserve fiber length [2, 3, 5].   It is also known that initial contact of the resin and glass fiber must be done gently and is best accomplished by coating the glass fiber with resin melt [4]. The process gently coats continuous length glass fiber with resin in controlled percentages, chops the glass fiber into consistent, specified lengths between 6 mm to 25 mm while imbedded in molten resin, and feeds the hot mixture directly into the screw and barrel of an injection molding press. Since the material is hot when fed into the injection press barrel, longer fiber lengths can be processed and maintained. The in-line compounding process is available for licensing. Equipment is available as an add-on to the molder's existing injection press. This paper describes the features and advantages of in-line compounding for long fiber thermoplastic injection molding.

The In-Line Compounding-Injection Molding Process

The in-line molding process is represented by the schematic drawing in Figure 1. Thermoplastic resin pellets are fed into the hopper of the resin "shooter." The shooter is a typical injection barrel capable of melting resin, homogeneously mixing and injecting the melt into the process at high rates and pressures. Continuous length glass fibers are pulled from the supply creel and into the process die by the high-pressure flow of molten resin. The viscous entrainment die is designed to meter glass fiber and molten resin, keeping the glass fiber percentage within close tolerances. The glass fiber strand and molten resin mixture is pushed from the viscous entrainment die at 122 m to 183 m per minute. The process starts and stops instantaneously, as dictated by the material feeding requirements of the injection press barrel. An inline chopper cuts the glass fiber imbedded in the molten thermoplastic resin as it exits the viscous entrainment die. The chopper's cutting chamber is heated to maintain the cut mixture in the molten state and this cut mixture is directed through a nozzle positioned directly above the injection press screw. Glass fiber cut lengths of 6 mm through over 25 mm are possible. The process is capable of controlling glass fiber percentages within a narrow range. A total variation of less than 1% by weight is typical.

A single input signal from the injection press controls is required for the system to operate. When the injection press screw is turning, the system is delivering molten material. The system stops delivering material when the injection press screw stops turning.

Four significant process advantages occur when chopped glass fiber and molten resin are fed into the injection press barrel. 1) Conventional pultruded pellets in lengths of 25 mm or longer are difficult to feed. The mixture from the new process system is flexible, allowing very long fiber lengths to be processed without experiencing feeding problems. Cut lengths of 50 mm or greater would be possible if the injection press were large enough to handle them.   2) The resin has already been melted allowing for gentle mixing and maximizing retained fiber length of any given chop length. 3) The screw and barrel wear associated with pellets composed of partially melted resin and glass fiber is eliminated.   4) The resin has undergone a single melt history, minimizing degradation and improving physical properties. Table 1 summarizes the properties found in a typical part made of 40% long glass fiber reinforced polypropylene.

Figure 2 shows the new system mounted on a 230 ton injection press. The system is compact and efficient, in comparison with other in-line compounding systems, which involve weight feeders (with attendant material losses), compounding extruders, and accumulators, all mounted on an injection press. Figure 3 is a close up of the fiber / resin mixing chamber, viscous entrainment die and hot fiber chopper. The new in-line compounding injection molding process is initially targeted to mold composite parts from 0.25 kg to about 1.35 kg in size on presses with clamping capacities of 200 to 500 tons. Future larger systems employing the same principles are under development.

Economics

In-line compounding of long fiber thermoplastics for injection molding provides a compelling cost advantage. The same raw materials used to produce pultruded long fiber thermoplastic pellets are used in the new system. The economic advantage of in- line compounding and direct feed of the press is derived from the efficiency of the process and the elimination of a "middle man" processing step, thereby resulting in as much as a 50% reduction in raw material costs vs. purchased pellets.

References

1. R. C. Hawley, U.S. Patent 6,186,769 (2001), *Resin and Fiber Compounding Apparatus for Molding Operations*
2. R. C. Hawley, U.S. Patent 5,165,941 (1992), *Extruder Apparatus and Process for Compounding Thermoplastic Resin and Fibers*
3. R. C. Hawley, U.S. Patent 5,185,117 (1993), *Process for Compounding Thermoplastic Resin and Fibers.*
4. R. C. Hawley, U.S. Patent 4,312,917 (1979), *Fiber Reinforced Compound Composite Structure and Method of Manufacturing Same*
5. R. F. Jones, *Guide to Short Fiber Reinforced Plastics,* Hanser Publishers, Munich 1998

Table 1 Product Properties

Physical Properties	Direct molded LFTP
Fiber Length	12 mm
% Glass Fiber	40
Polymer	Polypropylene
Tensile Strength, MPa	125
Tensile Modulus, MPa	10,350
Flexural Strength, MPa	167
Flexural Modulus, MPa	7,800
Notched Izod, J/m	382
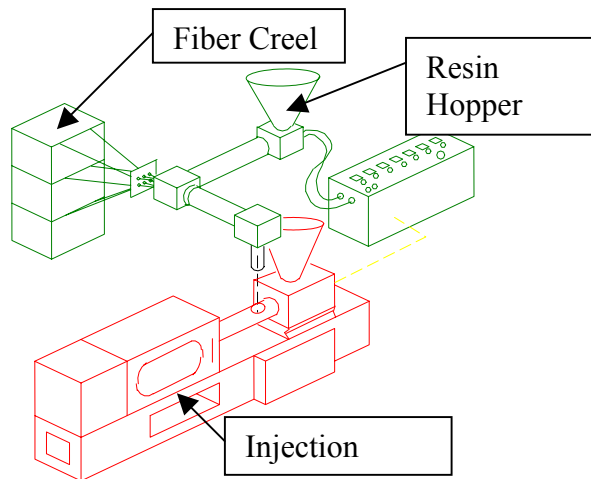
Figure 1
In-Line Molding System Schematic

Figure 2
In-Line Compounding System

Figure 3
Fiber chopper

PROCESS FOR ORIENTING DISCONTINUOUS FIBERS IN THERMOPLASTICS

Y. S. Kim and T. S. Creasy

Polymer Technology Center
Texas A&M University
M.S. 3123, 100 Engineering/Physics Building
College Station, TX 77843-3123
Corresponding Author's e-mail: tcreasy@tamu.edu

SUMMARY: Equal channel angular extrusion (ECAE) can affect the alignment of materials at the molecular level. This process method is used to create novel metallic and polymer materials. The present work looks at ECAE as a method of producing high-value recycled short-fiber composites. Commercial glass fiber/polyacetal rods processed with ECAE were inspected to determine the effect of the process on fiber length and orientation at both room temperature and at 73 °C. The initial fiber orientation had a uniform distribution function about the major axis of the rods in the range of 11.8 to 56.0 degrees and the fibers were 105.6 ± 35.6 μm long. Processing at 73 °C did not change the length of the fibers, but it aligned them to a loglogistic distribution with a mean angle of 23.5 ± 18.2°. At room temperature the process both aligned the fibers and reduced their length by 23%. The authors conclude that temperature adjustments control the strength of the interface, which has an impact on the fiber fracture process, but not the flow mechanics, which control the fiber orientation.

KEYWORDS: ECAE, extrusion, recycling, short fiber, fiber fracture, fiber orientation.

INTRODUCTION

Equal channel angular extrusion (ECAE or ECAP) is a novel process that affects microstructures through extreme, uniform simple-shear [2]. Although the total strain history is large the material regains its initial shape when the process cycle is complete; it can be processed again if greater plastic deformation is beneficial. This extreme strain generates novel properties at the molecular level [3, 4]. Prior research with ECAE shows that the process aligns inclusions in metals and crystallites in semicrystalline polymers. Metal powders processed with the method can be consolidated and given specific textures. These effects might lead to benefits in new and

---

[2] Z.Y. Liu et al., The effect of cumulative large plastic strain on the structure and properties of a cu–zn alloy, Materials Science and Engineering A, 242 (1- 2) (1998) 137-140

[3] Z.Y. Xia, H.J. Sue and T.P. Rieker, Morphological evolution of poly(ethylene terephthalate) during equal channel angular extrusion process, Macromolecules, 33 (23) (2000) 8746-8755

[4] Z. Xia et al., Dynamic mechanical behavior of oriented semicrystalline polyethylene terephthalate, Journal of Polymer Science, Part B, 39 (12) (2001) 1394-1403

recycled composites with a thermoplastic matrix polymer because ECAE can produce alignment in a bulk material.

Equal channel angular extrusion (ECAE or ECAP [5]) is a novel process that applies extreme strain to a material through uniform, simple shear [6]. Segal describes the process as rigid body motion of the material except for a moving thin layer that receives severe plastic deformation [6]. A finite element method (FEM) model of the process appears in Fig. 1; the darkest regions represent the steel die and the shaded portion is a model of a nylon billet subjected to the process. The top of the billet is forced downward until it plastically deforms in the shearing plane. The shearing plane appears as the shaded region 45 degrees from the vertical.
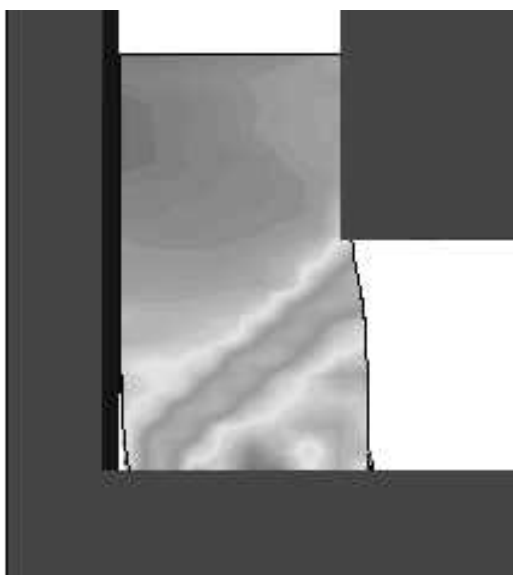
Fig. 1. FEM model of ECAE. The shaded region oriented 45 degrees from the vertical direction is the high shear strain plane. Portions of the billet above this plane have a negative vertical velocity and portions to the right of this plane have a rigid body velocity to the right.

The fracture of brittle fibers in polymer melt flow has been studied in detail [7, 8]. ECAE provides the novel opportunity to process in the solid state and have a useable material with new capabilities after extreme deformation. Before it reaches the shearing plane, the material undergoing ECAE is moving with solid body motion in the direction of the entrance channel. After passing the shear plane, the particles of the body are moving with the same magnitude of velocity, but directed at an angle of to the initial solid body motion. During the transition---the passing through the shear plane---the fiber can encounter bending and tensile stresses as its

---

[5] Liu Z. Y., et al. (1998) The Effect of Cumulative Large Plastic Strain on the Structure and Properties of a Cu–Zn Alloy, Materials Science and Engineering A, A242(1-2):137-140

[6] Segal V.M. (1995) Materials Processing by Simple Shear, Materials Science and Engineering A, A197(2):157-164

[7] S.Y. Fu and B. Lauke, Effects of fiber length and fiber orientation distributions on the tensile strength of short-fiber-reinforced polymers, Composites Science and Technology, 56 (10) (1996) 1179-1190

[8] T.S. Creasy, S.G. Advani and R.K. Okine, Non-linear response of a long, discontinuous fiber/melt system in elongational flows, Rheologica Acta 35 (4) (1996) 347-355

trailing portion attempts to move with the initial sold body velocity and its leading portion attempts to move with the new velocity vector. A brittle, solid, body in a flow with a velocity gradient or sharp transition must either move with the velocity of its centroid or fracture into two fibers [8, 9]. The gradient or transition in velocity introduces strain in the fiber through the stress transfer at the fiber-matrix interface. The effect of this transition region is found from the experiments described below.

EXPERIMENTS

Material Studied

The specimens were commercially extruded cylindrical rods of polyacetal (Delrin™ 570), which is a semicrystalline thermoplastic. Polyacetal has a glass transition temperature (Tg) of -30°C, a thermal deflection temperature (TDT) under an 0.5-MPa load of 167°C and a melting point (Tm) of 178°C. Short glass fiber filler at a loading of up to 20% weight was added to the polymer by compounding and conventional extrusion. The dimensions of the rods were 12.7-mm diameter by 121 mm in length. Three pieces were processed via ECAE and one piece was analyzed as the 'as-received' condition of the composite.

Experimental Methods

The fiber mass fraction and mean fiber length were measured after the polymer was burned away [10]. Fiber orientation was measured by optical microscopy of cross-sections [11]. The data were processed using a rigorous statistical approach; at least 60 samples of each measurement were taken. Processing conditions included one pass at 73 °C and two passes at room temperature (RT).

RESULTS

Fiber Length

The fiber length distributions appear in Fig. 2. Although the initial fiber length distribution narrows—the shorter fibers are not affected, but the longer fibers are shortened—when the material receives plastic deformation at 73 °C, the change in mean fiber length is not statistically significant. The colder process at room temperature did significantly reduce the mean fiber length from 105.6 ± 35.6 μm to 81.0 ± 32.2 μm after a single pass through the die. This was a significant reduction in the fiber length. However, a second pass did not reduce the fiber length to a significant degree.

[9] S.F. Shuler, D.M. Binding, R.B. Pipes, Rheological behavior of 2-phase and 3-phase fiber suspensions, Polymer Composites, 15 (6) (1994) 427-435
[10] creasy kang ireland in press
[11] creasy kang j thermoplastic composites

Fiber Orientation

ECAE aligned the fibers when the material was processed at either temperature. The statistical distribution of the fiber angles changed from a uniform probability density function to a loglogistic distribution after a single pass. All three process conditions brought the mean fiber angle to about 23°. The second pass at room temperature did not shift the mean fiber angle farther.

CONCLUSIONS

Based on the measured effects of ECAE processing on the short fiber composites, the authors state these conclusions:

1) Fiber length may be a strong function of the processing temperature. If the matrix is softer— weak interface—the fiber cannot be loaded to its fracture stress.
2) Fiber orientation is not a strong function of the processing temperature. The same mean fiber angle was obtained with each process condition.
3) Number 1 above implies that using a specific processing temperature might control fiber length.

Conclusion number 2 has not been noted for ductile inclusions. Ductile inclusions become fibrous after multiple ECAE processing passes and they continue to align with the major axis of the extrudate. The results here are novel because they indicate that brittle, fiber shaped inclusions approach a fixed angle that is away from the extrusion axis.
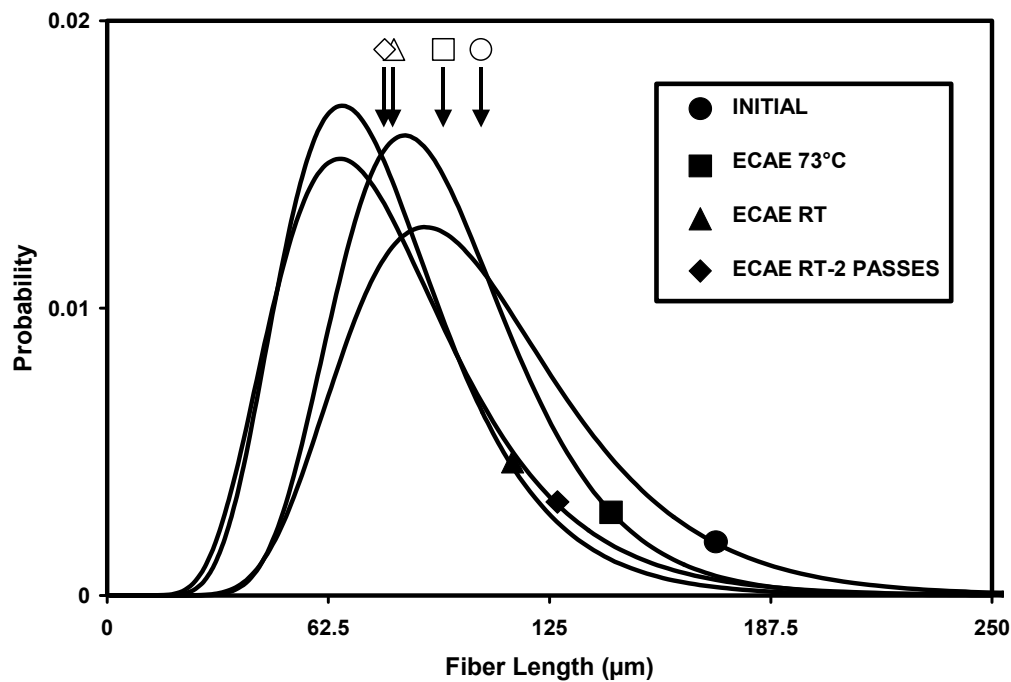
Fig. 2. The initial fiber length is not significantly reduced when the composite is processed at 73 °C, but the process at RT does reduce the fiber length during the first pass. A second pass produces no further reduction in length. [10]
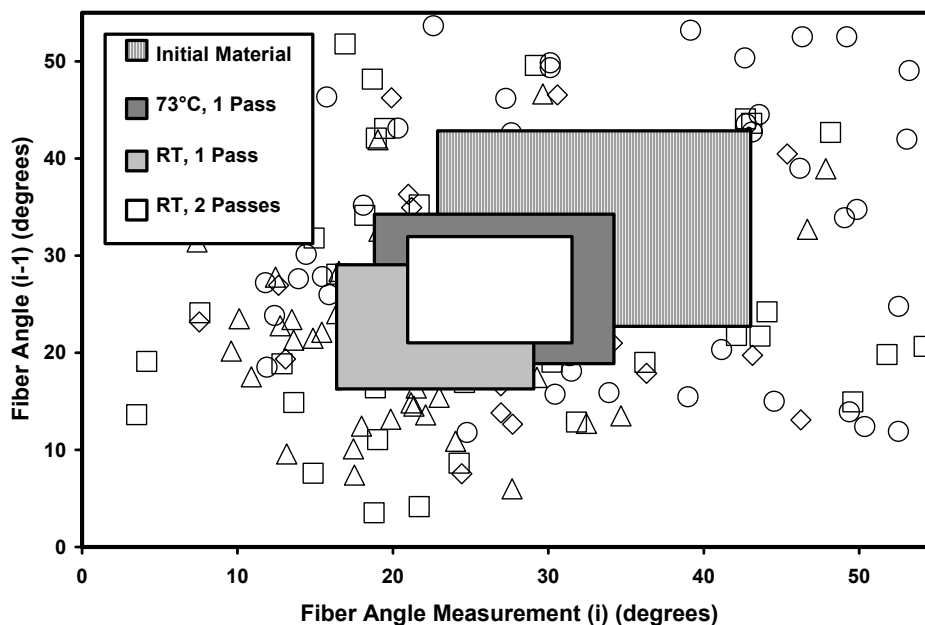
Fig. 3. The lag chart shows the range of fiber angles found in initial and processed short fiber composite. Each rectangle encloses the interquartile range—middle 50%--of the fiber angles measured for the condition. ECAE moves the center of each rectangle toward a mean fiber angle of 22°.

REFERENCES

2.   Z.Y. Liu et al., "The effect of cumulative large plastic strain on the structure and properties of a cu–zn alloy," *Materials Science and Engineering A*, Vol 242 , no. 1- 2, 1998, pp. 137-140.

3.   Z.Y. Xia, H.J. Sue and T.P. Rieker, "Morphological evolution of poly(ethylene terephthalate) during equal channel angular extrusion process," *Macromolecules*, Vol 33, no. 23, 2000, pp. 8746-8755.

4.   Z. Xia et al., "Dynamic mechanical behavior of oriented semicrystalline polyethylene terephthalate," *Journal of Polymer Science, Part B*, Vol 39, no. 12, 2001, pp. 1394-1403.

5.   Liu Z. Y., et al., "The Effect of Cumulative Large Plastic Strain on the Structure and Properties of a Cu–Zn Alloy," *Materials Science and Engineering A*, Vol A242, no. 1-2, 1998, pp. 137-140.

6.   V.M. Segal, "Materials Processing by Simple Shear," *Materials Science and Engineering A*, Vol A197, no. 2, 1995, pp. 157-164.

7.   S.Y. Fu and B. Lauke, "Effects of fiber length and fiber orientation distributions on the tensile strength of short-fiber-reinforced polymers," *Composites Science and Technology*, Vol 56, no. 10, 1996, pp. 1179-1190.

8.   T.S. Creasy, S.G. Advani and R.K. Okine, "Non-linear response of a long, discontinuous fiber/melt system in elongational flows," *Rheologica Acta* Vol 35, no. 4, 1996, pp. 347-355.

9.   S.F. Shuler, D.M. Binding, R.B. Pipes, "Rheological behavior of 2-phase and 3-phase fiber suspensions," *Polymer Composites*, Vol 15, no. 6, 1994, pp. 427-435.

10.   T.S. Creasy and Y.S. Kang, "Fiber fracture during equal channel angular extrusion of short fiber reinforced thermoplastics," *Journal of Materials Processing Technology* In Press.

11.   T.S. Creasy and Y.S. Kang, "Fiber Orientation during Equal Channel Angular Extrusion of Short Fiber Reinforced Thermoplastics," *Journal of Thermoplastic Composites* Vol 17, 2004, pp. 205-227.

Twin Screw Extrusion Processing of Graded Composite Materials

Frederick M. Gallant [1] and Hugh A. Bruck[1]

[1] *Department of Mechanical Engineering, University of Maryland, College Park, MD 20742, emails: gallantfm@ih.navy.mil and bruck@eng.umd.edu*

SUMMARY: A new method for fabricating graded composite materials with continuous gradient architectures has been developed using the technology of continuous processing with a Twin-Screw Extruder (TSE). While TSE processing has been investigated for controlling the fabrication of homogeneous composites in steady-state operating conditions, there is a lack of knowledge concerning the processing of gradient architectures using transient operating conditions. Therefore, there is a need to characterize and model the relationship between the extruder screw geometry, transient operating conditions, and the gradient architecture that evolves in the extruder. In this investigation, recent interpretations of the Residence Time Distributions (RTDs) and Residence Volume Distributions (RVDs) for polymer composites in the TSE are used to develop a process model for predicting compositional gradients in the direction of extrusion. In situ optical measurements are used to verify the gradient architectures. The process model that has been developed in this research effort will serve as the basis for determining the operating conditions and screw configurations that produce a desired gradient architecture.

INTRODUCTION

There is a great deal of interest in tailoring structures so the functional requirements can vary with location. In most cases, this will involve varying the materials that are used at specific locations within the structure resulting in discrete interfaces throughout. These discrete interfaces often limit structural performance by introducing weaknesses or impeding transport process. Attempts at mitigating these problems have led to the concept of Functionally Graded Materials (FGMs). FGMs are structures that possess gradual variations in material behavior that enhance material and/or structural performance [1]. For example, at one point the material may be hard and at another point it may be soft. The description of this functional variation is known as the gradient architecture (*Figure 1*) [2]. Currently, there is a challenge to manufacture FGMs using scalable processes that can easily control the evolution of the gradient architecture in a continuous manner. Manufacturing technologies for processing FGMs are categorized as either transport-based or constructive processes [1]. Constructive manufacturing processes primarily

produce discretely layered gradient architectures, and include: powder densification, deposition, and lamination techniques. Transport-based processes primarily produce continuous gradient architectures, and include: mass transport, thermal diffusion, inertial separation, and melt infiltration.
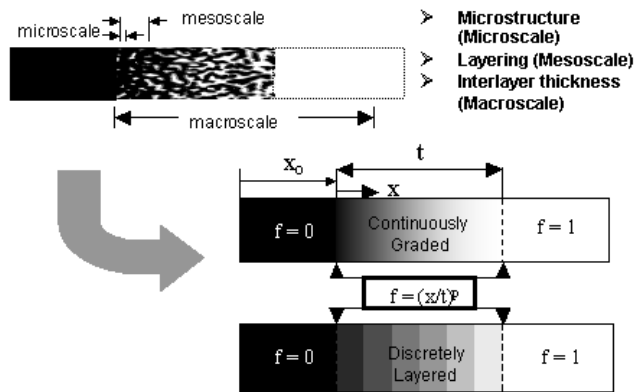
Figure 1. Description of gradient architectures for graded composites [2]

A transport-based manufacturing technology that has yet to be used for manufacturing FGMs is the Twin Screw Extrusion (TSE) process. This paper elucidates on the fabrication of graded polymer composites with continuous gradient architectures using TSE processing technology. Steady-state Residence Volume Distribution (RVD) models are used to describe the TSE process. Convolution of these RVD models with feed input conditions are then used to predict the 1-D composition gradients that evolve during the Twin Screw Extrusion process. Optical measurements are used to verify the composition gradients predicted by the RVD models.

CONTINUOUS PROCESSING OF POLYMER COMPOSITES USING TWIN SCREW EXTRUSION
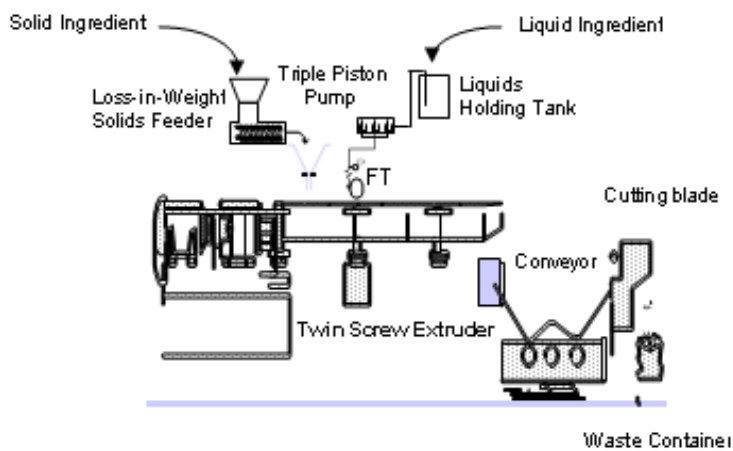
Figure 2. Schematic of Twin Screw Extrusion process

TSE processes are utilized to manufacture a number of consumer and industrial goods from snack foods and medical tubing to plastic pellets and military propellants. The continuous nature of this process has many advantages over batch types, so it has found widespread utility across diverse industries that process polymers and polymer composites. The advantages tend to be universal: economy, quality, and flexibility. Thus, TSE processing is a promising technology for producing graded composite materials.

At the heart of the TSE process is the extruder, which is highly configurable and flexible allowing for the optimization of processing for many different types of materials (*Figure 2*). Unlike discrete batch processes that require a number of process steps and facilities, the continuous nature of the TSE process allows for the combination of process steps to reduce

facility requirements. By continuously processing materials, it is possible to produce larger quantities with greater consistency (i.e., no batch to batch variation). The process also lends itself to on-line analysis allowing for the quick detection of anomalous conditions or quality that can be used to automatically remove material into a waste container.

RESIDENCE DISTRIBUTION MODELING OF TSE PROCESS

To control gradient architectures manufactured with the TSE process, it is necessary to develop a model of the process. Material transport through a fully intermeshing twin screw extruder is accomplished by screw geometry and screw motion [3]. Because of the complex dependence of material transport on evolving material properties, screw configuration, and operating conditions, the quantitative residence time of material in the system, characterized by the residence time distribution (RTD), has become a convenient way to express the cumulative effect of all processing and material parameters. The RTD is typically normalized in order to describe the probability, $e(t)$, that a given quantity of material will reside in the extruder for a time, t, as follows:

$$e(t) = \frac{c(t)}{\int_0^\infty |c(t')| dt'} \tag{1}$$

where $c(t)$ is a filtered probe response obtained from the extruder [4]. The RTD can be used to quantify various characteristics of the TSE process, such as the dampening that occurs as a result of backmixing in the extruder [5]. A model has been developed to predict the RTD based on a series of ideal mixers [6]. The general form of the RTD model, $f(t)$, for a series of n ideal mixers is as follows:

$$f(t) = \frac{a^n}{(n-1)!} (t - t_d)^{n-1} e^{-a(t - t_d)} \tag{2}$$

It consists of two parameters: (a) the delay time, t_d, predicted from operating conditions and screw configuration, and (b) a shape factor, a, determined experimentally. The RTD can be converted to the volume domain, equation (3), to obtain a Residence Volume Distribution (RVD) that has been shown to be independent of operating conditions and only dependent upon screw geometry [7]. Thus, the RVD can be used to uniquely identify (i.e., fingerprint) a screw design. The RVD and its associated general mixing model are given as follows:

$$g(v) = \frac{c\left(\frac{v}{Q}\right)}{\int_0^\infty \left|c\left(\frac{v}{Q}\right)\right| dv} = \frac{e\left(\frac{v}{Q}\right)}{Q} = \frac{a_v^n}{(n-1)!} (v - v_d)^{n-1} e^{-a_v(v - v_d)} \tag{3}$$

By converting residence distribution model from the time to the volume domain, it is possible to directly predict the spatial distributions of material in a gradient architecture independent of operating conditions.

Figure 3. Graded polymer composites manufactured using the TSE process

PREDICTION AND MEASUREMENT OF COMPOSITION GRADIENTS

The TSE process is naturally suited to producing continuous composition gradients. These composition gradients can be achieved either by dynamically changing the relative feed rate of ingredients, or by varying the operating conditions. Examples of graded polymer composite fabricated by changing the ingredients in the TSE process can be seen in *Figure 3*.

Based on the RVD model in equation (3), the 1-D composition gradient, *f[z(v)]*, can be predicted by convolving the feed input conditions, *h(v),* for the extruder with the RVD model as follows:

$$f[z(v)] = \int_{o}^{v} g(v-v')h(v')dv' \tag{4}$$

A RVD representative of the TSE process and a prediction of the gradient evolution from convolution of the RVD with impulse, step, and ramp input conditions can be seen in *Figures 4a* and *4b* respectively.

(a)   (b)
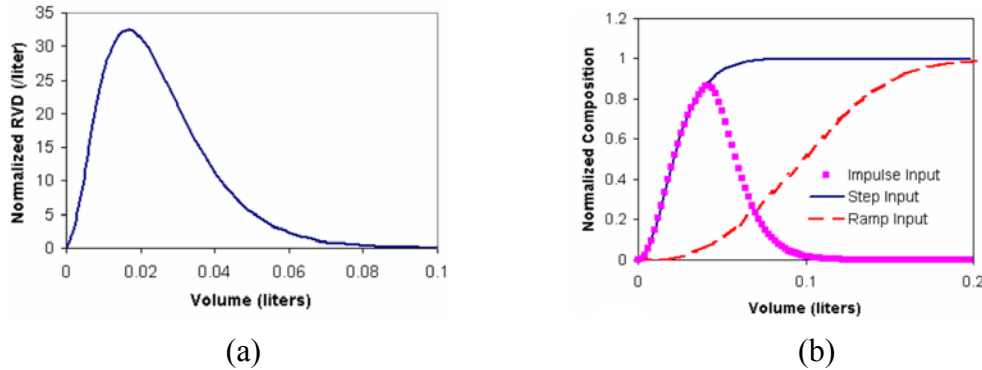
Figure 4. (a) RVD representative of TSE process, and (b) prediction of gradient architecture from convolution of RVD with impulse, step, and ramp input conditions

The 1-D composition gradient that evolves in the TSE process has been characterized using in situ optical measurements of the composite ingredients. The optical measurement system consisted of a bifurcated fiber optic cable inserted into a probe that screws into a Dynisco-profiled barrel instrumentation port. The twin-screw extruder used in these experiments was a laboratory scale Werner & Pfleiderer model ZDSK-28 with co-rotating fully-intermeshing screws. A model polymer composite system was chosen for this experiment that consisted of 200 μm KCl particles and DuPont Dow Engage 8401, a high melt index polyolefin elastomer (POE). The RTD for this material system and the screw configuration along with an experimental fit to of equation (2) can be seen in *Figure 5a*. The gradient architectures that evolved for step and ramp changes from 40 wt% to 60 wt% particle input can be seen in *Figure 5b*. The general variation in the gradient architecture is qualitatively very similar to the predicted variations seen in Figure 5. Thus, the convolution model exhibits excellent potential for predicting 1-D composition gradients in polymer composites fabricated in the TSE process.
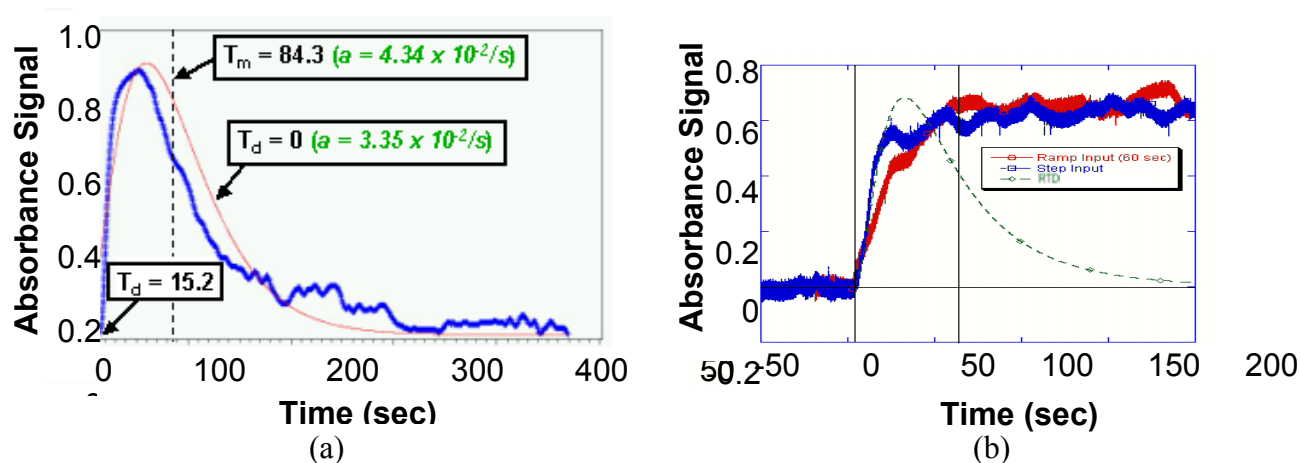
Figure 5. Experimental optical measurements of (a) RTD and (b) gradient architectures for step and linear changes in input conditions

CONCLUSIONS

TSE processing has been used to fabricate continuously graded polymer composites. Residence distribution models were used to characterize the TSE process. These models were then convolved with feeder input conditions to predict the 1-D composition gradients that evolve in the TSE process. Experimental studies were conducted using a model polymer composite system consisting of an elastomer with KCl particle reinforcement. In-situ optical measurements were used to characterize the RTD and gradient architectures that evolved from step and linear changes in KCl particle reinforcement from 40 wt% to 60 wt%. These measurements were qualitatively similar to the predictions from the convolution model, indicating that the convolution model has excellent potential for predicting gradient architectures in TSE-processed polymer composites.

ACKNOWLEDGEMENTS

REFERENCES

1.   Suresh, S. and Mortenson, A., *Fundamentals of Functionally Graded Materials*, Institute of Materials, London, UK (1998).

2.   Bruck, H.A., Evans, J.J., and Peterson, M.L., "The Role of Mechanics in Biological and Biologically Inspired Materials," *Experimental Mechanics*, 42, 361-371 (2002)

3.   Rauwendaal, C., *Polymer extrusion*, first ed., Hanser Publishers, New York (1986).

4.   Gao, J., Walsh, G.C., Bigio, D., Briber, R.M., and Wetzel, M.D., "A Residence Time Distribution Model for Twin Screw Extruders", *AICHE Journal*, 45, 2541-2549 (1999).

5.   Danckwerts, P.V., "Continuous Flow Systems: Distribution of Residence Times." *Chemical Engineering Science*, 2, 1-18 (1953)

6.   Gao, J., Walsh, G.C., Briber, R.M., and Wetzel, M.D., "Mean Residence Time Analysis for Twin Screw Extruders", *Polymer Engineering and Science*, 40, 227-237 (2000)

7.   Gasner, G.E., Bigio, D.I., Marks, C., Magnus, F., and Kiehl, C., "A New Approach to Analyzing Residence Time and Mixing in a Co-Rotating Twin Screw Extruder", *Polymer Engineering and Science,* 39**,** 286-298 (1999)

Sheet Molding Compound (SMC) Processing

Jose M. Castro [1] and Michael Rabinovich [1]
[1] *Department of Industrial, Welding, and Systems Engineering, The Ohio State University*

Columbus, Ohio 43210
castro.38@osu.edu

SUMMARY: A spiral flow tool can bee used to gain insight into the dynamic interactions of the SMC during the compression molding process. In contrast to flat plate molding, the spiral flow tool simulates a very long flow; while collecting processing parameters during molding with respect to time. A mathematical model has been developed and experimentally verified for the spiral flow tool. A new method of determining the friction coefficient using the spiral flow tool is proposed, which yields similar results to flat plate molding.

KEYWORDS: Sheet Molding Compound, SMC, spiral flow tool, compression molding

INTRODUCTION

Sheet Molding Compound (SMC) is a fiber reinforced polymer matrix composite material that offers an array of beneficial properties that are demanded by many modern applications. Automotive, aerospace, marine, and industrial/consumer industries increasingly use SMC to take advantage of its performance. SMC is composed of polymerized or cross-linked resin, reinforcement fibers, filler, and various additives.
Throughout the years, the spiral flow tool has evolved in its design that would better accommodate the SMC, which included widening the flow channel and mimicking the actual compression molding process with shear edges.

THE SPIRAL FLOW TOOL

The spiral flow described in this paper is equipped with a data acquisition system that allows for collecting responses exhibited by the SMC, and a special hydraulic package that exerts a constant force on the material during the molding process, with the force specified by the operator.

   The spiral flow tool's data acquisition system consists of 5 sensors that collect pressure and temperature inside the mold at 5 different positions. Besides the temperatures and pressures at these locations, the hydraulic force that is applied on the material is recorded as the material is molded. The LVDT provides data on the relative mold half's position during mold closing.

Lastly, the spiral flow tool provides a length value at which the material stopped flowing. A schematic of the spiral flow tool used in this research is shown in Fig. 1.
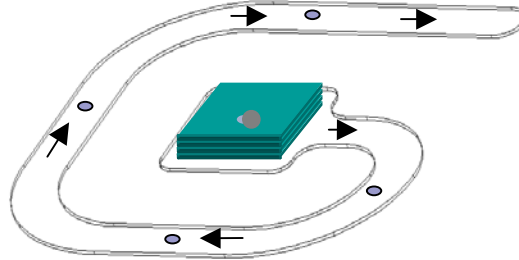
Fig. 1. Design of the spiral flow tool described in this paper. Dots represent the positions of temperature and pressure sensors. Arrows represent the direction of the material flow. The rectangles in the center represent the SMC charge.

MATHEMATICAL MODELING OF THE SMC INSIDE THE SPIRAL FLOW TOOL

Castro and Abrams [1] have proposed a model to represent SMC flow based on the pioneering work of Tucker [2, 3, 4, 5], Barone and Caulk [6, 7] and Marker and Ford [8]. The model consists of a material that flows by extension (bulk), with a thin lubricating layer on the surface (resin rich layer), which behaves as a power law fluid. They have also proposed a method to calculate the friction coefficient and resistance to extension. The model for the spiral flow tool is based on this model.

The spiral flow tool's molding process can be represented in three stages. Stage I starts when the SMC comes into contact with both halves of the mold and ends when the material fills up square section of the mold. Stage II picks up at the end of Stage I and ends when the hydraulic forces reaches maximum. Stage III is effective when Stage II ends and lasts until the flow stops [11].

Stage I could be described by the 2-directional SMC model, Eqn. 1.

$$F(t) = \frac{4\eta V U(t)}{h(t)^2} + M \frac{2U(t)V^{n+2}}{h(t)^{2n+3} W^{n+1}(n+2)(2^{n+1})} \tag{1}$$

F(t)=Force on SMC (compacted)
V=volume of SMC
h(t)=part thickness
U(t)=closing Speed
W=width of the part (6")
M=m/δn (lubricating layer)
η= resistance to extension
n= paste power law index

Stages II and III are based on a model that assumes a combination of one-dimensional flows, described by Eqn. 2 and illustrated in Fig. 2. This is a reasonable assumption to make, and has been verified by experiments where a small section of a colored charge maps out the flow of SMC [11]. Stages I and II occur in the first few seconds of the molding process, with not a very significant material flow, which means that Stage III is the most important stage to understanding the behavior of the material because Stage III lasts for more than 10 seconds and represents most of the material flow. The above model has been shown to represent the experimental data fairly well [11].

$$F(t) = 2 \cdot \left[\begin{array}{l} \dfrac{4 \cdot \eta \cdot U(t)}{h(t)} \cdot L_m(t) + \dfrac{M \cdot 2 \cdot U(t)^n}{h(t)^{n+1} \cdot (n+1)} \left(L_m(t)^{n+2} - \dfrac{L_m(t)^{n+2}}{n+2} \right) + \\[2ex] + \left(\dfrac{16 \cdot \eta \cdot U(t)}{h(t)} + \dfrac{2 \cdot M \cdot U(t)^2}{h(t)^{n+1} \cdot (n+1)} \left(2^{n+2} - \dfrac{2^{n+2}}{n+2} \right) \right) \cdot 6 + \\[2ex] + \dfrac{4 \cdot M \cdot U(t)^n}{h(t)^{n+1} \cdot (n+1)} \left(6 \cdot L_m(t)^{n+1} - \dfrac{6^{n+2}}{n+2} \right) \end{array} \right] \qquad (2)$$

Lm(t)=Flow length, calculated from the conservation of mass assumption
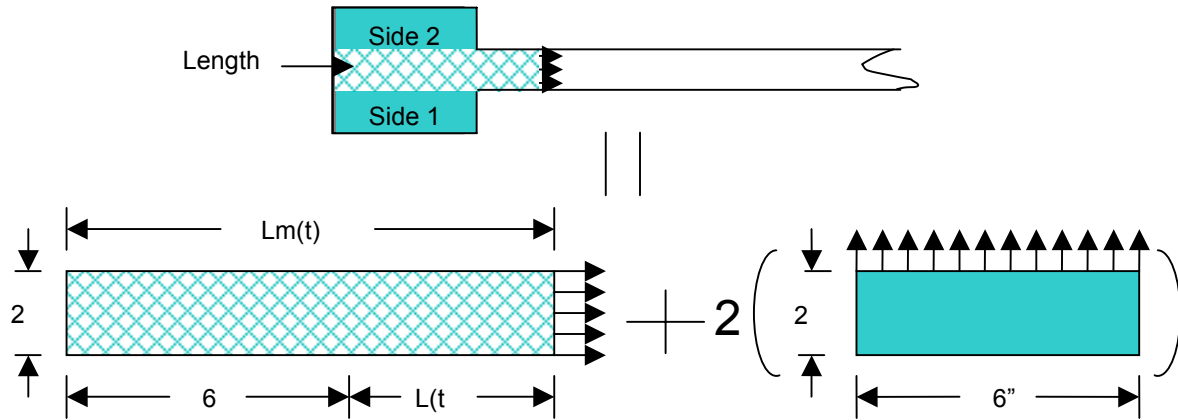
Fig. 2. Breakdown of the geometry used to model Stages II and III.

The data from the pressure transducers can be used to calculate the lubricating layer parameter $(M=m/\delta^n)$ by using the LVDT data and pressure readings [11].

$$\frac{m}{\delta \cdot n} = M = \frac{(p_i - p_{i+1})(h(t)^{n+1}(n+1))}{(2 \cdot (U(t))^n)(x_{i+1}^{n+1} - x_i^{n+1})} \qquad (3)$$

p=pressure from the transducer
x=position inside the mold

SPIRAL FLOW TOOL VERSUS FLAT PLATE MOLDING FOR OBTAINING MATERIAL PARAMETERS

Previous work has been done using flat plate molding for determining the material flow parameters. Flat plate molding has the advantage over the spiral flow tool with its simpler geometry, but the spiral flow tool has the advantage of simulating an extensive flow of the material.

Equation 2 could be solved by iterations for the part thickness (h) and the closing speed (U), from which the length of flow could be calculated. Fig. 3 shows a plot where the predicted length of flow values is compared to the experimentally measured values. The predictions were made using the material parameters measured with the flat plate molding, done by Boylan and Castro [10].
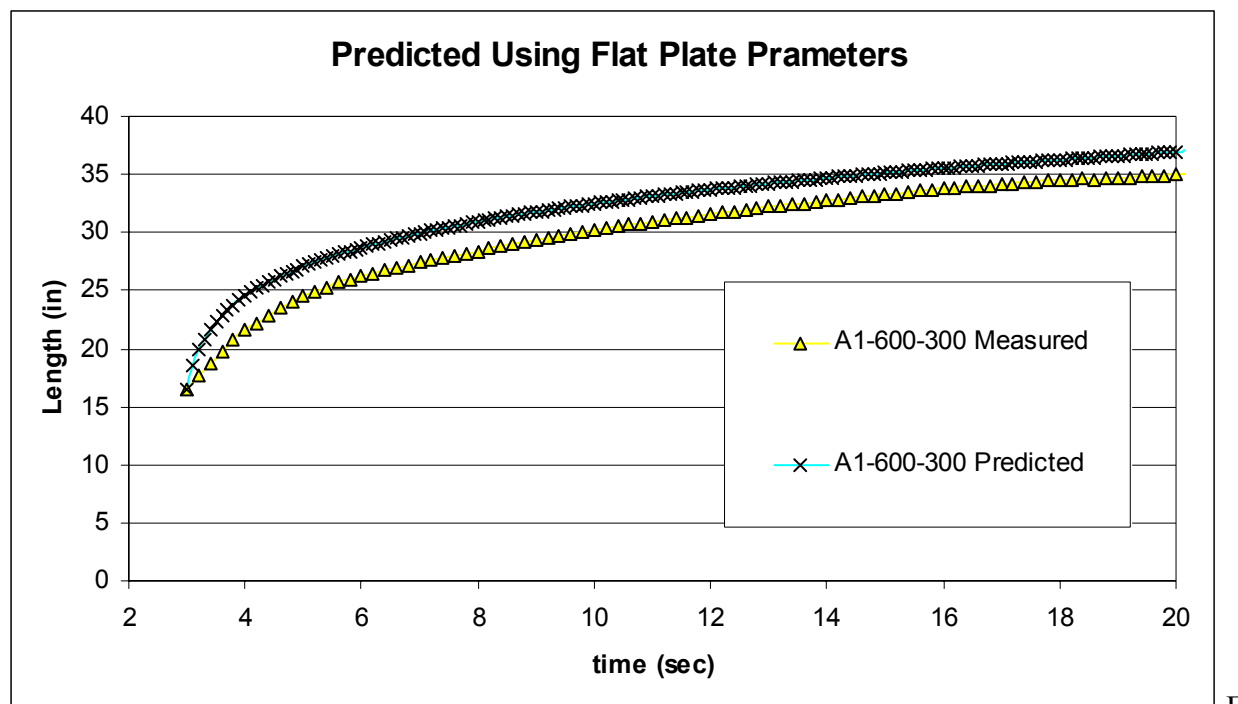
Fig. 3 Predicted flow length in the spiral flow tool using flat plate measured material parameters.

It should be noted that the spiral flow tool experiments are only repeatable within one inch of the final flow length. The model predictions using the flat plate parameters produce values that are close to the actual experiments.

A comparison between the lubricating parameters from the spiral flow tool using Eqn. 3 and the flat plate molding is displayed in Table 1.

Table 1. Comparison of the lubricating layer parameter from two different methods.

	Spiral Flow	Flat Plate
Low Filler – Low Glass	1.3	1.27
Low Filler – High Glass	4.1	4.36
High Filler – Low Glass	1.5	2.17

The lubricating layer parameter (M) obtained from the spiral flow tool closely matches to the values obtained from the flat plate molding. However, efforts to determine the resistance to extension parameter (η) with the spiral flow tool produced inconsistent results.

CONCLUSIONS

The spiral flow tool which was previously used as a qualitative tool to evaluate SMC can also be used to determine the lubricating layer parameter M, with similar results to flat plate molding. The flow of SMC inside the spiral flow tool could be predicted with the material parameters obtained from flat plate molding. The resistance to extension parameter (η) cannot be obtained from the spiral flow tool easily and needs to be investigated further.

ACKNOWLEDGEMENTS

REFERENCES

1.	Abrams, L. and J. Castro. *Predicting Molding Forces in SMC Compression Molding.* In ANTEC 2000. 2000. Orlando, Florida.
2.	Advani, S.G. and C.L. Tucker, *A Numerical Simulation of Short Fiber Orientation in Compression Molding.* Polymer Composites, 1990. p.164.
3.	Tucker, C.L and E.W. Liang, Polymer Composites, 1995. p.70.
4.	Osswald, T.A. and C.L. Tucker, *Compression Mold Filling. Simulation for Non-Planar Parts.* International Polymer Processing, 1990. p.79.
5.	Lee, C.C. and C.L Tucker, *Flow and Heat Transfer in Compression Mold Filling.* Journal of Non-Newtonian Fluid Mechanics, 1987. p. 245.
6.	Barone, M.R. and D.A. Caulk, *A Model for the Flow of a Chopped Fiber Reinforced Polymer Compound in Compression Molding.* Journal of Applied Mechanics, 1986. p. 361.
7.	Barone, M.R. and D.A. Caulk, *The Effects of Deformation and Thermoset Cure on Heat Conduction in a Shopped Fiber Reinforced Polyester During Compression Molding.* Int. J. Heat Mass Transfer, 1979. p. 1021-1032.

8.   Marker, L. and B. Ford. *Rheology and Molding Characteristics of Glass Fiber Reinforced Sheet Molding Compounds.* In Reinforced Plastics/Composites Institute. 1977.

9.   Lee, L. J., Marker, L. F., and Griffith, R.M *The Rheology and Mold Flow of Polyester Sheet Molding Compound.* Polymer Composites, 1981.

10.   Boylan, Sarah *Applications in Sheet Molding Compound Compression Molding.* M.S. Thesis, The Ohio State University, 2002.

11. Castro, J., Rabinovich, M., and Leach, B. *Mathematical Modeling of the Spiral Flow Tool for Sheet Molding Compound (SMC).* Numiform, The Ohio State University, 2004.

Modeling Flow-Induced Orientation of Fibers Using a New Closure Model

Dilip K. Mandal [1], Andre Benard [1], and Charles A. Petty [2]

[1] *Department of Mechanical Engineering, Michigan State University*
2555 Engineering Building, East Lansing, MI, 48824
[2] *Department of Chemical Engineering and Materials Science, Michigan State University*
2527 Engineering Building, East Lansing, MI 48824
And Corresponding Author's e-mail:benard@egr.msu.edu

SUMMARY: The microstructure and rheology of suspensions can be characterized by using low-order statistical moments of the orientation distribution function. This is illustrated by calculating the orientation dyad and the fiber induced stress for Couette flow between two eccentrically situated cylinders. Other geometries are also considered. Under the conditions studied, the eigenvalues of the orientation dyad remain nonnegative throughout the flow domain. The results are compared with other theories for the microstructure that show unrealizable behavior under the same conditions.

KEYWORDS: *fiber suspensions, fiber orientation, non-Newtonian, closure model, finite elements*.

INTRODUCTION

The properties of short fiber composite are strongly influenced by the orientation of the fibers in the final product. Advani and Tucker [1] discuss the utility of predicting the local microstructure of composites during processing by using low-order moments of the distribution function for the orientation unit vector. This approach, albeit appealing for its low computational cost, unfortunately requires a statistical closure model for the orientation tetrad. In this paper, the microstructure induced by Couette flow between two eccentrically situated cylinders is calculated by using a *fully symmetric quadratic* (FSQ-) closure for the orientation tetrad developed by Petty *et al.*[2]. For comparison, the microstructures predicted by using a *hybrid* closure (see Advani and Tucker [1]) and a *quadratic* closure (see Doi and Edwards [3]) are also presented.

MICROSTRUCTURE THEORY

With $\underline{p}$ defined as a unit vector oriented parallel to the major axis of a rigid fiber, the fraction of fibers having orientation coordinates on the unit sphere in the range $0 \leq \theta \leq \theta + \Delta\theta$ and $0 \leq \phi \leq \phi + \Delta\phi$ is given by

$$P\{0 \leq \theta \leq \theta + \Delta\theta, 0 \leq \phi \leq \phi + \Delta\phi\} = \Psi(\theta, \phi, t) \sin(\theta)\, d\theta\, d\phi \tag{1}$$

where $\Psi(\theta, \phi, t)$ is the orientation distribution function for fibers. For fiber suspensions with an aspect ratio L/d $\gg 1$, $\Psi(\theta, \phi, t)$ is governed by Smoluchowski's equation (see Bird *et al.* [4]; Doi and Edwards [3]; Larson [5]):

$$\frac{D\Psi}{Dt} + \frac{\partial}{\partial \underline{p}} \cdot \left[(\underline{p} \cdot \nabla\underline{u} - \underline{p}\,\underline{p}\,\underline{p} : \nabla\underline{u})\,\Psi \right] = D_R \frac{\partial}{\partial \underline{p}} \cdot \frac{\partial \Psi}{\partial \underline{p}}. \tag{2}$$

A realizable orientation distribution function must satisfy the following normalization condition

$$\int_0^{2\pi} \int_0^{\pi} \Psi(\theta, \phi, t) \sin(\theta)\, d\theta\, d\phi = 1. \tag{3}$$

In eqn (2), D_R is a rotary diffusion coefficient and has units of 1/time.

Low-order moments of the orientation distribution function are used to characterize the microstructure of fiber suspensions. For example, the second moment, or orientation dyad, is defined as

$$<\underline{p}\,\underline{p}> \equiv \int_0^{2\pi} \int_0^{\pi} \underline{p}\,\underline{p}\, \Psi(\underline{p}, t) \sin(\theta)\, d\theta\, d\phi. \tag{5}$$

An evolution equation for $<\underline{p}\,\underline{p}>$ consistent with eqn (2) is

$$\frac{D<\underline{p}\,\underline{p}>}{Dt} = (\nabla\underline{u})^T \cdot <\underline{p}\,\underline{p}> + <\underline{p}\,\underline{p}> \cdot \nabla\underline{u} - 2 <\underline{p}\,\underline{p}\,\underline{p}\,\underline{p}> : \underline{\underline{S}} - 6 D_R \left(<\underline{p}\,\underline{p}> - \frac{1}{3}\underline{\underline{I}} \right). \tag{6}$$

In the above equation, $\nabla\underline{u}$ is the velocity gradient and $\underline{\underline{S}}$ is the strain rate. It is noteworthy that the orientation tetrad directly impacts the microstructure by directly coupling with the strain rate, $<\underline{p}\,\underline{p}\,\underline{p}\,\underline{p}> : \underline{\underline{S}}$. Solutions to eqn (6) are symmetric and have the required property that $\mathrm{tr} <\underline{p}\,\underline{p}> = 1$ provided that: 1) the closure model for $<\underline{p}\,\underline{p}\,\underline{p}\,\underline{p}> : \underline{\underline{S}}$ is symmetric, and 2) $\mathrm{tr}\,(<\underline{p}\,\underline{p}\,\underline{p}\,\underline{p}> : \underline{\underline{S}})$ reduces to $<\underline{p}\,\underline{p}> : \underline{\underline{S}}$. The three orientation tetrads examined hereinafter have these two features.

A *fully symmetric quadratic* (FSQ-) closure for the orientation tetrad was introduced by Petty *et al.* [2] in order to preserve the six fold symmetry and contraction properties of $<\underline{pppp}>$. The closure is defined by the following set of equations:

$$<\underline{p}\,\underline{p}\,\underline{p}\,\underline{p}> = (1-C_2)<\underline{p}\,\underline{p}\,\underline{p}\,\underline{p}>_1 + C_2 <\underline{p}\,\underline{p}\,\underline{p}\,\underline{p}>_2 \text{ , where} \tag{7}$$

$$<\underline{p}\,\underline{p}\,\underline{p}\,\underline{p}>_1 \equiv -\frac{1}{35} S[\underline{\underline{I}}\,,\,\underline{\underline{I}}] + \frac{1}{7} S[\underline{\underline{I}}\,,\,<\underline{p}\,\underline{p}>], \text{ and} \tag{8}$$

$$<\underline{p}\,\underline{p}\,\underline{p}\,\underline{p}>_2 \equiv +\frac{2}{35} <\underline{p}\,\underline{p}>:<\underline{p}\,\underline{p}> S[\underline{\underline{I}}\,,\,\underline{\underline{I}}]$$
$$+ S[<\underline{p}\,\underline{p}>\cdot<\underline{p}\,\underline{p}>\,,\,<\underline{p}\,\underline{p}>\cdot<\underline{p}\,\underline{p}>]. \tag{9}$$
$$-\frac{2}{7} S[\underline{\underline{I}}\,,\,<\underline{p}\,\underline{p}>\cdot<\underline{p}\,\underline{p}>]$$

The result of the operation $S[\underline{\underline{A}}\,,\,\underline{\underline{B}}]$ yields a fully symmetric tetradic-valued operator formed from the two indicated symmetric dyadic-valued operators. In general, C_2 depends on the eigenvalues of the orientation dyad. At the nematic state (perfectly aligned), C_2 must be equal to 1/3. At the smectic state (i.e., 2D isotropic state), C_2 must be equal to 1/2. For the calculations presented hereinafter, C_2 is approximated as 0.37 for all orientation states.

Other closures for the orientation tetrad include the quadratic closure used by Doi and Edwards [3] for liquid crystalline polymers:

$$<\underline{pppp}> = <\underline{pp}><\underline{pp}>, \tag{11}$$

and the hybrid closure used by Advani and Tucker [1] for suspensions:

$$<\underline{pppp}> = 27\det(<\underline{pp}>)<\underline{pppp}>_1 + (1-27\det(<\underline{pp}>))<\underline{pp}><\underline{pp}>. \tag{12}$$

Unlike the *fully symmetric quadratic* (FSQ-) closure defined above, eqns (11) and (12) do not satisfy the six fold symmetry and contraction properties of the exact orientation tetrad. However, they do satisfy the two conditions identified below eqn (6).

The foregoing theory directly influences the rheology of the fiber suspension through an elastic contribution to the deviatoric component of the stress:

$$\underline{\underline{\tau}} = 2\mu \underline{\underline{S}} + k <\underline{pppp}>:\underline{\underline{S}}. \tag{13}$$

In the above equation, μ is the shear viscosity of the continuous phase and the elastic coefficient k, which is proportional to the viscosity, depends on the volume fraction and the aspect ratio of the fibers (Bird *et al.*[4]; Bhave *et al.* [6]). For the calculations presented in this paper, $\mu = 1.5$ N-s/m^2, k = 3.0 N-s/m^2, and $\rho = 1260$ kg/m^3.

The velocity and pressure fields are determined by solving the continuity equation,

$$\nabla \cdot \underline{u} = 0 ,$$ (14)

and the equation of motion:

$$\rho \frac{D \underline{u}}{D t} = -\nabla P + \nabla \cdot \underline{\underline{\tau}} .$$ (15)

Computational Approach

A Petrov-Galerkin finite element method with 496 quadratic elements and 2,108 nodes was used to develop a steady state solution to eqns (6), (14), and (15) with $D_R = 0$ (see Yu and Heinrich [7]). The radius of the larger cylinder R = 100mm and the radius of the smaller cylinder r = 50 mm. The two cylinders have an offset of 25-mm (see Figure 1). A no-slip boundary condition was imposed on the velocity at solid fluid interfaces. The angular velocity of the outer cylinder is $0.336 \, \nu/R^2$, where ν is the kinematic viscosity of the fluid. The inner cylinder is stationary. A similar problem was analyzed by Feng and Leal [8] for liquid crystalline polymers by using a quadratic closure for the orientation tetrad.
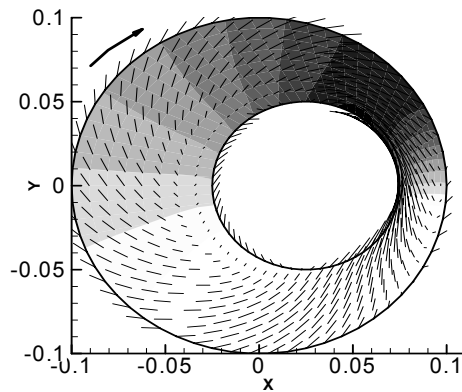
Figure 1 Distribution of the orientation director and the pressure field in the gap between a rotating cylinder and a stationary eccentric cylinder predicted by using the *FSQ-closure* for the orientation tetrad. Shorter director lengths indicate a nearly isotropic microstructure and longer director lengths indicate a highly aligned (nematic-like) microstructure. The darker gray scales identify relatively high-pressure regions; the lighter gray scales identify relatively low-pressure regions. The smallest eigenvalue associated with the director is 1/3 and occurs in regions where the strain rate is small.

A steady state solution was developed by solving an initial value problem with

$$<\underline{p}\,\underline{p}>_o = \frac{1}{3}\underline{\underline{I}}. \tag{16}$$

Quiescent initial conditions were specified for the velocity and pressure fields. A successive substitution scheme (Picard iteration) with a relaxation factor of 0.5 was used to solve the set of non-linear equations. A first order implicit scheme was used with a time step of approximately $0.05R^2/\nu$. The Reynolds number Re ($\equiv \Omega R^2/\nu$) = 0.336.

The eigenvector associated with the largest eigenvalue of the orientation dyad is defined as the microstructure director $<\underline{N}>$. All the eigenvalues of $<\underline{p}\,\underline{p}>$ are real and satisfy the inequality $0 \leq \lambda \leq 1$. Models for the orientation dyad that satisfy this feature are realizable. The eigenvectors of the anisotropic component of $<\underline{p}\,\underline{p}>$, defined by

$$\underline{\underline{b}} \equiv <\underline{p}\,\underline{p}> - \frac{1}{3}\underline{\underline{I}}, \tag{17}$$

are the same as the eigenvectors of $<\underline{p}\,\underline{p}>$. The eigenvalues of $\underline{\underline{b}}$ and the eigenvalues of $<\underline{p}\,\underline{p}>$ are related by

$$\beta = \lambda - \frac{1}{3}. \tag{18}$$

Therefore, $\frac{1}{3} \leq \lambda_{max} \leq 1$ and $0 \leq \beta_{max} \leq \frac{2}{3}$. The vector field defined by $\underline{n} \equiv \beta_{max} <\underline{N}>$ can be used to characterize the local microstructure of a suspension. For an isotropic microstructure, $\underline{n} = \underline{0}$; for a highly aligned nearly nematic microstructure, $\underline{n} \cong \frac{2}{3}<\underline{N}>$.

RESULTS AND CONCLUSIONS

Figures 1 and 2 show the distribution of the scaled director $\underline{n} \equiv \beta_{max} <\underline{N}>$ for the FSQ-closure, hybrid closure, and the quadratic closure, respectively. The FSQ-closure for the orientation tetrad gives a realizable microstructure whereas the hybrid closure and the quadratic closures produce small regions where the maximum eigenvalue of the orientation dyad is larger than unity, which is an unphysical result.
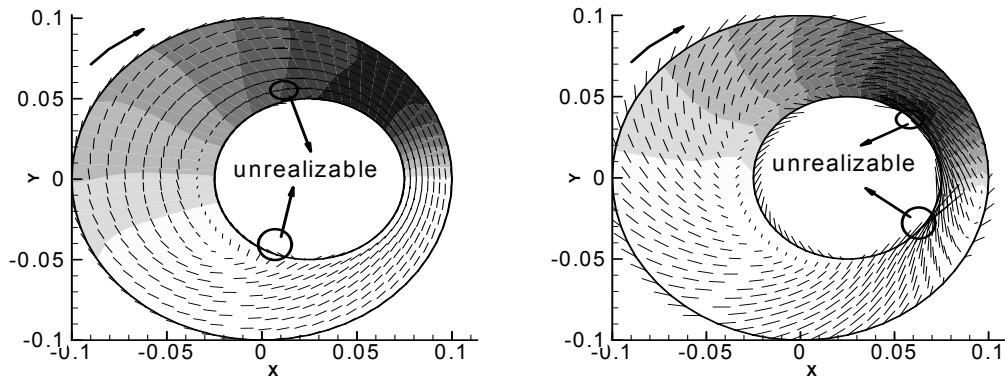
Figure 2. Distribution of the orientation director and the pressure field in the gap between a rotating cylinder and a stationary eccentric cylinder predicted by using the hybrid (left) and the quadratic (right) closures for the orientation tetrad.. The maximum eigenvalue associated with the director for the orientation dyad predict by the hybrid closure is 1.03 and 1.4 for the quadratic closure, which are unphysical. The smallest eigenvalue associated with the director is 1/3 and occurs in regions where the strain rate is small. A small unrealizable region develops in the flow field as indicated in the figures above.

The overall microstructure produced by the FSQ-closure and the quadratic closure are similar (see Figures 1 and 2); however, the hybrid model defined by eqn (12) produced a qualitatively different microstructure for the same complex flow field. The pressure distribution was similar for all three models. A recirculating region close to the small cylinder developed on the large gap side. Note that the fibers are randomly oriented in this region. Outside the circulating region, the fibers tend to orient with the velocity field. The fibers tend to be highly aligned in the small gap region where the strain rate is high.

REFERENCES

[1] Advani, S.G & Tucker, C.L, Closure approximation for three-dimensional structure tensors, Journal of Rheology, 34:367-386, 1990.

[2] Petty, C. A., Parks, S. M. & Shao, S. M., Flow Induced Alignment of Fibers, in Proceedings of *12th International Conference on Composite Materials*, ICCM12/TCA, Paris, July 5-9, 1999.

[3] Doi, M. & Edwards, S. F., *The Theory of Polymer Dynamics*, International Series of Monographs on Physics 73, Oxford University Press, 1998.

[4] Bird, R.B., Armstrong, R.C. & Hassager, O. *Dynamics of Polymeric Liquids*, Volume 2, John Wiley, 1987.

[5] Larson, R. G., *The Structure and Rheology of Complex Fluids*, Oxford University Press,1999.

[6] Bhave, A. V., Menon., R. K., Armstrong, R. C. & Brown, R. A., A Constitutive Equation for Liquid-Crystalline Polymer Solutions, *Journal of Rheology*, 37(3), 413-441,1993.

[7] Yu, C.-C & Heinrich, J.C., Petrov-Galerkin methods for the time dependent convective transport equation, Journal for Numerical Methods in Engineering, 23:883-901, 1986.

[8] Feng, J. & Leal, L.G., Simulating complex flows of liquid-crystalline polymers using the Doi Theory, Journal of Rheology, 41:1317-1335, 1997.

THERMOPLASTIC PROCESSING

Thermoplastic Liquid Composite Molding: Production and Characterization of Composites Based On Cyclic Oligomers

Hilde Parton [1], Ignaas Verpoest [1]

[1] *Department of Metallurgy and Materials Engineering, K.U.Leuven*
Kasteelpark Arenberg 44, B-3001 Leuven, BELGIUM
Corresponding Author's e-mail: hilde.parton@mtm.kuleuven.ac.be

SUMMARY: The use of low viscous polymeric precursors like cyclic butylene therephthalate oligomers, which can react to form a thermoplastic matrix, allows thermoset production techniques such as resin transfer molding to be used for the production of continuously reinforced thermoplastic composites. Given that the matrix is polymerized inside a closed mold and in the presence of fibers, the relation between the matrix and composite properties has been studied for different preforms. In order to assess the experimental data, the composite properties were predicted with the classical laminate theory. Although most fibers and more specifically their sizing do not completely inhibit polymerization, some do lead to inferior matrix properties which affect the non-fiber dominated composite properties. In order to assess the feasibility of producing large parts with this production technique, a thermoplastic leaf spring prototype was manufactured. Even though some optimization is still required to improve process reproducibility, the resulting product quality was satisfactory. Moreover, most of the problems occurring during processing are inherent to the RTM process and not related to the matrix system.

KEYWORDS: thermoplastic, RTM, cyclic oligomers

INTRODUCTION

The main problem during the processing of thermoplastic composites is the impregnation of the fibrous reinforcement with highly viscous resins. Therefore, liquid composite molding techniques are typically associated with thermoset resins. Recently, however, more attention has been paid to in situ polymerization techniques, where impregnation is facilitated by injecting polymeric precursors, which then react to form a thermoplastic matrix. The low viscosity of these precursors allows for the use of liquid molding techniques like resin transfer molding for the production of continuously reinforced thermoplastics.

This paper reports on the characterization of continuously reinforced thermoplastics made by RTM as well as the production of a thermoplastic leaf spring prototype.

PRODUCTION AND CHARACTERIZATION OF A4-SIZED PLATES

Materials

The prepolymers used in this study were the cyclic butylene therephthalate oligomers (CBT$^{®}$ resin) supplied by Cyclics Corporation. These oligomers are precursors for the thermoplastic polybutylene therephthalate (PBT). The number of butylgroups in the oligomer mixture varies from two to seven, resulting in a melting range from 130-160 °C. Before processing, the oligomers were dried overnight at 110 °C to remove residual moisture, which could interfere with the polymerization reaction. The tin-based catalyst (Fascat™ 4101) is commercially available from Atofina Chemicals Incorporated.

Four types of glass fiber reinforcements were used, which were all dried overnight at 110 °C before processing. These reinforcements were used to produce composites of 2 mm thickness. The first fabric (S-UD) supplied by Saertex Wagener GmbH, is a non-crimp unidirectional fabric with a total areal density of 951 g/m². Although this fabric is mostly unidirectional, a small amount of 90° fibers (27 g/m²) was added to ensure for fabric stability. Three layers of this fabric were used, resulting in a total fiber volume fraction of 54 %. A biaxial ($\pm$ 45°), non-crimp fabric (S-B) from Saertex was also used. The measured areal density of the fabric is 590 g/m². Four layers were used to reach a fiber volume fraction of 46 %.

Ahlström Fiber Composites supplied a second type of non-crimp fabric, which consists out of three layers, 0°, 90° and a random mat. The areal density of these individual layers was determined experimentally resulting in respectively 1217, 60 and 53 g/m². Two layers of these fabric were used (0, R, 90)$_s$ to reach a fiber volume fraction of 52 %.

Eurocarbon B.V. developed a braid for a leaf spring prototype. Each layer of this braid consists for 84 % out of 0° fibers, whereas the $\pm$ 45° fibers only encompass 16 % of the total areal weight, which is 1200 g/m². Two layers of this fabric were used, resulting in a total fiber volume fraction of 48 %. The unidirectional fibers are not of the same type as the $\pm$ 45° fibers. In order to use this braid into the plate mold, the braid was cut open.
PBT Twintex from Vetrotex Renforcement S.A., which is a 2 × 2 twill weave, was used as a reference material. The areal density is 1030 g/m² with a fiber weight fraction of 65 % in 2.5 mm thick composite.

Production of flat plates

The production of glass fiber reinforced polymerized CBT (GF-pCBT) closely resembles the well-known RTM process for thermoset composites. The oligomers are heated to a temperature (190 °C) above their melting point, after which the catalyst (0.45 wt%) is added. The resulting mixture is stirred for a well-defined time (15 s), before it is vacuum infused into the closed mold, containing the fibrous reinforcement. During this stirring time, polymerization already commences, resulting in a continuously increasing viscosity and thus a limited time window for mold filling. Once the mold is completely filled, in- and outlet ports are closed after which sufficient time (30 min) should be available to complete the polymerization reaction and cold crystallization.

Characterization of pCBT

The characterization methods used for the determination of the matrix properties, which are described in detail elsewhere [1], include gel permeation chromatography (GPC) en differential scanning calorimetry (DSC).

Fig. 1 shows the GPC results for different pCBT composites. It is clear that both the degree of conversion and the molecular weight decrease when fibers are present during polymerization. It was previously demonstrated that the degree of conversion is underestimated by a few percent for the fiber reinforced pCBT [1], therefore, the remaining oligomer content for most composites is satisfactory. Although ECA-UD has an oligomer content of less than 10 %, visual observation of the composites revealed fiber-matrix incompatibility. In the vicinity of the fibers, the matrix was yellowish, compared to bright white for unreinforced pCBT. This color difference also translates in the lowest measured molecular weight.
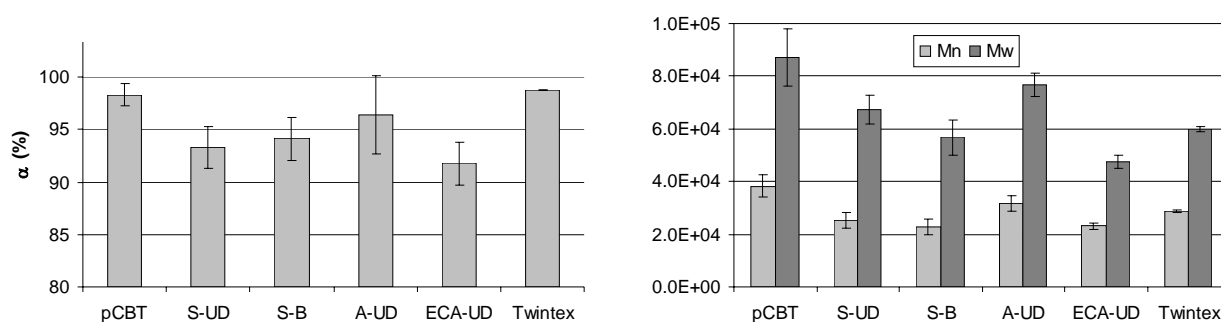
Fig. 1 GPC results

The degree of crystallinity was determined by DSC measurements, Fig. 2. There is no major difference between the unreinforced and reinforced pCBT. Compression molded Twintex-PBT has however a significantly lower degree of crystallinity. PBT is usually crystallized from the melt, as is the case for the Twintex PBT. pCBT on the other hand can start crystallization before polymerization is fully completed, resulting in a different degree of crystallinity, depending on the polymerization temperature and a different crystalline structure. The difference in crystalline structure strongly influences the matrix toughness, but will not be further discussed here [2].
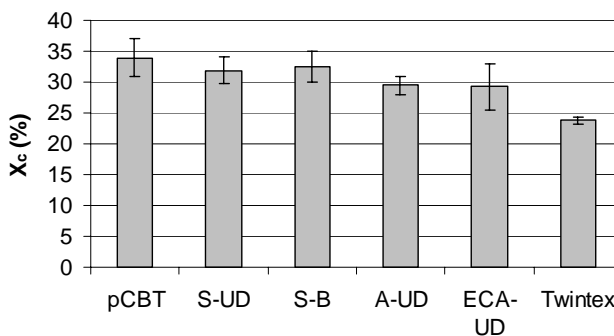
Fig. 2 Degree of crystallinity

Mechanical properties

The mechanical properties of the composites are tested in three point bending according to ASTM D790-84. The moduli of the composites were compared to the theoretical properties, calculated according to the classical laminate theory. The transverse unidirectional properties were calculated with both the equations of Chamis and those of Thai-Hahn ($\eta = 0.5$) [3].
Both the experimental and theoretical moduli are shown in Fig. 3. The longitudinal modulus is a fiber dominated property and should therefore not be affected by poor matrix polymerization. The somewhat larger discrepancy for the ECA-UD samples can be explained by a deviation of the fiber orientation due to the nature of the fabric (cut-open braid).

The transverse modulus is on the other hand a matrix- and interface dominated property. Although it is known that predicting the non-fiber dominated properties is less accurate, the deviation of almost 50 % for the ECA-UD samples clearly indicates inferior matrix properties, which was confirmed by the GPC results, which show the lowest degree of conversion and the lowest molecular weight for the ECA-UD matrix.
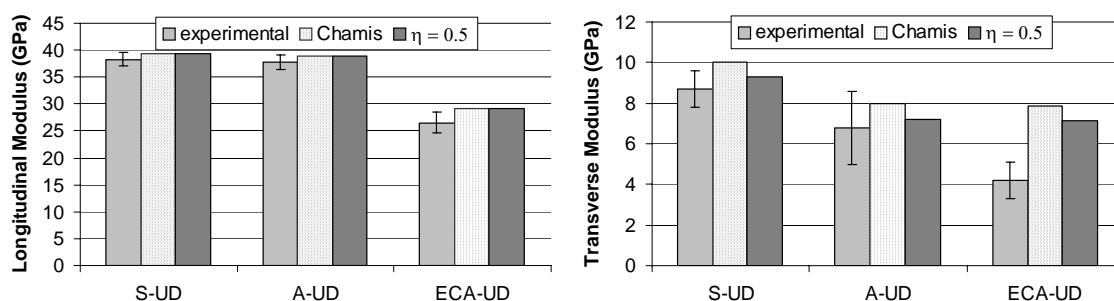
Fig. 3 Mechanical properties compared to theoretical predictions

LEAF SPRING PROTOTYPE

Materials

The braided preform for the leaf spring consisted out of 6 layers of braiding (ECA-UD), braided over a metal template, which was removed after the braiding process. Unfortunately, the template was a little bit too wide, resulting in difficulties in placing the preform into the mold cavity. The total weight of the leaf spring preform was 2.1 kg.

Two matrix materials were used, namely CBT® resin, which was described above and for comparative reasons, an epoxy resin Epikote 828 with curing agent Epicure DX-6514 was also used to produce two prototypes.

Production of thermoplastic leaf springs

In order to enlarge the time window for fiber impregnation with the reactive mixture, the oligomer melt (2 kg) was kept at 170 °C as compared to 190 °C for the production of the flat plates. Lowering the temperature of the oligomer-catalyst mixture, decreases the reaction speed and thus the viscosity of the entering liquid. In order to complete polymerization in a reasonable timeframe and to optimize the matrix properties, the mold temperature was still kept at 190 °C. Stirring time for the catalyst/oligomer mixture was 45 s. The resin mixture was injected into the mold with an overpressure of maximum 2.5 bar and assisted by an underpressure of 0.8 bar. Fig. 4 shows the set-up for the production of the thermoplastic leaf spring. In order to enhance mold filling, an injection channel along the length of the leaf spring was foreseen.
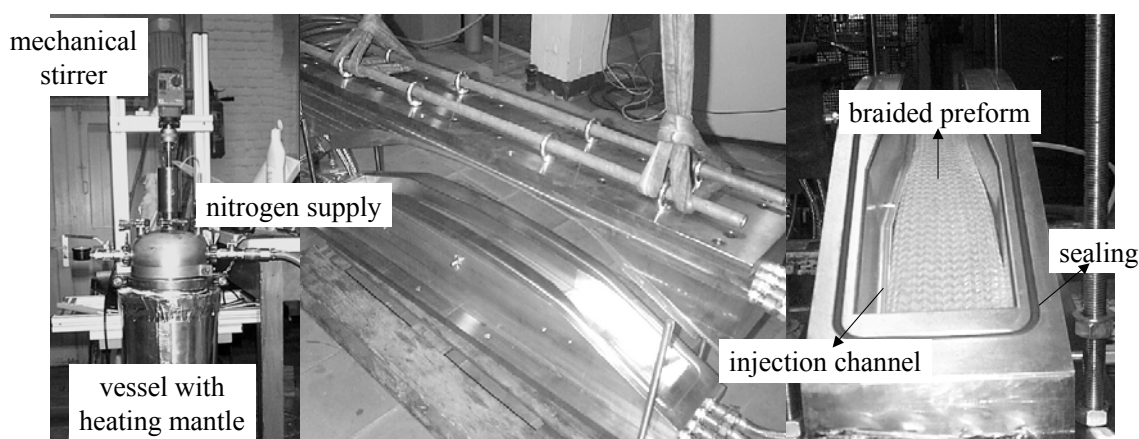
Fig. 4 Set-up for production of leaf spring

Table 1 gives an overview of the processing parameters and filling times needed to produce the leaf spring prototypes. For the production of the leaf springs, there were two major parameters changed, namely the position of the mold and the filling of the distribution channel. The mold was rotated in order to enhance air evacuation by placing the vents at the highest point. The distribution channel was filled with roving and or partially closed with sealing in order to on one hand slow down the resin flow inside the channel and on the other hand to avoid short cut flows due to imperfect fitting of the preform.

Table 1 Processing parameters for leaf spring production

	Epoxy 1	Epoxy 2	pCBT 1	pCBT 2	pCBT 3	pCBT 4	pCBT 5	pCBT 6
mold rotation	0°	0°	0°	180°	180°	180°	90°	90°
distribution channel	empty	empty	empty	roving	roving	roving	roving+ sealing	roving + sealing
overflow time	75	90	60	120	100	N.A.	90	N.A.
filling time	600	900	300	300	300	375	420	270

From the production of these prototypes, it became clear that the process is not yet very reproducible. Both the time to reach the first overflow and the time to reach air-free overflow (filling time) changes although other parameters are kept constant. There was no major difference in the irreproducibility between the very low viscous oligomers and the epoxy resin. Even though there are a number of factors that have to be taken into account, such as the pressure profile, the fiber preform plays a major role.

The preform was braided around a mandrel with the inner section of the mandrel being 60 mm wide. This leads to a preform width of around 70 mm, which is substantially larger than the 66.5 mm of the actual leaf spring. Compression of the braid to fit into the mold cavity causes the transverse permeability to decrease 22 %, calculated with the formulas of Gebart [4]. The amount of prefrom compression changed from one production run to another. Sometimes fibers from the outer braid were trapped inside the injection line and/or distribution channel, therefore altering the transverse permeability and thus causing process irreproducibility.

Another effect of the need to compress the fiber preform in the middle section, is the impossibility to closely fit the preform to the mold cavity in the widening region of the leaf spring. This leads to gaps exceeding 3 mm between the fiber preform and the mold cavity. In combination with a non-perfect fit of the preform at the outer sides of the leaf spring, short cut flows are almost unavoidable. These short cut flows are responsible for the sometimes very sudden overflow. It is therefore crucial to produce a preform, which fits perfectly inside the mold cavity without major handling.

The time for this resin-catalyst combination to complete polymerization and crystallization is only 30 minutes, which, in an automated process, can be the total cycle time, since the mold does not need to cool down before demolding. For this prototype set-up however, a minimum cycle time of 3 hours was needed due to thermal cycling of the mold, preform preparation excluded. The prototype is shown in Fig. 5 and weighed 2.9 kg after proper trimming.

Fig. 5 Leaf spring prototypes

Testing of leaf spring prototype

The leaf spring prototypes were tested in four point bending mode as shown in Fig. 6. A maximum load of 10 kN was obtained, which corresponds to a roller displacement of 250 mm. At this large displacement, strain in the outer fiber was only 2 %. A short-term cyclic loading was also applied, leading to a constant spring constant of 30 N/mm.
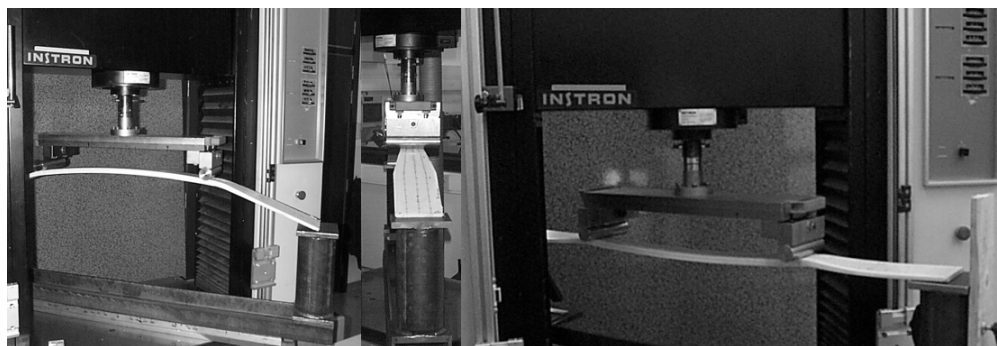
Fig. 6 Testing of leaf spring prototype

CONCLUSIONS

Liquid molding technologies were used to manufacture continuously reinforced themoplastic composites by utilizing polymeric precursors that were polymerized in situ. Although most fibers and more specifically their sizing do not completely inhibit polymerization, some do lead to inferior matrix properties which affect the non-fiber dominated composite properties such as the transverse modulus in unidirectional composites.

Scaling-up the process was assessed by the production of a thermoplastic leaf spring prototype. Although optimization of the braided preform is necessary to improve process reproducibility, the encountered problems were inherent to the RTM process and not related to the resin system. The final product quality and mechanical properties were satisfactory.

ACKNOWLEDGEMENTS

REFERENCES

1 H. Parton and I. Verpoest, "Reactive processing of textile reinforced thermoplastics", *14th International Conference on Composite Materials*. 2003: San Diego. p. CDrom paper 1201.

2 H. Parton, J. Baets, P. Lipnik, J. Devaux and I. Verpoest, "Liquid molding of textile reinforced thermoplastics", *11th European Conference on Composite Materials*. 2004: Rhodos, Greece.

3 P. K. Mallick, "Fiber-reinforced composites". 1993, Marcel Decker: New York. p. 547.

4 B. R. Gebart, "Permeability of unidirectional reinforcements for RTM", *Journal of Composite Materials*.Vol. 26(8), p. 1100-1133. (1992)

Liquid Molding of Carbon Fabric Reinforced Nylon Matrix Composite Laminates

Selvum Pillay, Haibin Ning, Uday K. Vaidya, and Gregg M. Janowski

Department of Materials Science and Engineering, The University of Alabama at Birmingham, 254 BEC, 1150 10th Avenue South, Birmingham, AL, 35294.
Corresponding Author's e-mail: uvaidya@uab.edu

ABSTRACT: This manuscript describes the processing techniques and processing windows used to produce carbon fiber reinforced, nylon matrix composite panels. Anionic polyamide 6 resin (casting grade) was polymerized *in situ* after infusion. Careful time and temperature control were necessary to obtain total fiber impregnation with subsequent complete polymerization. These advances will permit the use of affordable thermoset manufacturing processes such as Vacuum Assisted Resin Transfer molding (VARTM) or Resin Transfer Molding (RTM) to produce thermoplastic-matrix composite structures. The processing parameters, methodology and limitations of using VARTM for nylon matrix composites are highlighted. Static and low velocity impact response of the panels are presented and compared to traditional thermoplastic and thermoset composites. DSC scans show full polymerization of the resin was achieved. SEM evaluation show full wet-out of the preform was achieved at both the macroscopic and microscopic level. The properties of the panels produced using the process developed has been equivalent to, or superior, compared to reported values of other carbon thermoset composite panels manufactured using VARTM.

KEYWORDS: VARTM, reactive resin, Nylon, PA6.

INTRODUCTION

The use of thermoplastic composites has gained steady favor over traditional materials such as steel in structural and semi-structural applications. The current US market for such materials is in excess of one billion pounds per annum, half of which is consumed by the automotive industry [1, 2]. This utilization is driven by specific strength, damping, corrosion resistance, and impact resistance. However, these composites are limited to products that can be manufactured using traditional thermoplastic processes like injection molding, compression molding and extrusion. These processing techniques typically result in short fiber lengths and cannot use continuous fiber woven fabrics. Recent developments in processing and materials technology strive to improve the mechanical properties, especially in impact, of thermoplastic composites, which require maximum fiber length (3, 4). Thermoplastic resins, like PEEK, PEKK, reinforced with woven fabric can be processed using an autoclave under very high temperatures and pressures, a very expensive processing approach. Vacuum assisted resin transfer molding (VARTM) has been very well developed and is now a proven low-cost manufacturing technique for thermoset

resin composites. VARTM offers a closed mold system that allows zero Volatile Organic Compounds (VOC's), and it uses a single sided tool, which reduces cost. Unfortunately, the high melt viscosity of thermoplastic resins generally precludes the use of VARTM due to poor impregnation or mold fill.

Thermoset infusion techniques can be used for thermoplastics by either significantly lowering the viscosity of the resin or reducing the flow distance. By accomplishing this, the advantages of thermoplastics over thermosets of cost, faster cycle times, superior impact properties, and recyclability can be brought to composite materials and structures.

There has been substantial interest recently in liquid molding of thermoplastic resin composites using the matrices anionic polyamide 12 (5, 6), cyclic PBT (7, 8), and anionic polyamide 6 (9, 10). The current study will utilize polyamide 6 (PA6), a well known commodity thermoplastic resin that has been used extensively for nylon casting applications. In this research, a process is developed for the use of PA6 as an effective matrix for infusion into a carbon fabric preform. Mechanical property data will be presented that indicates that these composites possess high modulus, tensile strength, and impact resistance.

MATERIALS AND PROCESSING

Caprolactam monomer, Bruggolen C10 catalyst, and Bruggolen C20P activator were used to form the polyamide 6 resin and were supplied by Bruggemann Chemical U.S., Inc. This system is used extensively by the polymer casting industry to cast near-net-shapes. The short polymerization times make the system ideal for casting. The monomer is melted ($T_m = 69^{\circ}C$) in two parts, one containing the initiator and one containing the catalyst. The two parts are then either mixed and poured into the mold or mixed via an injection head and injected into the mold. Reaction injection molding of nylon block copolymers were first done by H. Mooji, DSM, Netherlands. (11).The 3K tow size, 4 harness satin weave carbon fabric with an areal density of 0.02 g/cm^2 was supplied by US Composites.

The carbon fabric was washed with acetone to remove the lubricants and sizing. Twenty layers of the carbon fabric were placed between two layers of porous Teflon cloth and then laid onto the tool surface. The preform was then bagged and sealed using high temperature bagging film and tacky tape.

The viscosity of the resin is a function of the levels of catalyst and initiator, temperature, and time. Various combinations were investigated to achieve both full wet-out of the preform and full polymerization. The caprolactam was heated to $100^{\circ}C$ until it was liquid. The catalyst and activator were then added, and the solution was brought to a molten state. The catalyst is sensitive to moisture, and the caprolactam oxidizes rapidly at these temperatures. Therefore, storage and processing must be done in a dry nitrogen environment. The resin was then infused into the preform via an infusion line. Once the resin reached the end of the preform, the infusion line was clamped off, and the temperature was raised to $150^{\circ}C$ to polymerize the nylon. PA6 anionically polymerized from solution has a higher degree of crystallinity compared to the same material crystallized from the melt. (10).

DSC scans were conducted to establish the degree of polymerization. Scans on initial samples showed a number of peaks at temperatures ranging from $70^{\circ}C$ to $220^{\circ}C$. This implies that there

was a large percentage of the monomer in the system and full polymerization was not achieved. Figure 1 shows a DSC scan of a fully polymerized panel. Only one sharp peak is observed at 220°C, the melting temperature of PA6. The sharpness of the peak indicates a high degree of crystallinity, which is characteristic of PA6 anionically polymerized from solution.

One limitation of using liquid molding techniques for thermoplastic resin is the high melt viscosity. This leads to poor wet-out of the fibers both macroscopically (tows) and microscopically (filament). The viscosity of the Caprolactam, initiator and catalyst at 100°C is low enough that macroscopic (a function of the flow) and microscopic (due to capillary action) wet-out is achieved. The SEM images shown in Figure 2 show the wet-out at the filament level. It can be observed that the fiber is completely coated by the resin in both the cross sectional and the longitudinal view of the fibers.
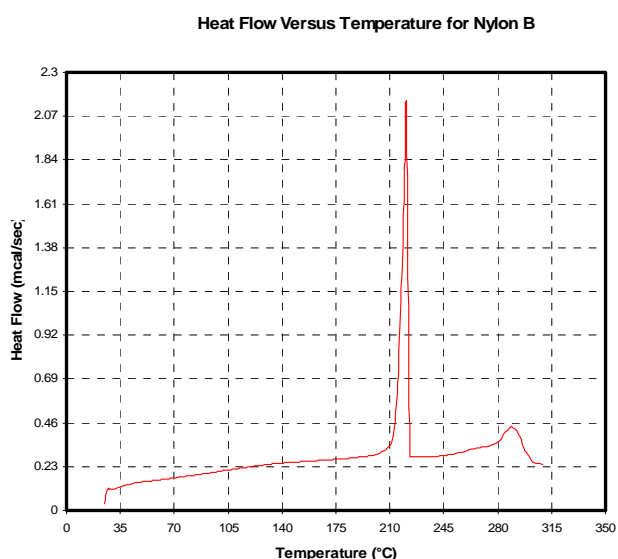
Figure 1: DSC scan of carbon /PA6 samples. Note the sharp peak at 220°C and no peaks lower than 220°C, which implies full polymerization.
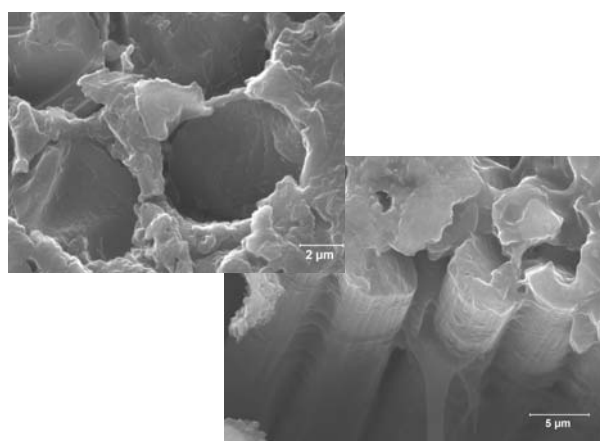
Figure 2. SEM image showing cross section and longitudinal carbon filaments and PA6 resin. The filaments are fully wet-out with resin.

MECHANICAL TESTS

Tensile

Tensile tests were conducted according to ASTM D 3039M using samples of dimensions 12.5 x 250 mm cut from the panel. The sample ends were tabbed with an epoxy glass material, dimensions 12.5 x 63 x 0.85 mm, with the tab ends tapered to 5°. The tabs were bonded to the sample using a Three Bond™ thermoplastic adhesive. Samples were tested in a servo-hydraulic tensile test machine at a displacement rate of 2 mm/minute with a gage length of 120 mm. The change in length of the sample was measured using a clip-on extensometer, which was detached prior to failure.

The average modulus and ultimate tensile strength (UTS) values were 64.86 GPa and 822 MPa, respectively. The modulus was marginally lower than reported values for carbon/ epoxy (V_f = 50%) of 70 GPa. However, the UTS is above the reported value of 600 MPa. The sample failed within the gage, and failure was mainly fiber dominated. Figure 3 shows a typical failed sample.

Figure 3. Typical failed sample in tension, failure occurred in the gage.

Flexure

Three point bend tests were conducted according to ASTM D 790M. Samples of dimension 10 x 80 x 4 mm were prepared from the panel. The tests were conducted on a SATEC power screw universal test machine. The support span was set at 64 mm, and the rate of cross head motion was 1.7 mm/minute. The average flex modulus and flex strength was 45 GPa and 490 MPa, respectively. The mode of failure was tensile face fracture and delamination.

Impact

Low velocity impact (LVI) tests were conducted using a Dynatup 8250 impact-testing machine equipped with a load cell of capacity 1590 kg (3500 lbs). A hemispherical shaped head tup of diameter 19.5 mm and mass 0.12 kg was used. The total mass including the tup mass, impactor and the holding bolts was 0.24 kg for the hemispherical impactor. The samples were clamped using a pneumatic assist mechanism, such that 76.2 mm (3") diameter of the sample face was exposed to the impactor. The force-time, energy-time and load-deflection response of the samples were measured. Damage initiation and progression was monitored.

Figure 4 illustrates a typical force-time-energy curve for the carbon / nylon composite sample. The energy to peak load and the peak force were normalized with respect to the thickness. The average values of E/t and F/t were 62097.95 J/m and 1873.306 kN/m, respectively. The failure mode was observed to be primarily tensile fracture of the back surface. Figure 5 shows the tensile face of an impacted sample. The impact energy absorbed by the carbon / PA6 samples were found to approximately 27% greater than reported values for rubber toughened SC15 epoxy / carbon samples.
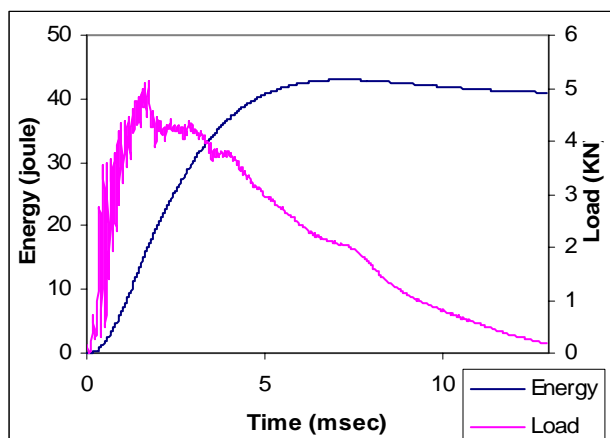
Figure 4 Typical Force / Energy – Time curve for carbon / PA6 composite sample.

Figure 5 Tensile face of typical impacted sample.

SUMMARY

Vacuum Assisted Resin Transfer Molding, a method that is well established for thermosets, has been effectively used to infuse carbon fabric performs with PA6 resin. The processing parameters were established to provide a low viscosity of the resin for a long enough time for full wet-out of the preform and good fiber impregnation. The method was significantly modified to accommodate the differences of the thermoplastic resin, especially with regard to temperature and moisture control. The DSC scans showed that the resin was fully polymerized. The sharp peak in the scan is an indication of a high degree of crystallinity. The SEM images show that macroscopic and microscopic fiber impregnation was achieved.

The preliminary impact, tensile and flexure data show that the thermoplastic composite possesses properties equivalent to or superior to thermoset composites. When compared to reported values, the ultimate tensile strength is superior using the PA6 resin. The impact data shows that the PA6/carbon panel is superior to SC 15, a specially developed thermoset resin for impact. Further tests need to be conducted and compared to equivalent carbon/epoxy composites for meaningful comparisons.

REFERENCES

1. Hartness, T., Husman, G., Koenig J., and Dyksterhouse J., The characterization of low cost fiber reinforced thermoplastic composites produced by the drift process. *Composites: Part A* **32**, 1155-1160 (2001).

2. Composite Fabricators Association, www.cfa-hq.org.

3. Thomason, J.L., and Vlug, M.A., Influence of fiber length and concentration on the properties of glass fiber-reinforced polypropylene: 1. Tensile and flexural modulus. *Composites: Part A* **27A** 477-484, (1996).

4. Bush, S.F., Torres, F. G., and Methven, J. M., Rheological characterization of discrete long glass fiber (LGF) reinforced thermoplastics. *Composites: Part A* **31** 1421-1431, (2000).

5. Zingraff L., et al., Reactive processing and forming of polyamide 12 thermoplastic composites, 23rd Europe SAMPE conference proceedings, 2002, pp 237-248

6. Luiser, A., Bourban, P.E. and Manson, J.A.E., *In Situ* Polymerization of Polyamide 12 for Thermoplastic Composites. ICCM-12, Paris, 1999.

7. Ciovacco, J. and Winckler, S.J., Cyclic thermoplastic properties and processing, 45th International SAMPE Symposium, 2000, Long Beach, CA.

8. Hilde Parton and Ignass Verpoest, Reactive Processing of Textile Reinforced Thermoplastics, ICCM 14, 2003, San Diego, CA.

9. Van Rijswijk, K., Vlasveld, D.P.N., Brsee, H.E.N. and Picken, S.J., Vacuum injection of anionic polyamide 6, Proceeding of ICCST 4, 2003, Durban, South Africa.

10. Vlasveld, D.P.N., Van Rijswijk, Bersee, H.E.N., Beukers and Picken, S.J.N., Process Considerations for Liquid Molding of Composites Based on Anionic Polyamide 6, ICCM 14, 2003, San Diego, CA.

11. Mooij, H., SRIM Nylon Composites, Advanced Materials: Cost Effectiveness, Quality Control, Health and Environment, SAMPE / Elsevier Science Publishers B. V. 1991.

Processing Window for Vacuum Infusion of Fiber-Reinforced Anionic Polyamide-6

Ir. K. van Rijswijk[1], Ing. K. Koppes[2], Dr.ir. H.E.N. Bersee[1], Prof.ir. A.Beukers[1]

[1]Faculty of Aerospace Engineering, Delft University of Technology,Kluyverweg 1, 2629 HS, Delft, The Netherlands: Email: K.vanRijswijk@LR.TUDelft.NL
[2]Afdeling Luchtvaarttechnologie, Hogeschool INHOLLAND Haarlem, Haarlem, The Netherlands

SUMMARY: In order to manufacture durable wind turbine blades for offshore application in a sustainable way, Delft University of Technology is currently developing vacuum infusion technology for reactive processing of thermoplastic composites. This paper presents a processing window for Anionic Polyamide-6 (APA-6), a reactive thermoplastic system produced by DSM Fiber Intermediates. Injection times, polymerization rates and degree of conversion for various processing temperatures and resin formulations are determined.

KEYWORDS: anionic polyamide-6, thermoplastic composites, vacuum infusion, processing window, viscosity, degree of conversion.

INTRODUCTION

Following international agreements on reduction of CO_2-emission, the Dutch government has formulated the ambitious target to have 6,000 Megawatt wind power installed offshore in 2020. A knowledge program is initiated by the WE@SEA foundation (Wind Energy at Sea), which reflects the combined effort of public and private interest towards realizing this target. In the next decades, more than 1,000 turbines need to be installed in the North Sea. The two main requirements formulated by WE@SEA for the 3,000 blades to be constructed are durability and sustainability. The blades should be more fatigue resistant to increase the current lifetime of 20 years and to reduce preventive and corrective maintenance visits, which are currently required 4 to 6 times a year, costing 7 to 12 k€ per visit. In the light of producing green energy, effort is put in the development of economic and environmental friendly manufacturing processes, procedures for installation and dismantling, and the destruction and re-use of materials.

Delft University of Technology is currently developing a process for manufacturing large thermoplastic composite (TPC) blades. Due to the higher toughness of the matrix, TPC potentially offer a higher resistance to fatigue than their thermoset counterpart currently applied, such as fiber-reinforced epoxies and vinylesters. In addition, TPC can be remolded upon melting, opening the door for re-use of the blade material. In order to produce blades with lengths in excess of 50 meter, the currently most widely applied manufacturing process for turbine blades, vacuum infusion, is maintained. This process utilizes a low viscosity resin that is injected in a mold with pre-placed fibers, followed by a curing step. Since the viscosity of thermoplastic polymer melts is too high, reactive processing is required: a low viscosity monomer melt is injected between the fibers, followed by in situ polymerization of the thermoplastic matrix.

This paper presents a processing window for processing of Anionic Polyamide-6 (APA-6), a reactive thermoplastic system produced by DSM Fiber Intermediates. Injection times, polymerization rates and degree of conversion for various processing temperatures and resin formulations are determined.

EXPERIMENTAL

Chemistry

Polyamide-6 (APA-6) was obtained through anionic polymerization of ε-Caprolactam. The lactam monomer was molten (T_m = 79 °C) and mixed with the activator (Hexamethylene Diisocyanate) and the catalyst (Caprolactam Magnesium Bromide), all supplied by DSM Fiber Intermediates [1]. By heating up this mixture to 130-180 °C, polymerization is completed within 30 minutes. Polymerization time can be adjusted between 2 to 60^+ minutes, by changing the amount and type of activator and catalyst. In general, activator and catalyst are added in a 1:1 ratio of 0.6 mol%. This is referred to as a 1-1 formulation. In this paper, various x-y formulations are used (e.g. 2-1 refers to the addition of 1.2 mol% activator and 0.6 mol% catalyst).

Rheology

Viscosities were measured in a Bohlin V88 concentric cylinder viscometer (speed = 6, spindle type 6) for various resin formulations at various temperatures. An experimental setup with Nitrogen supply provided a water and oxygen free environment for polymerization. Repeated measurements demonstrated the consistency of this test. After injection, viscosities were measured continuously up to a value of 1 Pa·s. From past experiences, this value is regarded as the upper limit for the injection window.

Degree of conversion

The degree of conversion (X) of the polymerization of APA-6 in heated reaction tubes was determined for various resin formulations at various temperatures. At regular time intervals, polymerization was terminated by quenching the closed tubes in ice water. Samples were grinded, weighed (m_{tot}) and refluxed overnight in demineralized water. After filtering and rinsing, samples were weighed again (m_{pol}). Whereas the Caprolactam monomer dissolves easily in water, the APA-6 polymer does not. The degree of conversion was determined according to Eqn. 1.

$$X = \frac{m_{pol}}{m_{tot}} \cdot 100\%$$

$$(1)$$

RESULTS AND DISCUSSION

Rheology

Viscosity-time relations are presented in Fig. 1, for 1-1 and 2-2 formulations polymerized at 140, 150 and 160 °C (T_{pol}). It can be seen that less time is required to reach the 1 Pa·s limit for a higher polymerization temperature. The same can be concluded for the addition of more activator and catalyst. The viscosity remains extremely low (< 0.1 Pa·s) during most of the injection time, which facilitates fiber wetting and increases the flow rate of the resin through the fibers. Upon reaching the 1 Pa·s limit, the spindle with the polymerizing Caprolactam was removed from the setup and quenched in liquid Nitrogen. Determination of the degree of conversion correlated the 1 Pa·s viscosity limit to a 10 % conversion limit.
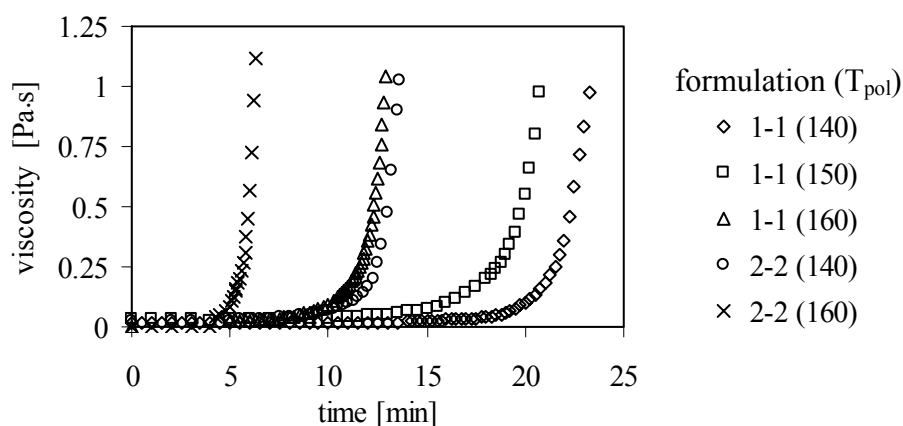
Fig. 1 Viscosity-time relations for anionic polymerization of Polyamide-6

Degree of conversion

Fig. 2 shows the degree of conversion in time for 1-1 and 2-2 formulations polymerized between 130 and 180 °C. As expected, higher polymerization temperatures and the addition of more activator and catalyst increase the polymerization rate. For the 1-1 formulation, polymerization at 130 °C is extremely slow. This can be explained by the semi-crystalline nature of APA-6. During formation of APA-6, which takes place well below its melting point (T_m = 220 °C), polymerization and crystallization occur as two competitive processes. At 130 °C, crystallization is the more dominant process and reactive sites can become trapped in the crystals very easily. As a result, polymerization is slowed down or even halted [2].

Final degree of conversion

The parameters changed not only influence the rate of polymerization, but also the final degree of conversion and hence the material properties. Residual Caprolactam acts as plasticizing agent for the APA-6 matrix for conversions below 95% [2]. Moreover, leftover Caprolactam will either diffuse to the product surface, making the product tacky and unpaintable, or in case of

composites it might diffuse to the fiber surface where it can significantly weaken the fiber-matrix interface. The final degree of conversion obtained in this study (conversion after 45 minutes) was determined for various formulations at a polymerization temperature of 140 °C, Table 1. Conversions obtained correspond to values found in literature [3]. It can be seen that increasing the amount of catalyst reduces the final degree of conversion, whereas the addition of more activator has no effect. The reason for this is that for every catalyst molecule added a MgBr cation is introduced, whose positive charge needs to be compensated for by a Caprolactam anion throughout the polymerization. Caprolactam left over to compensate for the cations is inevitable and determines the maximum obtainable degree of conversion, in other words a conversion of 100% is not achievable [4]. In literature, conversions of 98 % and higher have been reported for various activator/catalyst combinations [5]. Additional Caprolactam in the final product is caused by other phenomena (processing conditions, pollutions, …) and should be kept to a minimum.
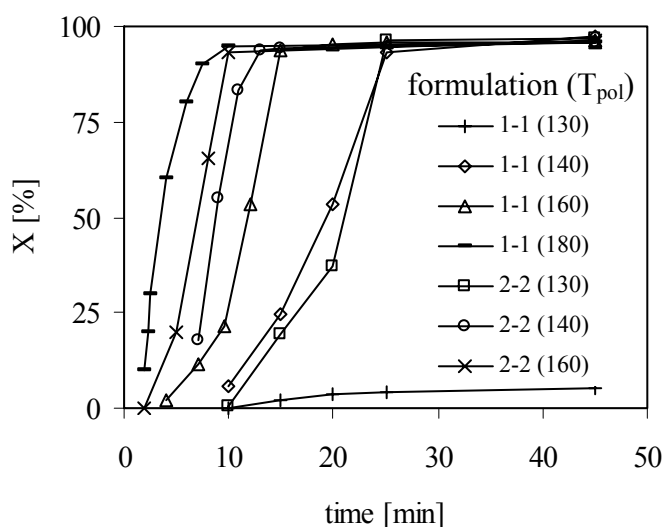
Fig. 2 Degree of conversion-time relations for anionic polymerization of Polyamide-6

Table 1 Final degree of conversion at a polymerization temperature of 140 °C

Formulation	Final degree of conversion [%]
1-1	97
2-1	97
5-1	97
1-2	94
2-2	94
1-5	93
5-5	93

Processing windows

For both the 1-1 and 2-2 formulation a processing window for various polymerization temperatures is constructed, see Fig. 3. A degree of conversion of 10 %, which correlates to a viscosity of 1 Pa·s, determines the end of the injection window. In the rheology experiments, the time to reach 10 % conversion appeared to be longer than in the experiments with the reaction tubes quenched in liquid Nitrogen. The explanation for this is that a single rheology test requires more reactive mixture (450 ml vs. 30 ml in a reaction tube). Consequently, heating up the material takes longer and polymerization is delayed. It can be concluded that part thickness is also an important parameter in constructing the processing window. The processing windows presented make use of the results obtained from the reaction tube tests and, therefore, are more

representative for manufacturing of thin walled composites. After 95 % conversion, the product can be demolded. It can be clearly seen that by adding more catalyst, the polymerization is much faster up to a degree of conversion of 90%. However, compensating for the higher concentration of cations takes its toll in terms of a longer processing time to reach 95% conversion.
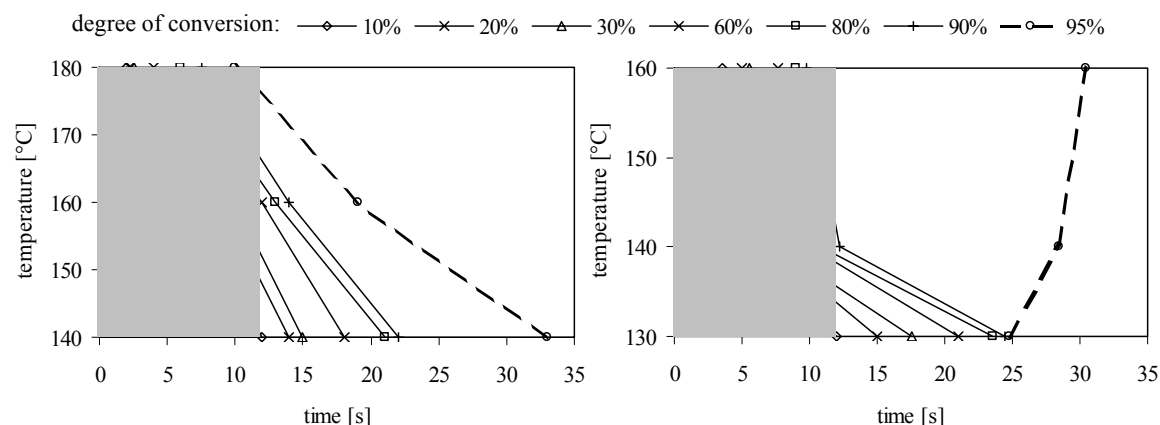
Fig. 3 Vacuum infusion processing windows for 1-1 (left) and 2-2 (right) formulations of Anionic Polyamide-6. Gray area represents the injection window, dotted line indicates demolding time.

CONCLUSIONS

A processing window for vacuum infusion of fiber reinforced Anionic Polyamide-6 was constructed for two resin formulations. Time to complete infusion and time to demold are indicated. Addition of more catalyst reduces the final degree of conversion, due to compensation for the higher number of metal cations present. This compensation also causes the polymerization process to slow down significantly above conversions higher than 90%. It was shown that besides resin formulation and polymerization also the part thickness has a strong influence on the processing window.

ACKNOWLEDGEMENTS

REFERENCES

1. www.dsm.com
2. A.A.van Geenen, DSM Fiber Intermediates, "Anionic Polyamide – Chemistry and Processing", personal communications.
3. Udipi, K., Dave, R.S., Kruse, R.L. and Stebbins, L.R., Polyamides from lactams via anionic ring-opening polymerization: 1. Chemistry and some recent findings, Polymer, Vol. 38, Number 4, p. 927-938, 1997.
4. A.A. van Geenen, DSM Fiber Intermediates, personal communications.
5. Ricco, L., Russo, S., Orefice, G. and Riva, F., Anionic Poly(ε-caprolactam): Relationships among Conditions of Synthesis, Chain Regularity, Reticular Order, and Polymorphism, Macromolecules, Vol. 32, p. 7726-7731, 1999.

Stamp-Forming of Reactive-Thermoplastic Carbon Fiber/Pa12 Composite Sheet

M.D. Wakeman[1], L. Zingraff[l], P. Blanchard[2], J.-A. E. Månson[1]

[1]*Ecole Polytechnique Fédérale de Lausanne (EPFL),*
Laboratoire de Technologie des Composites et Polymères (LTC),
CH-1015 Lausanne, Switzerland
Email: jan-anders.manson@epfl.ch

[2]*Ford Motor Company, Ford Research Lab,*
2101 Village Road, Mail Drop 3135,
Dearborn, MI 48121, USA
Email: pblanch3@ford.com

SUMMARY: Stamp-forming trials were performed on prepreg sheets of carbon fiber reinforced PA12. A thermoplastic resin transfer molding technique was used as an interim process for experimental CF/PA12 sheet production. Design of experiment techniques were used to determine statistically significant parameters prior to more detailed investigation of void content evolution. Having demonstrated the effectiveness of the stamping process, coupled impregnation and polymerization models, linked to a technical cost model, were used to establish the feasibility of a continuous reactive impregnation line to supply such a stamping process. Over-injection molding of scrap stamped composite sheet onto the formed component was shown to integrate the structural stiffness of textile composites with the added functionality and shape stiffness of flow molding techniques, giving a closed loop recycling route.

KEYWORDS: *Stamp-forming, reactive-thermoplastic systems, continuous impregnation line*

1. INTRODUCTION

In response to driving forces requiring weight reduction in automotive structures, a stamp-forming process has been developed using carbon fiber fabrics impregnated with a reactive thermoplastic material system. This approach has been developed for large manufacturing volume applications with an emphasis on reducing production costs. This was achieved by rapid, non-isothermal stamping of a novel carbon fiber reinforced polyamide material, which offers a reduction in semi-finished material costs. Carbon fiber reinforced plates were produced via thermoplastic resin transfer molding (TP-RTM). The objectives were to identify the dominating stamping parameters and to investigate the effects of 3 activator concentrations (influencing polymer viscosity) on final stamped part quality. The potential of scaling the plaque RTM production process to a continuous reactive impregnation line was then investigated with coupled impregnation, polymerization and cost models. As a trimming operation was required after stamp forming of the blank, over-injection molding of recycled material onto a stamped composite sheet was studied as a means of cost effective recycling of scrap material.

2. MATERIALS AND CF/APLC12 PREPEG PROCESS

---

[1] To whom all correspondence should be addressed

2.1 Material system

A reactive thermoplastic system, with in-situ polymerization of low viscosity monomer, was used to reduce fiber bed impregnation times [1]. This consists of a cyclic amide monomer (laurolactam) that, once activated, polymerizes in the fiber bed into polyamide 12 via an anionic ring-opening reaction (APLC12). The polymerization kinetics and the final molecular weight are controlled by the type and concentration of initiator and activator, together with process temperature. Three activator concentrations of 2%, 2.7% and 4% used in this study yield theoretical molecular weights of 45k g/mol, 27k g/mol and 23k g/mol.

2.2 Thermoplastic RTM process

Thermoplastic resin transfer molding was used to produce the plates (56% V_f) (Figure 1) stamped in this study [2]. The injection unit consists of two tanks/gear pumps/pipes conveying the initiator and activator (liquid system) and monomer from the tanks to the mixing head. The monomer is molten during processing while the liquid system is at room temperature; both are held under nitrogen giving a neutral environment. Immediately prior to injection, the monomer and liquid system are combined in a static mixing head. A RTM tool with a line gate was used to produce plates measuring 450mm x 550mm. For a 1mm plaque thickness, two layers of a 5-harness satin CF weave (440 g/m^2) were used [0/90]$_s$. At a tool temperature of 180°C, activated monomer was injected into the fiber bed, and heating continued to a peak temperature of 200°C, which was then held to complete polymerization. Following the polymerization phase, the tool was cooled prior to demolding. These steps were achieved in less than 60 minutes. Typical CF/APLC12 properties were: tensile stiffness and strength of 56GPa and 600MPa (ASTM D638), flexural stiffness and strength of 55GPa and 450MPa (ASTM D790), and a compressive

Figure 1   CF/APLC12 plate cross section (before heating/stamping): porosity =3.5%

strength of 155 to 260MPa, for 1 and 3mm thick plaques respectively (ASTM D3410).

3.   STAMP-FORMING TRIALS

3.1   Processing facility

Processing of the CF/APLC12 plates was performed by non-isothermal stamping. The facility (Figure 2a) consisted of a fast response medium wave 12 zone infra red oven with upper and lower pyrometer control. This was linked by a shuttle system to a fast acting hydraulic press, with typical transfer times of 2s. Trials were conducted with both a flat plaque tool and with a generic double curvature tool (Figure 2b). This incorporated a 6-zone segmented blankholder system (individually controlled temperature and pressure levels), and enabled consideration of deformation mechanisms and measurement of coupon-based mechanical properties.
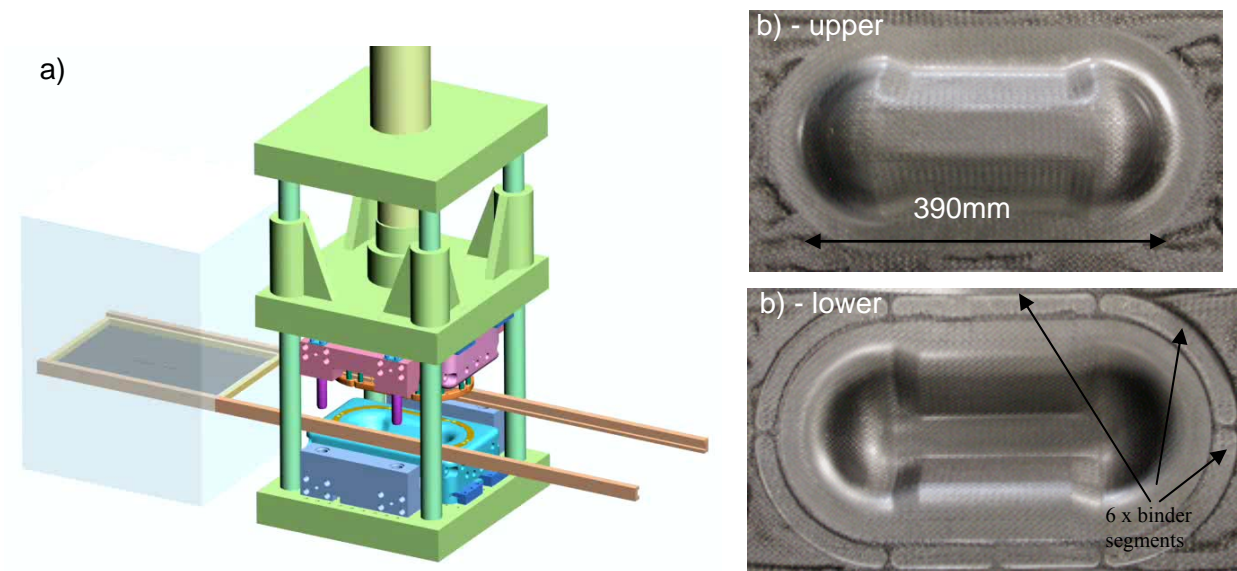
Figure 2   a) Stamp-forming cell   b) stamped CF/PA12 generic component

3.2   Preheat studies

Preheat cycles, typically 120s to 280°C, were determined using thermocouples. The material exhibited limited deconsolidation (compared with commingled yarn [2]), and maximum porosity was below 10% after heating to between 180 and 280°C. Marginally increased deconsolidation occurred for higher activator levels (and hence lower viscosities). Any deconsolidation from the preheat cycle should ideally be reduced during the final stamping process.

3.3   Determination of dominant stamping process parameters

The influence of material preheat temperature (200°C, 280°C), tool temperature (20°C, 120°C), stamping rate (12mms^{-1}, 166mms^{-1}), and time at pressure (10s, 30s) on compressive strength of 1mm thick flat plaque was investigated using a 16 run Taguchi array. Pressure was set at 40bar, after which in-plane flow of matrix material can occur. Compressive strength data was analysed. Statistically significant trends (90%) were that higher tool temperatures and increased stamping rates increased the compressive strength. Time at pressure was not statistically significant, and hence 10s was used thereafter for 1mm thick parts to give a cost effective process.

3.4 Effect of APLC12 activator concentration and preheat temperature

The influence of preheat temperature (180°C, 235°C, 270°C), and activator concentration (2, 2.7, 4%) was studied (9-run array). Parameters held constant were: tool temperature (120°C), stamping rate (166mm/s), pressure (40bar), and time at pressure (10s). Figure 3 shows compressive strength versus process conditions. Higher preheat temperatures increased compressive strength until a reduction at 270°C was approached (oxidative degradation). Increased activator concentrations, reducing Mw and lowering viscosities, increased compressive strength. PA12 degradation reduced properties at higher temperatures. After stamping, porosities were typically 3% for 1mm structures (Figure 4).
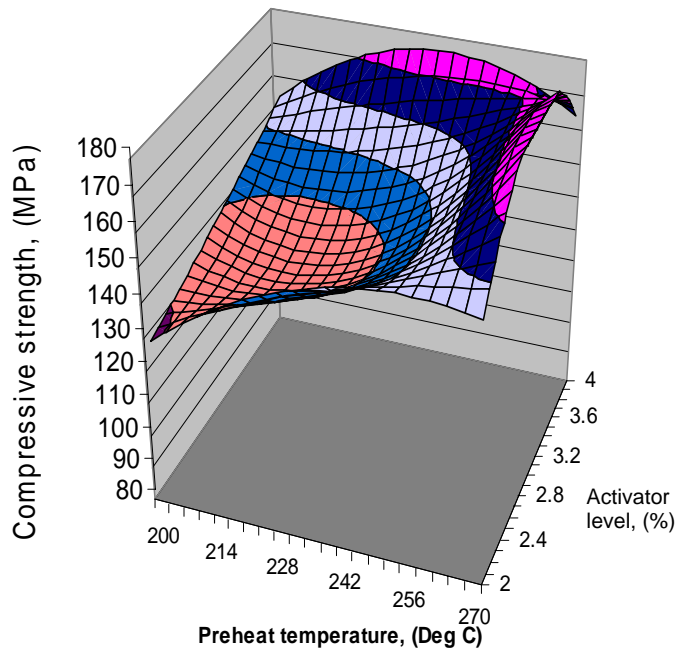
Figure 3   MLR model of CF/APLC12 study

Figure 4   CF/APLC12 stamped sheet cross-section (preheat temperature = 200°C, stamping rate = 166mms^{-1}, 2% activator level) void content =3.1 %

3.5 Over-injection molding trials

Recycled CF/APLC12 was compounded with virgin PA12 (adjusting the CF M_f to 40%) and over-molded onto a 3mm thick CF/APLC12 stamping. A standard injection cycle was used, with the CF/APLC12 stamping prewarmed ($<T_m$) to facilitate in-situ fusion bonding during over-injection. Hence the intrinsic stiffness of stamped sheet was combined with the functionality and shape stiffness of injection molding, while giving a closed loop recycling route for stamping trim. Figure 5 shows the ribbed plate structure.
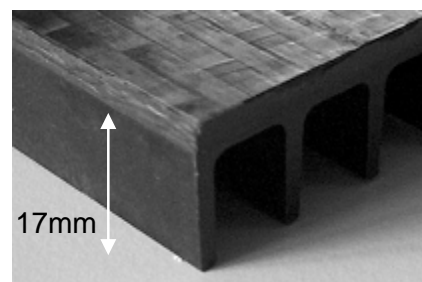
Figure 5 Over-injected stamping

4. CONTINUOUS REACTIVE IMPREGNATION LINE

Having demonstrated the stamp-forming of CF/APLC12 sheet produced by a batch TP-RTM process, a concept for a continuous reactive impregnation line was developed (Figure 6). Molten activated monomer would be sprayed onto fiber textiles passing continuously through an impregnation chamber and subsequently a polymerization oven, after which cooling and compaction would occur via calendaring rollers. Full preconsolidation would be of limited gain

due to preheat stage deconsolidation. A high line rate should result with low pulling forces (an impregnation die is not used) compared with an injection-pultrusion process [3]. Reduced equipment investment compared with conventional double-belt press preconsolidation processes should also occur. A model coupling impregnation mechanisms and reaction kinetics [1] of the APLC12 system was therefore developed to predict the line speeds for such a reactive impregnation line. This was then used as an input into a technical cost model [4] to estimate the final impregnated sheet cost per kg. The following approach and assumptions were taken:

- pressure applied by the spray system gives a constant driving impregnation pressure;
- material delivery rate is constant with time;
- material viscosity varies with time and the degree of polymerization;
- degree of conversion in the impregnation chamber is assumed zero (i.e. all polymerization is assumed to initiate and complete in the polymerization oven)
- time taken for the material to increase from 180°C to 245°C is assumed instantaneous.
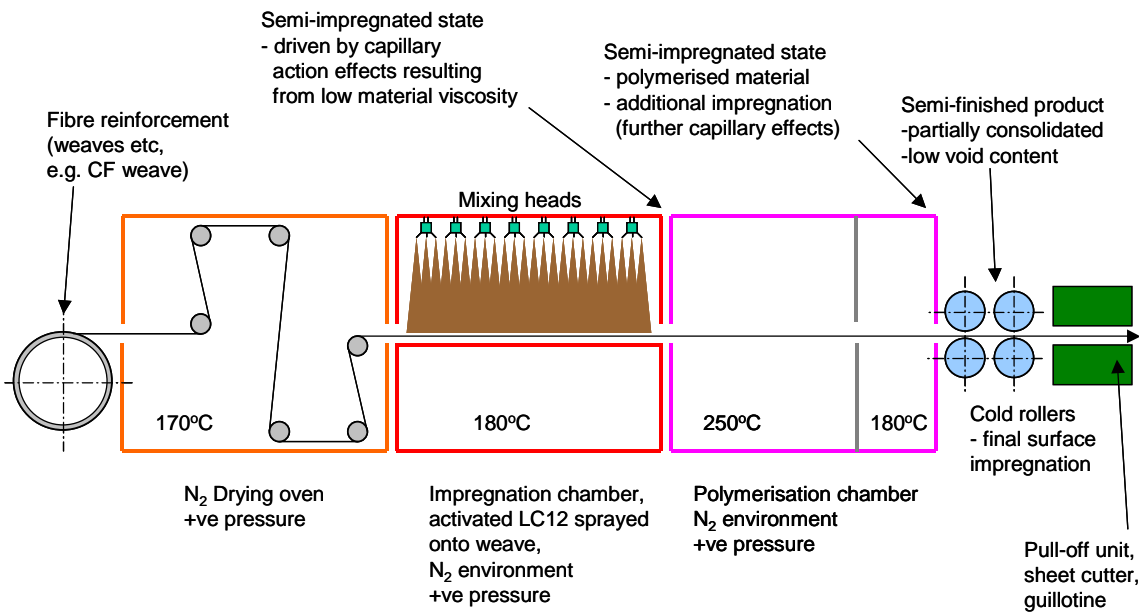
Figure 6   Continuous reactive impregnation line: textile carbon impregnated with APLC12

4.1   Impregnation and polymerization

Polymerization of the sprayed activated monomer will initiate before entering the polymerization chamber. Therefore, with viscosity versus time $\eta\,(t)$ a function of the degree of conversion and hence varying during impregnation, infiltration length depends on viscosity build up and hence the integral form of Darcy's law was used:

$$L^2 = \frac{2K}{\left(1-V_f\right)}\left(P_a + P_c\right)\int_0^{t_{final}} \frac{dt}{\eta(t)} \tag{1}$$

After finite difference integration, this can be rewritten as:

$$L^2 = \frac{2K}{\left(1-V_f\right)}\left(P_a + P_c\right)\sum_{i=1}^{n}\left(\frac{1}{2.14\cdot\exp\left(-0.028T_i + \left(12.08 + 0.016T_i\right)\beta_i\right)}\right)\frac{t_{final}}{n} \tag{2}$$

Where: L is impregnation depth at time t_{final}, K fiber bed permeability (Z-direction), P_a spray system pressure, P_c capillary pressure, V_f carbon fiber volume fraction, T_i temperature (in °C) at time I; and β the degree of conversion at time i.

Upper and lower bounds, detailed in Table 1, were substituted in Equ. (2) to evaluate the continuous line. The upper bound transverse permeability was calculated based upon a quadratic fiber arrangement geometric approximation as 1.7×10^{-12} m². This compared well with experimental data for the 5-harness satin weave of 14.1×10^{-12} m² for a V_f of 47% (lower bound). The capillary pressure depends on V_f and the infiltration velocity, and hence the upper and lower range of measured capillary pressures was used. An additional driving pressure results from the impingement speed of the sprayed droplets. The depth of impregnation, for a 5m long impregnation zone, was calculated numerically by a time summation of 1s steps; from zero to the time available for impregnation, with activated monomer penetration predictions in Figure 7.

Table 1   Upper and lower bound assumptions for continuous line model

Symbol and designation		Upper bound	Lower bound
L	depth of impregnation	variable of interest	variable of interest
K	fiber bed permeability in the Z-direction	1.4×10^{-11} m²	1.7×10^{-12} m²
P$_a$	pressure of the spray system	10,000 Pa	1,000 Pa
P$_c$	capillary pressure	1,400 Pa	500 Pa

For low line speeds (0.25 - 1 m/min), the infiltration time was sufficient for the viscosity to significantly increase, subsequently limiting the infiltration depth, as shown by the plateau. For the lower case, impregnation of a 2 mm thick textile required 6s, or at a line speed of 50 m/min, an infiltration zone length of 5 m enabled impregnation of a 2 mm thick textile. For the upper case, 2mm thick sheet could theoretically be produced above 50m/min with a 1m-impregnation zone. Hence the increasing activated monomer viscosity does not represent a significant limiting effect on line speed when infiltration is considered.
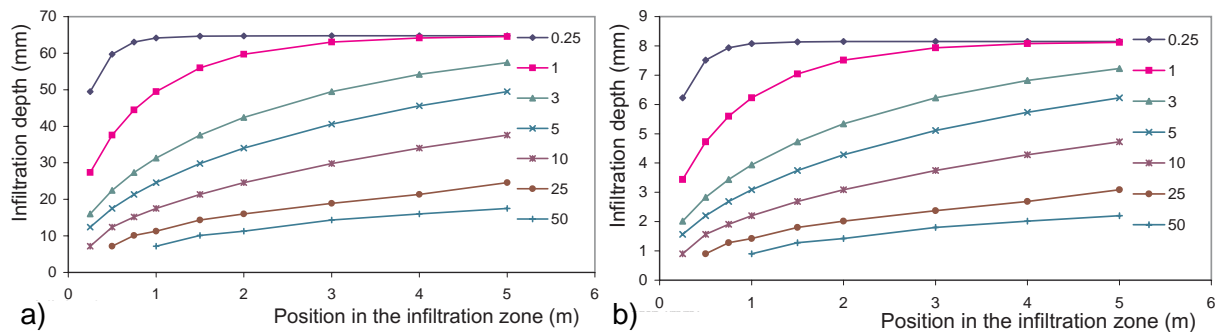
Figure 7   Depth of impregnation vs. impregnation zone position vs. line speeds (m/min); 2 wt.% of liquid system: a) Upper, b) lower bound

Following impregnation of the fiber bed, it was assumed that all polymerization occurs in the polymerization chamber at 250°C. This neglects the 10% conversion in the impregnation chamber (2 minutes at 180°C). The time required to reach 99.5% conversion (2% activator) at 250°C was 218 s, enabling the effect of line speed on polymerization zone length to be

determined. For the lower case, a line speed of 5m/min and a 2mm impregnation depth would require impregnation and polymerization chambers of 0.5m and 18m respectively; chamber length reduces further to 0.25m and 11m for a line speed of 3m/min. For the upper case the depth of impregnation did not limit line speeds in that an impregnation depth of 7mm was still possible at 50m/min for a 1m-long impregnation zone.

4.4 Technical cost modeling (TCM) of the prepregging line

Based upon an X-brace concept for the Ford Thunderbird [4], the cost (excl. tax/profit) of using a continuous line at 3m/min to produce CF/APLC12 preforms (1.5m wide and 1.7 mm thick) was considered (Figure 8). Upper (2 M€) and lower (1 M€) line cost estimates were modeled. Costs were calculated for utilization-based (Ut) scenarios (i.e. cost per minute) and 1, 2 and 3 shift-
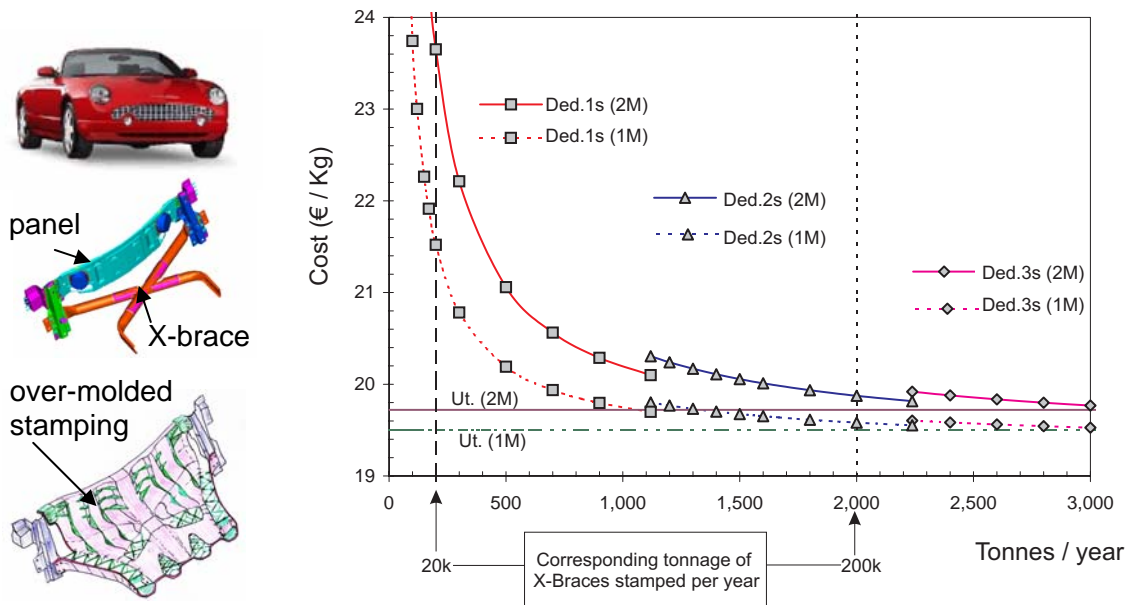
Figure 8   a) Concept application, b) CF/APLC12 prepreg cost/ kg vs. tonnes/year

based dedicated (Ded.) scenarios (line amortised over one product or client). A carbon fiber cost of €15/kg was used. For the X-brace component, a preform weight of 10kg was required to replace a steel part of 19.3kg. This required a 2.75m long CF/APLC12 preform (ρ = 1.43 g/cm^3). At a line speed of 3m/min, 3,700 tons/year could be produced (or 5.5 s for 1kg of preform).

For utilization-based prepreg lines (assuming full line capacity usage), equipment costs had a limited influence. With an arbitrary 30% increase for taxes and profit, the CF/APLC12 prepreg cost of 25.6 €/kg would offer a significant reduction versus commercially available materials. Where full production capacity could not be assumed, a dedicated-based scenario should be considered. Stamp-forming 20k or 200k X-brace/year would require 1 shift production to supply 200 tons/year or 2 shifts for 2000 tons/year. Prepreg costs would be (upper case, excl. tax and profit) 23.6 and 19.9 €/kg respectively.

5.   CONCLUSIONS

Stamp-forming trials of CF/APLC12 plate, produced by a TP-RTM process, were performed to demonstrate process feasibility. To reduce prepreg cost compared with commercial products, a continuous reactive impregnation line was modeled. The line speed was predicted based upon coupled impregnation and polymerization models. For a prepreg line rate of 3m/min, a TCM was used to show the considerable cost potential of CF/APLC12.

6.   ACKNOWLEDGEMENTS

7.   REFERENCES

1. Luisier, A., P.-E. Bourban, J.-A.E. Månson, "Time-Temperature-Transformation Diagram for Reactive Processing of PA12". Applied Polymer Science, 2001, 81, p.963-972.
2. Wakeman, M.D., Zingraff, L., Kohler, M., Bourban, P.-E., Månson, J.-A.E., "Stamp-forming of carbon fiber/PA12 composite preforms" ECCM10, June 3rd-7th 2002, Brugge, Belgium
3. Luisier, A., P.-E. Bourban, and J.-A.E. Månson, " Reaction injection pultrusion of PA12 composites: process and modeling", Composites: Part A 34 (2003) 583–595
4. Wakeman, M.D., Månson, J.-A.E., "Design and Manufacture of Textile Composites" Chapter 11: Cost analysis, Ed. A. Long, Woodhead, to be published summer 2004

Resin Transfer Molding Of Anionically Polymerized Polyamide 12

V. Michaud, L. Zingraff, J. Verrey, P.-E. Bourban and J.-A.E. Månson

Ecole Polytechnique Fédérale de Lausanne (EPFL)
Laboratoire de Technologie des Composites et Polymères (LTC)
CH-1015 Lausanne, Switzerland
Corresponding Author's e-mail: jan-anders.manson@epfl.ch

SUMMARY: The infiltration of Lactam12 monomer and activator system into non-crimp fabrics or satin weave carbon fabrics is presented herein, with emphasis on the specific features of this system, as compared to traditional thermoset RTM. Capillary effects are shown to be significant, and their magnitude to depend on the fiber bed architecture, volume fraction and on the matrix flow-rate. In addition, the main sources for void content in the final parts are identified. The polymerization and solidification shrinkage are quantified to account for at most 9 % in the matrix. The infiltration process is studied in details to assess the role of flow rate on the formation of voids. Optimal flow conditions are determined to minimize void content during liquid molding. Finally, as the monomer is kept under Nitrogen, diffusion and solubility of Nitrogen in the monomer are characterized, to indicate that Nitrogen bubbling during injection is a major cause of voids in the final part. The average void content is reduced from initially 17% to below 1% in flat composite plates with optimized process conditions. In parallel, complex shapes including thickness variations and hollow cores are produced, demonstrating the strong potential of this material system.

KEYWORDS: reactive thermoplastic, polyamide 12, capillary effects, void reduction

INTRODUCTION

Resin Transfer Molding is traditionally reserved to thermoset matrix composites, where it finds a wide number of applications. For thermoplastic matrices, this technique is in general not possible because of the high viscosity of the matrix. Solvent processing would be feasible but is not environmentally acceptable. The infiltration of the monomer of a given thermoplastic polymer together with an activator provides an elegant solution: the monomer viscosity is often very low (comparable to that of water or molten metals), so injection is easy and requires low pressures. The polymerization reaction then proceeds within the fiber bed [1]. Among potential systems, the Lactam 12 is anionically polymerized (APLC12) using a liquid activator and catalyst system to form Polyamide 12 (PA12). The monomer and activator system can thus be mixed in the liquid state and injected as in conventional RTM, to yield PA12 matrix composites. Although very similar in concept to thermoset RTM, the APLC12 process raises a number of specific issues. Emphasis has been placed on the definition of optimal process windows for the infiltration process, and on improving the quality of the final part, in terms of final conversion

rate, but also in terms of void content. This paper reviews recent research at LTC on infiltration of APLC12 into non-crimp fabrics or satin weave carbon preforms. After a brief description of the materials and the process, the role of capillary effects will be highlighted, as well as the strategy for void reduction, based on the analysis of matrix shrinkage, flow rate optimization and diffusion and solubility of gases in the monomer. Differences and similarities with thermoset processes, in particular with epoxy matrices, will be pointed out.

MATERIALS

The resin system consists of a cyclic Lauryllactam monomer, which polymerizes into Polyamide 12 via an anionic ring-opening reaction. The monomer is stored above its melting temperature of 154°C, under a Nitrogen flow to prevent its degradation with oxygen. The liquid activating system contains both activator (carbodiimide) and catalyst (sodium-caprolactam) in solution [2,3], and is kept at room temperature, also under Nitrogen. Stored separately in an inert atmosphere, the reactants have an infinite shelf life. The polymerization is sensitive to both the purity of the compounds and the presence of moisture, oxygen and other products such as amines and acids. The polymerization kinetics are characterized as a function of temperature and activator content together with the evolution of the viscosity of the system with time and temperature [2, 3]. With 1.5% activator content, the viscosity of the resin is measured to be initially $\eta=2.3\ 10^{-2}$Pa·s at 180°C, and to increase slowly within the first 80s. The time for complete polymerization is about 50 min at 190°C and is reduced to 20 minutes at 210°C. A Time-Temperature-Transformation diagram is also established to help define the processing window for this system [2]. It is found that because of a phase separation between the partially converted polymer and the monomer, as well as because of the long polymerization kinetics, the infiltration and polymerization should be performed above the melting temperature of the polymer (175°C). This, in turn, implies that the mold be cooled down after polymerization is complete, in order to remove the part. The need to cycle the mold temperature up to above 180°C certainly represents an economic burden and an increase in the total cycle time compared to thermoset RTM, since thermoset parts can be de-molded hot when the vitrification time is reached.

The fabrics were all manufactured with Tenax 5N21 high tensile strength carbon fibers. This fiber was selected because its sizing does not inhibit the polymerization reaction. Commercial epoxy type sizings cannot be used, as the presence of oxygen and amino groups reduces the extent of polymerization. Two types of fabrics were investigated, a 5-harness satin weave of 440 g/m^2, and a bi-axial ±45° fabric of 626g/m^2, stitched with PA66 threads.

EXPERIMENTS

The thermoplastic liquid composite molding process consists in the following steps, which are very similar to thermoset RTM with a flow-rate controlled equipment. The molten monomer and liquid activator are pumped separately to a mixing head connected to the mold to enable injection of activated monomer. With the laboratory scale equipment available, the maximum flow rate achievable is 0.1l/min. The mold contains the reinforcement preform through which

infiltration occurs. All the process is run at a minimum of 175°C. After complete polymerization, the mold is cooled down, enabling solidification and crystallisation of the PA 12 matrix.

Two molds were used in this investigation. A small mold was developed to monitor the position of the flow front during infiltration, the inlet pressure and the mold temperature (Figure 1). APLC12 composites were thus processed at different flow rates with the two fabric types. Polished sections of the obtained plates (170 x 230 mm^2) were analysed under a microscope, and the void content was quantified by image analysis.
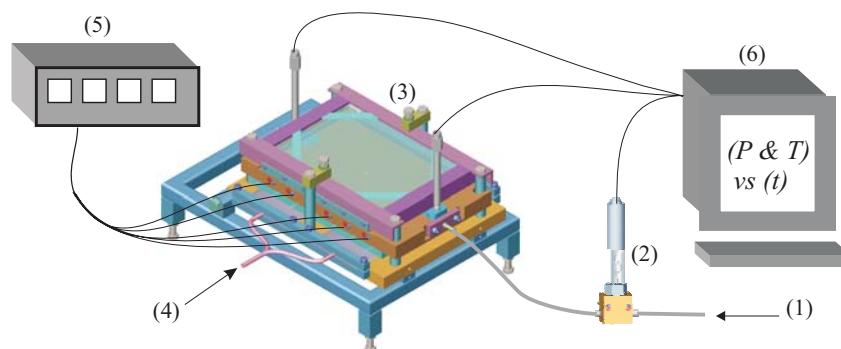
Fig. 1. Infiltration set-up, with: (1) Inlet for activated Lactam 12; (2) High accuracy pressure transducer; (3) Mold composed of a heated steel half-mold and a glass upper half-mold; (4) Compressed air inflating hoses to close the mold; (5) Heat regulation system; (6) Computer + acquisition system.

A large mold was manufactured to produce demonstration parts, which includes several features typical of a car floor-pan (hollow crossbeams, thin monolithic walls and various thicknesses) that could not be manufactured in a direct stamping operation. Figure 2 shows the bottom half of the mold. Both molds are designed to withstand temperatures up to 250°C since the polymerization of the matrix occurs at about 190°C or above. Additional details on the large mold are given in Ref. [4].

CAPILLARY PHENOMENA

A great potential of APLC12 compared to thermoset RTM is the very low viscosity of the infiltrating resin, thus reducing infiltration times or the need for high flow-rates. Also, as the infiltration is run at high temperature, it seems preferable that the resin pressure remains low in the mold, to alleviate the additional need for expensive frames or clamping equipments. This is the reason why low flow-rates are investigated. In this framework, it thus becomes relevant to investigate the magnitude of the capillary pressure drop at the flow front $\Delta P\gamma$, which is often neglected in thermoset RTM, where the inlet pressure is in general much higher than $\Delta P\gamma$ values [5]. A technique presented by Verrey *et al.* [6] is used to evaluate the capillary pressure drop in a dynamic experiment from the curve of inlet pressure increase versus time, assuming that the flow

is saturated [7]. For NCF fabric, with a volume fraction fibers of 50%, and a flow rate of 0.1l/mn, a value of $\Delta P\gamma$ =-13.8±3.0kPa is obtained. The negative value indicates that the LC12 wets the reinforcement, so that flow is enhanced. Also, as the maximum inlet pressure reached during infiltration is about100kPa above the
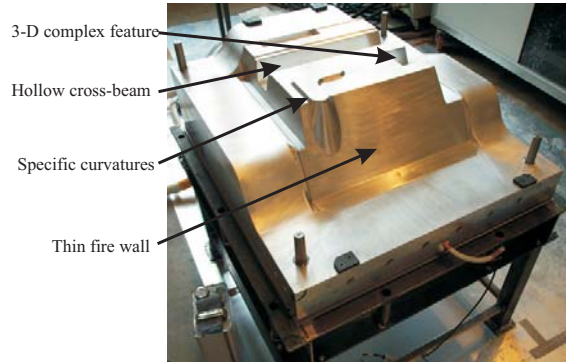
Figure 2. Lower part of the mold designed for thermoplastic components.

atmospheric pressure, $\Delta P\gamma$ represents a minimum of 14% of the pressure differential driving the flow. Similar experiments performed on NCF with an epoxy matrix have shown that effects of a similar magnitude are found for epoxy, but with an opposite sign, indicating that viscous forces tend to counteract the flow of epoxy during infiltration, although both systems are wetting according to thermodynamics [6]. This also observed directly on parts manufactured with interrupted experiments, as shown in Figure 3. When the injection is stopped, capillary forces induce a rise of resin within the bundles, leading to an unsaturated flow front. The capillary rise is of about 1 cm for the epoxy system, whereas it reaches 10 cm in the LC12 system. This indicates that the LC12 system can be injected at very low pressure, and let to infiltrate under its own capillary forces, with reasonable flow kinetics.

Similar experiments were performed with the satin weave fabric, for volume fractions of 40 to 48%, with varying flow-rates. The results are given in Figure 4, where $\Delta P\gamma$ is plotted as a function of a modified capillary number $Ca=\dfrac{Q\quad\eta}{A(\ 1-V_f\ )\gamma_{ma}}$, where Q is the flow-rate, A the cross-section of the fabric, η the viscosity of the matrix and γ_{ma} the surface tension of the matrix. The capillary pressure drop is still found to be negative, and increases slightly with the flow-rate, as expected from Tanner's law for dynamic wetting [7]. The magnitude is however much lower than found with the NCF fabric at a capillary number of Ca=0.0033. This was also observed with epoxy resins, and indicates that the local arrangement of bundles within the fabric plays a large role in its propensity for capillary infiltration. This should thus be checked if the process is sought to rely on capillary infiltration.

Epoxy   LC12

Saturated flow front   Unsaturated flow front

■ Dry fabrics   ■ Unsaturated region   ■ Saturated region
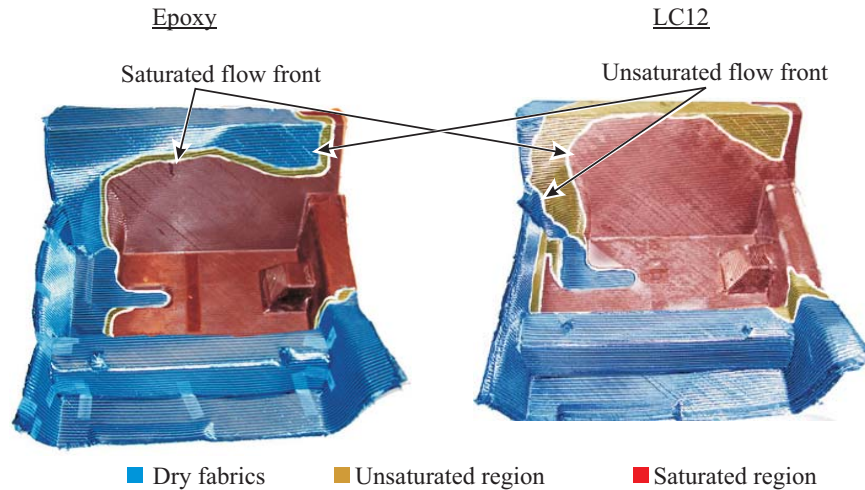
Figure 3. Non-saturated flow front in incomplete parts with Epoxy and LC12, respectively.
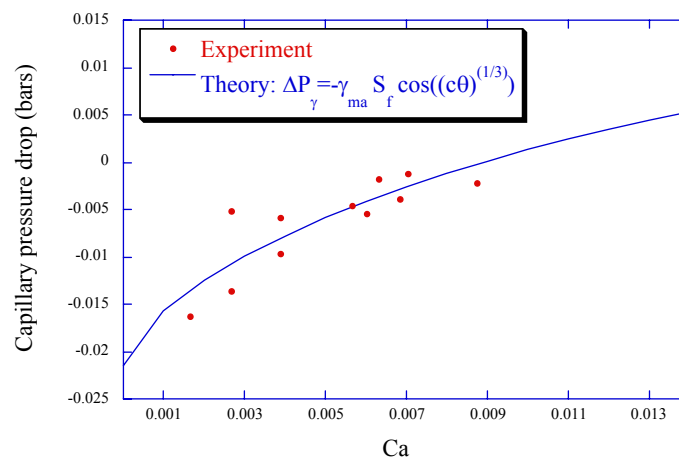
Figure 4. Capillary pressure drop as a function of *Ca* for the satin weave.

PART QUALITY

A necessary requirement for the APLC12 RTM process to reach a mature stage is a part quality comparable to that obtained with thermoset RTM. A first issue to address is the residual monomer content in the part. High levels of conversion are now achieved provided that the fiber sizing does not inhibit polymerization, that the preform be thoroughly flushed with Nitrogen before the infiltration, and that enough time, as indicated by the cure kinetics diagrams, is allowed for the system to polymerize before cool-down. The second issue is the residual void content in the part. Concerning this last point, a large body of knowledge has been gathered in the case of thermoset RTM [8-15], which can be quite directly applied to reactive thermoplastic processes. These studies identified the causes for void formation to include the diffusion of gases in the resin during storage, mechanical air entrapment during infiltration, nucleation of voids due to chemical reaction between the resin and the reinforcement or the release agent, leakage of the mold, inhomogeneity in the reinforcement. These phenomena result in different types of voids such as dry spots (large un-impregnated zones), macroscopic voids (entrapped air during the

infiltration process), microscopic voids (incompletely infiltrated bundles), voids created by moisture or gas liberation in the resin, or voids created by cavitation due to resin shrinkage. Following guidelines established in the literature, these points were investigated for the APLC12 system.

Matrix shrinkage

The volume evolution of LC12 upon polymerization and cooling was measured by monitoring the location of the free surface of a small amount of silicon oil placed above the molten system in a graduated test-tube [16,17]. The influence of the cooling rate and of the amount of activator were investigated. Opposite to the case of epoxy [18], no detectable shrinkage was observed during polymerization. However, shrinkage was measured during cool-down, since a fraction of the material crystallizes upon cooling below the Polyamide 12 melting temperature (174°C), while the amorphous fraction remains rubbery until the glass transition temperature (40°C). At low cooling rate (about 1.5°C/min), a volume shrinkage of 9.3% was measured, whereas at high cooling rate (about 5.5°C/min) a slightly lower value of 8.6% was obtained. By increasing the liquid activating system to LC12 ratio, a slight decrease in total shrinkage was measured, from 9 to 8.3 for an activator content ranging from 1.5 to 9 %. In summary, for most cases, the maximum void content arising from cooling shrinkage is about 9 % in the matrix, and will be reduced in the composite proportionally to the volume fraction of reinforcement. Nevertheless, care should be taken to ensure a controlled cooling of the part, as in thermoplastics molding and metal foundry practice.

Flow velocity

As observed and quantified for thermoset and model resins, the infiltration velocity, directly related to the flow rate in the present case, may influence the formation and the location of voids in the final part [13-15]. This is explained by the relative magnitude of the capillary versus viscous forces during infiltration, as represented by the capillary number *Ca*. Below a critical value of the capillary number, the capillary effects dominate so that the bundles are infiltrated ahead of the flow front. This may lead to gas entrapment in the inter-bundles spaces. Above the critical capillary number, the viscous forces dominate and inter-bundle flow may lead, resulting in micro-porosities inside the fiber bundles. Ideally this critical capillary number should correspond to the value at which the capillary pressure drop crosses 0 in Figure 4, at *Ca*=0.009.
A series of plates was thus manufactured with the satin weave, for different values of the flow-rate leading to capillary numbers between 0.002 and 0.01. The void content was measured, counting separately the inter-bundle void content, and the intra-bundle void content, on polished cross-sections, taken at various locations in the plate, near the inlet and in the middle. The results are given in Figure 5. First, a very large void content is observed in all cases, 6% being the minimal value observed. Secondly, a trend as predicted by the analysis of Patel *et al*. [13-15] is indeed observed. Microscopic observations support the hypothesis that inter-bundle voids dominate at low Ca, whereas intra-bundle voids dominate at high Ca. Finally, a "critical" Ca value is found at about 0.007, within the range of the value predicted above.
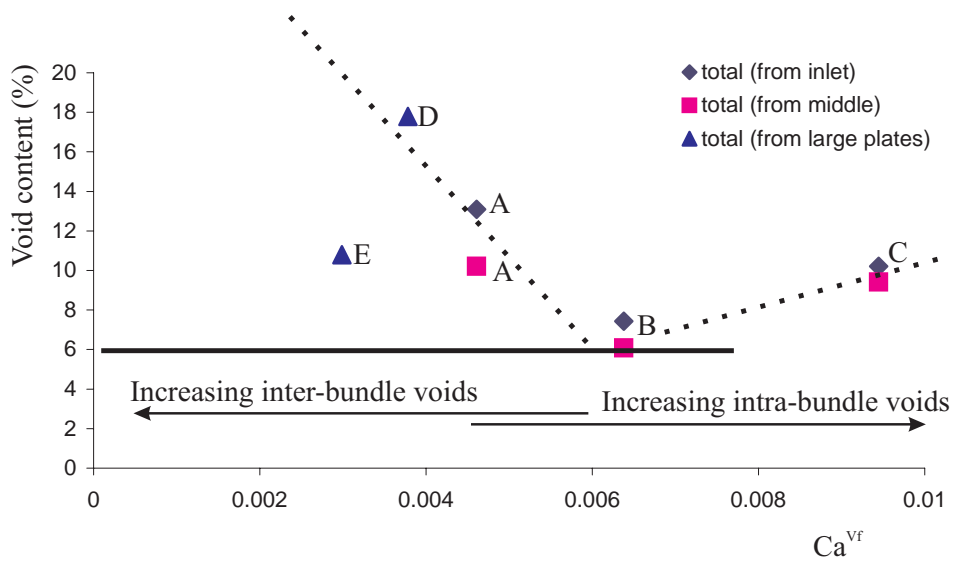
Figure 5. Void Content versus experimental Capillary number *Ca* for the satin weave.
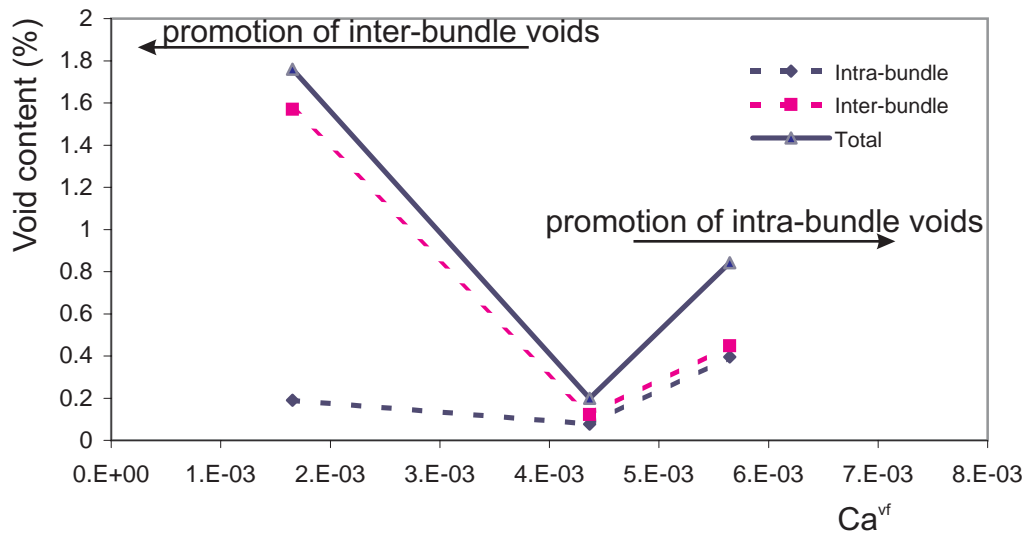
Figure 6. Void content versus experimental capillary number *Ca*, for degassed monomer and the satin weave.

Diffusion of Nitrogen

In thermoset composite molding, the resin is often degassed before injection to remove the air potentially entrapped during mixing. In APLC12 RTM, the monomer pellets are melted in the tank under Nitrogen, and the molten monomer is then kept under flowing Nitrogen, as recommended by the manufacturer to prevent its degradation. The solubility and diffusion coefficients of N_2 into the molten monomer are thus the critical parameters to evaluate this potential source of voids. Due to a lack of available data, the diffusion coefficient D of Nitrogen

in molten Lactam and the Henry's law coefficient H were experimentally determined by adapting the approach developed by Lundström for thermoset resins [10]. The D value ranges between 0.2 to $1.2.10^{-10}$ m/s^2, in a temperature range between 150 and 200°C, and the H value decreases between 4 and $0.5\ 10^{-5}$ s^2/m^2 in the same temperature range [16,17]. This indicates that if the monomer is initially free of Nitrogen, and stirred slowly, the flowing gas environment should only affect a top layer in the tank. However, since the monomer is melted under Nitrogen, a lot is initially entrapped. When the monomer is injected, its temperature raises from 175°C in the tank to up to 200°C in the mold, thereby releasing Nitrogen, since its solubility decreases with increasing temperature, at atmospheric pressure. To test this hypothesis, a special tank was designed, in which the monomer was melted and kept under vacuum. Several plates were manufactured as described earlier, but with the degassed monomer. The results of void content versus capillary number are given in Fig. 6. It is clear that this was a key factor, as the void content remains consistently below 2%, even though the same trend is observed with an optimal capillary number for best part quality.

CONCLUSION

The infiltration of APLC12 monomer and activator system into non-crimp fabrics or satin weave carbon preforms was reviewed, with emphasis on the specific features of this system, as compared to traditional thermoset RTM. The process windows for this system are now established for part production. The capillary effects are shown to enhance flow, in particular for the NCF fabrics, which are more tightly assembled. It seems thus possible to rely heavily on capillary effects to spontaneously infiltrate APLC12 into fabrics. The part quality was assessed, and it is shown that one can define optimal process parameters to minimize the void content, and that a key issue is to limit the diffusion of Nitrogen in the molten monomer before infiltration. This system thus offers a viable alternative to thermoset RTM, if thermoplastic reinforced parts are to be produced with a complex shape.

ACKNOWLEDGEMENTS

REFERENCES

1   Bourban, P.E., *Liquid Molding of Thermoplastic Composites*, in *Comprehensive Composite Materials*, A. Kelly, Editor. 2000. p. 965-977.
2   Luisier, A., Bourban, P.-E., and Månson, J.-A.E., 2001, Applied Polymer Science, (81), 963-972.
3   Luisier, A., Bourban, P.-E., and Månson, J.-A.E., 2002, Journal of Polymer Science, Part A: Polymer Chemistry, (40), 3406-3415.
4   Verrey, J., Michaud, V. and Månson, J.-A.E., "Processing of complex parts with thermoplastic RTM Techniques", 24th International SAMPE Conference, Paris, April 2003, K. Drechsler Ed. pp.553-561.
5   Michaud, V. and Mortensen, A., "Infiltration processing of fiber reinforced composites: governing phenomena", Composites part A, 32, pp.981-996, 2001.
6   Verrey, J., Michaud, V. and Månson, J.-A.E, "Capillary Effects in Liquid Composite Molding with Non-Crimp Fabrics", paper # 1658, proceedings of ICCM 14, San Diego, CA, 14-18 July 2003.
7   Berg, J., "Wettability", Surfactant Science Series, Vol.49, Marcel Dekker, INC, 1993, 531p.
8   Chen, Y.T., Davis, H.T., and Macosko, C.W., 1995, Aiche Journal, (41), 2261-2273.
9   Lundström, T.S., 1997, Composites Part A, (28A), 201-214.
10   Molnar, J.A., Trevino, L., and Lee, L.J. in Proc *44th annual conference, Composites Institute, The Society of Plastics Industry, Inc.,1989*, 1989, 1-10
11   Parnas, R.S. and Phelan, F.R. Jr, 1991, Sampe Quarterly, (23), 53-60.
12   Parnas, R.S., Salem, A.J., Sadiq, T.A.K., Wang, H.-P., and Advani, S.G., 1994, Composite Structures, (27), 93-107.
13   Patel, N. and Lee, L.J., 1995, Polymer Composites, (16), 386-399.
14   Patel, N., Lee, V., and James Lee, L., 1993, Polymer Composites, (14), 161-172.
15   Patel, N., Rohatgi,V., and Lee, L.J., 1995, Polymer Engineering and Science, (35), 837-851.
16   Zingraff, L., Bourban, P.-E., Michaud, V. and Månson, J.-A.E., "Liquid composite molding of anionically polymerized polyamide 12", paper # 1849, proceedings of ICCM 14, San Diego, CA, 14-18 July 2003.
17   Zingraff, L. "Void formation and transport during Liquid Composite Molding and Forming of reactive thermoplastic composites", EPFL PhD Thesis n°2906, 2003.
18   Eom, Y., Boogh, L., Michaud, V., Sunderland, P. and Månson, J.-A.E., "Stress initiated void formation during cure of a three-dimensionally constrained thermoset resin", Polymer Engineering and Science, Vol.41, n°3, March 2001, pp.492-503

Simulation and Control of the LCM-Process with Future Matrix Systems

Weyrauch, F.; Stadtfeld, H. C.; Mitschang, P.

Institut fuer Verbundwerkstoffe GmbH
Erwin-Schroedinger-Strasse 58, 67663 Kaiserslautern, Germany

Corresponding Author's e-mail: florian.weyrauch@ivw.uni-kl.de

SUMMARY: To increase the efficiency of LCM (Liquid Composite Molding) it is important to increase the number of manufactured parts and to assure a constant quality. Therefore, a concept to design and develop a controlled LCM process will be presented in this paper. The concept is based on a decision tree. A modular program package was developed to implement such a decision tree or a process chart in LabView®. An experimental verification to react on a Race-Tracking-Effect will be presented. In a second study in-situ polymerizing PBT was used and was injected by a completely automated and controlled RTM-Process (Resin Transfer Molding).

KEYWORDS: RTM, Race-Tracking-Effect, Controlled Process, Decision Tree, CBT, PBT

INTRODUCTION

To produce complex and high stressed parts, resin injection processes like RTM are used more and more often. For economic efficiency it is recommended to reduce the rejection of a part and to speed up the process time without reducing the part quality. The use of fixed open loop control can result in different shapes of the flow front and this can result in an incomplete filled part. The use of a closed-loop control is recommended. Different authors use offline algorithms which are defined in the design phase. An example is the stepwise opening of a gate when flow front reaches the gate position [1, 2]. In this case a simple ON/OFF switch is needed which turn to 'ON' when a sensor detects the resin at the gate location. Another example of an offline designed control is the use of an algorithm based on a decision tree [34]. The advantage is that only point sensors are needed to react on different situations inside the mold and the decision tree can be designed during the mold design.

CONTROLLED RTM-PROCESS

The Institut fuer Verbundwerkstoffe GmbH uses such a decision tree to design a controlled RTM process. The first step to design the decision tree is the selection of different relevant disturbances. One example for a disturbance is the wrong positioning of fabric layers inside the mold. In this case there could be a gap between the fabric and the edge of the mold. In this gap the resin flows rapidly forward and changes the desired shape of the flow front. This is a very

common effect and is called Race-Tracking-Effect [5, 6]. The result can be that a certain region is surrounded by resin and the entrapped air can not leave, causing a dry spot in the fabric.
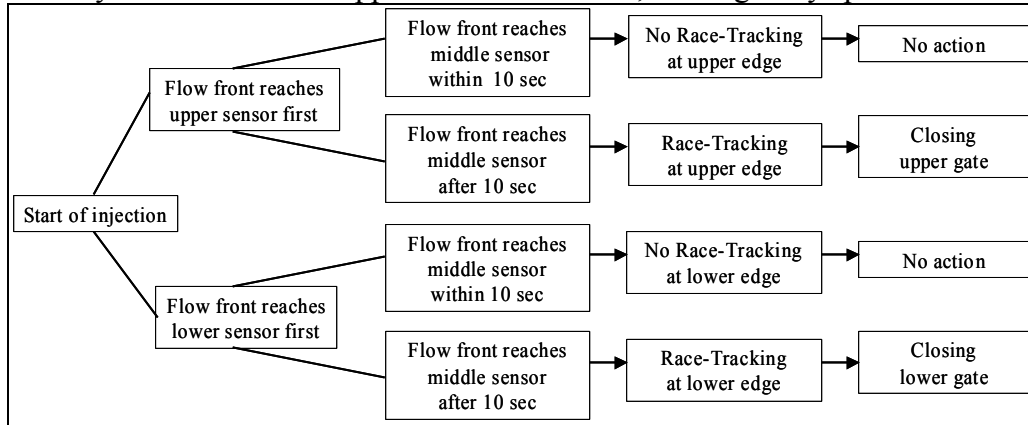
Fig. 7: Decision tree to react to the Race-Tracking-Effect
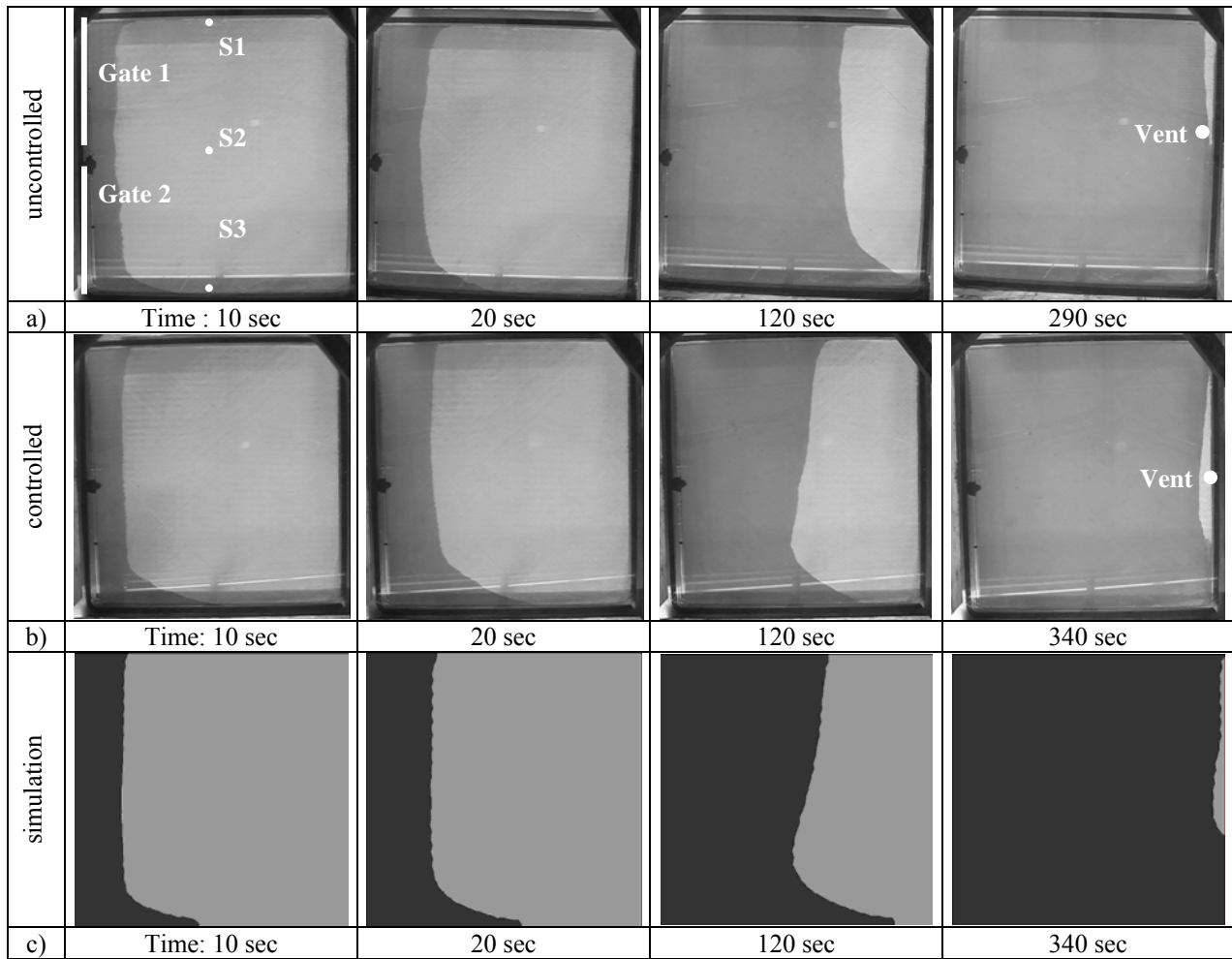
Fig. 8: Comparison between injection without control (a), with control (b), and with the simulation of controlled injection (c)

In Fig. 7 a decision tree to control an injection into a quadratic mold with either a Race-Tracking-Effect at the upper or lower edge is shown. On the left side of the mold two line gates were used to inject the resin. Three sensors in the middle axis perpendicular to the flow direction are needed to decide if there is a Race-Tracking-Effect and if so, at which edge it occurs. In Fig. 8 the flow front of an uncontrolled (a) experiment is compared with a controlled (b) experiment at several time steps. In the shown case the Race-Tracking-Channel is located at the lower edge. The movement of the flow front can be seen by the darker, already filled, areas. Within the controlled experiment the last filled area is around the vent and the part is filled completely. Within the uncontrolled test the upper right edge stays dry because the entrapped air can not disappear through the vent. The result is an incompletely filled component. The disadvantage of the controlled process is that it takes a little longer to fill the cavity but this will be compensated by receiving a completely filled component. In the third row (c) of Fig. 8 the filling simulation used to get the parameters to design the decision tree is shown. It can be seen that the simulation (c) and the experiment (b) are almost identical.

To implement the decision tree into the injection environment, which is controlled by a measurement computer, a system of modules was developed. Modules for all tasks of a controlled injection were programmed to be used with the Software LabView[®]. These are the modules to collect the data of the different sensors, the modules to handle the actuators (valves, pressure pots), and the modules to build up the decision tree. For example, to design the decision tree there are modules which wait for a certain event or branches dependent on the status of a switch, or they stop further decisions if an emergency button is pressed. The decision tree can easily be programmed by 'Dragging and Dropping' the modules inside the LabView[®] environment.
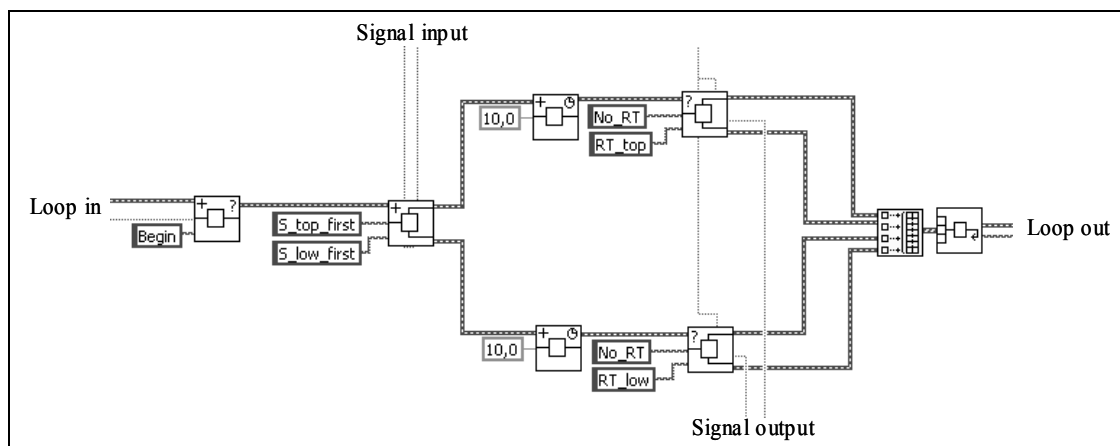
Fig. 9: Decision tree to influence the Race-Tracking-Effect designed within LabView[®]

As can be seen in Fig. 9, the programmed decision tree looks similar to the plotted one (Fig. 7). This results in an user friendly program because it is easy to read and easy to maintain. The decision tree modules can also be used to program a flow chart of an injection process. A further advantage of such a computer controlled process is that the documentation of every process step is easy to be handled.

Controlled injection with in-situ polymerizing PBT

The control concept was also used for producing plates with an in-situ polymerizing polybutylene terephtalate (PBT). The used system was CBT$^{®}$ Resin a product of Cyclics Corporation. The advantages of this system are that it has a very low viscosity at injection temperature and polymerizes into solid PBT within a short cycle time [7]. CBT$^{®}$ Resin is a low molecular weight oligomer material, which is available e.g. granule or powder form and melts above 150°C. During heating up the viscosity decreases to 20 mPas at 180°C. The polymerization takes place inside the heated mold using a catalyst. The polymerization is finished in less than 10 minutes (200°C mold). If the mold is cooler than 220°C the PBT is solid and can be removed from the mold without cooling down the mold. Therefore, reheating the mold prior to the next injection is redundant. This aspect and the short polymerization time results in a very short cycle time, making the process attractive for economic serial production.
A problem occurring in several injections with CBT$^{®}$ Resin is associated with this short cycle time and the low viscosity. Therefore, the flow velocity of the CBT$^{®}$ Resin is high and the fibers inside the mold are moved by the fluid. This can be solved, for example with a new positioning of gates and vents, but for an existing mold another solution is needed. Former injections were achieved in a vacuum process using a 2-component CBT$^{®}$ Resin system. After opening the gate, the CBT$^{®}$ Resin flows inside the mold driven by the pressure difference of 1 bar. This leads to a high flow rate in the beginning of the injection. To prevent this the injection process was changed and a pressure pot was used. A pressure pot offers the ability to start the injection with a slight increase of the injection pressure. Due to the fact that it is not trivial to calculate the forces moving the fibers inside the mold, the pressure ramp was defined as follows. Increasing the pressure from 0 bar to 2 bar in 30 seconds and keeping this pressure until the end of the injection. The end of the injection is detected by a temperature sensor which is placed inside the pipe from the gate into the resin trap (Fig. 10). At this position the sensor is outside of the heated mold and if the hot resin reaches the sensor, a clear increase of the temperature can be seen (Fig. 11 left). Thus, this method is a very easy way to check if the resin reaches a vent. This signal is used by the control to close the gate. The gate and the vent were opened and closed by automatic valves which clamp the flexible tubes.
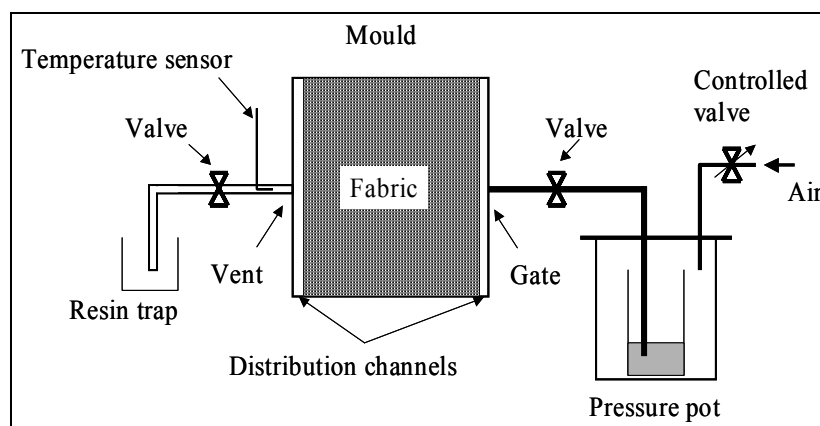
Fig. 10: Experimental set-up

In Fig. 11 (left) the time curves of the injection pressure inside the pot and the temperature at the vent are shown. In the first 30 seconds the pressure ramp can be seen. 9 seconds later the temperature at the gate increases rapidly from 42°C to 190°C and the valve at the vent closes. After further 60 seconds the gate valve closes and the pressure inside the pressure pot drops down. This time is needed to be sure that the micro-impregnation of the fibers is completed. With this controlled injection process the problem with the fiber movements was solved and good parts were injected. A second advantage of this controlled process is that less CBT® Resin is needed because of the short time the valve closes after the cavity is filled. This is not possible if the process is handled manually. The designed process is very robust and the used equipment like the sensor or the pressure pot are standard products. Thus, this is an easy and cost efficient way to inject the resin using a controlled process. A plate injected with this controlled process using a ±45° non crimped carbon fiber fabric is shown in Fig. 11 (right).
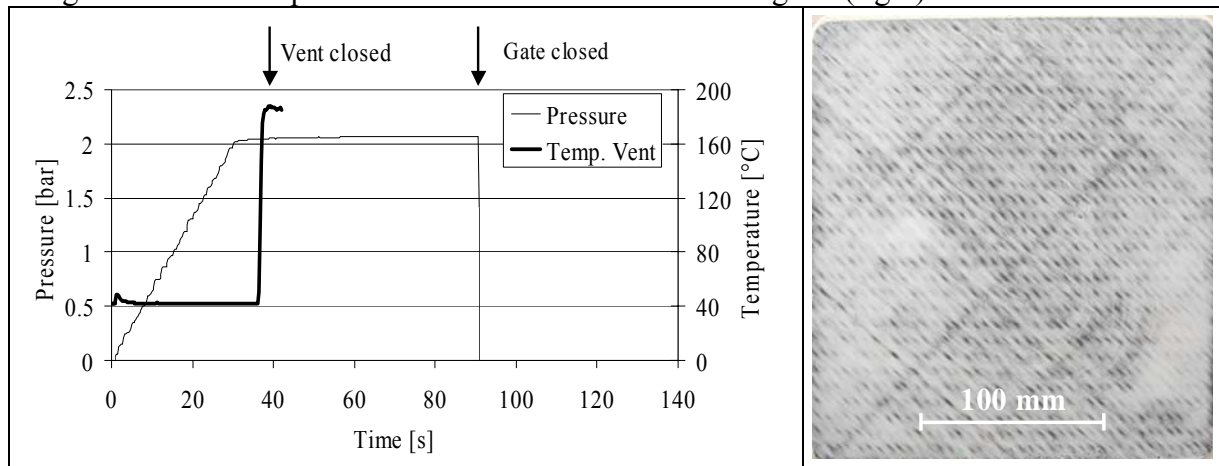
Fig. 11: Measured injection pressure and temperature at the vent position and injected plate

CONCLUSION
In this paper a controlled LCM-process was introduced. With the help of the developed modules it is very easy for engineers to create an efficient control for injection processes like RTM. The advantage of a controlled process is that the rate of rejected parts can be decreased, while a constant, well documented quality can be guaranteed.

ACKNOWLEDGEMENTS

REFERENCES

[1] Dirk Heider, C. Hofmann J.W. Gillespie, Jr.: "Automation and control of large-scale composite parts by VARTM processing", *'45th International SAMPE Symposium and Exhibition Science of Advanced Materials and Process Engineering Series*, Vol. 45', SAMPE(Ed.), Long Beach, CA, May 21-25 2000, pp. 1567-1575.

[2] Moon Koo Kang, Jae Joon Jung, Woo Il Lee: "Analysis of RTM process with controlled multiple gates resin injection", *Composites Part A,* Vol. 31 (2000), pp. 407-422.

[3] E. M. Sozer, S. Bickerton, S. G. Advani: "On-line strategic control of liquid composite mold filling process". *Composites Part A*, Vol.31 (2000), 9, 1383-1394.

[4] Bickerton S, Stadtfeld HC, Steiner KV, Advani SG: "Design and application of actively controlled injection schemes for resin-transfer molding", *Composites Science and Technology,* Vol. 61 (2001): pp. 1625-1637.

[5] Simon Bickerton ; Hubert Stadtfeld ; Karl Steiner ; S.G. Advani: "Active control of resin injection for the RTM Process", *Proceedings of the 13th Technical Conference on Composite Materials ASC Baltimore Maryland*, Sept. 1998, pp.232-245

[6] P. Mitschang, A.Ogale, J. Schlimbach, F. Weyrauch, C. Weimer: „Preform Technology: a Necessary Requirement for Quality Controlled LCM-Processes", *Polymers & Polymer Composites*, Vol. 11 No. 8, 2003, pp.605-622

[7] R. Eder: „Cyclic Thermoplastics – Properties and Processing", *Proceedings "IVW Status-Kolloquium"*, Kaiserslautern, Germany, 8. + 9.11.2001, Vol. 25, pp. 33 – 43

Resin Film Infusion of Cyclic PBT Composites: Consolidation Analysis

Síora Coll [1,(i)], Adrian Murtagh [1,(ii)], Dr. Conchúr Ó Brádaigh [1,(iii)]

[1] *Composites Research Unit, Department of Mechanical Engineering, National University of Ireland Galway, University Rd, Galway, Ireland:* [(i)]*Email; s.coll@nuigalway.ie*
[(ii)] *Email: adrian.Murtagh@nuigalway.ie*
[(iii)] *Email: conchur.obradaigh@nuigalway.ie*

SUMMARY: The focus of this paper is to examine the mechanisms involved in the consolidation of stitched glass fiber reinforced cyclic polybutylene terephthalate (CBT™) during processing, with a particular emphasis on sandwich structures. A pre-preg form of the material was processed under vacuum using a resin film infusion technique on a flat plate heated mold with topside heating and temperature and displacement are recorded. The final application of these structures is aimed at the manufacture of wind turbine blades in the wind power industrial sector, where sandwich structures are typically used. CBT™ is a new low viscosity thermoplastic matrix, suitable for the manufacture of structural composites for automotive, electrical, sports equipment, powder coating, and wind power applications. Consolidation is examined as a function of the processing parameters - temperature, vacuum pressure and time, and mechanisms of intimate contact, autohesion and fiber impregnation are considered for a prediction model.

KEYWORDS: resin film infusion; cyclic polybutylene composites; consolidation; sandwich structures; thermoplastic matrix; intimate contact; autohesion; fiber impregnation.

INTRODUCTION

The CBT™ system holds a number of advantages over thermoset systems including improved toughness, damage tolerance and ease of recycling of composite parts. CBT™ has a low processing viscosity (below 20 mPa.s at 180°C) which allows rapid and thorough wet-out of fiber reinforcements[1,2]. The combination of low viscosity, rapid reaction or polymerization cycles, and the benefit of isothermal processing (hence the ability to demold at higher temperatures) leads to a shorter overall process time. The polymerization reaction emits no exotherm, which eliminates the problem of 'hot-spots' that may damage parts in the mold, or cause internal stresses or warping. This also greatly reduces cycle times in large parts where thermoset thick walled sections currently pose a threat of overheating unless processed slowly. This is particularly applicable to wind turbine blade 'root section' manufacture where slow cycle times increase cost and lower productivity. Most other sections of wind turbine blades are based on composite sandwich structures, which offer excellent stiffness and strength for low weight[3]. In this case, glass fiber reinforced CBT™ skins are separated by thick, lightweight, high

temperature, closed cell foam core – the thicker the core, the higher the flexural stiffness and strength of the panel – for minimum weight gain [4].

The resin film infusion process has increased in popularity for the manufacturing of structural composites for aerospace, automotive and military applications, and has been identified as an alternative cost-effective manufacturing technology to RTM [5]. The combination of an open mold and a vacuum bag reduces the tooling cost of the resin film infusion process, and facilitates the manufacture of large structures, such as wind turbine blades.

During the RFI processing of thermoplastic matrix composites, consolidation may be characterized by three major steps: intimate contact, autohesion, and fiber impregnation[6]. Consolidation of thermoplastic composites can be considered as an autohesion process in which molecular chains diffuse across the interface and entangle with neighboring chains. The interface is created by intimate contact achieved by an applied pressure [7].It is believed that the strength of the interply bonds depends mainly on two mechanisms: intimate contact and diffusion bonding. During fiber impregnation, the matrix is introduced into the space between the fibers. It is important to predict the thickness reduction of the material after processing in order to design for accurate tolerances, and allow for assembly of large structures such as wind turbine blades. Therefore, this paper focuses on the consolidation behavior of glass fiber reinforced cyclic PBT.

MATERIALS

The monomer used in these trials is cyclic butylene terephthalate oligomers (CBT™), and are supplied by Cyclics Corporation. The form of material used here is a one-part 'pre-preg'. The pre-preg supplied is unidirectional, stitched glass fabric (951 g/m^2), dry on one side, and with a coating of pre-catalysed resin on the other, and is technically an intermediary between pre-preg and resin film material. Due to the design of the material a large degree of debulking is observed once vacuum is applied, represented by figure 1. A plot showing the debulking of ten layers of pre-preg material at room temperature is shown in figure 2, which illustrates a 42% decrease in thickness for a 12 ply laminate. The further trials discussed in this paper do experience the 'debulking' phenomenon, however consolidation is the main point of focus.
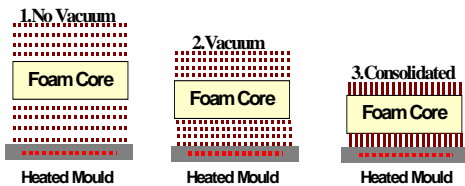
Fig.1: Debulking Phenomenon
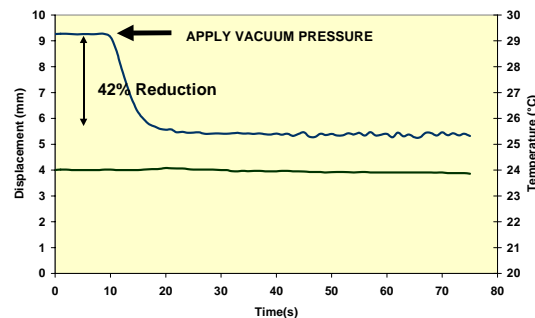
Fig.2: Debulking at room temperature

The pre-preg was dried under vacuum at 120°C for 12 hours, and purged periodically with nitrogen to remove any residual moisture, as moisture acts as an inhibitor to the polymerization reaction. Thick parts are processed with thermocouples placed at intervals between layers to monitor the temperature throughout the part. For sandwich panels, the CBT™ resin is processed

'in-situ' with a high temperature closed cell foam, thus ensuring an excellent bond between the two surfaces. The foams used in these trials include a high temperature Polyisocyanurate (PIC) foam and a developmental grade of PET foam.

EXPERIMENTAL

The tooling used in these experiments is a stainless steel flat plate mold, capable of rapid heating rates, precise temperature control, uniform temperature distribution, and accurate temperature monitoring capabilities. A portable heated top plate is used to ensure uniform heating. An ideal process temperature-time plot for processing of CBT™ is outlined below (fig.3), and is described in four stages; stage 1: initial temperature ramp, stage 2: drying stage (120°C), stage 3: secondary temperature ramp, and stage 4: secondary dwell (190°C). The critical stage in this process is the secondary temperature ramp, or stage 3, at which point the melt viscosity starts to decrease[8]. Temperature was measured using a temperature data logging system, reading temperatures from thermocouples located at various points in the lay-up. This data logging system also recorded displacement by using data from a linear variable differential transducer (LVDT). Vacuum pressure was monitored using a digital vacuum gauge.
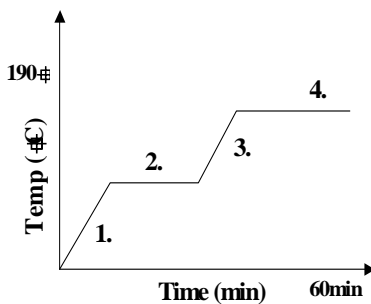
Fig.3:Ideal Temperature-Time Profile for Profile for Processing of CBT™
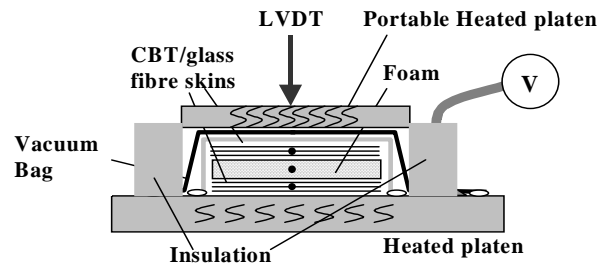
Fig.4: Tool Schematic

The apparatus described was used to study the behavior of CBT glass fiber reinforced parts, and sandwich structured parts using the same materials. Figures 5&6 below are plots taken from the process cycle of a 12 ply, unidirectional glass fiber reinforced CBT™ part, and a sandwich structured part consisting of six layers of unidirectional glass fiber with a PIC foam core (thickness=6mm), respectively. In figure 5, a slight decrease in thickness may be observed as the temperature is increased from room temperature to 120°C. This is due to the nature of the pre-preg material which is quite 'boardy' and becomes slightly more pliable as the temperature is increased. During the drying stage, the part thickness reaches an stable value, as the temperature is stabilised at 120°C. The matrix remains in solid form at this stage. A slight decrease in thickness may be observed between 130°C and 140°C as the resin starts to soften, and this is followed by a more rapid decrease as the temperature is increased to the processing temperature of 190°C. The part thickness decreases rapidly, within a few minutes. The rapid increase in temperature causes the viscosity of the resin to decrease dramatically (from 150mPa.s to <20mPa.s),and flow readily, leading to the impregnation of the glass fiber as the resin fills the spaces between the fibers thus resulting in a 65% decrease in thickness.

Figure 6 shows a similar pattern for the sandwich panel. The initial increase in the thickness of the part, as highlighted in section 'A', is due to the foam core, which expands slightly due to off-gassing once temperature is applied, however the degree of expansion is negligible, (<0.5mm). This effect was studied in trials measuring the effect of temperature on the foam alone. Again, the thickness of the part decreases rapidly as the temperature rises. Section 'B' exhibits a thickness 'recovery'. It is hypothesized that this phenomenon is a viscoelastic recovery of the matrix due to an increase in the partial pressure within the vacuum bag as the resin starts to flow, and vacuum channels are limited. The low viscosity of the resin at high temperatures means that it is imperative that the resin is not encouraged to flow outside of the fiber reinforcement as this will increase the volume fraction of the composite part, which has implications for mechanical properties. The effects of squeeze flow have been examined in this study and it has been shown that displacement is much greater for parts where squeeze flow has occurred.
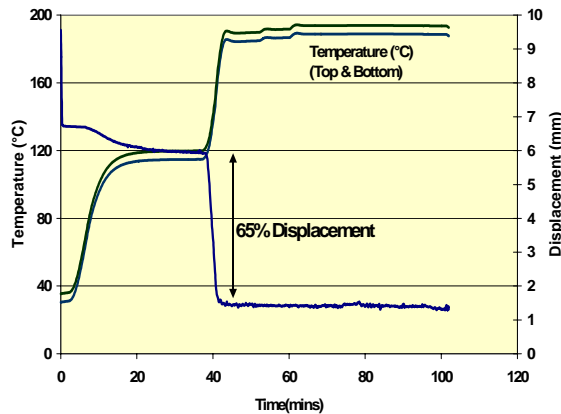
Fig.3: Displacement:12 ply UD laminate
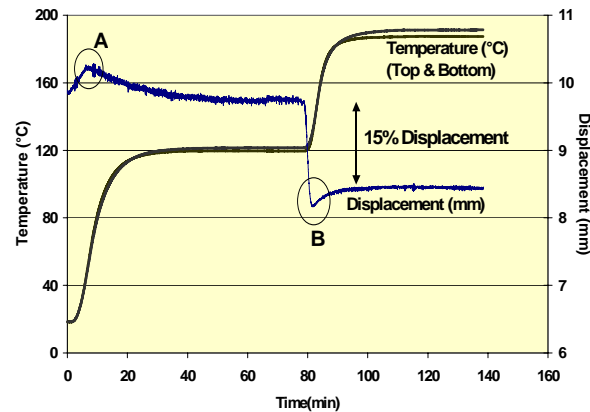
Fig.4: Displacement:6 ply UD; foam core

MODELING

In consolidation models to date, based on pressure evolution analysis[9,10], it is assumed that the applied pressure is transmitted to the matrix as well as to the fiber reinforcement. The forces in the resin and the fibers balance the applied load thus;

$$P_{app} = P_f + P_r \tag{1}$$

Where P_{app} is the applied pressure, P_f is the fiber pressure, and P_r is the resin pressure.
Consolidation at process temperature without vacuum pressure results in the plies bonding together by resin bridges, however large voids visible to the eye are present between the plies suggesting that no intimate contact is developed under these conditions. Therefore, to complete intimate contact, pressure must be applied to complete the resin bridges. The Lee & Springer model of the degree of intimate contact in unidirectional fiber-reinforced thermoplastics represents the initial ply surface as a series of equisized rectangles, with the present voids also represented as equisized triangles [11]. Based on this geometry, the deformation of the rectangular resin elements can be defined as;

$$b(t) = b_0 \left[1 + \frac{5\phi P_{app} t}{\eta} \left(1 + \frac{w_0}{b_0} \right) \left(\frac{a_0}{b_0} \right)^2 \right]^{\frac{1}{5}} \tag{2}$$

where b(t) is the width of the rectangular elements at time t, η is the viscosity, w_0, a_0 and b_0 are the initial dimensions of the rectangular resin elements, φ is a constant for the pressure distribution and P_{app} is the applied pressure. Intimate contact is achieved once b(t) is equal to $b_0 + w_0$. Based on this equation, the time needed to complete intimate contact t_{ic} is;

$$t_{ic} = \left[\left(\frac{b_0 + w_0}{b_0} \right)^5 - 1 \right] \left(1 + \frac{w_0}{b_0} \right)^{-1} \left(\frac{a_0}{b_0} \right)^{-2} \left(\frac{\eta_0}{5\phi P_{app}} \right)$$

(3)

where η_0 is the shear viscosity (10 Pa/s) and is expressed as:

$$\eta_0 = 6x10^{13} \exp\left(\frac{-0.779}{T} \right) \tag{4}$$

where T is the temperature in degrees Kelvin. The constants were determined based on data supplied by the manufacturer. The viscosity of the resin is greatly dependent on the temperature to which it is exposed, and this relationship is important when considering the final step in the consolidation process, fiber impregnation. Impregnation is achieved by heating the lay-up to a temperature at which the matrix becomes liquid enough to penetrate the remaining space between the fibers, The depth of the fibers penetrated by the matrix in a given time can be described by Darcy's Law[12]:

$$v_{flow} = \frac{K}{\eta} \frac{dP}{dx}$$

(5)

where v_{flow} is the flow rate of the matrix through the fiber bed, K is the permeability, η is the viscosity, and dP is defined as $P_{atm} - P_{par}$ where P_{atm} is perfect vacuum, or atmospheric pressure, and P_{par} is the partial pressure within the vacuum bag, which for perfect vacuum, is assumed as negligible. Therefore equation (5) becomes:

$$\frac{d\zeta}{dt} = \frac{4K_p}{\eta} \frac{P_{atm}}{\zeta - \zeta_0} \tag{6}$$

where $K_p = K/(1-V_f)$ where V_f is volume fraction, and ζ_0 is the thickness of the fiber tow, and ζ is the thickness of the non impregnated zone. Integrating and solving, gives:

$$\zeta(t) = \zeta_0 - \sqrt{\zeta_0^2 - 2\left[\zeta_0 \zeta_i - \frac{4K_p}{\eta} \left(P_{atm} - P_{par} \right) t \right]} \tag{7}$$

This model gives an approximation for the thickness of the impregnated zone as a function of time, and temperature, and at constant pressure.

CONCLUSIONS & FURTHER WORK

An experimental study has been carried out on the consolidation behavior of cyclic polybutylene terephthalate resin (CBT™) and a prediction model has been put forward. Experimental results show that at constant pressure (vacuum pressure) the change of viscosity with respect to temperature is the main governing factor behind the consolidation of the composite parts. Once polymerization of CBT™ commences the viscosity of the resin starts to increase until crystallization is complete. The model gives an approximation of thickness. Work is ongoing to complete comparisons of experimental and numerical results. Areas to be investigated include the effect of fiber orientation on consolidation – to date, unidirectional fibers only have been used. Further work will also investigate the consolidation behavior of very thick parts, in excess of 40 ply's.

REFERENCES

1. Roman H.J. Eder. Steven J. Winckler, Processing of Advanced Thermoplastic Composites using Cyclic Thermoplastic Polyester, in Proceedings of the *22nd SAMPE Europe International Conference*, CNIT Conference Center, La Défense, Paris, 2001
2. Cyclics Corporation; Manufacturers data - http://www.cyclics.com
3. Dayton A. Griffin, Sandia National Laboratories Report, (2002-1879), Blade System Design Studies Volume 1: 'Composite Technologies for Large Wind Turbine Blades'.
4. Geoff Green, Chris Feely, Leonard Hollaway (ed), *Handbook of Polymer Composites for Engineers,* Woodhead Publishing Ltd, Abington, Cambridge, England, 1994, Chapter 6.4
5. V.Antonucci, M.Giordano, L.Nicolais, A.Calabro, A.Cusano, A.Cutolo, S.Inserra, Resin flow monitoring in resin film infusion process, *J. Mat. Processing Technology* 143-144 (2003) 687-692
6. R.Phillips, D.A.Akyüz, J.E.Månson, "Prediction of the consolidation of woven fiber-reinforced thermoplastic composites", *Composites Part A: Applied Science and Manufacturing,* Volume 29, Issue 4, 1998, Pages 395-402
7. Po-Jen Shih, "On-line Processing of Thermoplastic Composites", PhD thesis, Faculty of the Virginia Polytechnic Institute & State University, Feb.19, 1997
8. S.M.Coll, A.M. Murtagh, C.M.Ó Brádaigh, *Resin Film Infusion of Cyclic PBT Composites: A Fundamental Study*, Proc. of the 25th SAMPE Europe International Jubilee Conference, Paris Expo, Paris, Porte de Versailles, 2004
9. Gutowski, Cai, Baeur, Boucher, Kingery, Wineman, *J. Comp. Mat.* 1987, 21
10. Dave, Kardos, Dudukovic, *Polym. Comp.*, 1987, 8(1), 29
11. W.I. Lee, & G.S. Springer, *J. Comp. Mat.,1987,21,1017*
H. Lin, S. Ranganathan, S.G.Advani, "Consolidation of Continuous-Fiber Systems", Flow & Rheology in Polymer Composites Manufacturing, Ed. S.G.Advani, 1994, Els. Sc. 9(6),

Perspectives for Reactive Molding of PPA as Matrix for High-Performance Composite Materials

Niccolo Pini, Chiara Zaniboni, Stephan Busato, Paolo Ermanni

Center of Structure Technologies, ETH Zurich
Leonhardstrasse 27, LEO B3, CH-8092 Zurich, SWITZERLAND
pini@imes.mavt.ethz.ch

SUMMARY: While Liquid Composite Molding (LCM) technologies for thermoset composites are increasingly used for manufacturing high quality structural components, LCM technologies based on thermoplastic matrices are still in development. Reactive thermoplastic LCM processes are at present applicable only to a few engineering polymers. This work presents perspectives for reactive molding of a high-temperature resistant polyphtalamide (PPA). Thermoanalytical, rheological and optical tests were performed to assess the behavior of low melting PA 6T/6I oligomers with increasing temperature and to monitor the polymerization and crystallisation reactions. The raw oligomeric material first undergoes a solid-liquid phase transition at around 135°C. At this stage its behavior is highly thixothropic and its viscosity around 10^5 mPa·s. At higher temperatures the viscosity of the oligomeric melt decreases further until a high temperature crystallisation process occurs at about 180°C. Polymerization starts at about 220°C and ends at 290°C. During the reaction the polymer crystallises as soon as it is formed with an achievable degree of crystallinity considerably higher than that of melt-crystallised samples. In accordance with the results, a viable processing technology based on powder impregnated intermediate materials is proposed.

KEYWORDS: PPA, reactive molding, oligomers, *in-situ* polymerization, powder impregnation.

INTRODUCTION

The potential of composite materials for lightweight structures is nowadays broadly recognised and exploited, even though several drawbacks prevent their more widespread adoption in modern technologies [1,2]. State-of-the-art high-performance thermoset composites show low damage tolerance and out-of-plane toughness [2], two factors limiting their application in safety critical parts. Furthermore their temperature resistance is mostly poor. From these points of view high-performance thermoplastic composites perform clearly better, but they require complex processing routes, which make them expensive and inadequate for geometrically complex parts [1,2].
The problems in processing thermoplastic composites arise mostly from their high viscosity in the molten state [2,3], which antagonizes the impregnation of the fiber bed. The processing window is usually quite narrow excluding a further viscosity reduction by temperature increase

without degradation. A viscosity reduction could be achieved by using solvents, which however would have to be removed after impregnation.

A more recent approach consists in performing *in-situ* polymerization of precursor materials [3,4], in principle similar to the curing of thermoset resins. Low molecular species – monomers or oligomers – with low melt viscosity impregnate the fiber bed, then react after impregnation to form a polymer.

Because of the often delicate polymerization conditions, not many thermoplastic polymers can be *in-situ* polymerized. So far the following systems have been commercially promoted: Laurinlactam monomers producing PA12 (EMS Chemie, Switzerland) [3], "Fulcrum" producing TPUR (Dow Plastics, USA), CBT oligomers producing PBT (Cyclics Corp., USA) [4]. These processes yield well-known engineering thermoplastics, thus reducing the innovation potential and commercial impact of the *in-situ* technologies. In order to achieve a breakthrough for the latter, a reactive system delivering a high-performance polymer is needed.

Polyphtalamides (PPA) fill in the gap between engineering polymers and high-performance polymers such as polyphenylenesulfide (PPS) and polyetheretherketone (PEEK). PA 6T/6I is a cocondensation product of terephtalic and isophtalic acids with hexamethylenediamine with outstanding thermal properties: its melting point T_m is around 325°C, while its glass transition temperature T_g is 138°C. The heat deflection temperature HDT at 1.8 MPa is as high as 120°C [5].

The production process of PA 6T/6I at EMS Chemie involves a pre-condensation step, in which monomers condensate to oligomers (up to 10 repeating units). In a second step these oligomers condensate further to a polymer under loss of a small amount of water, making them potentially applicable in LCM processes.

The aim of this work is to study the suitability of these oligomers for LCM processes by characterising them from a thermal (DSC, TGA) and rheological point of view. Furthermore, optical analysis is performed in order to assess the polymer's microstructure.

EXPERIMENTAL

PA 6T/6I oligomers (XE 3733 VK) were kindly donated by EMS Chemie, Domat-Ems, Switzerland. Because of their sensitivity to moisture, the oligomers were dried at 80°C and 4 mbar for at least 24 hours before polymerization.

Thermal Analysis

DSC analysis was performed on a Perkin Elmer DSC 7 with nitrogen as purge gas in order to prevent high-temperature oxidation. Powder samples were tested in the temperature range from 80°C to 350°C with different thermal profiles in order to assess the progress of the polymerization reaction.

TGA Analysis was performed on a Perkin Elmer Pyris 1 TGA in nitrogen atmosphere from 80°C to 600°C at a heating rate of 10°C/min.

Rheological Analysis

The oligomer powder was pressed to pills with 20 mm diameter at 145°C and 160 MPa. The viscosity of the oligomers was measured on a plate-plate Paar Physica UDS 200 rheometer at different constant temperatures.

Optical Analysis

The microstructure of the polymer was observed by optical analysis of thin sections (microtome Leica RM2155 and optical microscope Leica RX DMA). Cryo-fracture was performed on polymerized samples and the fracture surface observed with a Scanning Electronic Microscope (SEM).

RESULTS AND DISCUSSION

Thermal Analysis

A typical DSC temperature scan from 80°C to 350°C at 10°C/min is shown in Fig. 1. In the heating curve (upper curve) four peaks can be clearly identified.
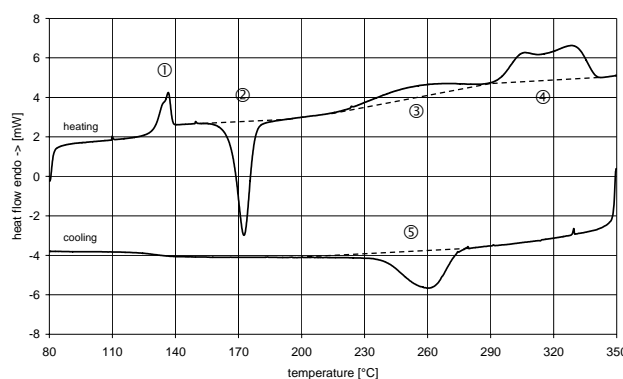
Fig. 1 DSC scan at 10°C/min under nitrogen of the oligomers XE 3733 VK.

Peak 1 at about 133°C represents the endothermal melting peak of the oligomers. Its enthalpy strongly depends on the sample history, which affects the degree of crystallinity of the sample.
Between 135°C and 170°C the sample is in a molten state. At peak 2 the oligomers undergo a high temperature crystallisation. Oligomers are short chain molecules: in the solid state their mobility is strongly reduced but in the melt they can easily rearrange and crystallise in a paraffin-like structure (fully extended chain crystals) without any entanglement between the chains. The stability of this configuration is further increased in the case of polyamides, which can form hydrogen bonds between the chains. Peak 2 could also be interpreted as a first polymerization step, but the narrow peak is more typical for crystallisation processes and TGA analysis does not show evidence of volatile reaction by-products at this temperature, which would be expected in case of a polycondensation.

Between 220°C and 290°C peak 3 can be identified as a broad endothermal peak. This peak is the superposition of three processes, namely polycondensation, crystallisation of the formed polymer and evaporation of the reaction by-product water. At 290°C the oligomers have completely reacted. The polymer crystallises as soon as it is formed: the temperature range of peak 3 corresponds namely to the temperature range where the crystallisation driving force is very large, as can be deduced from the position of crystallisation peak 5.

Peak 4 between 290°C and 340°C is a broad double melting peak of the polymer. This broad melting range mirrors the broad crystallisation range between 215°C and 290°C.

In the cooling curve (lower curve in Fig. 1) only one crystallisation peak from the melt can be identified between 290°C and about 220°C.

TGA experiments under nitrogen at 10°C/min showed that up to 200°C no volatile by-products are emitted. Therefore, DSC peaks 1 and 2 are no polycondensation peaks. Between 220°C and 290°C about 3.5 wt% water is released, due to the polycondensation reaction taking place in correspondence to DSC peak 3.

It is interesting to note that the melting enthalpy of the *in-situ* polymerized PA 6T/6I (ΔH^m=54.1 J/g) is about 33% higher than that of the melt-crystallised polymer (ΔH^m=40.7 J/g). This implies that the crystallinity of *in-situ* polymerized PA 6T/6I is 33% higher than that of the melt-crystallised polymer.

Heating of the oligomers only to 290°C followed by cooling to 80°C (Fig. 2) showed complete absence of any peaks in the cooling curve, thus implying that the oligomers reacted completely during the heating phase. On second heating of the *in-situ* synthesised polymer to 350°C only the melting peak between 305°C and 330°C can be observed.

These findings open up new opportunities to process PPA directly into a solid phase at lower than melting temperatures.
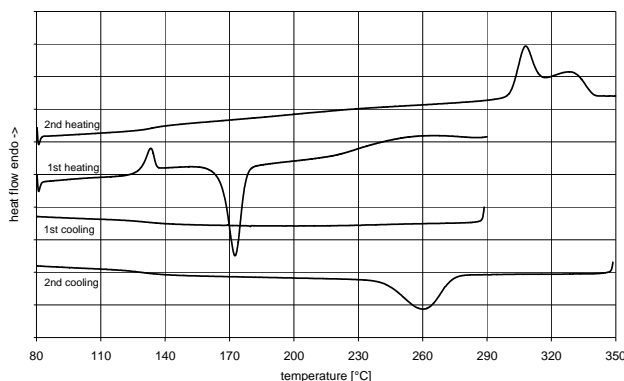
Fig. 2 DSC scan at 10°C/min under nitrogen of the oligomers XE 3733 VK. First heating to 290°C, then cooling to 80°C. Second heating to 350°C and cooling to 80°C.

Rheological Analysis

During processing the viscosity of the oligomers changes by several orders of magnitude. As expected, both viscosity and pot life of the material strongly decrease with increasing temperature (Fig. 3). Furthermore molten samples showed a pronounced shear thinning behavior, which causes the low viscosity to be evident only at higher shear rates.

The lowest observed viscosity of about 50 Pa·s at 180°C is still too high to allow injection of the oligomers in Resin Transfer Molding-like processes, but it is one order of magnitude lower than that of thermoplastic melts, so ensuring a more efficient fiber impregnation.

Optical Analysis

The polymer's microstructure was presumed to be of a spherulitic type. However, microscopical analysis of thin sections under polarised light did not unsheathe single overstructures like spherulites but only a smeared cluster of optically active crystals.

SEM analysis of cryo-fractured samples delivered pictures of fracture surfaces typical for brittle semi-crystalline polymers. A cellular structure could be identified on the surface with a cell width in the order of 0.1 μm, which could be the prints of the very single crystals.
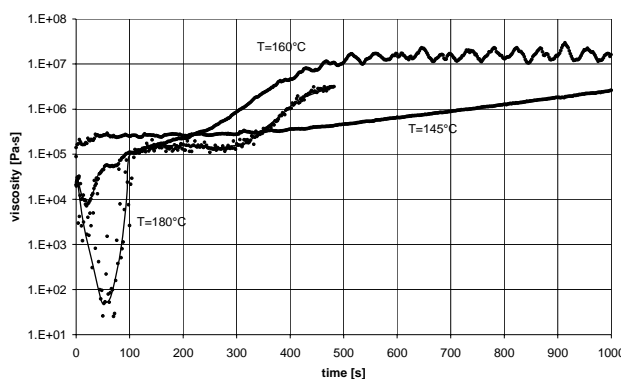
Fig. 3 Oligomer viscosity as function of dwelling time at three constant temperatures: 145°C, 160°C and 180°C (shear rate D = 20 s^{-1}).

CONCLUSIONS

The investigations presented open up a new way to process high-performance composites materials with PPA matrix. The unique thermal and rheological properties of the studied oligomers allow the manufacturing of oligomer powder impregnated reactive intermediate materials. The low viscosity of the molten oligomers can be fully exploited during the forming step, so that a faster – according to Darcy's Law – fiber impregnation can take place. After impregnation with the molten oligomers the temperature has to be increased up to the polymerization temperature, which is lower than the melting point of the polymer. After polymerization the part can be theoretically directly demolded. This processing route is expected to reduce cycle time, tooling and energy costs and deliver at the same time a high-temperature resistant high-performance composite material with an excellent price-performance ratio.

ACKNOWLEDGEMENTS

REFERENCES

1.　T.G. Gutowski, "Advanced Composites Manufacturing", John Wiley & Sons, Inc., 1997
2.　D.C. Leach, "Continuous Fiber Reinforced Thermoplastic Matrix Composites", in "Advanced Composites", ed. Partridge, I.K.; Elsevier Applied Science, 1989, pp. 43-109
3.　A. Luisier, "In-situ polymerization of lactam 12 for liquid molding of thermoplastic composites", Thèse No. 2453 (2001), EPF Lausanne
4.　R.H.J. Eder, S.J. Winckler, "Processing of advanced Thermoplastic Composites using Cyclic Thermoplastic Polyester", thanks to Mr. Rösch of Cyclics Corporation Europe
5.　www.knovel.com: online polymers database

Thermoplastic Composites – Products, Processes and Applications

Michael P. Knox

Saint-Gobain Vetrotex America, Inc.
3410 Briarfield Blvd., Suite B, Maumee, OH,43537 USA
Michael.P.Knox@Saint-Gobain.com

SUMMARY: The segment of materials known as continuous fiber reinforced thermoplastic composites (CFRTP) occupy a unique processing methodology vastly different than traditional thermoplastics (injection molding, blow molding, thermoforming) and thermosets (SMC molding, filament winding, pultrusion, infusion). This uniqueness hinders the commercial development of applications using CFRTP. For CFRTP to flourish as a valid material segment, fast and efficient transformation processes will need to be developed and industrialized.

KEYWORDS: Thermoplastic composite, continuous fiber reinforcement, diaphragm forming, thermoform stamping,

INTRODUCTION

This paper serves to identify commercially availability of the following.

1.) Thermoplastic composite materials technologies
   a. Melt impregnation
   b. Powder impregnation
   c. Low viscosity reactive thermoplastics
   d. Commingled fibers
2.) Transformation processes
   a. Vacuum bag molding / vacuum infusion
   b. Diaphragm forming
   c. Thermoform stamping
   d. Pultrusion and filament winding
3.) Commercial applications for the above processes
4.) Conclusion

THERMOPLASTIC COMPOSITE MATERIAL TECHNOLOGIES

Melt Impregnation

Melt impregnation is a well established and documented impregnation technique that has roots in the process of making long fiber reinforced thermoplastic injection molding compound. Imperial Chemical Industries (ICI) developed a strong patent position throughout the 1980's (1).
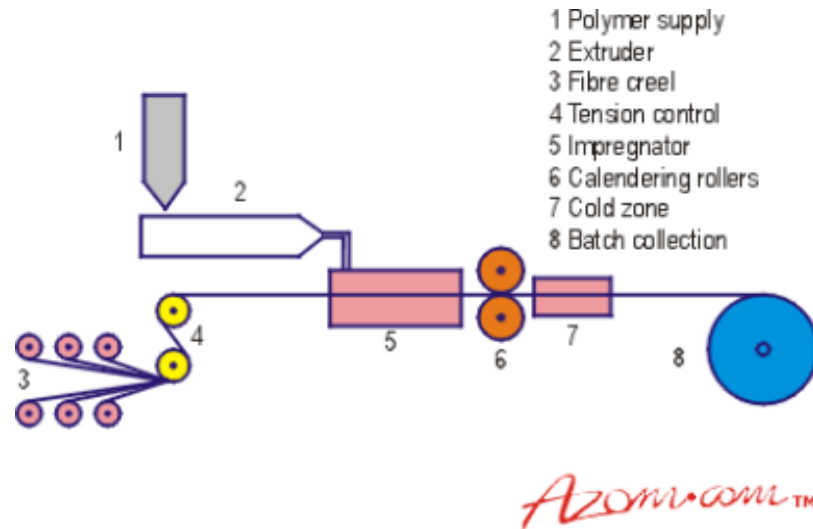
Fig. 1 Schematic of melt impregnation

The key technological component of the process is the impregnation die. Generally speaking, the impregnation die contains a "bath" of molten polymer. In the bath, the fiber roving is guided over and under a series of bars to spread the roving, and provide shearing forces on the roving. These basic actions act to wet out the individual fiber filaments in the fiber roving. Bates (2) reports on the quality of fiber wet out as a function of roving inlet tension, pull speed, number and diameter of cylindrical pins, temperature of polymer, outlet die diameter and pulling tension. He concludes that

A unique impregnation die was studied by Weustink and van Keulen (3) for thermoplastic filament winding. It was concluded that by using conical, co rotating impregnation bars the fiberglass roving "spread" better resulting in better impregnation at high line speeds.
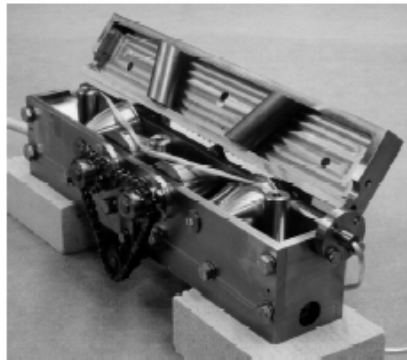
Fig. 2 The die system used by Weustink

Two relatively new melt impregnation techniques have been patented. US Patent 6186769 by Hawley identifies a "pushtrusion" process whereby the polymer processing pressure is used to impregnate and move the glass roving through the die system. US Patent 6709995 by Dyksterhouse expands on his two previous patents 6656316 and 5911932. This technology is predicated on heating the fiberglass roving well above the melt temperature of the polymer.

Again, the main commercial application of the melt impregnation technology is in the manufacture of long fiber injection molding compound; however, there is good interest in thermoplastic pultrusion and filament winding where recyclability, zero emissions, part toughness, and post forming are encouraging attributes.

Powder Impregnation

Powder Impregnation is a widely accepted technology to make thermoplastic prepreg or semipreg. Prepreg is considered fully consolidated; while semipreg needs to be processed for full consolidation. Although there are variants of this process (4), electrostatic powder coating (EPC) appears to be the primary technology. In EPC, the polymer is finely ground and charged oppositely than that of the fiber. The fiber is then run through a "fluidized bath" whereby particles of polymer are attracted into the fiber. From here, the fiber can be wire coated to encapsulate the powdered polymer and fiber, or the fiber / powder can be put through hot rollers to partially or fully impregnate the fiber. Yet another approach would be to use an additional binder to hold the powder in place. The benefit of this is that the fiber is soft and flexible. Several companies employ these types of processes – **Baycomp** (Canada), **Hexcel Applied Fiber Systems** (US), **Cytec** (US), **Sulzer** (Switzerland).

Low Viscosity Reactive Thermoplastics

Two new encouraging emerging technologies are gaining commercial momentum in the CFRTP segment. **Fulcrum™** is based on a thermoplastic urethane (TPU) polymer. The key to this impregnation technology is the reversal of the polymerization process in the melt stage that results in extremely low melt viscosity; hence easy wet out of the reinforcing fibers. These materials are referred to as depolymerizable repolymerizable thermoplastics (DRTP) When

cooling, the molecular weight increases to that of a typical thermoplastic. The Fulcrum technology is specifically designed for thermoplastic pultrusion where toughness, recyclability and post forming are desired attributes.

The second technology is from Cyclics Corporation. **Cyclics®** is a cyclic polybutylene terephalate (CPBT) based polymer that when polymerized becomes PBT – a very useful and effective engineering thermoplastic. The CPBT oligomers when processed at low temperatures (180 – 200ºC) have a very low melt viscosity; hence making it very easy to wet out fiber reinforcement. Catalyst is required to start the polymerization reaction. Catalysts have been designed to be very slow or very fast. This flexibility lends itself to a wide range of processes and applications from reaction injection molding type processes to vacuum infusion of very large parts.

One interesting aspect of this technology is that once fully reacted, the molded part can be demolded instantly. The crystalline melt point of PBT is 225ºC – well above the processing temperature of the CPBT.

Commingled Fibers

NASA was one pioneer in the technique of commingling reinforcing fibers with thermoplastic fibers as a route for post impregnation during processing. This solution allowed flexibility in product forms. Commingled fiber yarns or rovings can be used as-is, or can be knitted, woven or braided into a higher performing composite product. These advanced forms drape and conform easily to form complex parts (5).

The concept of commingling was taken to new levels when Saint-Gobain Vetrotex introduced the **Twintex®** product. Twintex is commingled E glass with thermoplastic fibers. Polypropylene (PP) is the first commercial thermoplastic used as it is lightweight and inexpensive. Twintex is made at the bushing level during the glass fiberization step. Due to the industrial nature of the process, it is a very economical, high production process.
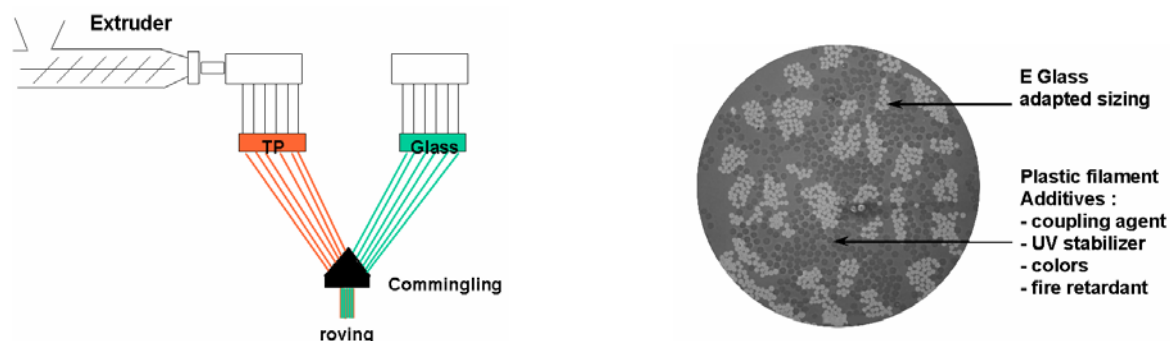
Fig. 3 In-line commingling and an actual cross section of commingled roving

This high volume industrial process has helped the CFRTP market segment expand greatly as price points are competitive with alternative material solutions like wood, metal and thermoset composites. The technology is flexible in terms of product forms and applications. Direct **roving** can be pultruded or filament wound. It can be woven into a compliant **fabric** and vacuum bag molded, diaphragm formed or laminated into a preconsolidated sheet. The preconsolidated **sheet** can be used as-is for flat panel applications, or it can be used as a semi finished good for thermoform stamping or compression molded. Lastly, the roving can be readily converted into long glass **molding compound** for injection molding. The data below shows the range of performance from this one core technology.
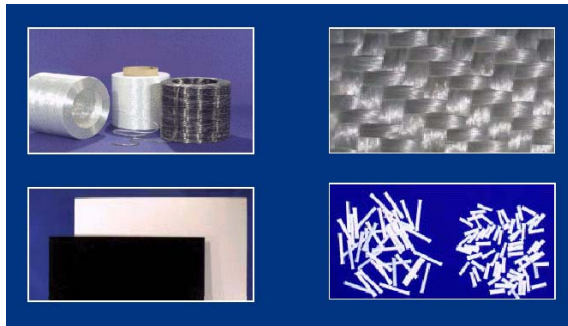
Material	Strength (MPa)	Modulus (MPa)
20% IM compound	61	3,650
40% IM compound	86	5,870
Balanced Fabric	240	13,000
Unbalanced Fabric	400	24,000
Unidirectional	700	38,000

Fig. 4 Product various product forms and tensile data for these forms

TRANSFORMATION PROCESSES

The transformation of these materials into molded articles is a critical area for future growth of commercial applications. Simply stated, there is a lack of accepted technology in the market to support growth. Below, several commercial processes will be discussed.

Vacuum Bag Molding
Vacuum bag molding of CFRTP has roots in thermoset infusion. Compliant CFRTP materials are laid in a mold, a bag is placed over the tool, vacuum is drawn, then the tool is heated until the product is fully melted and cooled.
Vacuum bag molding is suitable for applications where 5 – 15 parts per day are required. Extremely large structures, and variable wall thicknesses are achievable.
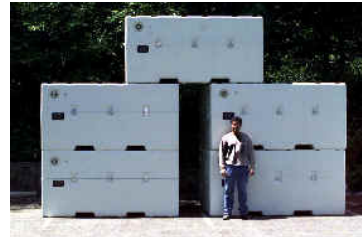
Fig 5 Rigid inflatable boat made by Halmatic (UK), and military shipping containers molded by Integrated Technologies (USA)

Diaphragm Forming

There is good potential for diaphragm forming to become industrial process for the transformation of CFRTP raw materials. The schematic below shows a double diaphragm process. This process is much like traditional thermoforming, but with electrometric diaphragms. The CFRTP material (fabric or sheet) is placed in between the diaphragms. The diaphragms are then clamped; **not** the CFRTP material. This allows the material to conform to the mold while the diaphragms act to constrain the material from wrinkling or folding. Once the diaphragms are clamped, vacuum and heat are applied to melt and remove voids (and to consolidate if unconsolidated raw materials are used). The diaphragms are moved over the tool where vacuum and pressure are used to form the part in a one sided cold tool. Parts are then demolded.
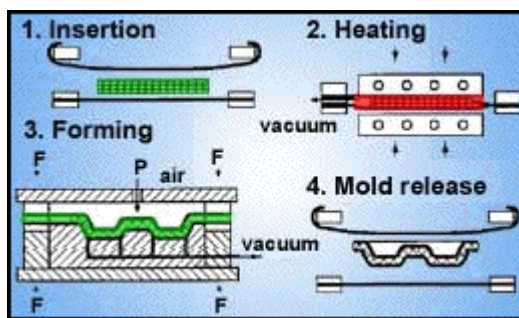
Fig 6 Double diaphragm forming schematic, and a decorative canoe seat made by a diaphragm forming process (photo courtesy of **Diaphorm, Inc**. (US)).

The diaphragm forming process is characterized as a medium series production process for applications requiring 50 – 200 parts per day. The process results in constant thickness, and parts need trimming. Single diaphragm forming is very amenable to variety of decorative surface films, and is very competitive in cost to compression molding (6).

Thermoform Stamping

Stamping of CFRTP sheets is fairly well established in the industry, but not on a large scale, high volume basis. Most processes are captive to the specific processor. Thermoform stamping is characterized by using non shear edge matched tooling that can be matched metal, or metal / rubber. One advantage of rubber is quasi hydrostatic pressure on near vertical walls due to the compression of the rubber. One disadvantage is poor surface aspect on the part due to the lack of a highly polished surface. The CFRTP product is heated, then shuttled to the pressing area by a specialized clamping frame. Pressing requirements can be as low as 50 pounds per square inch of part.

Unlike diaphragm forming where the diaphragms constrain the fabric from wrinkling or folding, the thermoform stamping process uses a clamp frame that allows the CFRTP product to "displace" (versus "flow") as the fabric is drawn (pushed) into the tool. The specific clamping

points, and amount of tension on the physical displacement are keys to having the CFRTP product conform to the tool surface with predictable and consistent fiber orientation.

The subject of stamping CFRTP materials is covered in great detail at the National Research Council of Canada (7,8).
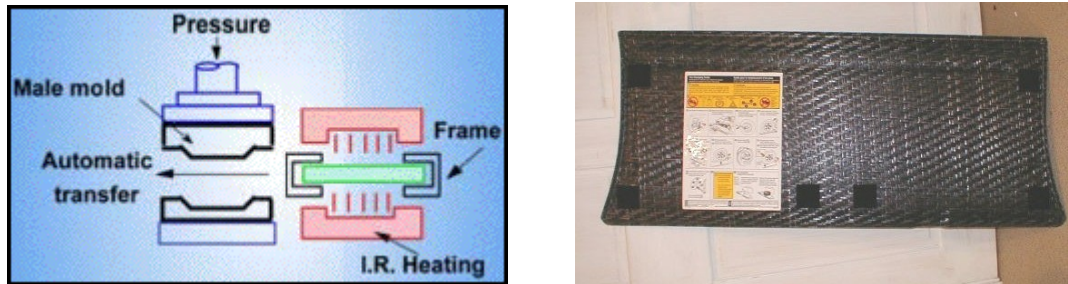
Fig 7 A schematic for the thermoform stamping process and a Saturn Vue load floor made by stamping a sandwich panel of CFRTP skins onto a PP honeycomb core.

Pultrusion and Filament Winding

Progress has been made in the area of thermoplastic pultrusion and filament winding especially with the use of commingled fibers and DRTP where the ease of impregnation leads to fast line speeds.

Pictured below is a filament wound water storage tank, and a thermoplastic composite fence profile. Both applications exploit the toughness and durability characteristics of CFRTP.

Fig 8 Filament wound CFRTP pressure vessel and a pultruded fence profile.

CONCLUSION

The benefits of CFRTP materials are numerous and clear – no VOC, readily recyclable, toughness, durability, post forming, eliminating of painting, can be welded… Absent is a clear and distinct process base to transform CFRTP materials into useful articles. The applications and processes above are just a beginning.

REFERENCES

1.   US Patents 4541884, 4549920, 4559262, 4624886, 4735828, 4783349, 5019450

2   P. Bates, "Modeling the Melt Impregnation Process", *LFT 2003 Conference*, Brussels Belgium.

3.   T. Weustink, F. van Keulen "Optimal Spreading of Fiber Bundles through an Impregnation Device with Convex Rolls", Delft University of Technology

4.   S. Black, "Thermoplastics provide attractive options", *High Performance Composites,* July / August 2001, Pages 20 - 26.

5.   R. Ford, Azom.com "Advanced Thermoplastic Composites", 2004

6.   T. Johnson, V. Brachos, V. Borbone "Costs of TPC Molding: Economical Production Technology for Low and High Volume 3-D TPC Parts", *Automotive Composites Conference*, Troy, MI, 2002

7.   G. Lebrun, J. Denault, P. De Lucas, "Thermoforming / Stamping of Continuous Fiber Reinforced Thermoplastic Composites", *Composites 2001*, October 2001

8.   G. Lebrun, J. Denault, M. Bureau, "Influence of Consolidation and Forming Parameter in the Molding of Continuous Fiber Reinforced Thermoplastic Composites", *Automotive Composite Conference*, Troy, MI 2002

Intraply Shear Characterization of a Fiber Reinforced Thermoplastic Composite

W.F. Stanley[1], P.J. Mallon[2]

[1]*Composites Research Center, Dept. of Mechanical and Aeronautical Engineering,*
University of Limerick, Ireland: Email: Walter.Stanley@ul.ie (corresponding author)
[2]*Irish Composites Ltd., Spiddal, Co. Galway, Ireland: Email: pat@irishcomposites.com*

ABSTRACT: Acquiring complex curvature shapes during thermoforming of thermoplastic composites involves flow phenomena such as interply slip, intraply shear and squeeze flow. To date the intraply shear mechanism is the least well understood. Approaches have been made to determine both longitudinal and transverse steady intraply shear viscosities of molten unidirectional continuous fiber-reinforced composites in the past but with conflicting results. The present study concentrated on experimentally establishing the intraply shear behavior of carbon fiber reinforced polyetheretherketone (APC-2). To induce true intraply shear in a composite laminate APC-2 panels, were cut and ground into long, square-faced blocks, which were then rotated through 90°. A series of experiments was carried out in which a central plate was drawn out at constant velocity using a custom-built pull-out shear apparatus. Values of longitudinal and transverse shear viscosities were determined for shear rates between 0.025 and 0.02 s^{-1}. The viscosity was highly shear-rate dependent, and was best modeled using a 'power-law'. At a rate of 0.01s^{-1} the longitudinal viscosity was in the 1 MPa.s range, and approximately 2.5 times the transverse value. These values are several orders of magnitude greater than those determined using more traditional means, such as torsional rheometry, but agree with results obtained using a picture frame test method.

KEYWORDS: Thermoplastic, unidirectional composite, intraply shear, viscosity.

INTRODUCTION

Many modern composites consist of a highly viscous resin or matrix reinforced by long, continuous strands of virtually inextensible fibers. These composites are often supplied in the form of tape-like sheets referred to as preimpregnated tapes or 'prepregs' in which the fibers have been highly collimated and aligned in the matrix in order to maximise their reinforcing potential. This alignment of the fibers together with their inextensibility makes the properties of the bulk composite highly directional or strongly anisotropic, with preferred directions along and transverse to the fibers. Forming complex shapes from sheets of preimpregnated thermoplastic composite, in their melt state, may be considered as a difficult process when compared to the forming of unreinforced thermoplastic sheet, or indeed, sheet metal [1]. For a thermoplastic composite such as APC-2, comprising approximately 60% by volume carbon fibers embedded in a PEEK matrix, however, circumstances are complicated by the high degree of anisotropy associated with this composite, and successful part manufacture is not as straightforward [2]. Deformation of the composite is constrained by the fiber reinforcement but facilitated by the

matrix, which acts as a form of lubricant in between individual fibers and between plies of different orientation, decreasing the internal friction during the motion of fiber bundles in a laminate, thus lowering the forming forces [3-6].

To model the flow and deformation of strongly anisotropic materials in a commercial forming process, mathematicians (Spencer [7], Rogers [8]) have developed macroscopic theories in which constitutive equations are used to relate the state of stress at any point and time in the material to the strain or rate-of-strain. The simplest form of these equations, which assumes the case of a highly anisotropic viscous liquid reinforced by a single family of inextensible fibers, consists of two important rheological parameters, these being the longitudinal viscosity η_L, which is associated with shearing along the direction of the fibers, and the transverse viscosity η_T, which is associated with shearing perpendicular to the fiber direction. Clearly, if models of this type are to be successfully employed in the simulation of composite forming, then an accurate experimental database for η_L and η_T is vital.

In this paper a custom-built experimental apparatus designed to provide experimental values for the longitudinal and transverse viscosities of a thermoplastic composite system undergoing steady-shear deformation is introduced. The operation of the instrument is based on the principle of drawing a thin, flat plate from a composite specimen using a constant pull-out velocity and measuring the pull-out force as a function of the plate's displacement from its initial position. By aligning the fibers parallel or normal to the pull-out direction the anisotropic behavior of the test specimen can be characterized, and through appropriate mathematical analysis, the readings of pull-out force can be converted into corresponding values of longitudinal and transverse shear viscosity.

DEFROMATION BEHAVIOR

For unidirectional thermoplastic composites, four principal mechanisms have been identified and observed to occur when manufacturing parts from preimpregnated tape [3]. These are (i) resin percolation through the fibers (ii) transverse flow of the fibers (iii) interply slip of the individual plies across one another and (iv) intraply shearing of the individual fibers within each ply. To realise acceptable wrinkle free complex or double curvature parts some form of shear mechanism must be present to allow for the fiber re-orientation. During the shaping stage, fibers must be displaced relative to each other within individual plies, due to the shear stresses that are induced. As each fiber within a ply is separated from its neighbours by an amount of viscous polymer this is the material that is sheared during deformation and the mechanism of accommodating inter-fiber shear is called intraply shear. Two types of intraply shear can occur within a ply, namely axial and transverse as illustrated in Figure 2.1. Axial intraply shear must be present whenever a double curvature shape is to be formed successfully and wherever the relative orientation between neighbouring plies changes.

(a)   (b)
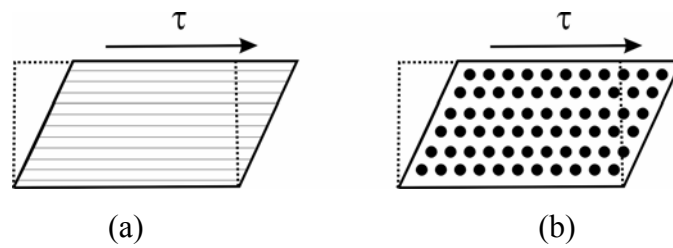
Figure 2.1: Two modes of intraply shear in composite materials: (a) axial or longitudinal and (b) transverse.

To date it appears that relatively few experimental studies into the characterization of the intraply shear mode of deformation in commercial composite systems have been made. More effort has concentrated on trying to characterize fully the interply slip of these advanced composites. A number of successful research studies have been carried out on the 'model' composite systems consisting of long, rigid and virtually inextensible fibers embedded in a liquid, Newtonian matrix, at room temperature whereby the intraply shear behavior was much more readily achievable throughout their composite structure than the models' commercial counterparts [9-12].

APPARATUS

An illustration of the complete experimental apparatus, with a sample to be tested *in situ*, is given in Figure 3.1, highlighting the three principal influences on the composite material during an experiment, namely the normal pressure over the surface area, the application of heat and the lateral straining action.
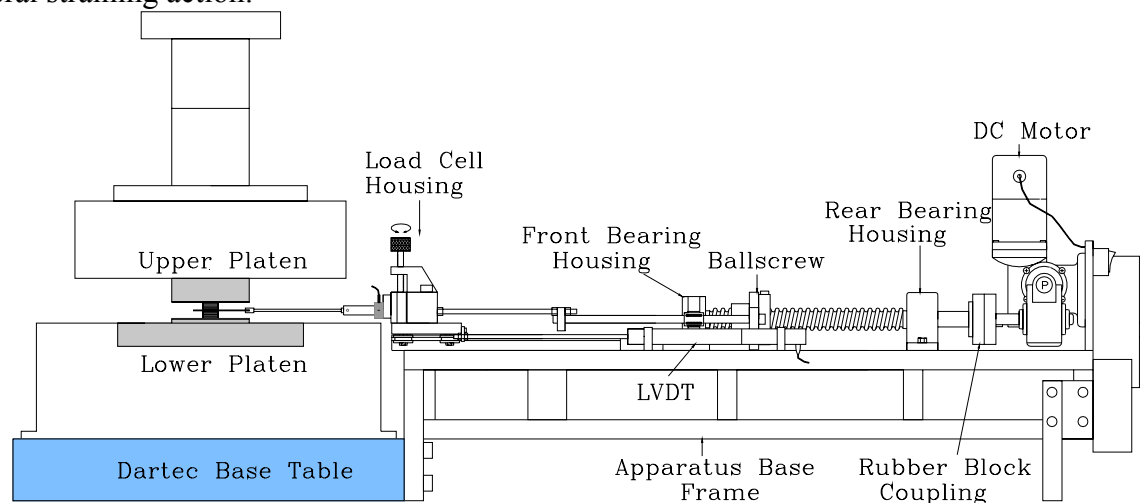
Figure 3.1: Complete shear apparatus, indicating main parts of the rig.

The vertical gap height and normal pressure was controlled using a commercially available hydraulic straining unit, Dartec 100 kN RK, the heating was effected using cartridge heaters embedded in steel platens. The shearing action was achieved and monitored using the custom built experimental rig.

The drive mechanism of the shear rig used to generate the desired (constant) pull-out velocity consisted of a motor driven ball-screw. This was attached through a connecting shaft to a main housing, which sat on a sliding trolley. The trolley was fitted with four contoured wheels that ran on the mating rail or track. The main housing supported the load cell, a 10 N maximum capacity Model 31 from Cooper Instruments (U.S.A.) Ltd., with a linearity rating of ±0.15% F.S. The load cell had two male threads along its main axis. One of these threads screwed into a T-slide on the main housing, thereby facilitating a change in the load cell height (for centralisation) by rotating a threaded shaft fitted to the slide. The other end of the load cell, called the active stud, was screwed into a rod of machineable glass ceramic, commercially known as MACOR, to minimise the conduction of heat from the composite to the load cell. Next, was a stainless steel rod to enable correct angular alignment of the pull-out plate, i.e. horizontal. A titanium tube, of outside diameter 3 mm and wall thickness 0.5 mm, was screwed directly to this steel rod. At the other end, a steel clip joined the titanium extension tube to the titanium pull-out plate. A ±25 mm linear variable differential transformer (LVDT) supplied by RDP Electronics (U.K.) Ltd., model number DCT1000C (±0.5% linearity), was employed to measure the pull-out plate displacement. The LVDT armature was connected to the rear of the housing trolley.

SPECIMEN PREPARATION

Early shear tests were performed on composite blocks consolidated under higher than recommended pressures in order to achieve a thick 'single' ply of unidirectional material, i.e. to overcome the formation of resin rich interlayers. However, subsequent shear tests resulted in interply slip of the plies. In order to encourage intraply shear in the composite and preclude the effect of the resin layers on the deformation process a novel approach would have to be adopted in order to induce the deformation sought. The only practical solution to this problem was to align blocks of composite such that the individual planes or layers of the plies were perpendicular to the line of action of the pull-out force as depicted in Figure 4.1.
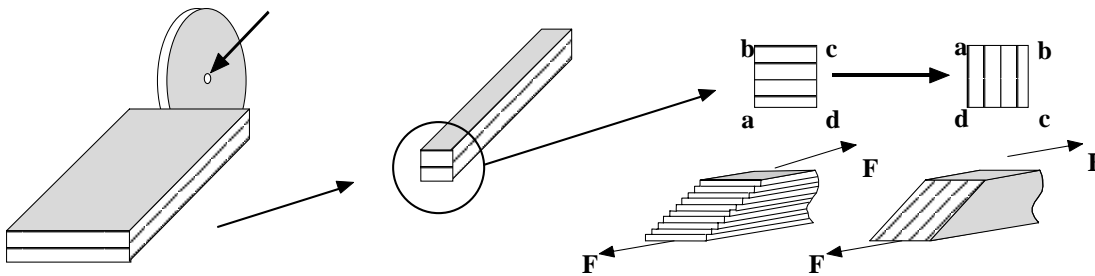
Figure 4.1: Schematic of the composite machining process and desired deformation.

Panels comprising 80 plies of unidirectional APC-2 were manufactured in an autoclave. The consolidated panels were then machined using a diamond tipped 'slitting' saw to have a constant height of 10 mm of varying lengths.

EXPERIMENTAL PROCEDURE

One half of the assembly of blocks to be tested was placed on the lower platen according to prescribed datum lines. A thermocouple probe tip was placed in close proximity to the side of the composite in order to monitor the temperature as close as possible to the assembled blocks, but without disturbing them. Prior commissioning tests were carried out to check the temperature distribution throughout the upper and lower composite block assemblies by inserting thermocouple probes into predrilled holes in the specimens and monitoring time the time taken to achieve near isothermal conditions within the material with a set point temperature of 380°C. The central titanium pull-out plate was, already attached to the extension arm, was simultaneously laid on top of the composite and into the ceramic attachment affixed to the load cell. The upper half of the composite assembly was then placed on the titanium plate directly above the block, or blocks, below. Finally, the upper platen was lowered into position, such that it made slight contact pressure with the whole assembly. When the composite attained the required temperature the motor of the shear rig was activated and the load - deflection readings were logged. The predominant pull-out velocity was set at 0.1 mms⁻¹. The effect of normal pressure on the intraply shear behavior was also limited due to the size of the assembled blocks used in the test programme, i.e. their relatively small surface area, and correspondingly, the minimum recordable normal force on the composite. A complete series of experiments was carried out on blocks of composite, with increasing block, hence fiber, length. All of these composite blocks sheared through the thickness in a truly intraply shear mode of deformation up to and including blocks of 10 mm length. With the sample length greater than 10 mm, the increased fiber length prevented the composite from shearing. A comprehensive test series was also performed in which the pull-out velocity was varied to investigate a shear rate effect on the shear behavior.

A similar programme of experimentation was carried out with the fibers aligned in a direction transverse to the pull-out force. It became evident that during the transverse shear tests that the composite tended to deform more readily than when aligned in the longitudinal direction, up to a certain extent of shear. Thereafter, the pull-out plate began to slip relative to the composite blocks, and the tests degenerated to simple friction tests. Again, a comprehensive test series was also performed in which the pull-out velocity was varied to investigate a shear rate effect on the shear behavior. Two images are given in Figure 5.1, (a) and (b), taken of a 6 mm sample sheared at 0.2 mms⁻¹, longitudinal direction, and two photographs of a 20 mm in length composite block sheared at 0.1 mms⁻¹, transverse direction (c) & (d).

(a)   (b)   (c)   (d)
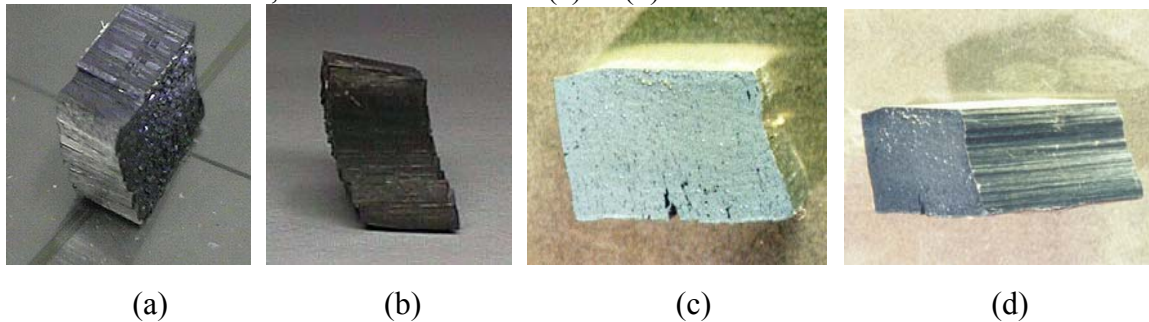
Figure 5.1: Images of samples of APC-2 post shear; (a) & (b) longitudinal direction, (c) & (d) transverse direction.

RESULTS

The full range of viscosity values extracted from the results of the test programme in the longitudinal direction is given in Figure 6.1 (a). Three distinct values of shear rate were applied during the testing phase. These corresponded to pull-out velocities of 0.025, 0.1 and 0.2 mms^{-1}. Pull-out velocities above 0.2 mms^{-1} were tried but did not result in a successful test, i.e. the pull-out plate slipped thereby instigating zero degree of intraply shear within the composite blocks. The titles in the legend of this graph refer to the block or fiber length. The viscosity values were calculated by using the average force value over the range of displacement from 1.25 to 2.25 mm of shear, when the fibers were uniformly distributed and the structure of the material was least disturbed. There exists a shear-thinning effect in the shape of the viscosity curve. There also existed a fiber length effect on the viscosity values obtained, i.e. for increasing fiber lengths the viscosity increased for all values of shear rate.

The power-law model can be used when the shear-rates being studied are not negligibly small and can use a small number of experimentally determined values to provide an empirical method for determining viscosity data. Its basis lies in the logarithmic plot of shear stress versus shear rate. The apparent viscosity, or shear–dependent viscosity, is not absolute but a function of the shear rate,

$$\eta = \frac{\tau}{\dot{\gamma}} \qquad (6.1)$$

A linear region of the logarithmic plot suggests the following relationship,

$$\tau = K(\dot{\gamma})^{n} \qquad (6.2)$$

then, an expression for the viscosity, η, reduces to:

$$\eta = K(\dot{\gamma})^{n-1} \qquad (6.3)$$

n is called the power-law index and K is called the 'consistency'. The plot of shear viscosity versus shear rate, Figure 6.1 (b), indicates that a power-law model could be applied to the composite deformation behavior, the form of which is given in equation 6.4.

(a)   (b)
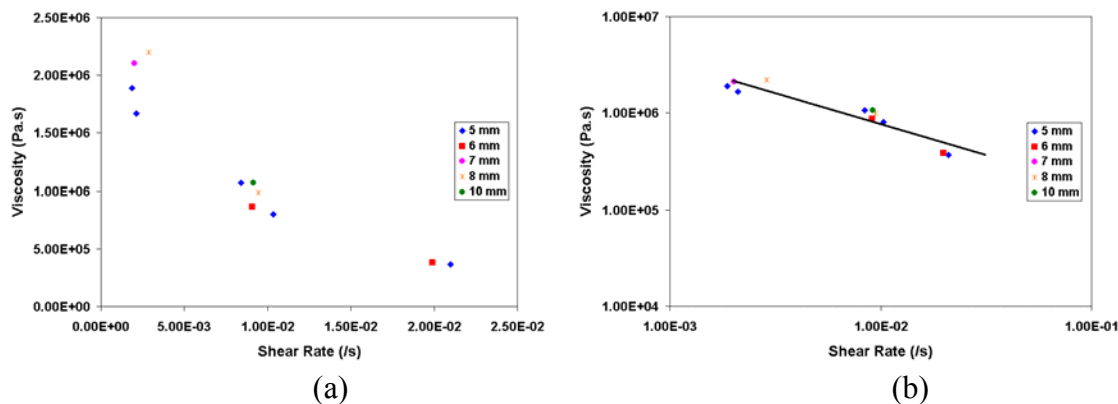
Figure 6.1: (a) Viscosity values for APC-2, for increasing values of shear rate – longitudinal direction; (b) Power-law region indicated from the tests.

$$\eta_L = 39637(\dot\gamma)^{-0.646} \qquad\qquad (6.4)$$

A similar analysis was applied to the force-displacement data collated from the tests performed in the transverse direction. The viscosity – shear rate dependence plot is given in Figure 6.2 (a).

(a)   (b)
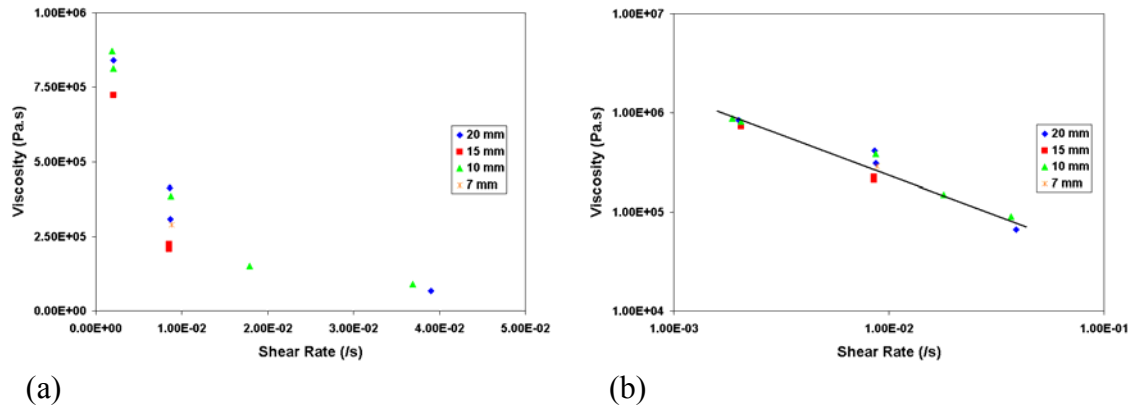
Figure 6.2: (a) Viscosity values for APC-2, for increasing values of shear rate – transverse direction; (b) Power-law region indicated from the tests.

The magnitudes of the viscosity values for the composite, with the fibers aligned in the transverse direction, turned out to be 40 % (approx.) of those when the blocks were aligned in the longitudinal direction. Again, shear thinning, the viscosity fall-off with increasing shear rate, was evident for the material during this phase of experimentation. No discernible fiber length effect was evident in the viscosity values collated. A power-law model was also applied to the results with the following equation determined from the graph in Figure 6.2 (b).

$$\eta_T = 6720.1(\dot\gamma)^{-0.7798} \qquad\qquad (6.5)$$

DISCUSSION

The values collected for the intraply shearing viscosities for the thermoplastic composite presented in this study far exceed those arrived at by oscillatory and torsional shear testing [13-15]. Values for steady flow and dynamic viscosities for both longitudinal and transverse shear varied between 3,200 Pa.s and 7,400 Pa.s. The longitudinal viscosities were on average higher by a factor of 1.3 than the transverse values. The findings from this research are in the MPas. range, three orders of magnitude in difference. A significant factor that may have influenced the torsional rheometry and oscillatory shear results would be the formation of resin-rich layers between the surfaces of the composite and the platens of the test rig. When the oscillatory deformation was applied to the samples, a large proportion of the resulting shear may occur purely within the resin-rich layers, and only a small amount being transmitted through to the bulk of the composite.

However, the resultant values arrived at through the picture-frame technique [16-18] and the transverse squeeze flow experiments [19,20] are comparable. Figure 7.1 (a) compares the power-law model proposed by the current findings and that presented by McGuinness et al [18] from the experiments done using the picture-frame method, longitudinal direction.

(a)   (b)
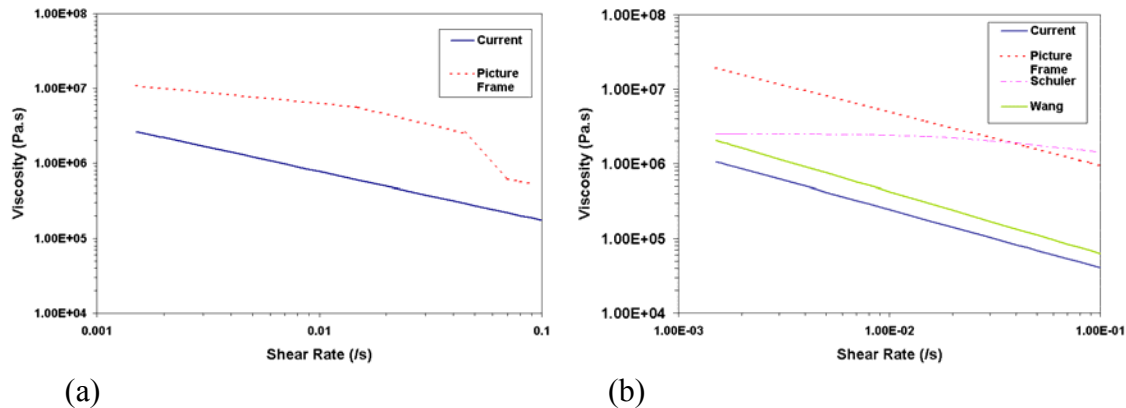
Figure 7.1: (a) Comparison of the power-law model from the current study and that proposed by McGuinness [18] for APC-2 in the longitudinal direction; (b) Comparison of the power-law model from the current study and the models proposed by McGuinness [18], Schuler [19], and Wang [20] for APC-2 in the transverse direction.

The power-law model proposed by McGuinness is not constant across the range of shear rates of interest at a temperature of 380°C. Thus the behavior could be described by using two power-law models that give viscosity values over particular shear-rate ranges, resulting in the distorted shape of the plot in Figure 7.1(a). In the transverse direction, the transverse flow experiments, in addition to the picture-frame work can now be compared with the current research. The testing temperature used throughout the range of experiments was between 370°C and 390°C. The models proposed by each researcher to describe the transverse shearing flow behavior are plotted in Figure 7.1(b). Again, McGuinness used a power-law to model the viscosity of the composite in the transverse direction. In this instance, one model described the behavior over the full range of shear rates used. Schuler and Advani [19] employed a Carreau model for the transverse shear viscosity of APC-2 at the testing temperature of 370°C. Wang and Gutowski [20] used a power-law model with parameters n = 0.17 and K = 9300 Pa.s^n. As with the longitudinal case, the transverse shear values from the picture-frame experiments far exceed those from the current investigation. The larger sample size (200 mm^2) could have cased the higher viscosities due to some degree of fiber entanglement, the probability of which would be higher with an increase in the sample dimensions. A limitation of the results or viscosity values arrived at using the picture-frame technique is that cross-ply laminates (32 ply $[0_4/90_4]_{2S}$) were used as the test samples and the force response from these tests were approximately 25% higher than the unidirectional tests, although it was not possible to deduce the viscosity values from these tests due to the complicating factor of the surrounding compliant diaphragms. Therefore, the unidirectional values of shear viscosity could be far less than 75% of the cross-ply values. Moreover, by the very nature of the rhombus deformation induced in the sample, there was a through-thickness effect also. Schuler has applied a Carreau model to describe the transverse flow behavior of APC-2 at 370°C. A 10°C increase in temperature would reduce the viscosity by approximately 17% [21]. This would account for some of the difference in the magnitude of values from this transverse flow experiment and the current study. However, over the range of shear-rates used during the current study, the viscosity values are in the Newtonian plateau in Schuler's proposed Carreau model. Only, towards the higher rates of shear, does his viscosity dependence change over to the power-law behavior. One difficulty in interpreting squeeze flow experiments is the

non-uniform nature of the flow field of the samples, which can induce large variations in shear rates throughout the material, and thus affect the overall shear rate dependence. In a similar type of experimental technique, Wang [20] applied a power-law model to describe the transverse flow of APC-2. The results compare rather favourably with current results, with the viscosity values of the current study approximately half the transverse flow values.

CONCLUSIONS

A custom built shear apparatus has been developed and applied to investigate the steady-shear deformation of a commercial high fiber volume fraction carbon fiber reinforced thermoplastic composite material. The rheological behavior of the composite has been investigated for different pull-out shear rates both along and transverse to the principal fiber directions. A novel specimen block design was introduced. Assemblies of 5 to 20 mm long blocks, 10 mm square, were tested in the rig. When values of viscosity for the composite were plotted against the shear rate, shear-thinning response or behavior was evident. The viscosity measured from the tests was approximately 2 MPa.s at the lowest shear rate of 2.5×10^{-3} s^{-1} in the axial direction. This value reduced by a factor of ten approximately, with a tenfold increase in shear rate. The transverse viscosities were consistently less than the longitudinal viscosities for all shear rates. The highest viscosity measured was approximately 0.9 MPa.s at 2×10^{-3} s^{-1}. The longitudinal values of shear viscosity were approximately 2.5 times the corresponding transverse values. A power-law model was also used to describe the shear behavior in the both directions. The values of viscosity determined during this current study were far greater than those determined using oscillatory shearing techniques. A picture-frame experiment, however delivered results of a similar magnitude to values found in this study. The results were also compared to two transverse shear/squeeze flow investigations. The results for one of these studies were modeled using a Carreau expression, but were significantly different from the current results, modeled using a power-law, although still in the MPa.s range. Another investigation, this time with the results modeled using a power-law, were quite comparable with the current results.

REFERENCES
[1] Advani, S. G. (ed), "*Flow and Rheology in Polymer Composites Manufacturing*", Composite Materials Series, Volume 10, Elsevier, 1994.
[2] Cogswell, F. N., and Groves, D. J., " The Melt Rheology of Continuous Fiber Reinforced Structural Composite Materials", Proceedings Xth International Congress on Rheology, Sydney, 1988.
[3] Cogswell, F. N., "The Experience of Thermoplastic Structural Composites During Processing", *Composites Manufacturing*, Volume 2, Number 3 / 4, 1991, pp. 208-216.
[4] Bersee, H. E. N., and Robroek, L. M. J., " The role of the Thermoplastic Matrix in Forming Processes of Composite Materials", *Composites Manufacturing*, Volume 2, Number 3 / 4, 1991, pp. 217-222.
[5] Martin, T. A., Bhattacharyya, D., and Pipes, R. B., "Deformation Characteristics and Formability of Fiber-Reinforced Thermoplastic Sheets", *Composites Manufacturing*, Volume 3, Number 3, 1992, pp. 165-172.
[6] O'Bradaigh, C. M., McGuinness G. B., and Pipes, R. B., "Numerical Analysis of Stresses and Deformations in Composite Materials Sheet-Forming: Central Indentation of a Circular Sheet", *Composites Manufacturing*, Volume 4, Number 2, 1993, pp. 67-83.

[7] Spencer, A. J. M., "*Deformations of Fiber-Reinforced Materials*", Oxford University Press, 1972.

[8] Rogers, T. G., "Squeezing Flow of Fiber-Reinforced Viscous Fluids", *Journal of Engineering Mathematics*, Volume 23, 1989, pp. 81-89.

[9] Roberts, R. W., and Jones, R. S., "Rheological Characterization of Continuous Fiber Composites in Oscillatory Shear Flow", *Composites Manufacturing*, Volume 6, Number 3 / 4, 1995, pp. 161-167.

[10] Roberts, R. W., and Jones, R. S., "Fiber Walk-out during Small Amplitude Oscillatory Shear of Continuous-Fiber Composites", *Composites Science and Technology*, Volume 58, Issue 6, 1998, pp. 855-869.

[11] Goshawk, J. A., and Jones, R. S., "Structural Reorganisation during the Rheological Characterization of Continuous-Fiber Composites in Plane Shear", *Composites: Part A*, Volume 27A, 1996, pp. 279-286.

[12] Stanley, W.F., Roberts, R. and Mallon, P.J., "The Characterization of the Shear Deformation Behavior of Fiber-Reinforced Composites", Sixth International Conference on Automated Composites ICAC, Bristol, 23-24 September 1999, pp 31-44.

[13] Kaprielian, P. V., and Rogers, T. G., "Determination of the Shear Moduli of Fiber Reinforced Materials by Centred and Off-Centred Torsion", Proceedings 34th SAMPE International Symposium, Nevada, May, 1989.

[14] Groves, D. J., "A Characterization of the Shear Flow in Continuous Fiber Thermoplastic Laminates", *Composites*, Volume 20, Number 1, January 1989, pp. 28-32.

[15] Bellamy, A. M., Groves, D. J., and Stocks, D. M., "Anisotropic Rheology of Continuous Fiber Thermoplastic Composites", *Composites*, Volume 23, Number 2, 1992.

[16] Nestor, T. A., and O'Bradaigh, C. M., "Experimental Investigation of the Intraply Shear Mechanism in Thermoplastic Composites Sheetforming", *Key Engineering Materials*, Volumes 99-100, 1995, pp. 19-36.

[17] McGuinness, G. B., and O'Bradaigh, C. M., "Characterization of the Processing Behavior of Unidirectional Continuous Fiber Reinforced Thermoplastic Sheets", Proceedings 4th International Conference on Flow Processes in Composite Materials, University of Aberystwyth, Wales, September, 1996.

[18] McGuinness, G. B., and O'Bradaigh, C. M., "Characterization of Thermoplastic Composite Melts in Rhombus Shear: The Picture-Frame Experiment", *Composites: Part A*, Volume 29A, 1998, pp. 115-132.

[19] Schuler, S. F., and Advani, S. G., "Transverse Squeeze flow of Concentrated Aligned Fibers in Viscous Flow", Journal of Non-Newtonian Fluid Mechanics, Volume 65, Number 1, July, 1996, pp. 47-74.

[20] Wang, E. L., and Gutowski, T. G., "Laps and Gaps in Thermoplastic Composites Processing", *Composites Manufacturing*, Volume 2, Number 2, 1991, pp. 69-78.

[21] Cogswell, F. N., "*Thermoplastic Aromatic Polymer Composites*", Butterworth-Heinemann, 1992.

In-Mold Coating of Thermoplastic Substrates-Wall Slip and Improved Rheological Model

Narayan Bhagavatula and Jose M Castro

Department of Industrial Systems and Welding Engineering
The Ohio State University, Columbus, OH 43210
And Corresponding Author's e-mail: castro.38@osu.edu

SUMMARY: For thermoplastic parts like automotive body panels, the current industrial practice is to paint them for protection against outdoor exposure or to improve surface appearance. Painting is environmentally unfriendly and costly. Furthermore, a non-environmentally friendly adhesion promoter typically needs to be used before painting. In-mold coating (IMC) is a cost effective and environmentally benign alternative to painting. IMC is carried out by injecting a liquid low viscosity thermoset material onto the surface of the thermoplastic part while still in the mold. The coating then solidifies and adheres to the substrate. A Hele-Shaw based mathematical model and a corresponding computer code based on the Control Volume Finite Element Method (CV/FEM) has been developed to simulate the flow during the IMC process assuming the coating to be a power law fluid [5]. The continuous deformation of the thermoplastic substrate caused by the coating injection is analyzed by means of the PVT relationship of the substrate. Although the simulation works well for predicting fill patterns as discussed in [5], pressures were found to deviate from experimentally recorded results. A one-dimensional simulation is presented in this paper to show that including wall slip and using an improved rheological model better predicts the pressure distribution.

KEYWORDS: In-mold Coating, Wall slip, Sisko Model, Power law model.

INTRODUCTION

In-mold coating (IMC) has been successfully used for many years for exterior body panels made from a fiber reinforced polymeric composite material named Sheet Molding Compound (SMC) by compression molding. The coating is a thermoset liquid, used to fill the surface porosity typical in these composites and to improve their surface quality in terms of functional and cosmetic properties [1]. When injected onto a cured SMC part, IMC cures and bonds to provide a paint-like surface [2]. Because of its distinct advantages, IMC is now being considered for injection molded thermoplastic parts. Similar to IMC for SMC, IMC for thermoplastics could be used either as a topcoat or as a primer. As a primer, it will replace the currently used adhesion promoter. The long term goal is to completely eliminate both the priming and painting operation altogether. With current materials, the potential to eliminate the adhesion promoter is large [3, 4]; however, more research is needed to completely eliminate painting. For a successful IMC operation, there are two key concerns that need to be addressed. The first one is the location of the injection nozzle. It should be located such that the thermoplastic part is totally covered and

the potential for air trapping is minimized. The selected location should be cosmetically acceptable and should also be accessible for ease of maintenance. The second one is that the clamping force available needs to be higher than the hydraulic force generated by the coating so that the mold does not open during IMC injection. For IMC for SMC, this is not a key issue since SMC molds have shear edges that act as a seal in case the mold opens. The goal of this research work is to develop a computer simulation tool to predict the pressure distribution and the fill pattern to enable the identification and screening of potential IMC nozzle locations and to determine the required clamping force. In a previous paper [5], we presented a two-dimensional model based on the Hele-Shaw approximation to predict the flow of IMC, assuming the coating to be a power law fluid. Though the simulation tool predicts experimental fill patterns reasonably well, the pressures were not properly predicted. This could be due to wall slip as often found in flow through micro channels. To demonstrate this effect, we introduced a slip boundary condition into the 1-D pressure governing equation presented in [6]. It was shown that as we introduce a non-zero value to the slip coefficient β, the simulated pressures move towards the experimental values as shown in Fig.1. Thus slip at the wall during filling of the mold could be one of the reasons we obtain lower than predicted pressures [7]. Additionally, the coating material has shown evidence of an upper Newtonian plateau at the high shear rates encountered during coating. Thus, an improved rheological model instead of the power law would also help in predicting pressures more accurately. In this paper, we use an improved rheological model, namely, the Sisko model, in conjunction with the slip boundary condition in a 1-D flow case to illustrate how the introduction of additional modeling parameters is a step in the right direction towards predicting pressures more accurately.
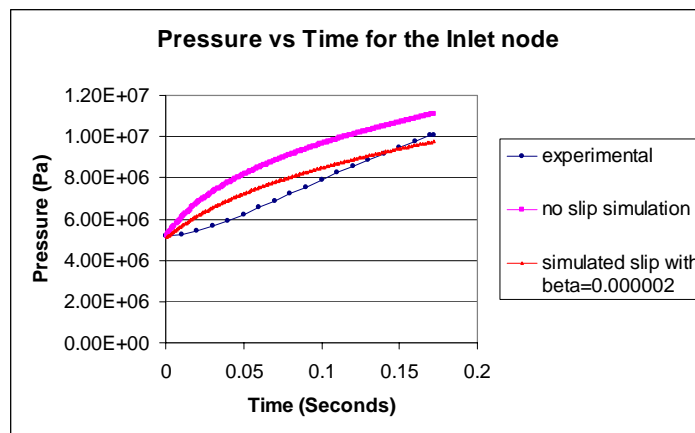
Fig.1. Numerical vs. Experimental Pressures

MATHEMATICAL MODELING

For a simple rectangular part, the coating flow from a line injection port can be approximated as a one-dimensional flow as shown schematically in Fig. 2. The following assumptions are made:

1) Isothermal flow, since, due to the very thin gap, the coating reaches the wall temperature in a very short time [4];
2) Quasi-steady-state flow with inertial terms neglected;
3) Lubrication approximation: $v_x = v_x(z, h(x))$;
4) The gap available for IMC flow can be expressed as [4] :

$$h = h_S (1 - \frac{V}{V_0})$$ (1)

where h_S is the thickness of the thermoplastic substrate, V is the specific volume of the thermoplastic substrate and is a function of the IMC pressure under the assumption of isothermal flow, V_0 is the specific volume of the thermoplastic substrate at the average (bulk) temperature just before the coating injection starts.

The viscosity of the coating liquid is modeled using the Sisko model:

$$\eta = \eta_\infty + m\dot{\gamma}^{n-1}$$ (2)

where η_∞ is the upper Newtonian Viscosity, m and n are constants.

Fig.2. Schematic of 1D IMC flow

With the above assumptions, the momentum balance equation can be simplified to:

$$\frac{\partial p}{\partial x} = \frac{\partial}{\partial z}[\eta(\frac{\partial v_x}{\partial z})]$$ (3)

where p is the pressure of the coating and v_x is the velocity of the coating. The boundary conditions are given by:

$$v_x = v_s = \beta\left(\frac{\partial v}{\partial z}\right)\bigg|_{z=0}; \quad \text{at } z = 0$$ (4)

$$\frac{\partial v_x}{\partial z} = 0; \quad \text{at } z = h/2$$ (5)

where β is the slip coefficient.
Integrating Eqn. 3 using the boundary conditions, and substituting Eqn. 2 in the resultant equation, we obtain an expression for the pressure gradient in terms of the velocity and viscosity parameters:

$$\frac{\partial p}{\partial x}\left(z - \frac{h}{2}\right) = [\eta_\infty\left(\frac{\partial v_x}{\partial z}\right) + m\left(\frac{\partial v_x}{\partial z}\right)^n]$$ (6)

This equation needs to be solved numerically since the pressures cannot be calculated explicitly in terms of flow rate. Further, the coating thickness is a function of the specific volume of the thermoplastic that is related to pressure and needs to be solved numerically. Finite Difference Method (FDM) was used to solve the equations numerically. Nested iteration

loops were used to solve for pressures. At a fixed spatial step, that is used to track the flow front location, using the inner loop, the pressures were obtained for using iterative solutions for velocity and pressure at a particular coating thickness. For each time step, the flow front is advanced by one spatial step, and then the pressure distribution and the coating thickness distribution are obtained by iterative solution of Eqn.1 and PVT relationship as defined in [5]. The whole procedure is repeated until filling is completed.

RESULTS AND DISCUSSION

Fig.3 shows the comparison between the experimentally observed pressures (at transducer location) and various numerically obtained results for coating a thermoplastic (ABS) flat plate of dimensions 0.152m x 0.152m x 0.002m. The flow rate used was 3.679E-07 m^2/s. *n* and *m0* values were 0.3085 and 0.0935 respectively. It can be seen that the experimental results are not adequately predicted by the available filling simulation codes. Based on the preliminary experimentally determined viscosity values, η_∞ was found to be approximately 0.075 Pa-s. Using this value in the 1-D flow case and checking for various values of slip coefficient β, it was observed that at a particular value, the predicted pressures adequately match the experimentally observed values. The general trend seen is that increasing η_∞ increases the slope of the curve whereas decreasing β, the slope decreases.
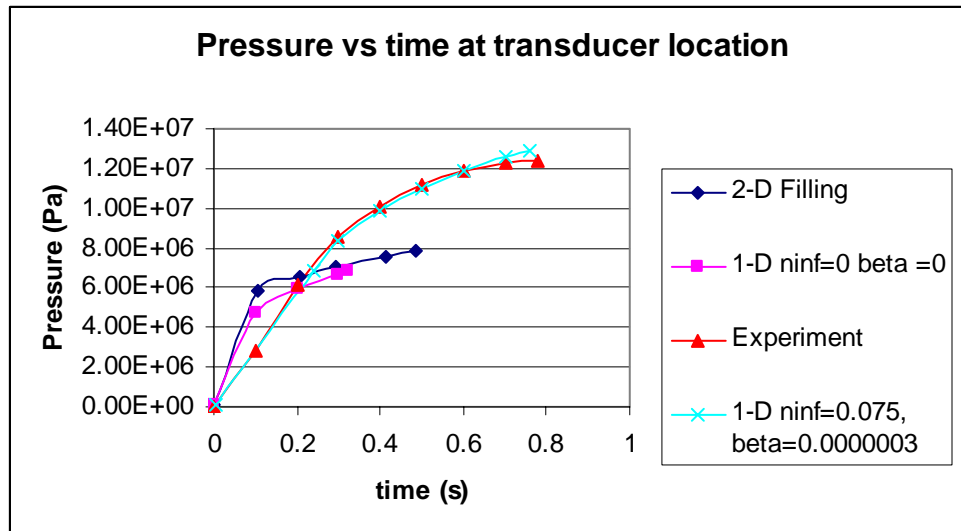
Fig.3 Comparison between the experimentally observed pressures (at transducer location)

CONCLUSIONS AND FUTURE WORK

A computer code has been developed for coating flow in one direction. The code includes an improved viscosity model, namely, the Sisko model and boundary condition allowing slip at the wall. Preliminary results indicate that these are steps in the right direction towards being able to predict the pressure distribution during coating flow. More work is needed to properly characterize the coating materials at high shear rates and to evaluate the slip coefficient. The computer code also needs to be extended to 2-D cases so that the coating of actual parts can be simulated.

REFERENCES

1) Haglund R, 1998, *In Mold Top Coating on Automotive Exterior SMC panels*, Thesis, Lund Institute of Technology, 39.

2) Straus E J, McBain D, and Wilczek F, 1997, *Reinforced Plastics*, 41.

3) Cabrera-Rios M, Zuyev K S, Chen X, Castro J M and Straus E J, 2002,*Polymer Composites* 23, 5.

4) Chen X, 2003, *PhD thesis*, The Ohio State University, Columbus, Ohio.

5) Chen X, Bhagavatula N and Castro J M, 2003, *Modeling and Simulation in Material Science and Engineering*,11, 1.

6) Zuyev K S, Chen X, Cabrera-Rios M, Castro J M and Straus E J, 2001, *Journal of Injection Molding Technology*, 5,2.

7) Bhagavatula N, Castro J M, 2004, *Numerical Methods in Industrial Forming Processes NUMIFORM 2004,* to be published.

Production of Complex 3D Parts Made of Continuous Fiber Thermoplastic Composites:
Development of a New Tooling Concept

J. Denault[1], G. Lebrun[2], P. Gagnon[1], D. Boucher[3] and B. Fisa[3]

[1]*Industrial Materials Institute, National Research Council Canada, 75, de Mortagne, Boucherville (Quebec) Canada J4B 6Y4, johanne.denault@cnrc-nrc.gc.c*
[2]*Currently at Composites Atlantic Ltée, 17000, rue Charles, suite 500, Mirabel (Quebec) Canada J7J 1X9, g.lebrun@qc.aira.com*
[3]*Department of Mechanical Engineering, École Polytechnique de Montréal, C. P. 6079, Succ. Center-Ville, Montreal (Quebec) Canada H3C 3A7, bohuslav.fisa@polymtl.ca*

SUMMARY: New tooling concept was developed to address the shortcomings of existing forming processes of continuous fiber reinforced thermoplastic (CFRTP),. This technology allows high volume production of good quality parts while keeping the development and fabrication costs low. Highlights of the technology include: molding of deep parts with small draft angles, better laminate conformation over the complete mold surface, uniform consolidation pressure over the whole part area , elimination of the need to know the final thickness distribution, reduced risk of premature laminate solidification during molding, reduced risk of excessive friction between the laminate and the mold cavity in the last portion of mold closure and elimination of the risk of mold locking due to the lateral expansion of the rubber punch.

KEYWORDS: Continuous fiber thermoplastic composites, thermoforming, tooling, stamping, sheet handling system, sheet car system.

INTRODUCTION

A great number of forming methods have been developed to mold CFRTP parts. Among these, the most familiar is undoubtedly the matched-die process, not only because of the extensive use of such tooling in the automotive industry for sheet metal forming but also because the machining of two rigid mold halves is a practice common to many processing techniques. In the matched-die technique, the mold halves are machined to the part geometry from steel or aluminum blocks. They are then installed between the platens of a press, which is mounted with moving frames for the clamping of the composite sheet and the sheet displacements between adjacent ovens and the press. Due to thickness variations of the laminate induced during forming, the size and geometry of both mold halves must be such that, once the mold is closed, the cavity thickness must perfectly match the final part thickness distribution to ensure a uniform

consolidation pressure over the part area. This aspect is even more critical when deep parts with small draft angles are stamped because in such cases, the increased shear deformations of the laminate are combined with the lower consolidation pressures over the side walls (the component of the press closing force normal to the side walls being much lower in such case).

To avoid these drawbacks of the matched-die process, a rubber-forming technique can be used. This process is similar to the matched-die technique except that the male half of the mold is made of highly deformable rubber, molded to or slightly larger than the part geometry. The main advantage of using a rubber punch is that during the mold closure the rubber deformation allows the application of a quasi-constant pressure over the part area, the deformed rubber punch acting as an incompressible fluid, thus ensuring a better laminate consolidation and allowing more flexibility in the punch design. Also, the lower thermal conductivity of the rubber punch reduces the cooling rate, giving more time to mold the part before premature solidification can occur. However, a good knowledge of the mechanical and thermal behavior of the rubber and of the deformation of the punch during mold closure must be developed, to control the increased friction between the laminate and the side cavity walls which can lead to mold locking prior to complete closure and to the collapse of the punch for parts having a large depth to width ratio. Increased laminate friction can also lead to premature cooling of the molten matrix and affect the surface finish of the part. Finally, if the punch size and geometry differ from those of the cavity, two cavities have to be machined, one for the cavity itself and one for the molding of the punch, increasing the fabrication time and cost.

To avoid relying on costly and inefficient trial-and-error practices as it is often the case in the development of new processing technologies, and considering the complexity of the thermoforming-stamping process of CFRTP parts, significant research effort has been devoted to the development of numerical tools to predict the laminate behavior during the forming process and the mechanical behavior of molded parts [1, 2]; the most successful to date being the PAM-FORM^{TM} analysis simulation program developed by ESI Software Inc. (France). In parallel to these developments, many research activities are dedicated to the understanding of the macro- and micro-mechanical behavior of composite materials during molding [3-5], which is essential for the development of efficient forming tools for CFRTPs. In this paper, a new tooling concept is presented. This technology allows the high volume production of good quality parts while keeping the development and fabrication costs low. Highlights of the technology include: molding of deep parts with small draft angles, better laminate conformation over the complete mold surface, uniform consolidation pressure over the whole area of the part, elimination of the need to know the final part thickness distribution, reduced risk of premature laminate solidification during molding, reduced risk of excessivefriction between the laminate and the mold cavity in the last portion of mold closure and elimination of the risk of mold locking due to the lateral expansion of the rubber punch.

EXPERIMENTAL

The consolidated thermoplastic commingled twill 2/2 weave fabric (26 oz/yd^2, glass only) of PP and 60% w/w of continuous E-glass fibers glass fibers used for the development of this technology was obtained from Vetrotex Certainteed (Twintex™).

RESULTS AND DISCUSSION

The thermoforming stamping is a processing technology derived from the thermoforming of plastic sheet and stamping of metal. It essentially consists in the transformation of preconsolidated and non consolidated continuous fiber thermoplastic composite plate under three dimensional part. The suitable conditions for thermoforming continuous glass fiber polypropylene composite are:

- Using an oven with IR elements to heat the laminate to about 200 °C.
- Transfer of the heated laminate to the forming unit (mold) in less than 5 seconds.
- Closure of the mold in less than 5 seconds while ensuring an efficient laminate stretching with the support/clamping system. Mold closure must be fast enough to avoid premature matrix cooling but slow enough to avoid laminate wrinkling during the forming phase
- Application of a minimum forming pressure for the laminate consolidation.
- Removal of the part from the mold after part has cooled to below 100 °C

New technology

In order to eliminate some of the problems encountered with the matched-die and the rubber-forming processes, a new tooling concept has been developed. In principle, this new concept keeps most of the advantages of the matched-die and the rubber-forming processes and removes most of their disadvantages. Figure 1 shows a schematic representation of the process. The concept is based on a mold punch made of a flexible diaphragm maintained by a rigid composite structure. During molding, a vacuum is applied inside the rigid structure and, via holes drilled through its walls, the diaphragm is maintained retracted against the structure. This allows the laminate to move freely along the side walls during mold closure, avoiding friction between the laminate and the tool. In a first step, the substructure forms the bottom part of the mold, similar to the matched-die process, and in a second step, the vacuum in the sub-structure is changed for air pressure to allow the diaphragm to conform the side walls of the part. The flexural strength of the parts molded from this processing technology in comparison with other techniques is presented in Figure 2.

Principal advantages over the matched-die and the rubber forming processes obtained with this concept are:

- It permits the conversion of a preconsolidated or of a non consolidated continuous fiber thermoplastic composite plate into a three dimensional part
- Reduces the risk of premature cooling along the side walls
- Decreases mold cost
- Reduces thickness variations over the part surface due to the application of a uniform pressure by the diaphragm
- Renders part consolidation more uniform
- Allows cycle times similar to the matched-die process because the sub-structure can rapidly push the laminate to the bottom of the mold
- Is a low cost process with the possibility to mold medium to high volumes of parts
- Keeps all the advantages of the rubber forming process with respect to the conformation of small radius edges and corners

- Allows the possibility to use composite membranes made by stacking rubber layers of different hardness an properties for better results concerning the forming of small geometric features of the part
- Avoids the drawback associated with the high coefficient of thermal expansion of rubber materials for which, in the rubber forming process, the size of the punch have to be designed by taking into account thermal expansion of rubber
- Avoids friction between the rubber diaphragm and the tools because the rigid composite base acts as an abrasion protector while the sides of the diaphragm, under vaccum, do not slide on the laminate. Only normal pressures are then sustained by the diaphragm, thus preserving its integrity for a longer period
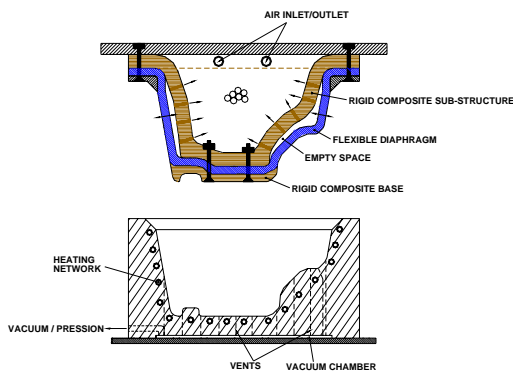
Fig. 1 Diaphragm and sub-structure concept tooling design.
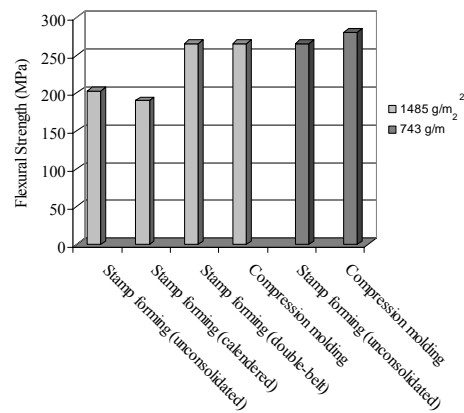
Fig. 2 Comparison of the flexural strength for different molding process.

The sheet handling system is another critical component of the molding process as it ensures transfer of the sheet from the oven to the forming unit and acts as a tensioning system on the laminate to avoid wrinkles in the part. Conventional thermoforming sheet handling systems for unreinforced plastics are not appropriate for thermoforming composite laminates because of the stiffness of the fibers. Figure 3 shows a sheet handling system that has been developed to mold laboratory scale parts. For larger parts, the following requirements have been taken into account in the design:

- Minimise the contact between the melted laminate and the outside part of the mold to avoid premature cooling.
- Ensure appropriate clamping and sufficient membrane tension on the laminate.
- Allow enough displacements of the sheet boundaries and follow the movements of theses boundaries during forming.
- Minimize material waste.
- Keep a good control of the sheet position during the forming phase.
- Do not disturb the IR rays of the heating system during the heating stage.
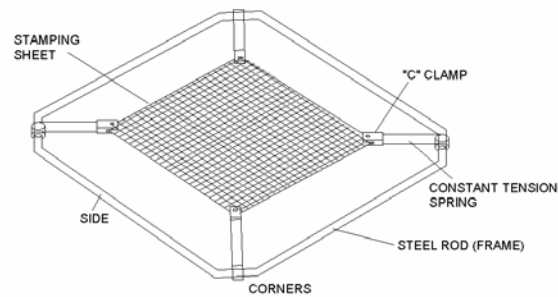
Fig. 3 .Sheet handling support for continuous fiber thermoplastic composites.

Figure 4 illustrates the importance of the location of the clamps of the clamping system. It was demonstrated that, depending on the orientation of the molten laminate as compared to the mold geometry and orientation, the clamps must be positioned at specific locations around the periphery of the sheet and the tension force they apply to the sheet at these locations must be properly adjusted to ensure a good conformation of the part.

(a)

(b)
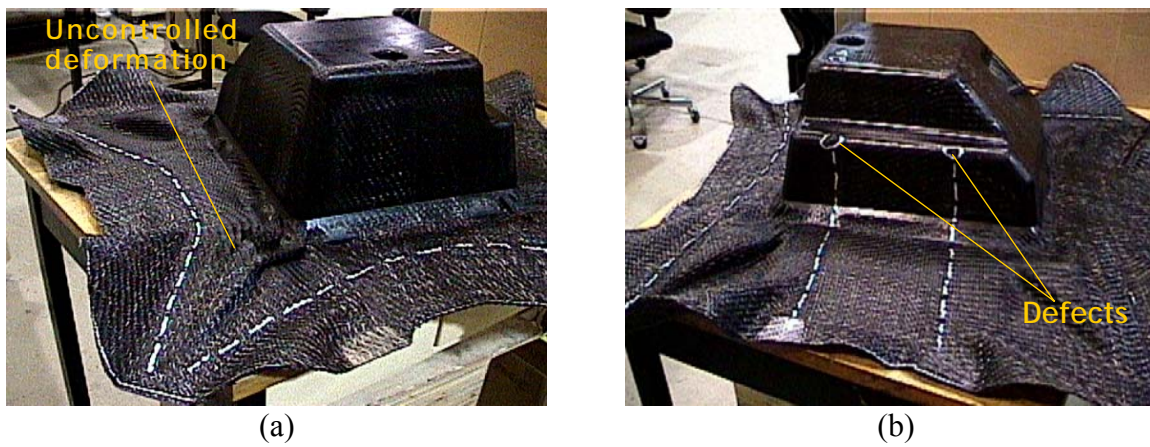
Fig. 4 . Part molded with a non-optimized sheet supporting clamps position. a) Uncontrolled fabric deformation at corners and b) Side edges defects induced by excessive tension induced in the fibers by the clamping supports..

CONCLUSION

In this paper, new tooling concept is presented. This technology allows production of good quality parts at high volume production while keeping low the development and fabrication costs. Advantages of this technology include: molding of deep parts with small draft angles, better laminate conformation over the complete mold surface, elimination of the need to know the final thickness distribution of the part, and short processing cycles, decrease time and cost required for production set up.

REFERENCES

1. De Luca, P., Lefébure, P., Pickett, A.K., Vodermayer, A.M. and Werner, W., 28th Int. SAMPE Tech. Conf., November 4-7, 1996, Seattle, USA.
2. Hsiao, S.-W. and Kikuchi, N., *Appl. Mech. Eng.*, 177, 1-34 (1999)
3. Lebrun, G. and Denault, J., American Society for Composites, 15th Tech. Conf., Sept. 25-27,2000, College Station, Texas, U.S.A.
4. Hou, M. and Friedrich, K.., *Applied Composite Materials*, 1, 135-153 (1994).
5. Bureau, M. N. and J. Denault, *Polymer Composites*, 21, 636-644 (2000).

RESIN TRANSFER MOLDING

Carbon Fiber Reinforced Composites and the Automotive Industry: A New Frontier?

David Steenkamer, Daniel Houston and Jeffrey Dahl

Research and Advanced Engineering, Ford Motor Company
2101 Village Road, MD3135, Dearborn, MI 48121-2053
dsteenka@ford.com

SUMMARY: Over the past fifty years, composites have become accepted in the automotive industry as an alternative material to steel for the production of exterior closure panels, semi-structural and structural parts. Composite components can now be found across the entire gamut of vehicles produced by the automotive industry including passenger, sports, and luxury cars, light- and medium-duty trucks, sport utility vehicles, and mini-vans. The vast majority of these composites are reinforced with either short or chopped glass fibers and they provide weight savings of 15 - 30% relative to a comparable steel part. As the automotive industry strives to improve fuel economy and reduce emissions of future vehicles, greater weight savings are needed. Aluminum and magnesium offer mass savings relative to steel of 50 - 60%. For composite materials to compete with these lightweight metals, carbon fiber must be utilized as the reinforcing fiber. This paper will present the preliminary results of experimental studies into the use of chopped carbon fiber in sheet molding compound (SMC) and structural reaction injection molded (SRIM) composites. While cost is a long-term business issue that will affect the proliferation of carbon fiber composites in the automotive industry, these studies have shown that technical issues including the fiber form and surface treatment exist that affect chopping, molding, and performance of carbon fiber reinforced composites. These technical issues must be addressed if carbon fiber composites are to become a viable alternative to aluminum and magnesium.

INTRODUCTION

Over the past fifty years, composites have become accepted in the automotive industry as an alternative material to steel for the production of exterior closure panels, semi-structural and structural parts. Composite components can now be found across the entire gamut of vehicles produced by the automotive industry including passenger, sports, and luxury cars, light- and medium-duty trucks, sport utility vehicles, and mini-vans. Relative to steel, composite materials provide the automotive industry with a variety of benefits including parts consolidation, design/styling flexibility, corrosion resistance and lower capital investment. The vast majority of these composites are reinforced with either short or chopped glass fibers

and they provide weight savings of 15 - 30% relative to a comparable steel part. As the automotive industry strives to improve fuel economy and reduce emissions of future vehicles, greater weight savings are needed. Aluminum and magnesium offer mass savings relative to steel of 50 - 60%. For composite materials to compete with these lightweight metals, carbon fiber must be utilized as the reinforcement. Thus, this paper will present the preliminary results of experimental studies into the use of chopped carbon fiber in sheet molding compound (SMC) and structural reaction injection molded (SRIM) composites.

CHOPPABLE CARBON FIBER

Carbon fiber rovings are typically single-ended type materials as they have traditionally been used in fiber conversion processes such as weaving, braiding, stitch bonded fabrics, and pre-preg manufacture or in composite fabrication processes such as pultrusion and filament winding. This presents a problem for the automotive industry. Specifically, the automotive industry uses large quantities of compression molded SMC and SRIM composites because of the low investment associated with these processes relative to steel stamping and the fast cycle times (i.e., 1 - 4 minutes). Historically, these materials and processes have employed a multi-ended glass fiber roving, which is an entirely different product form, as it chopped during the compounding stage for SMC or during the performing stage for SRIM. Although several carbon fiber roving variants have been and are currently under development at several suppliers, they all seem to fall short of optimum when compared to glass fiber rovings designed for chopped fiber applications. As a result, a myriad of processing issues exist when attempting to fabricate carbon fiber sheet molding compound (CF-SMC) or carbon fiber preforms for SRIM such as fiber fuzzing, substantial fiber 'fly' and excessive filamentization of the chopped material.

CARBON FIBER REINFORCED SMC COMPOSITES

In 2002, the North American transportation industry (i.e., automotive and heavy truck) consumed over 200 million lbs. of SMC [1]. The formulation of this material can be tailored to meet the demands of the application (i.e., Class "A" body panel, under-the-hood component or structural part). For structural applications, vinyl ester resins are typically used to meet the operating temperatures and 50% by weight, glass fibers are used as the reinforcement to provide the stiffness and strength required. To achieve the greatest weight savings relative to steel, the initial studies on CF-SMC have replaced all of the glass fiber with carbon fiber.

To fabricate the test panels for this study, single-ended 12K PAN carbon fiber SMC was compounded on a conventional line and maturated in a temperature and humidity controlled room. After thickening to the desired viscosity, plies of a pre-determined size and shape were cut from the roll and stacked up to form the charge. The charge was then placed onto the core of the tool and compression molded into test plaques.

Tensile and compression tests were performed on specimens machined from the composite plaques in both the 0° (parallel to the compounding machine) and 90° (cross the compounding machine) directions and the results are provided in Table 1.

To put this data into perspective, it should be noted that this material was reinforced with 55% by weight carbon fibers resulting in a composite with a specific gravity of 1.5. The data in Table 1 clearly indicates that there is a significant amount of variability in the CF-SMC as the coefficients of variation (COVs) ranged between a low of 9% and a high of 21%. In some cases (most notably tensile modulus and compressive strength), the CF-SMC exhibits anisotropy. With the amount of scatter in the data, it is hard to determine how real this phenomenon is or if the 0° and 90° data overlap. However, if an automotive design approach (typically mean minus three standard deviations) is used, the combination of the COVs and the anisotropy dramatically decreases the design allowable. Finally, by comparing the properties in Table 1 to those of 50% by weight glass fiber reinforced SMC [2], it is clear that the use of carbon fiber substantially increases the tensile modulus but there is much less of a benefit of incorporating this reinforcement in terms of increasing tensile and compressive strengths.

Table 1: Mechanical properties of CF-SMC *

Property	Carbon Fiber SMC	
Test direction	0°	90°
Tensile modulus, GPa	43 (21%)	36 (14%)
Tensile strength, MPa	212 (19%)	205 (12%)
Poisson's ratio	0.26	0.40
Compressive strength, MPa	234 (11%)	292 (9%)

The data in parentheses is the coefficient of variation associated with the property.

CARBON FIBER REINFORCED SRIM COMPOSITES

For this portion of the study, chopped carbon fiber performs were fabricated using the Ford Programmable Preforming Process (F3P) and then molded into a composite via SRIM with a polyurethane resin. With the F3P process, carbon fiber rovings were processed through an Aplicator SMART chopper gun and a flat panel preforming tool was used for preform fabrication. The flat panel preforming tool is 700 x 700 mm and the consolidation thickness can be varied with the use of stop blocks at the four corners of the tool.

For these experiments, a total of three different materials were tested: two carbon fiber rovings and one glass fiber roving. The experimental carbon fiber rovings tested are designated as Carbon Roving A and B. Carbon Roving A is a multi-ended roving containing a total of approximately 48k filaments that have been split into 8 bundles containing approximately 6k filaments per bundle. Carbon Roving B was also a multi-ended roving but it contained a total of 36k filaments by combining 12 bundles with each containing 3k filaments. The glass fiber used was a gun roving, which is mainly used in the spray-up process, but it has also been successfully used in chopped fiber performing processes.

During visual examination of the carbon fiber preforms fabricated at low areal densities (<1000 g/m^2), it was noticed that an excessive amount was light transmitted through the perform.

When these performs were placed on a light table (Figs. 1 and 2), it was evident that regions of zero fiber content were present. This phenomenon was not evident in glass fiber preforms fabricated at areal densities yielding the same fiber volume fraction. Based upon these visual issues, preliminary screening experiments were conducted in an attempt to determine what factors contributed to the formation of the zero fiber regions. The results of these studies indicated that preform processing parameters did not contribute significantly and, therefore, could not be used to reduce the amount of zero content regions within the preform. The main factor was determined to be the particular type of carbon fiber roving used in preform fabrication with Carbon Roving A being the worst case. If regions of zero fiber existed, then in order to maintain the overall areal density within the plaques, regions far exceeding the nominal were also present.
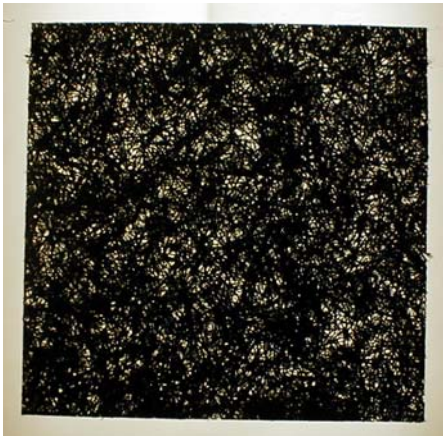
Fig. 1: Carbon Roving A @ 500 g/m^2 Fig. 2: Carbon Roving A @ 1000 g/m^2

In addition to the light transmission study, the perform permeabilities were also measured by using Darcy's Law in a rectilinear permeability rig. Three pressure transducers were used to obtain pressure data and are located at 33, 115 and 218 mm from the injection point. The fluid used was a mixture of 82% by weight glycerol and 18% by weight water with a viscosity of approximately 56 mPa·s. Pressure data between the three transducers was used to calculate the permeability. All preforms were fabricated using the same preform processing conditions yielding a fiber volume fraction of 40% for a 3.0 mm cavity thickness. This corresponds to a preform areal density of 2160 g/m^2 for carbon fiber and 3072 g/m^2 for glass fiber.

As shown in Table 2, the preform with Carbon Roving B exhibits decreased permeability when compared to the preform with Carbon Roving A. This is probably caused by the increased number of individual bundles present within the preform. This provides an increased number of fiber contact points and an overall increased surface area for fluid contact thereby increasing the resistance to flow and yielding lower permeability. Conversely, the permeability of the glass fiber preform is comparable to that of Carbon Roving A; however, the glass fiber roving contains approximately 12 times as many bundles as Carbon Roving A. Based on the permeability data and the differences highlighted above, it is believed that as carbon fiber rovings approach bundle geometries comparable to glass fiber rovings, which is necessary for uniform fiber dispersion, the permeability of carbon fiber preforms will be substantially lower when compared to glass fiber preforms.

In terms of mechanical testing, tensile tests were performed on specimens machined from SRIM composite plaques formed with Carbon Roving A as well as the baseline glass roving. By comparing the properties of these materials (Table 3), it is clear that the use of carbon fiber almost doubled the tensile modulus; however, the use of carbon fiber actually led to a decrease in both the tensile strength and strain to failure. The authors attribute these results to the findings of the light transmission studies in which high and low areal density regions were found in performs with carbon roving A. This also explains the greater variability in the CF-SRIM composites as the COVs were greater than those measured for the glass fiber-SRIM composites.

Table 2: In-plane permeabilities of chopped, random fiber preforms

Material Type	Thickness (mm)	Fiber Volume Fraction (%)	Wetted In-Plane Permeability (Darcy)	COV (%)
Carbon Roving A: 8 x 6k	3.0	40	145	27
Carbon Roving B: 12 x 3k	3.0	40	59	25
Glass Roving OC 357 D-AA	3.0	40	125	21

Table 3: Mechanical properties of glass and carbon fiber reinforced SRIM composites *

Property	Polyurethane/Glass Fiber	Polyurethane/Carbon Fiber
Fiber volume fraction, %	38	40
Tensile modulus, GPa	15.2 (8%)	27.9 (22%)
Tensile strength, MPa	247 (12%)	200 (13%)
Tensile strain, %	2.30 (7%)	0.80 (17%)

* The data in parentheses is the coefficient of variation associated with the property.

SUMMARY

As the automotive industry strives to improve fuel economy and reduce emissions of future vehicles, greater weight savings are needed. Aluminum and magnesium offer mass savings relative to steel of 50 - 60%. For composite materials to compete with these lightweight metals, carbon fiber must be utilized as the reinforcing fiber. This paper presented the preliminary findings of experimental studies into the use of chopped carbon fiber in SMC and SRIM composites. While cost is a long-term business issue that will affect the proliferation of carbon fiber composites in the automotive industry, these studies have shown that technical issues also exist. Specifically, the variability and anisotropy in the CF-SMC must be reduced and the chemistry must be optimized in order to improve the adhesion of the vinyl ester resin to the carbon fibers in order to increase the tensile and compressive strengths. With regards to CF-SRIM composites, a great deal of improvement is needed to reduce variability within carbon fiber preforms to levels normally associated with glass fiber.

Based upon the test results presented, it appears that with an improvement to the product form, preform characteristics can also be improved to benefit not only the preforming process but also the molding process and mechanical performance of composite.

REFERENCES

1.   Automotive Composites Alliance, 2002 Model Year Passenger Car and Truck Thermoset Composite Components, Troy, Michigan, 2002.

2   D. Denton, The Mechanical Properties of an SMC-R50 Composite, Owens-Corning Fiberglas Corporation, 1979.

Evaluation of the Vibration Assisted RTM Technique in the Production of Real Parts

Nikos G. Pantelelis

National Technical University of Athens, Department of Mechanical Engineering, Building M, Zografou Campus, 15773, Athens, Greece, pande@mail.ntua.gr
and
Synthesites SA
POBox 64078, 15710, Athens, Greece, synthesites@freemail.gr

SUMMARY: To promote the intermixing between micro and macro resin flows through fibers using dynamic means few ideas have been proposed such as the audio frequency vibrations applied to the injection pressure and the VIARTM technique. In the latter the mold and the preform are vibrated together during and/ or after the filling process by applying external mechanical vibrations to the mold eliminating air traps and improving wetting. For the evaluation of the VIARTM technique and the identification of the flow phenomena an improved test rig has been developed to explore the repeatability of the process and the dependence of the performance on the frequency that the mold is vibrated at. Trials indicate that vibrations contribute towards the balancing between the capillary and the channel flow resulting in improved fiber impregnation and elimination of racetracking. Moreover the filling time is reduced maintaining the injection pressure or lower injection pressure is required for the same filling time with respect to the classic RTM case. The use of VIARTM to a real geometry composite part reveals its advantages.

KEYWORDS: RTM, vibrations, flow

INTRODUCTION

The main characteristic of liquid composite molding is the flow phenomena that take place during the filling stage where the resin impregnates the dry fibers. The void formation during the filling process is one of the major problems of Resin Transfer Molding especially when the tendency is to increase the fiber volume fraction and decrease the filling time. Many studies have dealt with the mechanisms of void formation where the air (as well as gases that are produced during the chemical reactions) are entrapped in the fiber preform structure, thus small or large voids are formed in the composite part, deteriorating part quality significantly [1]. Unfortunately, in practice variability in the preform placement and uneven compaction of the fibers may alternate significantly the theoretically calculated flow paths and, consequently, to increase voids and air-bubbles.

In order to eliminate these problems, the vibration assisted resin transfer molding (VIARTM) has been proposed [2], based on the application of external mechanical vibrations to the mold and the fiber preform during and/ or after the filling cycle transforming the "static" RTM process to a "dynamic" one. For the evaluation of the VIARTM technique a new improved test rig has been

developed to perform a new round of trials with the aim to explore the repeatability of the process and the dependence of the performance on the vibration frequency. Furthermore, VIARTM is evaluated for a real RTM part geometry.

Void formation mechanism

In Liquid Composite Molding the problem of the formation of small (air-bubbles) and/ or large (dry spots) voids occurring during fiber impregnation is well known. For an acceptable composite part from RTM process the targets are to eliminate completely dry-spots which destroy the quality of a composite part and to minimise significantly the size of the remaining air-bubbles in the part. In all dry fabrics' impregnation the existence of two different flow paths is evident: the macro flow or inter-tow flow is developed through the micro channels that are formed in random manner by the compaction of the fabrics in the cavity, dominated by the hydrodynamic pressure and the micro flow or intra-tow flow, which is formed when the resin impregnates the fiber bundles, governed by the capillary pressure. When the flow rate is high, air bubble generation can be observed inside the fiber tows whereas the opposite phenomenon (air-bubbles are formed at the micro- channels) occurs when the flow rate decreases.

For the reduction of the void generation the proposed technique is employed for the balancing enhancement of these two simultaneous flows towards a homogeneous flow. The idea of enhancing the intermixing between micro and macro flows using dynamic means is not new. Baig and Gibson [3] and Song and Ayorinde [4], introduced audio frequency flow vibrations to enhance the productivity and the quality of the process. Both teams developed mechanisms that generated high-frequency vibrations to the resin entering the cavity at the inlet gate. Although advantages of these techniques were claimed to be a significant decrease of the filling time, the reduction of voids and a more effective resin impregnation of the fibers these were not confirmed in practice as flow-induced vibrations at the inlet port vanish at the flow front, together with the hydrodynamic pressure.

On the contrary, in the VIARTM technique the mold and the preform are vibrated together during the filling process by applying external mechanical vibrations to the mold. Parameters that could affect the process and need to be studied are the frequency, the magnitude and the direction of the external vibrations with respect to the cavity shape.

Results

For the evaluation of the VIARTM technique a test rig has been built with a flat circular cavity with 340 mm diameter and 3 mm nominal thickness. The cavity was formed using a 3mm spacer between an aluminium and an acrylic flat plates of 25 mm thickness, each.

The transparent acrylic plate has been used as the upper tool in order to track continuously the flow behavior of the resin during the filling cycle using a digital video camera. The resin enters into the cavity from a central inlet gate and overflows from a single outlet gate at the perimeter of the cavity when the filling cycle is concluded. The materials used for the trials were a polyester resin (Norpol 4190) with a rather high viscosity (700 cps @ room temperature) and 7 plies of a plain weave thick glassfiber fabric. To eliminate the deformations from fiber compaction and injection pressure the acrylic plate was reinforced with steel beams, maintaining

a uniform part thickness. The trials were repeated several times in order to ensure the repeatability of the obtained results.

Min	1	5
Case 1 (RTM)		
Case 2 (VIARTM 15 Hz)		
Case 3 (VIARTM 17 Hz)		
Case 4 (VIARTM 30 Hz)		
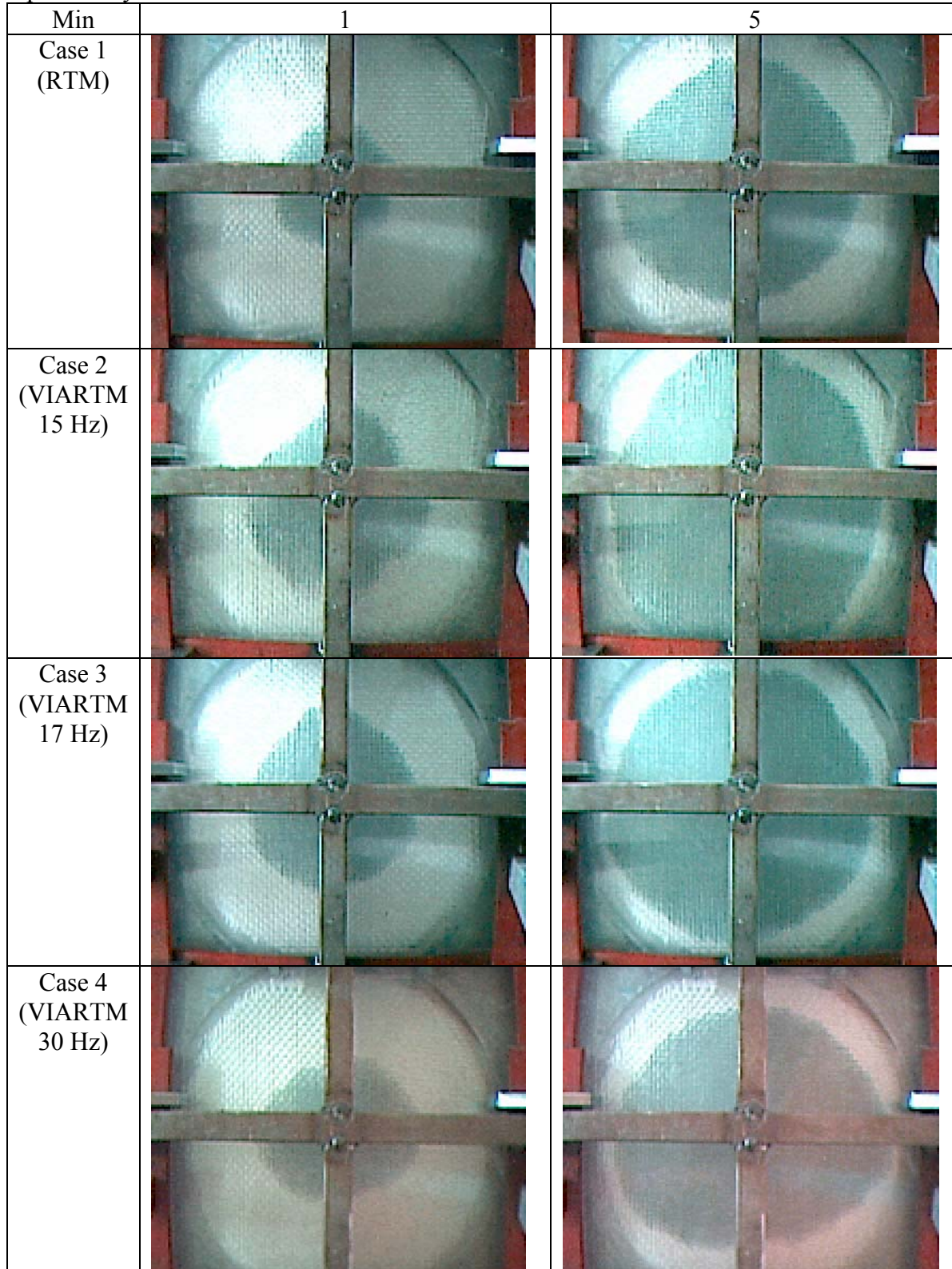
Figure 1. Filling patterns with RTM and VIARTM during a corresponding filling cycle.

At the present study the mechanical vibrations were generated using a conventional AC motor coupled with a cam mechanism creating a 2 mm vibration magnitude where the excitation frequency may vary from 1 to 60 Hz. To study the effect of different vibrations' directions with respect to the horizontal plane of the cavity, in the 15 Hz case (case 2) in-plane vibrations were applied, in the 17 Hz case (case 3) random vibrations and perpendicular vibrations at the 30 Hz case (case 4). Regarding the snapshots at figure 1 which were taken from the corresponding video captures for each test case some very useful observations can be made. The 15 Hz case 2 proves the faster test case having a difference of more that 2 minutes from the total 7 minutes filling time of the classic RTM case 1. The 17 Hz case 3 seems to be slightly slower than case 2 and as can be seen in the snapshots, at the 5th minute the resin has the same pattern as in the 7th minute in the classic RTM. The 30 Hz case 4 (perpendicular vibrations) was marginally faster than classic RTM. With respect to the full filling cycle, as can be seen in table 1, a significant reduction of 33% of the filling time for the VIARTM case 2 has been attained with respect to the classic RTM test case 1 whereas for the other two VIARTM cases the filling times presented no significant differences comparing to case 1.

Table 1. Experiments for the circular cavity varing the vibration frequencies.

Case	Vibration (Hz)	V_f (%)	Thickness (mm)	Filling time (min)	Flexural modulus (MPa)	Flexural Strength (MPa)
1	-	36.8	3.60	12.15	2016	457.0
2	15	35.6	3.80	8.07	1830	469.9
3	17	36.0	3.75	10.50	1847	452.8
4	30	35.8	3.75	12.56	1753	490.5

In order to explore the effects of vibrations to the mechanical properties of the composite part, five coupons (25x80) from each composite disc were cut and tested in accordance to the ASTM D790 standard. Comparing the flexural strengths of the coupons cut from each disc, the coupons produced in the classic RTM (case 1) and in case 3 (random 17 Hz) presented the lowest values, coupons of case 2 (15 Hz) presented rather higher value whereas coupons of case 4 (30 Hz) presented a 10% increase with respect to the classic RTM (case 1). Comparing the flexural modulus (table 1) a 10% decrease is apparent for the coupons of all the VIARTM cases with respect to the RTM case.

| Figure 2. The geometry of the composite part | Figure 3.a. No racetracking was observed | Figure 3.b. No racetracking was observed (right side). |
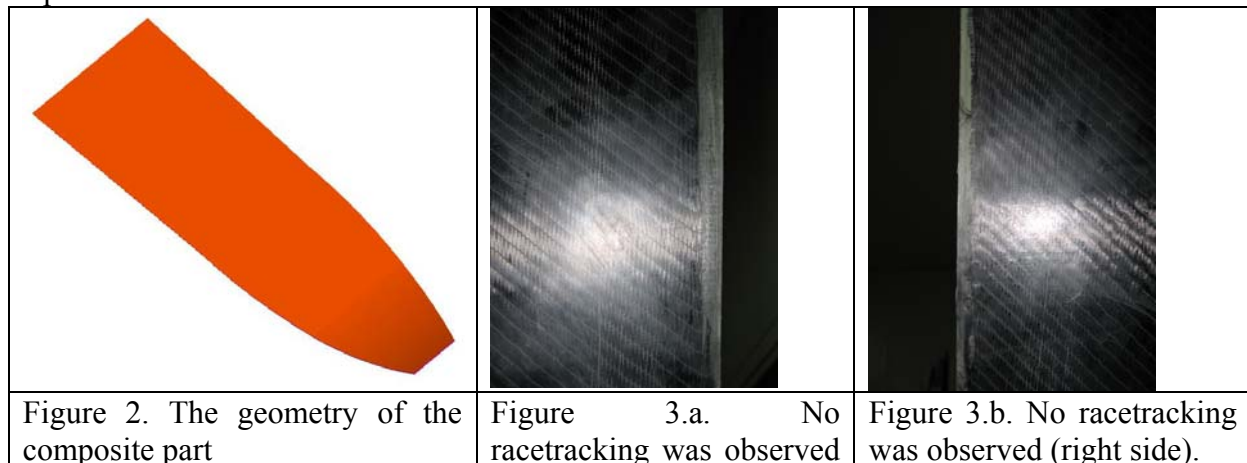
	(right side).	

In order to further explore the behavior of the VIARTM in real geometry parts a long flat part (750 mm) with variable width (from 70 mm to 190 mm) and thickness in the longitudinal direction was selected (fig. 2). The thickness varied from 1.0 mm at the widest edge to 2.5 mm at the narrowest edge resulting in a variable fiber volume fraction from 24% up till 60% using two layers of biaxial (0/90) carbon fiber NCF from Saertex and an epoxy resin heated at 40° C for reducing its viscosity to 200 cps. A central gating and one outlet gate at each narrow edge were used. This specific set-up was chosen as the longitudinal flow was also unbalanced: the most difficult region for impregnation was on one end and the easiest at the other end. To make things worse the fabrics were deliberately cut randomly narrower allowing enough space for racetracking. As the injection pressure was set to 0.4 MPa it was impossible to fully impregnate the part without using vibrations. The resin reached only the easiest outlet gate after 5 minutes and went halfway towards the other direction. On the contrary, using vibrations it took 2 minutes for the resin to reach the easiest outlet gate and 5.2 minutes the second gate. Moreover, no racetracking was observed (figures 3.a and 3.b). Although the mold was made from aluminium no problems were encountered for the installation of the vibration mechanism (at 40 Hz and a magnitude of 1 mm).

Conclusions

An alternative technique was tested in depth for the enhancement of resin impregnation through the fiber preforms in RTM. Applying vibrations at the mold and the preform, resin impregnation is improved especially in the case of high volume of fraction (V_f) and woven fabrics where most of problems in the classic RTM occur. However, further experiments are essential in order to study the resin impregnation in higher V_f (up to 65%) as well as to introduce measurements techniques to get a better insight of the effects of vibrations at the inter and intra fiber tow resin impregnation.

Results indicated that there is an obvious change in the flow of the resin through the fibers indicating that vibrations contribute towards the increase of the capillary pressure and as a result effective resin impregnation through the fibers is attained. However, further studies are essential in order to explore in details the effects of mold vibrations in the mold filling, the resin curing and the final mechanical properties of the composite part.

Acknowledgements

References

1. M.K. Kang, W.I. Lee, H.T. Hahn, "Formation of microvoids during resin-transfer molding process", Composites Science and Technology, 60 (2000), 2427-2434.

2. N. G. Pantelelis and A.E. Kanarachos, Vibration assisted resin transfer molding (VIARTM), 13th International Conference on Composite Materials, China, 2001. (Reprinted as a Society of Manufacturing Engineers Technical Paper, EMO 1-343).

3. B.S. Baig and R.F. Gibson, "Vibration Assisted Liquid Composite Molding", Proc. 11th Annual ESD Advanced Composites Conference, 1995, Dearborn, USA, pp.645

4. F. Song, and E.O. Ayonrinde, "Model development in the simulation of vibration assisted liquid composite molding", Proc. 11th Annual ESD Advanced Composites Conference Dearborn, USA, (1995), pp.203-212.

Development of a Polyamide Copolymer Resin Transfer Molding System for Thermoplastic Composites

Mark Greaney, Conchúr Ó Brádaigh

Composites Research Unit

Department of Mechanical Engineering,
National University of Ireland, Galway.

SUMMARY:

The present study evaluated a process for fabricating anionically polymerized carbon-fiber reinforced polyamide plaques. Vacuum assisted resin transfer molding (VARTM) was used to impregnate a dry carbon-fiber bed with a low viscosity molten catalyst, activator and monomer mixture. Polymerization occurred in-situ forming a solid thermoplastic polymer matrix composite. Also investigated were the potential benefits or detriments associated with using polyamide copolymers as opposed to homopolymers for the matrix material. The tooling employed were both rigid and semi-rigid matched molds. The entire fabrication process was completed in a matter of minutes. The present investigation showed that the matrix fulfilled the requirements for direct liquid impregnation of fiber-reinforced preforms. The matrix viscosity was low. Once impregnated the melt was solidified in a reasonable amount of time. And the resultant matrix had high enough properties to give good mechanical and physical stability to the composite.

KEYWORDS: anionic polymerization, thermoplastic, copolymer, polyamide

INTRODUCTION

Direct impregnation of fiber-reinforced composites by a liquid matrix allows large, complex, and repeatable parts to be fabricated with low tooling costs and cycle times. As opposed to thermosets, thermoplastic matrices offer the advantages of high impact strengths and the ability to be recycled. Due to high melt viscosities, thermoplastics are generally not used for high volume-fraction resin injected parts. The employment of an activated melt, which polymerizes in-situ, overcomes this problem. The process outlined herein relies on two monomers; caprolactam and laurolactam, which when combined with the activator and catalyst solution form the copolymer polyamide 6/12.

Currently the advanced composite market is dominated by thermoset-based resins. However thermosets have several intrinsic disadvantages that in today's environmentally aware society are becoming increasing problematic. The two most prevalent problems with thermosets are their inability to be recycled and the harmful emissions that can be produced during processing.

The advantages of VARTM include low tooling costs, the ability to form complex shapes, and the ability to control fiber orientation and volume-fraction. VARTM is suitable however, only for resins with very low viscosity ($\mu \ll 1$ Pa·s). A VARTM copolymer system must satisfy the following 4 criteria: (i) The monomers can be melted under an inert atmosphere. (ii) The monomers, activator, and catalyst can all be mixed thoroughly prior to injection. (iii) The tool must be airtight during impregnation and polymerization. (iv) The tool must be able to maintain a constant temperature for a period of time and then cool down. [1]

The melting temperature of the copolymers examined in this project depends on the polymer ratio and varied between the melt temperatures of PA 12 (178 ^{o}C) and PA 6 (220 ^{o}C). Because the predominantly PA 6 mixtures have a melt temperature above their polymerization temperature the entire process can be considered isothermal. In industrial terms this means that a mold need not have a temperature cycle. That is to say that the fabrication process can have $T_{injection} = T_{polymerization} = T_{demolding}$. This is advantageous for mass production of parts as the cycle time is not dependent on the molding tool's heat up or cool down rate.

Materials

The problem of thermoplastic material's high melt viscosities can be overcome by using the anionic polymerization processing technique. Anionic polymerization is a quick and clean method of producing polyamide materials. Conversion to high molecular mass polymer is almost instantaneous and does not have any by-products. All that is required is the monomer, a catalyst, an activator and a means to heat and mix them together. EMS Chemie A.G. in Switzerland developed a catalyst and activator solution used in the present study for anionic polymerization. Named GRILONIT, it has a viscosity < 1 Pa.s and can be stored indefinitely in an inert atmosphere. Unlike previous thermoplastic composite matrix systems there is no need for separate pre-blended monomer-catalyst and monomer-activator solutions that slowly polymerize over time.

From a mechanical and physical property standpoint it can be beneficial to mix two monomers, polymerize the mixture, and form a copolymer. The optimal copolymer would take the best properties, applicable to the particular situation, from their respective homopolymers to create a material that is ideally suited to its intended purpose. The monomers discussed here, caprolactam and laurolactam, form PA 6 and PA 12 respectively.

Tenax 5N21 carbon-fiber woven into a 2/2-twill fabric was used for all reinforced processing and testing. The density of the carbon-fiber was 1770 kg/m^3. The weight of the fabric was 440 g/m^2. The 2/2 twill fabric used in the present study was quite drapeable unlike most thermoplastic pre-pregs, which tend to be stiff and "boardy." A desktop heated composite tool was designed and used to create both reinforced and un-reinforced plates. Plates were also

created on an industrial-sized, double daylight, hydraulic composite press. Both employed matched rigid molds.

It was found through testing un-reinforced samples that PA 6 had the most suitable mechanical properties for a composite matrix. PA 6 was also found to process more readily as its monomer precursor had a lower melt temperature and lower viscosity than PA 12. Polyamide 6 has one great drawback however, its moisture absorption. Immersed in water it can absorb up to 9.5% by weight in moisture. This can lead to dimensional changes, mechanical and physical property changes, internal stresses, and in the case of a composites, delamination. Polycaprolactam based composites are therefore suitable only for applications where moisture absorption and dimensional stability are not of critical importance. [2]

Anionically Polymerized Lactam Composite Injection Process

The entire polymerization process in terms of composite fabrication is quite straightforward. It can be broken down into three main stages, which consist of the mixing, the injection, and the polymerization. The mixing stage begins by placing measured amounts of monomers consecutively into a conical flask and melting the mixture in an oil bath. The melting temperature of caprolactam is 69 ^{o}C and that of laurolactam is 151 ^{o}C. A temperature of 175 ^{o}C was chosen.

This was done so that the melt would not polymerize during the mixing process, but when injected the by placing temperature would only need to be raised by a few degrees in order to accelerate the polymerization process. After the caprolactam / laurolactam mixture has been thoroughly melted and mixed, the injection portion of the process is ready to begin.

During the injection the GRILONIT is added to the co-monomer melt and the entire mixture is stirred for approximately 30-60 seconds depending on volume. As the melt enters the mold and wetts the fibers the pressure must be monitored carefully to ensure laminar flow. If the flow is turbulent it creates voids in the finished composite structure that can cause stress concentrations or act as crack initiators.

When enough of the mixture has flowed through the fiber bed into the outlet trap, the inlet and outlet are sealed. The temperature of the mold is raised to the polymerization temperature. The panels outlined in this study were polymerized at 200°C for 20 minutes. Higher temperatures accelerate polymerization. Figure 1 illustrates a schematic of the APLC process.
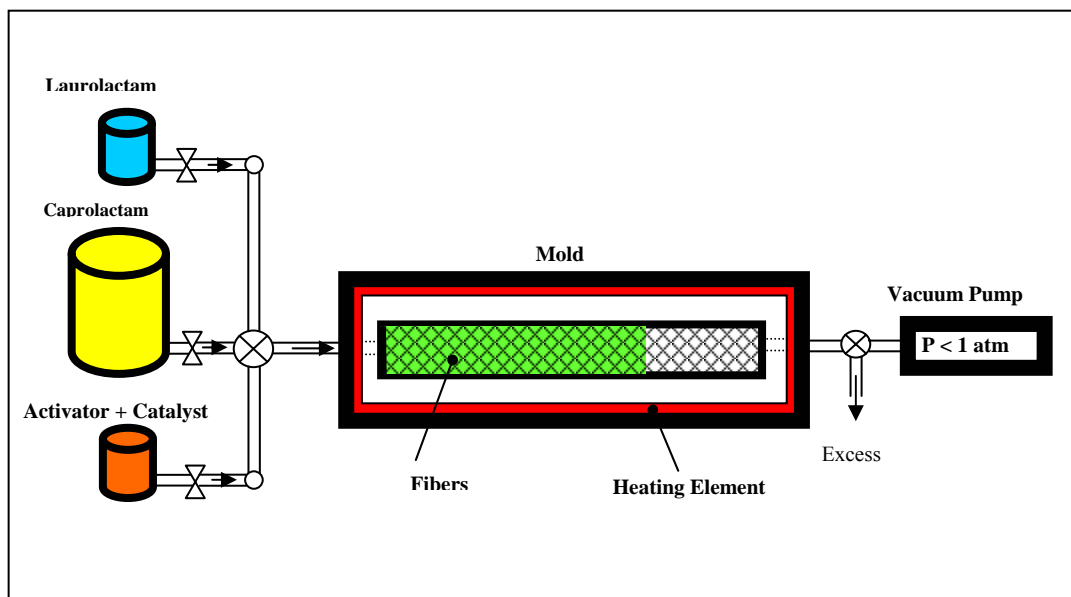
Figure 1 VARTM APLC Process

RESULTS

Mechanical and physical tests were carried out at the National University of Ireland, Galway and the Composites Testing Lab Ltd. Galway, Ireland. Tensile and flexural composite samples at 60% volume fraction were tested according to ASTM standards. The results of the tests are detailed in Tables 1 and 2. Values in parentheses are percentage standard deviations.

Table 1 Tensile and Flexural Testing

Material	Tensile		Flexural	
	E (Gpa)	Strength (MPa)	E (GPa)	Strength (MPa)
PA 12	56.3 (1.3)	768.0 (3.7)	49.11 (7.1)	404.8 (5.1)
90/10 PA 6/12	55.0 (3.0)	684.5 (1.3)	52.00 (4.4)	478.4 (4.7)
95/5 PA 6/12	62.3 (3.3)	773.8 (2.6)	52.93 (7.6)	400.6 (3.7)

Table 2 Anionically Polymerized Polyamide Moisture Absorption Properties

Material	Equilibrium (50% Rel. Humidity)	24 Hr. Immersion	2 Hour Immersion @ 100 ^{o}C
PA 12	0.30 (3.3)	0.17 (5.9)	0.65 (3.1)
90/10 PA6/12	0.61 (6.6)	1.02 (6.9)	3.14 (3.5)
95/5 PA6/12	0.56 (3.6)	0.88 (2.3)	2.76 (2.9)
PA 6	0.53 (7.5)	0.68 (4.4)	2.06 (5.8)

While all of the materials exhibited good moisture absorption performance throughout the tests, the trends between them were somewhat unexpected. The results showed that the addition of

laurolactam to a caprolactam melt actually increased the moisture absorption. This would suggest that in the present study there are no benefits, in terms of moisture performance, in using a copolymer as opposed to a homopolymer.

CONCLUSIONS

Anionic polymerization using the GRILONIT system proved to be a quick, clean, and reliable method of producing polyamide 6, polyamide 12, and polyamide 6/12. Both the polymers and copolymers exhibited good tensile and flexural strengths as well as relatively low moisture absorption. The composites fabricated in this project were impregnated using low pressure (< 1 bar). The plate manufacturing cycle time was also low. The wetting of the fiber bed (injection time) took as little as 10 seconds. Polymerization time, in this case, was 20 minutes. Higher temperatures accelerate the polymerization process leading to even shorter cycle times.

Thermoplastic composite materials have considerable potential for the composite industry. Their ability to be recycled and their improved toughness offer distinct advantages over their thermoset counterparts. Other benefits such as vastly reduced cycle times, ease of storage, and ease of handling, create the potential for mass production. Traditionally it has not been easy to mold thermoplastic-reinforced composites due to the high viscosity of the matrix material. High temperatures and pressures were required to fully impregnate the fiber beds. Thermoplastic liquid composite molding proved to be virtually impossible. The employment of an activated monomer melt eliminates the problems associated with high viscosity. Applications of the current system include automotive parts. These can involve structural parts for cars such as bumpers, hoods, as well as interior components such as dashboards and panelling. APLC's could also be formed into sandwich structures, which could then make up self-supporting exterior panels on busses, trucks, and other large automotives.

In conclusion, the anionic polymerization of polyamide copolymers as a matrix for advanced composites proved to be successful. The VARTM processing method was a simple and effective way of impregnating a carbon-fiber bed. The resulting composite materials exhibited good mechanical and physical properties thereby creating a potential for effective use in a variety of diverse applications.

REFERENCES

[1]   Ó Máirtín, Pádraig, *"Development of a Liquid PA-12 Molding System,"* NUI, Galway 1999, M.Eng.Sc. Thesis

[2]   Kohan, Melvin I., *"Nylon Plastics Handbook,"* Cincinnati 1995, Hanser/Gardiner Publications, Inc.

Integrated In-Plane Infiltration Simulations in the Design of Liquid Composite Processing

C.Lekakou, E.C.Heardman, M.Easton and M.G.Bader

School of Engineering, University of Surrey, Guildford, Surrey GU2 7XH, UK
And Corresponding Author's e-mail: C.Lekakou@surrey.ac.uk

SUMMARY: This study adopts the two-phase flow approach in the infiltration of a porous fibrous preform, considering a varying degree of fluid saturation across the preform. The infiltration simulations have been integrated with the numerical results of forming simulations based on the solid mechanics, finite element approach. The local fiber orientation and local fiber fraction predicted from the forming simulations are used in a permeability model to predict the in-plane distribution of permeability components across the shaped preform. The predictions of FLOWPOR, an in-house developed two-phase flow algorithm for both orthogonal and non-orthogonal structured grids, are successfully compared with experimental data of the flow progress in in-plane radial diverging flow, in-plane radial converging flow and flow in a hemispherical hat preform geometry.

KEYWORDS: infiltration, flow, simulations, permeability, liquid processing, composites.

INTRODUCTION

Composites manufacturing via the liquid processing route is a multi-stage process involving at least two totally different types of materials, the fiber reinforcement and the liquid curing resin. Hence, the computer modeling of such processes comprises the integration of simulations using numerical algorithms from multidisciplinary areas, covering both solid and fluid mechanics.

The first stage includes the computer simulation of the forming of fiber reinforcement, following a solid mechanics approach in this study. The required input data comprise the mechanical properties of the fiber reinforcement. Results of the forming simulation include the distribution of fiber orientation and fiber volume fraction which are going to affect both the permeability distribution of the fiber preform and the mechanical properties of the composite product. The current study utilizes the results of forming simulations using the finite element solid mechanics approach, where the fabric is considered as a solid deforming sheet with measured mechanical properties and friction properties between the fabric and the mold [1].

A major element of an integrated process analysis is the modeling and prediction of the permeability variation across the preform due to the deformation occurring during forming. In woven and other bidirectional fabrics, shear is the main mode of fabric deformation when the fabric is formed over a double curvature mold geometry.

The present study has used the most advanced model so far of predicting permeability as a function of shear angle in in-plane shear, being developed by Heardman et al [2]. The model needs as input data only the permeability of the unsheared fabric.

Once, the permeability distribution is predicted, analysis of the filling stage is carried out using Darcy's law. RTM-dedicated software packages include LIMS, developed by the University of Delaware [3], and RTMFLOT, developed by Ecole Polytechnique de Montreal [4]. Both these algorithms are based on the finite element numerical technique in solving for the pressure field, and the mass conservation equation for calculating the advancement of flow front.

However, flow simulation of the filling stage might not be well established yet in cases with large regions of partially saturated porous medium during the filling operation. This has been the reason for discrepancy in some permeability measurements reported in the literature. One of the explanations has been linked with the difference between the fronts of the flow in the meso-channels between the fiber yarns and the micro-flow between fibers inside individual fiber yarns, which can be of course translated into the existence of a partially saturated zone during filling. Antonelli and Farina [5] carried out computer simulations of basic mold geometries using the ABAQUS finite element software package which considers two-phase flow through the porous medium, a liquid and a gas phase. In this method, the flow advancement is illustrated from the contour plots of the degree of saturation and it is possible to identify a partially saturated region by the flow front during filling. Unfortunately, no comparisons with experimental data were published in that study [5].

The present study includes modeling of flow through a porous medium of inhomogeneous permeability following the two-phase flow approach. A computer algorithm, FLOWPOR, has been developed for flow across both orthogonal and non-orthogonal structured grids and it has been validated by comparing predictions with experimental data of flow progress. The case-studies used in the computer simulations include radial outwards flow across a flat fibrous preform, reverse converging flow across a flat fibrous preform, and infiltration of a hemispherical hat preform with fluid injected at the center of the hat.

NUMERICAL SIMULATIONS AND RESULTS

The two-dimensional in-plane flow through a rectangular plate with central fluid injection was considered in Case-study I. The Newtonian infiltrating fluid was silicone oil of a viscosity of 104 mPa s which was injected under a constant injection pressure of 0.21 MPa. A rectilinear numerical grid of 25x25 nodes was considered in the computer simulations and the predictions from both ABAQUS and FLOWPOR compared well with the experimental data. It must be noted that the value of permeability inputted in the simulations has been derived from the experimental data of Case-study I.

Case-study II comprises the infiltration of an almost square-shaped fibrous preform plate of in-plane dimensions 248x246 mm, where the infiltrating fluid was injected at the preform perimeter under a constant pressure of 0.1 MPa while the mold was under vacuum of –0.1 MPa (so the injection pressure difference was 0.2 MPa).

The filling process consists of a radial converging flow. The value of permeability inputted in the simulations using either ABAQUS or FLOWPOR has been derived from the experimental data of radial diverging flow of Case-study I. Figure 1(a) presents the advancement of flow front at the mid-lines of symmetry (Lfill = 0.5(Xfill + Yfill)) as a function of time, as predicted by ABAQUS, which lies behind the experimental data. On the other hand, the predictions of FLOWPOR in Figure 1(b) agree very well with the experimental data. We believe that the main reason for this is that FLOWPOR predicts a larger unsaturated area behind the flow front in converging radial flow than ABAQUS which must be also true experimentally. Hence, the converging radial flow may be essentially faster than the diverging radial flow due to the fact that as the flow accelerates during filling in the converging flow, the micro-infiltration of fiber yarns takes longer to complete resulting in a larger unsaturated area during filling. Figure 1(c) presents a very good correlation of the pressures predicted by FLOWPOR with the corresponding experimental data from a pressure transducer located on the x mid-line, 25 mm from the center of the mold (radius of transducer port = 2 mm).

(a) (b) (c)
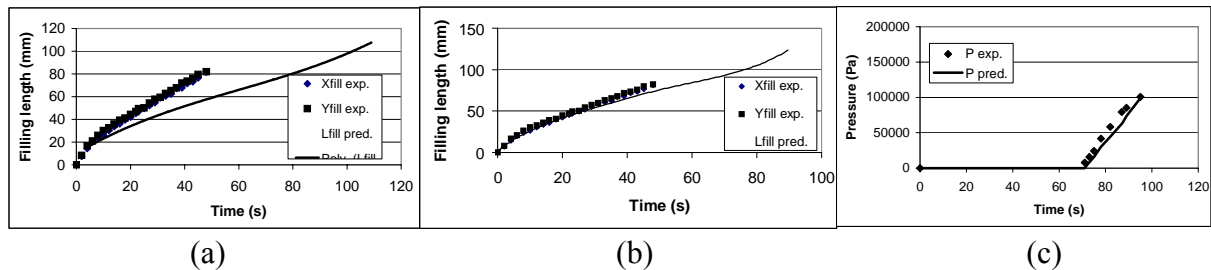
Fig.1. Case-study II: converging flow: predictions by (a) ABAQUS (b) and (c) FLOWPOR.

Case-study III involved RTM flow in a hemispherical hat preform with central injection. Initially, a constant homogeneous porous preform thickness of 4 mm was considered which would result in $V_f = 0.55$ in a unsheared fibrous preform (eg. at the dome of the hemispherical hat geometry). The forming simulations predicted a maximum shear angle of 45° at the edge of the dome on the diagonal of the fabric which yields $V_f = 0.78$ at that location. This is certainly higher than the expected packing fiber volume fraction for woven fabrics ($V_{f,max} = 0.62-0.65$) and such a molding would not be possible to be manufactured using RTM in the hemispherical hat geometry of homogeneous thickness of 4 mm.

An RTM experiment was carried out allowing for a larger homogeneous thickness of 5 mm. In this, flow-channelling and leaking was observed in the flow across the flow dome due to inadequate compression locally in the dome, whereas the flow progressed in smooth manner on the flat surface of the hat geometry, through the fibrous porous medium and in a petal pattern. Regarding computer simulations of the flow in the hemispherical hat geometry, ABAQUS exhibited numerical instabilities and only FLOWPOR gave fully numerical converged solutions in all case-studies during the whole filling. Fig.2 presents the numerical predictions of FLOWPOR. Due to symmetry, only quarter of the hemispherical hat geometry was employed in the flow simulations. A smooth flow progress through the fibrous preform in the dome part was predicted by FLOWPOR, due to the fact that only Darcy's flow was included in the FLOWPOR and there was no model of Poisseuille flow in FLOWPOR to predict flow leaking.

The flow patterns predicted on the flat rim display the petal pattern of the experimental results with the flow progressing faster at the mid-lines of the preform due to the higher permeability there, whereas the permeability is lower at the diagonal positions near the dome edge because of the higher shear angles there and the resulting higher local fiber volume fractions.

(a)   (b)
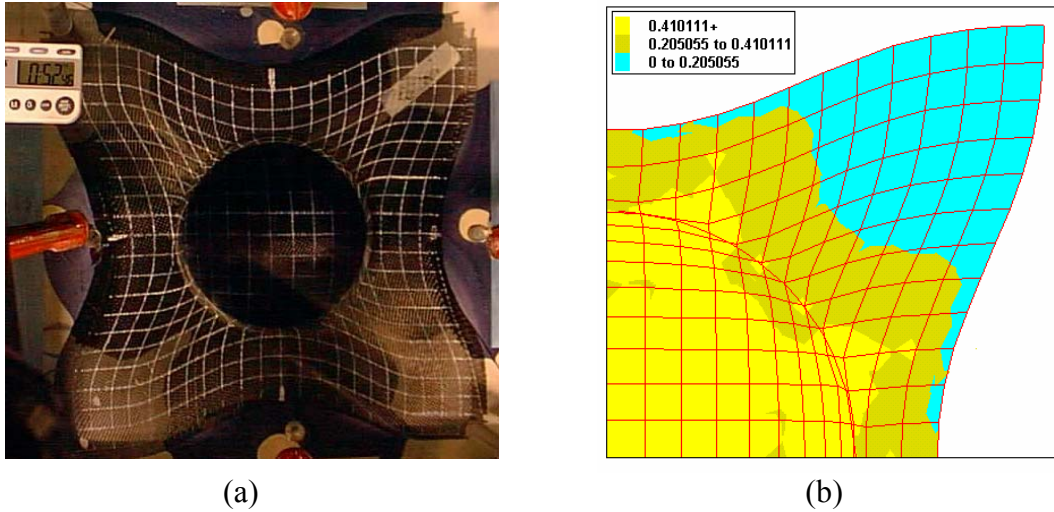
Fig.2. Case-study III: Flow progress in RTM through a hemispherical hat preform:
(a) experiment; (b) FLOWPOR predictions.

Case-study IV involved RIFT flow through the hemispherical hat preform. The manufactured laminate had a thickness distribution, which together with the predicted interfiber angles from the forming simulations, yielded a predicted permeability distribution presented in Fig.3(a) and (b). The predicted local permeabilities were higher in RIFT than in RTM due to the lower V_f values in RIFT. In general, the agreement between the FLOWPOR predictions and the experimental results (Fig.3(c)) of the flow progress is very good in both the infiltration times and the corresponding flow advance, and the shape of the advancing flow front which is approximately circular.

(a)   (b)   (c)
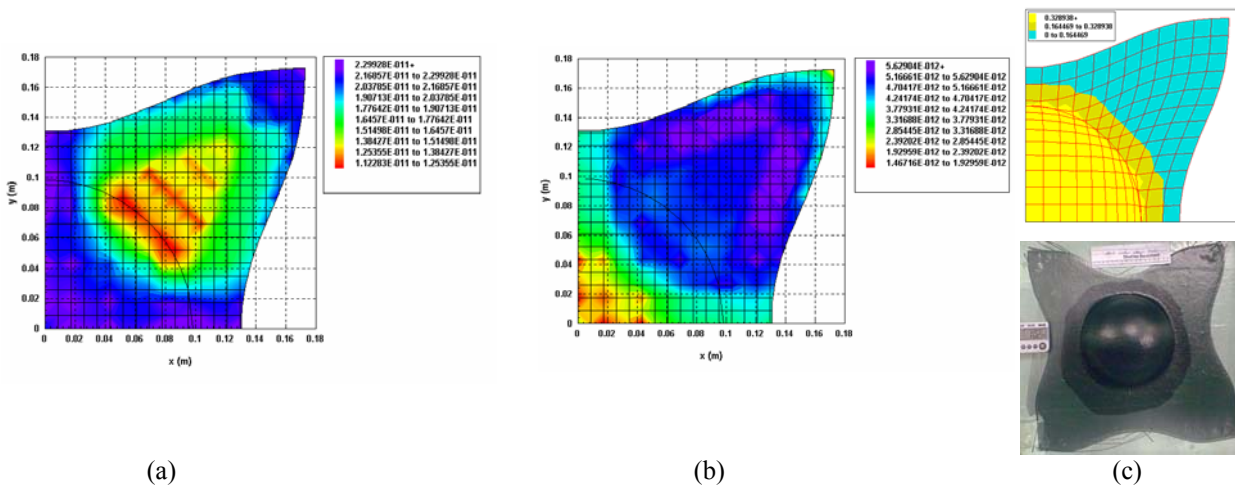
Fig.3. Case-study IV: Flow progress in RIFT through a hemispherical hat preform:
(a) K_{xx} predictions; (b) K_{xy} predictions; (c)top: FLOWPOR predictions; (c)bottom:experiment.

CONCLUSIONS

The predictions of both ABAQUS and FLOWPOR agreed very well with the experimental data in the case of in-plane, radial diverging flow, a configuration often used in measurements of the in-plane permeability of fiber preforms. However, the case-study of in-plane converging flow highlighted the need of accurately predicting the unsaturated region behind the flow front: in this case, only the predictions of FLOWPOR, a two-phase flow code, agreed well with the experimental data of flow advancement and pressure.

The infiltration of a hemispherical hat preform with central injection proved an interesting and demanding case-study both experimentally and numerically. The infiltration simulations were integrated with the results from forming simulations based on the solid mechanics finite element approach, using ABAQUS Explicit. The RTM mold needed to be specially designed in terms of inhomogeneous preform thickness to accommodate the high fiber fraction, highly sheared preform regions. A permeability model was used successfully to predict the permeability distribution across the porous fibrous preform on the basis of the distribution of local fiber orientation predicted by the forming simulations. ABAQUS presented some numerical instabilities in the infiltration simulations for the hemispherical hat geometry whereas FLOWPOR yielded numerical convergence in all case-studies. The predictions of FLOWPOR were successfully validated with existing experimental data in the in-plane infiltration of a RIFT process in terms of infiltration times and shape of flow front.

REFERENCES

1. L.Dong, C.Lekakou and M.G.Bader, "Processing of composites: simulations of the draping of fabrics with updated material behavior law", *J.Composite Materials*, Vol.35, no.2, 2001, pp.138-163.

2. E.C.Heardman, C.Lekakou and M.G.Bader, "In-plane permeability of sheared fabrics", *Composites A*, Vol.32, no.7, 2001, pp.933-940.

3. S.G.Advani and P.Simacek, "Modeling and simulation of flow, heat transfer and cure", Chapter 8 in "*Resin transfer molding for aerospace structures*", Kluwer Acad.Publ., 1998.

4. F.Trochu, R.Gauvin, D.M.Gao and J-F.Boudreault, "RTMFLOT-An integrated software environment for the computer simulation of the resin transfer molding process", *J.Reinf.Plastic Comp.*, Vol.13, no.3, 1994, pp.262-270.

5. D.Antonelli and A.Farina, "Resin transfer molding: mathematical modeling and numerical simulations", *Composites A*, Vol.30, no.12, 1999, pp.1367-1385.

Definition of a Process Performance Index Based on Gate-Distance and Incubation Time for Liquid Composite Molding Processes Design

F. Sánchez[1], C. Zhang[2], Z. Liang[2], B.Wang[2], J.A. García[3], F. Chinesta[4]

[1]Universidad Cardenal Herrera CEU. Escuela Superior de Enseñanzas Técnicas C/ San Bartolomé 55, E-46115 Alfara del Patriarca, Valencia (Spain), sanchezf@uch.ceu.es
[2]Department of Industrial Engineering, FAMU-FSU College of Engineering, 2525 Pottsdamer Street, Tallahassee, FL 32310-6046, chzhang@eng.fsu.edu
[3]Universidad Politécnica de Valencia. Dpto Ing. Mecánica y Materiales, Camino Vera s/n, 46022, Valencia (Spain), jugarcia@mcm.upv.es
[4]Laboratoire de Mécanique des Systèmes et des Procédés - ENSAM Paris, 151 Boulevard de l'Hôpital, F-75013 Paris (France), francisco.chinesta@paris.ensam.fr

SUMMARY: The success of filling and curing stages in a liquid composite molding (LCM) depends on many variables such as locations of gates and vents, temperature distribution, flow rate, injection pressure, etc. A great challenge to obtain high quality finished parts is to accurately predict flow pattern, and temperature and conversion profiles using simulation for process design optimization. With the predicted process performance measures, the LCM process can be optimized through locating the gates and vents properly. In this study, a process performance index based on gate-distance and incubation time for liquid composite molding processes is defined. This index allows the consideration of both resin flow and curing issues in process design optimization. Another advantage of using this index in process optimization is that the computation involved is very efficient as only two-dimensional calculation is required. This makes the index very useful in LCM process design optimization where lengthy iterative stochastic search algorithms such as genetic algorithms are used. In this study, the new index is used to optimize the resin transfer molding (RTM) process design, considering both resin flow and curing. The effectiveness of the approach is illustrated through a number of examples which involve race tracking, varying permeability areas, different filling conditions, etc.

KEYWORDS: Fixed Mesh Resolution, RTM, Liquid Composite Molding, Incubation time, Optimization.

INTRODUCTION

Mold conforming processes of materials made from liquid resins and, in particular, Resin Transfer Molding (RTM), are increasingly used in the fabrication of polymeric matrix composites reinforced with fibers. These processes are based on the reinforcement impregnation with a low viscosity resin, from which composites parts are conformed after the curing reaction.

The polymerization starts when the resin components are mixed just before the injection (see Fig. 1). The elapsed time since the reactive components are mixed, also known as incubation time [3, 7] is directly related with the resin curing conversion. The incubation time depends on the traveled path of each fluid particle throughout the mold, and therefore is not always easily to predict it.

The resin gelling time can be delayed and controlled by using different inhibitor concentrations in the polymerization resin agents as the fluid flows, see for instance [1, 2]. In [2] Comas-Carmona, Advani et al. used the correlation of the gelling time and the concentration of the inhibitor as follows:

$$\ln(t_{gel}) = a + bC_{hardener} + cC_{accelerator} + dC_{inhibitor} \tag{1}$$

Where a, b, c, d, are constants to be determined for each resin, and C refers to the concentration of the chemical agents. Since the time to gel and the incubation time are directly related, the LCM process can be optimized through locating the gates and vents properly in order to reduce cycle time, avoid dry spots and obtain spatially homogenized curing.
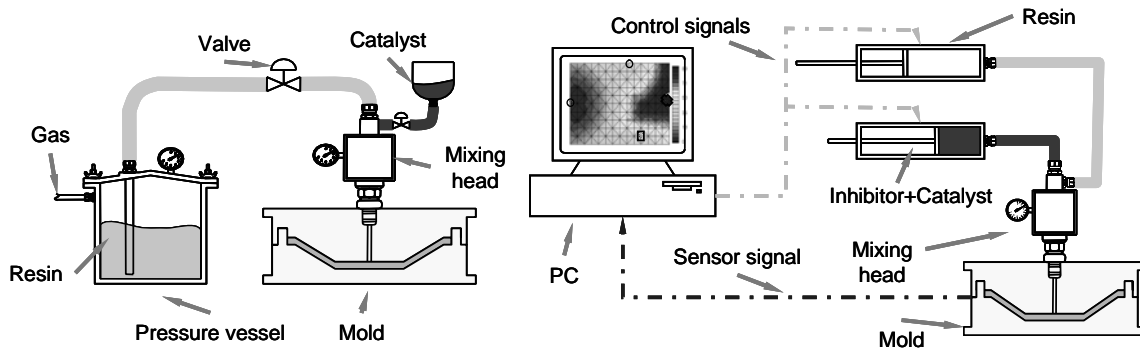
Fig. 1. Schematic resin injection system without control (left) and with PC-based control providing automatic mixing of resin components at injection gate (right)

PROCESS OPTIMIZATION AND RESIN FLOW INDEX.

The success of filling and curing stages in liquid composite molding (LCM) depends on many variables such as locations of gates and vents, temperature distribution, flow rate, injection pressure, etc. Traditionally the selection of gate and vent locations in mold design is based on the experience and trial and error attempts. Many research studies have been conducted to reduce cycle time by using computer simulation and optimization. Zhang, Wang et al, employed in [4] and [5] a process performance index based on gate-distance of the resin located on the flow front at different time steps. A good process should have short filling time and a desired resin flow pattern (small standard deviation) as shown in Fig. 2.

A process performance index was proposed as follows:

$$Q = \frac{T \times \sum_{k=1}^{m} \sqrt{\frac{\sum_{i_k=1}^{n_k} (d_{ik} - \bar{d}_k)^2}{n-1}}}{m} = \frac{T \times \sum_{k=1}^{m} q_k}{m} \tag{2}$$

where:

Q: overall process performance index (the lower the better)

q_k: intermediate flow front index for flow front k

m: number of flow fronts taken from the simulation model

n_k: number of nodes on flow front k

d_{ik}: distance from node i on flow front k to the outlet.

$\bar{d}_k$: average distance from nodes on flow front k to the outlet.

T: Total mold filling time.

This index has been redefined in this work in order to include the incubation time as a variable related with a optimal curing performance. The new index is completed as follows:

$$QD = \frac{T \times D \times \sum_{k=1}^{m} q_k}{m}$$

$$D = \frac{\sum_{i=1}^{n_f} D_i}{n_f} \quad ; \quad D_i = \max_{j=1}^{nn_i}(E_j) - \min_{j=1}^{nn_i}(E_j) \tag{3}$$

where:

QD: overall process performance index (the lower the better).

D: resin incubation time dispersion index defined for all filled nodes.

D_i: filled node i dispersion index (see Fig. 3).

E_j: incubation time for node j.

nn_i: number of nodes connected with node i.

n_f: number of filled nodes.
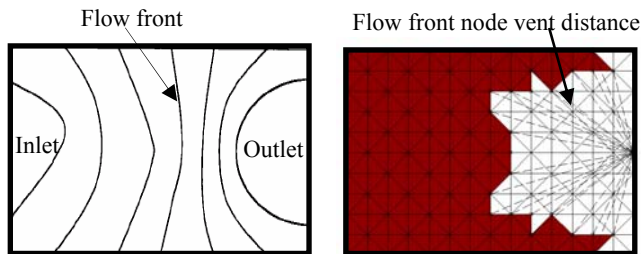
Fig. 2. Desired Flow front shape (left) and distances between flow front nodes and vent (right).
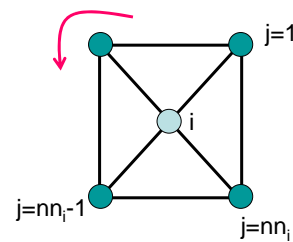
Fig. 3. Dispersión index D_i definition

NUMERICAL SIMULATIONS

In order to validate the resin flow index, a series of simulation experiments have been conducted to check how the index represents the RTM process behavior. In all cases a mold of 100 mm x 140 mm, a thickness of 6.4 mm, a permeability of 2.714 e-10 m^2 with 50 % fiber volume, a viscosity of 0.1 Pa·s, and a constant flow rate injection of 0.5 cm^3/s, has been used. Three cases with different permeability conditions (10, 50, 0.1 and 0.02 times the uniform permeability) as shows Fig. 4 have been studied. In case 1a, the resin is injected with constant inhibitor concentration during filling, and in case 1b three sensors separately located in the mold allow to control the inhibitor concentration in order to obtain spatially homogenized curing. The gate incubation time is set to be the time in that the fluid presence sensor detects resin. A similar sensor-based control technique was implemented with satisfactory results by Comas-Carmona, Advani et al. in [2]. It can be observed in Fig. 5 that the index QD defined in equation (2) is better in the second case and, as was expected, Q does not show this behavior. The coloring map of the dispersion index predicts this proper homogenized curing. In Fig. 6 is shown the variation of the resin incubation time dispersion index D for both cases at each time step. The three peaks of the controlled case correspond to the sensor signals. Case2 and Case3 are also shown in Fig. 5.

It can be noticed that without changes in the inhibitor concentration, both index Q and QD agree that Case2a represent the best filling conditions and Case3b the worst ones.
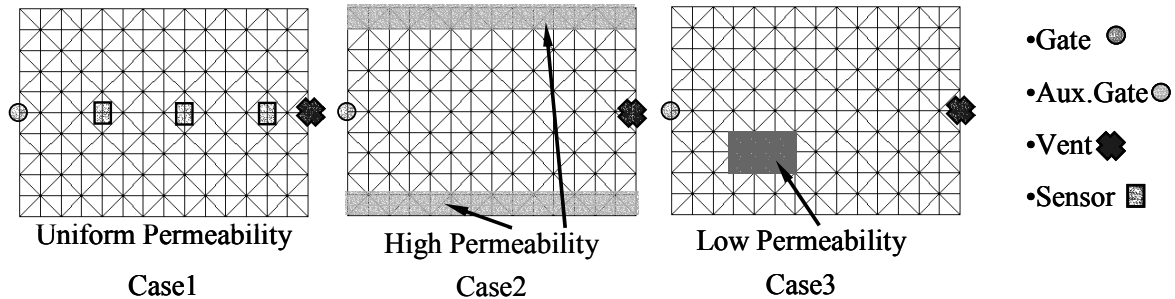
Fig. 4. Simulated conditions for the RTM part
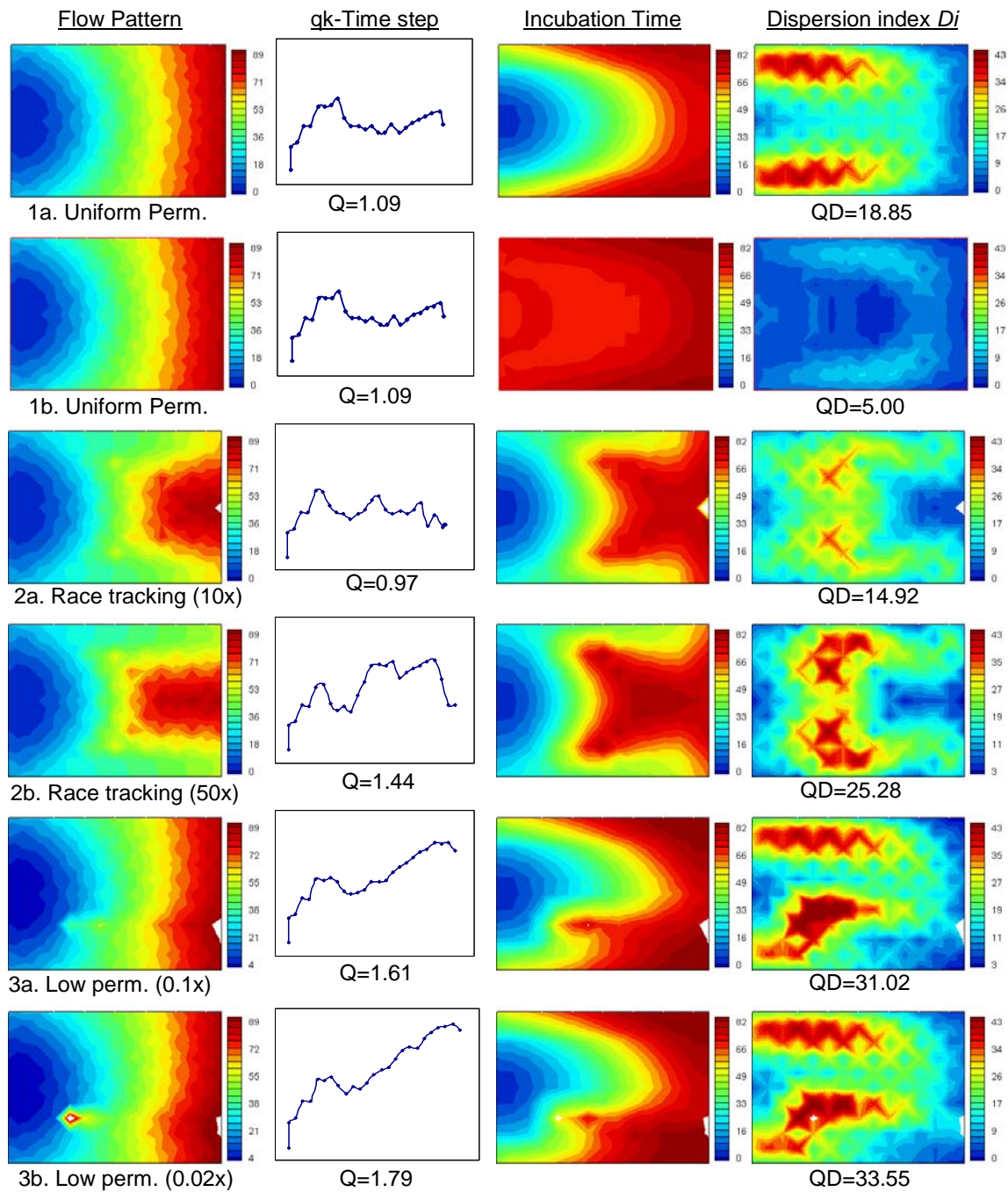
Fig. 5. Illustrations for different simulation cases.
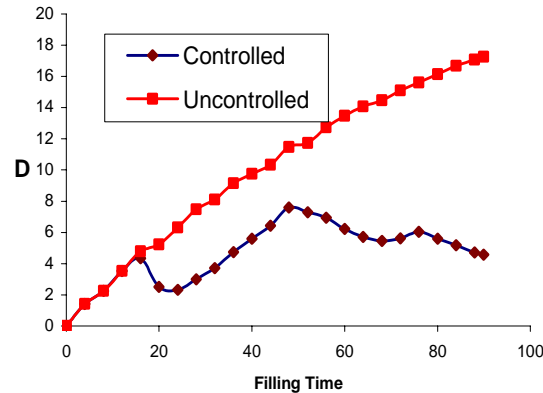
Fig. 6. Time evolution of the resin incubation time dispersion index D for case 1

CONCLUSIONS AND FURTHER WORK

This index allows the consideration of both resin flow and curing issues in process design optimization. Another advantage of using this index in process optimization is that the computation involved is very efficient as only two-dimensional calculation is required. This makes the index very useful in LCM process design optimization where lengthy iterative stochastic search algorithms such as genetic algorithms are used. It may be necessary to redefine the cost weight of considering more than one injection gate or the control of the inhibitor concentration for optimization purposes.

ACKNOWLEDGEMENTS

REFERENCES

1. Comas-Cardona, S. Ziaee, S.G. Advani, *Spatially homogeneus gelation in Liquid Composite Molding*, Polym. Eng. Scie. Vol.42 num 8, p 1667-1673. (2002).
2. Comas-Cardona, S. Ziaee, S.G. Advani, *Etude et contrôle de la polimérisation homogène dans les procédés LCM*, Revue des Composites et Matériaux Avancés Vol.13 (2003).
3. Ll. Gascón, F. Sánchez, J.A. García, F. Chinesta, *A flux limiter technique for the calculation of the incubation time in LCM*, to appear in European Scientific Association on Material Forming, ESAFORM (2004).
4. S. Jiang, C. Zhang, B. Wang, *A process performance index and its application to optimization of the RTM process*, Polymer Composites 22 (5), 690-701, (2001)
5. J. Luo, Z. Liang, C. Zhang, B. Wang, *Optimum tooling design for resin transfer molding with virtual manufacturing and artificial intelligence*, Composites part A 32,877-888, (2001).
6. D. Rouison, M. Sain, M. Couturier, *Kinetic study of an unsaturated polyester resin containing an inhibitor*. Journal of Applied Polymer Science, 89, 2553–61, (2003).
7. F. Sánchez, J.A. García, Ll Gascón, R. Torres, I. Ordeig, *A fixed mesh strategy for the calculation of the incubation time in LCM*, European Scientific Association for Material Forming, ESAFORM, pp. 679-682, Vol. I, (2003).

Processability Analysis of Thick Braided Composites Manufactured with RTM Technology

S. Laurenzi[1*], M. Griccini[1], E. Lalia Morra[2], E. Anamateros[2], M. Marchetti[1]

[1] Department of Aerospace and Astronautic Engineering, University of Rome "La Sapienza", Rome, Italy: s.laurenzi@aerorisc.diaa.uniroma1.it

[2] Agusta-Westland S.p.A, Aerospace Composites Center, Anagni, Italy: e.laliamorra@it.agusta.com

SUMMARY: Thick braided carbon fiber/epoxy resin composites have recently become relevant structural materials in the field of aerospace and aeronautics. The aim of the present work is to investigate the effect of Resin Transfer Molding (RTM) process on braided composites for the fabrication of a helicopter transmission traditionally made with metallic materials. Several experiments have been conducted at different braided angles in order to study the relationship between braided angle, permeability and the flow transverse through thickness of the laminates and volume fraction.

KEYWORDS: Resin Transfer Molding, permeability, braided composites

INTRODUCTION

Metallic materials are traditionally used in the fabrication of transmissions, but they are susceptible to corrosion. Composite materials are known to have far better corrosion resistance and damage tolerance than metallic ones. In addition to the better overall performance, the composite top case weighs 40% less than the original cast metallic design. Braided structures are highly comfortable to conical structure. Braiding is a highly automated textile process. The carbon fibers are placed in the proper orientation in a precise and consistent manner using automation, which results in lower manufacturing costs and more repeatable processes. The advantages of braiding compared to standard tape and fabrics include strength in third dimension, improved fatigue resistance, more efficient distribution of mechanical stresses, conformability to complex shapes, reduced scrap and reduced labor costs. In combination with resin transfer molding process (RTM), it provides the capability of producing low-cost, high-quality components. The aim in RTM is to impregnate the reinforcement with resin as fast as possible, before the resin cures, while minimizing undesirable features such as voids and non-uniform wetting. In the case of helicopter transmissions, a dedicated tooling design analysis has to be performed in order to guarantee the completion of wetting process of the preform, because of the high thickness of the part and its non uniformity with abrupt increases. Furthermore, the pore space deforms as the preform is compressed, stretched, or folded inside a mold.

In this work, the resin flow front through the thick preform has been investigated for three types of braided materials, considering several experiments at different braided angles in

order to study the relationship between braided angle, permeability and thickness of the laminates for a specific volume fraction. It has been observed that for thickness more than 11 mm, the difference of flow front between the top and bottom of the preform starts to be consistent, meaning that the transverse flow through thickness cannot be considered negligible.

Furthermore, for cylindrical braids the tow spacing increases with reducing braid angle, resulting in the creation of flow channels that appear dominate the permeability.

This study is important to estimate the permeability profile of a braided preform, without which simulation models would not provide information useful for process design.

MATERIALS AND METHODS

Three types of 6K T300 carbon braided reinforcements have been used. In Table 1 material properties are shown for a 45 ° fibers orientation.

Table 1

Code	Weight (g/m)	Weight (g/m2)	Diameter (mm)
B-120-06	68	277	78
B-120-05	136	480	90
B-144-05	81	370	70

By changing the diameter of cylindrical braided, the braided angle is changed and a different weight for unit area is assumed. This aspect has been considered.

The resin used for tests has been the epoxy high temperature curing Hexcel RTM6. In fig 1 the resin viscosity profile is shown.
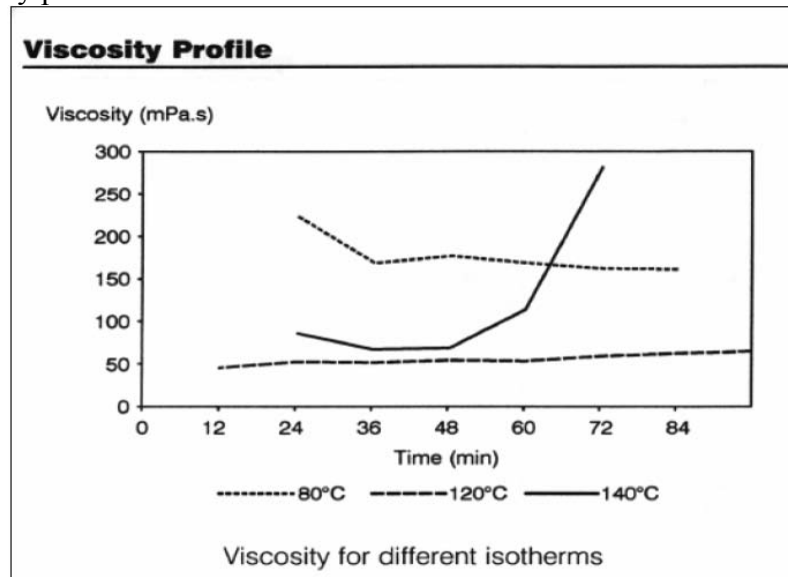
Fig. 1: Resin viscosity profile

Specimens Manufacture

Flat braided reinforcements were cut from cylindrical mandrels, with each layer retained using masking tape at edge as in Fig. 2.
The fiber volume fraction of the preform has been determined by the well known formula

$$V_{ff} = \frac{n\,A}{h\,\rho}$$ (1)

where h is the thickness of the frame (8 mm, 11 mm, 15 mm), ρ is the average density of material (1.7 g/m³), n is the number of layers varying to keep constant the fiber volume fraction for several h, A is the weight for unit area. The fiber volume fraction was 0.67 for all experiments.
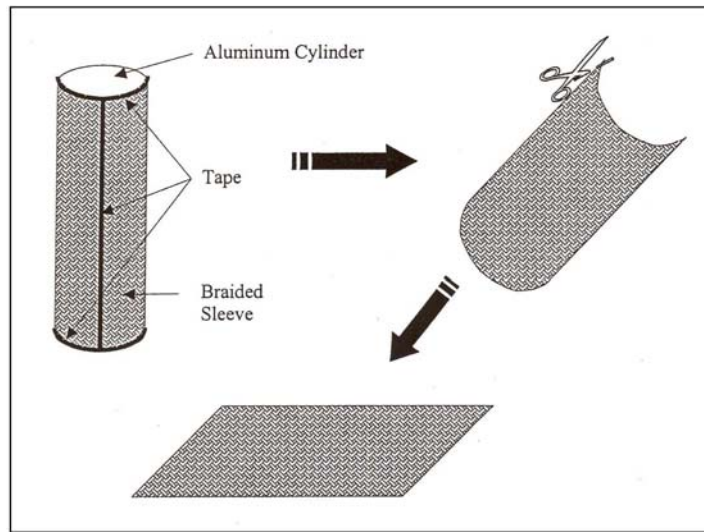
Fig. 2: Procedure to cut the braided layers

Samples have been produced at range of braided angles of 30°, 45°, 60°. Fig. 3 shows how a shape cell of a braided preform varies with the braded angle. So, several mandrels have been used, because of determined braided angle are obtained with specific diameter of cylindrical braided.
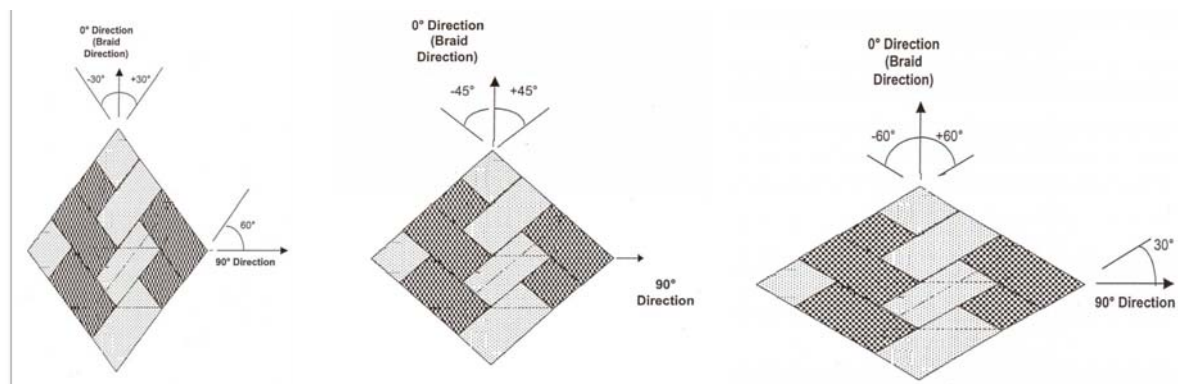
Fig. 3: Braided angles used for the experiments

Permeability Measurement

The permeability tests were performed in a rectangular RTM mold. The bottom and top mold is made of 5 cm thick glass so that the flow front progress can be observed visually. The thickness of the mold has been adjusted by using different frames. A grid had been drawn on the top and bottom glass to measure the fluid flow front position.

The permeability have been measured at different braided angles. All the permeability tests were carried out preheating the material at 80 °C and maintaining the mold at 120 °C. The fluid was injected into the mold under a predetermined constant air pressure (2 bar) and linear flow apparatus. During the test, a video camera recorded the fluid flow process at both sides of the mold. The flow front position at different times was obtained with the help of image grabbing system and some specifically developed software.

To establish the effect of the braid angles and thickness, a minimum of three permeability tests were carried out at each braid angle for a determined thickness and volume fraction. The permeability value has been determine with the classical Eqn. (2):

$$K_x = \frac{\mu \Phi \, slope \, of \left[x^2{}_f(t_f) \right]}{2 \Delta P}$$

(2)

where Φ is the porosity and μ is the viscosity of the resin. To study the effect of the thickness on the wetting preform, three frames have been used at specific volume fraction.

RESULTS

Following is the permeability as a function of braided angle for the different materials analyzed in the case of mold thickness equal to 8 mm. Each point is the average of three experimental data.
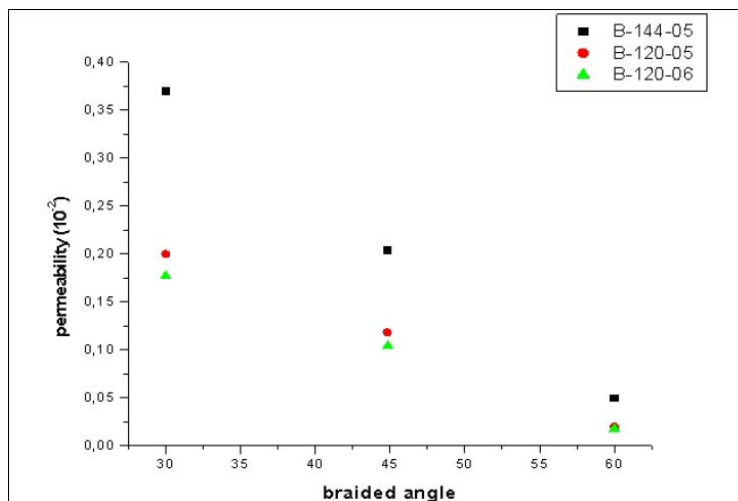
Fig. 4: Permeability parallel to mandrel axis with thickness equal to 8 mm

CONCLUSIONS

In RTM applications, resin flow induced defects, voids and dry spots are known as the largest source of quality and reproducibility problems. These defects are often caused by unbalanced resin flows, which are directly related to the fiber preform permeability variation. In our case, possible sources of this problem can be a local variation of braided angle during preform preparation and braided angle change for conical shape. In our experiments we studied the effects in variation of the braided angle on the permeability parallel to the mandrel axis. It is visible that, for all materials in exam, the permeability decreases with increasing of the braided angle. This appears to be due to the change in tow spacing with braided angle. The tows become non-linear with the flow direction, producing an additional resistance to flow of the resin. The permeability value is substantially the same with the changing of the thickness for a specific volume fraction, but the difference of the space run by the flow front between the top and bottom of the preform increases with thickness. These results imply that the transverse flow through thickness cannot be considered negligible. This phenomenon appears relevant for B-120-05, where the pore space between the tows is less than the other two materials studied, and will be taken in consideration for future simulation of the flow of entire conical structure for the process design.

REFERENCES

1. T. Kruckenberg and R. Paton, "Resin Transfer Molding for Aerospace Structure", Kluwer Academic Publisher 1998.
2. D. Stover, "Resin-transfer molding for advanced composites", *RTM,* Advanced Composites, pp. 60-80, 1990.
3. R. Davè, "A Unified Approach to Modeling Resin Flow During Composite Processing", *Journal of Composite Materials*, Vol. 24, pp. 22-41, 1999.
4. J. Coulter and S. Guceri, "Resin Impregnation During the Manufacturing of Composite Materials Subject to Prescribed Injection Rate", *Journal of Reinforced Plastics and Composite,* Vol. 7, pp. 200-213, 1988.
5 S. G. Advani and E. M. Sozer, "Process Modeling in Composite Manufacturing", Marcel Dekker, Inc. New York-Basel.
6 Y. Luo, I. Verpoest et al., "Permeability measurement of textile reinforcement with several test fluids", *Composites part A ,*Vol. 32, pp.1497-1504, 2001.
7 L. Ding, C. Shih, Z. Liang, C. Zhang, and B. Wang, "In situ measurement monitoring of whole-field permeability profile for liquid composite molding processes", *Composites part A,* Vol. 34, pp. 779-789, 2003.
8 V. M. A. Calado, and S. G. Advani, "Effective average permeability of multi-layer preforms in resin transfer molding ", *Composites science and technology,* Vol. 56, pp.519-531, 1996.

VACUUM INFUSION PROCESSES

Separating Bubbles By Superficial Capillary Flow

A Yusuf, W M Banks and D Kirkwood

Department of Mechanical Engineering
University of Strathclyde
James Weir Building, 75 Montrose Street
Glasgow G1 1XP
Scotland
afendi@fkm.utm.my or wmb@strath.ac.uk

SUMMARY: In an earlier analysis [1], it was found that using bubble film is the best method for removal of volatile components and dissolved gases. The bubble film thickness may reduce to around 0.1 μm before break up and this allows diffusion at molecular level without nucleation. Formation of bubble film on the other hand, can provide a larger diffusion surface area. At one end, the bubble is playing an important role in removing the volatile component and dissolves gaseous and at another, the bubble itself is the problem and very difficult to eliminate. The separation of bubbles by means of capillary superficial flow process is found to provide a possible solution to get bubble free resin mixture prior before infusion. Therefore the process of mixing, degassing, bubble straining and infusion can be carried out concurrently to form a continuous supply system.

The paper develops the above work being undertaken at the University of Strathclyde to seek to reduce the formation of bubbles in the resin infusion manufacture of composite structures.

KEYWORDS: bubble film, volatile component, dissolves gaseous, capillarity, imbibition, drainage, infusion, degassing.

INTRODUCTION

Developments in the field of advanced composite materials over the past decades have significantly altered their current and future potential role in structural applications. Composites offer structural designers materials of higher strength, stiffness and lower distortion than previously available engineering materials. Epoxy resin composites are one example of such a material. These composite systems are finding widespread use in the transportation, marine, aerospace and even sporting goods industries. As these structures are becoming more optimized, in order to reduce weight and material cost, the requirement on mechanical properties are increasing in terms of performance and consistency.

Vacuum infusion is one of the manufacturing techniques used to give increased performance. It is suitable for large load carrying composites and sandwich structures. The vacuum infusion process virtually eliminates styrene emissions, making for a cleaner and healthier workplace.

This process not only improves the air quality, but also reduces non-construction solid waste products significantly. Resin infusion under flexible tooling (RIFT) is a variant of vacuum driven resin transfer molding in which one of the solid mold faces is replaced by a polymeric film. One variant of the process is known commercially as SCRIMP

During the manufacture of composite components by resin infusion bubbles may develop during mixing due to air entrapment, local pressure variation and out-gassing of volatile components and dissolved gases. Bubble problems during composite impregnation results in higher void content. The void content distribution in the final laminate leads to inhomogenous problems in impregnation. Bubbles in a viscous fluid are very difficult to eliminate. It is possible to bring a bubble closer to the surface for diffusion but viscosity governs the drainage on the bubble film; therefore, smaller bubbles take a longer time to break up.

THE FLUID AND BUBBLE

The fluid on this occasion is epoxy resin RSL 135i (viscosity 1100 mPas) and amine type hardener RSH 137i (viscosity 50 mPas) supplied by PRF composite. The mixture of 33g hardener for 100g of resin as recommended by the supplier at 25 ^{0}C giving a viscosity of 200 mPas. During the pouring of the resin, there are always some entrained air bubbles. The big bubbles (over 1 mm in diameter) rise easily to the surface and take a few seconds to clear. The small bubbles (less than 1 mm in diameter) move much slower to the surface. Theoretically, the terminal velocity [4] of the rising bubble can be represented as

$$U = \frac{2}{9} \frac{\rho g r^2}{\mu} \tag{1}$$

The same things also happen during pouring of the hardener, being much less viscous than the resin, the bubble releases to the surface almost instantly. Since the resin is much heavier and viscous than the hardener, the two remain separated like water and oil. The stirring action to mix the resin and hardener creates more bubble and also much smaller bubble (dust like particle).

During the degassing process, the bubbles grow bigger in size and rise to the surface easily as buoyancy forces predominant. While the bigger bubbles disperse on to the surface, the much smaller bubbles only rise slowly to the surface. The pressure variation does not have any effect on the terminal velocity of a rising bubble. These smaller bubbles may take hours to rise to the surface.

It is essential to have bubble free resin before vacuum infusion starts. If the infusion starts immediately after degassing, the unreleased bubbles may migrate into the lamination. During curing, the shrinkage of the resin will pull the bubble surface in between the fiber tow creating higher void content. Therefore, the degassing time needs to be extended to allow the bubbles to clear the resin

THE FILTERING MEDIUM

The filtering medium used in this experiment is made of woven fine fibers. It is supplied in sheet form and the pore size is very fine, the estimated range being from 50 to 100 microns distributed randomly. The thickness is about 2 mm. Each fiber is so thin that it can only be seen in a microscope, which can magnify at least 1000 times [6]. In just one square centimeter of the woven cloth, the fiber passes over itself 30,000 times (which means that each gram of the cloth contains 39,000 meters). It is almost unimaginable. The cloth feels smoother and softer than the finest terry. Rather than using fine mesh this woven micro fiber cloth was considered to be appropriate since the bubble size developed in the experiment varies from dust like particles.

IMBIBITION AND DRAINAGE

In the studies of multiphase flow through porous medium [2], it is shown that capillarity governs most of the permeation process. The present of bubbles represents the non-wetting fluid, and the resin mixture therefore may be termed wetting fluid. The movement of these wetting and non-wetting fluid in between the solid medium by means of superficial capillary flow cause imbibition and drainage.
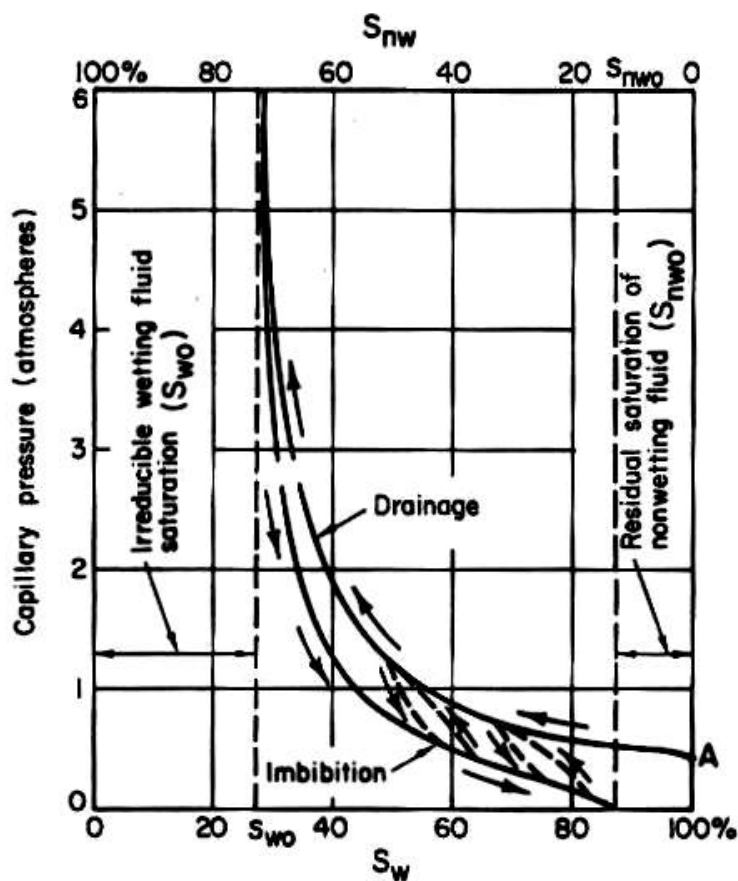
Figure 1: Typical capillary pressure – wetting fluid saturation curves illustrating hysteresis [2].

Due to the complexity of random configuration in natural porous mediums [5], capillary tube has been taken in most experiments as to ideally represent the actual mono-system. For a single bubble of non-wetting fluid to be forced in to a capillary (to promote drainage), slightly higher pressure needs to be induced compared to the process of imbibition by the wetting fluid that takes place naturally by the capillary pressure. With reference to figure 1 in unsaturated flows, Snwo indicates the amount of entrapped air that is the non-wetting fluid. At Snw ≤ Snwo, the non-wetting fluid ceases to flow.

Bond in 1928 [3] proposed a simplified formula for a critical diameter at which a gas bubble or liquid droplet is midway between rigid and fluid state:

$$d_{cr} = 2\sqrt{\frac{\sigma}{\Delta \rho g}} \qquad (2)$$

For epoxy resin surface tension σ = 32 dyne/cm (32 x 10^{-3} N/m) and resin density ρ = 1.1028 g/cm^3 (1102.8 kg/m^3) and taking g = 9.813 m/s^2, the bubble critical diameter d_{cr} = 0.003439 m (3.439 mm). Therefore, considering bubble diameters lower than this critical diameter (e.g. 1 mm to dust like particle) they are as rigid as can be theoretically accepted.

To explain what happens to the bubbles (as they cannot pass through the woven cloth), the following equation drawn from Young-Laplace equation should be able to verify the condition. Pressure P inside a bubble [4] of radius r is given by

$$P = \frac{4\sigma}{r} \qquad (3)$$

The pressure inside a small bubble is greater than that inside a large one. When small and large bubbles are connected, the smaller ones inflate the larger and collapse. Therefore, the result of the coalescing bubbles that cannot penetrate through the filter will increase in buoyancy properties to rise and diffuse to the surface.

RESULT AND CONCLUSION

A simple experiment has been carried out to verify the above theoretical approach. A bubbly resin was poured in to a cup-like container, made of the woven micro fiber cloth, placed in a vacuum pressure at 90 mbar. The excess resin which permeated through the filter was collected at the bottom of the vacuum chamber. It was found that the collected resin contained no visible bubbles. However, there was a small amount of dust like particles present. These dust like particles diminished as the vacuum pressure was relieved.

For the conclusion, bubbles created during mixing, transferring and degassing can be separated using a porous medium (fine fiber filter) due to superficial capillary flow. Therefore, bubble free resin can be produced, prior to the vacuum infusion process without waiting for the bubbles to clear by themselves, which consumes a longer period of time.

REFERENCES

1.   Afendi Yusuf, W M Banks and D Kirkwood, "The Means to Void Content Reduction in Vacuum Infusion Process", *Proc. of Advanced Composite Manufacturing Center (ACMC/SAMPE) Conference on Marine Composites,* pages 17-25 (2003).

2.   Jacob Bear, "Dynamics of Fluids in Porous Media", *American Elsevier Publishing Company* (1972).

3.   Tomasz Kiljanski and Marek Dziubinski, "Centrifugal Degassing of Highly Viscous Newtonian Liquids", *The Canadian Journal of Chemical Engineering*.Vol.79, pages 449-454 (2001)

4.   P.D. Howell, "The Draining of a Two Dimensional Bubble", *Journal of Engineering Mathematics*, *Kluwer Academic Publishers*.Vol 35, pages 251-272 (1999)

5.   Eyvind Aker, " A Simulation Model for Two-Phase Flow in Porous Media", *Thesis for The Degree of Candidates Scientiarum*, Department of Physics, University of Oslo(1996).

6.   KBM Miljöprodukter AB, http://www.kbm.se/eng.htm

In-Mold Coating of Composites Manufactured by the Resin Infusion Between Double Flexible Tooling Process by Means of Co-Infusion

Posen Chiu, Okenwa I. Okoli, H-P Wang

Florida Advanced Center for Composite Technologies
Florida A&M University – Florida State University College of Engineering, 2525 Pottsdamer Street, Tallahassee, FL 32310
Corresponding Authors' e-mail: Okoli@eng.fsu.edu

SUMMARY: As composite materials gain wider acceptance within the transportation industry, it is pertinent to investigate the available coating processes with a view to reduce emissions and associated costs. This work aims to develop a methodology for in-mold coating components manufactured using the Resin Infusion between Double Flexible Tooling (RIDFT) process.

RIDFT is a neoteric two-stage manufacturing process that involves; 1) infusion of resin between two flexible silicone membranes until thorough wetting of the fibers is achieved, and 2) vacuum forming, where the membranes are pulled over a one-sided mold.
The viability of in-mold coating RIDFTed components was investigated. This work-in-process, reports on successes and challenges presented, during the co-infusion of a polyurethane enamel paint (DuPont Imron 5000) and a vinyl ester resin (Derakane 470-45).

KEYWORDS: Resin infusion, co-infusion, in-mold coating, composites

INTRODUCTION

Over the past four decades, polymer composites have been presented as the material of the future due to their advantages of high strength to weight ratios, corrosion resistance, and functional integration [1]. Nonetheless, the production economics of polymer composites tend to limit their application in the mass production sector. The lead times to manufacture are simply too high. Several production processes are available, with the liquid composite molding techniques being the most amenable to mass production.

Techniques such as resin transfer molding (RTM), vacuum assisted resin transfer molding (VaRTM), and their variants have been successfully implemented for the manufacture of polymer composite components. Once manufactured, composite components undergo a series of finishing processes to prepare the substrate for painting. Some of the current painting methodologies are not only laborious, time consuming and expensive, but may result in the release of materials that are harmful to the environment.

This work will assess the viability of in-mold coating composites made by the RIDFT process by means of co-infusion.

RIDFT is a two-stage process – resin infusion and wetting, followed by vacuum forming. As shown in Fig. 1, dry reinforcement is placed between two membranes. After securing the membranes, resin is infused under a vacuum. The next stage is vacuum forming, during which the membranes are drawn over a male mold (final product shape) by applying a vacuum. The use of a one-sided mold provides huge cost benefits when compared with the RTM process. A cost savings of 24% has been demonstrated when compared with SCRIMP [1].

Step 1: Load fiber   **Step 2: Seal Machine**   **Step 3: Infuse Fiber**

Step 4: Seal Chamber   **Step 5: Vacuum Form Part**   **Step 6: Demold**
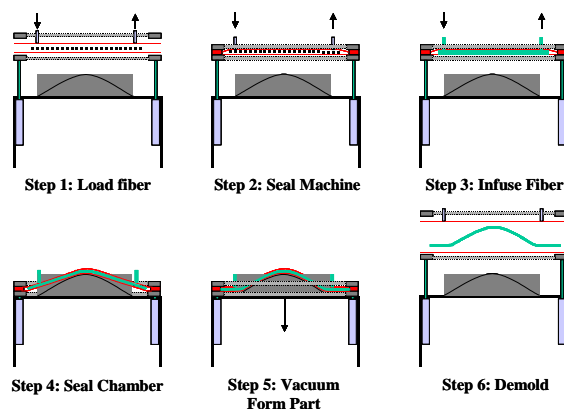
Fig. 1   The RIDFT process [1]

The automotive coatings market has been significantly influenced by the macroeconomic environment, the drive towards lower costs and higher efficiency, technology innovation and sound environmental practice [2]. Environmental concerns have led the trend to reduce solvent use in coating applications. The latest technology and materials development promise to lower assembly paint-line emissions, eventually eliminating solvents in paint, while improving scratch resistance and the overall durability of a vehicle finish.

It is imperative that methodologies are sought to reduce the costs associated with painting, as well as the negative environmental impacts. In-mold coating (IMC) of composite components may address these issues. IMC has been successfully used for many years for exterior body panels made from compression molded Sheet Molding Compound (SMC) to improve their surface quality in terms of functional and cosmetic properties [2]. When injected onto a cured SMC part, IMC cures and bonds to provide a paint-like surface. Another method for in-mold coating is the use of thermo-formable paint films.

Several forms of in-mold coating have been researched, including the metal plating of sheet molding compounds (SMC) [3], and in-mold coating of injection molded plastics [4]. McCarthy *et al* [5] discussed the effects of implementing paint films on different fiber structures. Castro *et al* [6] offered the process model for in-mold functional coating of thermoplastic substrates. Toro and Okoli [2] reported on the use of paint films on RIDFTed composite parts. They established the viability of the use of thermo-formable paint films with the RIDFT process.

This work describes the preliminary results of in-mold coating assessment studies of RIDFTed components. A room temperature cure vinyl ester resin was used with DuPont Imron 5000 paint.

APPROACH

Based on the work by Gillio *et al* [7], a simplified schematic of the co-injection setup is shown in Fig. 2. In the majority of cases, the flow of a polymer inside a mold filled with a stationary fiber bed is modeled using Darcy's law (Eqn. 1).
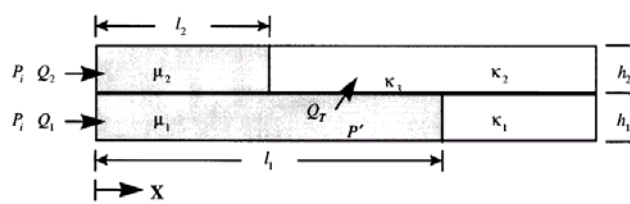
Fig. 2 Schematic of the one-dimensional flow model in CIRTM [7]

The macroscopic velocity, *u*, is given by:

$$u = \frac{k}{\mu}\frac{dP}{dx}$$

(1)

where *k* is the permeability of the fiber preform, μ is the viscosity of the resin, and *dp/dx* is the pressure gradient in the flow direction.

In co-injection, the top and the bottom preforms could have different permeabilities and the resins injected could have different viscosities, leading to different resin velocities between the top and the bottom halves of the mold. The injection is assumed to be at the same pressure since this is the case in the majority of VARTM type processes [7]. In such a case the velocities of the two flow fronts will be given by:

$$u_1 = \frac{k_1}{\mu_1}\frac{P_i}{l_1}$$

(2)

$$u_1 = \frac{k_2}{\mu_2}\frac{P_i}{l_2}$$

(3)

The RIDFT set-up is illustrated in Fig. 3.
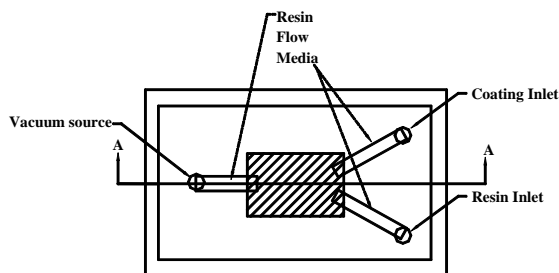
Fig. 3(a)   RIDFT IMC (Top view)
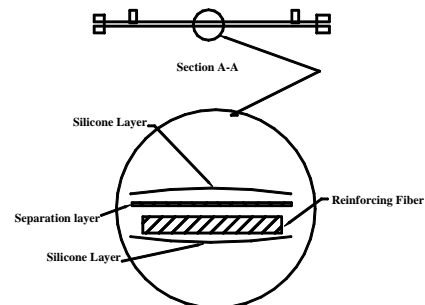
Fig. 3(b)   RIDFT IMC (Detailed)

The resin and coating material were infused through separate flow media under vacuum. A layer of FERRO Prepak material was used to separate the paint and resin to prevent mixing during infusion. The paint is infused first followed by the resin, which dissolves the separation layer on contact.

RESULTS AND DISCUSSION

A series of experiments were performed. Initial tests used an impermeable vacuum bag as the separation layer. Resin Derakane 470-45 was co-infused successfully, demonstrating the viability of the experimental set-up. The bagging material was obviously unsuitable for a separation layer for IMC due to adhesive incompatibilities. Other materials were assessed including the FERRO # MCO8 Prepak material. Initial infusion with coating and resin showed promise. However, since the coating material is more viscous than the resin (30:1) and permeability $k_1 > k_2$, when infused concurrently, the resin filled the mold faster than the paint. Additionally, the resin depletes the separation material on contact. Therefore, it was necessary to first infuse the paint, and then infuse the resin.

Fig. 4(a) Non-coated and IMC RIDFTed components
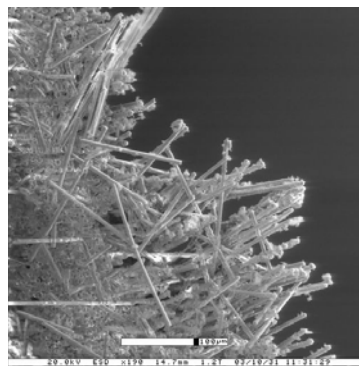
Fig. 4(b) Microstructure of IMC RIDFTed component showing poor interfacial bonding

As can be observed from the samples shown in Fig. 4(a), co-infusion was implemented. The resin and paint were co-infused into the flexible diaphragms. However, the separation layer did not perform as required, allowing the paint to seep through, and mix with the resin. This may have resulted in the paint interfering with the fiber-matrix interface. Fig. 4(b) is the microstructure of a failed IMC specimen. It shows extensive fiber pullout, which is indicative of a poor fiber-matrix bond. This poor interfacial bond may have resulted in the radical difference in storage modulii observed in the non-coated and coated parts. See Figs. 5 (a and b). Material selection is on- going to determine a more suitable separation layer material. Other paints will also be evaluated.
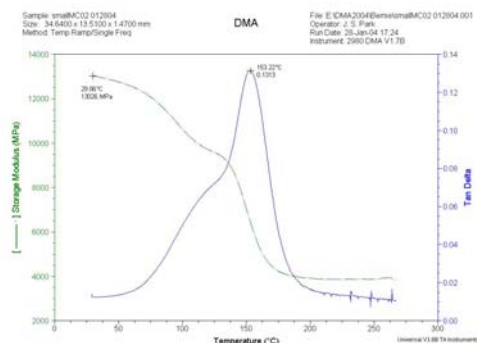
Fig. 5(a) DMA diagram showing composite storage modulus of 13026MPa and Tg is 153.22°C, for a RIDFTed composite part.
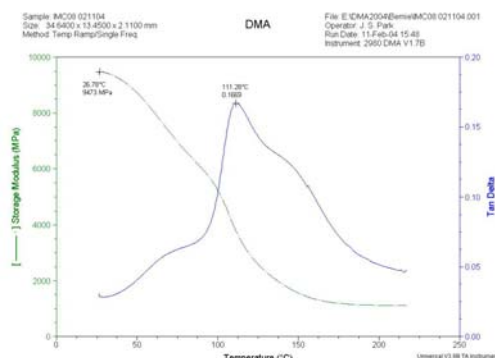
Fig. 5(b) DMA diagram showing composite storage modulus of 9473MPa and Tg is 111.28°C, for IMC RIDFTed part.

SUMMARY AND CONCLUSION

In this experimental study, co-infusion was implemented. The resin and paint were co-infused in-between the flexible diaphragms. However, the separation layer did not perform as required, allowing the paint to seep through, and mix with the resin. Material selection is on going to determine a more suitable separation layer material. Other paints will also be evaluated in future work.

The ability to in-mold coat a composite will certainly advance their manufacturing. Nonetheless, the methodology for sustaining or improving mechanical properties and appearance of products should be the premise of implementing IMC. In applying in-mold coating into the process today known as RIDFT, its unique approach to integrating flexible coatings with substrates is a natural fit for market segments such as automotive, agricultural, construction equipment, marine, lawn and garden, and aerospace.

ACKNOWLEDGEMENTS

REFERENCES

1. J.R. Thagard, O.I. Okoli, Z. Liang, H-P Wang, C. Zhang. "Resin Infusion between Double Flexible Tooling: Prototype Development", *Composites: Part A* 34, (pp. 803–811), 2003.

2. N. Toro, O.I. Okoli. "In-Mold Coating of Composites Manufactured with the Resin Infusion between Double Flexible Tooling Process", *Proc. CFA 2003*.

3. N. Yamamoto, N. Yagi. "Development of Metal Plating on FRP Exterior Body Panels". *JSAE Review,* 16, (pp. 179-183), 1995.

4. J.W. Rayle, D.W. Cassil. "Advancements in Injection In-mold Coating Technology", *Metal Finishing*, September 1995.

5. S.P. McCarthy, T.M. Ellison, Q. Guan, A.K. Delusky. "The Effect of Reinforcing Fiber Length on Surface Properties of Thermoplastic Composites Made by Surface Finishing/Compression Molding", *Proc. NSF Workshop on Composite Sheet Forming, Lowell, MA, U.S.A.,* September 5-7, 2001.

6. K.S. Zuyev, X. Chen, M. Cabrera-Rios, J. M. Castro, E.J. Straus. "In-Mold Functional Coatings of Thermoplastic Substrates: Process Modeling", *Journal of Injection Molding Technology,* 5, No. 2, (pp. 80-97), 2001.

7. E. F. Gillio, S. G. Advani, J. W. Gillespie Jr. "Investigation of The Role of Transverse Flow In Co-Injection Resin Transfer Molding", *Polymer Composites.* 19(6), (pp.738-746), 1998.

Design and Performance of a New VARTM Resin Injection Line

Ajit R Nalla [1], Benoit Lelievre [2], James Glancey [3]

[1] *Department of Mechanical Engineering, University of Delaware*
[2] *IUP de Lorient, Université de Bretagne Sud, Lorient, France*
[3] *Department of Mechanical Engineering, University of Delaware, Newark, Delaware-19716,Email:jglancey@me.udel.edu (corresponding author)*

SUMMARY: Improving control of the resin flow and resulting flow front within a mold during VARTM will be an important development that significantly improves molded part quality. Additionally, current practices like extending injection times to minimize dry spot formation result in excessive resin waste as well as increased cycle times. To improve process controllability during VARTM, a new and innovative resin injection line was designed and tested. The injection line, which consists of individual segments each independently operated, allows for the control of resin flow to different locations within the mold. Several generations of prototypes have been used to demonstrate that a simple vacuum-based actuation technique for each line segment provides the most cost effective configuration that meets the performance requirements. Current research is focusing on optimal design geometry that improves dynamic response and minimizes hysteresis-like behavior.

KEYWORDS: VARTM, injection, smart line, flow control, segments.

INTRODUCTION

Liquid composite molding processes such as VARTM (Vacuum Assisted Resin Transfer Molding) offer numerous advantages over other processes because of the low tooling costs and it's applicability to large structures. VARTM basically consists of the following steps: 1) Placement of a stack of dry fiber reinforcements known as a preform over a tooling surface which is enveloped and sealed with a flexible plastic bag and tacky tape; 2) Applying a vacuum and drawing resin into this assembly through the injection line under vacuum and filling the entire space between the preform fibers in the mold; and 3) Curing of the resin in the mold. To achieve a defect free part with out dry spots and voids, it is essential to saturate the entire space between the preform fibers. The inherent variations in the key process parameters such as the preform permeability (k), fluid viscosity (µ), fiber volume fraction (V_f) and the compaction pressure along with the preform preparation and preform placement fundamentally influence the permeation of the resin through the preform. The formation of dry spots and voids that results in the manufacture of defect parts has created a genuine need for better flow control approaches in VARTM.

REVIEW OF CONTROL TECHNIQUES FOR VARTM

Improved control of resin flow has been attempted in the past with several approaches. Feedback control [3] of the VARTM process was developed to adjust vacuum levels at several vent locations within the mold. The system was based on computer-controlled pressure regulators and venturi pumps; vacuum sensors were used to measure in-situ vacuum levels at different locations in the system. This system, which was able to control accurately and quickly the vacuum levels in the vents, showed potential for flow front control. Flow rate control [2] during VARTM processing was developed in which the system applied a computer-controlled vacuum differential between the injection and vent gate with feedback from a precision scale. The controller was implemented in Lab VIEW to support the data acquisition and actuation and was applied to various molding applications to improve both processability and part quality. In another study, an Intelligent Process Control (IPC) system [1] was developed to fully automate the VARTM process, to allow material, process and part traceability and to ultimately reduce scrap and end-user costs through sensor-based real-time quality control. Based on this work, a sequential resin injection system was proposed, developed and implemented which helped in reducing the resin fill time. Recently, enhancement of flow in VARTM using localized induction heating was attempted in which an induction heating was used as a method of locally reducing the resin viscosity to counteract the effects of localized low permeability regions within the preform [4].

Each of the control techniques mentioned above for VARTM utilize distribution lines for resin injection and vacuum supply, and provide very limited controllability of the resin flow within the mold. As a result, dry spots and void formation continue to limit the complexity of the mold designs as well as production efficiency. An alternative control method that shows promise for improved resin control in VARTM by manipulating the flow from different segments or regions of the mold is examined in [7]. The underlying basis for this new resin injection technique is presented in this paper.

OBJECTIVE

The objective of this research is to propose a design and examine the performance of a new, segmented VARTM resin injection line. This paper discusses the design strategy for the line segments, the actuation method employed to control these segments, and the effectiveness of the line as a means to control resin flow from an injection line.

SEGMENTED INJECTION LINE DESIGN

Conceptual Design

The "Segmented Injection Line" consists of multiple segments that can be individually actuated thereby controlling the resin flow to different parts of the mold. Initially several different actuation methods including piezoelectric-based devices, magnetism, hydraulic and electromagnetic restrictive materials were accessed to determine the best method of actuation. A simple vacuum-based actuation technique for each line segment proved to be the most cost effective technique that meets the performance requirements. The design of the vacuum-based injection line is presented herein.

The conventional VARTM methods typically use an omega tube [Fig. 1] for the injection line. The resin reservoir is attached to one end of the tube, and the vacuum applied to the mold draws resin through the tube, out the bottom and into the preform. With this configuration, resin flows out from the entire length of the tube, and cannot be regulated unless the supply of resin to the tube is terminated. To improve the controllability of the resin flow from an injection line, independent segments within the line were created. This new configuration is illustrated in Fig 2. A circular tube with several perforations along its length that act as ports for the flow of resin into the mold is placed on top of the preform. Once the
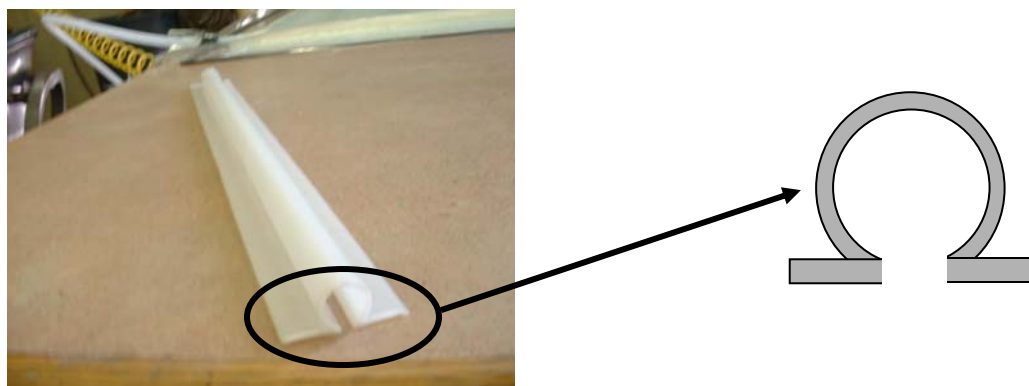
Figure 1: Conventional Omega Tube currently used for both the resin injection line and the vacuum line.
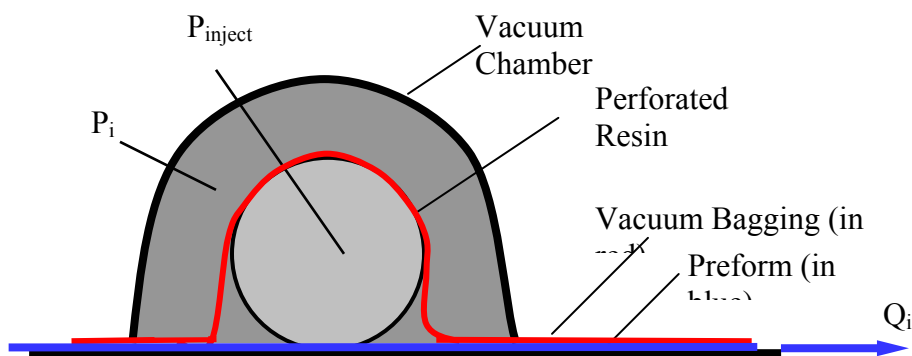
Figure 2: Typical cross-section of the segmented injection line.

tube is in place, the vacuum bag is placed over the entire mold, including the perforated tub. This circular tube is part of the conventional VARTM set up replacing the omega tube. However, unlike conventional VARTM techniques, an additional vacuum chamber is placed on the vacuum bag over the perforated tube. As a result, when a vacuum is applied to the mold, the vacuum bag is drawn against the perforated tube, and resin cannot flow from the holes. However, when a signal pressure, P_i is applied, the bag can be lifted off the perforated tube, thus allowing resin to flow from the tube into the preform. Using this approach, independent injection line segments can be created along the perforate tube with independent vacuum chambers [Fig 3a].

The resulting constitutive law for the i_{th} injection line segment will be:

$$\text{if } P_i > P_{inject}, \ Q_i = 0 \tag{1}$$

$$\text{if } P_i < P_{inject}, \ Q_i > 0$$

where P_i is the absolute pressure in the vacuum chamber and P_{inject} is the absolute pressure in the perforated resin tube.

Prototype Development

Several different design configurations were examined for the segmented line. For testing purposes, a semi-circular shaped plexi-glass vacuum chamber with both ends sealed was partitioned to create independent segments of injection line.   This accommodated visual inspection of the bag and tube during operation. The chamber was placed over the injection line and sealed tightly to the vacuum bag [Fig 3]. Vertical dividers along the chamber segmented the injection line into the desired number of independent segments. A separate small vacuum line (i.e. the actuation signal) was then connected to each section of the vacuum chamber, thus allowing independent opening and closing of each segment.

(a)   **(b)**
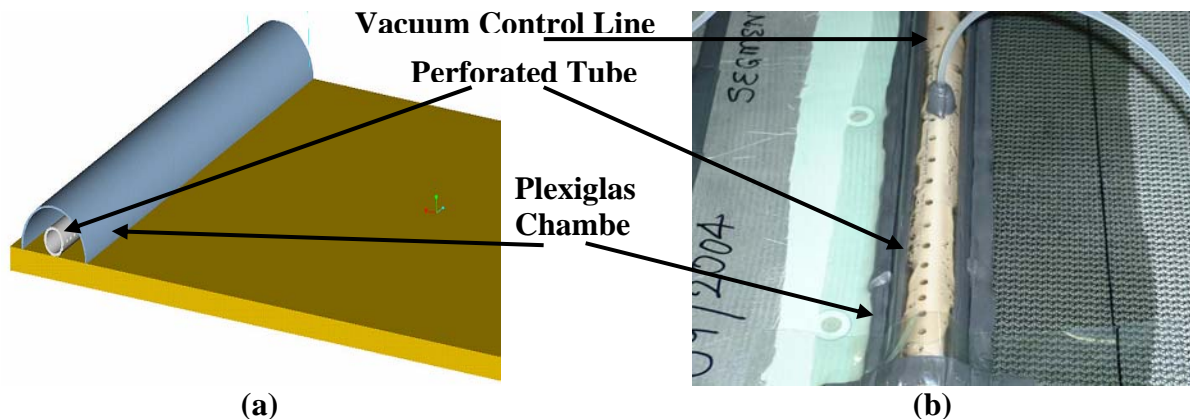
Figure 3: Solid model (a) and early prototype (b) of one segment of the new injection line.

PROTOTYPE TESTING AND PRELIMINARY RESULTS

Several experiments were conducted to evaluate the performance of the segmented injection line. Initial tests with a single line segment were used to verify the constitutive behavior described in Equation 1. In general, performance was very good as long as the vacuum bag was properly placed over the perforated tube. The intimate contact between the vacuum bag and tube necessary for the bag to seal the perforations required that no wrinkles were present in the bag. Subsequent testing of the single line segment did reveal however, that resin bleeding within the mold would allow the flow front to creep, even after the line segment was turned off. As illustrated in Fig 4, after the segment was closed, the resin flow front continued to propagate into the unwetted mold about 75 mm. As a result, the actual flow front behavior using the segmented line may, in some instances, be confounded by resin bleeding, and the ability to predict and/or control the resin movement within the mold will require a more sophisticated approach than the simple constitutive law proposed in Equation 1.
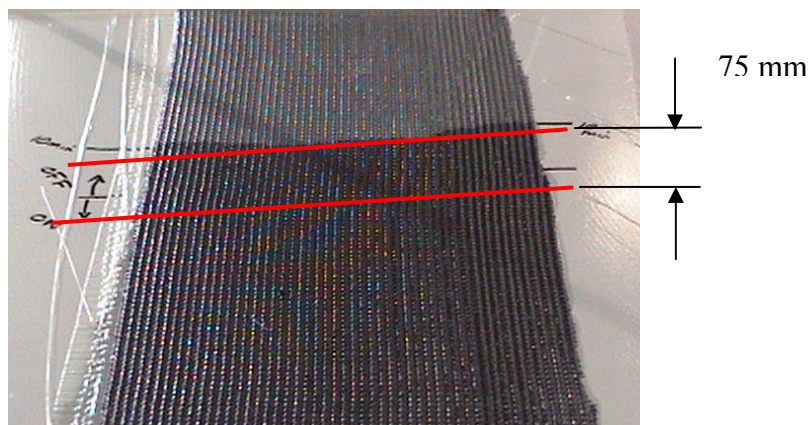
Figure 4: Evidence of resin bleeding 10 minutes after closing the injection line segment.

To investigate the dynamic behavior of the segmented injection line, a 3-segment prototype was fabricated and instrumented with pressure transducers. Pressure within each vacuum chamber segment, along with the resin supply pressure was monitored during various experiments. Of particular interest was the step response of each line segment; a typical test result is shown in Fig 5 for a step-close scenario. In general, the response time to close the segments was relatively high averaging 3 to 4 s. By comparison, the time to open a line segment averaged only 50 ms. This hysteresis-like behavior can be attributed to the fundamental difference between opening and closing a segment. When turned off, the vacuum bag cannot achieve the intimate contact necessary to seal the perforations in the tube until the resin in the vacuum chamber has been displaced into the mold. This phenomenon can be observed in Fig 6. As a result, the response time can be relatively long, especially as the resistance to flow in the mold increases during injection. However, when a line segment is turned on, the vacuum bag can pull away from the perforated injection tube relatively quickly since the resistance to resin flow through the tube and perforations is low. These effects can be substantially reduced by optimizing the vacuum chamber design, thus minimizing the volume of resin that must be displaced, especially during closing.
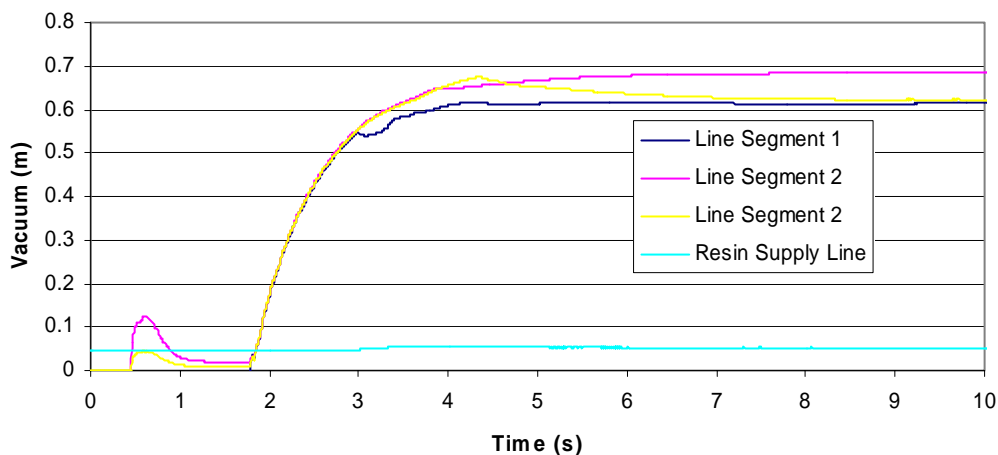
Figure 5. Step response of the segmented resin injection line.

200
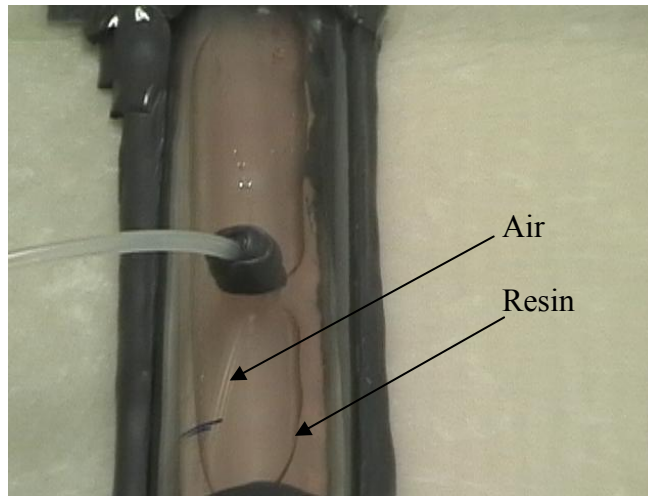
Figure 6. View of one injection line segment during a step response test.

CONCLUSIONS

A multi-segment injection line for VARTM has been design and tested. This new line, which consists of individual segments each independently operated, allows for the control of resin flow to different locations within the mold. Several generations of prototypes have been used to demonstrate that a simple vacuum-based actuation technique for each line segment provides the most cost effective configuration that meets the performance requirements. Experiments using both single and multi-section injection line prototypes prove this configuration is capable of controlling the resin flow from each segment. Dynamic performance tests during opening and closing (step response) operations suggest significant hysteresis-like behavior can occur; this effect can be minimized in future designs with proper vacuum chamber geometry.

ACKNOWLEDGEMENTS

REFERENCES

1. Heider, D. (Center for Composite Materials, University of Delaware); Gillespie Jr., J.W.; Pike, T.L.; Thomas, G.E.; Steele, T.; Florence, J., Intelligent process control for affordable VARTM processing of DoD structures, Source: International SAMPE Symposium and Exhibition (Proceedings), v 48 I, 2003, p 657-669.
2. Heider, D. (Center for Composite Materials, University of Delaware); Epple, S.; Gillespie J.W., Jr., Flow rate control during Vacuum-Assisted Resin Transfer Molding (VARTM) processing, Source: International SAMPE Symposium and Exhibition (Proceedings), v 46 I, 2001, p 1061-1071.
3. Heider, D. (Univ of Delaware); Graf, A.; Fink, B.K.; Gillespie, J.W. Jr. Feedback control of the vacuum assisted resin transfer molding (VARTM) process, Source: Proceedings of SPIE - The International Society for Optical Engineering, v 3589, 1999, p 133-141.
4. Johnson, R.J. (Composites Processing Laboratory, Department of Mechanical Engineering, University of Connecticut); Pitchumani, R., Enhancement of flow in VARTM using localized induction heating, Source: Composites Science and Technology, v 63, n 15, November, 2003, p 2201-2215.
5. Walsh, S.M. (U.S. Army Research Laboratory); Mohan, R.V. Sensor-based control of flow fronts in vacuum-assisted RTM, Plastics Engineering, v 55, n 10, October, 1999, p 29-32.
6. Hsiao, K.-T. (Center for Composite Materials, University of Delaware); Gillespie J.W., Jr.; Advani, S.G.; Fink, B.K .Role of vacuum pressure and port locations on flow front control for liquid composite molding processes Source: Polymer Composites, v 22, n 5, October, 2001, p 660-667.
7. Ajit R Nalla , James Glancey , Benoit Lelievre, Theoretical and experimental evaluation of a segmented injection line for resin flow control in VARTM- FPCM-7 (2004)The 7th International Conference on Flow Processes in Composite Materials, Newark, Delaware, USA, 7 ~ 9 July. 2004.

Vacuum Source Volumetric Flow and the Vacuum Infusion Process

Patrick E. Mack, CCT

Verdant Technologies, Inc.
310 Bourne Avenue
Box 15 / Building 50
East Providence, RI 02916
e-mail: patrick.mack@verdantresins.com

SUMMARY: Vacuum infusion processing has enjoyed a resurgence of interest in recent years as a primary mode of fabrication over traditional open mold processing. This renewed interest is driven by economic, environmental and engineering concerns as closed mold processing is recognized as being a cleaner, more efficient process than open molding. To facilitate vacuum infusion implementation, process simulation models are often used to gain an understanding of and to optimize the processing parameters for a given part. Simulation models to date derive resin flow characteristics, i.e. velocity, in part by way of the pressure gradient at the resin flow front. Although these simulations have been found to be generally accurate further process optimization may be realized through consideration of the effects of the vacuum source's volumetric flow rate on the infusion process. This paper seeks to lay the groundwork for future model development by expanding our understanding of these effects and their implications.

KEYWORDS: vacuum source volumetric flow; *Darcy Weisbach Friction Factor Equation*; extended *Bernoulli* equation.

INTRODUCTION

While composites find their roots in closed mold processing modern derivatives such as resin transfer molding (RTM) and were born of the desire to reduce the acquisition costs associated with aerospace composites. Generally what we think of as vacuum infusion processing (VIP), be it surface infusion or interlaminar infusion, are second order derivatives of RTM developed with the intention of meeting the cost/performance profile of a commercial (aka open mold) composite. Process simulation models for VIP naturally followed a like path from RTM. While significant model development specific to VIP is prevalent throughout the literature [1-3], no mention is made of the vacuum source volumetric flow rate relative to the resin flow rate. Rather, motive force is defined specific to the established pressure gradient at the flow front between the vacuum and the resin. However, numerous field accounts of varied infusion rates with different pumps and vacuum tube diameters, other variables remaining constant, led us to believe otherwise.

RESEARCH OBJECTIVE & APPROACH

Clearly the discovery of a correlation between vacuum source volumetric flow rate and resin flow velocity would, at a minimum, impact seemingly rudimentary decisions such as vacuum pump selection, and could ultimately shift our approach to process implementation enabling broader application within the market. Thus our research sought to determine whether or not the volumetric flow rate of a vacuum pump make a difference in the resin flow velocity and parallel infusion rate, and if so, determine how might we account for this in future models.

To approach the question a standard vacuum/laminae cell was developed in which resin flow velocity was characterized via distance over time. Two such experiments would be performed wherein all variables within the cell were maintained constant, bar the cells vacuum tube inlet diameter. In this manner the volumetric flow rate afforded by the pump was altered between the experiments.

EXPERIMENTAL

The standard vacuum/laminae cell is shown schematically (top view) in Figure 1 where the laminae consisted of 600 g/m^2 chopped strand mat/Polybeam™ 720/600 g/m^2 chopped strand mat measuring 304.8-mm in width by 2133.6-mm in length. The general assembly of the standard cell is representative of interlaminar infusion, shown schematically in Figure 2, where the Polybeam™ 720 is a reinforcing interlaminar infusion media. Referring again to Figure 1, upon assembly of the laminae (1), a single vacuum port (3) was fitted adjacent to the flow medium, and spiral cut tubing (2) for resin input was fitted on the

Figure 1.

opposite edge of the flow medium. The cell was set up such that the ensuing flow front path would run perpendicular to the lamina length. A flexible vacuum bag was then fitted and sealed about the laminae, the resin input tube sealed with a clamp and vacuum drawn. To facilitate flow front progression time demarcation a clear vacuum bag was used.
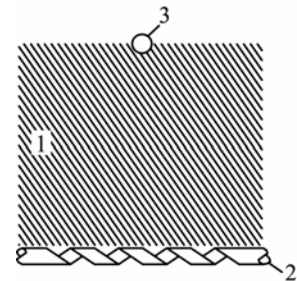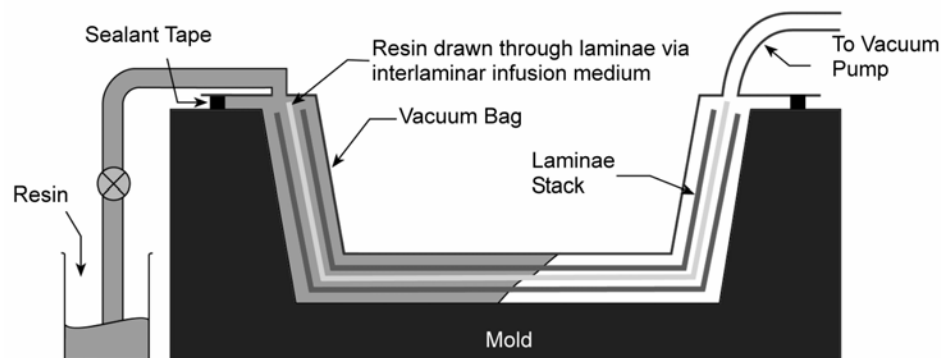
Figure 2. Interlaminar Infusion Illustration.

A gauge affixed to a standard resin trap read vacuum. When vacuum reached 96.5 kPa , the clamp was removed from the resin inlet tube, and the tube was subsequently placed in initiated polyester resin (~ 0.10 Pa•s). The resin clamp was reaffixed to the inlet tube when the resin front reached the vacuum port. Time interval demarcations were recorded every 30 seconds from the time of resin introduction to infusion completion. Two such experiments were performed wherein all variables within the cell were maintained constant, bar the cells vacuum tube inlet diameter. One experiment was run with a 19.05-mm ID vacuum tube as a control based on the pump inlet diameter (also 19.05-mm), and the other with a 9.525-mm ID vacuum tube. In this manner the volumetric flow rate afforded by the vacuum source was altered between the experiments.

RESULTS AND DISCUSSION

Figure 3 comparatively graphs the resin flow front velocity between that of the control (19.05-mm Vac.) and of the reduced (9.525-mm Vac.) vacuum source volumetric flow rate. One can clearly see a difference between the two. Given this measurement the question turns to whether or not the observed difference correlates to the change in volumetric flow rate.
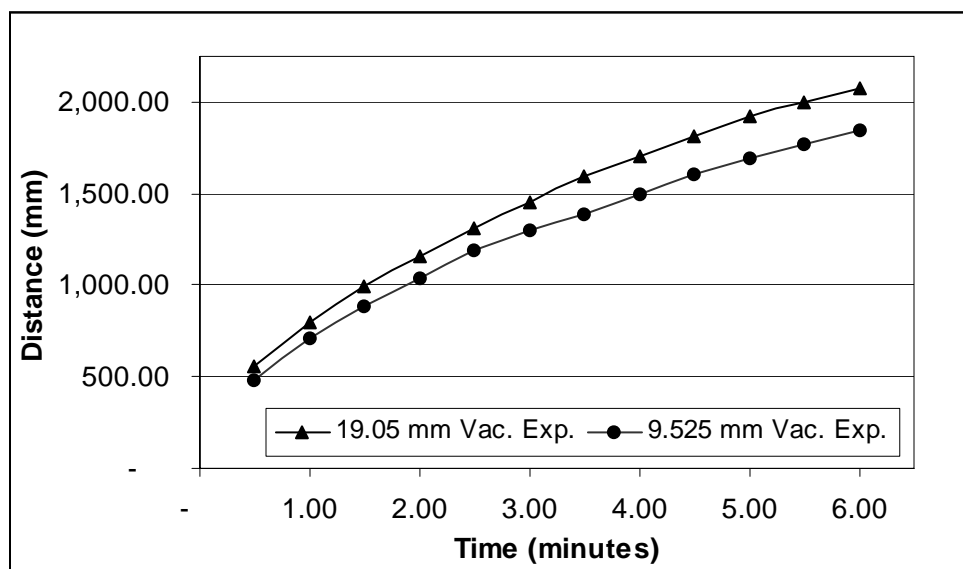
Figure 3. Infusion Rate Comparative.

The answer can be found by looking at the fundamentals of pumps in general. Pumps convert mechanical (rotational) energy into fluid (kinetic) energy, measured often as head. Head refers to the height of a liquid column which the pump could create using the kinetic energy that is generated. Vacuum producing devices maintain a system at a desired pressure or remove gas (fluid) from a vacuum system at a rate S_p, which is defined as a volume flow rate of gas per unit of time, $S_p = dV/dt$. Common units used for pumping speed are liters per second, cubic feet per minute (cfm), or cubic meters per second, all of which are expression of kinetic energy. Thus, as applied to our experiment, gas laws can be used to model the kinetic energy loss (or head loss) in our system, as attributed to the friction created by reducing the diameter of our vacuum tube.

The determination of frictional head loss can be attained through application of the *Darcy Weisbach Friction Factor Equation* (Eq. 1) as applied to our experimental set-up specific to the vacuum tube in question and our known pumping speed at the given pressure (96.5 kPa).

$$h_l = f\left(\frac{L}{D}\right)VP \qquad (1)$$

Where

VP = Pressure required to accelerate fluid from zero velocity to some velocity (V) and is proportional to the kinetic energy of the fluid stream.
L = length
D = diameter
f = friction factor

Through application of Eq. 1, in reducing the cross sectional area of the vacuum tube we find an 11.2089% drop in the systems kinetic energy, realized through the effective reduction in net CFM at the given pressure. Figure 4 graphs the 9.525-mm Vac. Predicted as derived through application of the 11.2089% kinetic energy loss against the control cure. Note the strong correlation between the 9.525-mm Vac Predicted and that of the experimental result.
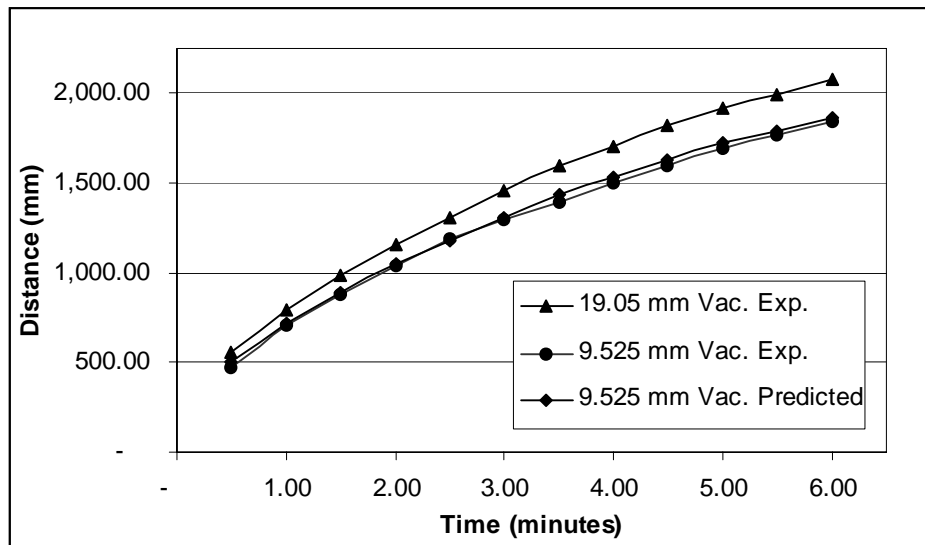
Figure 4. Infusion Rate Comparative vs. Predicted

SUMMARY AND CONCLUSION

The experimental results and model show good correlation and present compelling evidence regarding the role of vacuum source volumetric flow rate and resin flow velocity. From a practical standpoint one should consider the implication of flow rate in pump selection for a given application. Care should also be taken in infusion cell setup so as not to restrict the available kinetic energy (i.e. don't unnecessarily restrict the vacuum lines). Additionally care should be taken by those engaged in research activities where results may be skewed by differences in vacuum source volumetric flow rate (i.e. pre-form permeability testing).

With regards to simulation modeling our current research suggests that the role of vacuum source volumetric flow rate can be quantified by adding a term to Bernoulli's equation (2) to balance the pump energy (h_A)

$$\frac{p_1}{\gamma} + \frac{V_1^2}{2g} + z_1 + h_A - h_L = \frac{p_2}{\gamma} + \frac{V_2^2}{2g} + z_2 \qquad (2)$$

REFERENCES

1. A. Hammami, B.R. Gebart, "Analysis of the Vacuum Infusion Molding Process", *Polymer Composites*, Vol. 21, No.1, Pages 28-40 (February 2000).
2. K. Han, S. Jiang, C. Zhang, B. Wang, "Flow modeling and simulation of SCRIMP for composites manufacuturing", *Composites: Part A*, 31, Pages 79-86 (2000).
3. K.J Ahn, J.C. Seferis, L. Letterman, "Autoclave Resin Infusion Process: Analysis and Prediction of Resin Content", SAMPE Quarterly, Pages 3-10, (January 1990).
4. L. Joubaud, F. Trochu, J. Le Corvec, "Simulation of the Manufacturing of an Ambulance Roof by Vacuum Assited Resin Infusion (VARI)", Composites 2002 Convention and Trade Show, Composites Fabricators Association, (2002).
5. I. Granet, *Fluid Mechanics Fourth Edition*, Prentice Hall, (1996).
6. *Industrial Ventilation – A Manual of Recommended Practice*, 21st Edition, American Conference of Governmental Hygienists, (1992).

Low Cost Aerospace Composites

Maarten Labordus
Center of Lightweight Structures TUD-TNO
Kluyverweg 1, 2629 HS Delft, The Netherlands
Corresponding Author's e-mail: M.Labordus@ind.tno.nl

SUMMARY: A new low cost resin system has been used to produce a composite elevator. Vacuum infusion has been used as low cost, non-autoclave room temperature production process. The innovative design which is characterized by a high degree of integration helps reducing assembly cost. A top-down certification approach, in combination with a fully computerized process control helps to speed up the implementation of these new materials, processes and designs and bring down the certification costs. This is demonstrated by the design and production of a simplified elevator construction.

KEYWORDS: Vacuum infusion, vinylester, certification, top-down, building block

INTRODUCTION

Resin infusion in aerospace applications has traditionally been focused on pressure injection in stiff molds. This process is commonly referred to as Resin Transfer Molding or RTM. Several resin systems have been and are being used with the pressure injection process, like RTM6 and Cycom 890. A number of parts have been produced and certified for this pressure injection process. Although good product quality can be achieved, this process is very expensive and inflexible for design changes. Only limited part sizes are possible. Recent developments have focused on cost reduction by switching from pressure injection to vacuum infusion. This will greatly reduce the mold costs since only one mold halve is needed and the clamping system is obsolete. However, for aerospace applications, still the expensive resin systems are used which require infusion at elevated temperatures. This implies that the mold geometry needs to be compensated for thermal expansion mismatches and that some sort of heating equipment needs to be installed on or around the mold. Also the use of a one-sided tool has still limited the level of integration of parts. This research describes a new approach, were a room temperature processing and room temperature curing vinylester resin system is used. A free-standing post-cure can ensure a T_g up to 230°C. New preforming methods and innovative tooling systems have allowed for a high level of integration. This is demonstrated by the production of a simplified elevator construction. The following chapter deals with some design aspects of the demonstrator product. The third chapter describes the production steps taken. In chapter four, some comments on certification issues are given. The paper ends with conclusions and recommendations.

DEMONSTRATOR DESIGN AND PRELIMINARY ANALYSIS

A composites redesign was made of an aluminium elevator of a business jet. Several concepts for a lighter and cheaper elevator were considered, where "design for manufacturing" was the leading requirement. This will consequently lead to concepts with a high potential for cost reduction. An evaluation was made among three materials: aluminium (original baseline design), Carbon T300-epoxy and Carbon IM7-vinylester, and two structural concepts: the stiffened skin and the sandwich concept.

Three load cases are analysed: maximum pressure distribution, balance weight loads and damage tolerance (one hinge failure). From this analysis, performed both by analytical and finite element methods, a optimal design evolved, together with a first estimate of laminate lay-ups and thickness'. This design is shown schematically in . The design consists of a fully integrated spar-rib center box, an upper and lower skin with integrated local sandwich stiffening elements and several leading edge and hinge close-out ribs. For repair ability considerations, it was decided not to integrate the trailing edge with the skins, but to use a detachable structure. The materials selected were IM7 plain weave fabric from Hexcel Schwebel (SGP203-CSDH-49) and Daron hybrid vinylester (Daron XP 45-A-2 + Daron XP 40-B-1). To overcome tolerance problems normally associated with vacuum infusion, a mold design is foreseen where all the assembly surfaces are defined by the stiff mold system. Due to the flexibility of the vacuum infusion process, any design changes like a (local) increase of laminate thickness, can be easily implemented without a major redesign of the mold system. The design of this structure has been based on mechanical properties resulting from a short screening program of the selected material combination. The new design showed a 30% weight reduction with respect to the baseline concept.
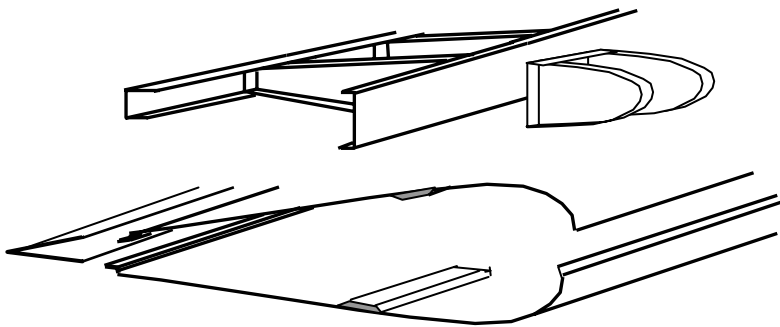
Figure 5: Schematic concept of elevator design

DEMONSTRATOR PRODUCTION

For demonstration purposes, it was decided not the produce a complete full scale elevator, but rather a simplified demonstrator with some critical features. A three rib structure was chosen with ribs at the minimum and maximum distances as they occurred in the elevator design. If it proves to be possible to infuse this part, the infusion of the complete elevator should also be possible with the proposed infusion strategy. A combination of flow simulations (Figure 6) and practical infusion experiments have led to an infusion strategy from an inlet channel along the lower side of the front spar to several outlet points located at the upper side of the rear spar in between the ribs. The production can be divided into two steps: vacuum infusion of composite parts and the assembly. The assembly of the demonstrator will be rather conventional and will include bonding and applying mechanical fasteners.
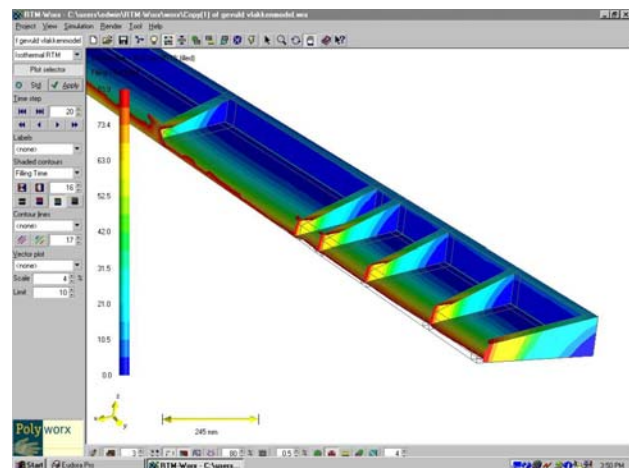
Figure 6: Flow simulation in RTMWorx (ref. 1)

The main focus of this paper will be on the vacuum infusion process. A mold system has been designed and constructed according to the proposed infusion strategy. The spar and rib laminates are preformed with a novel, patent pending preform method. Additional unidirectional tapes are interleaved in the flanges to increase the bending stiffness. To avoid tolerance problems during assembly, all bonding surfaces are defined by stiff mold surfaces. To ensure a reasonable surface quality on the vacuum bag side of the laminate, preshaped vacuum bags and nylon cowl plates are used.
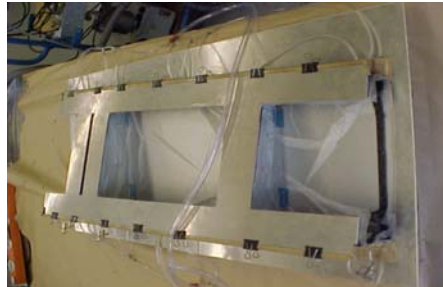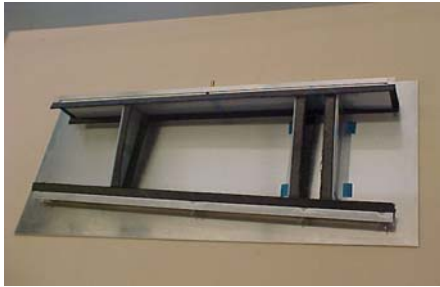
Figure 7: Mold with preforms (left) and mold sealed with preshaped bags and closing plate (right)
When the mold is completely sealed and the air tightness is checked, the resin is mixed according to the recipe in chapter 4. The resin is degassed for 5 minutes at 5mbar absolute pressure with a piece of Scotchbrite as bubble nucleator (ref. 2). The actual infusion is performed at 50mbars absolute pressure. After infusion, the pressure was increased to 200mbars absolute pressure before the resin inlet was closed. The whole procedure of checking air tightness of the mold, setting the pressures during infusion and curing and the opening or closing of resin inlets can all be computer controlled. After a 24hrs room temperature cure, the part is demolded. A freestanding post cure of 1hrs@120 $^\circ$C, 1hrs@150 $^\circ$C, 1hrs@180 $^\circ$C and 1hrs@210°C followed to achieve the 180°C T_g-wet. For the other parts like the skins and the leading ribs, a similar procedure was performed. The resulting components are shown in Figure *8*.
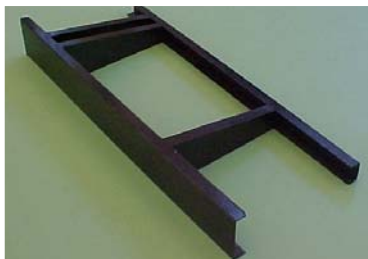
Figure 8: The integrated rib-spar structure (left), a skin (middle) and a leading edge rib (right)
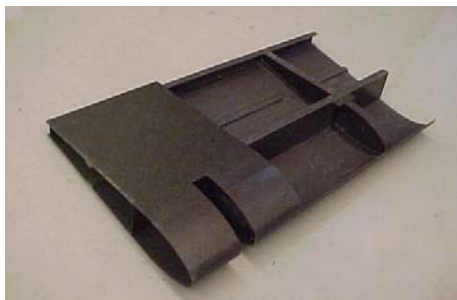
For demonstration purposes, these components are only assembled by a bonding film. In the actual elevator, there will also be a need for rivets at critical locations. The resulting demonstrator is shown in Figure 9.

Figure 9: The demonstrator after assembly

CERTIFICATION CONSIDERATIONS

Aerospace is normally not associated with low costs. Especially when aerospace certified composites are involved, the costs can be enormous. The introduction of new low cost materials or new low cost production processes is hampered by the traditional *building-blocks* certification approach. For composites, testing on coupon scale will rarely give insight in the failure mechanisms of the complete composite structure. However, the traditional building block certification approach involves an enormous amount of tests on coupon scale. For a new material or process, all these tests have to be performed all over again. This has lead to the situation that, even for so-called innovative programs like the JSF development, which has been focused on affordability, very traditional and expensive production processes like prepreg autoclaving are still being used and only use is made of already certified materials. Therefore, to be able to make real progress, a different certification approach is proposed. Laminate analysis software like Kolibri (ref. 3) will be used to determine the required engineering constants. The input for this software follows from a small screening program on physical and mechanical properties. FEM calculations are been carried out to validate the structural design. A full scale test under the most extreme conditions will have to show the design meets the airworthiness requirements. Flight spectrum fatigues tests can also be replaced by single stage testing for composite structures since fatigue in composite structures is not a material issue but a design issue. Also the time and cost consuming product control step can be omitted if a proper process control system is implemented. The aim is to certify the minimal product quality which can be achieved within a prescribed process window. This certification approach of building and testing structures in combination with process control, rather than the traditional building block approach will drastically reduce the introduction time and cost of new materials and processes.

CONCLUSIONS AND RECOMMENDATIONS

It has been shown that it is possible to produce high quality composite parts with a high degree of integration. By using the most optimal process, material and design options for each situation, major weight and cost savings can be achieved. The process control system has also proven its value. Working with vacuum as driving force for the resin does imply the need of proper degassing of resin prior to infusion in order to achieve an aircraft worthy product quality. Preferably, a continuous degassing procedure should be developed, rather than the batch wise degassing applied in the laboratory. In an actual production environment, a large degree of automation and a flow oriented production set-up should be aimed for. The new, patent pending preforming processes allows for such a flow production and automation. The Center of Lightweight Structures has also been working on computer controlled process control for resin infusion processes.

REFERENCES

1. Koorevaar, A. Journee Atlantec, ISITEM – UIT Nantes, 3-4 Februari, 1994, pg. 94
2. Labordus, M, *Avoiding voids by creating bubbles*. Proceedings of the 20th International SAMPE Europe Conference. Paris April 13th-15th, 1999. Center of Lightweight Structures TUD-TNO
3. http://www.clc.tno.nl/projects/recent/kolibri.html

ACKNOWLEDGEMENTS

Composite End Closures for an Autonomous Underwater Vehicle

Valeria Antonelli, Maarten Labordus and Peter Nederveen

Center of Lightweight Structures TUD-TNO
Kluyverweg 1, 2629 HS Delft, The Netherlands
Corresponding Author's e-mail: V.Antonelli@lr.tudelft.nl

SUMMARY: This paper presents some of the results obtained within the framework of the EC funded MAST-III project: "Lightweight Composite Pressure Housings for Mid-Water and Benthic Applications". The primary objective of this project was to gain experience in the design and fabrication of deep-water pressure resistant, fiber reinforced plastic (FRP) structures. This was demonstrated by designing and producing the battery container made entirely of FRP. This battery container is part of an autonomous underwater vehicle with a 2000 meters operational depth capability. In an unmanned underwater vehicle, this battery pack container is the largest structure. The scope of this paper is to show the design procedures and production methods of the end closures and transition rings of the pressure vessel. Some experimental results and their verification will also be presented.

KEYWORDS: Drape, vacuum infusion, marine application, thick-walled composites

INTRODUCTION

The pressure vessel is the core of an AUV (Autonomous Underwater Vehicle), whose schematic layout is shown in
Figure *10*, and is used for the containment of the battery pack, which supports the vehicle itself and the entire payload contained in it.
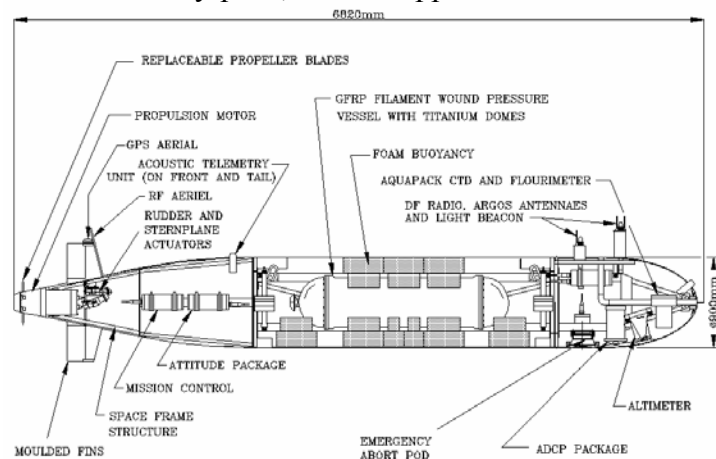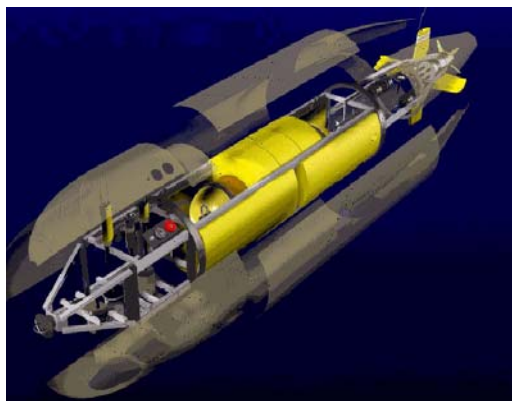
Figure 10: AUTOSUB - schematic layout.

The most important requirements that were taken into account for the design of the domes were:
- a maximum operating depth of 2000 m and ultimate design depth of 3000 m;
- an internal diameter of 450 mm;
- easiness of connection with cylinder;
- the minimisation of unusable space;
- lightness;
- producability (production technique being vacuum infusion).

DESIGN

During the preliminary design three possible shapes where evaluated: the classic hemispherical shape, a quasi-ellipsoidal which is normally used for pressure vessels subjected to internal pressure [2] and a spherical section. These three shapes where evaluated on basis of the given list of requirements with the help of the Finite Element Method and Drape, varying material (CFRP and GFRP) and thickness. The computer program Drape® [1] was used to predict the shear deformation (the so-called trellis effect) of the fabric layers during their draping onto the mold. As it was expected, the hemispherical shape is the one which needs the more material per blank, but also the one which causes the smallest locking angle. On the other hand the spherical section is the one which requires the least amount of material per blank and also the one that would be easily producible.
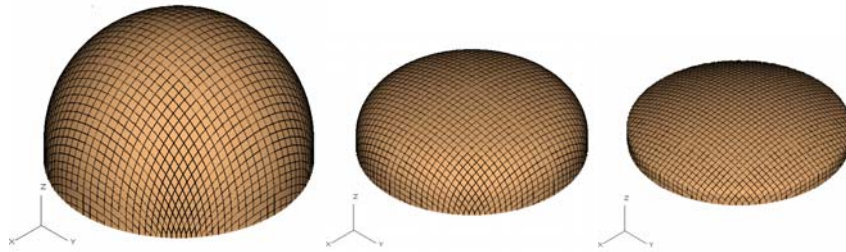
Figure 2: Results of fiber shearing in the three different shapes obtained by DRAPE.

Through the Finite Element Analysis, buckling behavior and strength of the three shapes were analysed. Since the buckling behavior of the end closures is depending on the behavior of the cylinder to which they are connected, also half of the filament wound cylinder was included in the model. Both linearised eigenvalue analysis and linear static analysis have been carried out.
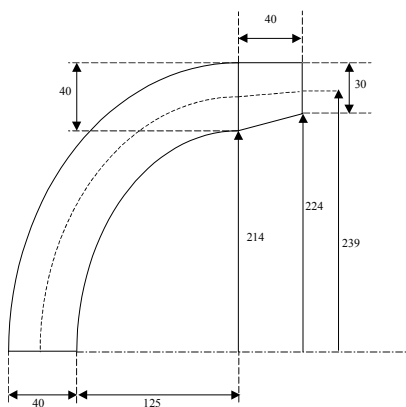
Figure 3: Dimension of the dome

The design load consisted of a uniform external pressure of 30.0 MPa on the entire structure. The design load included a safety factor of 1.5 as prescribed by the requirements. The results for the different designs, obtained by the FE-Analysis and the DRAPE analysis were evaluated for producability, material cost and weight. The ellipsoidal shape was finally chosen, being the one that performed better in terms of production and weight. This design was further developed in order to make a product which could be extractable from the two molds. Figure 3 gives the basic dimensions of the dome. In figure 4, shows the transition rings to connect the domes to the filament wound cylinder.

This configuration, quite unusual and requiring a certain degree of precision during machining, was chosen for two main reasons: the V-seal configuration in fact provides protection of the sealing surfaces on the cylinder transition ring by recessing them into a V-section groove and facilitates the fitting of the transition rings because of the V-shape. The presence two O-rings, one per ring surface, allows a good sealing protection.

Figure 4: Titanium transition rings

PRODUCTION OF THE DOMES

Carbon domes will be produced with a vacuum infusion process. To ensure a good geometry definition, two stiff molds are used. However, only vacuum is used to force the resin into the mold. This makes the process more critical for leakages, but simplifies the mold-construction. Double O-rings are used for sealing of the mold. Carbon Injectex fabric is used, since this material has a high permeability and allows for a fast impregnation of the reinforcement. The material is also very drapeable to allow for preforming without wrinkles.

Figure5. The two mold halves

Size and shape of the blanks has been determined with the program DRAPE [3]. DRAPE is also used to calculate the thickness increase due to shearing. With this information, it can be determined which layers have to be cut to a smaller diameter to achieve the correct product thickness.

Figure 6: Finished product

When all the layers are placed in the mold, the mold is closed, sealed and the resin inlet and outlet hoses are applied.

The Epikote 860 epoxy resin system requires infusion at $60^{\circ}C$; therefore the complete mold system is heated. The resin components are also heated to infusion temperature and mixed. After mixing, the resin is degassed at a pressure level below infusion pressure. This is done to avoid outgassing of dissolved components in the resin during the infusion. The degassing method used is described in more detail in reference 4. When the mold is completely filled, the resin inlet is kept open to allow continuous resin feeding to compensate resin shrinkage. The prescribed cure cycle is started. After curing, the parts can be removed from the mold. Then the transition rings are bonded onto the domes and a protective coating is applied. The finished domes are shown in figure 6.

TESTING

Six domes were manufactured and they where all tested. Two sets were tested back-to back without a central cylinder. The first set was tested in a long-term test, deployed at 2000 meters depth, to verify its long-term behavior. The second set was destructively tested to verify the predicted strength. Prior to the test, a scan of the structure was made to verify the quality of the product. Strain gauges where placed in the domes to verify the strength of the material both inside and outside the structure, in order to be able to capture also eventual bending. The test was carried out at IFREMER, in the 1000 bar ACB tank. The domes showed a perfectly linear behavior up to failure, which happened at an external pressure of 542 bar. The theoretical results showed good accordance with the tests. The last test was the full-scale test of the demonstrator. In this test the domes were positioned at the ends of a carbon fiber cylinder produced by filament winding. Also in this second test both domes and cylinder where fully instrumented to verify the strength at failure and the buckling pressure of the cylinder. Failure occurred in this case at 398 bar, due to buckling of the cylinder. The domes remained intact up to failure of the cylinder. The numerical predictions were also in good accordance with the test results, demonstrating the possibility of designing thick walled composite structures by means of finite element analysis.

CONCLUSIONS

The present paper has shown feasibility of carbon fiber reinforced epoxy domes for deep-water application. The major difficulty was the ability to design a product which was not only fulfilling the structural requirement, but that could also be manufactured with the vacuum infusion technique.

ACKNOWLEDGEMENT

REFERENCES
[1]   http://www.soc.soton.ac.uk/autosub/
[2]   Biezeno C.B. Grammel R., *Technische Dynamik,* 2. Auflage, Springer-Verlag, Berlin/Göttingen/Heidelberg (1953).
[3]   Bergsma O.K., *Three Dimensional Simulation of Fabric Draping,* Delft University press, 1996
[4]   Labordus, M. Hoebergen, A. Söderlund, J. Åström, T. *Avoiding voids by creating bubbles, Degassing of resin for the vacuum injection process*. Proceedings of the 21st International SAMPE Europe Conference. Paris, La Defence, April 18th – 20th, 2000

PROCESS CONTROL

Theoretical and Experimental Evaluation of a Segmented Injection Line for Improved Resin Flow Control in VARTM

Ajit R Nalla [1], James Glancey [2], Benoit Lelievre [3]

[1] *Department of Mechanical Engineering, University of Delaware*
Email:Nalla@me.udel.edu
[2] *Department of Mechanical Engineering, University of Delaware, Newark, Delaware-19716*
Email:jglancey@me.udel.edu (corresponding author)
[3] *IUP de Lorient, Université de Bretagne Sud, Lorient, France*

SUMMARY: During the infusion of resin into a closed mold that contains a preform in the VARTM process, resin flow is often affected by the inherent variations in permeability resulting from the part design as well as the variability associated with the mold lay-up. Current injection methods used for VARTM provide very limited control of the resin flow within the mold; this can result in part defects including dry (unfilled) regions and voids. Improved control of resin flow appears possible with several approaches including the development a multi-segment resin injection line that provides real time modifications to the flow front. The objective of this paper is to study the performance of a segmented, controllable (smart) resin injection line that can be used for real time control of the resin flow to different parts of the mold thus reducing part defects. Simulations of different smart injection line configurations for various mold geometries using several FEA models are studied, and the effectiveness of the smart line injection is analyzed under different scenarios including variable mold permeabilities as well as more complex geometric features in the mold. Simulation results indicate there is a significant decrease in the void area with some part designs using the segmented injection line. Optimal flow control is achieved by changing the lengths of the injection line segments and using suitable control strategy; both of which are mold and part dependent. The effectiveness of this methodology is verified with experiments that use feedback from resin sensors and actively control the resin flow in the mold.

KEYWORDS: VARTM, injection, simulation, flow control, dry spots, voids.

INTRODUCTION

VARTM (Vacuum Assisted Resin Transfer Molding) is a liquid composites manufacturing process that offers numerous advantages over other processes because of the low tooling costs and the manufacturing benefits for large structures. In VARTM, a stack of dry fiber reinforcements known as a preform is placed over a tooling surface and is enveloped and sealed with a flexible plastic bag and tacky tape. Drawing vacuum through a vent line compacts the preform and conforms it to the tool surface and the resin is drawn into this assembly through the injection line by connecting the resin reservoir to the tooling. The pressure difference of one atmosphere between the resin reservoir and the vacuum vent port drives the resin into the assembly to impregnate the empty spaces between the fibers.

After the resin reaches the vent port, a reasonable amount of time is allowed for the resin to bleed out of the vent before terminating the injection from the resin reservoir. This not only saturates the spaces between the fiber tows, but also insures the fiber tows also become fully wetted with resin. The vacuum may be maintained for an additional time after injection is completed to allow resin to equilibrate and to maintain the compaction pressure and deformation.

The preform permeability (k), fluid viscosity (μ), fiber volume fraction (V_f) and the compaction pressure are the parameters that fundamentally influence the permeation of the resin through the preform. The preform permeability, a function of the preform microstructure, often exhibits large variabilities there by creating local areas of either high or low permeabilities. Due to these variations, the actual resin flow pattern often deviates from the desired flow pattern thereby creating areas into which the resin doesn't permeate; these regions of unfilled preform are termed dry spots and voids. The formation of dry spots and voids result in the manufacture of defect parts which is a major disadvantage of the VARTM process. Hence, there is a genuine need for better flow control approaches in VARTM to compensate for permeability variations, and therefore reduce or eliminate the dry spots and voids.

Current methods used for VARTM that utilize distribution lines for resin injection and point or line sources of vacuum provide very limited controllability of the resin flow within the mold. As a result, dry spots and voids continue to limit the complexity of the mold designs as well as production efficiency. Previous research attempted to control flow using feedback of resin position [5], flow rate control [2], intelligent process control [1], localized induction heating [4] and differential vacuum [6]. Despite the availability of advanced, adaptive control methodologies, very little practical value can be derived from these techniques for VARTM until improved methods for actuation of the flow within a mold are developed. Alternative control methods that show promise for better flow control in VARTM include controlling the resin flow from different segments or regions of an injection line, and changing the local permeability of either the distribution media or the preform. This paper focuses on the improved control of the resin flow in VARTM using a segmented injection line.

OBJECTIVE

The primary objective of this paper is to investigate the potential improvements in control of resin flow using a segmented injection line. In this effort, our goal was to study the effect of the segmented injection line, which we call as a "Smart Line" of injection, in providing real time control of resin flow. Specific performance metrics, including resin flow front controllability and void formation are used in this paper to compare this approach to conventional VARTM injection methods.

MATERIALS AND METHODS

The development of a smart segmented injection line was achieved by creating controllable segments of the line which can be turned on or off to control the flow of resin. Details of the design of a multi-segment, "Smart Line" are presented in Ref [10].

The smart line configuration is based on simulations used to understand the relationship between the segment length and the resulting controllable region within the mold. The independent design parameters in this approach as shown in Figure 1 are the number of segments within the injection line (1, 2, 3, . . .), length of the individual segments (L1, L2, L3, . . .), control action distance (CD), length of the mold (L), width of the mold (W), local and bulk permeabilities of the preform. The corresponding dependent parameters would be the flow front pattern, void area and fill time. The individual segments of the injection line can be turned on or off depending on the situation. Control action distance (CD) would be the distance from the injection line at which a segment is opened or closed.
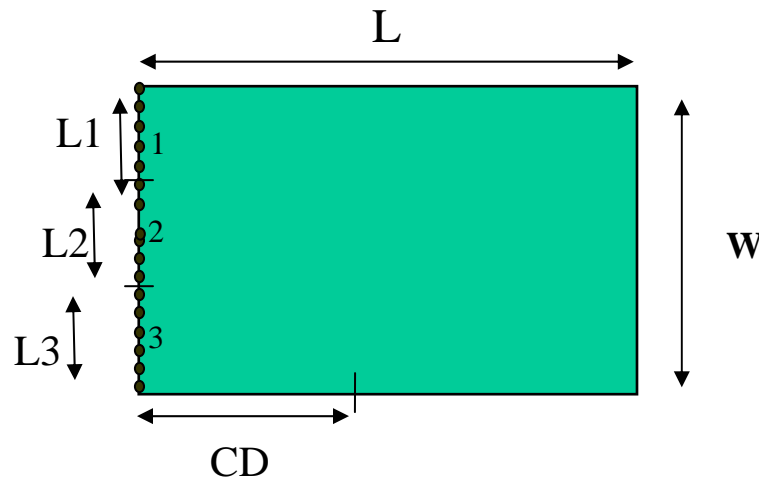
Figure 1: A simple rectangular preform that includes a segmented injection line.

To study the effects of the segmented injection line in steering the resin to all parts of the mold and to achieve the desired flow front pattern, we considered various preform patterns including molds with: different permeability regions, inserts, and race tracking channels. Once a heterogeneous preform pattern was selected, the flow pattern of the resin through this mold using the conventional VARTM method and a single injection line was first studied. An open loop (uncontrolled) flow pattern was observed as the resin progressed more quickly through the regions of higher permeabilities leaving the regions of low permeabilities dry. This resulted in the formation of the dry spots and voids. Next, for the same preform pattern, the various resin flow patterns were computed using LIMS (Liquid injection simulation software developed at the Center for Composites Materials, University of Delaware) [7, 8, 9]. The segmented injection line configuration was examined with different numbers of segments and varying lengths of the individual segments as well as different control action distances. From this, the relationship between the various line segment configurations and the controllable mold regions was determined.

By the analysis of all this data obtained using LIMS, the best suited control strategy for the selected preform pattern that prevented void formation was determined in terms of the number of segments of the injection line required (1, 2, 3 or more), lengths of the various segments (L1, L2, L3 and so on…) and the control action to be taken at different control action distances (CD). Experiments were conducted using the control strategy data obtained from this analysis, and the results are presented in the next section.

RESULTS AND DISCUSSIONS

Experiments were performed to validate the simulation results for various preform patterns. Conventional VARTM set up using a single line injection and modified set up using a segmented injection line were used for experiments, and is illustrated in Fig 2. The ability of segmented injection line to steer the resin in a desired pattern through a heterogeneous preform pattern is analyzed in this section. The preform pattern of 80 cm x 60 cm size with a high permeability region of size 30 cm x 20 cm was selected for analysis [Fig3]. The resin flow patterns for the selected preform pattern using the conventional VARTM set up with
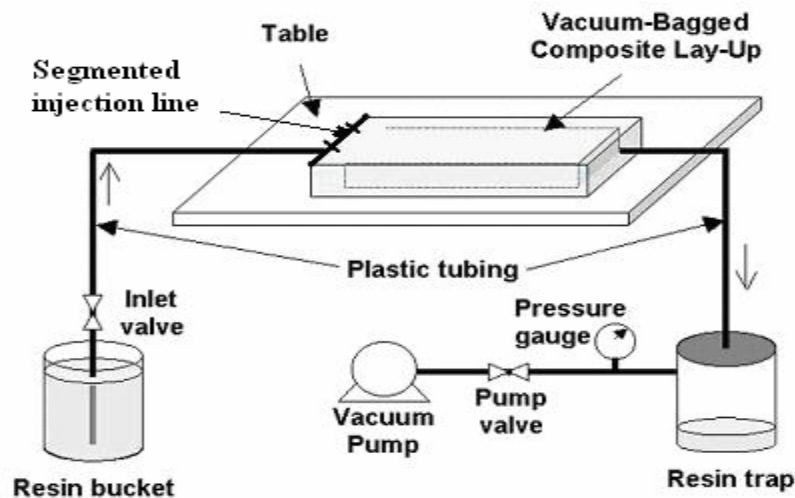
Figure 2: Experimental VARTM setup.

a single injection line were studied by running simulations with LIMS software, and then validated experimentally. Table 1 contains the details of the mold as well as the segmented line configuration used in both the simulations and experiments. As illustrated in Figures 4 and 5, it was observed that for conventional the VARTM method using a single injection line, the resin raced through the high permeability region thereby leaving the flow lagging in the other part of the mold which had lower permeability. This resulted in the formation of the dry spot on the top corner of the mold as seen in the Fig 5. The simulated and experimental results obtained for the conventional VARTM set up using single line injection are plotted at various filling stages in the mold and presented in the Fig 4, 5. Comparison of this data confirms that the simulated and experimental results were very similar.

A subsequent experiment was conducted using the modified set up with a prototype segmented injection line.

The number of segments and the control strategy required to steer the resin uniformly through the mold was determined by running a number of simulations for various injection line configurations using LIMS; the corresponding best configuration for the injection line is presented in Table 1. At the start of the injection both the segments of the injection line were kept open. Once the flow reached the higher permeability region, the second segment of the injection line was closed and the resin was allowed to impregnate only through the first injection line segment. This control action was taken at a distance of 20 cm from the point of injection along the length of the mold.

This decreased the resin flow velocity through the high permeable region and the desired resin flow pattern steering the resin uniformly to all parts of the preform pattern was achieved. This eliminated the dry spot that had formed in the conventional VARTM tests. The simulated and experimental results obtained for the modified VARTM set up using the segmented injection line are plotted at various filling stages in the mold and are presented in the Fig 6 and 7. The simulation and experimental results were found to be virtually identical. The effectiveness of the segmented injection line is validated by achieving the controlled resin flow pattern through the heterogeneous preform pattern selected. Additionally, the effectiveness of this methodology was studied by extending experimental and simulation analysis to preform patterns with induced race tracking, inserts and other homogeneous and heterogeneous patterns. Results again confirmed that improved preform filling could be achieved with the segmented injection line when compared to conventional VARTM injections methods.

Table 1: Control action strategy and segmented line configuration with reference to Fig 1

Parameter	Value	Units
L	80	cm
W	20	cm
L1	20	cm
L2	40	cm
L3	0	cm
CD	20	cm
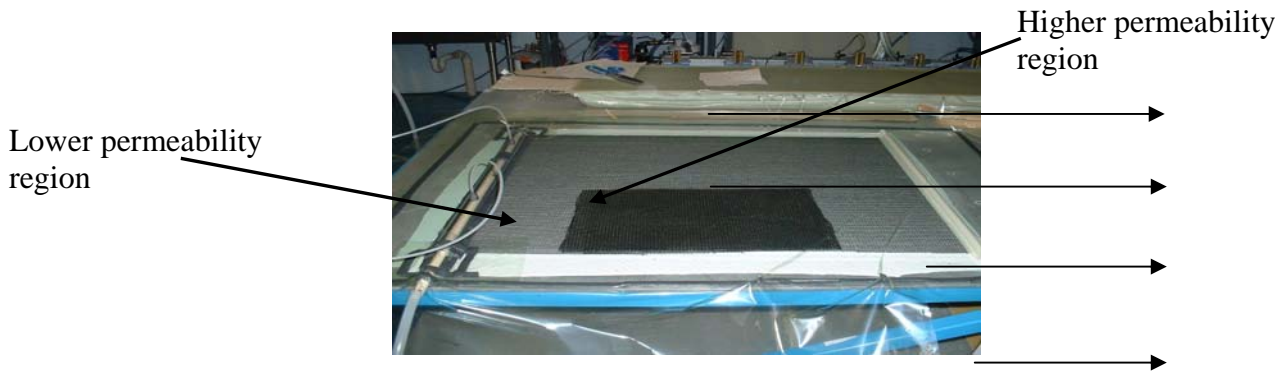
Figure 3: Preform pattern and modified set up using segmented injection line

Dry spot
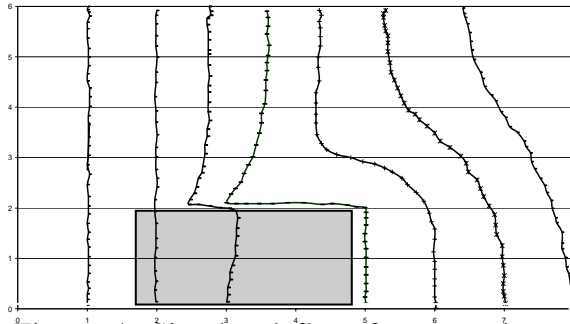
Figure 4: Simulated flow front vs. time for VARTM using single line injection
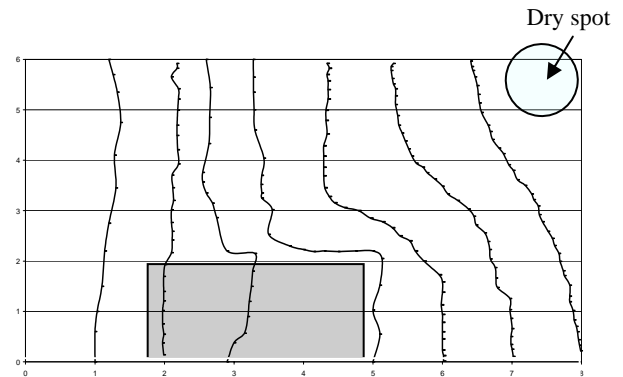
Figure 5: Experimental flow front vs. time for VARTM using single line injection
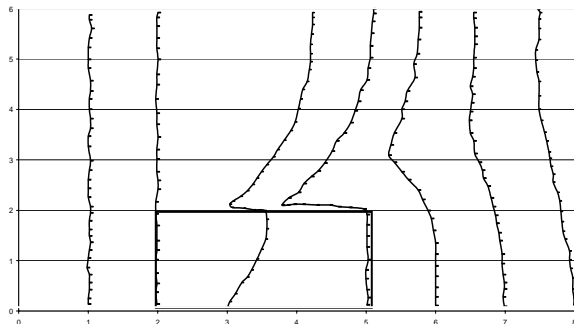
Figure 6: Simulated flow front vs. time for VARTM using segmented injection line
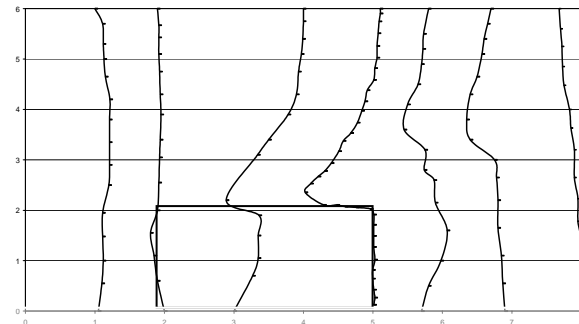
Figure 7: Experimental flow front vs. time for VARTM using segmented injection line

CONCLUSIONS

The capability of controlling the resin flow in VARTM using a novel segmented injection line was demonstrated through both simulations and experiments. This technique has proven to be a very important strategy in achieving better flow control, especially where variations in permeability and complex mold shapes are present. Results indicate there is a significant decrease in the void area with the segmented injection line. Optimal flow control is achieved by changing the lengths of the injection line segments and using suitable control action; both of which are mold dependent.

ACKNOWLEDGEMENTS

REFERENCES

1. Intelligent process control for affordable VARTM processing of DoD structures Heider, D. (Center for Composite Materials, University of Delaware); Gillespie Jr., J.W.; Pike, T.L.; Thomas, G.E.; Steele, T.; Florence, J. Source: International SAMPE Symposium and Exhibition (Proceedings), v 48 I, 2003, p 657-669.
2. Flow rate control during Vacuum-Assisted Resin Transfer Molding (VARTM) processing Heider, D. (Center for Composite Materials, University of Delaware); Epple, S.; Gillespie J.W., Jr. Source: International SAMPE Symposium and Exhibition (Proceedings), v 46 I, 2001, p 1061-1071.
3. Feedback control of the vacuum assisted resin transfer molding (VARTM) process Heider, D. (Univ of Delaware); Graf, A.; Fink, B.K.; Gillespie, J.W. Jr. Source: Proceedings of SPIE - The International Society for Optical Engineering, v 3589, 1999, p 133-141.
4. Enhancement of flow in VARTM using localized induction heating Johnson, R.J. (Composites Processing Laboratory, Department of Mechanical Engineering, University of Connecticut); Pitchumani, R. Source: Composites Science and Technology, v 63, n 15, November, 2003, p 2201-2215.
5. Sensor-based control of flow fronts in vacuum-assisted RTM Walsh, S.M. (U.S. Army Research Laboratory); Mohan, R.V. Source: Plastics Engineering, v 55, n 10, October, 1999, p 29-32.
6. Role of vacuum pressure and port locations on flow front control for liquid composite molding processes Hsiao, K.-T. (Center for Composite Materials, University of Delaware); Gillespie J.W., Jr.; Advani, S.G.; Fink, B.K. Source: Polymer Composites, v 22, n 5, October, 2001, p 660-667.
7. P.Simacek, E.M.Sozer, and S.G.Advani, User manual for DRAPE 1.1 and LIMS 4.0 Tech. report, CCM, University of Delaware (1998).
8. M.Bruschke and S.G.Advani, Polymer composites, 11, 398 (1990).
9. P.Simacek, E.M.Sozer, and S.G.Advani, SPE Annual Technical Conference –ANTEC, Conference Proceedings, 44, 2327 91998).
10. Ajit R Nalla, Benoit Lelievre, James Glancey. Design and Performance of a New VARTM Resin Injection Line. FPCM-7 (2004) The 7th International Conference on Flow Processes in Composite Materials, Newark, Delaware, USA, 7 ~ 9 July. 2004.

Optical Fiber Sensor for Monitoring Flow and Resin Curing in Composites Manufacturing

C.Lekakou[1], S.Cook[1], Y Deng[1], T.W.Ang[2] and G.T.Reed[2]

[1] School of Engineering, University of Surrey, Guildford, Surrey GU2 7XH, UK
[2] School of Electronics, Computing and Mathematics,
University of Surrey, Guildford, Surrey GU2 7XH, UK
And Corresponding Author's e-mail: C.Lekakou@surrey.ac.uk

SUMMARY: An optical fiber has been used as an intensity-based sensor for the monitoring of the fluid front infiltrating a reinforcing fiber mat in composites manufacturing. The sensor length comprised the fiber core, initially surrounded by air or vacuum and subsequently covered by the infiltrating fluid. Two configurations were tested where a step-change or a continual output signal was obtained, respectively. In the latter case, the sensor used in this study demonstrates an improvement of up to two orders of magnitude over conventional monitoring techniques used for this application. This performance is coupled with more obvious advantages of low cost, compatibility with composite fabrication, and ease of use. The sensor was also used to monitor the curing of resin, where the power output was falling as the surrounding resin was curing. The sensor was successful at determining the gel point which was in agreement with rheological data.

KEYWORDS: Optical fiber, sensor, flow, curing, composites.

INTRODUCTION

Infiltration of fiber mats by polymeric liquids in composites manufacturing is generally described by Darcy's law as flow through a porous medium. In one or two-dimensional in-plane flows, flow monitoring is required in the measurement of the in-plane permeability of fiber mats and for purposes of process monitoring and control during manufacturing. Flow/curing sensors positioned at the mold surface include pressure transducers, thermistors and dielectric sensors and may be used in the case of non-transparent molds when the flow cannot be monitored visually. In cases of inhomogeneous permeability and thick laminates, flow sensors are needed between fiber layers to monitor flow variations across the thickness of the fiber mat and flow racing effects where the fluid may race along certain macro-channels between certain fiber layers. SMARTweave [1] is an example of such a sensor comprising a grid of carbon filaments on two non-intersecting planes; it functions on the basis of change in electric conductivity as the infiltrating liquid fills the gap between two crossing carbon filaments. However, its applicability is sometimes limited if it is used within carbon fiber mats due to similarities in electric conductivity between the carbon filament sensor grid and the carbon fiber mat.

Hence, this study focuses on the idea to develop an optical fiber-based sensor system. Optical fibers have been used successfully as cure sensors [2,3] in polymers by relying on changes in the refractive index of the polymer resin as it cures. Fluorescence-based optical fiber sensors have been further investigated for flow monitoring of a polymer resin containing a fluorescent dye [4], where the fluorescence intensity measured by the sensor increased linearly with the sensor length covered by the advancing resin.

PRINCIPLE OF OPERATION

The suggested principle of operation is based on the propagation of light along an optical fiber by total internal reflection if the angle of incidence of a light beam is greater than a critical angle, θ_c, determined from Snell's law

$$\theta_c = \sin^{-1}\left(\frac{n_2}{n_1}\right) \tag{1}$$

where n_1 and n_2 are the refractive indices of the fiber core and its surrounding medium, respectively. Commercial optical fibers consist of a central core surrounded by a layer of cladding of refractive index n_2, where $n_1 > n_2$. An outer plastic coating provides mechanical protection. The losses in the light transmission through such a fiber are proportional to the fourth power of the frequency of the transmitted light, hence the use of low frequency light is preferred: in this study, red light was used as the lowest frequency region of the visible light. Snell's law results in a cone of acceptance of the transmitted light by the optical fiber the angle of which is defined by the numerical aperture, NA, calculated by the relation:

$$NA = \sqrt{n_1^2 - n_2^2} \tag{2}$$

Hence, the greater is NA the lower are the light losses. The number of propagating modes, M, supported by the optical fiber is then given by the equation

$$M = 2\pi^2 \alpha^2 (NA)^2 / \lambda^2 \tag{3}$$

where α is the radius of the fiber core and λ is the wavelength of light. In this project, the length of the optical fiber prepared to act as a flow sensor consisted only of the core, so that the surrounding medium, air, vacuum or process fluid, would act as cladding.

The core of the sensing length of the optical fiber will be initially surrounded by vacuum or air of a refractive index $n_2 = 1$. It will be subsequently covered by the propagating process fluid which will be generally of higher refractive index than air, namely: $n_{2,\,epoxy}$ in the range of 1.44(uncured) to 1.58(cured); $n_{2,\,polyester}$ in the range of 1.53(uncured) to 1.57(cured); $n_{2,\,silicone\;oil}$ = 1.402(often used in permeability measurements). These may be compared with the refractive index of materials used as cladding in commercial optical fibers, for example acrylic where n_2 = 1.37 to 1.49.

Prospective core materials for the optical fiber include silica with $n_1 = 1.45$ to 1.46, lead oxide doped glass with $n_1 = 1.62$, poly(methyl methacrylate) with $n_1 = 1.49$, cured epoxy with $n_1 = 1.57$ and polystyrene with $n_1 = 1.6$. The loss of the optical fiber will vary as the core is increasingly covered by the liquid due to the fact that increasingly fewer modes of light will be able to propagate. The loss will increase with increasing coverage, but will also be a function of both the refractive index and loss coefficient of the liquid. Hence, a particular propagating process fluid has to be matched with the appropriate optical fiber core material.

EXPERIMENTS AND RESULTS

A specially manufactured optical fiber was supplied by Fibercore Ltd consisting of silica core of 125 μm diameter and an acrylic coating of 250 μm external diameter. A laser source of 650 nm wavelength and less than 1 mW power was coupled into one end of the fiber, whilst the output end was connected to a "Fotec" optic power meter to measure the power of the light output. An output of 130 μW was measured in this manner using the optical fiber without any liquid present.

Alternatively, a mid-zone of the optical fiber was stripped of its acrylic coating (air-clad sensor length) and the optical fiber was embedded between glass fiber, reinforcing fabric layers to monitor the flow progress of an uncured epoxy resin in resin infusion under flexible tool (RIFT) (see Fig. 1).
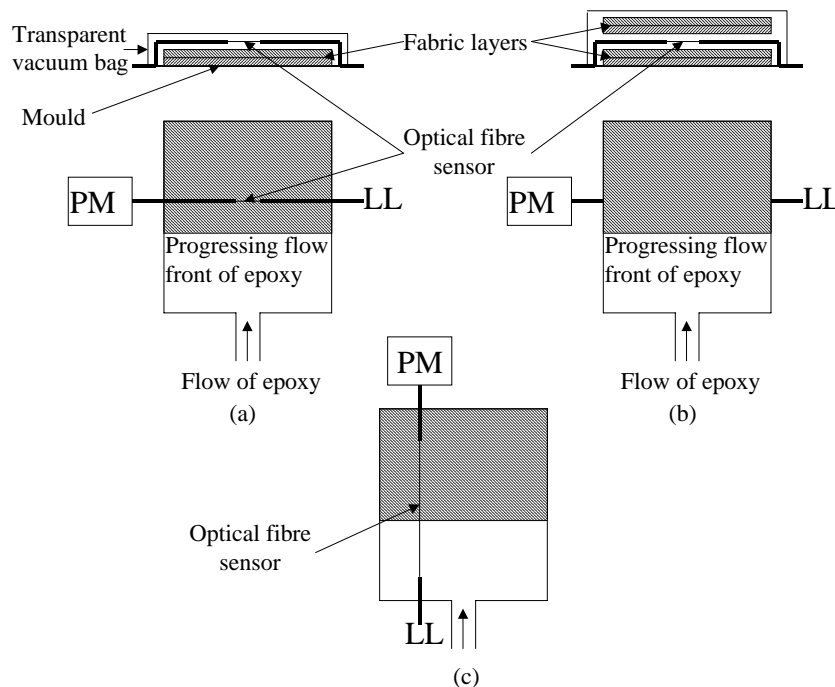
Fig.1. Monitoring the flow front in RIFT where the optical fiber sensor is placed normal (a) and (b) or parallel (c) to the flow direction. LL: laser light; PM: power meter.

In the experiment in Fig.1(a), as soon as the epoxy fluid reached the sensing length the output detected by the power meter fell to about 20% of the value measured when the sensing length was air-clad. Given that the fluid progress at the top fabric layer was monitored visually and with a camera, it was concluded that the step-change in the power meter signal gave an excellent indication of the time at which the flow front covered the fiber. In the experiment in Fig.1(b) where the optical fiber was placed between fabric layers, the signal of step-change in the output measured by the optical power meter was received before the flow was observed to reach the same marked position in the top layer. This clearly indicates flow racing in the middle-layer region which, in turn, demonstrates the effectiveness of this simple sensor in this aspect of composites manufacturing.

In the experiment in Fig.1(c), a 100 mm air-clad sensor zone was prepared and the optical fiber was placed parallel to the flow direction on the top glass fabric layer. The sensor was then covered gradually by the flowing epoxy while the light output was measured by the power meter and the length of fiber sensor covered by epoxy was monitored using a camera. Fig.2 presents the results in which the detected power output falls as the epoxy propagates along the sensor. The reason for this is that the refractive index of the uncured epoxy, n_2, is very close to n_1 of the silica core leading to more weakly confined modes. As the length of the fiber sensor is surrounded partly by air and partly by epoxy, there is a correlation between the optical loss and the extent of coverage by epoxy, as expected. Fig.2 has been constructed by normalising the power output $P_{ep,x}$, obtained when a length x of the sensor is covered by epoxy, to the power output $P_{ep,0}$, obtained when the whole length of the sensor zone was air-clad. The obtained experimental data has been fitted to the exponential loss equation

$$\frac{P_{ep,x}}{P_{ep,0}} = e^{-\alpha x} \qquad (4)$$

This results in a loss coefficient $\alpha=0.766$ cm^{-1}, or expressed in dBs, a loss of 3.3 dB/cm. Taking a typical sensitivity of an optical power meter to be of the order of 1 μW, and the resolution to be 1 μW, then for a typical $P_{ep,0}$ of 130 μW in this study we are able to resolve optical fiber coverage by liquid of up to 6.4 cm, with a resolution of 490 μm. Obviously increasing the optical power will increase the total length that can be measured, and better resolution can be obtained by using an optical power meter with improved resolution. For example, if we increase $P_{ep,0}$ to 1 mW, the fiber coverage increases to 9.1 cm, with a resolution of 65 μm.
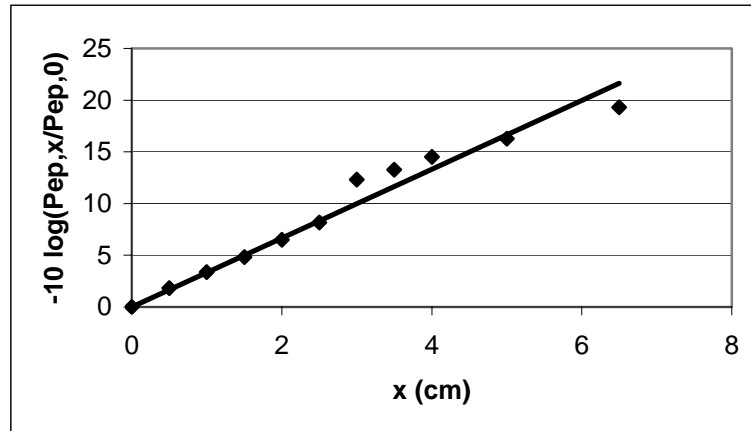
Fig.2. Continual output power signal obtained when a 100 mm flow-sensor zone was placed in the flow direction: experimental data and logarithmic fit according to equation (4).

The last experiment involved the monitoring of curing of the Araldite epoxy system using an optical fiber with a core of $n_1=1.65$, made by Oxford Electronics Ltd. The result is presented in Fig.3(a) in which the power output decreased as the refractive index of epoxy increased during curing. The output stabilised at about 400 min which agrees with the gel point observed in the viscosity rise in a corresponding rheology experiment in Rheometrics, Fig.3(b)

(a)

(b)
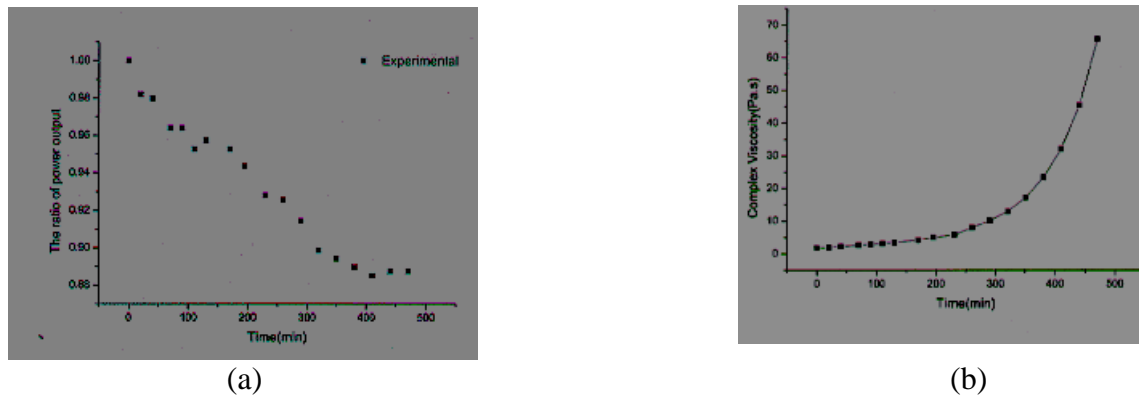
Fig.3. Curing of epoxy: (a) normalised power output from the optical fiber sensor; (b) viscosity data from Rheometrics.

CONCLUSIONS

We have demonstrated that a simple, intensity-based optical fiber sensor can be used for the monitoring of flow and curing in composites manufacturing, placed either at the surface of the molding or between fiber layers. The sensor has good resolution and accuracy and is particularly suited to detect flow racing effects or dry spots in critical regions.

REFERENCES

1. U.K.Vaidya, N.C.Jadhav, M.V.Hosur, J.W.Gillespie and B.K.Fink, *Smart Materials & Structures*, Vol.9, no.6, 2000, 727.

2. M.A.Afromowitz, *J. of Lightwave Technology*, Vol.6, no.10, 1988, 1591.

3. P.A.Crosby and G.F.Fernando "The application of optical fiber sensors in advanced reinforced composites: Chapter 3 - Cure monitoring", Optical Fiber Sensor Technology, Vol.III, eds. K.T.V.Grattan and B.T.Meggitt, Publ. Kluwer Acad.Publ., 1999.

4. S.R.M.Kueh, S.G.Advani and R.S.Parnas, *Proceedings ICCM-12*, Paris, 1999.

On-Line / Off-Line Control of Mold Filling in Liquid Composite Molding

Jeffrey M. Lawrence, and Suresh G. Advani,
Center for Composite Materials and Department of Mechanical Engineering
University of Delaware, Newark, DE 19716

SUMMARY: Prohibitive costs are preventing Liquid Composite Molding processes from gaining greater popularity. The high costs are due to lack of automation and repeatability. Variations inherent in the preform cutting and placement process lead to unpredictable resin infusion patterns which form regions devoid of resin. This compromises the structural integrity of the composite and the part scraped. Control during the filling stage of Liquid Composite Molding processes have been shown to redirect the flow providing a greater percentage of acceptable manufactured composite parts. However, many of the current techniques have various limitations. Many off-line control approaches depend on anticipation of problems, and on-line approaches are geometrically limited and can be computationally intensive if executed during manufacturing. The present work combines off-line and on-line approaches to fill the mold containing fabrics in an attempt to eliminate their shortcomings and reduce the limitations. First, off-line computationally intensive control algorithms based on the specific part geometry and locations for the sensors and injection gates are created. Next, on-line control is initiated with the off-line parameter guidelines. The approach will be presented and illustrated with several case studies to demonstrate geometrical independence in a simulation environment.

KEY WORDS: Resin Transfer Molding, Numerical Simulation, Active Control

INTRODUCTION

In Liquid Composite Molding (LCM) processes, a dry preform stack is placed into a mold. The mold is sealed, and a liquid thermoset resin is injected into the mold. The resin flows through the preform, displacing the air in the gaps between the fibers pushing it out through the vents. Once the filling is complete, the resin is allowed to harden, and the final composite part is removed from the mold. Due to the nature of the fiber preform material and the process of cutting and placement in the mold, the flow behavior is complex and may result in dry spots (regions devoid of resin). These mechanically weak regions of the part require the entire part to be discarded. Current research efforts have focused on utilizing fluid flow techniques to ensure that the fluid will entirely displace all of the air in the mold and fully saturate the preform. Slight deviation in preform placement in the mold can cause fiber free channels between the preform edges and the mold walls. The resin can race through these channels as the resistance to flow is much less than within the preform and reach the vent before the complete preform is impregnated. Active flow control will compensate for material and fiber preform cutting and placement variability and help to reduce wastage and increase the yield.

FUNDAMENTALS OF DEPENDENCE MAP CONTROL

The first concept to establish is that of the actual flow front and the target flow front at a given instant. The objective of the controller is to minimize the difference between the actual and target flow fronts. As control is lost (or not taken) the two will diverge. The schematic seen in Figure 1 explains this difference.
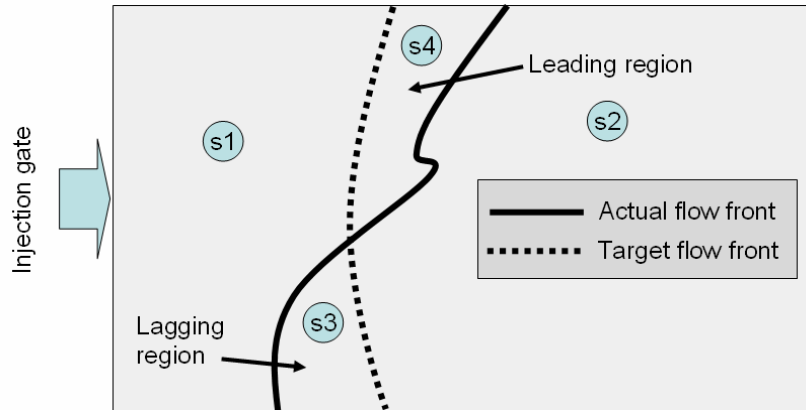
Figure 1: Schematic of disturbance in mold filling depicting the actual and target flow fronts, as well as the concepts of the leading and lagging region

At the instant pictured in Figure 1, a disturbance (unknown) has caused the fluid to flow faster in some regions of the mold, and to flow slower in other regions. The areas where the actual fluid is flowing faster then the target flow pattern will be called the leading regions and those where the actual fluid is flowing slower than the target pattern will be called the lagging regions. In LCM, the only way to correct for a lagging region is by opening an injection gate near that lagging region. The only way to correct for a leading region is to close any open gates near the leading region. The vents in this case have no influence on the fluid flow. Since the only control available for each gate is to either be open (allowing fluid to inject) or closed (preventing fluid from injecting), the controller has to determine which of the gates to open and which to close. Gates near a particular flow region will influence the flow in that region [1]. Therefore, qualitatively, gates near leading regions should be closed in order to slow the flow and gates near lagging regions should be opened to accelerate the flow. This however is an ambiguous solution, as gates near both lagging and leading regions need a clear command as to what to do. Therefore, a quantitative approach needs to be developed. First, each sensor in the mold will tell the system weather or not the fluid has reached that point. Then, the virtual sensor status is checked from the target flow front. Then, each sensor is classified as lying in a lagging (s3 in Figure 1), leading (s4 in Figure 1), or no-action region (s1 and s2). Figure 2a assigns a sensor state value for each of those conditions.
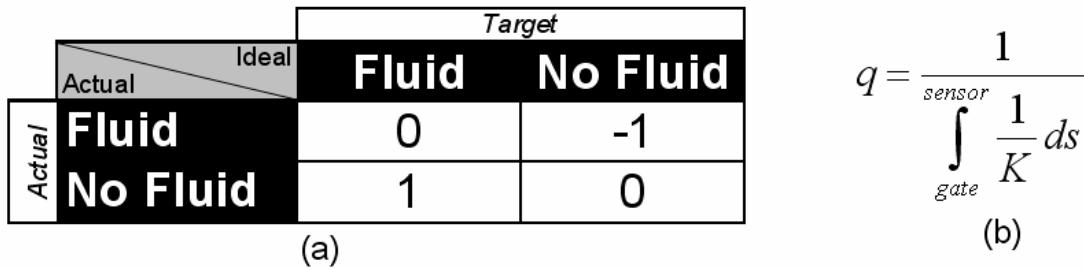
Figure 2: (a)The comparison of the sensor status for the actual and target flow fronts for the sensor state value (0, 1, -1). (b) The flow conductance (q) is the inverse of the integrated permeability (K) of the preform

With the sensor state value, the sensors have a way of communicating to the gates weather the fluid needs to be accelerated (by opening) or retarded (by closing). In order to decide which sensors to respond to, each sensor must be weighted according to its relationship with the gate in question. This will be accomplished through the flow conductance (q), which is qualitatively defined as the effect a particular gate will have on a particular location in the mold, and quantitatively defined by the equation in Figure 2b. The flow conductance is calculated from the gate in question to each sensor in the mold. The path that is used to calculate the flow conductance is optimized by using an A* algorithm [2, 3]. To determine the ultimate state of the gate, the sum-product between the sensor state value and the flow conductance is taken, which results in the action value. If the resultant action value is positive, the gate will open, and if it is negative it will close. In the balanced case that the action value is exactly zero, the gate will remain in its current state (opened or closed). This same process is then repeated for every gate in the mold. When this is done, the flow conductance will be calculated between each gate and each sensor. The matrix of these flow conductance values is called the dependence map. After these calculations, the fluid advances, and the analysis is repeated during each time step of the entire filling process. There are a few auxiliary rules that are amended to the general construct above. The first rule is that gates that are not covered by fluid should not be opened. This prevents multiple flow fronts, weld lines, and other unfavorable flow conditions. The second rule is that once a gate has been opened and closed, it may not be re-used. This is to prevent "dead" gates that will no longer provide controllability to the system from being used. The third, and final rule is that if a situation exists where all of the gates in the mold are set to be closed, the single gate with the lowest action value is to be opened. This is to temporarily allow the filling to continue, until a target gate is found.

VALIDATION

With the control approach fully defined, it is now necessary to validate the approach. In order to have better control over the processing parameters, virtual experiments will be used in the validation. The virtual experiments will be done using computer simulation of the filling stage using the computer simulation software Liquid Composite Molding Simulation (LIMS) [4].

In order to conduct the virtual experiments, a finite element mesh must be prepared, a nominal permeability distribution must be applied to the elements in the mesh, and initial injection gates must be selected to generate the target flow pattern. The mesh with the initial and control gates along with the target flow pattern can be seen in Figure 3.
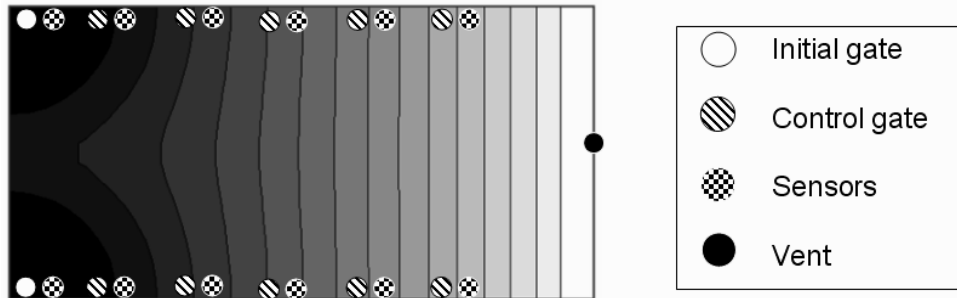
Figure 3: The initial injection gates, target flow front pattern, and control gates and sensors

Now that the target flow pattern is defined, the dependence map containing the flow conductance values between each gate and sensor is generated with the A* algorithm. With these two tasks complete, the off-line portion of the control strategy is complete. To perform the on-line portion of the control, disturbances are added to the system.
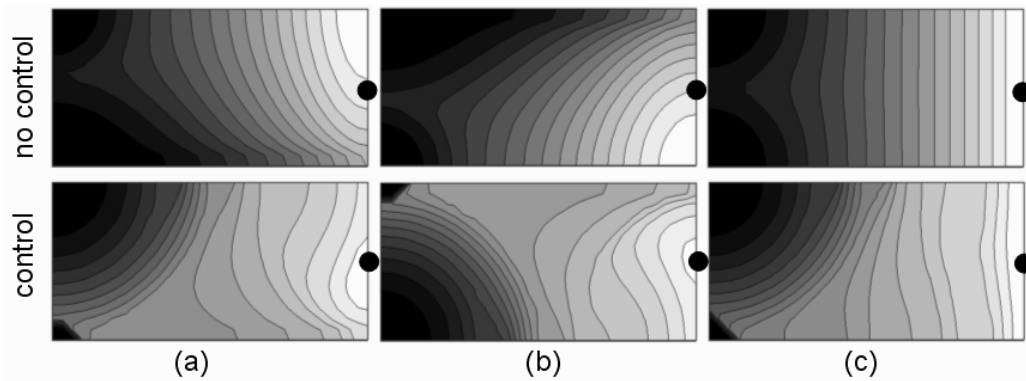
Figure 4: Examples of the controller's effect. The top shows the flow progression with no control applied and the bottom pictures show the same cases with flow control. The vent is indicated by the black circle.

The most common flow disturbance that occurs in the RTM process is race tracking, where fluid flows faster along air gaps created along mold edges [5].Three virtual experiments will be conducted for this validation. Case (a), will contain a race tracking channel along the bottom edge of the mold. Case (b) will perturbed with a race tracking channel along the top edge of the mold. Case (c) will be the nominal case, with no disturbances present. This last case will test the robustness of the system to be sure that flow control is maintained when there are no disturbances. Each case is run with and without control using LIMS.

The resultant flow front patterns can then be examined to see if the controller maintained the flow front progression according to the target pattern. Next, the on-line portion of the control is used, where the action values are calculated, and the results checked against the three auxiliary rules. This control technique does not depend on pre-classifying the disturbances. Therefore, no additional effort or modification to the controller is needed for any case. Figure 4 show the resultant flow progression with no control and then with control for all three cases (a-c). As seen in Figure 4, in each case, the flow patterns were restored to resemble those in the target case. These examples validate the control approach and demonstrate its flexibility to handle any disturbance in the mold.

CONCLUSIONS

A new approach was developed to apply control to the filling stage of LCM processes. The controller was built with the goal in mind that the system would be transferable to an actual composites manufacturing operation and will add versatility to the range of disturbances that the controller could correct. The technique was developed, based on the concept of a dependence map. An example was presented that demonstrated that the system was able to maintain control of the flow progression despite several unpredicted and unplanned disturbances.

ACKNOWLEDGEMENTS

REFERENCES

1.   Gokce, A. and S. G.Advani, *Gate effectiveness in controlling resin advance in liquid composite molding processes.* Journal of Manufacturing Science and Engineering, 2003. 125(3): p. 548-555.

2.   Sharai, Y. and J.-I. Tsujii, *Artificial Intelligence: Concepts, Techniques and Applications.* 1982: John Wiley & Sons.

3.   Al-Hasan, S. and G. Vachtsevanos, *Intelligent Rout Planning for Fast Autonomous Vehicles Operating in a Large Terrain.* Robotics and Autonomous Systems, 2002. 40: p. 1-24.

4.   Simacek, P. and S.G. Advani, *Desirable features in a Mold Filling Simulation for Liquid Molding Process.* Polymer Composites, 2004. in press.

5.   Bickerton, S. and S.G. Advani, *Characterization and Modeling of Race Tracking in Resin Transfer Molding.* Composite Science and Technology, 1999. 59(15): p. 2215-2229.

Variability in Liquid Composite Molding Techniques: Process Analysis and Control

N. C. Correia, F. Robitaille, A.C. Long, C.D. Rudd

School of Mechanical, Materials, Manufacturing Engineering and Management, University of Nottingham, Nottingham NG7 2RD U.K.

Christopher.Rudd@nottingham.ac.uk

SUMMARY:

The present work aims to develop tools to understand and control the manufacturing repeatability in LCM processes such as resin transfer molding (RTM) and vacuum infusion (VI a.k.a VARTM). One major cause of flow repeatability is studied: the natural variation in reinforcement permeability. This is done by implementing a Monte-Carlo solution to the problem of flow through porous media. Reliability improvements are proposed by using this "real-life" virtual flow environment to design the appropriate active control strategies. In addition, the reliability differences between VI, where the flexible tooling induces transient thickness and permeability, and standard RTM, are explored. It is shown that specific models are required to analyse the impact of variability in different LCM techniques and how different control techniques affect the probable outcome of an injection.

KEYWORDS: Liquid Composite Molding, Statistical Methods, Monte-Carlo, Computational Modeling, Control.

INTRODUCTION

Modeling real flow through porous media is statistical in essence. It is commonly accepted that superficial density and compaction properties of textile reinforcements vary. It is also known that permeability exhibits a statistical nature, although these and other sources of injection risk are not normally taken into account [1]. The approach followed is based on the Monte-Carlo technique which, insofar as this work is concerned, can be outlined as a method involving the repeated simulation of the same case with different statistically generated properties. The main outcomes are the probabilities of specific flow occurrences such as final filling points, times and expected deviations from the ideal scenarios. Through these results one can characterize the efficiency of different filling strategies and produce control development tools. It can also be shown that ideal simulations of flow can overlook filling problems and, while sensible strategies can be used to avoid them, some might also result in longer filling times then are necessary.

Variations in permeability of reinforcements are therefore expected to promote differences in fill time, flow front perturbations, and cause incomplete mold filling. The same can be said for fiber angle or surface density of textiles for example. Hence, the fact that these properties are averaged in standard simulations involves a simplification of the physical process, which can be critical for the manufacturing of large series or expensive components. While sensible strategies can be used to prevent problems, they are often associated with operator expertise and can sometimes be overlooked in the design stages. The ability to quantify possible flow errors statistically could therefore be used as a manufacturing-design tool. Furthermore, computer assisted design of control schemes can only be done if one can understand and simulate natural variations in flow. The global objective of this work, which stems from which stems from past publications on this topic [1], is therefore to examine some scenarios where flow modeling, monitoring and control can be used to advantage to address some of the real-world difficulties.

BACKGROUND

Most background literature on statistical variations in flow deals with the problem of race tracking. Simply put, it is not possible to ensure that the cutting of textile reinforcements is perfect nor is their placement in the molds. Flow must therefore be controlled in order to achieve consistent production and prevent filling problems. This field has seen a significant amount of research, from the bulk-permeability work by Hammami *et al* [2] and Bickerton *et al* [3] to the control of of real cases by Mathur *et al* [4] and Hsiao *et al* [5] and experimental characterization work by Devillard *et al* [6].

A number of other factors can also influence LCM flow: experimental work published by Rudd *et al* [7] and Smith *et al* [8] explored, for example, the effect of textile draping on the permeability tensor and the mechanical properties of resulting laminates. As with most results found in the literature, these present a degree of scatter but the statistical nature of flow or mechanical properties is not explored since their work focussed on the fundaments of average behavior. Rudd *et al* [9], Lai *et al* [10] and Long *et al* [11] are examples of modeling approaches for draping, and of the draping effects on permeability: again, not investigating the nature of statistical variations as a possible origin of flow disturbance.

One other significant source of parameter variations is reinforcement permeability, which, as Bickerton *et al* [3] and Hoes *et al* [12] propose is not a constant value but follows a statistical distribution. A typical result is shown in Table 1, which contains the data used in these examples.

Table 1 – Statistical permeability data (Hoes *et al,* [12]).

Type	Matl.	Manuf.	Ref.	No. tests	Orient.	Mean	σ / mean
Plain woven	E-glass	Syncoglas	R 420	86	x	1.23×10^{-11}	14.1
					y	2.62×10^{-11}	21.7
					$ln\,(K_x/K_y)$	0.32 -	$\sigma = 0.08$

This statistical nature of flow properties of textile reinforcements is fundamentally different from the literature models of fiber orientation and fiber volume fraction used in the draping analysis, which are deterministic (a function of idealized textile architecture and mold geometry).

Note that this is not the case in recent race tracking studies where the stochastic nature of channel formation is integrated in the analysis. Given the importance and widespread use of flow simulation software in mold design and optimization, these input parameters are crucial to their accuracy. Consequently, real LCM flow does not follow the idealized scenarios but presents variations due to the statistical nature of the flow properties and geometry of the preform. These references are currently the main source of statistical permeability characterization data.

The effect of statistically distributed flow properties is discussed briefly in the following section through an implementation of the Monte-Carlo method.

IMPLEMENTATION OF NATURAL VARIABILITY IN FLOW MODELING OF LCM

Useful process models should reflect permeability variations by predicting the distribution in possible outcomes from any molding process. To model the effects of permeability and compaction variations on flow, predicted or measured distributions in properties must be incorporated in LCM simulations. In the present work, this is achieved by Monte-Carlo FE simulation which involves solving the same geometric problem a significant number of times insuring, each time, that the model contains different element properties (permeability and compaction). This is achieved by generating properties, by random selection from the relevant inverse probability distribution function (PDF), thereby resulting in them being normally distributed across a significant number of elements replicating experimental measurements and making all resulting models different and non-ideal. This procedure is repeated for all elements within the model: each will have a different permeability tensor and/or compaction properties, but permeabilities over a large number of analyses conform to the experimental normal distribution. Figure 5 shows the Monte-Carlo algorithm used.
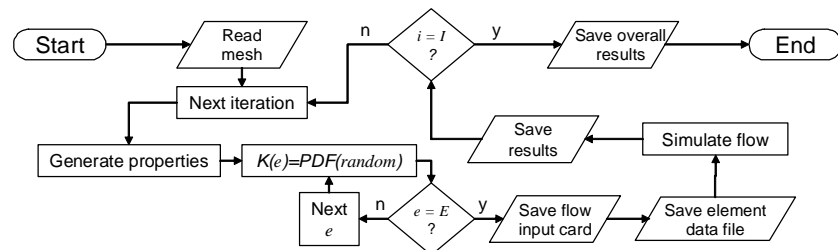
Figure 5 – Monte-Carlo algorithm proposed in this work. *e* and *E* represent the current and total number of elements and *i* and *I* the current and total number of iterations

The input files for these simulations are generated automatically by in-house software. These provide the range of filling patterns that might be expected, and also fill time and last point to fill (guiding gate and vent locations). From this, the likelihood of success for any combination of materials and injection strategy could be determined. Figure 6 illustrates this method by showing the predicted locations for the last point to be filled in a rectangular mold injected from all four corners, obtained from the statistical analysis of 15000 simulations done using LIMS.

Using the same methodology, a 2D LIMS simulation of VI can also be used to study variability for flow through compliant media.

The resulting variable permeability and fiber volume fraction and are shown in Figure 7. As can be observed, these properties are location dependent while simultaneously representing the expected reinforcement variability.
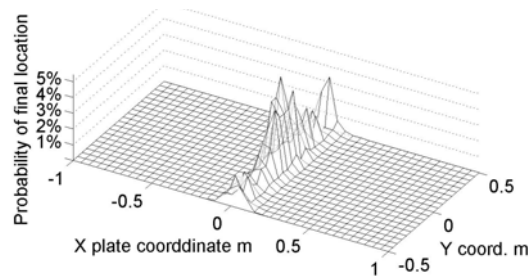
Figure 6 – Probability of final location from 15,000 simulations with Syncoglas RE 420
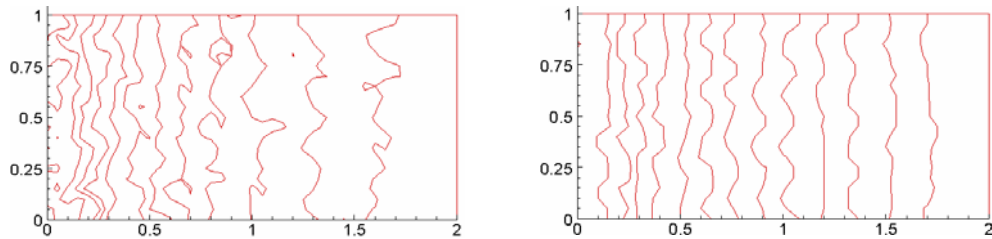
Figure 7 Evolution of permeability. Left) Iso-K lines: 7.75 E-11 m2 to 2.2 E-11m2 in 12 divisions. Right: Iso-vf lines: 40% to 55% in 16 divisions. Flow evolves from left (inlet) to right (outlet).

PROCESS CONTROL

Another application of the Monte-Carlo method is in the computer assisted development of active control systems. The control concept employed in this example uses flow front positions to analyze different control actions: the effectiveness of an action is assessed by computing the difference in saturation between the ideal and the controlled cases. Subsequently, the best control action is activated until the next control step phase is reached. . Figure 8 illustrates the result of a typical five stage virtual on-line control showing the potential benefits of flow front steering through variable inlet pressure at different injection ports.
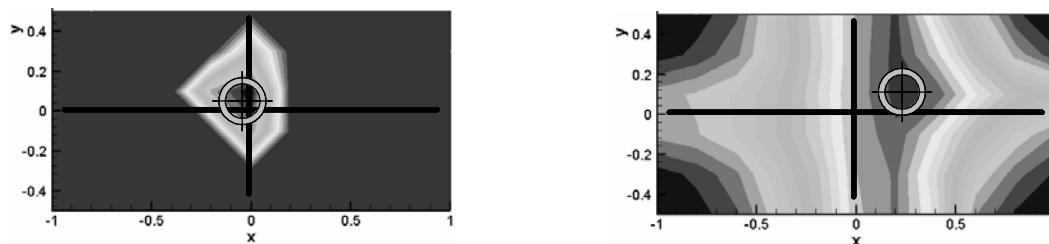
Figure 8 – Controlled injection filling (left) vs isochrones of the non-controlled injection (right)

Note that this is a simple approach to control but that the technique can be expanded, e.g. training neural networks to recognize filling patterns, uniquely quantify the statistical effectiveness of each approach and take the appropriate action.

CONCLUSIONS

This work discusses the developments on flow modeling of LCM processes, which were achieved through the application of the Monte-Carlo method. The method was described and demonstrated for non-compliant porous media case. It was shown that this method can be used to develop complex control approaches as it is able to statistically quantify the effect of different numbers of control steps or injection strategies. The adaptability of this method to different mold geometries and injection strategies also implies that new LCM control and optimisation tools could be industrially deployed. Finally, while the full impact of the statistical distribution of permeability and compaction on LCM techniques continues to require study, the introduction of Monte-Carlo techniques on virtual experimentation / process development could have a vast potential.

ACKNOWLEDGEMENTS

REFERENCES

1.   N. C. Correia, F. Robitaille, A. C. Long And C. D. Rudd, "Analytical And Numerical Studies Into The Vacuum Infusion Process: In-Plane Flow In Compressible Porous Media." *Proc. of International conference on composite materials ICCM 14 San Diego USA July 2003*

2.   Hammami A., Gauvin R. And Trochu F. "Modeling the edge effect in liquid composites molding". *Composites Part A: Applied Science and Manufacturing*, Volume 29, Issues 5-6, Pages 603-609 (1998).

3.   Bickerton, S. And Advani, S.G. "Characterization and Modeling of Race-tracking in Liquid Composite Molding Processes" *Composites Science and Technology*, Volume 59, Issue 15, Pages 2215–2229 (1999).

4.   Mathur, R., Advani, S.G. And Fink, B.K. Use of Genetic Algorithms to Optimize Gate and Vent Locations for the RTM Process. Polymer Composites, Volume 20, Issue 2, Pages 167-178 (1999).

5.   Hsiao, K.-T., Devillard, M. And Advani, S.G. "Streamlined Intelligent RTM Processing: From Design to Automation" *Proc. of 47th International SAMPE Symposium and Exhibition*, Volume 47, Pages 454–465 (2002).

6.   Devillard M.; Hsiao K-T.; Gokce A.; Advani S.G. "On-Line Characterization of Bulk Permeability and Race-Tracking During the Filling Stage in Resin Transfer Molding Process". *J. Comp. Materials*, Volume 37, Issue 17, Pages 1525-1541 (2003).

7.   Rudd, C.D., Long, A.C., McGeehin, P. and Smith, P. "In-plane permeability for simulation of liquid composite molding of complex shapes". *Polymer Composites*, Volume 17, Issue 1, Pages 52-59 (1996).

8.   Smith, P., Rudd, C. D., And Long, A. C. "The effect of shear deformation on the processing and mechanical properties of aligned reinforcements". *Comp. Sci. and Technology* Volume 57, Pages 327-344 (1997).

9.   Rudd, C.D., Long, A.C., Mcgeehin, P., Cucinella, F., And Bulmer, L.J, "Processing and mechanical properties of bi-directional preforms for liquid composite molding". *Comp. Manuf.* Vol. 6, Pages 211-219 (1995).

10.   Lai, C.-L. And Young, W.-B. "The Effects of Preforming Induced Variable Permeabilities on the RTM Molding Flow". *Polymer Composites,* Volume 20, Issue 2, Pages 225-239 (1999).

11.   Long, A.C., Souter, B.J., Robitaille, F. And Rudd, C.D. (2002) Effects of fiber architecture on reinforcement fabric deformation. Plast. Rubber and Comp. **31**(2): 87-97.

12.   Hoes, K., Dinescu, D., Vanheule, M., Sol, H., Parnas, R., Belov, E. And Lomov, S., "Statistical distribution of permeability values of different porous materials". *Proc of the Tenth European Conference on Composite Materials (ECCM10) June 3-7, Brugge, Belgium.* (2002)

Active Flow Control in a VARTM Process Using Localized Induction Heating

Richard J. Johnson and Ranga Pitchumani [1,2]

[1,2]*Composites Processing Laboratory, Department of Mechanical Engineering,*
University of Connecticut, Storrs, CT 06269-3139
Corresponding authors e-mail: pitchu@engr.uconn.edu

SUMMARY: Variabilities in preform permeability can lead to the formation of dry spots and nonuniform flow progression during mold filling in the vacuum assisted resin transfer molding (VARTM) process. Real-time flow control can improve fill uniformity and eliminate potential fill related defects. Flow control schemes commonly manipulate the inlet pressures or flow rates and have been shown in the literature to be limited in their ability to steer the flow in regions far from the inlet ports [1]. A viable solution to this problem is localized heating of the resin during the mold filling process, which can reduce the local viscosity of the flowing resin to compensate for spatial preform permeability variation. In this paper localized heating is achieved using an induction heater with carbon fiber susceptors embedded in the preform layup. This type of control must be applied to the VARTM process in such a way as to heat in the lagging regions while avoiding overheating and thus prematurely curing the resin. To this end, this paper presents a real time control strategy that is demonstrated in a lab scale experimental setup, and is shown to be successful in improving the uniformity of the flow during mold filling of heterogeneous preform layups.

KEYWORDS: Vacuum Assisted Resin Transfer Molding (VARTM), Induction Heating, Active Control, Permeability Variations.

INTRODUCTION

Vacuum assisted resin transfer molding (VARTM) is an attractive and affordable method of producing composite products. In this process, a fibrous reinforcement material, termed preform, is laid into a single hard sided mold and sealed with a vacuum bag. Vacuum is drawn on the system through the exit vents and catalyzed resin is drawn from the inlet ports through the porous preform material. Part defects often arise in this filling stage when the flow follows the path of least resistance entrapping a void in a region of local low permeability or when the last location within the mold to be filled is not adjacent to an exit vent. Thus achieving uniform fill and complete fiber saturation is an essential part of producing quality products. Despite an optimum process design, process and material parameter uncertainties as well as real time and run-to-run variabilities can cause deviations from design targets [2]. Therefore, reliable fabrication must employ real-time process control to realize complete fill despite practical unpredictabilities.

Conventional control schemes seek to vary inlet pressures or flow rates in RTM process, equivalently vacuum levels in the VARTM process, with the goal of steering the flow through a desired fill pattern. It has been shown that this type of control has diminishing capabilities as the flow front moves away form the controlled boundary [1]. Spatially localized control schemes are one way of increasing controllability in heterogeneous preform layups. Here, heat will be used to locally reduce resin viscosity and compensate for flow restriction in low permeability areas. The feasibility of this concept was investigated in a previous study [3, 4], where a numerical model was used to study the effects of induction heating on the flow enhancement. In addition, a simulated optimal control scheme was developed utilizing a numerical process model of non-isothermal mold filling for VARTM [5, 6]. The goal of the present study is to implement the previously developed control scheme on a standard VARTM process and perform experiments to evaluate the effectiveness of the control on a variety of preform layups.

APPROACH

Experimental Setup

A standard VARTM molding process consisting of a square mold with line inlet and outlet located at either end, venturi pump, resin trap and resin source container, was augmented with components for induction heating control, including an Ameritherm NOVA 1.0 induction heater with a pancake style coil, a motion control system, and a computer image capture system. These components were tied together by the software based control implemented in LabVIEW.   More detailed descriptions of this experimental setup can be found elsewhere [4].

During an experiment, preform layers are placed within the mold along with a carbon fiber susceptors layer. Resin is drawn into the mold with a vacuum and flow fronts were fed back from a CCD camera to the controler. Based on the information on the lagging areas of the flow front at each time instant, the induction coil was moved and powered such that the flow is steered to a desired pattern. These experiments were conducted using a glycerin and water mixture as the working fluid that closely matches the viscosity of an actual resin-catalyst system. The temperature dependence of the viscosity of glycerin, however, was found to be not as strong as that of the resin mixture. This substitution of working fluids therefore gives conservative estimates of the effects of local heating during the VARTM process.

Active Control

The active control of induction heating in the VARTM process has two main requirements: voltage and motion control. Induction coil voltage must be varied to provide significant aid for flow permeation in low permeability areas while ensuring that material temperatures are limited to within a prescribed value so as to minimize the effects of the cure reaction if an actual resin system were used. The induction coil must also be moved to insure that heating is applied to appropriate regions of the molded part.

A fundamental challenge of the chosen heating control method is that material temperatures must be limited so as not to gel the resin during the filling stage of the process.

To this end, an upper bound for material temperature is specified as $100°C$ in this study. It is not practical to feed back material temperatures from within the molded part, where the maximum material temperatures occur, so a feed-forward scheme was developed which solves a simplified energy equation based on a lumped capacitance approach to quickly estimate material temperatures [7]:

$$\rho c \frac{\partial T}{\partial t} = \frac{-c_f h}{d}\left(T - T_\infty\right) + q'''$$ (1)

In this equation h is the convection heat transfer coefficient [7], d is the molded part thickness, T is the resin saturated preform temperature, q''' is the volumetric heat generation, and T_∞ is the ambient temperature. The term, c_f, is a correction factor used to compensate for the simplifying assumptions of uniform temperature through the thickness, negligible conduction in every direction, and negligible advection. A value of $c_f = 0.45$ was found to most closely fit the analytical solution to the experimentally validated numerical model presented in [4, 6]. Estimated temperatures from the model (Eq. 1) are used to choose induction coil voltages that maximize the temperature without surpassing the upper bound and thus minimize the fill times. When combined with appropriate coil motion the objective is to achieve uniform flow progression throughout the fill. Control of the motion of the coil in the y-direction (along the overall flow direction) is such that the induction coil always follows the flow front, lagging just enough to not heat any unfilled areas. The desired motion of the coil in the x-direction (width-wise direction) is to supply heating to areas lagging behind the mean flow front, thus the coil is located in the x-direction such that it is aligned with the largest flow lag. The only desired heating areas across the width of the mold are those determined as stated above. Following this logic, the induction coil is turned off during its transit in the x-direction to the target.

RESULTS AND DISCUSSION

Experiments were performed on a rectangular mold of overall dimensions 30 *cm* × 30 *cm* using a preform layup with Owens-Corning M8610 continuous strand mat comprising the majority of the mold with a 15 *cm* × 15 *cm* centrally located, low permeability, woven mat insert. The results are discussed by considering one specific preform layup in this Section. The first frame in Fig. 1 depicts the preform layup, where the relatively high permeability continuous strand material is shown in white and the low permeability woven material is seen in grey.

Preform Layup	0% Fill	20% Fill	40% Fill

60% Fill	80% Fill	Completed Fill Fill Time = 990 s	Ending Fill 76% Fill
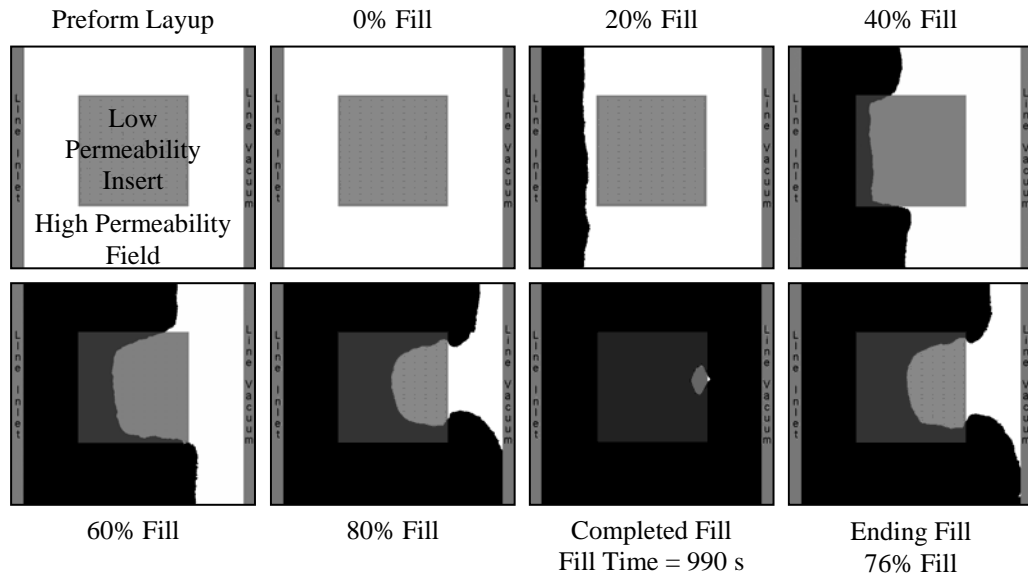
Fig. 1: Flow front progression without control (without heating).

Controlled (heated) and uncontrolled (unheated) runs were preformed and flow front information was collected in each experiment at five second intervals in the form of binary image captures. Data collected in the unheated case is presented in Fig. 1. The progress of the mold filling process is illustrated in the six frames following the preform illustration at even intervals of percent fill, defined as the volumetric percentage of the mold that has been filled. The final frame, titled ending fill, will be discussed later. The flow starts from the line inlet and progresses towards the central low permeability (woven mat) patch as indicated by the black areas. A lag develops as the flow enters the low permeability region; this lag continues to grow as the flow passes through the woven mat area. The flow lag is sufficiently large such that the flow pinches off a dry spot at the exit side of the low permeability area. This dry spot will become a defect in the final part and likely result in a part failure.

The heated (controlled) fill profiles for the same preform layup are shown in Fig. 2 following a similar format as in Fig. 1. During this fill, the control dictates coil positions and voltages to steer the flow to a desired uniform flow progression in which the flow fronts are strait lines parallel to the mold width. Here the flow progresses similarly to the unheated case at first; however, upon reaching the low permeability area, the flow is seen to be more uniform than that in the unheated case. For the case studied here, the improved uniformity provided by the control leads to a void-free fill, as observed in Fig. 2.
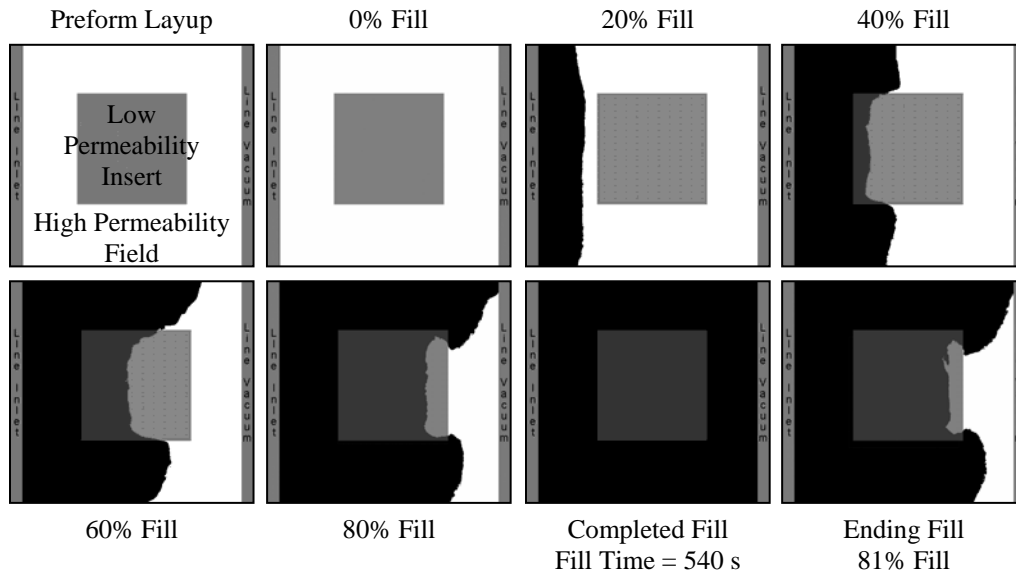
Fig. 2: Flow front progression with control (with heating).

Flow front geometry at the instant the flow reaches the end of the mold is indicated as the ending fill in Figs. 1 and 2. Flow profiles at this instant have important implications on the ability to successfully fill a mold in many liquid molding processes in that voids can be entrapped within the mold if the last location to fill is not adjacent to a vent. Ideally for a square mold configuration with a line inlet and line outlet, the flow would progress uniformly with flow fronts always being parallel to the inlet and outlet. Thus for a perfect fill, the percent fill at the instant the flow reaches the end of the mold would be 100% corresponding to a perfectly uniform profile. The control seeks to match this uniform profile during the entire fill and a good indication of its performance is the improvement of the ending fill shape. For the unheated case (Fig. 1) the ending percent fill noted in the last frame is 76%, and the corresponding profile has unfilled regions along most of the end of the mold as well as a significant portion of the low permeability area. The heated ending profile (Fig. 2) has a percent fill of 81% which is seen as an improvement, and moreover most of the low permeability region is filled at this instant.

Apart from improving the uniformity of the flow, the viscosity reduction achieved via local heating also speeds up the fill. The completed fill times noted in the seventh frames of Figs. 1 and 2 are 990 seconds for the unheated case and 540 seconds for the heated case. The significant improvement in fill time coupled with the improved flow uniformity has a practical impact on production. Additional studies and details on the control may be found in ref. [8], which the interested reader is referred to.

CONCLUSIONS

A flow control for the VARTM process based on localized induction heating was implemented on a lab-scale test bed and used to perform experiments on a heterogeneous preform layup with a centrally located low permeability region.

The control is designed to be independent of preform layup, allowing for compensation of unexpected preform permeability variation throughout the fill by locally heating and thus lowering the resin viscosity. Results show improved flow patterns when using the control, which can avoid entrapment of dry spots within the preform. In addition to improving flow uniformity, the control is able to significantly reduce fill times. Overall the localized induction heating flow control scheme was shown to provide practical improvements to a standard VARTM process.

ACKNOWLEDGEMENTS

REFERENCES

1.   D. Nielsen and R. Pitchumani, "Intelligent model-based control of preform permeation in liquid composite molding processes, with online optimization," *Composites A: Applied Science and Manufacturing*, Vol. 32, No. 12, 2001 pp. 1789.
2.   S. K. Padmanabhan and R. Pitchumani, "Stochastic modeling of nonisothermal flow during resin transfer molding processes," *International Journal of Heat and Mass Transfer*, Vol. 42, No. 16, 1999 pp. 3057.
3.   R. J. Johnson and R. Pitchumani, "Induction heating permeation enhancement for the VARTM process," *Proceedings of the 34th International SAMPE technical conference*, Vol. 34, No. 1, 2002 pp. 250.
4.   R. J. Johnson and R. Pitchumani, "Enhancement of flow in VARTM using localized induction heating," *Composites Science and Technology*, Vol. 63, No. 15, 2003 pp. 2202.
5.   R. J. Johnson and R. Pitchumani, "Simulated active flow control in a VARTM process using localized induction heating," *Proceedings of the 14th International Conference on Composite Materials*, 2003 Paper# 0861.
6.   R. J. Johnson and R. Pitchumani, "Simulation of active flow control based on localized preform heating in a VARTM process," *Composites A: Applied Science and Manufacturing*, 2004, Submitted.
7.   F. Incropera and D. DeWitt, *Fundamentals of heat and mass transfer, fourth edition*, New York: Wiley, 1996.
8.   R. J. Johnson and R. Pitchumani, "Implementation of Flow Control Using Localized Induction Heating in a VARTM Process," *Polymer Composites*, Submitted 2004.

MODELING AND SIMULATION: I NUMERICAL METHODS

New Approaches to Accelerate Calculations and Improve Accuracy of Numerical Simulations in Liquid Composite Molding

François Trochu, Edu Ruiz, Vincent Achim, Sofiane Soukane

Center de Recherches Appliquées Sur les Polymères (CRASP), Département de Génie Mécanique, École Polytechnique de l'Université de Montréal, H3C 3A7, Canada,
e-mail: *trochu@polymtl.ca*

Postal address:	P.O. Box 6079, Station "Center-Ville"
	Montreal (Quebec) Canada, H3C 3A7
Phone:	(514) 340-4711 ext. 4280
Fax:	(514) 340-5867

SUMMARY

Through-thickness flows occur typically in resin transfer molding in the case of thick parts of high fiber volume content containing multi-layer fibrous reinforcements or in thin parts when the mold is heated at a different temperature than the resin. In this latter case, viscosity changes through the thickness of the part. This results in irregular flows, usually faster in the skin when the mold is maintained at a higher temperature than the resin. Two new numerical approaches were devised to improve the accuracy of computer simulations of mold filling in Liquid Composite Molding (LCM). The motivation of this investigation is to avoid costly full 3D simulations and minimize the number of elements required to simulate mold filling. The first goal is achieved by using a mixed formulation based on a new prismatic non-conforming finite element. A mesh is extruded through the thickness of the composite in order to reflect accurately the detailed structure of the laminate and mold filling calculations are carried out on the extruded mesh. The second way to speed up calculations is to optimize the triangular in-plane mesh of the part. In order to evaluate the advantages of these new approaches in terms of accuracy and computer time, calculations performed with the new prismatic finite element are compared with finite element solutions obtained with 2D triangles and 3D tetrahedrons. The numerical performance of an optimized mesh is also assessed in terms of computer time and ability to conserve the resin mass during mold filling.

INTRODUCTION

Complex interactions caused by rheological, thermal, chemical and viscoelastic phenomena occur during composite processing. Several efforts have taken place to model these coupled phenomena. Different implementations using Taylor-Galerkin finite element (FE) formulation have been presented [1], but whenever the convective contribution to the total heat flux becomes important, temperature oscillations appear in the vicinity of the flow front.

An extension of these models using a stabilized Galerkin formulation coupled to a time Gear interpolation were shown to be unconditionally stable with no restriction on the time interval [2]. Unfortunately, for 3D simulations, much computer time is still required to solve these coupled systems. Extensive efforts through model simplification have consequently been made to decrease the computational time. Different approximations have been suggested typically based on mixed finite element and finite difference formulations [3, 4]. These methods are faster than a full 3D analysis, but neglect the through-thickness heat convection [3] and do not take into account the permeability and resin viscosity variations through the thickness of the part. Moreover, the finite difference formulation is not unconditionally stable and the grid usually needs to be refined as a function of Fourier's and Nusselt's numbers.

In order to solve the flow and heat problems in a novel way, a different way of combining finite elements (FE) and finite differences (FD) is proposed in this paper with different levels of coupling between the heat and flow equations. The fluid flow is solved with PAM-RTM [5]. Two numerical methods were implemented for the energy balance equation and resin cure. The first one is based on the new prismatic finite element, which approximates the heat exchange and resin cure in 3D parts. The second approach is a hybrid FE/FD formulation, in which the FE method is used to evaluate the in-plane heat exchange and the FD approximation solves the through-thickness heat flow.

The second way of speeding up calculations is based on constructing an optimum anisotropic mesh from the initial mesh of the mold cavity. On a fixed grid, the progression of the resin front is usually tracked by introducing a "level of resin saturation" inside each elementary volume of the mesh. The so-called "fill factor" [6] remains bounded between 0 and 1 (0 for an empty cell, and 1 for a fully saturated one). The new methodology is mainly based on the increase of the fill factor. The resulting mass accumulation in the "overfilled" elements is then redistributed to their immediate neighbors. This redistribution of resin results in newly filled elements without having to solve again the transport equations. However, resin redistribution on an isotropic mesh would very likely alter the real shape of the resin front, thus leading to inaccurate results. Therefore, in order to retain the maximum possible accuracy on the position of the flow front in time, the new proposed anisotropic refinement criterion will tend to stretch the mesh elements perpendicularly to the flow direction.

GOVERNING EQUATIONS

Based on volume averaging techniques, Darcy's law is often used to model the resin flow through porous media. It establishes a relationship between the average fluid velocity $\langle \bar{v}_r \rangle$ and the pressure gradient ∇P:

$$\langle \bar{v}_r \rangle = -\frac{[\mathbf{K}]}{\phi \, \mu_r} \langle \nabla P \rangle \tag{1}$$

where $[\mathbf{K}]$ is the permeability tensor, μ_r the resin viscosity and ϕ the porosity of the porous medium (fibrous reinforcement).

Assuming that the reinforcement is a not a deformable medium, the following equation of mass conservation may be considered:

$$div\left(\frac{[\mathbf{K}]}{\mu_r}\langle\nabla P\rangle\right) = 0 \tag{2}$$

Castro-Macosko [7] model is used to predict the viscosity variations due to resin conversion that may occur during impregnation.

To model heat transfer, the whole system including the mold, resin and fibrous reinforcement is considered. The "lumped" approximation assumes that the fibers and the surrounding fluid are at an averaged temperature. Following this approach any averaged physical property may be estimated by the rule of mixture, based on the mass fractions of the lumped components. In the case of dominant convection, the heat balance equation includes a source term $f(T)$ arising from the heat generated by resin polymerization. Therefore it is written in the following form:

$$\frac{\partial T}{\partial t} + \bar{v}\cdot\nabla T = f(T) \tag{3}$$

At the flow front, a Dirichlet boundary condition may be imposed based on the temperature of the dry fibrous reinforcement or a flux boundary condition is derived by a backwind approximation to estimate the heat transferred by the incoming resin. At the interface between the mold and the fluid, a heat transfer condition is usually imposed.

Neglecting species diffusion, the mass balance can be expressed as:

$$\phi\frac{\partial \alpha}{\partial t} + \bar{v}\cdot\nabla\alpha = \phi\dot{H} \tag{4}$$

where $\dot{H}$ is the rate of heat generated by resin polymerization. Reaction kinetics is usually described by Kamal-Sorour [8] model.

FINITE ELEMENT / FINITE DIFFERENCE FORMULATION

To solve the flow and heat problems, a new approach is proposed by combining finite elements (FE) and finite differences (FD) with different levels of coupling between the heat and flow equations. The fluid flow is solved with PAM-RTM [5]. Two numerical methods were implemented for the energy balance equation and resin cure. The first one is based on a new prismatic finite element, which approximates the heat exchange and resin cure in 3D parts. The second approach is a hybrid FE/FD formulation, in which the FE method is used to evaluate the in-plane heat exchange in the part and the FD approximation solves the through-thickness heat flow.

The numerical solution is obtained by the standard Galerkin method as implemented by Bohr [2]. In order to avoid spurious oscillations, a Lesaint-Raviart formulation with discontinuous FE is used to solve the transport problem.

Using the Galerkin formulation, the weak form of equation (3) is expressed as:

$$\int_\Omega w\left(\frac{\partial T}{\partial t} + \bar{v}\cdot\nabla T\right) d\Omega = \int_\Omega w\, f\, d\Omega + \int_{\Gamma_d}\left|T^+ - T^-\right|(\hat{n}\cdot\bar{v})\, d\Gamma_d \tag{5}$$

for any test function w belonging to the space $F(\Omega)$, where T^+ and T^- are the temperature values on the two sides of the boundary Γ_d. The finite element solution of equation (5) is obtained by an iterative process. Beginning with the elements adjacent to the injection gate, the temperature field is calculated explicitly by an upwind scheme. The heat convection is finally solved using a Gear implicit scheme for the time derivative formulated as:

$$\int_\Omega w\left(\frac{1.5T^n - 2T^{n-1} + 0.5T^{n-2}}{\Delta t} + \bar{v}\cdot\nabla T^n\right) d\Omega = \int_\Omega w\, f\, d\Omega + \int_{\Gamma_d}\left|T^{n^+} - T^{n^-}\right|(\hat{n}\cdot\bar{v})\, d\Gamma_d \tag{6}$$

where indices n, n-1 and n-2 account for the current and previous time steps respectively.

To evaluate the temperature field, a classical predictor-corrector method is used. The temperature is predicted by the diffusion equation and corrected by the convection solution. The iterative procedure consists of advancing half a time step in conduction and the other half in convection. Conforming shape functions are used in order to insure temperature continuity at the finite element nodes. Similarly, a 4th order Runge-Kutta method is used to predict the evolution of the polymerization reaction. The degree of cure obtained is transported on the geometrical domain by a Lesaint-Raviart integral formulation like temperature in equation (6).

The crossing time F_t at each mesh node was obtained from a first filling simulation on a coarse mesh from which the anisotropic remeshing algorithm can be initiated. Mesh anisotropy is achieved by constructing the anisotropic size map that will indicate how stretched the elements will be [9]. At any point X in a triangulated domain Ω, a metric tensor M is known and is represented by a d x d positive symmetric matrix (d = dimension of Ω). In 2D this matrix can be written as:

$$M(X) = \begin{bmatrix} a(X) & b(X) \\ b(X) & c(X) \end{bmatrix} \tag{7}$$

with $a(X) > 0$, $c(X) > 0$ and $a(X)c(X) - b(X)^2 > 0$. The distance between two points A and B belonging to the geometric domain Ω is redefined as:

$$dist(AB) = \int_0^1 \sqrt{\left(\frac{\partial s(t)}{\partial t}\right)\cdot M(s(t))\cdot\left(\frac{\partial s(t)}{\partial t}\right)}\cdot dt \tag{8}$$

where $s(t)$ is a parametric representation of the path connecting A and B.

The gradient of the scalar variable F_t provides information about the flow direction and can be used as the reference variable for remeshing. Using linear functions to interpolate F_t, constant gradients are obtained inside each triangle of the mesh.

A local averaging is performed to derive the values G of the gradient at the element nodes. Using these values, equation (9) can be integrated over the total filling time in order to define a particle trajectory starting from any vector position X on a node of the mesh

$$\frac{dX}{dt} = \frac{G}{\|G\|} \qquad (9)$$

Results and conclusion

The extrusion of the shell mesh of Fig. 1 into layers with different material properties led to 60,000 prismatic elements and 40,000 nodes. For a comparable accuracy to 3D simulations, a typical filling calculation based on this new approach required only 45 mn to run on an IBM IntelliStation M-Pro PC with a Pentium III (1.0 GHz) processor.
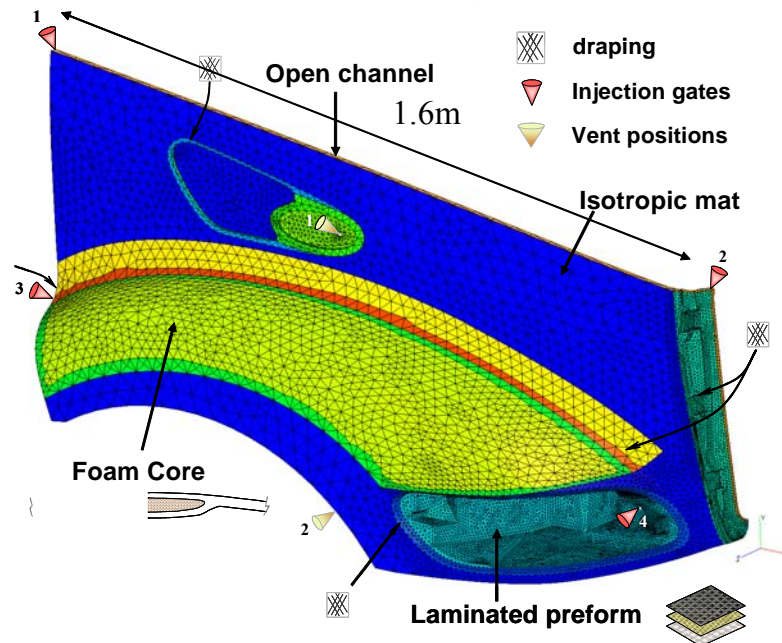
Fig.1 Mesh of an automotive fender

All possible coupling combinations have been tested for the automotive hood of Fig. 2. An example of mold filling simulation is shown in Fig. 3 (top), in which each colour corresponds to a different crossing time of the resin in the mold cavity. The degree of cure has also been predicted as shown in Figure 3 (bottom) at the end of the filling process. Figure 4 compares the performance of each type of coupling. For a comparable accuracy the time required to run a full 3D finite element analysis using tetrahedrons decreased from about 44h to 1h 40mn with the new prismatic element and 25mn for the hybrid formulation. The two new numerical schemes are stable, accurate and provide a solution at a relatively low computer cost.
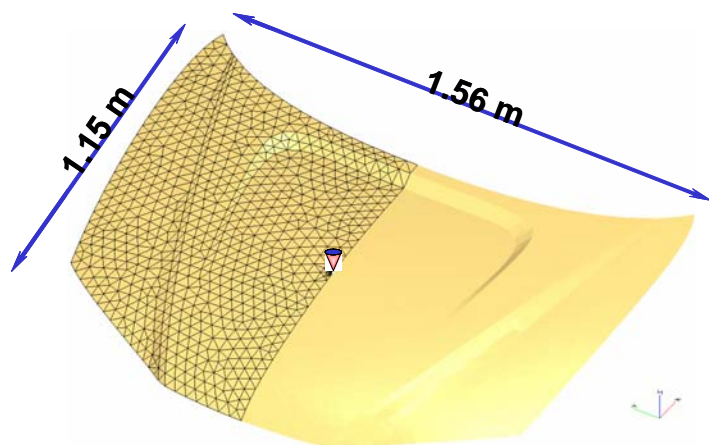
Fig. 2 Mesh of an automotive hood
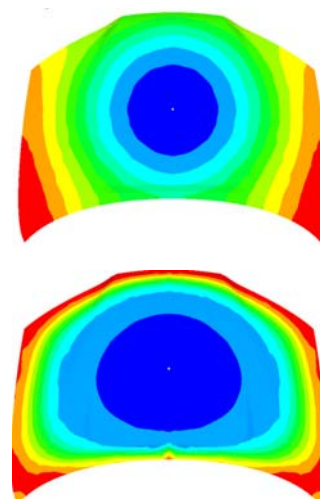
Fig. 3 Views of the hood showing mold filling in time (top) and degree of cure at the end of filling (bottom)
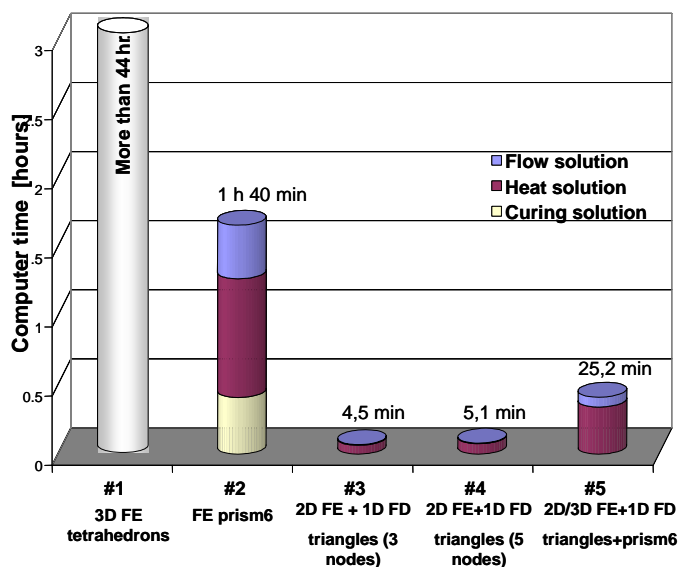
Figure 4 Comparison of computer times required for each model

A simple squared part is used as a test case to demonstrate the remeshing approach. As shown in Fig. 5, the part consists of 3 different zones. Zone 2 has a permeability two orders of magnitude higher that the two remaining ones. A filling simulation is performed by injecting at the left bottom corner of the squared part using the isotropic mesh (1000 triangles) shown in Fig. 6. The simulation took 46 seconds on an IBM 2.8 GHz Z Pro Intellistation with no overfilling of the elements during resin progression. The gradient of the resulting filling times was used to produce the anisotropic mesh (2000) elements shown on Fig. 2. The same filling simulation is again performed on the new mesh.

The total computational time including remeshing was 26 seconds on the same computer. It can be seen that the front progression is conserved and even smoother compared to the isotropic mesh.
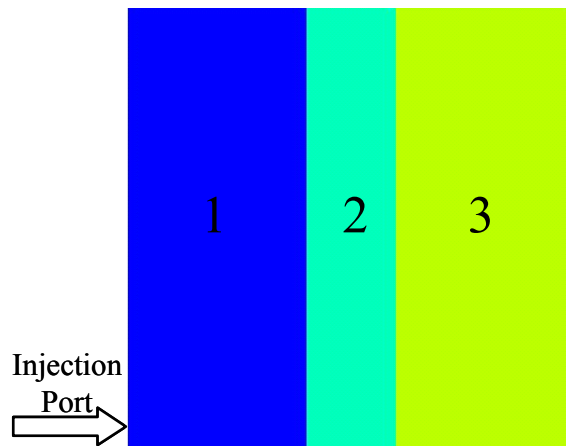
Fig. 5 Base case for the remeshing approach
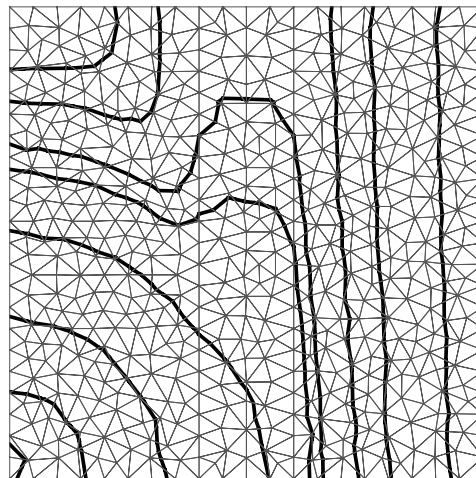
Fig.5 Resin front on isotropic mesh
(No overfill)
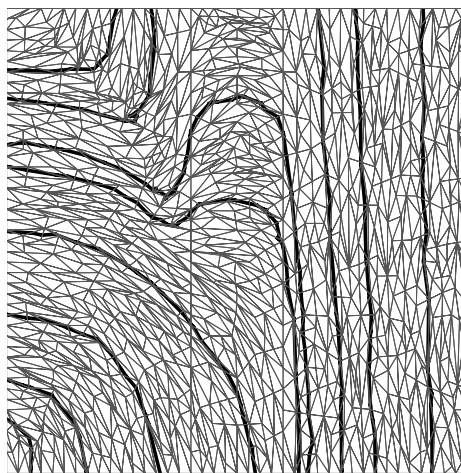
Fig. 6 Resin Front on Anisotropic mesh
(Overfill factor of 2)

REFERENCES

[1] Guyonvarch G., Audet M., Qian Y. Y., Trochu F., Delaunay D. Validation of Non-Isothermal Resin Transfer Molding Simulations. *Joint European Conference JEC.* Paris, April 24-26 1996.

[2] Bohr E. « Etude des Échanges Thermiques dans la Fabrication des Composites par les Procédés d'Injection sur Renfort ». *Mémoire de Maîtrise en Sciences Appliquées. Dep. Génie Mécanique.* École Polytechnique de Montréal. 2000.

[3] Bruschke M. V., Advani S. G. A Numerical Approach to Model Non-Isothermal Viscous Flow Through Fibrous Media with Free Surfaces *International Journal for Numerical Methods in Fluids.* 1994; **19**:575-603.

[4] Ngo N. D., Tamma K. K. Non-Isothermal 2D Flow/3D Thermal Developments Encompassing Process Modeling of Composites: Flow/Thermal/Cure Formulations and Validations. *International Journal for Numerical Methods in Engineering.* 2001; **50**:1559-1585.

[5] PAM-RTM, ESI-Group, www.esi-group.com

[6] Trochu F., Gauvin R. and Gao D.-M, "Numerical Analysis of the Resin Transfer Molding Process by The Finite Element Method", *Advances in Polymer Technology,* Vol. 12, No. 4, 1993.

[7] Castro J .M., Macosko C. W., Perry S. J. *Polymer Commun.* 1984; **25**:82.

[8] Kamal M., Sourour S. Kinetics and Thermal Characterization of Thermoset Cure. *Polymer Eng. Sci.* **13**(1):59-64, 1973.

[9] – E. Béchet, E. Ruiz, F. Trochu and J.-C Cuillere, "*Adaptive mesh generation for mold filling problems in resin transfer molding*", Composites: Part A **34** (2003) 813-834

ACKNOWLEDGEMENTS

Some Numerical Schemes for the Numerical Treatment of the Advection Equation in Liquid Composites Molding Processes

F. Sánchez[1], J.A. García[2], Ll. Gascón[3], F. Chinesta[4]

[1] *Universidad Cardenal Herrera CEU. Escuela Superior de Enseñanzas Técnicas C/ San Bartolomé 55, E-46115 Alfara del Patriarca, Valencia (Spain), sanchezf@uch.ceu.es*
[2, 3] *Universidad Politécnica de Valencia. Camino Vera s/n, 46022 Valencia (Spain) jugarcia@mcm.upv.es [2], llgascon@mat.upv.es, [3]*
[4] *Laboratoire de Mécanique des Systèmes et des Procédés - ENSAM Paris, 151 Boulevard de l'Hôpital, F-75013 Paris (France). francisco.chinesta@paris.ensam.fr*

SUMMARY: Liquid Composites Molding (LCM) processes simulation involves an efficient treatment of the advection equation governing the evolution of different process variables (volume of fluid, heat transfer, incubation time, etc). In a previous work [1], a second-order scheme with flux limiters has been developed for the integration of the advection equation, which governs the volume fraction evolution. Due to the fact that other properties, like the incubation time, are not defined in the empty part of the mold, some numerical difficulties are found during the process updating [2]. Then the scheme described in [1] must be modified to solve the extra difficulty introduced by the advection equation governing the evolution of the incubation time. This paper describes a new flux limiter technique, based on TVD schemes [3], for the calculation of the incubation time and the fluid fraction in mold filling simulation in thin cavities with replaced fiber mats using a fixed mesh.

INTRODUCTION

In LCM (Liquid Composite Molding) processes several properties must be transported by the flow: curing reaction, temperature, incubation time, fluid fraction, etc. In this work different schemes for the numerical treatment of the advection equation that governs the evolution of a generic fluid property are proposed. The application of the integration of the fluid presence function and the incubation time is achieved by using a new flux limiter strategy that allows to obtain accurate results in bidimensional LCM simulations.

In order to analyze the accuracy of the different techniques proposed in this work, we consider the resolution of the advection equation that governs the evolution of a generic fluid property J:

$$\frac{dJ}{dt} = \frac{\partial J}{\partial t} + \underline{v} \cdot \nabla J = S \tag{1}$$

An appropriate technique for the discretization of eq.(1) consists in applying the Leisant-Raviart technique (discontinuous finite element method). We can write the conservative form of the eq.(1) as

$$\int_{\Omega^e} \left(\frac{\partial J}{\partial t} + Div(J\underline{v}) - J \ Div \ \underline{v} \right) d\Omega = \int_{\Omega^e} S d\Omega \tag{2}$$

where Ω^e represents an element of a finite element mesh of the fluid domain $\Omega_f(t)$. From eq.(2), using the divergence theorem and taking into account the fluid incompressibility, results

$$\int_{\Omega^e} \frac{\partial J}{\partial t} d\Omega + \int_{\partial\Omega^{e+}} J\underline{v}\underline{n}ds + \int_{\partial\Omega^{e-}} J\underline{v}\underline{n}ds = \int_{\Omega^e} S d\Omega \tag{3}$$

where $\partial\Omega^{e+}$ denotes the outflow boundary and $\partial\Omega^{e-}$ the inflow boundary of the element Ω^e, respectively.

One of the main difficulties related to eq.(3) is that the function J associated to the fluid is not defined in the element boundaries along which are applied the boundary integrals. If we consider a constant value in the element, the discontinuous finite element method assumes that on the outflow boundary the function J is equal to the existing value inside the element Ω^e, i.e. $J(\underline{x} \in \partial\Omega^{e+}) = J^e$ and that on the inflow boundary the function J is given by its value in the upstream element, i.e. $J(\underline{x} \in \partial\Omega^{e-}) = J^{e-}$. Thus, eq.(3) can be rewritten in the equivalent form:

$$\frac{\partial J^e}{\partial t} \left| \Omega^e \right| = -J^e \int_{\partial\Omega^{e+}} \underline{v}\underline{n}ds - J^{e-} \int_{\partial\Omega^{e-}} \underline{v}\underline{n}ds + S^e \left| \Omega^e \right| \tag{4}$$

where $\left| \Omega^e \right|$ denotes the volume of Ω^e. Considering a first order explicit approximation of the time derivative, we can write (4) as

$$J_e^{n+1} = J_e^n - J_e^n \frac{\Omega^+}{\left|\Omega^e\right|} + J_{e-}^n \frac{\Omega^-}{\left|\Omega^e\right|} + S_e \Delta t \tag{5}$$

where we define the inflow and outflow fluid volumes as $\Omega^- = q^- \Delta t$ and $\Omega^+ = q^+ \Delta t$, being q^+ and q^- the outflow and inflow flow rates, respectively. In the above equation, the subscript for the property J, denotes the considered element and the superscript indicates the time step.

A FIRST ORDER TECHNIQUE FOR THE CALCULATION OF THE FLUID PRESENCE AND INCUBATION TIME

The evolution of the volume fraction, I, and the incubation time, E, are given as a general linear advection eq. (1) where for the volume fraction, $J=I$, $S=0$, and for the incubation time $J=E$ and $S=1$, with the initial conditions:

$$I(\underline{x}, t=0) = \begin{cases} 1 & \underline{x} \in \Omega_f(t) \\ 0 & \underline{x} \notin \Omega_f(t) \end{cases} \quad ; \quad E(\underline{x}, t=0) = \begin{cases} 0 & \underline{x} \in \Omega_f(t) \\ \text{Not defined} & \underline{x} \notin \Omega_f(t) \end{cases}$$

Then the discretization form of the governing equation of the fluid fraction, I, is defined from eq.(5) considering $J=I$ and $S=0$:

$$I_e^{n+1} = I_e^n - I_e^n \frac{\Omega^+}{\left|\Omega^e\right|} + I_{e-}^n \frac{\Omega^-}{\left|\Omega^e\right|} \tag{6}$$

On the other hand, the incubation time is defined as the elapsed time since the resin components were mixed just before the injection. The value of the incubation time E is then set to zero in the injection nozzle and varies throughout the filled part of the mold, but it is not defined on the empty one. The discretization form of the equation governing the evolution of the incubation time is obtained from eq.(5) considering $J=E$ and $S=1$:

$$E_e^{n+1} = E_e^n - E_e^n \frac{\Omega^+}{\left|\Omega^e\right|} + E_{e-}^n \frac{\Omega^-}{\left|\Omega^e\right|} + \Delta t \tag{7}$$

A first problem appears if we consider the time t for which an element Ω^e starts its filling process from its upstream element Ω^{e^-}. To illustrate this limitation we consider the situation where the outflow volume is null, $\Omega^+ = 0$, then eq.(7) establishes that solution at t_{n+1} is dominated by solution existing in the element in the previous instant, even when this element is empty and E is then not defined. In order to solve, properly, the eq.(7) we use the method described in [2], by multiplying eq.(7) by the fluid fraction I and eq.(6) by the field E and sum both resulting equations, it results in solving eq.(1) for $J=EI$ and $S=I$ whose discretised form is given by

$$(EI)_e^{n+1} = (EI)_e^n - (EI)_e^n \frac{\Omega^+}{\left|\Omega^e\right|} + (EI)_{e-}^n \frac{\Omega^-}{\left|\Omega^e\right|} + S_e \Delta t \tag{8}$$

where taking S as I evaluated in the time $n+1$ then $S^e = I_e^{n+1}$ and yields

$$E_e^{n+1} = \frac{(EI)_e^n}{I_e^{n+1}} - \frac{(EI)_e^n}{I_e^{n+1}} \frac{\Omega^+}{\left|\Omega^e\right|} + \frac{(EI)_{e-}^n}{I_e^{n+1}} \frac{\Omega^-}{\left|\Omega^e\right|} + \Delta t \tag{9}$$

It is important to notice that in order to obtain E_e^{n+1} will be necessary the previous resolution of I_e^{n+1}. Moreover we assume that only exists inflow volume in a given element when the upstream element is completely filled i.e. $\Omega^- \neq 0$ only if si $I^{e^-} = 1$, and exists outflow volume from a given element when it is completely filled, that is $\Omega^+ \neq 0$ only if $I^e = 1$. This condition is included in the formulation by means the parameter δ defined by

$$\delta_e = \begin{cases} 1 & if \quad I_e = 1 \\ 0 & if \quad I_e < 1 \end{cases} \qquad and \qquad \delta_{e-} = \begin{cases} 1 & if \quad I_{e-} = 1 \\ 0 & if \quad I_{e-} < 1 \end{cases} \tag{10}$$

If we include this condition in eq.(5), the discretization of the advection equation for a general variable can be rewriten as

$$J_e^{n+1} = J_e^n - \delta_e^n J_e^n \frac{\Omega^+}{\left|\Omega^e\right|} + \delta_{e-}^n J_{e-}^n \frac{\Omega^-}{\left|\Omega^e\right|} + S_e^{n+1} \Delta t \tag{11}$$

A FLUX LIMITER TECHNIQUE FOR CALCULATION OF THE FLUID PRESENCE AND INCUBATION TIME

In order to extend the previously described first order schemes to second order with flux limiter ones for the resolution of the advection eq.(1), we change the notation and rewrite the eq.(11) as follows:

$$J_e^{n+1} = J_e^n - \frac{\Delta t}{A(e)} \underline{v}_e \sum_{j=1}^{3} l_{ej} \hat{\underline{f}}_{ej} \underline{n}_{ej} + \Delta t S_e^{n+1} \quad \text{with}$$

$$\hat{\underline{f}}_{ej} = \hat{\underline{f}}_{ej}^{UP} = \frac{1}{2} \left\{ \left(\delta_e J_e + \delta_j J_j \right) - \text{sgn} \left(\underline{v}_e \cdot \underline{n}_{ej} \right) \left(\delta_j J_j + \delta_e J_e \right) \right\}$$

(12)

where $A(e)$ is the area of the element e, j represents a neighbour triangle element, $\underline{n}_{ej}$ is the outward unit vector on the common edge of the triangles e and j, l_{ej} is the length of that edge and the velocity vector of element e is $\underline{v}_e$, see Fig.1.

The extension of the above scheme to second order is described by eq.(12) replacing $\hat{\underline{f}}_{ej}$ by $\hat{\underline{f}}_{ej}^{SW}$ defined by:

$$\hat{\underline{f}}_{ej}^{SW} = \hat{\underline{f}}_{ej}^{UP} + \frac{1}{2} \chi \left(r_{ej} \right) \left(\text{sgn} \left(\underline{v}_e \cdot \underline{n}_{ej} \right) - \frac{\Delta t}{d_{ej}} \underline{v}_{ej} \cdot \underline{n}_{ej} \right) \left(\delta_j J_j - \delta_e J_e \right)$$

(13)

where the average velocity between elements e and j is defined by v_{ej} and d_{ej} represents the distance between barycentres of the triangles e and j. The superscript UP denotes first order upwind scheme and SW second order with Sweby flux limiter (4). Note that we include again the use of the parameter δ defined by

$$\delta_k = \begin{cases} 1 & if \quad I_k = 1 \\ 0 & if \quad I_k < 1 \end{cases} \quad \text{for} \quad k = e, j$$

(14)

and r_{ej} is defined by

$$r_{ej} = \begin{cases} \min_{k \neq j, \cos \theta_{ek} < 0} \left\{ \dfrac{\delta_e J_e - \delta_k^e J_k^e}{\delta_j J_j - \delta_e J_e} \right\} & if \quad \cos \theta_{ej} > 0 \\[4mm] \min_{k \neq j, \cos \theta_{ek} < 0} \left\{ \dfrac{\delta_k^j J_k^j - \delta_j J_j}{\delta_j J_j - \delta_e J_e} \right\} & if \quad \cos \theta_{ej} < 0 \end{cases}$$

(15)

in which θ_{ej} (Fig.1) denotes the angle between $\underline{n}_{ej}$ and the velocity vector of element e, the definition of the Superbee flux limiter is then given by

$$\chi_{SB}(r) = \max \left\{ 0, \min \left\{ 2r, 1 \right\}, \min \left\{ r, 2 \right\} \right\}$$

(16)

For the integration of the fluid presence function I, we take $J=I$ and $S=0$ in eq.(12) and for the resolution of the incubation time, $J=EI$ and $S=I$. It is easy to note that if we take

$$\delta_k = 1 \quad if \quad I_k \leq 1 \quad \text{for} \quad k = e, j$$

(17)

the condition (17) means that neighbour elements can exchange fluid without complete its own filling previously.

NUMERICAL SIMULATIONS

In order to evaluate the accuracy of the different schemes described, we consider a saturated mold as depicted in Fig.2. In that case, the exact resolution of the pressure and velocity distribution are known and then they do not contribute to the numerical errors induced by the discretization of the advection equation. A comparison of the different fluid presence function integration schemes proposed is shown in Fig.3. It can be noticed that the use of the Superbee flux limiter allows to compute a more accurate solution in the neighbourhood of the discontinuity associated with the flow front. Moreover, as it was expected, the use of δ defined by eq.(14) instead of eq. (17) allows to avoid the diffusive flow front. Fig.4 shows the incubation time along a flow streamline in the elements comparing exact solution with the different ones given by eq.(12). Here once again the use of the Superbee flux limiter shows a more accurate solution. The convergence analysis shown in Fig.5 has been carried out for a complete mold filling. The error is defined by the L_2 norm at the solutions computed for different mesh sizes. The order of convergence is two times higher when the Superbee flux limiter is used instead of the first order upwinding scheme. Fig.6 depicts the incubation time distribution and the filling flow pattern of a U-Shaped mold of 500x260x10 *mm*. The constant flow rate is 4 cm^3/s. and the porosity is 0.5. It is interesting to note how the fluid located in the left upper part of the mold, even just closed to the injection nozzle, stops and gets 'older'.
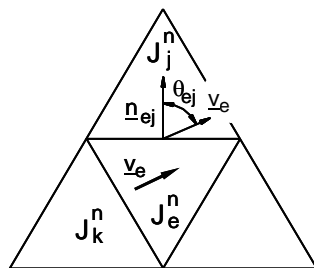
Fig.1.   Discretization nomenclature
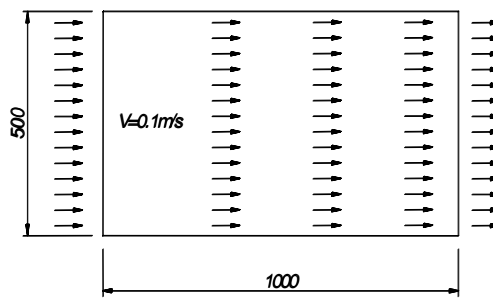
Fig.2.   Saturated flow conditions
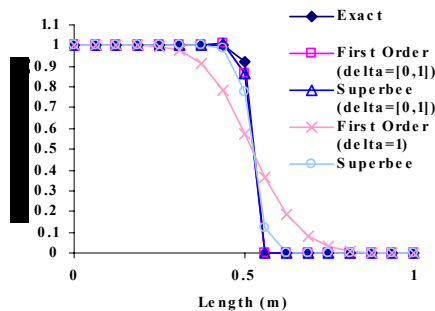
Fig.3.   Schemes comparison used to compute *I*
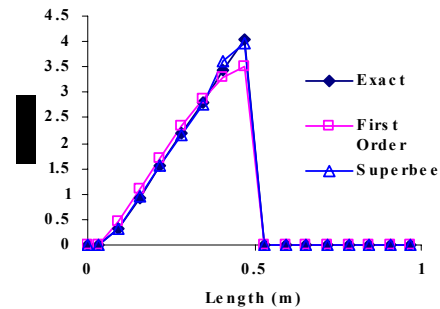
Fig.4.   Schemes comparison used to compute *E*
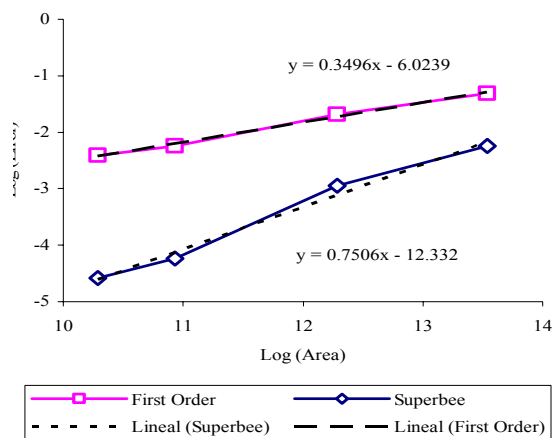
Fig.5.   Convergence analysis
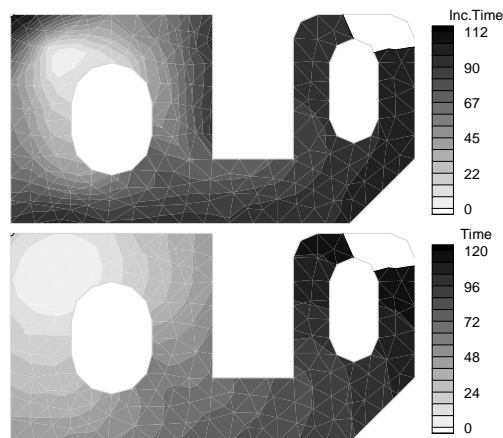
Fig.6.   Incubation. time and flow pattern

CONCLUSIONS

A new approach to solve the advection equation of a general fluid variable using a second order flux limiter technique has been defined and tested. A fixed mesh numerical algorithm has been completed and improved for simulate both the bidimensional flow behavior and the incubation time in LCM process.

ACKNOWLEDGEMENTS

REFERENCES

1. García J.A., Gascón Ll., Sánchez F.,Chinesta F. *Mold Filling Simulation in RTM Processes*, Revue des Composites et Matériaux Avancés, Vol.13 (2003),85-97.
2. F. Chinesta, T. Mabrouki, A. Ramón, *Some difficulties in the flow front treatment in fixed mesh simulations of composites forming processes*, ESAFORM 2002.
3. Harten, *High Resolution Schemes for Hyperbolic Conservation Laws*, J. Comput. Phys. 49 (1983) 357-393.
4. Sweby P.K., *High Resolution Schemes Using Flux Limiters For Hyperbolic Conservation Laws*, SIAM J. Numer. Anal. (1984) 995-1011.

Numerical Method to Predict Void Formation during the Liquid Composite Molding Process

Zuzana Dimitrovová[1] and Suresh G. Advani[2]

[1] *Researcher of IDMEC / IST and Invited Auxiliary Professor of DEM / ISEL*
Av. Rovisco Pais, 1, 1049-001 Lisbon, Portugal: zdimitro@dem.ist.utl.pt
[2] *Professor, Department of Mechanical Engineering and Center for Composite Materials*
University of Delaware, Newark, DE 19716: advani@udel.edu
Corresponding author's email: zdimitro@dem.ist.utl.pt

SUMMARY: Void formation during the injection phase of the liquid composite molding process can be explained as a consequence of the non-uniformity of the flow front progression. This is due to the dual porosity within the fiber perform (spacing between the fiber tows is much larger than between the fibers within in a tow) and therefore the best explanation can be provided by a mesolevel analysis, where the characteristic dimension is given by the fiber tow diameter of the order of millimeters. In mesolevel analysis, liquid impregnation along two different scales; inside fiber tows and within the open spaces between the fiber tows must be considered and the coupling between the flow regimes must be addressed. In such cases, it is extremely important to account correctly for the surface tension effects, which can be modeled as capillary pressure applied at the flow front. Numerical implementation of such boundary conditions leads to ill-posing of the problem, in terms of the weak classical as well as stabilized formulation. As a consequence, there is an error in mass conservation accumulated especially along the free flow front. A numerical procedure was formulated and is implemented in an existing Free Boundary Program to reduce this error significantly.

KEYWORDS: void formation, surface tension, capillary pressure, mass conservation, free boundary flow, mesolevel analysis, dual porosity.

INTRODUCTION

Liquid Composite Molding is a composite manufacturing process in which fiber preforms consisting of stitched or woven bundles of fibers, known as fiber tows, are stacked in a closed mold and a polymeric resin is injected to impregnate all the empty spaces between the fibers. Fiber tows are usually millimeters in diameter and consist of bundles of 2000 to 5000 fibers [1]. An important step is to ensure saturation of all the fiber tows and regions in between them in order to avoid voids formation. Due to the dual porosity in woven fiber preforms, resin progression is not uniform, and a transition region where the flow has not yet stabilized and saturated, is formed along the macroscopic flow front. This region is very sensitive to voids formation. The best way to analyze this flow is at the mesolevel, i.e at the scale of fiber tows.

MESOLEVEL ANALYSIS
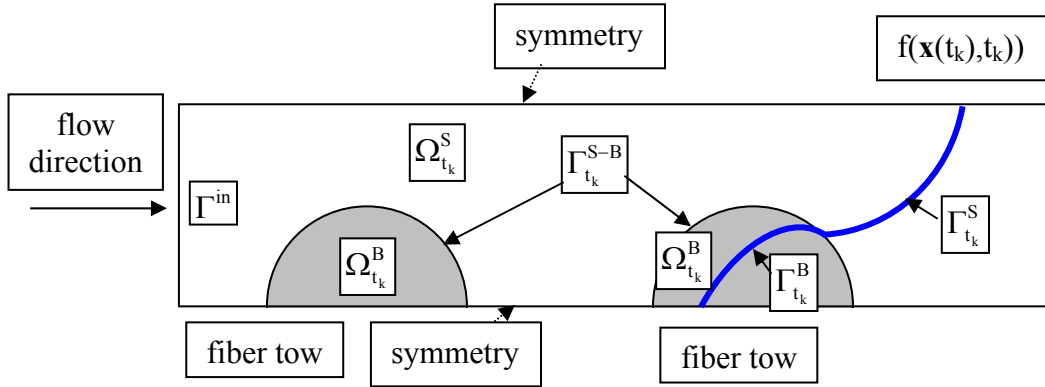
Fig.1 Flow domain, regions and boundaries designation

In mesolevel analysis, liquid flowing along two different scales must be considered. Single scale porous media (fiber tows represented in Fig. 1 by grey half-circles) and open spaces (white spaces) are presented in the same unit cell which will allow one to couple the flow in these two different regimes. Fiber tows have uniformly distributed pores, therefore sharp flow front can be assumed as the resin impregnates. Moreover quasi steady state assumption can be exploited. As the flow is slow, inertia terms can be neglected, implying that one can assume Stokes flow in the inter-tow spaces $\Omega_{t_k}^S$ (white space between Γ^{in} and $\Gamma_{t_k}^S$) and Darcy's flow in saturated intra-tow region $\Omega_{t_k}^B$ which need to be solved at each discretized time t_k. In fact, Darcy's law must be modified to Brinkman's equations, in order to account for viscous stress at the interface between these two regions ($\Gamma_{t_k}^{S-B}$), which rapidly decreases with the distance from $\Gamma_{t_k}^{S-B}$. In summary, the following equations must be satisfied at each time step, t_k:

$$\text{in inter-tow spaces: } \nabla \cdot \mathbf{v} = 0 \text{ and } \nabla p = \mu \Delta \mathbf{v} \quad \text{in } \Omega_{t_k}^S \tag{1}$$

(Stokes equations),

$$\text{in intra-tow spaces: } \nabla \cdot \mathbf{v}^D = 0 \text{ and } \nabla p^f = \mu \Delta \mathbf{v}^D - \mu \mathbf{K}^{-1} \cdot \mathbf{v}^D \quad \text{in } \Omega_{t_k}^B \tag{2}$$

(Brinkman's equations),

where $\mathbf{v}$ is local velocity vector, p is local pressure, μ is resin viscosity and ∇ stands for spatial gradient, $\Delta = \nabla \cdot \nabla$. $\mathbf{v}^D$ is Darcy's velocity vector, i.e. the phase averaged velocity related to the intrinsic phase average $\mathbf{v}^f$ by $\mathbf{v}^D = \phi_t \mathbf{v}^f$, where ϕ_t is intra-tow porosity. p^f stands for intrinsic phase average of the local pressure and $\mathbf{K}$ is absolute permeability tensor.

If fibers inside the tows are rigid, impermeable and stationary, the following boundary conditions, under usual omission of the air pressure, must be fulfilled at the free front:

$$\boldsymbol{\sigma}_t^v = \mathbf{0} \text{ and } \left(\boldsymbol{\sigma}^v \cdot \mathbf{n}\right) \cdot \mathbf{n} - p = \sigma_n^v - p \approx -p = -p_c = -2\gamma H \quad \text{at } \Gamma_{t_k}^S, \tag{3}$$

$$p^f = P_c \quad \text{at } \Gamma_{t_k}^B. \tag{4}$$

Here $\boldsymbol{\sigma}^v$ is local viscous stress, $\boldsymbol{\sigma}^v_t$ tangential vector of the viscous stress vector, σ^v_n normal component of the viscous stress and $\mathbf{n}$ the outer unit normal vector to the free front in Stokes region $\Gamma^S_{t_k}$. p_c and P_c stand for local and global (homogenized) capillary pressure, γ is resin surface tension and H is mean curvature. Progression of the free boundary can be determined according to:

$$\frac{Df}{Dt} = \frac{\partial f}{\partial t} + \mathbf{v} \cdot \nabla f = 0 \quad \text{at } \Gamma^S_{t_k}, \tag{5}$$

$$\frac{Df}{Dt} = \frac{\partial f}{\partial t} + \frac{\mathbf{v}^D}{\phi_t} \cdot \nabla f = 0 \quad \text{at } \Gamma^B_{t_k}, \tag{6}$$

where $f(\mathbf{x}(t),t)=0$ is implicit function describing the moving sharp flow front (dark line in Fig. 1), $\mathbf{x}$ is spatial variable and t is time. Other boundary conditions such as symmetry, periodicity and inlet conditions at Γ^{in} are related to the particular problem under consideration.

We have formulated the governing equations for free boundary flows in intra- as well as inter-tow spaces and developed numerical techniques to address the movement of the flow at the mesolevel scale which we call the Free Boundary Program (FBP). Numerical simulations can track the advancement of the resin front promoted by both hydrodynamic pressure gradient and capillary action [2-5]. In such simulations it is extremely important to account correctly for the surface tension effects, which can be modeled as capillary pressure applied at the flow front. Unfortunately essential boundary conditions of this kind make the problem ill-posed, in terms of the weak classical as well as stabilized formulation. As a consequence there is an error in mass conservation accumulated especially along the free front. This can affect significantly normal velocities at the free front and distort the next front shape. Due to the explicit integration along the time scale, such errors are irreversible. Several stabilization techniques were implemented in FBP to eliminate this effect [3-5]. In this article we will present more appropriate techniques for stabilization, based on weak formulation of the problem. The methodology implemented in Darcy's region is well-known, although rarely used in real simulations. It is presented e.g. in [6]. The recalculated outlet velocities have superior convergence properties [7]. In Stokes region the correction of the outlet velocities we are presenting have not yet been published to our knowledge. Both methodologies are implemented in FBP.

FLOW FRONT RECALCULATION AND CORRECTION

Following [6], outlet normal velocities can be recalculated in Darcy's region according to:

$$\left(q^h, \tilde{v}^{D,h}_n\right)_{\Gamma^B_{t_k}} = B\left(q^h, p^{f,h}\right) - L\left(q^h\right) \quad \forall q^h \in \hat{P}^h. \tag{7}$$

B and L represent bi-linear and linear form of the weak formulation, new outlet velocities with superior convergence properties are $\tilde{v}^{D,h}_n$, q^h is trial pressure and $p^{f,h}$ is the solution already obtained in a standard way. Trial pressures space, $\hat{P}^h$, consists now solely from functions originally omitted because of the pressure essential boundary condition.

Efficiency of this technique can be shown on a simple example:

$$\Delta u = 1 \quad \text{in } [-1,1] \times [-1,1],$$
$$u = 0 \quad \text{at the boundary } \partial([-1,1] \times [-1,1]). \tag{8}$$

Numerical results were obtained by thermal analysis in ANSYS (u thus represent temperature). In Fig. 2 results are compared on one of the straight boundaries. Mesh of quad elements was used as 6×6 (tf 6), 10×10 (tf 10) e 200×200 (tf 200). Normal heat flux tf 200 for 200×200 mesh can be already assumed as exact. Recalculated normal flux on 6×6 and 10×10 meshes is designated as "tf-cal 6" and "tf-cal 10". It is seen that the coincidence with the exact values is just excellent.
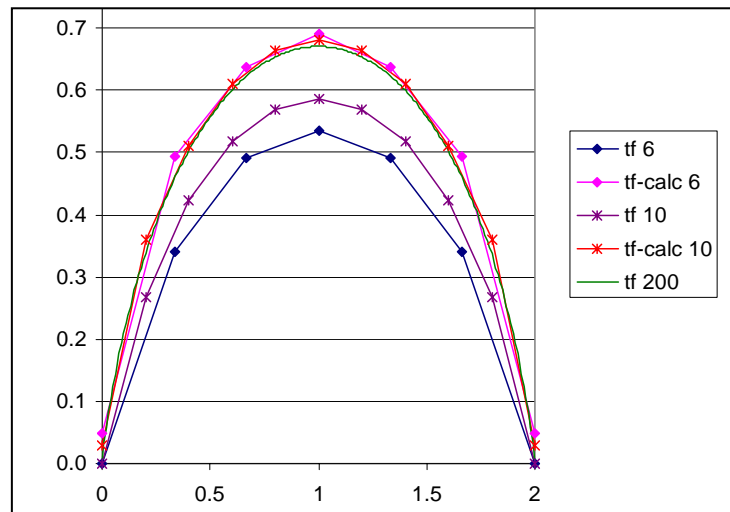
Fig. 2. Normal thermal fluxes of the problem specified in (8). Notice that recalculated fluxes on 6x6 and 10x10 meshes (tf-calc 6 and tf-calc 10) do as good a job as a mesh of 200x200 (tf 200)

In the Stokes region the following scheme is used:

$$\left(q^h, w_n^h\right)_{\Gamma_{t_k}^S} = \left(q^h, \nabla \cdot \mathbf{v}^h\right) \quad \forall q^h \in \hat{P}^h,$$
$$\tilde{v}_n^h = v_n^h - w_n^h, \tag{9}$$

where w_n^h is an auxiliary value of the normal velocity, used to correct the originally obtained normal velocities, v_n^h. In this case incompressibility condition is completely separated from the weak formulation. Efficiency was verified directly on ANSYS fluid element FLUID 141, where pressure and velocities are nodal variables. Test problem for unit viscosity and mass free fluid is specified in Fig. 3a) and results are shown in Fig. 3b).

Also here the recalculated outlet normal velocities fit the solution well for the very fine mesh. In this test problem pressure does not correspond to the capillary pressure, because the aim was only to test the efficiency of such methodology.
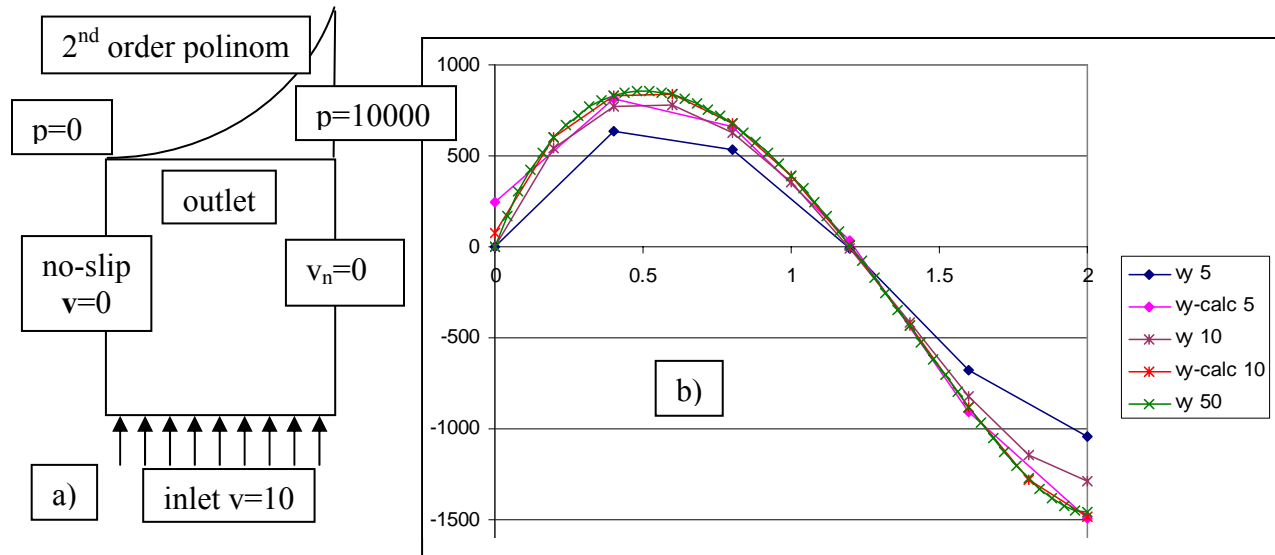
Fig. 3 (a) Fluid problem definition, (b) original values vy 5, vy 10 and vy 50 on 5x5, 10x10 and 50x50 quad meshes and recalculated vy-calc 5 and vy-calc 10 outlet normal velocities

CONCLUSION

Presented stabilization techniques are very efficient as shown in the simple test examples. They permit calculation of frontal normal velocities with sufficient precision even for coarse meshes. They are included in the post-processing part of FBP. Their implementation ensures better mass conservation at the global as well as the local level. It makes it possible to obtain a front shape that is not only more exact but also smoother. The computational time is reduced as coarser meshes can be used to obtain stable and accurate answers and it also allows one to step through larger time steps during the impregnation process.

ACKWNOLEDGMENTS

REFERENCES

1.   S. G. Advani, M. V. Bruschke and R. S. Parnas, "Resin transfer molding", In: Advani SG, editor. *Flow and rheology in polymeric composites manufacturing.* Amsterdam, Elsevier Publishers, 1994, pp. 465-516.

2.   Z. Dimitrovová and S. G. Advani, "Analysis and characterization of relative permeability and capillary pressure for free surface flow of a viscous fluid across an array of aligned cylindrical fibers", *Journal of Colloid and Interface Science,* Vol. 245, 2002, pp. 325-337.

3.   Z. Dimitrovová and S. G. Advani, "Free boundary viscous flows at micro and mesolevel during liquid composites molding process", CD of communications of *14th International Conference on Composites Materials*, San Diego, California, EUA, 2003.

4.   Z. Dimitrovová and S. G. Advani, "Numerical simulation of free boundary viscous flows at all length scales of LCM process", CD de comunicações do *3th International Conference on Computational & Experimental Engineering and Sciences*, Corfu, Grécia, 2003.

5.   Z. Dimitrovová and S. G. Advani, "Mesolevel analysis of the transition region formation and evolution during the liquid composite molding process", *Computers & Structures*, accepted, 2004.

6.   T. J. R. Hughes, G. Engel, L. Mazzei and M. G. Larson, "The continuous Galerkin method is locally conservative", *Journal of Computational Physics*, Vol. 163, 2000, pp. 467-488.

7.   I. Babuška and A. Miller, "The post-processing approach in the finite element method - Part 1: Calculation of displacements, stresses and other higher derivatives of the displacements", *International Journal for Numerical Methods in Engineering*, Vol. 20, 1984, pp. 1085-1109.

Simulation of Isothermal RTM Filling Using SPH Method

S. Comas-Cardona[1], P.H.L. Groenenboom[2], C. Binetruy[1] and P. Krawczak[1]

[1] *Ecole des Mines de Douai, Technology of Polymers and Composites Department*
941 rue C. Bourseul, BP 838, 59508 Douai, France
[2] *ESI-BV, Gebouw Kortland, Nieuwe Tiendweg 11a,*
2922 EN Krimpen aan den IJssel, The Netherlands
Corresponding Author's e-mail: binetruy@ensm-douai.fr

SUMMARY: Resin Transfer Molding (RTM) can be a very attractive single-step process for sandwich structure manufacturing. During an RTM injection, the pressure field developing while saturating the fiber-reinforced skins can lead to large shifting or deformation of the foam core material. Such effects induce poor dimensional accuracy of skins and core thickness. Moreover, filling time and injected resin amount can be significantly increased as a result of foam core crushing. In order to model this type of hydro-mechanical coupling, the use of mixed Finite Element and Smoothed Particle Hydrodynamics (FE-SPH) method is presented in this study. This method combines Lagrangian particles and finite elements, modeling respectively the resin and the sandwich core. Computed pressure responses during the filling stage are compared to sandwich manufacturing test results. The potential of this original numerical method is discussed.

KEYWORDS: Smoothed Particle Hydrodynamics method, resin transfer molding, hydro-mechanical coupling, sandwich manufacturing

INTRODUCTION

Resin Transfer Molding (RTM) can be a very attractive single-step process for sandwich structures manufacturing. The two fiber-reinforced skins and the core are laid up in a mold cavity. Both skins are saturated and bonded to the core while resin is injected. During sandwich manufacturing using RTM, the pressure field developing while saturating the fiber-reinforced skins can experimentally lead to large shifting[1,2] or compression[2,3] of the core. Such effects are damaging to the part because they induce poor dimensional accuracy of both skin and core thickness. Also, filling time and injected resin amount can be significantly increased due to the core crushing.

Previous works focused on addressing similar manufacturing issues and this hydro-mechanical coupling using finite element methods (FEM)[2,4], mixed control volume / finite difference methods (CVM/FDM)[5] or even a one-dimensional Lagrangian formulation[6]. However, when the geometry of the flow domain changes, due to a free surface or interfaces with moving structures, special solutions are required within these numerical schemes. In this paper, it will be shown how the Smoothed Particle Hydrodynamics (SPH) method provides an attractive alternative solution to simulate such cases.

This method has previously been used to simulate isothermal RTM filling [7] and gave fairly good qualitative results in terms of resin flow front profiles.

This study particularly focuses on flow-induced foam core compression during sandwich manufacturing. In order to model this hydro-mechanical coupling, a mixed FE-SPH method has been chosen. An SPH package is available within the commercial simulation tool PAM-CRASH (ESI, France) and has been further developed to solve for viscous flow in porous media. The following section presents a brief review of flow within porous media and the SPH method. Then, pressure responses computed from the filling simulations will be compared to sandwich manufacturing test results where hydro-mechanical coupling is present. Finally, the potential of this alternative and generic numerical method is discussed.

FUNDAMENTALS

Fluid flow dynamics within porous media

It is possible to derive the conservation of mass and momentum equations for flow in porous media from the conservation equations for a two-phase medium in which one of the materials is fixed in space[8]. Considering constant fluid viscosity and laminar flow, and a proper scaling analysis for RTM, the equations to be solved (conservation of mass and momentum) are respectively:

$$\frac{\partial \eta}{\partial t} + \nabla(\eta \vec{u}) = 0 \qquad (1)$$

$$\eta \left\{ \frac{\partial \vec{u}}{\partial t} + \vec{u}(\nabla \cdot \vec{u}) \right\} = -\phi \nabla P + \eta \vec{g} - \phi^2 \mu K^{-1} \cdot \vec{u} \qquad (2)$$

where ϕ is the fluid volume fraction or porosity, $\vec{u}$ the fluid velocity, μ the viscosity, P the pressure, g the gravitational acceleration, K the permeability and η the apparent density defined as: $\eta = \phi \rho$, where ρ is the fluid density. In this study, in order to simulate the flow for all regions of the computational domain, whether porous or not, Eqn. 2 provides the basis of the solution with the viscous drag term only being used within the porous regions.

Smoothed Particle Hydrodynamics

The SPH method is a Lagrangian and mesh-less method which was originally developed to solve astrophysical problems [9,10] and has later been applied also to the flow of compressible fluids[11]. However when pressure wave propagation is not of prime interest, as in this study, the use of an artificial equation of state for nearly incompressible liquids is quite suitable[11]. In SPH, the fluid is represented by a population of particles that interact with each other. Properties are averaged within a sphere of influence. Fundamentals and details of the method are widely available in the literature [9-11].

The interaction of the particles with the finite elements, representing respectively the resin and the foam in this study, is modeled by the sliding interface algorithms available within PAM-CRASH. The use of such interaction between the SPH and finite elements has already been validated for a wide range of applications.

EXPERIMENTAL

Material characterization

An exhaustive materials characterization has been performed at room temperature in order to feed the code with material input data. A non-reactive Newtonian fluid (Di-Octyl Phtalate, DOP) is used. Its viscosity, measured using a Brookfield viscometer, is 0.07 Pa.s. The permeability of the woven fabric (1500S3, Chomarat Composites) was measured for fiber volume fractions varying from 0.43 to 0.57. The variation can be fitted to a second order polynomial as:

$$K = 1.08 \times 10^{-8} V_f^2 - 1.42 \times 10^{-8} V_f + 4.6 \times 10^{-9} \qquad (3)$$

where V_f is the fiber volume fraction and the permeability K is in m^2. The areal weight of the fabrics is 1500 g.m^{-2}. The foam core (NA1100, Alvéo) has also been characterized in compression. For the pressure levels used in this study, the foam can be considered as a linear elastic material and its bulk modulus is 1.2 MPa. Finally the unsaturated fabrics have been tested in compression using a tensile test machine with a cross-head speed of 0.5 mm.min^{-1}. Previous work showed that such mechanical behavior can be fitted to a power law relationship[12]:

$$\sigma = 19.30 \, V_f^{9.32} \qquad (4)$$

where σ is the compressive stress in MPa.

Sandwich manufacturing

Sandwich panels are manufactured at room temperature using a mold whose cavity dimensions are 500 x 200 x 16 mm^3 (Fig. 1). The mold cavity is filled up with a 10 mm-thick soft closed-cell polyethylene foam core and two skins each consisting of 3 plies of glass woven fabric. The fiber volume fraction reached in both skins is close to 53%. Once the mold is closed, a fluid (DOP) is injected at constant flow rate (15 cl.min^{-1}).
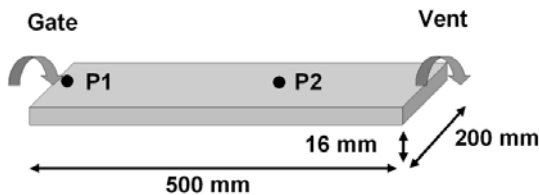
Fig. 1 Experimental setup.
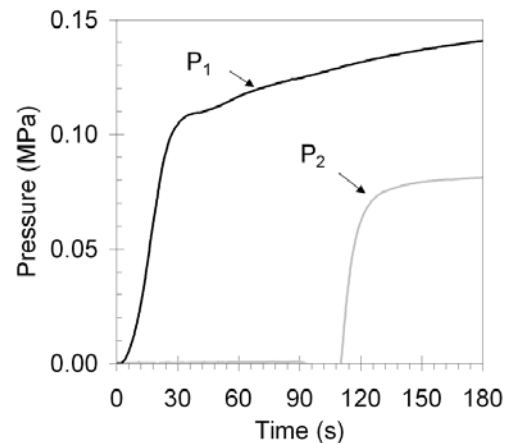
Fig. 2 Experimental pressure responses (P$_1$: at the gate. P$_2$: 29 cm from the gate).

Pressure at the injection gate (P1) and 29 cm away from the gate (P2) are monitored and recorded throughout the injection (Fig. 2). The pressure response at the gate location (P1 curve) can be separated into two regions. In the first one (until 25 s), the linearity between pressure and time verifies Darcy's law while the foam core is not deformed. After 25 s of injection, foam core compression occurs due to a local pressure built-up in the mold cavity. In the neighborhood of the gate, both porosity and permeability of the porous media increase, creating a discontinuity in slope of the pressure response – the resistance of the fluid to flow through the porous media decreases [3].

SIMULATION

Before using the mixed FE/SPH method to solve for hydro-mechanical coupling during sandwich manufacturing, the method has been quantitatively validated for isothermal RTM filling of monolithic composite parts. Comparisons of flow front positions and pressure distributions were made with the FEM-based commercial simulation tool PAM-RTM (ESI, France) and gave excellent agreements.

Lagrangian particles and finite elements are combined to model resin and sandwich core respectively (Fig. 3). The fluid response is transferred to the foam core using contact algorithms. The skins are modeled as porous regions in which Lagrangian particles are evolving. The foam is modeled as an elastic material which is initially loaded under compressive stress. This initial compressive load is calculated from the equilibrium between the fiber reinforcement and the foam compression at the closing of the mold [3]. When the foam is being compressed, more volume becomes available to the flow of resin, either by expansion of the porous material, or by the creation of a thin layer of free volume between the foam core and the porous material. Practical limitations do not allow to include this effect directly in the geometry of the computational model, but it is possible to derive simple mathematical expressions for the porosity and permeability as a function of the local core displacement. User-defined subroutines allow to include this effect in the simulations.
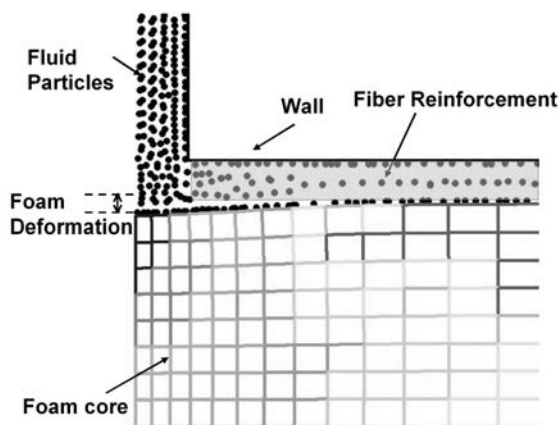
Fig. 3 Close-up of the foam deformation at the gate. Grayscale of the FE mesh represents the stress levels in the foam.
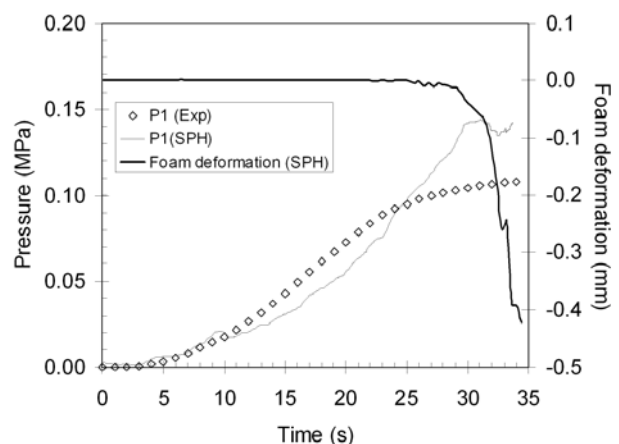
Fig. 4 Injection pressure and foam deformation

Figure 4 shows the simulation results compared to experimental data. Injection pressure responses match very well. After an initial pressure built-up, the increase slows down once the foam starts to deform. The experimental and numerical pressure responses are in excellent agreement. The foam deformation at the gate is also given from the simulation. Figure 3 is a close-up look at the foam deformation in the neighborhood of the injection gate after 35 s of injection. Because of technical issues it was not possible to measure it experimentally, using a contact-less displacement sensor for instance, since the experiments were carried out in an industrial mold. However, the foam core deformation (few tenths of millimeters) and the pressure response effects obtained in this study from the simulation, are in the same range as those obtained by Binetruy et al.[3] and Wirth et al.[2] for RTM using similar experimental conditions. Finally, the results of the study show that the simulation tool should be very sensitive. As a matter of fact, few tenths of millimeters of foam core crushing have a tremendous effect on the pressure response at the injection gate.

CONCLUSION

The mixed FE-SPH method has been successfully validated to solve for hydro-mechanical coupling in RTM. The accuracy of the method allows to properly predict the pressure and core crushing response during the injection. The mixed FE-SPH method is very generic and versatile, and should have the potential to solve for non-isothermal fluid flows.

ACKNOWLEDGEMENTS

REFERENCES

[1]: Al-Hamdan A., Rudd C.D. and Long A.C., Dynamic core movements during liquid molding of sandwich structures, *Comp. Part A*, **29A**, 273-282 (1998)

[2]: Wirth S. and Gauvin R., Experimental analysis of core crushing and core movement in RTM and SRIM foam cored composite parts, *J. Reinf. Plast. Comp.*, **17**(11), 964-988 (1998)

[3]: Binetruy C. and Advani S.G., Foam core deformation during liquid molding of sandwich: Modeling and experimental analysis, *J. Sand. Struc. Mat.*, **5**(4), 351-376 (2003)

[4]: Pham X., Trochu F. and Gauvin R., Simulation of compression resin transfer molding with displacement control, *J. Reinf. Plas. Comp*, **17**(17), 1525-1556 (1998)

[5]: Han K., Lee L.J. and Liou M., Fiber mat deformation in liquid composite molding. II: Modeling, *Polym. Comp.*, **14**(2), 151-160 (1993)

[6]: Farina A., Cocito P. and Boretto G., Flow in deformable porous media: Modeling & simulation of compression molding processes, *Math. Comput. Model.*, **26**(11), 1-15 (1997)

[7]: Sawley M., Cleary P. and Ha J., Modeling of Flow in Porous Media and RTM using SPH, *2nd Int'l Conference on CFD in Minerals and Process Industries, CSIRO*, Melbourne, Australia (1999)

[8]: Pillai K.M., Governing equations for unsaturated flow through woven fiber mats. Part 1. Isothermal flows, *Comp. Part A*, **33**(7), 1007-1019 (2002)

[9]: Lucy L.B., A Numerical Approach to the Testing of Fusion Process, *Astron. J.*, **88**, 1013-1024 (1977)

[10]: Gingold R.A. and Monaghan J.J., Smoothed particle hydrodynamics: Theory and application to non-spherical stars, *Mon. Not. R. Astr. Soc.*, **181**, 375-389 (1977)

[11]: Monaghan J.J., Simulating free surface flows with SPH., *J. Comput. Physics*, **110**, 399-406 (1994)

[12]: Tolls S. and Manson J.A.E., An analysis of the compressibility of fiber assemblies, *Proceedings FRC Conf.*, 25/1-25/10 (1994)

MODELING AND SIMULATION:
II PROCESS DESIGN AND OPTIMIZATION

Optimization of Mold Filling Parameters during the Injection Compression Molding Process

M. J. Buntain, and S. Bickerton

Center for Advanced Composite Materials, Department of Mechanical Engineering,
The University of Auckland, Private Bag 92019, Auckland, New Zealand.
e-mail: s.bickerton@auckland.ac.nz

SUMMARY:

The Injection Compression Molding process is a variant of the Liquid Composite Molding group, and requires careful specification of processing parameters if the potential benefits are to be realised. A method has been developed for determining optimal processing parameters for reduction of resin injection pressures, total compaction loads and process cycle times. Response Surface optimization Methodology was applied, providing an efficient method for identifying optimal solutions without the requirement of an exhaustive search of the design space. A 2D Finite Difference flow simulation has been applied to predict the transient resin injection pressures and total compaction forces that are generated during Injection Compression Molding processes. Two optimization scenarios are presented, where different weightings have been placed on the importance of minimizing clamping force, injection pressure and cycle time. The results illustrate how optimum processing parameters can vary depending on the specific requirements of different manufacturers.

KEYWORDS: Injection/Compression Molding, Liquid Composite Molding, Optimization

INTRODUCTION

The Injection Compression Molding (I/CM) process is one of the many Liquid Composite Molding processes that have been developed over the past few decades. I/CM involves liquid resin being injected through a porous fiber reinforcing preform, held within a partially closed two-piece rigid mold. After the required volume of resin has been injected, the mold cavity is reduced to its final thickness. This final phase of compaction forces the resin to flow through the remaining dry areas of the preform and compacts the fiber reinforcement to the designed fiber volume fraction. The resin is then cured, allowing the final composite part to be demolded. I/CM is similar to the more recognized Resin Transfer Molding (RTM) process, where resin is injected into a porous fiber reinforcing preform held in a mold cavity at the final part thickness. Relative to RTM, I/CM can provide reductions in required clamping forces or cycle times. To realize these potential benefits, careful specification of the processing parameters is required [1,2].

In specifying an I/CM process, several design variables must be selected. The choice of the injection flow rate, mold cavity thickness during resin injection, and the rate of compression during the final compaction phase are critical. Non-optimal processing parameters can result in excessive manufacturing cycle times or the requirement of oversized injection and compaction machinery. Through optimization of design variables considering both physical and economic requirements, an ideal processing solution can be identified for a specific mold geometry. To allow for efficient optimization of the I/CM design variables, a Response Surface Methodology (RSM) optimization algorithm has been adopted and coupled with a finite difference process simulation. The results of this study illustrate the strong dependence of any optimal solution to the specific requirements of a particular manufacturing scenario.

PROCESS SIMULATION

A 2D Finite Difference simulation has been developed to predict required resin injection pressures, total vertical compaction loads and process cycle times. This simulation is applicable to any axisymmetric part geometry where the resin is injected at the center of the mold. The resin pressures generated within the mold cavity have been modeled using Darcy's law, requiring the permeability of the intended fiber reinforcing material to be known. Several permeability tests were completed on a chopped strand mat material, to allow a realistic approximation of permeability to be applied. The reinforcing material compaction behavior has been modeled using a "mixed elastic" compaction stress model where the effects of stress relaxation, compaction rate dependency and resin lubrication effects are accounted for. The total clamping force applied to the mold is calculated, being composed of forces due to reinforcement compaction and generated resin pressure. Full details of the process modeling development have been presented elsewhere [3,4].
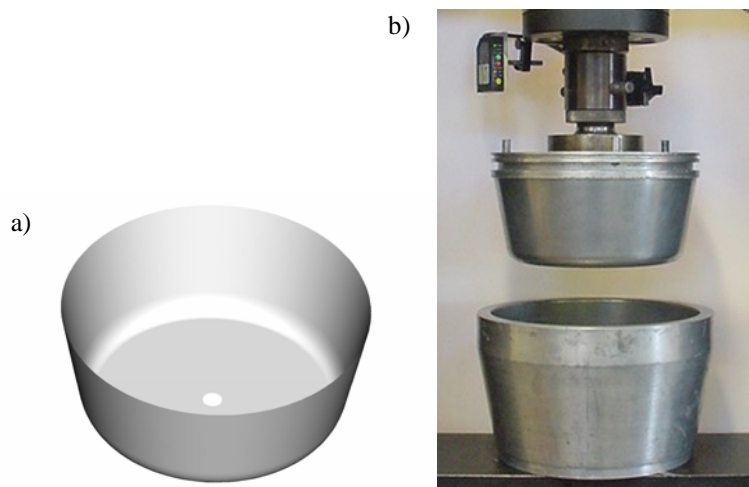
Fig. 1 a) Model of part geometry addressed in experimental study. b) Mold installed for experimentation.

To verify the accuracy of the process simulation, an experimental program has been completed [4]. Both RTM and I/CM Experiments were completed in a conical basin shaped mold having a central injection gate.

The fluid injection pressures and total vertical compaction loads were recorded during a range of experiments, where the cavity thickness during the resin injection phase, the rate of resin injection and the rate of compaction during the final compression phase were varied. The part geometry used in the verification of the mold filling simulation is pictured in Fig. 1. Sample clamping force traces recording during three I/CM experiments are shown in Fig 2, and are compared to simulated force traces. Comparison of process simulation and experimental results have provided good confidence in the application of the process simulation within the optimization study described below.
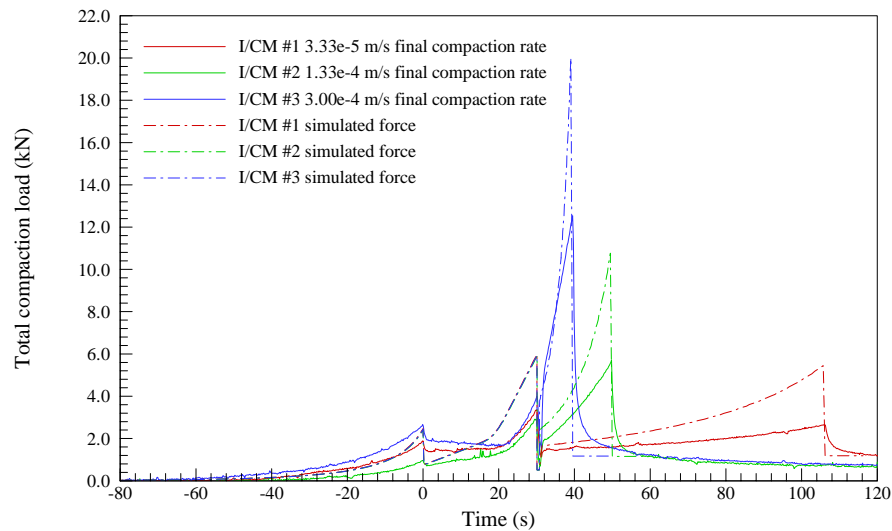
Fig. 2 Comparison of three experimental and simulated compaction force results

I/CM OPTIMIZATION METHODOLOGY

In this study three critical design variables have been varied to achieve an optimized process, the cavity thickness during the resin injection phase, the applied resin injection pressure at the injection gate, and the mold clamping force applied during the final phase of compression. An ideal I/CM process will result in a process with minimal injection pressure and clamping force, that is completed in a minimal process cycle time. These requirements are conflicting as a minimal injection pressure and clamping force will inevitably result in a maximum cycle time. This has prompted the development of a weighted process Performance Indicator (PI), provided in Eqn 1. W_F, W_P and W_t are weighting factors, and can each be set between 0.0 and 1.0, effectively ranking the importance of minimizing the maximum clamping force, injection pressure and process cycle time respectively. The PI developed has been used as an objective function during optimization, with a smaller value of PI representing a more ideal process.

$$P.I. = W_F \cdot \frac{F_{max\ process}}{F_{max\ allowable}} + W_P \cdot \frac{P_{max\ process}}{P_{max\ allowable}} + W_t \cdot \frac{T_{process}}{T_{cycle\ max\ allowable}} \qquad (1)$$

A Response Surface Methodology (RSM) algorithm has been applied in this study, through the HyperOpt (formally SOSopt) optimization platform.

RSM has been used extensively in the optimization of products and processes where multiple design variables can be altered to improve measures of design performance [5]. RSM is a numerical search method that uses an iterative approach to converge upon an optimal design solution. The concept behind RSM is that given the objective function values of a set of design solutions, a mathematical approximation of the objective function can be formulated. If there are two design variables in the problem then the approximation of the objective function can be visualized as a 3D surface, giving the methodology the 'response surface' title. The mathematical approximation of the objective function allows numerical techniques to be used to approximate the design variables that would result in the minimum objective function value. When a minimum value of an approximated objective function or 'response surface' has been determined then more design solutions can be evaluated in that region of the design space allowing a new mathematical approximation of the objective function to be formulated. As more design points are added to the response surface, the error between the approximated and actual objective function decreases. When sufficient design points are added to achieve a required level of convergence, then the design variables that result in the minimum of the approximated objective function can be assumed to be optimal.

Two optimization case studies are presented here using different weighting factors in the Performance Indicator to represent different manufacturing scenarios that may occur in industry. The geometry studied is the large circular tray of diameter 1.28m pictured in Fig 3. The final part thickness was set at a uniform 4.0mm, producing a target fiber volume fraction of 30% using a chopped strand mat reinforcing material. Resin viscosity was set at 0.13 Pa.s, typical of a low viscosity resin system used in LCM processes.
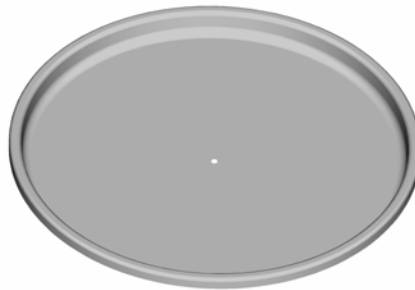
Fig. 3 Mold geometry utilized in the optimization study.

The PI weighting factors applied in each study, and the optimal solutions identified are outlined in Table 1. Study A places a large emphasis on minimizing the clamping force and a moderate emphasis on minimizing the process cycle time with $W_F=0.6$ and $W_t=0.3$. Study B places the main emphasis on minimizing the cycle time with very little requirement placed on minimizing the forces or injection pressures with $W_t=0.8$ and both W_F and W_P set at 0.1.

Table 1. Outline of case study objectives and optimal results identified.

	Study A			Study B		
	W_F	W_P	W_t	W_F	W_P	W_t
PI Weighting Factors	0.6	0.1	0.3	0.1	0.1	0.8
Compaction force (N)		765442			1740370	
Resin injection pressure (Pa)		250597			326417	
Cavity thickness during injection (mm)		16.0			22.9	
Minimum objective function value		0.380			0.2505	
Process cycle time (s)		144.6			56.82	
Iterations required to find optimum		21			22	

During the iterative RSM optimization process, many combinations of possible processing parameters are evaluated such that the effect of changing each can be gauged. The process parameters evaluated as the RSM optimizations progressed in each of these studies are presented graphically in Figures 4 and 5. At each iteration the resulting value of the objective function (PI) found from a set of processing variables is plotted against the primary vertical axis (at left), while the values of the input processing variables are normalized against maximum feasible values and plotted on the secondary vertical axis (at right). The optimization iteration number is plotted on the horizontal axis and it can be seen that as the optimization progresses the PI reduces (more optimal).
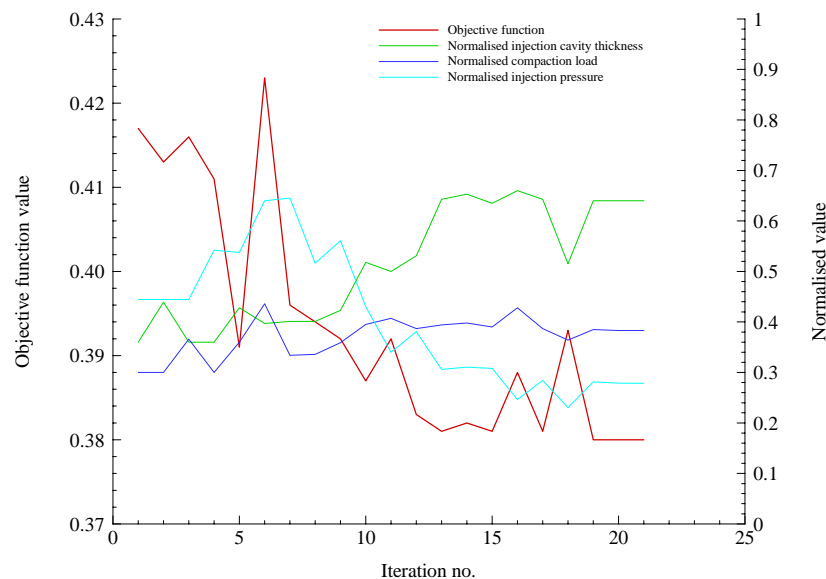
Fig. 4 Processes evaluated during study A RSM optimization.
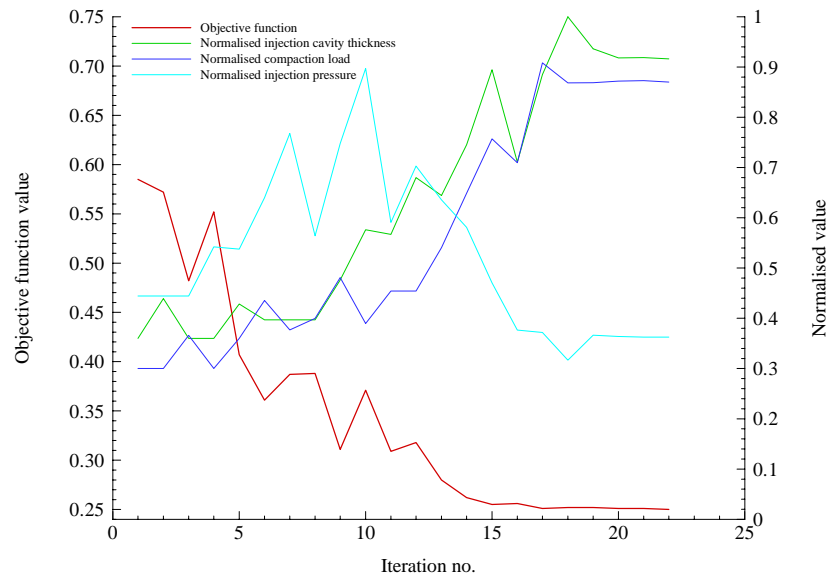
Fig. 5 Processes evaluated during study B RSM optimization.

DISCUSSION

It can be seen in Figures 4 and 5 that as the iterative RSM optimization progressed, the objective function (PI) continually dropped until converging upon an optimal solution. The optimal solution identified in each study was different, as expected with the weighting factors on minimizing injection pressure, clamping force and cycle time being different for each case. The optimal process identified by each study has selected injection pressures, clamping forces and process cycle times that reflect the performance indicator weighting factors that were applied. In study A, the optimal process identified requires clamping forces that are significantly lower that identified in study B. This is because the weighting placed on the importance of minimizing the clamping force is considerably higher in study A than in study B. The optimal process identified in study B results in a process where the cycle time is close to a third of that identified as optimal in study A. This is because the importance of minimizing the cycle time was high in study B.

CONCLUSIONS

This study has shown that for any I/CM manufacturing scenario where the requirements of reducing injection pressure, compaction force and process cycle time can be ranked, then optimal processing parameters for that process can be efficiently identified through the use of an RSM optimization algorithm. As I/CM is increasingly considered as an alternative to RTM, the greater number of process parameters to be specified must be acknowledged (i.e. cavity thickness at initial injection, mold closing speed during compaction phase).
The presented optimization methodology allows for efficient specification of an I/CM cycle that can closely match the requirements of each manufacturing scenario considered.

REFERENCES

1. X-T. Pham, and F. Trochu, "Simulation of Compression Resin Transfer Molding to Manufacture Thin Composite Shells", *Polymer Composites*, Vol. 20, pp. 463, 1999.

2. S. Bickerton, M.Z. Abdullah, "Modeling and Evaluation of the Filling Stage of Injection/Compression Molding", *Comp Sci and Tech,* Vol *63*, no. 10, pp. 1359, 2003.

3. S. Bickerton, M.J. Buntain, and P.A. Kelly, "Challenges for Modeling Filling during Liquid Composite Molding Processes", *Proceedings of the Polymer Processing Society 19th Annual Meeting*, Melbourne, July 7-10, 2003.

4. M.J. Buntain, "Optimization of Mold Filling during the Injection Compression Molding of Fiber Reinforced Plastics", ME Thesis, University of Auckland, New Zealand, 2003.

5. R.H. Myers, and D.C. Montgomery, "Response Surface Methodology, Process and Product Optimization Using Designed Experiments" 2nd ed., USA: John Wiley and Sons, Inc., 2002.

Evolutionary Algorithms Based Optimization of Filling Process in LCM

Boris Meier, Gion A. Barandun, and Paolo Ermanni

Center of Structure Technologies
ETH Zurich, Switzerland
boris.meier@imes.mavt.ethz.ch

SUMMARY: Simulation of LCM processes has been implemented in the in-house developed Finite Elements toolbox "FELyX" in 2-D, 2.5-D and 3-D. A Finite Element mesh with triangle, tetrahedral or brick elements is used. The program can be coupled to Evolutionary Algorithms, which are efficient methods for multi-parameter optimization. They have been successfully tested in structural optimization. Coupling to LCM simulation allows the determination of optimum process parameters including gate and vent locations as well as injection pressures and timing considering different objectives. Objective functions can be defined with respect to laminate's quality (no air entrapments) on the one hand and a short filling time on the other hand. The method was validated experimentally by optimizing the LCM process for complex 2-D and 2.5-D geometries. The obtained gate locations and injection pressures show remarkable improvements compared to heuristic optimization.

KEYWORDS: Liquid composite molding, simulation, evolutionary algorithms.

INTRODUCTION

Liquid composite molding (LCM) technologies are used for efficiently manufacturing structural composite parts of high quality. Further advantages are relatively low equipment and tooling costs as well as an excellent design flexibility.

Finding an optimal process configuration is usually the product of a long-term and expensive trial-and-error procedure. Reliable process simulation tools might contribute to significantly reduce production time, costs, and risks. There is commercial software available for LCM simulation.

Shojaei [1] presents a good review on the progress of modeling and simulation research in this field for the last two decades. In the field of optimization some research studies have been conducted coupling LCM simulation to Evolutionary Algorithms [2-6]. Special focus lies on definition of a process quality index that is needed as a measure of "optimization degree". There is still a need for further research, especially in 2.5-D and 3-D optimization. In our case we concentrate on efficient process cycles, i.e. short filling times and no dry spots.

BODY OF THE PAPER

Implementation of LCM simulation

FELyX (the Finite Element LibrarY eXperiment) [7] is an open-source finite element solver that has been developed at the Center of Structure Technologies, ETH Zurich. It is implemented in the generic programming language C++ and it includes a tool for structural analysis as well as for isothermal LCM simulation. Theory of LCM simulation has been discussed thoroughly in previous studies [1,8].

FELyX is able to store large amounts of data to hold the entire information of a finite element model. It stores all data in vectors templated with the appropriate data objects. The implementation in FELyX shows a high flexibility compared to commercial programs.

- Different element types can arbitrarily be mixed.
- Vents can be closed automatically as soon as the flow front reaches them.
- Gates can be opened and closed at any time, even time-dependency of pressure is applicable.
- Gates can be opened as soon as the flow front reaches them. This is useful for sequential injection.
- FELyX is independent from any pre- or post-processor since in- and output file formats can be adjusted.
- Additional element types may be added.
- Non-isothermal features could be implemented without reorganizing the whole code.
- New research results can be implemented immediately into the code.

Finally FELyX is at least as computationally efficient as commercial software.

Coupling to Evolutionary Algorithms

In order to develop optimal LCM manufacturing processes, the use of several simulation runs is unavoidable. There is a multi-objective optimization task with the two objectives of minimum injection time and complete fill.

According to the output parameters input parameters are varied. This could be done by any optimization procedure like heuristic optimization or by an optimization algorithm. Input parameters are gate and vent locations, gate pressures and timing of gates and vents.

Evolutionary algorithms are stochastic search methods that mimic the metaphor of natural biological evolution [9]. This method was implemented with the Evolving Object Library [10] and linked to FELyX (Fig. 1). It creates individuals of different process configurations. For each individual a simulation run is performed in parallel on an IBM cluster and the fitness is calculated with respect to the simulation's output parameters. The fitness determines which individuals will figure as parents for another generation of individuals (survival of the fittest).

Many LCM optimization studies in literature use node numbers as position variables of gates and vents. This does not seem to be appropriate since node numbers of similar value do not necessarily lie close to each other. Therefore a small change of node number could lead to a big change of the position of the node which leads to bad convergence behavior of the optimization algorithm. The present study uses Cartesian coordinates to describe locations.
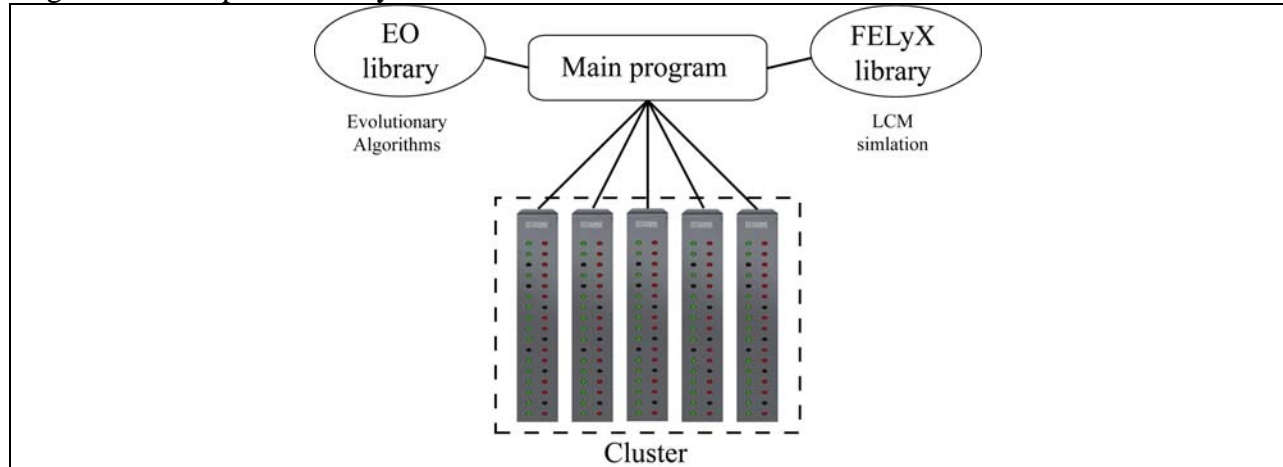
Fig. 1 Scheme of computational optimization procedure

Optimization in 2-D

A 2-D mold (550 mm x 125 mm) shown in Fig. 2 is considered. The numbers beside the gates denote the injection pressure in bar (10^5 Pa). Line injection at the bottom was left unchanged during the optimization.
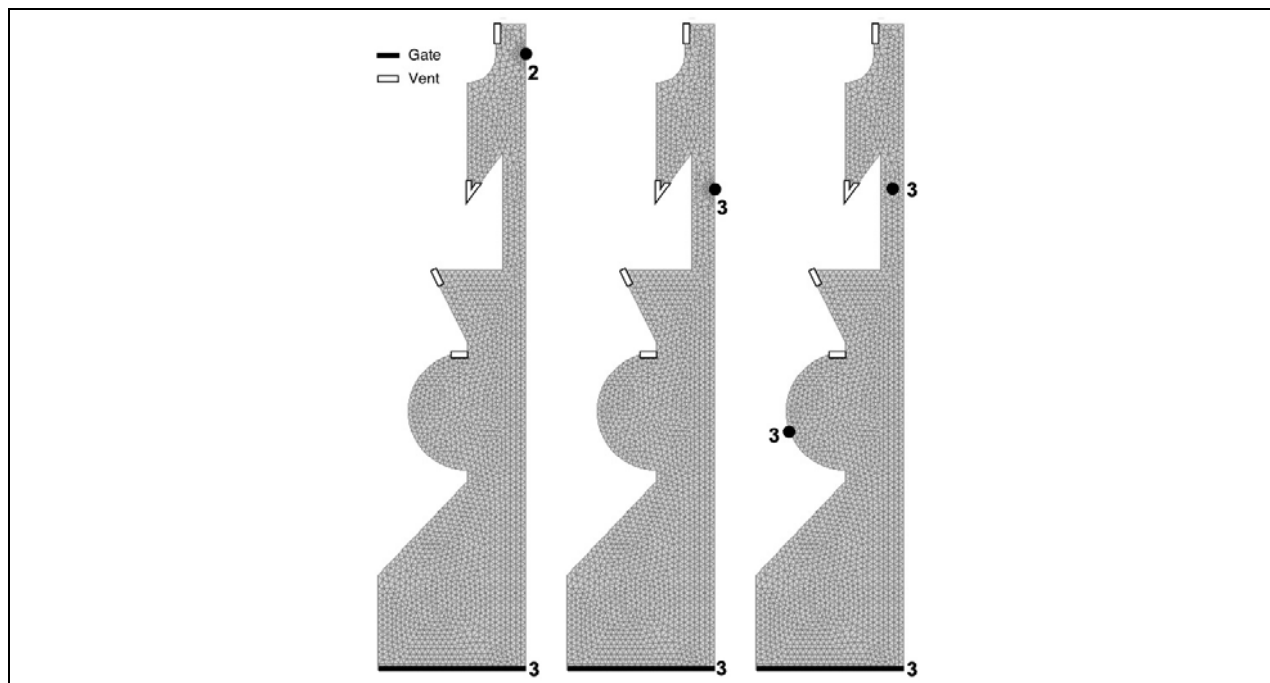
Fig. 2 Different process configurations
(left: original, center: 1 point gate optimized, right: 2 point gates optimized)

Original	1 point gate optimized	2 point gates optimized
319 s	225 s	106 s

Tab. 1 Filling time of different process configurations

The figure on the left-hand side shows the original process configuration developed during a diploma thesis, with a filling time of 319 s (Tab. 1). The figure in the center is the result of an optimization run with two variables: Gate position (right side) and pressure. As expected, the injection pressure was set to the maximum of 3 bar which leads to a much shorter filling time. In the figure on the right side an additional injection point is considered. The gate locations are considered to lie anywhere on the mold, i.e. there are 6 optimization variables now, four coordinates and two pressure values. The optimal configuration shows a remarkable improvement compared to the original process.

Injection pressure is usually applied to several nodes instead of one single node to avoid insufficient accuracy due to mathematical singularities [11].

Optimization in 2.5-D

A quarter of a wing-nose part (300 mm x 105 mm x 250 mm) shown in Fig. 3 is considered, having a preform permeability of 10^{-10} m^2 and the resins' viscosity is 0.1 Pa s. The part's thickness is 2 mm for z<=0 and 4 mm for z>0. Five vents are placed intuitively at the locations shown. The injection pressure is set to 3 bar.

The optimum spatial arrangement of three injection gates shall be obtained. Nine (3 x 3 coordinate components) variables optimization is performed using Evolutionary Algorithms. Population size is set to 30. After 50 generations the configuration shown in Fig. 3 turns out to be optimal. There are no dry spots and the filling time is at a minimum of 93 s.
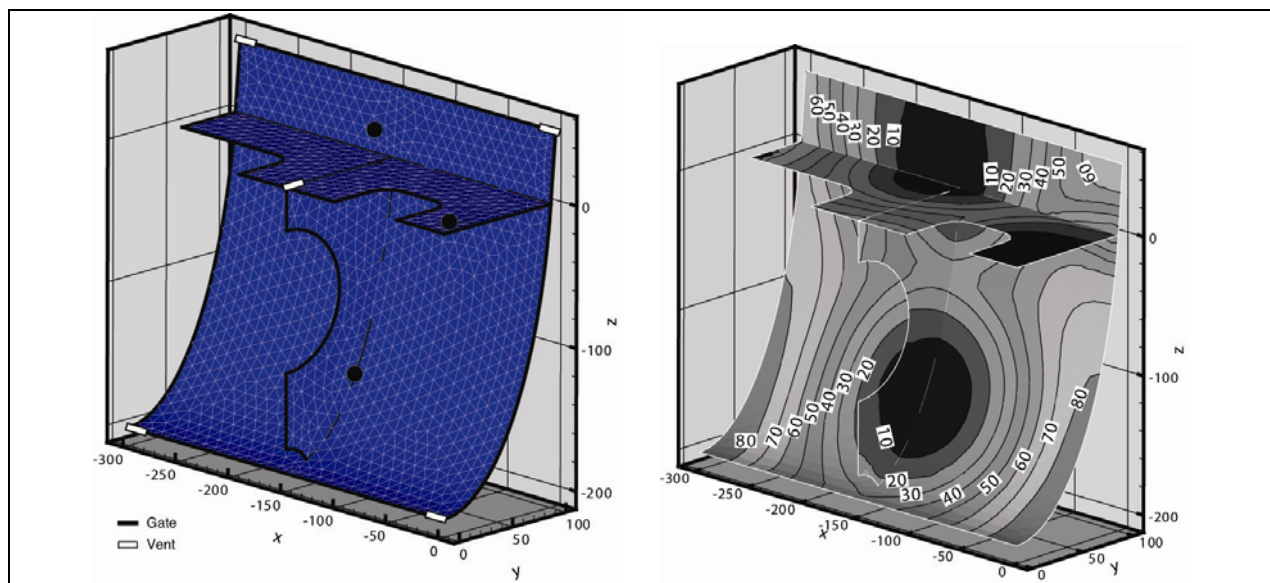
Fig. 3 Optimal process configuration and simulation result of a 2.5-D form
(left: mesh, gates and vents, right: isochrones)

Each injection gate is represented by three coordinates. Although the Evolutionary Algorithm identifies possible gate locations anywhere inside of the brick-like space spanned (-300<x<0, 0<y<105, -200<z<50) as indicated in Fig. 3, an additional algorithm finds the closest nodal points on the mold which are used as gates. A set of neighboring nodes can then be used by the FEM model to simulate the flow through the gate.

CONCLUSIONS

LCM simulation has been implemented. The simulation program is coupled to an optimization algorithm. Gate or vent locations are represented in the Evolutionary Algorithm in a new promising way that works in 2-D as well as in 2.5-D and 3-D. Results of optimization runs show efficient process configurations, that would hardly have been achieved by trial-and-error methods.

REFERENCES

1.   A. Shojaei and S. R. Ghaffarian, "Modeling and Simulation Approaches in the Resin Transfer Molding Process: A Review", *Polymer Composites*, Vol. 24, no.4, 2003 pp. 525.
2.   B. Y. Kim, G. J. Nam and J. W. Lee, "Optimization of Filling Process in RTM Using a Genetic Algorithm and Experimental Design Method", *Polymer Composites*, Vol. 23, no.1, 2002 pp. 72.
3.   S. Jiang, C. Zhang and B. Wang, "A Process Performance Index and Its Application to Optimization of the RTM Porcess", *Polymer Composites*, Vol. 22, no. 5, 2001, pp. 690.
4.   H.-W. Yu and W.-B. Young, "Optimal Design of Process Parameters for Resin Transfer Molding", *Journal of Composite Materials*, Vol. 31, no. 11, 1997, pp. 1113.
5.   W.-B. Young, "Gate Location Optimization in Liquid Composite Molding Using Genetic Algorithms", *Journal of Composite Materials*, Vol. 28, no. 12, 1994, pp. 1098.
6.   R. Mathur, B. K. Fink and S. G. Advani, "Use of Genetic Algorithms to Optimize Gate and Vent Locations for the Resin Transfer Molding Process", *Polymer Composites*, Vol. 20, no. 2, 1999, pp. 167.
7.   FELyX, The Finite Element library eXperiment, url: http://felyx.sourceforge.net (Version 0.31, 1.3.2004).
8.   A. Endruweit, "Investigation of the Influence of Local Inhomogeneities in the Textile Permeability on the Resin Flow in Liquid Composite Molding Processes", *Ph. D. thesis*, ETH Zurich (2003).
9.   P. Bentley, "Evolutionary Design by Computers", *Morgan Kaufmann Publishers, Inc.*, 1999.
10.   EO, Evolutionary Computation Framework, url: http://eodev.sourceforge.net (Version 0.9.3a, 1.3.2004).
11.   D. Modi, P. Simacek and S. Advani, "Sensitivity of Injection Gate Definition in Numerical Simulations of Mold Filling Processes", *unpublished*.

Monitoring Mold Filling and
Resin Cure in RTM

Murat Sozer[1], Goker Tuncol[2] and Alper Kaynar[3]

[1,2,3] *Koc University, Mechanical Engineering Department*
Rumeli Feneri Yolu, Sariyer, 34450, Istanbul, Turkey
[1]*Author to whom correspondence should be addressed, e-mail: msozer@ku.edu.tr*

ABSTRACT: Resin Transfer Molding (RTM) is used to manufacture continuous fiber reinforced polymeric composite parts. A thermoset resin is injected into a mold cavity previously filled with a reinforcing porous fabric preform. Both resin flow and properties of composite part are significantly affected by improper selection and preparation of material, and design of process parameters. In this study, thermocouple sensors were used to monitor both mold filling and resin cure. These sensors have advantages and disadvantages over other types of sensors such as pressure sensors. Fiber volume fraction measurements at different sections of panel parts indicated significant variations caused by several effects such as wash of fabric when resin reached a critical pressure, racetracking channels, and nonuniform compaction of mold plates. All these show that a smart control system is needed to automate RTM and reduce part rejection rate.

KEYWORDS: thermocouple, sensor, monitoring, RTM.

INTRODUCTION

In an RTM process, near-net-shape parts can be manufactured with high fiber content to meet mechanical strength and surface finish requirements [1][2]. In this process, a fabric preform is prepared by cutting and stacking glass or carbon fabric layers. The preform is draped over a tool surface. After the mold is closed, a thermosetting polymer is injected into the mold cavity to fill the empty space between the fibers. After complete filling, the ventilation and injection gates are closed. Typically, the filling time is several minutes or less. After the cure and solidification of the polymer, the mold is opened and the part is taken out.

A major issue in RTM process is incomplete mold filling due to the variations of raw material properties and then preparation. Since resin flow pattern is affected by these variations, a mold may not be filled completely, although it is filled completely under normal injection conditions in another injection. By using a control system such as that developed in [3][4][5][6][7][8], the variations in the process can be detected during the mold filling stage, and proper control actions can be taken to influence the flow pattern so that the mold cavity is filled completely. With a similar approach, in this study, an automated RTM system had the following five ingredients: (i) RTM injection machine from Radius Engineering [9], (ii) a modular mold, (iii) thermocouple sensors to monitor the mold filling and cure of resin, (iv) data acquisition cards and analysis computer program, and (v) mold filling simulation program, LIMS [10] developed by Suresh Advani, University of Delaware. This integrated system currently has some issues to be fixed for full automation, and they will be discussed here.

MOLD, MATERIALS and THERMOCOUPLE SENSORS

Mold

A general-purpose and research-based RTM mold was designed and then manufactured in a similar approach as in [6][8]. The bottom view of the lower mold part is shown in Figure 1. As seen in the figure, 45 multi-functional threaded holes (M20 = metric 20) are used for four different purposes: (i) inlet resin (injection gate), (ii) exit air (ventilation port), (iii) insert sensors into the mold cavity, (iv) to close the holes that are not needed. Some of the major characteristics of this mold are listed below:

- As many as 45 injection gates and ventilation ports are available on the mold.
- Visualization of mold filling through a transparent mold lid: This is needed to verify the success of the control system.
- Modular mold cavity: Many composite parts with different shape and dimensions can be manufactured by replacing a few modular sections of the mold.
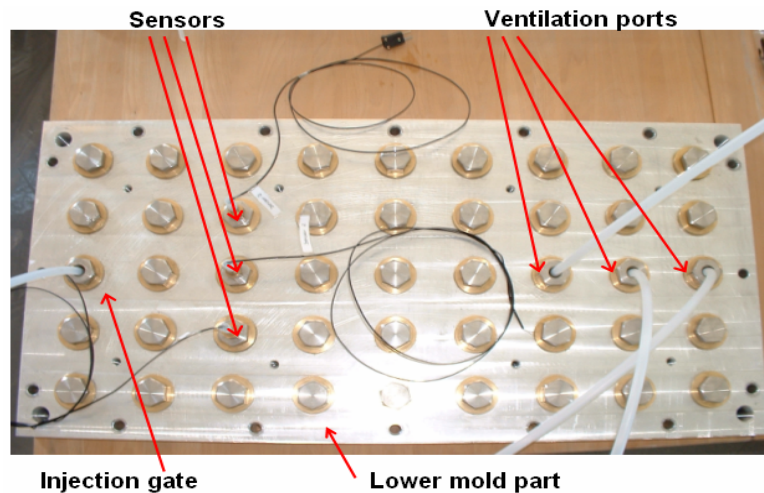
Figure 1. Bottom view of the lower mold part. There are 45 multi-functional bolts on the mold part. In this injection, 1 injection gate, 3 ventilation ports, and 3 sensors are used, and all the other multi-functional bolts are used as solid (i.e., no function).

Resin system

A room-temperature polyester, Dewester 196 (DYO Dewilux 511-0196) was used in the injections. The mixing ratio for cure reaction accelerator and curing agent was between 0.005 and 0.020 (weight based) depending on room temperature and storage time. Its viscosity at around $20^{o}C$ was measured to be about 0.77 Pa.s. However, this showed a significant variation with the storage time and from one batch to another. Its density was about 1.19 gram/cm^3 at the room temperature.

Fabric

E-glass plain weave fabric with an areal mass of 500 gram/m^2 was used. The fabric rolls were purchased from Fibroteks [11]. Warp and weft had the same width of about 4.5 mm. However, the empty spacing between them was about 3-4 mm in one direction and less than 1 mm in the other direction. Thirteen layers of fabric were cut and stacked, and then placed into the mold cavity with dimensions of 704 x 168 x 5 mm.

A fiber volume fraction of about 50% was achieved. Higher fractions could be obtained by compacting more layers of fabric under a press. The fabric preform had a length of 624 mm. The two empty channels with a length of about (704 – 624)/2 = 40 mm on both sides of the fabric were used to convert point injection and ventilation to line injection and ventilation.

Thermocouple Sensors

In RTM and similar processes, sensors are used to monitor mold filling and resin cure (cross-linking) for control purposes. Ideal sensors should not interfere with resin flow [12]. Some sensors (such as pressure transducers, thermocouples and direct current conductors) are placed on the surface of mold cavity, and they measure process variables such as resin pressure or temperature. Some other sensors (such as ultrasonic) are used externally [12]. One needs to consider the cost, ease of use, accuracy and reliability of the sensors when controlling mold filling and resin cure.

In this study, the following two J-type thermocouples were used: (i) National Instruments, 745685-J01, and (ii) Elimko Elektronik, 05T2JTTEA.

Compared to pressure sensors, major advantages of thermocouple sensors are: (i) they can be used for monitoring *both* mold filling and resin cure, (ii) they are cheaper.

In order to monitor the mold filling, the temperature of the polymer should be different from the ambient temperature. Although a room-temperature resin system was selected in this study, its temperature was raised above the room temperature by about 10°C before mixing the curing agent. This was easily achieved by heating the resin barrel of the Radius Engineering injection machine.

The designed thermocouple sensors are shown in Figure 2. A small copper part with high thermal conductivity was attached to the end of thermocouple in order to shorten the time delay in detecting the resin arrival.
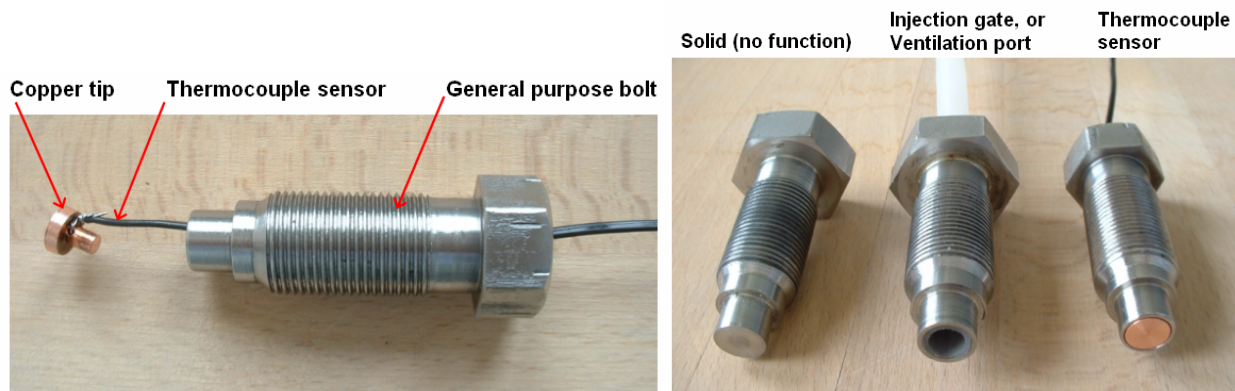
Figure 2: A thermocouple sensor and multi-functional bolts to be used on the lower mold part.

Three thermocouple readings were shown in Figure 3a during a mold filling. It took about 10 seconds to detect about 10°C temperature rise. Compared to pressure sensors, this is a disadvantage of thermocouple sensors used in this study. The control system works in such a way that when the temperature reading of a sensor indicates a specified ΔT, it is understood that the resin arrived there. In order to make a quicker detection of resin arrival, one may attempt to use a smaller ΔT such as a few degrees Celsius only. However, this might cause misdetection of resin arrival as there is a continuous noise in temperature readings as seen in Figure 3a. A filtering of noise is needed in order to have quick and reliable sensor readings.

Thermocouple sensor readings for three separate experiments were shown in Figure 3b during the cure and solidification stage. Due to the exothermic reaction, the temperature of the composite part increased gradually, and then decreased due to the conduction of the heat to the mold during cooling. It is clearly noticed in this figure that, as the curing agent mixing ratio was increased, the release of heat happened very quickly which also made the injection more difficult since the viscosity increased more rapidly.
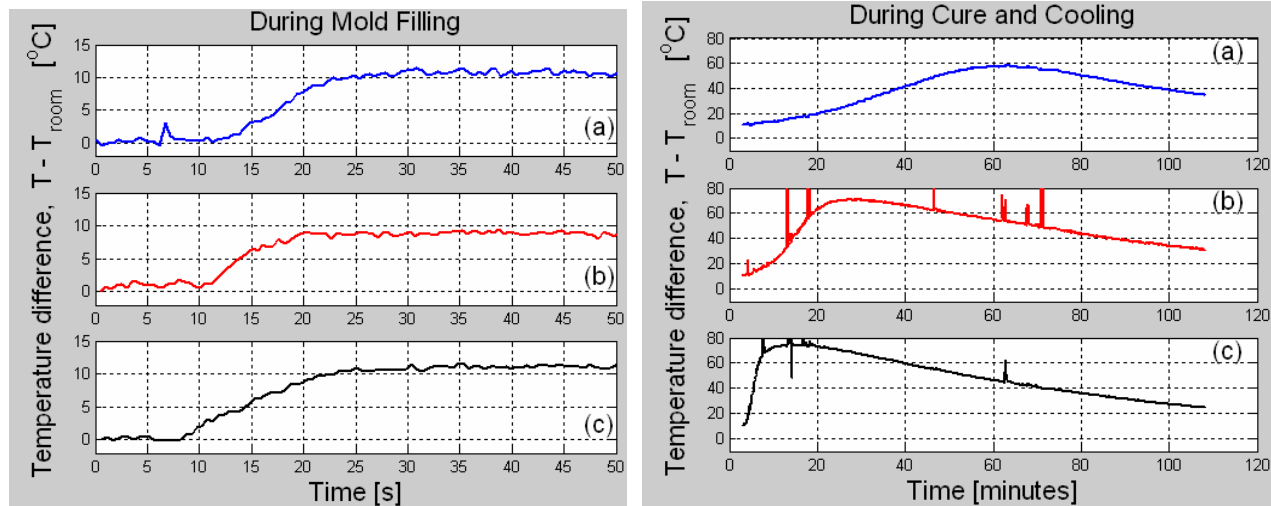
Figure 3. (Left): Temperature readings of three thermocouples during mold filling. (Right): Temperature readings of a thermocouple during cross-linking (cure) for three separate experiments. The mixing ratio of the "curing agent / polyester resin" is 0.005, 0.010 and 0.020 (weight based) in experiments (a), (b) and (c), respectively.

ISSUES

Although we tried to advance the RTM process toward more automation by using a control system, there are still some unresolved issues in this study. These are:

- Two-dimensional mold filling model was performed by using shell-like elements since the thickness dimension is much smaller than the in-plane dimensions. A sample mold filling simulation is shown in Figure 4 together with top view of the mold cavity and mesh. Due to insufficient compaction force applied by the bolts and stiffening bars, at some locations three-dimensional flow was observed through the transparent mold lid. The resin raced between the upper mold lid and the preform's upper side while the bottom side of the preform got saturated later. This condition is definitely a contradiction to the assumption of two-dimensional flow and corresponding mold filling simulations.

- Under constant flow rate injection, when the injection resin pressure reached above 15-20 bars approximately, wash (movement) of fabric preform was observed around the injection gate and also along the racetracking channels. In one of these extreme cases, where the maximum injection pressure reached 20 bars, the fabric preform was pushed toward the center, and wrinkled very significantly.

- Material properties (viscosity and gel-time) of Dewester 196 resin varied significantly as the room temperature changed from one injection to another, and also due to the storage time. The success of the control scheme and hence the injection depends on a reliable data base of the resin properties, which we are still working on.

- Upon a close examination of the part edges, it was observed that there is a less dense section of the reinforcing fabric adjacent to the mold wall. There are a few usually unavoidable reasons for this: (i) Some of the fiber bundles fall down from the fabric during the cutting and placement. (ii) Fiber wash due to high resin pressure.

- Specimens with 20 mm width were cut from one side of a part as shown in Figure 5. Average fiber volume fractions were measured as 0.23, 0.52, 0.58 and 0.50 along sections A, B, C and D, respectively. In order to investigate the variation of mechanical properties of specimen, a universal test machine was used as shown in Figure 6. The machine is capable of doing tension, compression and three-point bending (flexure) tests. However, the tests performed so far are inconclusive as the type of fracture is not consistent. The available punch of the machine has a fixture so thick that in some experiments it causes shearing. After modifying this fixture, the tests will be continued, and their results will be presented at the conference.
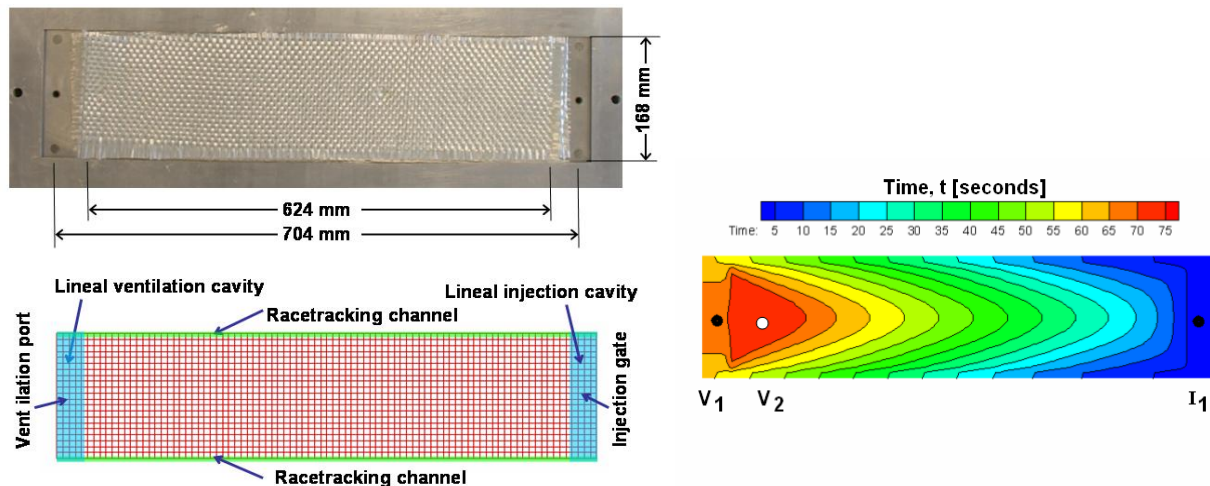
Figure 4. Mold filling simulation by LIMS [10] for a case with racetracking along the two sides. Different colors show the position of the resin flow front at different times. Simulation result suggests to activate a ventilation port at V_1 as well as V_2 in order not to entrap air, which will cause a dry spot otherwise.

Figure 5. Specimen to be cut from a composite part along the upper edge.
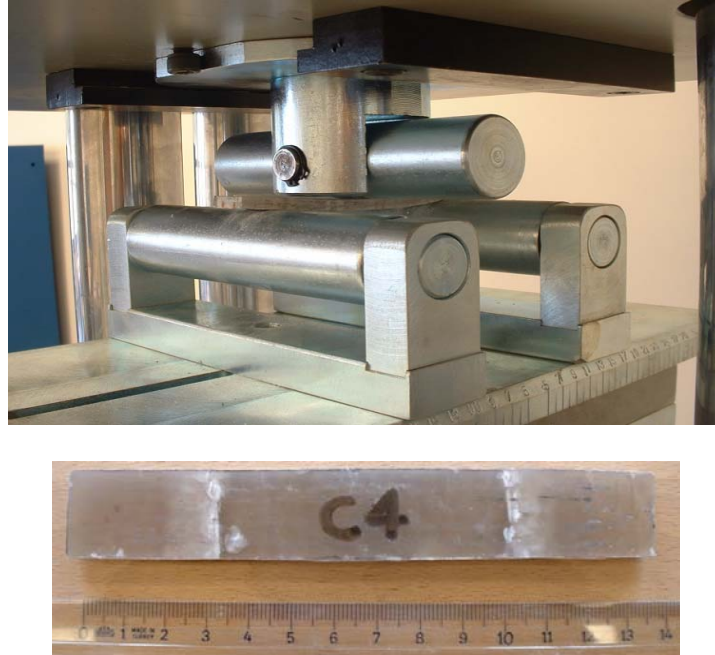
Figure 6. Three-point bending (flexure) test setup on a universal test machine; and a specimen

REFERENCES

[1] Advani, S.G., Sozer, E.M., ASM Handbook, Volume 21, Composites: Process Modeling, In volume chairs: D.B. Miracle and S.L. Donaldson, and chairperson: B.T. Astrom (editor), pp:423-433, Ohio, ASM International,

[2] Advani, S.G., Sozer, E.M., Process Modeling in Composites Manufacturing, Marcel Dekker, Inc., New York, (2002).

[3] Rice, B.P., Han, K., Lee, W.C., Intelligent process control for the resin infusion process, Proceedings of On-line Sensing and Control for Liquid Molding of Composite Structures, Annapolis, MD, (1999).

[4] Sozer, E.M., Bickerton, S., Advani, S.G., Use of sensors and simulations for strategic control of liquid composite mold filling process, CMA/SME, Composites Manufacturing and Tooling 2000 Conference and Tabletop Exhibits, Newport Beach, California, 167-190, (2000).

[5] Sozer, E.M., Bickerton, S., Advani, S.G., On-line strategic control of liquid composite mold filling process, Journal of Composites, part A: Applied Science and Manufacturing, 31:(12) 1383-1394, (2000).

[6] Stadtfeld, H.C., Sozer, E.M., Steiner, K.V., Advani, S.G., Approach towards an automated design environment for the resin transfer molding process, Proc 45th Int SAMPE 2000 Symp Exhibit 2000, 45(2), 1576–84, (2000).

[7] Hsiao, K.-T., Don, R.C., Estrada, G.A., Advani, S.G., Use of simulations, sensors and control methodologies to manipulate flow in liquid composites molding processes, Aerospace Congress & Exhibition, Seattle, WA, USA, (2001).

[8] Lawrence, J.M., Hsiao, K.-T., Don, R.C., Simacek, P., Estrada, G., Sozer, E.M., Stadtfeld, H.C., Advani, S.G., An approach to couple mold design and on-line control to manufacture complex composite parts by resin transfer molding, Composites: Part A, 33, 981–990, (2002).

[9] Radius 2100 cc Electric RTM Injection Cylinder, Radius Engineering, Inc., 3474 S. 2300 East, Salt Lake City, UT, USA.

[10] Simacek, P., Sozer, E. M., Advani, S.G., User Manual for DRAPE 1.1 and LIMS 4.0 Liquid Injection Molding Simulation, Technical Report UD-CCM 98-01, Center for Composite Materials, University of Delaware, Newark, (1998).

[11] Fibroteks Dokuma Sanayi ve Tic. A.S., Deniz mahallesi, Derince Sanayi Sitesi Yani, 41900, Derince, Kocaeli, Turkey.

[12] Heider D., Don, R., Thostensen, E.T., ASM Handbook, Volume 21, Composites: Cure Monitoring and Control, In volume chairs: D.B. Miracle and S.L. Donaldson, and chairperson: B.T. Astrom (editor), pp:692-698, Ohio, ASM International, (2001).

Process Simulation of LPM (<u>L</u>iquid <u>P</u>olymer <u>M</u>olding) in Special Consideration of Fluid Velocity and Viscosity Characteristics

Matthias Repsch[1], Ulrich Huber[1], Martin Maier[1],
Stefan Rief[2], Dirk Kehrwald[2], Konrad Steiner[2]

[1]Institut für Verbundwerkstoffe GmbH,
Erwin-Schrödinger-Straße 58, D-67663 Kaiserslautern
[2]Fraunhofer Institut für Techno- und Wirtschafsmathematik,
Europaallee 10, D-67657 Kaiserslautern

SUMMARY: Recently in RTM process technique in-situ polymerizing thermoplastics are a promising alternative for conventional thermoset matrix systems. The advantages of these systems are a low initial viscosity at the beginning of the process combined with the polymerization proceeding during injection. The low initial viscosity allows a fast mold filling even at a high fiber volume fraction which leads to a high fluid velocity especially at the beginning of the process. Additionally, the polymerization during injection leads to a change not only of the viscosity level but also of the viscosity characteristic to a shear rate dependent behavior. The high flow velocity as well as the shear dependent viscosity do not allow to model this kind of process by the generally accepted Darcy's Law which assumes low flow velocity and newtonian viscosity of the fluid. The intention of this paper is to investigate a high velocity fluid flow in a non-crimp fiber bed as well as the influence of visco-elastic fluid characteristic on the fiber bed microstructure.

KEYWORDS: Permeability, visco-elasticity, Newtonian, micro structure, Darcy's Law, high fluid velocity, viscosity characteristic, non-crimp

INTRODUCTION

RTM (Resin Transfer Molding) is a common process covered by the generic term LCM (Liquid Composite Molding) used to manufacture high performance parts. Recently an alternative for thermoset resins used in RTM is developing by in-situ polymerizing thermoplastics (ISPT). This kind of thermoplastics are polymerizing during mold filling which changes the flow behavior of the fluid from Newtonian to visco-elastic flow and causes a rise of viscosity by a factor of 100 starting from an initial viscosity of 17 mPas [1]. Due to these significant changes in flow characteristics it is necessary to adapt the process simulation software.

Most simulation tools are based on Darcy's law, which is one of the most common used empirical equation to describe flow through porous medias.

In its simplest formulation it takes the form:

$$v = \frac{K_f}{\eta_f} \cdot \frac{\Delta p}{\Delta x}$$

(1)

In this formulation v denotes the fluid velocity respectively the flow front speed, η_f represents the viscosity of the infiltrating fluid, K_f stands for the permeability of the porous media and $\Delta p/\Delta x$ represents the pressure gradient [2]. Darcy's Law is restricted to slow inertia free flow and a low, newtonian viscosity [3]. The key parameters in this equation are the permeability and in this particular case the viscosity. Usually the permeability is determined by one- or multidimensional flow experiments which are described elsewhere [3]. These experiments can for example be evaluated by the constant method, in which the permeability over the flow length is assumed to be constant. The following equation thus results directly by integration from Darcy's Law:

$$K_{const} = \frac{m \cdot \eta}{2 \cdot p_0}$$

(2)

In this formulation K_{const} denotes the permeability to be calculated, η represents the constant viscosity of the fluid, p_0 stands for the constant injection pressure and m represents the ascending slope of the straight line resulting from linearized experimental values in a diagram square of flow path over time. [4].

FLUID CHARACTERIZATION

Apart from the permeability the fluid viscosity plays a key role in the use of Darcy's Law. The change in viscosity over time and temperature as well as the dependency of the viscosity on the shear rate has to be included. Due to the difficult handling of ISPT systems a replacing fluid, a duromer system (Ly113 / Hy97) from the Huntsmann company was used for this study. For reference issues a standard vegetable oil with newtonian flow behavior was selected. The viscosity of the vegetable oil is ranging from 0,055 Pas at 20°C to 0,036 Pas at 27,5°C in which the all isothermal flow experiments have been executed.

To quantify the viscosity characteristics, measurements have been executed by using a plate-plate rheometer. The viscosity evolution of the epoxy resin at high shear rates and different temperatures is shown in fig. 1a. The initial viscosity is decreasing from 0,690 Pas at 20°C to 0,325 Pas at 27,5°C but at the same time the polymerization velocity is rising significantly. The shear rate dependency of the viscosity was measured in a range from 0,023 1/s to 225 1/s. The results are displayed in fig. 1b. These graphs illustrate that at low shear rates (> 10 1/s) the fluid viscosity is strongly shear rate dependent. Apparently the viscosity at shear rates lower than 0,1 1/s depends only on the shear rate but not on the degree of polymerization. This effect occurs because the macromolecular chains need only one energetic level to keep their degree of orientation independent from the chain length and therefore independent from the grade of polymerization. In respect of the shear rate dependency the epoxy is showing the same behavior as thermoplastic melts.
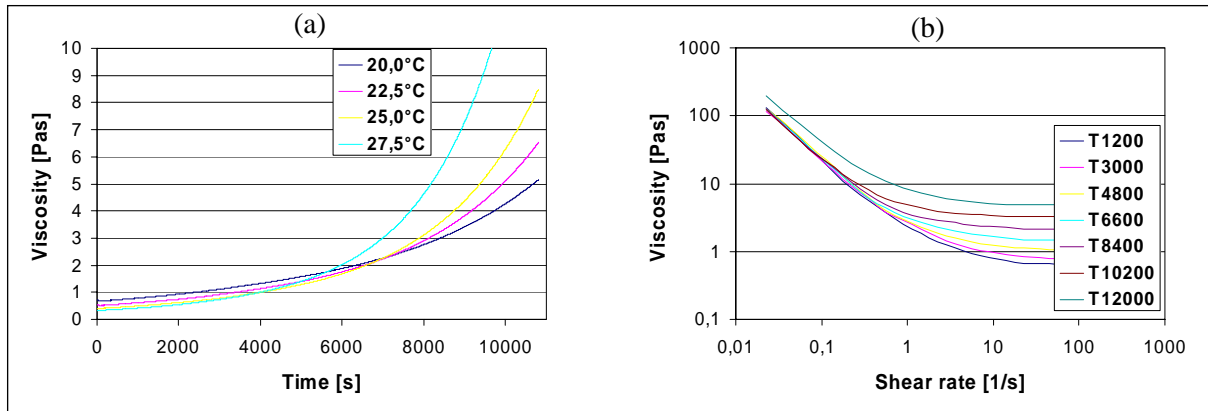
Fig. 1: a) Temperature dependent viscosity over time for the epoxy resin
b) Time dependent viscosity over shear rate for the epoxy resin

FLOW EXPERIMENTS

In order to get a reference, flow experiments were performed fulfilling the restrictions of Darcy's Law to sufficient low flow velocity and to shear rate independency of the fluid. Flow experiments have been carried out with vegetable oil using a fabric with a fiber volume content of 26% and an injection pressure of 0,2 bar. Fig. 2 (a) shows the square of flow path over time. It can be seen that the experiment displayed by graph 1 can be fitted quite well with a straight line through the origin of the diagram given by the Darcy's Law theory. This indicates that the experiment fulfills sufficiently the restrictions of Darcy's Law. Then, experiments with an injection pressure of 0,5 bar were executed. The results are shown by graph 2 in fig. 2 (a). It is obvious that the experimental values are differing from the straight line predicted by Darcy. Up to a flow length of approximately 0,17 m (0,03 m²) the flow is affected by inertia resulting in an overestimation of the flow front position by Darcy. From this point onward microstructural investigations are indicating flow channels which are apparently due to the higher pressure. This changes the permeability of the fiber bed resulting in a flow front velocity underestimated by theory.
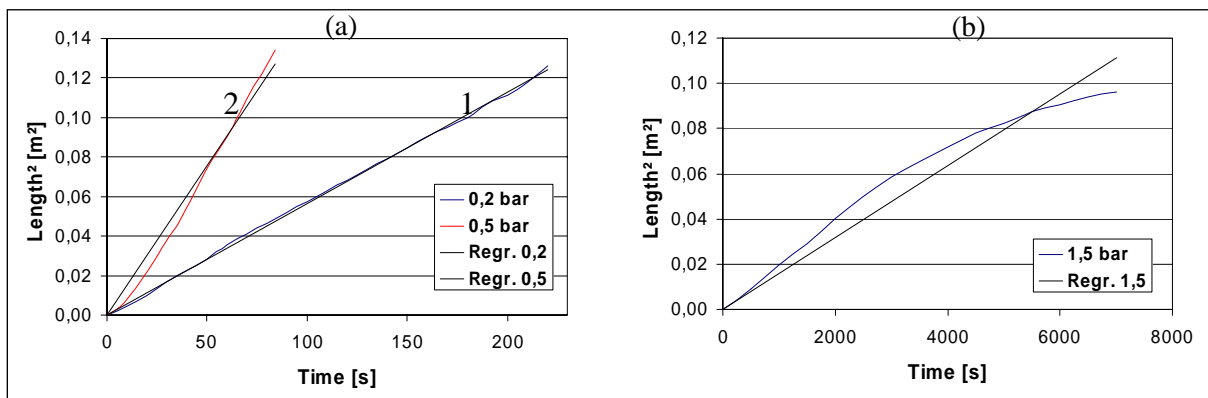
Fig. 2: Square of flow path over time at an injection pressure of 0,2 bar (a) and 0,5 bar (b)

In the next step the differences of Darcy- and visco elastic flow were quantified. Again, the experiment with vegetable oil and 0,2 bar injection pressure stands for reference. For this purpose a fiber volume fraction of 50%, an injection pressure of 1,5 bar and epoxy resin as fluid were used. Fig. 2 (b) shows the square of flow path over time of this experiment. Once more up to a flow length of approximately 0,17 m (0,03 m²) an inertia affected flow can be observed by a discontinuity in curve progression. A region of flow channel dominated the flow up to 0,24 m (0,06 m²) followed by the end section where the flow is decelerated because of a rising viscosity resulting from decreasing shear rates.

MICRO STRUCTURAL INVESTIGATION

The aim of the micro structural analysis was to investigate the influence of the fluid flow on the non-crimp fabric bed. The sample plates used for the investigation are produced with the same set of parameters mentioned in the paragraph above. In order to analyze the fluid influence polished cross-section cuts have been prepared from the plates impregnated by the epoxy resin. From this samples micrographs were taken to investigate the mesoscopic distribution of bundles, the developing flow channels inside the fiber bed and the distribution of the filament inside the bundles itself. The micrographs in fig. 4 are cut from the flow path length of 15 mm, 115 mm, 265 mm, 365 mm. It can be seen that the bundle distribution at the beginning of the flow path is nearly homogeneous. Picture 4 (b) and (c) at 115 mm and 256 mm flow length show, that with proceeding flow length a forming of flow channels takes place in the fiber bed influencing the flow front velocity during injection as already stated. This forming of flow channels can be observed reproducibly in all produced plates. In the boundary areas of the single fiber bundles a higher fiber volume fraction than in the mid area can be observed. A possible explanation for this effect is the transversal impregnation of the bundles [5]. Picture 4 (d) shows that the bundle distribution is again nearly homogeneous but the bundles are less compacted than at the beginning of flow. This change of the flow mechanism might be due to the lower flow speed and pressure gradient. It can be assumed, that the main flow switches from macroscopic to microscopic flow.

(a) 15 mm	(b) 115 mm
(c) 256 mm	(d) 365 mm
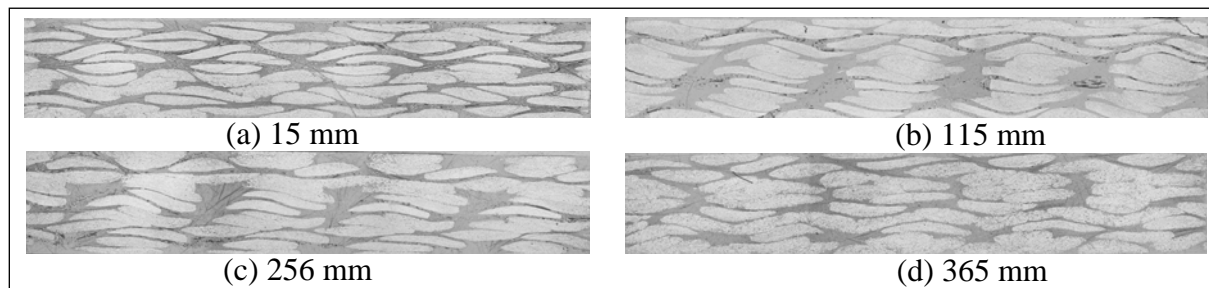
Fig. 4: micrograph of impregnated fiber bed at the (a) beginning, (b), (c)middle and (d) end of flow path

MICROSTRUCTURAL SIMULATION

In order to quantify the influence of the shear thinning characteristic of the fluid on the velocity distribution numerical simulations were performed. Fig. 5 shows the results of these simulations. The dimensionless flow speed v / v_{max} for a newtonian (center) and a shear-thinning fluid (left) in a highly resolved detail of a fiber bed, as well as for a newtonian (right top) and a shear-thinning (right bottom) fluid in the whole fiber bed at low resolution is displayed. All the results shown here are computed for periodic boundaries of the domain and a no-slip condition at the fiber boundaries. The results indicate that flow inside fiber bundles is negligible compared to flow between fiber bundles, and that for shear-thinning fluids the flow rate through the pores is higher than for comparable Newtonian fluids. This last result is in compliance to the experimental results which showed a higher flow front speed for the shear thinning fluid compared to the newtonian reference
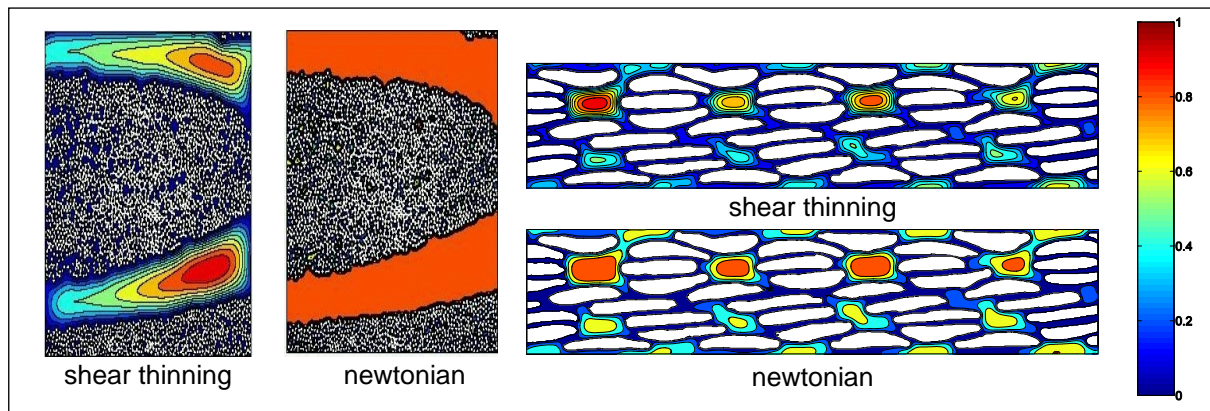
Fig 5: Dimensionless flow speed v / v_{max} for a newtonian and a shear-thinning fluid

CONCLUSION AND PERSPECTIVES

It can be stated that flow channel driven flow and therefore transversal impregnation of bundles is one of the most important mechanisms for transfer molding processes. From this arises the need to understand and to investigate the role of the microstructure during the process. One further aim is to detect the impregnation mechanisms on a micro structural level to achieve a more accurate flow simulation on a macroscopic scale.

REFERENCES

[1] R.H.J. Eder, Cyclics Thermoplastics - Properties and Processing, *IVW Schriftenreihe*, Volume 25, pp. 33-43, (2001)
[2] H.P. Darcy, Les Fontaines Publiques de la Ville Dijon, Victor Dalmont, Paris, 1856
[3] Huber, U., Zur methodischen Anwendung der Simulation der Harzinjektionsverfahren, *IVW Schriftenreihe*, Volume 26, Dissertation University Kaiserslautern, (2001)
[4] Flemming, M., Ziegmann, G. & Roth, S., Faserverbundbauweisen – Fertigungsverfahren mit duroplastischer Matrix, Springer-Verlag: Berlin and New York, 1999
[5] Huber, U., Maier, M.: Flow Behavior in saturated and unsaturated unidirectional fiber beds - a flow model, *Proceedings, FPCM-6 (2002)*, pp. 85-85, Auckland, New Zealand

A Knowledge-Based Flow Process Of Injection Molding in the Large Complicated Polymer Composite Manufacturing

H. K. Lee[1], Y. S. Kim[1], H. S. Lee[1], G. E. Yang[1] and H. G. Kim[2]

[1] Division of Mechanical & Aerospace System, Chonbuk National University,
City of Jeonju, 561-756, KOREA:geyang@moak.chonbuk.ac.kr
[2] Corresponding Author, Department of Mechanical Engineering, Jeonju University,
City of Jeonju, 560-759, KOREA:hkim@www.jeonju.ac.kr

SUMMARY: A knowledge-based flow process is presented for the large body injection-molding technology that is a difficult technique because of many factors and its interactions during molding process. DOE(Design of Experiment) is used to construct the optimal mold design condition and molding process. CAE(Computer Aided Engineering) is used for obtaining the mold process analysis and design, and CAI(Computer Aided Instruction) is introduced for the results of production molding process. The flow process of large body is systematically planned and finally constructed the knowledge-based flow process with DOE, CAE and CAI. The proposed flow process is implemented for molding process of automobile front bumper facia. It is found that the proposed knowledge-based flow process

INTRODUCTION

Injection molding has high productivity with accuracy and forming capacity of component parts. The plastic injection molding process has been used widely for mass production. However, it is difficult to produce large parts by injection molding. They have some problems of productivity and accuracy in molding process, compared to molding of the small parts. The large body molding technology is consequential for production of modular parts such as automobile component parts and aerospace parts[1,2].
For example, large bodies contain automobile front and rear bumper and instrument panel, and so on. Recently, the more automobile parts are produced in modular parts, being formed by LIMBT(Large Injection-Molded Body Technology). DOE can extract main factors and interactions among the factors to identify properties of injection molding process. Integration of DOE and computer aided technology supports a knowledge-based flow process for mold design to production molding in large injection-molded body technology.

This paper proposes a knowledge-based flow process for LIMBT, which can applied to automobile parts, such as bumper and instrument panel and so on.

CAE AND CAI

CAE and CAI can find results of variables for molding and production process. CAE is applied to analyze mold design and molding process. The polymeric flows in the filling phase can be approximated to a Hele-Shaw model[3]. Assuming an incompressible and non-Newtonian fluid, the equations for the filling phase of polymer can be written as the below equations[4]. These equations are continuity equation, momentum equation, and energy equation, respectively.

$$\frac{\partial u}{\partial x} + \frac{\partial v}{\partial y} + \frac{\partial \omega}{\partial z} = 0 \tag{1}$$

$$\frac{\partial p}{\partial y} - \frac{\partial}{\partial z}(\eta\frac{\partial v}{\partial z}) = 0 , \quad \frac{\partial p}{\partial y} - \frac{\partial}{\partial z}(\eta\frac{\partial u}{\partial z}) = 0 \tag{2}$$

$$\rho\, C_p(\frac{\partial T}{\partial x} + u\frac{\partial T}{\partial z} v\frac{\partial T}{\partial z}) = \eta\gamma^2 + k\frac{\partial^2 T}{\partial z^2} \tag{3}$$

where (x, y, z) are the Cartesian coordinates and (u, v, w) are the velocity components, respectively. T is the temperature, p is the pressure, ρ is the density, Cp is the specific heat and k is the thermal conductivity of the material whilst, η and γ are the shear viscosity and the shear rate.

CAI can be used to inspect the results of molding process and production process, which is corresponding to a follow-up experiment. The results to factors of injection-molded parts are found by the monitoring system and the 3D dimensional metrology. The 3D scanning inspections are based on 3 dimensional laser scanning and dimensional analysis. The measuring tolerances are within 20 μm with space geometry operations. The dimensional accuracy of parts is analyzed, compared with the geometric model of parts to check shrinkage and dimensions of the parts as shown in Fig. 1.
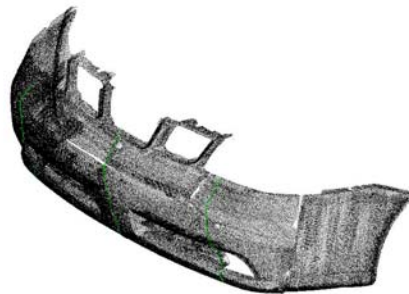
Fig. 1 3D scanning data and sectional dimension analysis

The monitoring system has pressure and temperature sensors, which are installed within the injection mold to detect molding temperature and pressure such as holding pressure and maximum pressure and temperature of melt polymer resins. The molding process factors are analyzed with the results calculated from CAE, and then compensated for accurate controlling the molding process and working conditions to construct a knowledge-based flow process. The monitoring system scheme is given in Fig. 2.
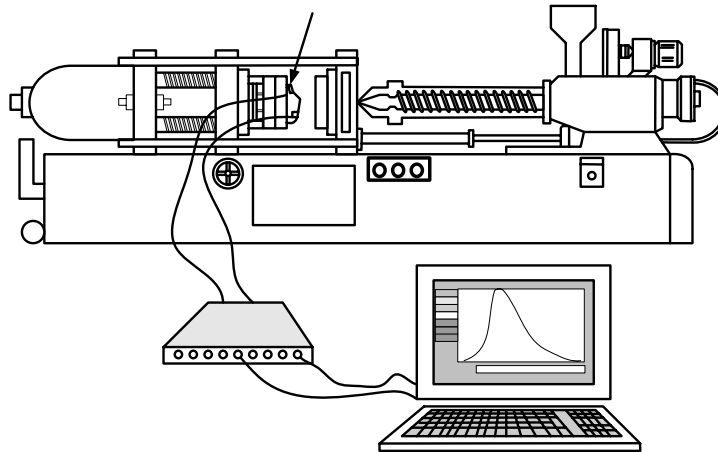
Fig. 2 Monitoring system scheme for injection molding process

DESIGN of EXPERIMENT

DOE has been used to systematically investigate process variables or product variables which can affect quality of parts. The DOE procedure consists of 4 steps: planning to define problems and objectives, screening to reduce the number of variables by defining the key variables, optimization to determine the optimal values and results for experiment factors, and verification to perform a follow-up experiment and confirm the optimal results.[5]

In mold design, main factors are main gate systems, side gate systems, and number of sub-gates, and so on. Fig. 3 shows gate systems and gate location. The geometrical shape and size of main gate and sub-gate are given with their location on the parts.
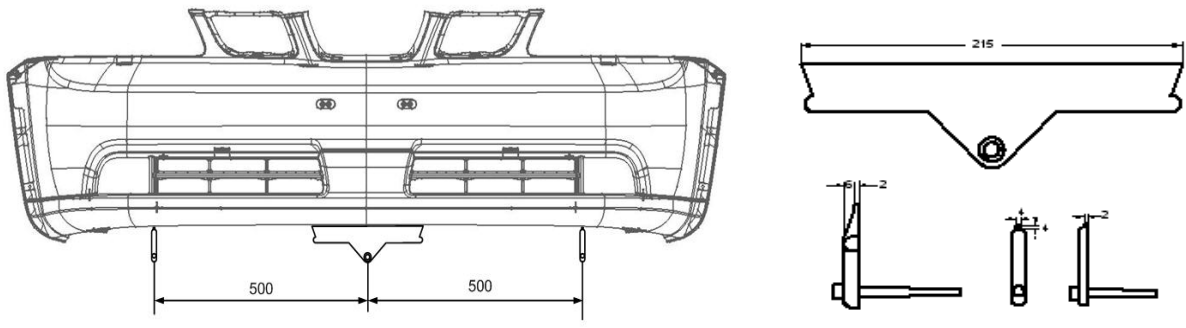
(a) Gate location   (b) Gate systems
Fig. 3 Gate systems and gate location

Main factors of molding process are holding pressure and mold temperature, and so on. The molding process can be analyzed by CAE system with the given conditions. The mesh generation and process analysis are shown in Fig. 4. And, the other important factor is cooling system, which can determine cycle time and shrinkage, and so on. However, the cooling channel is expensive and complicated so that the cooling system is fixed. The cooling channel is not considered as main factors in this study. Fig. 5 shows the cooling channel of the bumper facial injection mold.
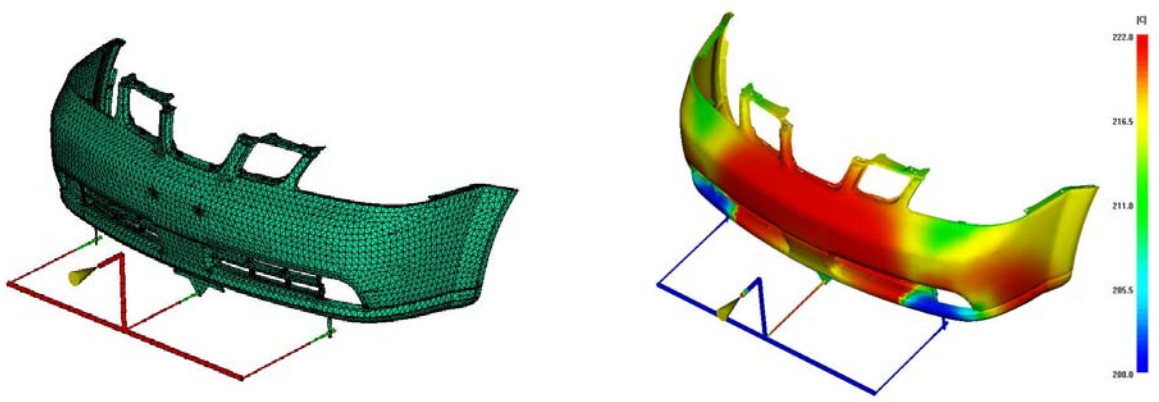
(a) Mesh generation   (b) Analysis of molding process
Fig. 4 Mesh generation and analysis of molding process
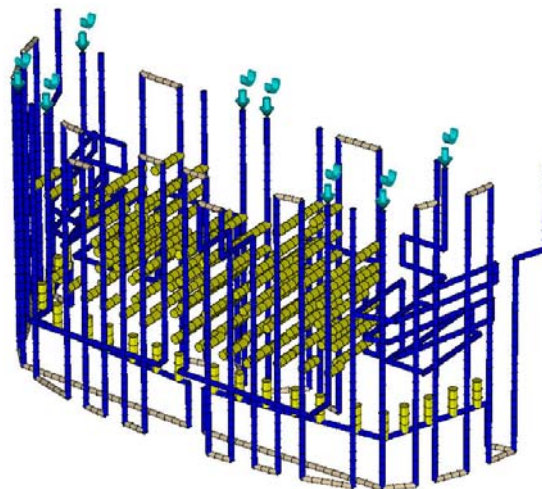
Fig. 5 Cooling channels of bumper facia injection mold

KNOWLEDGE-BASED FLOW PROCESS

The knowledge-based flow process is constructed on integration of computer aided technology and DOE. The DOE is applied in 3 steps; mold design process, molding process, and production process. Each step has many factors to affect the quality of its process. Results of DOE can be found by CAE in case of mold design process and molding process. And, Results of DOE in molding and production process is measured by CAI, which can measure values of variables in physical molding and production process. At the first time, main factors are simulated in 2 levels. The interactions among factors and main factors are selected. And then, the factors and interactions are simulated in 3 levels and repeat the previous process. For example, injection molding of bumper facia is planned and constructed based on the proposed knowledge-based flow process. Polymer resin of bumper is a kind of PP, reinforced with fiber to enhance physical properties. Table 1 explains the DOE in 3 steps of bumper facia.

Table 1 DOE schemes for injection molding of bumper facia

Items	Mold design process	Molding process	Production process
Main factors	Main runner system Sub runner system Gate system	Filling profiles Packing profiles Mold temperatures V/P change time	Injection pressure Injection velocity Packing profile Hot runner temperature V/P change time Metering volume Mold temperature difference
Level	2	2	3 or 2(mixed)
Orthogonal array	$L_8(2^7)$	$L_{81}(3^{40})$	$L_{18}(2 \times 3^7)$

CONCLUSIONS

The knowledge-based process of large injection-molded body is studied on integration of DOE and computer aided technology such as CAE and CAI. Large injection-molded body is complicated technology so that DOE are applied systematically in monitoring and controlling many factors of the process. CAE is applied in mold design process to optimize mold design and molding process. And, CAI is introduced in molding and production process to find optimal process conditions. For example, bumper facia reinforced with fiber is implemented on the knowledge-based process.

REFERENCES

1. H. S. Kim, J. S. Son, Y. T. Im, "Gate location design in injection molding of an automobile junction box with integral", Journal of Materials Processing Technology, Vol. 140, 2003, pp.110~115

2 H. Y. Kim, J. J. Kim, Y. J. Kim, " The injection molding analysis and the mold design for automotive plastic fender", J. of The Korean Society for Technology of Plastic, Vol.6, No.6, 1997, pp.489~499

3. H. P. Kim, Y. J. Kim, "A study on the effects of filling and packing phases on injection molding process", Trans. of the KSME, Vol. 10, No.2, 2002, pp.44~53

4. J. H. Yoo, H. S. Kim, "The effects of injection molding conditions of ploypropylene on the linear shrinkage and weight of molded parts" KSME, Vol.19, No.2, 1995, pp.322~329

5. J. Krottmaier, "Optimizing Engineering Designs", McGraw-Hill, New York, 1993.

MODELING AND SIMULATION:
III. FLOW AND CURE

Role of Filling Simulation in LCM Process Design

Pavel Šimáček[1] and Suresh G. Advani[1,2]

[1]*Center for Composite Materials, University of Delaware, Newark, DE 19716*
[2]*Department of Mechanical Engineering, University of Delaware, Newark, DE 19716 And*
Corresponding Author: advani@udel.edu

SUMMARY: Numerical simulations of the mold filling process in various Liquid Composite Molding (LCM) techniques, in which the fiber reinforcements represent the porous media and the polymeric resin is the impregnating fluid, have been successfully utilized for over a decade now. They continue to be under dynamic development and their utilization has expanded to design and optimization of the process, control of the impregnation process and adaptation to new LCM techniques such as the Vacuum Assisted Resin Transfer Molding (VARTM). This paper briefly describes the modeling and implementation of these features in a numerical simulation. We discuss these challenges in the framework of Liquid Injection Molding Simulation (LIMS) developed at the University of Delaware with examples that demonstrate its usefulness.

KEYWORDS: Process Modeling, Liquid Composite Molding, Flow in Porous Media, Process Control and Optimization.

INTRODUCTION

The Liquid Composite Molding refers to a number of processes that use liquid resin to impregnate the stationary fibrous preform. The two variations of this process that are of particular interest are Resin Transfer Molding (RTM) and Vacuum Assisted Resin Transfer Molding (VARTM).

During the RTM Process, the preform is placed into the mold cavity, the mold is closed and the resin is injected into the cavity under pressure. Once the liquid resin fills the mold cavity, it cures, during which the resin hardens due to the gelling of the polymer network forming the matrix of the composite, allowing the part to be de-molded. Note that the mold walls are considered rigid and preform is stationary during the injection. This technique is well known and has been traditionally applied to moderately large parts in various applications.
The VARTM process is similar, but the mold is one-sided. The fiber preform is placed on the mold plate. The other face of the preform is covered with a flow enhancement layer known as the distribution media and the assembly of the mold plate, preform and distribution media is encapsulated in a plastic bag. Vaccuum is drawn to compact and to hold the preform stationary. Vacuum pulls the resin into the distribution media and the fiber preform. Once the preform is saturated with resin, the part is cured and de-molded. This process is gaining popularity for manufacturing of larger parts, mainly because of lower tooling costs.

However, the one-sided mold complicates achievement of dimensional tolerances [1], though some heuristic remedies are available.

In this paper, we will address resin injection and preform saturation. It is useful to predict the resin flow during mold filling as it offers guidance for the selection of the injection gate location and the last regions to fill provide the location of vents in the mold to displace the air.

APPLICATIONS OF MOLD FILLING SIMULATION

The physical reality of the manufacturing process dictates what should be taken into account and included in the simulation to describe the process physics. Simulations have to address all significant issues that are encountered during the particular manufacturing process to be of value in manufacturing. In the wide range of LCM processes, different aspects of the impregnation physics become more (or less) significant. The simulation is then called upon to model these physical aspects.

Traditionally, the mold filling simulations were used to find the necessary vent location and to establish process pressure and time ranges [2-8]. This definitively proved to be more useful than the prohibitively expensive method of trial and mostly error to settle on gate and the vent locations to produce a composite structure without dry spots.

Although the introduction of the simulations helped in the selection of gates and vents in the mold during the manufacturing process, LCM processes tend to show significant variability in the input data. The imprecise cutting and placement of the preform is the most significant source of this variability. This makes it necessary to introduce optimization and control in the filling process to increase the yield despite this variability. Thus, the full potential of the simulations can be realized if one can use them for optimization of injection location(s) and other parameters [9-11], and to design robust adaptive injection systems for process control in the presence of variabilities [12].

Combining Elements of Various Dimensions: Distribution Media Model

The question whether a two-dimensional or three-dimensional model should be used to numerically simulate the mold filling has been raised since the first attempts to simulate RTM filling. The majority of LCM manufactured parts are geometrically thin shells. This suggests that simulation of the filling process using two-dimensional shell elements in three-dimensional space will be numerically efficient and be able to describe the flow accurately.
Unlike the plate, beam and solid elements in finite element stress analysis, the pressure and flow computation during the filling simulation allows one to combine 1-, 2- and 3-dimensional elements within a single mesh. Therefore, thick parts can be represented by three-dimensional elements and one-dimensional elements are superior in modeling runners and race-tracking channels. With the introduction of distribution media in VARTM processing, three-dimensional modeling becomes mandatory to capture the flow-front lag in the thickness direction.

The combination of two-dimensional element modeling of the distribution media and some geometric features, such as ribs, with the three-dimensional model of the preform allows one to resolve issues that arise due to large element aspect ratios (Figure 1).
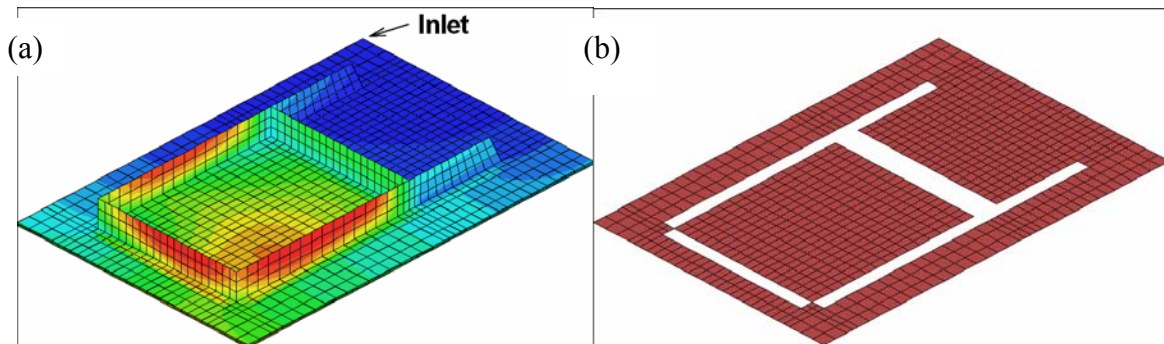
Figure 1: VARTM infused panel (modeled as 3D) with 2D ribs: (a) Simulation results (b) Two-dimensional model of distribution media that was placed on three dimensional mesh representing the fiber preform.

Combining Elements of Various Dimensions: Fiber Tow Saturation

In typical textile preform, the pores between the fiber tows are much larger than those within fiber tows. Consequently, the pressure driven flow fills them first, leaving unsaturated fiber tows behind the flow-front partially filled (Figure 2a.), where they act as a sink term until they are fully saturated. The phenomenon can be simulated by modeling the sink term by appending one dimensional element to each node in the mesh as shown in Figure 2b. The properties of this element are set to capture the behavior of the fiber tows, while the porosity of the original mesh is reduced to compensate for the volume of intra-tow pores. Simulation is run as usual, with the fill factor in the new nodes corresponding to the fiber tow saturation. The complete process may be automated using the scripting language within the simulation, since the material parameters are readily accessible. While the size of the system increases and the simulation performance somehow decreases, it is still possible to simulate injection into large and complex parts in very short (minutes) time frame as shown in Figure 2c, a box consisting of flat two-dimensional panels, with low level of race-tracking along the corners. Contour plot show the saturation of fiber tows. The lag between macroscopic flow-front and fully saturated fiber tows is emphasized [13].
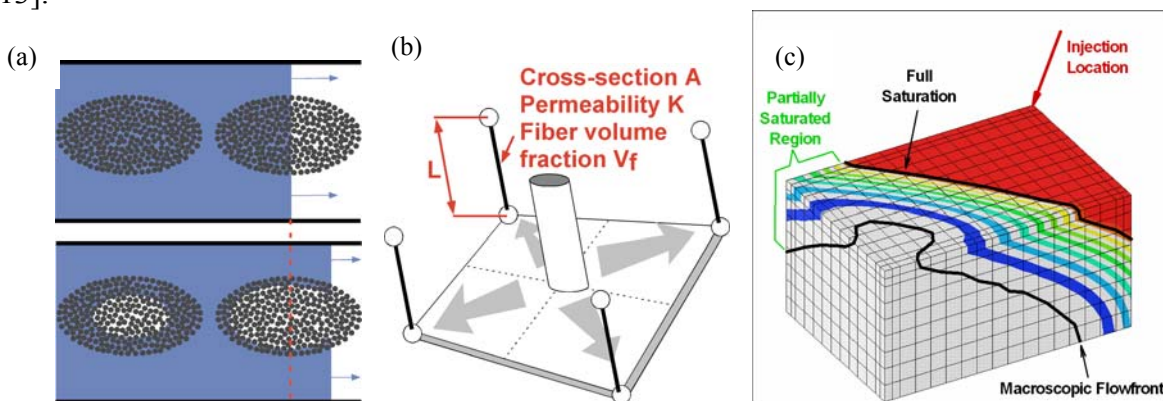
Figure 2 (a) Fiber tow saturation (b) Modeling fiber tow saturation with one dimensional elements appended to the mesh (c) Fiber tow saturation in a box mold with racetracking [13].

Optimization

Conventionally, one uses the filling simulation to verify existing part and process design and to ensure the cavity is filled without any dry spots. User might utilize the simulation as a tool to optimize the filling process, either to minimize the filling resources (time or required pressure) or to reduce the process sensitivity to expected variations in component properties [11]. In both cases, one usually varies the location of inlets and outlets to minimize the prescribed cost function.

Theoretically, the exhaustive search of optimal solution of the model problem is possible due to its discretized nature, but it is prohibitively time consuming in non-trivial cases. Hence, one either reduces the pool of admissible vent locations [15] or couples the simulation with optimization methods such as genetic algorithms [11,16] or similar techniques. Even then, the number of cases to be simulated is large. To handle this in real time, the simulation code must be very fast and the model must be simple and capture the necessary physics. Also, the input and output data for individual cases must be processed automatically by a computer (Figure 3). This requires a very tight coupling between optimizing code such as a genetic algorithm and the simulation package making it necessary to have an advanced scripting possible within the simulation code or/and runtime control of the simulation by the optimization code.
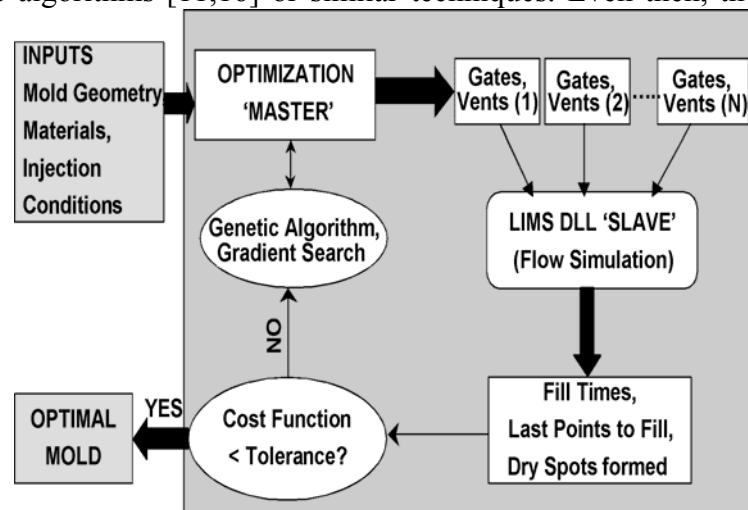
Figure 3: Flow Chart of RTM process optimization [13]

Sensing and Control

The material and process parameters in LCM manufacturing show evidence of variations [14,17-18]. Most commonly, the preform permeability can vary along the edges due to imperfect fit and non-repeatable placement, causing the resin to flow faster along the edges (race-tracking). Such race-tracking effects could significantly change the behavior of the predicted (or experimentally observed) flow front pattern [19]. As race tracking is a function of how the preform is placed and the edge effects, it is difficult to forecast its exact magnitude. To address this issue, one can monitor the situation in the mold via the use of flow sensors [20] and invoke corrective actions according to the sensor output. The corrective actions may include opening or closing inlets or vents or just modifying the injection parameters such as the flow-rates. The simulation is necessary to model possible scenarios, to find the "optimal" control actions and to verify the resulting control strategy.

Figure 4 shows an example of how one can use simulations to develop and test a control strategy to avoid dry spot formation by directing the flow of resin towards the vents by the opening and closing the auxilliary injection gates once the sensors have identified the correct scenario in action. Note that in order to deal with limits on driving pressure during VARTM processing, one commonly applies various sequential injection schemes to reduce the filling time. For such situations, the closing and opening of injection inlets may be triggered by resin arrival at specific locations, so this process can be classified as a rudimentary control.

To simulate sensing and control, the simulation program must provide two mechanisms. First, it should be able to search for the corrective action. This is fundamentally an optimization process. Thus, all of the requirements mentioned above will apply. Tight integration with control program that performs the search is necessary, though advanced built-in scripting can also accomplish the goal. Second, the simulation must provide the "virtual" sensor output during the filling process and allow changes in inlets and outlets during the filling process. This requirement is simple but very important. The coupling of the sensor output and control actions can be provided by an external program, which then controls the simulation, or preferably by an internal script, if the simulation supports any form of scripting.
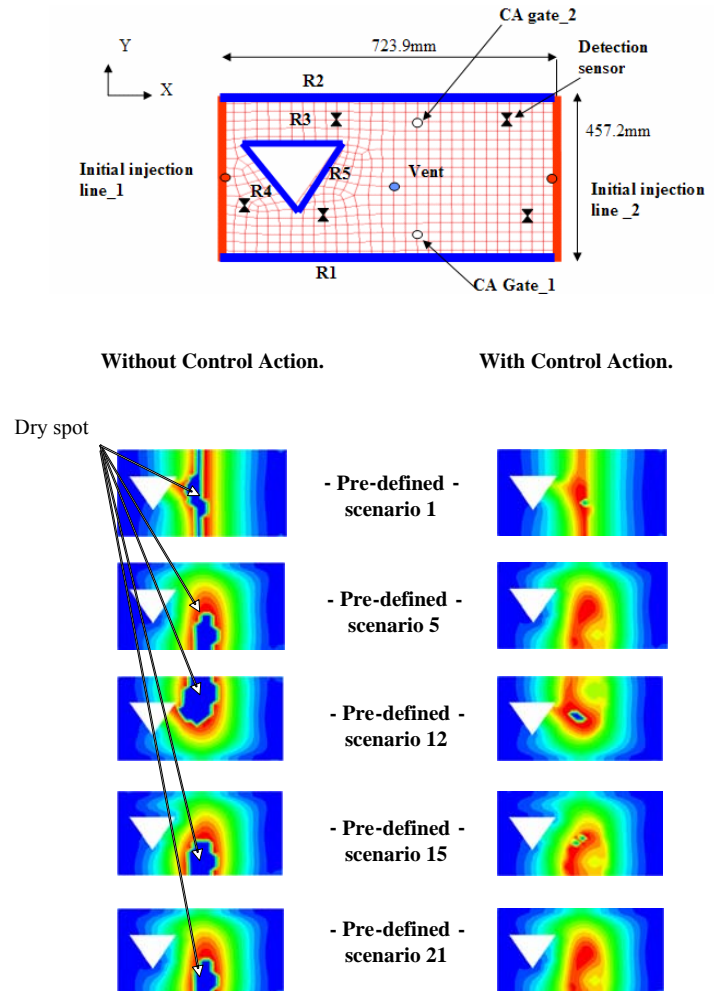
Figure 4: Simulation can evaluate all scenarios with forecasted race tracking and suggest control actions by injection resin from auxiliary gates to redirect flow to avoid dry-spots

CONCLUSIONS

The range of applicability of LCM simulations has significantly widened. This is caused by increasing attempts to optimize the manufacturing process, introduce process control and also because new derivatives of LCM process are being modeled. To successfully address various issues in LCM simulations such as race tracking, variability of material parameters, design of distribution media, prediction of time to saturate all the fiber tows in a preform, preform compression and injection gate and vent design, the simulation has to be flexible, accurate and fast.

It should have the (i) capability to model two-dimensional as well as three-dimensional problems, (ii) capability to include models of one-dimensional entities and be able to combine 1D, 2D and 3D sections in a single model (iii) allow for changes during the mold filling simulation and (iv) provide sufficient time resolution to model control action. Interface allowing for integration into other programs is always desirable.

The speed of computation, accuracy and changes during the mold filling simulation tend to contradict each other. Thus, the simulation package will always present a compromise between individual requirements. The success will depend not only on how the compromise is made but also on the actual use of the simulation that is bound to vary among its users. The simulation package LIMS (Liquid Injection Molding Simulation) has been in a continuous state of development over the last ten years at the University of Delaware. The goal is to keep the simulation flexible and fast, incorporate the correct process physics and validate the simulation with analytic solutions and experiments. It has been used successfully to simulate various aspects of RTM and VARTM injections, including optimization and control. Simulation execution and control from other applications is facilitated by a dynamic link library.

ACKNOWLEDGEMENT

REFERENCES

1. D. Heider, J.W. Gillespie, Jr. "Compaction Development During Vacuum-Assisted Resin Transfer Molding (VARTM)," *SAMPE Europe 2001, 22nd International Conference* March 27-29, (2001).

2. C.A. Hieber, S.F. Shen, "A finite element/finite difference simulation of the injection mold filling process," *J. Non-Newtonian Fluid Mech.* **7**, pp. 1-31, (1980).

3. T.A. Osswald, C.L. Tucker, C.L., *Polymer Eng. & Sci.* **28**, pp. 413-420, (1988).

4. M. Bruschke, S.G.Advani, " Finite Element/Control Volume Approach to Mold Filling in Anisotropic Porous Media," *Polymer. Composites* **11**, pp. 398-405, (1990).

5. R.W. Lewis, A.S. Usmani, J.T. Cross, "Finite Element Modeling of Mold Filling," *Finite Elements in the 90's*, ed.by E. Onate, J. Periaux and A. Samuelsson, Springer-Verlag/CIMNE, Barcelona, (1991).

6. V.R. Voller, Y.F. Chen, "Prediction of Filling Times of Porous Cavities," *International Journal Numerical Methods* **10**, (1995).

7. N.D. Ngo, R.V. Mohan, P.W. Chung, K.K. Tamma, "Recent Developments Encompassing Non-Isothermal/Isothermal Liquid Composite Molding Process Modeling/Analysis: Physically Accurate, Computationally Effective, and Affordable Simulations and Validations," *Journal of Thermoplastic Composite Materials* **6**, pp. 493-532, (1998).

8. F. Trochu, R. Gauvin, D.-M. Gao, "Numerical Analysis of the Resin Transfer Molding Process by the Finite Element Method." *Advances in Polymer Technology* **12**(4), pp. 329-342, (1993).

9. B. Minaie, Y.F. Chen, A.M. Mescher, "A Methodology to Obtaina Desired Pattern During Resin Transfer Molding," *Journal of Composite Material*, **14**, pp. 1677-1692, (2002)

10. M.Y. Lin, M.J. Murphy, H.T. Hahn, "Resin transfer molding process optimization," *Composites:Part A* **31**, pp. 361-371, (2000).

11. R. Mathur, B.K. Fink, S.G. Advani, "Use of Genetic Algorithms to Optimize Gate and Vent Locations for the Resin Transfer Molding Process," *Polymer Composites* **2**, pp. 167-178, (1999).

12. E.M. Sozer, S. Bickerton, S.G. Advani, "Use of Sensors and Simulations for Strategic Control of Liquid Composite Mold Filling Process," SME Technical Paper, *Composite Manufacturing and Tooling 2000*, (2000).

13. P. Simacek, S.G. Advani, "A Numerical Model to Predict Fiber Tow Saturation During Liquid Composite Molding," accepted in *Composites Science and Technology*

14. R. Mathur, "Model-Based Design Optimization Of Process Parameters For Composite Manufacturing Processes," Ph.D. Dissertation, University of Delaware (2002)

15. A. Gokce, S.G. Advani, *Materials and Manufacturing Processes*, Vol 19, No. 4, (2003)

16. B.Y. Kim, G.J. Nam, J.W.Lee, "Optimization of Filling Process in RTM Using a Genetic Algorithm and Experimental Design Method," *Polymer Composites*, **1**, pp. 72-86, (2002)

17. G. Carpenter, R. Leek, T. Donnellan, A. Rubel, "Simulation of Resin Transfer Molding for a Cubic Shell Geometry," *Heat and Mass Transfersin Materials Processing and Manufacturing, ASME HTD* **261**, pp. 133-145, (1993)

18. W.B. Young, M.T. Chuang, "Fabrication of T-Shaped Structural Composite Through Resin Transfer Molding," *Journal of Composite Material*, **16**, pp. 2192-2214, (1995)

19. S. Bickerton , H.C.Stadtfeld , K.V.Steiner, S.G.Advani," Design and application of actively controlled injection schemes for resin-transfer molding," *Composites Science and Technology*, (2001).

20. M. Devillard, K.-T. Hsiao, S. G. Advani, "On-line Race-tracking Characterization and Flow Control in Resin Transfer Molding," *34TH International SAMPE Technical Conference*,November 4-7, (2002).

A Numerical Study of Online Cure Kinetics Characterization during Liquid Composite Molding

KUANG-TING HSIAO
Department of Mechanical Engineering
UNIVERSITY OF SOUTH ALABAMA
Mobile, AL 36688-0002
e-mail: kthsiao@jaguar1.usouthal.edu

ABSTRACT

In Liquid Composite Molding (LCM), the resin impregnates the fiber preform and cures to form the composite part. The resin cure is an exothermic process and requires the mold heating profile to be optimized to reduce the cure cycle time and the cure induced thermal stress in the composite part. To optimize and control the cure cycle, it is necessary to obtain the resin cure kinetic parameters, which are usually measured offline by Differential Scanning Calorimetry (DSC) or Fourier transform infrared spectroscopy for neat resin and sometimes can be substantially varied due to the presence of fibers or the resin handling. In this paper, a model-based fitting technique to characterize the cure kinetics during LCM and its accuracy are studied numerically. A non-isothermal cure simulation of a composite part is performed based on a given set of cure kinetic parameters, which are the targets of the fitting process. The Genetic Algorithm is used to determine the cure kinetic parameters by matching the simulated temperature field based on the guessed cure parameters with the temperature history the composite part experienced. An uncertainty in temperature reading, which usually happens in real temperature measurement and control, is introduced to evaluate the accuracy and stability of this characterization technique with respect to various fitting periods during the cure process. Since the mold heating cycle will affect the cure history and the cure kinetics characterization, the influence of the mold wall temperature on the characterization accuracy is also investigated. The results show that by appropriately choosing the mold heating cycle, one will be able to enhance the accuracy and stability of the cure kinetics characterization within a reduced characterization period and hence can reserve more time for the following online cure optimization and control during the cure cycle. A numerical case study indicates great possibility of creating such a self-sufficient cure cycle optimizer by dividing the complete cure cycle into a cure characterization period and a cure optimization period.

KEYWORDS: Cure Kinetics Characterization, Cure Cycle Optimization, LCM, RTM, VARTM, Sensing and Control.

INTRODUCTION

In Liquid Composite Molding process such as RTM and VARTM, the liquid resin infiltrates the fiber preform inside a mold cavity due to the pressure difference between the resin injection gate and the vent. After the resin completely saturates the preform, the resin starts to cure and binds the fibers together to form solid composites.

During the resin infiltration stage, the resin cure process is usually inhibited to maintain the resin viscosity low because the goal is to have the pressure driven resin to impregnate the preform completely before the resin gels. In the resin filling stage, the flow of resin and mold filling pattern can be modeled and controlled effectively based on the well characterized preform permeability, porosity, and resin viscosity [1,2,3,4,5]. Once the resin fills the mold, one will have to control the cure cycle to obtain quality composite parts. The cure cycle optimization has several objectives: (i) to achieve high degree of cure (resin conversion), (ii) to minimize the accumulated residual stress and strain induced by non-uniform temperature and resin conversion the composites experienced during the exothermic cure process, (iii) to control the temperature of the composites from thermal degrading limit, (iv) to minimize the total time required to complete the cure process.

To design a good cure cycle, numerical modeling and optimization techniques have been applied to achieve the above-mentioned objectives by many researchers [6-11]. Due to the relatively small thickness compared with the in-plane dimensions of most of LCM parts, the cure process may be modeled as an 1-dimensional transient heat conduction problem coupled with a heat source term representing the reaction heat released by the polymer molecules cross-linking. The temperature of the mold walls can be controlled to influence the rate of resin cure (cross-linking) and hence achieve satisfactory temperature and cure history of the composites. Evolution strategies [6,7], gradient-based optimization techniques [8,9], and expert systems [10,11], have been used to control the cure cycle of composites. As many of the optimization techniques are coupled with numerical modeling, acquiring reliable and accurate thermal and cure kinetic parameters becomes very important for the cure cycle prediction and optimization. The resin cure parameters can be characterized off-line by using Differential Scanning Calorimetry (DSC) and ultrasound [12] or fitted directly from composites thermal history for complete cure cycles [13]. The direct fitting techniques based on composites temperature measurement may be more favorable for LCM processes due to the complexity of such processes and the uncertainty involved in resin handling such as catalyst concentration variation [14]; however, the confidence level of such type of fitting method have not been fully investigated.

In this paper, an evolution strategy (genetic algorithms) fitting technique has been coupled with 1-dimensional cure simulations to study the reliability of the direct fitting method under different temperature measurement noise levels. Furthermore, the feasibility of creating a self-sufficient cure cycle optimizer by dividing the complete cure cycle into a cure characterization period and a cure optimization period will be evaluated.

CURE PROCESS MODELING AND CHARACTERIZATION METHODOLOGY

The heat balance of the composites can be modeled as 1-dimensional heat conduction in the thickness direction as:

$$\rho_c c_{pc} \frac{\partial T}{\partial t} = \frac{\partial}{\partial z}\left(k_{czz} \frac{\partial T}{\partial z} \right) + \rho_r \varepsilon_r H_r \frac{\partial c}{\partial t} \tag{1}$$

where ρ_c, c_{pc}, k_{czz} are the density, specific heat capacity, and thermal conductivity-in the thickness direction of the composites respectively.

The heat generation rate due to the resin cure is described by the resin density ρ_r, the porosity ε_r, the reaction heat of resin H_r, and the resin cure rate $\partial c/\partial t$. The reaction model of the resin is given by [15]:

$$\frac{\partial c}{\partial t} = A \cdot \exp\left(-\frac{E}{RT}\right) \cdot c^m \cdot (1-c)^n \tag{2}$$

where c is the degree of cure (or conversion) and is ranged between zero and unit, A is the pre-exponential factor, E is the activation energy, R is the universal gas constant. The exponents m, n are ranged between zero and two, and $m + n \cong 2$ [13]. The values used in this numerical case study are listed in Table 1.

Parameters of Cure Kinetics				Thermal Properties of Composites & Resin			
H_r	399 kJ/kg	A	6879 s⁻¹				
R	8.314 J/mol-K	E/R	6480 K	ρ_c	1600 kg/m³	ρ_r	1186 kg/m³
		m	0.32	c_{pc}	1 kJ/kg-K	ε_r	0.5
		n	1.66	k_{czz}	0.72 W/m-K		

Table 1. Parameters of cure kinetics [15] and thermal properties [8] used in this numerical study.

The composite part is assumed to be 5 cm thick. Five nodes are used to simulate the heat conduction and cure process through the thickness. By giving a controlled mold wall heating cycle, the initial composites temperature ($T_0=293.17K$), and the initial resin conversion ($c_0=10^{-4}$), the temperature (T) and cure (c) history of the composites can be solved using explicit finite difference scheme from $t = 0$ to $t = t_{total}$. Then, the noise of measurement and control is introduced and hence the temperature measurement becomes $T_{exp} = T \pm \lambda \Delta T$ with $-1 \le \lambda \le 1$.

Based on the temperature measurement, a genetic algorithm optimizer is used to search the values of A, E, m, c_0 by minimizing the objective function from $t = 0$ to $t = t_s$ (which is the time to stop fitting):

$$\Omega_T(0, t_s) = \frac{1}{5t_s} \sum_{node=0}^{4} \int_0^{t_s} \left(T_{exp} - T_{fitting}\right)^2_{node} dt \tag{3}$$

where $T_{fitting}$ is the simulated temperature based on guessed cure parameters A, E, m, c_0.

RESULTS AND DISCUSSION

The baseline temperature and cure histories are shown in Figure 1. Assume the temperature measurement noise level is $\Delta T = 3K$, the fitted temperature and cure results for different values of t_s are shown in Figure 2 and Figure 3. Comparing Figure 2 and Figure 3 one observes that with fitting period $t_s=10000s$, the following temperature and cure predictions agree with the baseline much better than the case with short fitting period $t_s=5000s$. On the other hand, comparison between Figure 2 and Figure 4 shows that with the reduced measurement noise level $\Delta T = 1K$, better fitted results can be obtained for short fitting period $t_s=5000s$.

The results suggest that the confidence level of such direct fitting method increases as the measurement noise ΔT is reduced and the fitting period t_s is prolonged.
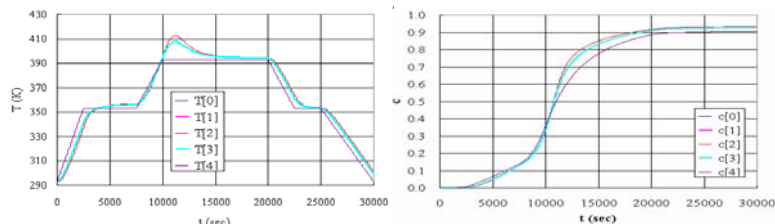
Figure 1. Baseline temperature and cure histories.
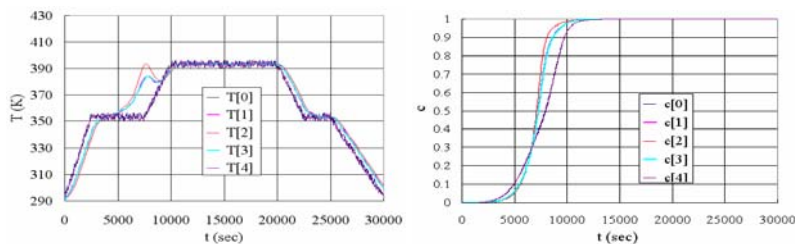
Figure 2. Fitted temperature and cure results for t_s=5000s and $\Delta T = 3K$.
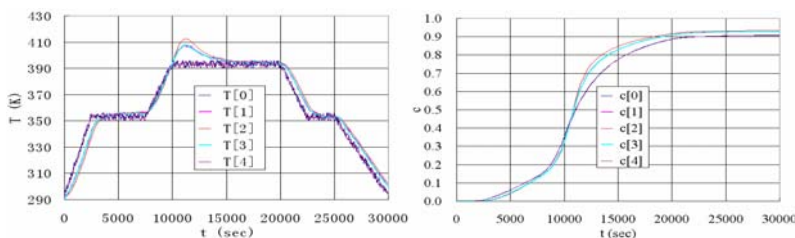
Figure 3. Fitted temperature and cure results for t_s=10000s and $\Delta T = 3K$.
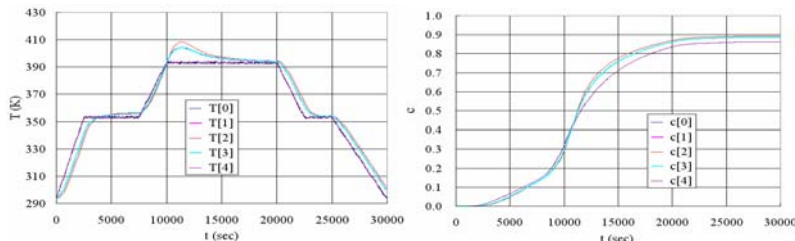
Figure 4. Fitted temperature and cure results for t_s=5000s and $\Delta T = 1K$.

To numerically investigate the feasibility of combining this online cure kinetics characterization technique with the online cure cycle optimization, a short fitting time t_s=5000s and a higher wall temperature are used during the cure kinetics fitting period. Based on the fitted cure parameters, the remaining cure cycle after t_s is optimized to achieve short cycle time and less thermal gradient and cure gradient in the thickness direction after $c > 0.70$. The noise is introduced through the whole cycle since the noise can be induced from both measurement and control system. The simulations of the integrated cure characterization and optimization are shown in Figure 5. The temperature and cure results of the optimized cure cycle are then calculated again by using the correct cure kinetic parameters listed in Table 1. The results represent the ideal and noise free data the composites should experience during the process and are shown in Figure 6.

Comparing Figure 5 and Figure 6, one can find that the fitting technique provides good temperature and cure predictions which agree well with the ideal data.
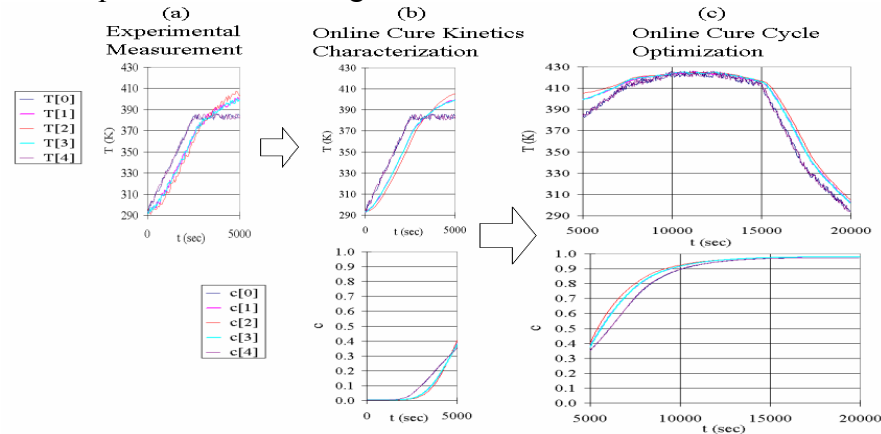
Figure 5.   Simulation of integrated cure kinetics characterization and cure cycle optimization (a) Simulated temperature measurement with $\Delta T = 3K$ until t_s=5000s.   (b) Fitted temperature and cure results. (c) Optimized cure cycle based on the fitted cure kinetic parameters.
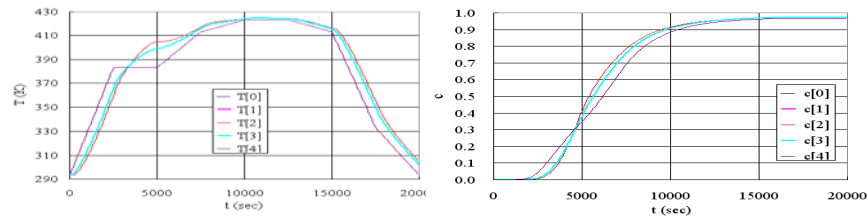
Figure 6.   Temperature and cure simulations for the optimized cure cycle using the correct cure kinetic parameters listed in Table 1.

CONCLUSION

To obtain reliable and accurate cure kinetic parameters is very important for LCM cure cycle management. A direct fitting technique consisting of a genetic algorithm optimizer and 1-dimensional cure simulator was developed to assess the confidence level of such a direct fitting approach subjected to different cure fitting periods, temperature measurement noise levels, and mold heating cycle. The results suggest that the confidence level of such a direct fitting method increases as the measurement noise is reduced and the fitting period is prolonged. Hence, it is concluded that the online cure kinetics characterization can be realized based on the direct fitting method if the mold heating cycle and the fitting period are carefully chosen. Furthermore, a simulated case study indicates that it is possible to combine such a cure characterization technique with the online cure cycle optimization to complete a self-sufficient cure characterization-optimization system for LCM processes.

REFERENCES

1. S. Advani and P. Simacek, "Modeling and simulation of flow, heat transfer, and cure (Ch:8). In: T.M. Kruckenberg, R. Paton (eds.), Resin Transfer Molding for Aerospace Structures. Norwell, MA: Kluwer Academic Publishers, pp. 225-281 (1998).

2. W. Young, "Gate location optimization in liquid composite molding using genetic algorithms", Journal of Composite Materials, Vol. 28, No. 12, pp. 1098-1113 (1994).

3. R. Mathur, B.K. Fink, S.G. Advani, "Use of genetic algorithms to optimize gate and vent locations for the resin transfer molding process" Polymer Composites, Vol. 20, No. 2, pp. 167-178 (1999).

4. J. M. Lawrence, K.T. Hsiao, R. C. Don, P. Simacek, G. Estrada, M. Sozer, H. C. Stadtfeld, Suresh G. Advani, "An approach to couple mold design and online control to manufacture complex composite parts by resin transfer molding," Composites Part A: Applied Science and Manufacturing, 33(7), pp. 981-990 (2002).

5. M. Devillard, K.-T. Hsiao, A. Gokce, and S. G. Advani, "On-line characterization of bulk permeability and race-tracking during the filling stage in resin transfer molding process," Journal of Composite Materials, 37(17), pp. 1525-1541 (2003).

6. N.G. Pantelelis, "Optimised cure cycles for resin transfer molding", Composites Science and Technology, Vol. 63, pp. 249-264 (2003).

7. D.J. Michaud, A.N. Beris, P.S. Dhurjati, "Thick-Sectioned RTM Composite Manufacturing, PartII. Robust Cure Cycle Optimization and Control", Journal of Composite Materials, Vol. 36, No. 10, pp.1201-1231 (2003).

8. M. Li and C.L. Tucker III, "Optimal Curing for Thermoset Matrix Composites: Thermochemical and Consolidation Considerations", Polymer Composites, Vol. 23, No. 5, pp. 739-757 (2002).

9. V. Antonucci, M. Giordano, K.-T. Hsiao, S. G. Advani, "A methodology to reduce thermal gradients due to the exothermic reactions in composites processing," International Journal of Heat and Mass Transfer, Vol. 45, pp.1675-1684 (2002).

10. D.E. Kranbuehl, P. Kingsley, S. Hart, G. Hasko, B. Dexter, A.C. Loos, "In situ sensor monitoring and intelligent control of the resin transfer molding process", Polymer Composites, Vol. 15, No.4, pp. 299-305 (1994).

11. V.K. Pillai, A.N. Beris, P.S. Dhurjati, "Intelligent curing of thick composites using a knowledge-based system", Journal of Composite Materials, Vol. 31, No. 1, pp. 22-51 (1997).

12. S.R. White, P.T. Mather, M.J. Smith, "Characterization of Cure-State of DGEBA-DDS Epoxy Using Ultrasonic, Dynamic Mechanical, and Thermal Probes", Polymer Engineering and Science, Vol. 42, No. 1, pp. 51-67 (2002).

13. D.J. Michaud, A.N. Beris, P.S. Dhurjati, "Thick-Sectioned RTM Composite Manufacturing: Part I- In-Situ Cure Model Parameter Identification and Sensing", Journal of Composite Materials, Vol. 36, No. 10, pp. 1175-1199 (2002).

14. M.S. Kessler, S.R. White, "Cure Kinetics of the Ring-Opening Metathesis Polymerization of Dicyclopentadiene", Journal of Polymer Science: Part A: Polymer Chemistry, Vol. 40, pp 2373-2383 (2002).

15. D.J. O'Brien, S.R. White, "Cure Kinetics, Gelation, and Glass Transition of a Bisphenol F Epoxide", Polymer Engineering and Science, Vol. 43, No. 4, pp863-873 (2003).

Simulation of the Vacuum Assisted
Resin Transfer Molding Process

Xiaolan Song [1], Alfred C. Loos [2], Brian Grimsley [3], Roberto Cano[3] and Pascal Hubert [4]

[1] *Materials Technology Center*
Southern Illinois University, Carbondale, IL 62901:xiaolan@siu.edu
[2] *Department of Mechanical Engineering*
Michigan State University, East Lansing, MI 48824
And Corresponding Author's email: aloos@egr.msu.edu
[3] *NASA Langley Research Center, Hampton, VA 23681,*
b.w.grimsley@larc.nasa.gov, r.j.cano@larc.nasa.gov
[4] *Department of Mechanical Engineering, McGill University*
Montreal, Quebec H3A2K6, CANADA:pascal.hubert@mcgill.ca

SUMMARY: A process model that includes the coupled phenomenon of resin flow and preform compaction was developed and used to simulate resin infiltration of a fibrous preform using the vacuum assisted resin transfer molding (VARTM) process. Flow of resin through the distribution medium and preform were modeled as flow through porous media. The finite element/control volume method was used to calculate the infiltrating fluid pressure distribution and track the progression of the flow front. The simulation results were compared with data obtained during infiltration of a carbon fiber preform with an epoxy resin. The parameters measured include the flow front location, resin pressure and preform thickness change. With accurate inputs, the flow front locations and resin pressure distribution can be accurately predicted. The predicted transverse displacements do not agree well with the experimental measurements. The reasons for the differences are discussed, and further investigations are recommended to develop a more accurate compaction model.

KEYWORDS: VARTM, Flow Modeling, Composite Materials, Composite Manufacturing

INTRODUCTION

Vacuum Assisted Resin Transfer Molding (VARTM) is a variant of the traditional RTM process in which one of the solid tool faces is replaced by a flexible vacuum bag. VARTM offers numerous cost advantages over traditional RTM, such as lower tooling cost and shorter start-up time. However, it has been well documented that resin infiltration of a fibrous preform is a complex process and often dry or unimpregnated areas can occur in the preform. In addition, the flexible nature of the vacuum bag makes it is difficult to control the cured thickness and fiber volume fraction of the composite. Due to the complex nature of the VARTM process, trial and error methods of process development are inefficient and expensive. The objective of this study was to develop and verify a comprehensive VARTM simulation model as a cost effective design tool.

MODEL DEVELOPMENT

The VARTM process consists of two important mechanisms, the flow of the resin through the preform and compaction and relaxation of the preform during infiltration. Hence, the simulation model of the VARTM fabrication procedure consists of a flow submodel and a compaction submodel.

Flow Model

The flow model was developed to track the flow of the resin through the distribution medium and the preform. Both the high-permeable distribution medium and the preform can be modeled as heterogeneous and anisotropic porous media. The resin fluid is assumed to be Newtonian and incompressible. Assuming that the flow is quasi-steady state, the governing equations for the flow problem are the continuity equation for an incompressible fluid, and Darcy's law of flow through a porous medium:

$$\nabla \cdot \vec{v} = 0 \tag{1}$$

$$\vec{v} = \frac{\vec{q}}{\phi} = -\frac{S}{\phi\mu}\nabla P_r \tag{2}$$

where, $\vec{v}$ is the interstitial velocity vector, $\vec{q}$ the superficial velocity vector, ϕ the porosity of the preform, μ the viscosity of the resin, S the permeability tensor of the preform, and P_r is the resin pressure.

Note that this is a moving boundary problem. The finite element/control volume (FE/CV) method [1] is utilized to track the progression of the flow front. At each time step, the Galerkin finite element method is used to solve for the pressure distribution in the fluid. The resin velocities are then calculated using Eqn. (2). With resin velocities obtained, the flow front location at that time is determined by means of the control volume technique.

Compaction Model

Due to the flexible nature of the vacuum bag, there is no direct control over the thickness or fiber volume fraction of the composite part. The compaction of the reinforcement preform is complex and depends on the compressibility and relaxation of the reinforcement under pressure, and the interaction between the reinforcement and the resin flow.

It is well accepted that during the flow of the resin in the fiber preform, the total compaction pressure is shared by the resin pressure and the pressure supported by the fiber network.

Therefore, Eqn. (3) is introduced to account for the transverse equilibrium inside the mold cavity during impregnation [2]:

$$P_c = P_r + P_n \tag{3}$$

where, P_c is the total compaction pressure, P_r is the resin pressure, and P_n is the effective compressive stress in the preform, often referred to as the net pressure applied to the preform.

For the VARTM process, the external pressure applied is the atmospheric pressure. At each time step, once the resin pressure distribution is obtained from the resin flow model, the pressure supported by the preform is computed using Eqn. 3. The normal strain in the preform along the transverse direction (ε) is a function of the net pressure applied to the preform.

The relationship between the compressive strain in the preform and the applied pressure is obtained by fitting the compaction test results to an empirical model. Two important phenomena are observed during the compaction experiments. First, because of the resin lubrication effect, the fiber sample saturated with resin is compacted more than the dry reinforcement under the same pressure. Second, the compressive response of the preform is not elastic and hysteresis occurs during the unloading process [3].

During the VARTM infusion process, before the resin front approaches, the dry reinforcement is under vacuum compression. Thus, the compressive strain of the preform can be calculated from the compaction response of the dry preform during the loading process. After the resin passes, the local net pressure applied to the preform decreases as a result of the increasing resin pressure. This is equivalent to an unloading process. Accordingly, the strain in the wet preform is determined by the compaction response of the resin saturated preform during the unloading process.

MODEL SIMULATIONS

The process simulation model was used to investigate resin infiltration of a 60.96 cm by 30.48 cm preform by the VARTM process. For the simulations, the properties of SAERTEX® multi-axial warp-knit (MAWK) carbon fiber fabric were used for the preform and A.T.A.R.D. Laboratories SI-ZG-5A epoxy were used for the resin. To assess the accuracy of the model, the flow patterns and the changes in resin pressure and preform thickness were measured during infiltration of the carbon preform. Fig. 1 shows the dimensions of the preform and the locations of the pressure sensors and Linear Variable Displacement Transducers (LVDT). Details of the instrumentation and the experimental procedures can be found in reference 4.
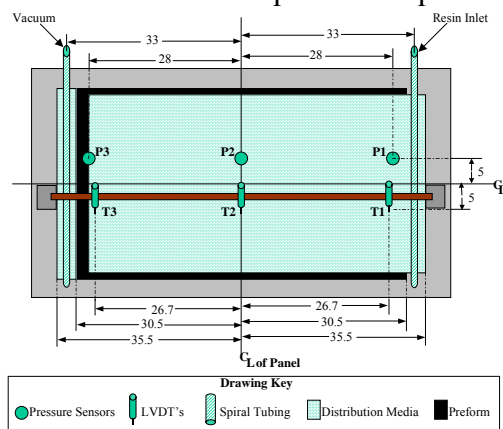
Fig. 1 Instrumented VARTM tool   Fig. 2 Cross-section of preform and distribution medium
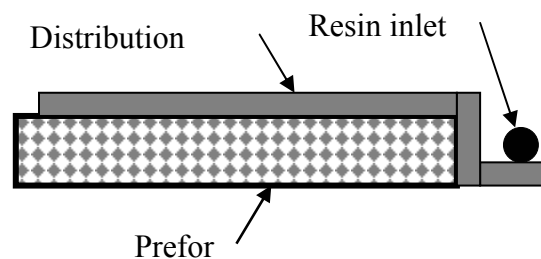
For the flat panels investigated in this study, resin flow is uniform across the width of the panels, except at the edges where there is no distribution medium. Hence, the resin velocity in the width direction is negligible and the resin infiltration of the flat preform can be modeled as a two-dimensional flow problem. Figure 2 shows the two-dimensional model of the preform and distribution medium. Linear two-dimensional quadrilateral elements were used to create the finite element mesh.

Shown in Fig. 3 is infiltration time versus flow front position at the top and bottom surfaces of the preform. The flow front at the top surface of the preform was recorded using a digital video camcorder. The bottom flow front position was obtained from the tool mounted pressure sensor responses recorded during the test. Overall, the agreement between the predicted and measured flow front position was very good.
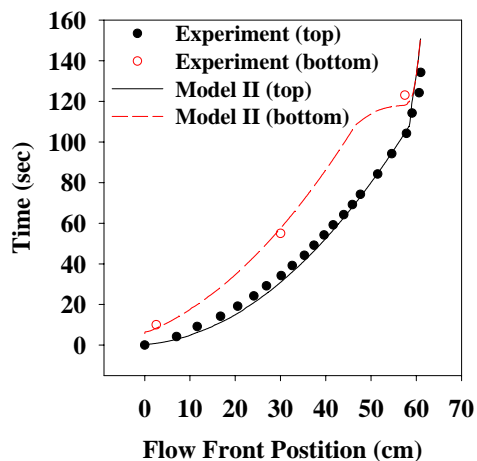
Infiltration time versus position
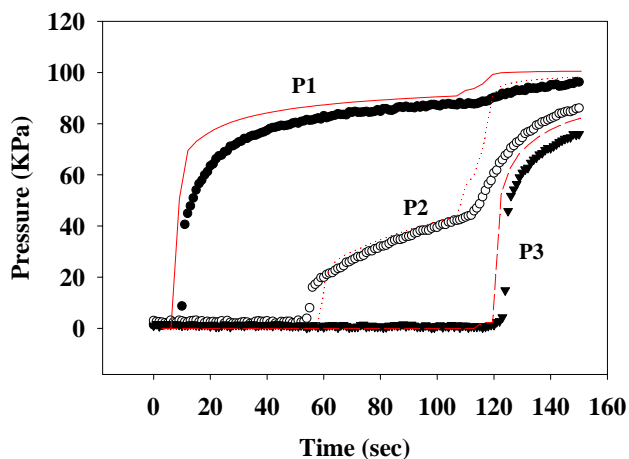
Fig. 3

Fig. 4 Pressure versus infiltration time

Resin pressure as a function of infiltration time is reported in Fig. 4. The solid lines represent the model predicted pressures, while the symbols represent the pressures measured by the three transducers mounted in the tool (Fig. 1). Agreement between the calculated and measured pressures at the three sensor locations was very good.
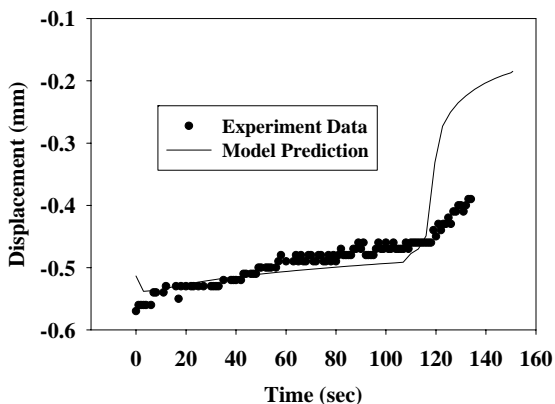
Fig.5 Displacement versus time at T1
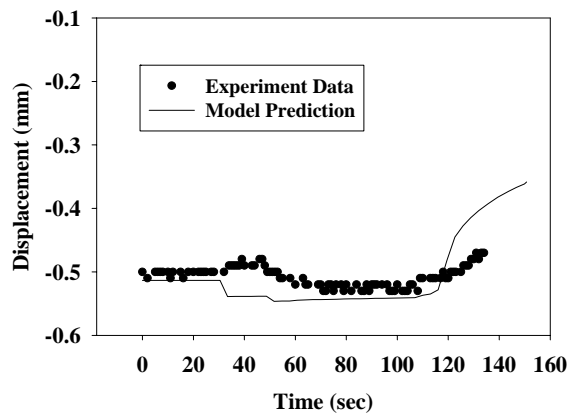
Fig. 6 Displacement versus time at T2

The measured and calculated displacements are compared in Figs. 5 and 6. Qualitatively, the calculated thickness changes of the preform agree well with the experimental measurements. Before the resin inlet opens, the dry preform is compacted under vacuum and initial displacements are induced. After the infusion process begins, the presence of the resin affects the compaction of the preform by two different mechanisms [3]. First, the lubrication effect of the resin causes rearrangement of the fiber network and an increase in the preform compaction.

This mechanism is called the wetting compaction effect of the resin. On the other hand, the increase of the resin pressure leads to a decrease of the pressure applied to the preform. Consequently, the amount of the preform compaction decreases. This is called the springback mechanism. During the infiltration process, the net compaction of the preform depends on the relative magnitude of the wetting and springback deformation mechanisms. Therefore, both the simulation and the experiment find that the compaction responses of the preform at the three LVDT positions are different. T1 moderately decreased after the resin passed by, while T2 increased after the flow front approached. After the flow front reached the end of the distribution medium, T1, T2, and T3 all decreased rapidly due to the sharp increase in the resin pressure. The sudden increase in preform thickness was observed at 115 seconds in the experiment, and the phenomenon was predicted to occur at 116 seconds in the simulation. Both the simulation and the experiment find that at the end of the infiltration process, T1 < T2 <T3. This indicates that the panel is less compacted on the resin inlet side and more compacted on the vacuum side.

CONCLUSIONS

In this investigation, a comprehensive Vacuum Assisted Resin Transfer Molding (VARTM) process simulation model was developed and verified. The model incorporates resin flow through the perform and compaction and relaxation of the perform. The computer model can analyze the resin flow details, track the thickness change of the preform, predict the total infiltration time and final fiber volume fraction of the parts, and determine whether the resin could completely infiltrate and uniformly wet out the preform.

ACKNOWLEDGEMENTS

REFERENCES

1. H. P. Wang and H. S. Lee, Fundamental of Computer Modeling for Polymer Processing, Chapter 8, ed. C. L. Tucker, Hanser Publishers (1989).
2. A. Hammami and B. R. Gebart, "Analysis of the Vacuum Infusion Molding Process," *Polymer Composites,* Vol. 21, no. 1, pp. 28-40 (2000).
3. B. W. Grimsley, P. Hubert, X. Song, R. J. Cano, A. C. Loos, and R. B. Pipes, "Flow and Compaction during the Vacuum Assisted Resin Transfer Molding Process," *SAMPE Technical Conference*, Vol. 33, pp. 140 – 153 (2001).
4. X. Song, "Vacuum Assisted Resin Transfer Molding (VARTM): Model Development and Verification," Ph.D. Dissertation, Virginia Polytechnic Institute and State University, Blacksburg, VA, April 2003.

Some Studies on Modeling the Unsaturated Flow in Woven, Stitched or Braided Fiber Mats in LCM

T. Roy, B. Z.Babu, R. S. Jadhav, M. S. Munagavalasa and K. M. Pillai[1]
Department of Mechanical Engineering
University of Wisconsin- Milwaukee
Milwaukee, WI 53201
Phone: (414) 229-6535
Fax: (414) 229-6958

Summary: The liquid composite molding (LCM) processes for manufacturing polymer composites involve injecting a thermoset resin into a fiber-packed mold cavity. Very often, the fiber preform behind the resin front is partially saturated during mold-filling giving rise to the unsaturated flow behind the flow front. This paper discusses the implications of the recent experimental, numerical and analytical work done by the authors' research group in advancing the state of research in this area. The experimental work describes the type of fiber mats in which the unsaturated flow is likely to occur, and the dimensionless parameters that are effective in predicting the unsaturated flow. Numerical work highlights the inadequacy of the conventional flow model when the 'sink' effect is not incorporated during the reactive and nonisothermal unsaturated flow in dual-scale porous media created by certain fiber mats. A new set of governing equations for such media is presented that incorporate the effect of delayed absorption of tows through various sink terms in the mass-balance, temperature, and cure equations.
Keywords: preform, unsaturated flow, sink, dual-scale porous media, RTM, LCM

Introduction

In Liquid Composite Molding process, a thermoset resin is injected into a mold cavity, which is packed with a preform made of fiber mats to create a cured part. LCM process includes Resin Transfer Molding (RTM), Vacuum Assisted RTM (VARTM), Seemann Composites Resin Infusion Molding Process (SCRIMP) and few others. All of the LCM technologies consist of the following major steps: the reinforcement of carbon or glass fiber is placed in the mold cavity, matrix material like thermoset resin is either injected under pressure or sucked into the mold cavity due to vacuum, once the fiber mat infiltrated, the matrix is allowed to cure and harden to its final shape, finally, the mold is opened and the part is taken out for final operations. For the thermoset type polymer-matrix composites, the solidification process is a cross-linking reaction that turns the resin into a hard brittle solid.

Numerical simulations of the mold-filling process in LCM provide a thorough insight in optimizing the mold design. Numerous softwares [1,2] are available to optimize the mold filling process.

---

[1] The author to whom correspondence should be addressed.

The basic assumption used in these simulations is that preform behind the flow-front is fully saturated with resin and the flow in such a region can be modeled using the equation of continuity (Eqn. 1) and Darcy'c law for momentum balance (Eqn. 2) given below.

$$\nabla.\mathbf{u} = 0 \ \dots\dots(1) \qquad \mathbf{u} = - (\mathbf{K}/\mu) \, \nabla P \ \dots\dots\dots(2) \qquad \nabla.[\mathbf{K}.\nabla P] = 0 \ \dots\dots\dots (3)$$

Here **u** is the volume averaged velocity of resin in fibrous porous media, P is the volume-averaged pressure, **K** is the permeability tensor of the fibrous performs and μ is the resin viscosity. For non-isothermal flows in porous media equation 1 and 2 can be combined with convection-diffusion type transport equations for energy and cure to predict temperature and degree of chemical reaction in the resin [3,4].

Previous work on the unsaturated flow

In the last few years it has been discovered that the physics used to simulate mold filling in LCM is inadequate for woven, stitched & braided fiber mats [5-7,9,13] which is being attributed to the dual-scale porous medium created due to the presence of large gaps between dense fiber tows. Figure 1(a) shows the schematic of a simple 1-D flow experiment used for detecting the unsaturated flow.

In figure 1(b), a typical "drooping" inlet-pressure history, a characteristic of the unsaturated flow [10], is compared with the inlet-pressure predicted by the conventional physics using Eqn. 3 after assuming full saturation behind a moving resin front.
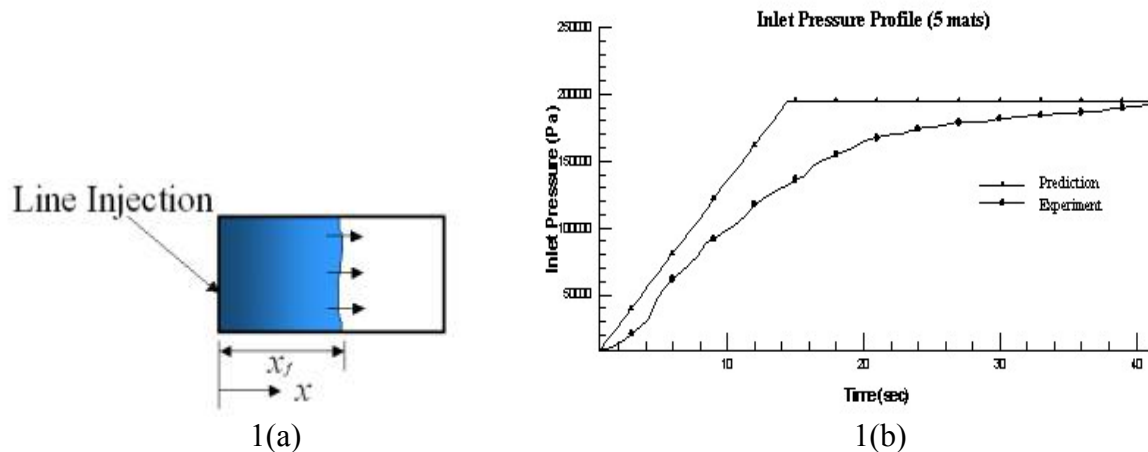
Figure 1.(a) Schematic of a simple 1-D flow experiment.
(b)Measured and theoretical inlet-pressure profiles for 5 biaxial stitched mats.
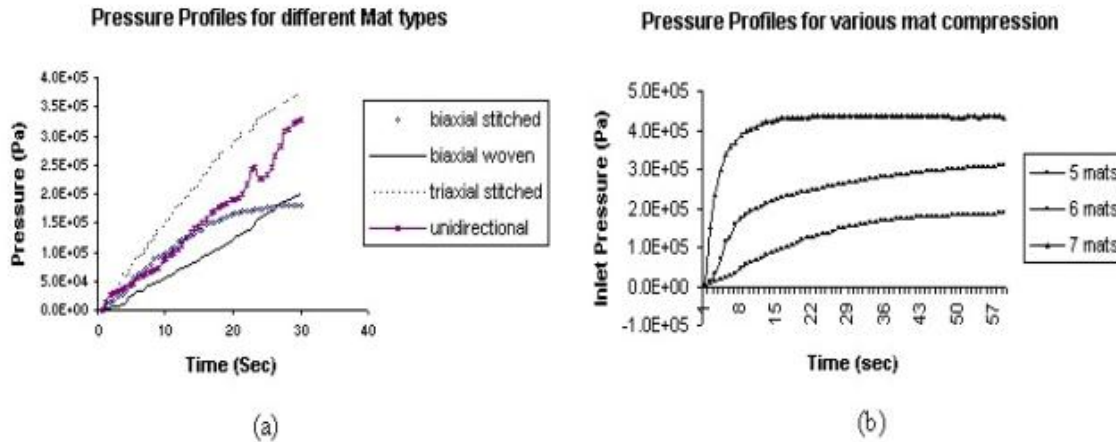
Figure 2: Comparison of measured inlet pressure history for various mat types and mat compression.

Recently, it has been observed that not all woven, braided or stitched mats showed the "droop" – only the stitched mats with long uninterrupted channels aligned along the flow direction manifested this aberrant behavior [9,10]. It was also observed that the inlet pressure profile becomes flatter with increasing number of mats (Fig. 2(b)). Theoretical models anticipated such a flattening of inlet pressure profile for the unsaturated flow as a direct function of the dimensionless parameters *pore volume ratio* and *sink effect index* [5-7]. These indices as an outgrowth of the sink model are demonstrably more scientific in modeling the unsaturated flow [12].

Validating the sink model using the pore volume ratio and sink effect index
Pore volume ratio (γ) and sink effect index (ψ) are defined as

$$\gamma = V_{tow}\, \varepsilon_i / V_{gap} \quad \text{....(4)} \qquad\qquad \psi = (K_t/K_{ch})(L/b)2\tau \quad \text{.....(5)}$$

where V_{tow} is the volume of tows, V_{gap} is the volume of gaps between tows, ε_i is the tow porosity, K_t is the tow permeability, K_{ch} is the channel permeability, L is the characteristic length in the flow direction, b is the characteristic length in the transverse direction and $\tau = \pi\, a\, b\, Ns$ is the tow area fraction which is equal to the total cross-sectional area of tows in a unit area of cross-section of the fiber mat. These dimensionless numbers characterize the magnitude of liquid absorbed by the tows and are a function of the relative resistance to flow in the tow and inter-tow regions, and the packing density of the tows. Recently, γ and ψ were computed from the micrograph samples of biaxial and triaxial stitched mats displaying the unsaturated flow [11]. (One of the micrograph of biaxial stitched mats is shown in Fig. 3.) It was observed that as γ and ψ increase, the `droopiness' of the inlet pressure profiles also increases [11], thus matching the trend predicted by the earlier sink models [6,7].
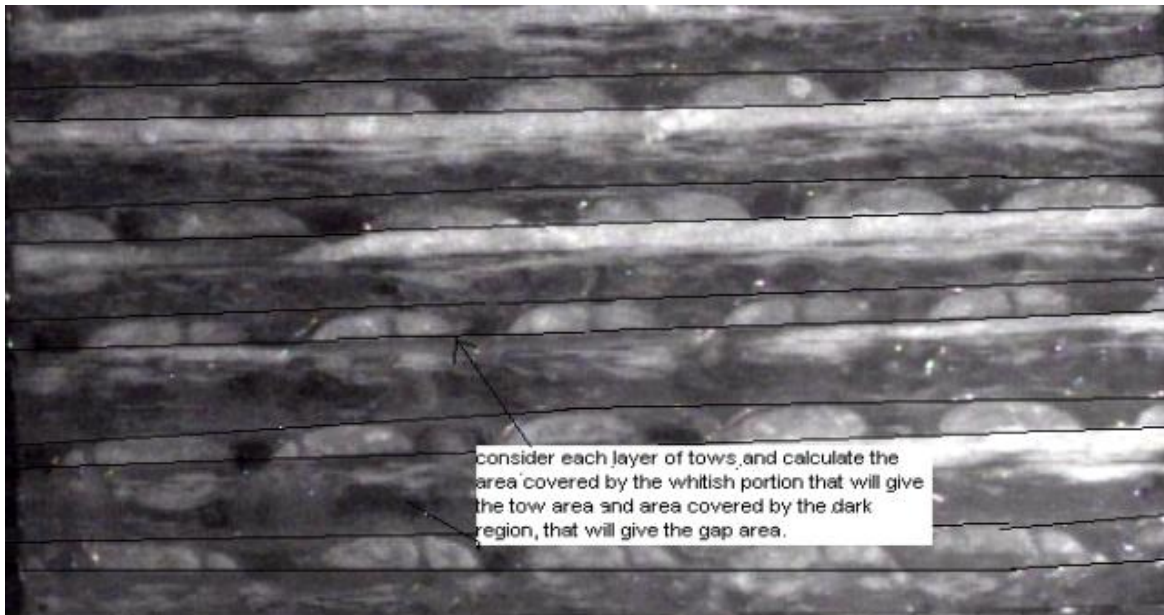
Figure 3: Measurement of tow area and gap area of a biaxial stitched mat. Tow area is the area covered by the whitish portion and gap area is the dark portion in each layer.

Study of temperature and cure distributions in dual-scale porous media
This numerical study was aimed at studying changes in temperature and cure distributions due to the sink effect in a dual-scale porous medium created by the stitched fiber mats. An iterative, control-volume approach based on energy and cure balances was used for developing discretized equations in the channels and fiber tows of the two-layer model of the dual-scale porous media [14,15].

A typical temperature distribution is shown in Fig. 4(a). Temperatures at the top edge represent the gap or inter-tow temperatures, whereas temperatures underneath it above the curve represent the inside-the-tow distribution. From the figure it is clear that resin near the curved micro front is at much higher temperatures as compared to the resin in the top, outer region. This can be attributed to the fact that the fibers in the mold are at a higher temperature as compared to the resin, when such fibers are "quenched" by the invading resin at the micro-front, the excess energy passes on to the resin resulting in an increase in temperature near the micro-front.

Similarly, the development of cure in the resin is shown in Fig. 4(b). The cure is at maximum near the micro-front region, which is due to the high temperatures developed inside tows behind the microfront. As a result, the rate of resin cure is also at a maximum. A significant difference in temperatures and cures of the outer (inter-tow) and the wetted inner (intra-tow) regions are observed. The effect of various parameters such as the ratio of liquid and fiber heat capacities, the fiber and resin thermal conductivities, the pore volume ratio, and the resin reaction rates are found to play an important role in the temperature and cure distributions inside and outside the tows.

<center>(a)   (b)</center>
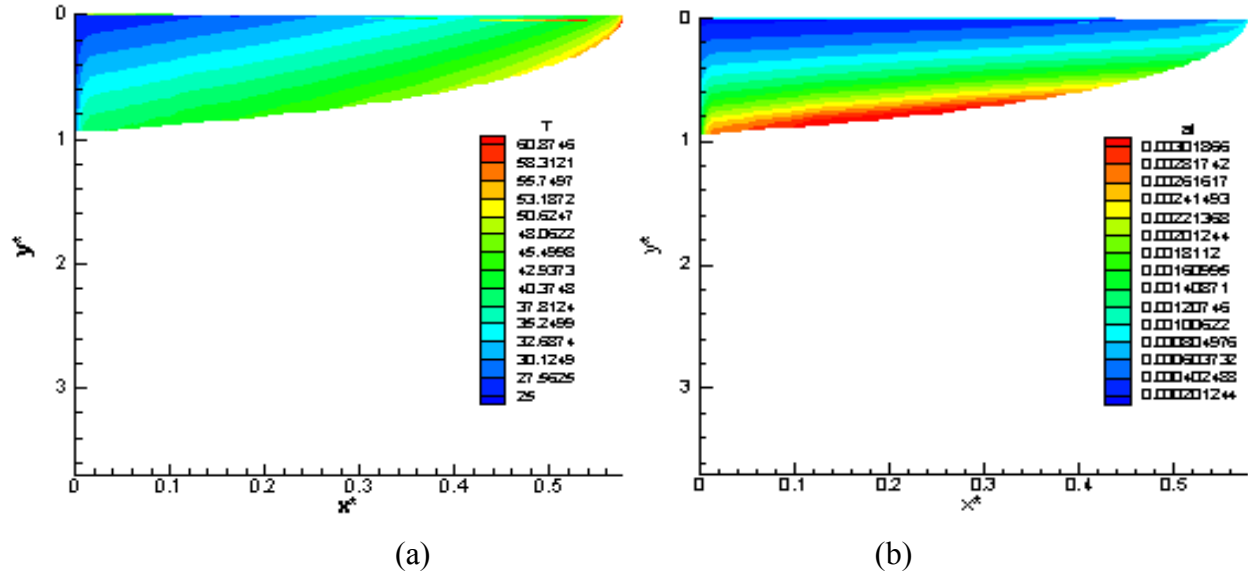
Figure 4: Temperature (a) and cure (b) distributions in a two-layered dual-scale medium.

Governing equations for the unsaturated flow

Pillai and Murthy recently developed the physics for modeling the unsaturated flow in dual-scale fiber mats observed during the LCM mold fillings [16, 17]. The mathematically rigorous phase-averaging method was employed to develop a new set of gap- and tow-averaged temperature and cure equations in the dual-scale media. These coupled equations can be used to model the unsaturated flow in fibrous dual-scale porous media under reactive, nonisothermal conditions. These equations for the gap and tow region are compiled in the following tables. (See [16,17] for details of the symbols.)

Table 1: Set of volume-averaged governing equations for the gap region.

Mass	$\nabla.<\mathbf{v}_g> = -S$
Momentum	$<\mathbf{v}_g> = -(\mathbf{K}/\mu).\nabla<P_g>^g$
Energy	$(\rho C_p)_l [\varepsilon_g \partial<T_g>^g/\partial t + <\mathbf{v}_g>.\nabla<T_g>^g] = \nabla.\mathbf{K}_{th}.\nabla<T_g>^g + \varepsilon_g\rho_g H_R f_c + Q_{conv} - Q_{con}$
Cure	$\varepsilon_g\partial<c_g>^g/\partial t + <\mathbf{v}_g>.\nabla<c_g>^g = \nabla.\mathbf{D}.\nabla<c_g>^g + \varepsilon_g f_c + M_{conv} - M_{diff}$

Table2: Set of volume-averaged governing equations for the tow region.

Mass	$\nabla.v_t = 0$
Momentum	$v_t = -(\mathbf{K}/\mu).\nabla P_t$
Energy	$[\varepsilon_t(\rho C_p)_l + (1-\varepsilon_t)(\rho C_p)_f]\partial T_t/\partial t + (\rho C_p)_l \mathbf{v}_t.\nabla T_t = \nabla.\mathbf{K}_{th,t}.\nabla T_t + \varepsilon_t\rho_g H_R f_c$
Cure	$\varepsilon_t\partial c_t/\partial t + \mathbf{v}_t.\nabla c_t = \nabla.\varepsilon_t \mathbf{D}_t.\nabla c_t + \varepsilon_t f_c$

Conclusions

In this paper we have discussed the unsaturated flow in Liquid Composite Molding process for different fiber mats. The 1-D unsaturated flow in stitched fiber mats, with inter-tow channels aligned with the flow direction, displays the drooping inlet-pressure history characteristic of the unsaturated flow. The droop in the inlet pressure history increases with increasing mat compression. Dimensionless numbers *pore volume ratio* and *sink effect index* are effective in predicting unsaturated flow in biaxial and triaxial stitched mats, and successfully validated the earlier unsaturated-flow theories. A numerical simulation of the reactive, nonisothermal flow in a two-layer, dual-scale porous medium predict high temperatures and resin cures inside tows, thereby contradicting the conventional temperature and cure models that predict high temperature and cures just behind the flow front. Various parameters, such as the ratio of liquid and fiber heat capacities, the fiber and resin thermal conductivities, the pore volume ratio, and the resin reaction rates, are shown to influence the temperature and cure distributions in such dual-scale media. Finally, a new set of governing equations for predicting resin temperatures and cures during the unsaturated flow in dual-scale porous media is presented. These equations, with new sink terms associated with convection and diffusion of heat and cure into the tows during the unsaturated flow, will help in an accurate simulation of the unsaturated flow in dual-scale fibrous media.

References

1. C-Mold User's Manual, Moldflow Corporation. www.moldflow.com
2. LIMS User's Manual, Center for Composite Materials, University of Delaware, Newark,DE 19716, USA.
3. C.L Tucker, III and R. B. Dessenberger. Governing equations for flow and heat transer in stationary fiber beds. In S. G. Advani, editor, *Flow and Rheolgy in Polymer Composites Manufacturing,* pages 257-323. Elsevier, Amsterdam, 1994.
4. S.G. Advani, editor. Flow and Rheology in Polymer Composites Manufacturing. Elsevier,1994.
5. Y.D.Parseval, K.M.Pillai, and S.G.Advani, A Simple Model for the Variation of Permeability due to Partial Saturation In Dual Scale Porous Media, *Transport in Porous Media*, Vol.27, p 243-264, 1997.
6. J.Slade, K.M.Pillai and S.G. Advani, Investigatioin of Unsaturated flow in woven braided and stitched fiber mats during mold-filling in Resin Transfer Molding, *Polymer Composites*, Vol 22, no 24, p 491-505 Aug 2001.
7. K.M. Pillai and S.G. Advani, A model for Unsaturated Flow in Woven Fiber Preforms during Mold Fillings in Resin Transfer Molding, *Journal of Composite Materials*, Vol 32, no 19, 1998.
8. C.L. Tucker III, editor. Fundamentals of Computer Modeling for Polymer Processing. Hanser Publishers, Munich, 1989.
9. B.Z.Babu and K.M. Pillai, New experimental findings on the Resin Impregnation Process in Woven, Stitched or Braided Fiber Mats in Liquid Composite Molding Process, *Proceedings of SAMPE 2002* at Long Beach, CA.
10. B.Z. Babu and K.M. Pillai, Experimental investigation of the effect of fiber-mat architecture on the unsaturated flow in liquid composite molding, *Journal of Composite Materials*. Vol. 38, No. 1/2004.

11. T.Roy, B.Z. Babu and K.M. Pillai, First steps towards quantitative validation of the unsaturated flow theories in Liquid Composite Molding, *Proceedings of ASME International: Summer Heat Transfer Conference*, Las Vegas (Nevada), July 21-23, 2003.

12. K.M. Pillai, Unsaturated flow in liquid composite molding processes: a review and some thoughts, *Journal of Composite Materials*, submitted the revised manuscript.

13. K.M. Pillai, Governing equations for unsaturated flow through woven fiber mats. Part 1. Isothermal flows, *Composites: Part A*, 33,1007-1019,2002.

14. Rajendra S. Jadhav and Krishna M. Pillai, Numerical Study of Heat Transfer During Unsaturated Flow in Dual-Scale Porous Media. *Numerical Heat Transfer, Part A*, 43:385-407,2003.

15. Krishna M. Pillai and Rajendra S. Jadhav, A Numerical Study of Non-Isothermal Ractive Flow in a Dual-Scale Porous Medium under Partial Saturation, *International Journal of Multiphase Flow,* under review.

16. K.M. Pillai, and M.S. Munagavalsa, Governing equations for unsaturated flow through woven fiber mats, Part2: Nonisothermal reactive flows, *Composites part A: Applied Science and Manufacturing*, n 35,2004,p 403-415.

17. K.M. Pillai, Governing Equations for Unsaturated Flow through Woven Fiber Mats: Part1 Isothermal Flows, *Composites Part A: Applied Science and Manufacturing*, v33,2002,p 1007-1019.

Modeling and Simulation of Liquid Compression Molding Using LIMS

M. Deleglise, C. Binetruy and P. Krawczak

Ecole des Mines de Douai, Technology of Polymers and Composites Department, 941 Rue Charles Bourseul, 59508 DOUAI : deleglise@ensm-douai.fr

SUMMARY: Injection Compression Molding is a fast Liquid Composite Molding (LCM) process in which resin is injected in a mold which is not completely closed. Once the desired amount of resin is injected, the mold is slowly closed and the resin is forced to impregnate the remaining dry fibrous medium until the desired fiber volume fraction or preform thickness is reached. The main advantage of this process as compared to Resin Transfer Molding (RTM), where the mold is fully closed before injecting, is the reduction of the mold filling time. The topic of this paper is to model the compression stage, that is the flow of resin through the preform while the preform is being deformed. The model consists in changing the geometry of the part between each calculation step and updating the fibrous material properties according to experimental data.

KEYWORDS: Simulation, Injection/Compression (I/CM, CRTM), Forced deformations

INTRODUCTION

Injection/Compression (I/CM) or Compression RTM (CRTM) process is a good alternative to Resin Transfer Molding (RTM) as it allows to reduce cycle time while ensuring good part quality. In both processes, fabric layers are previously laid up in the mold. Once the mold is closed, resin is injected. The part is de-molded at the end of the curing stage. The difference between the two processes lays in the closure position of the mold, as presented in Fig. 1. In RTM the mold is fully clamped during the injection, whereas in I/CM resin is injected before clamping the mold, either leaving a gap between the mold wall and the fabric, or injecting while the preform is not fully compacted. When the desired amount of resin is injected, a compression stage forces the resin to impregnate the whole preform. The simulation of compression based processes was addressed first on the material deformation side. For instance, Pillai et al. addressed this problem by characterizing a multi layered preform deformation and change in physical properties using a nonlinear elastic model [1-3] and by presenting a 3D-mesh generation method that keeps the preform layers integrity during the compression stage. Nevertheless, the topic of the compression driven flow during compression was not approached. Bickerton and Abdullah [4] developed an analytical model to predict the clamping force necessary during a I/CM process, using an elastic model and showed limitation via experimental results, proving the need to use a viscoelastic model to consider small deformations. The simulation of compression driven flow was previously addressed by Pham et. al. They modeled Compression Resin Transfer Molding (CRTM) for a 2D flow created by a 1D-compressive load using RTMFlot a computer-based program developed at the University of Montreal [5].

Mold pre-closing   **Injection stage**   **Compression stage**
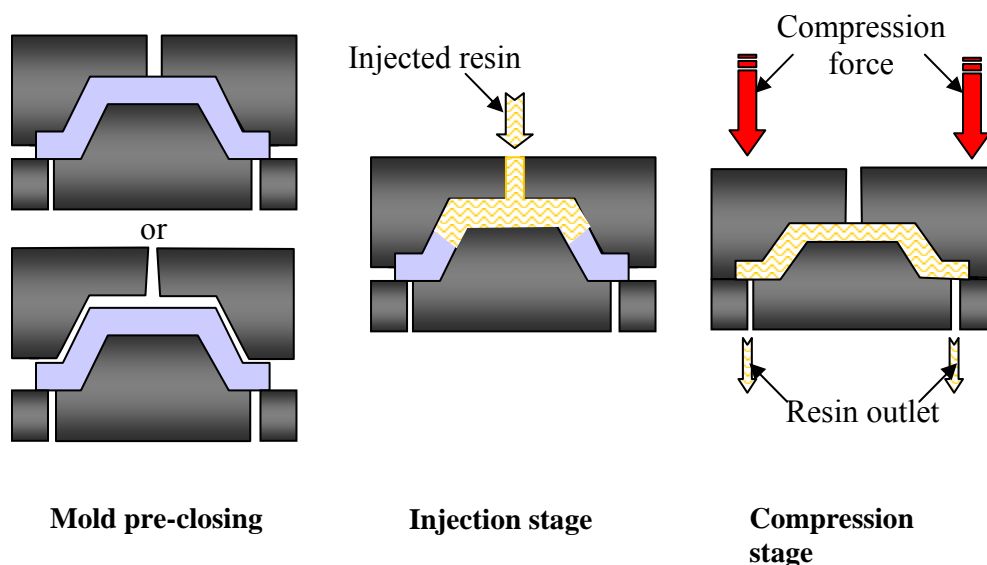
Fig. 1 : Injection/Compression process main stages

In this paper, we demonstrate the possibility of implementing the I/CM process in a simulation code called LIMS. This code developed at the Center for Composite Materials, University of Delaware, USA, is based on a control volume approach and is dedicated to the simulation of Liquid Composite Molding Technologies [6]. The advantage of LIMS is that one can access and modify any data as well as geometric features (nodes location for instance) between each calculation step, get information and take control actions without interrupting the simulation. The complexity of the I/CM process can thus be addressed using LIMS through dedicated algorithm and routine as one can change the geometry and update material properties at any time.

I/CM PROCESS MODELING

Two types of problems, presented in Fig. 2, are addressed:
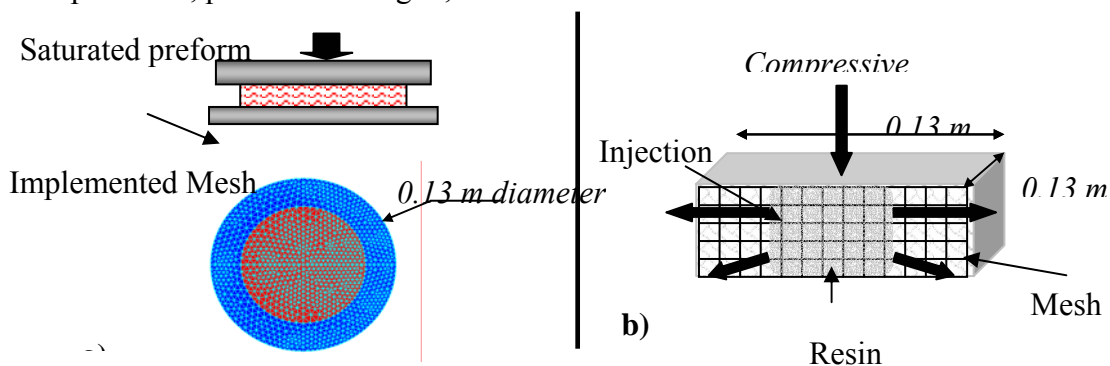
Fig. 2 : Consolidation (a) and Injection/Compression (b) processes and mesh presentation

- The consolidation step: a fully saturated fibrous preform is compressed to evacuate the excess of resin. The input geometry is a 2D shell mesh representing a plane perpendicular to the applied compressive load. A circular mesh shape is used as the resin flows radially (Fig. 2a).
- Injection followed by a compression stage (I/CM): resin is injected through the preform, then the preform is compressed and the resin flows towards the dried areas. In this case, the unidirectional compressive load creates a 2D in-plane flow. A rectangular mesh constituted of 50x20 rectangular elements is used as the representation of a slice of the part (Fig. 2b).

Assumptions

Although not required, the preform considered here is isotropic. A 1D-compression is set in the thickness direction with a constant deformation speed. Deformations in the in-plane directions are assumed negligible. The permeability is calculated from the fiber volume fraction according to experimental data obtained from the permeability tests performed for different fiber volume fractions on a balanced woven fabric (Lyvertex, Hexcel of 0.41 Kg/m^2) preform (Fig. 3).
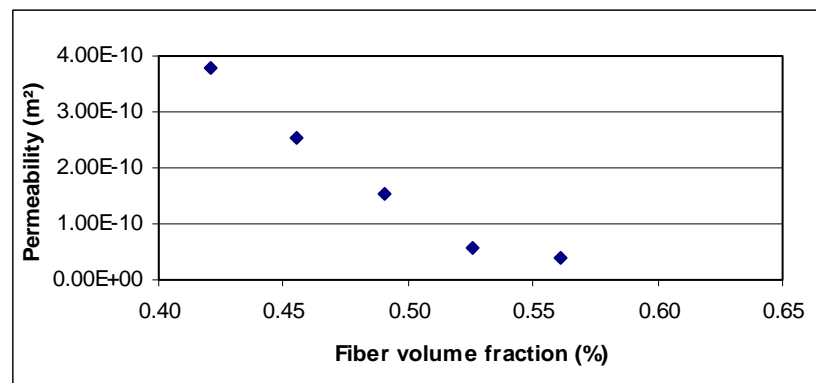
Fig .3 : Experimental permeability values for the studied preform

Algorithm

The principle of the simulation is to convert the vertical pressure load applied during the compression into progression of the resin flow front. The program is based on control of the amount of resin displaced. The algorithm is decomposed into the following steps :

- Set element properties (initial permeability K and volume fraction V_f, resin viscosity μ, elements thickness, …)
- Set injection gates (I/CM case) and vents
- Set nodes as filled nodes (consolidation case) or perform the injection until the desired amount of resin is injected (I/CM case)

- Compression loop
  - Set each filled node as an injection gate
  - Update the flow rate Q from the volume of resin moved out of the part

  $$Q = V_{comp}(1 - Vf) \frac{filled\ area}{Number\ of\ nodes\ filled}$$

  where V_{comp} is the compression velocity and V_f is the preform fiber volume fraction
  - Calculate the new part thickness

  $$h_n = h_{n-1} - V_{comp}(t_n - t_{n-1})$$

  where h and t represent the part thickness and time, respectively, the subscripts n and $n-1$ represent the current and previous calculation steps, respectively
  - Calculate the new perform volume fraction and permeability
  - Update material properties and mesh geometry
- Solve until the desired final thickness is reached

Results

The simulations are validated by controlling the injected volume with respect to time. The outputs are the resin pressure profile in the mold and the resin pressure at the center of the mold, presented in Fig. 4 and 5 respectively. Parameters used for the simulation for both cases are reported in Table 1.

Table 1. Simulation parameters

Parameter	Representation / unit	Value	Parameter	Representation / unit	Value
Injection flow rate	Q / $m^3.s^{-1}$	$1.67\ 10^{-5}$	Preform initial porosity	ϕ / %	70
Compression velocity	V_{comp} / $mm.min^{-1}$	0.5	Initial preform thickness	H_{init} / m	0.02
Resin viscosity	μ / Pa.s	0.2	Final preform thickness	H_{fin} / m	0.01
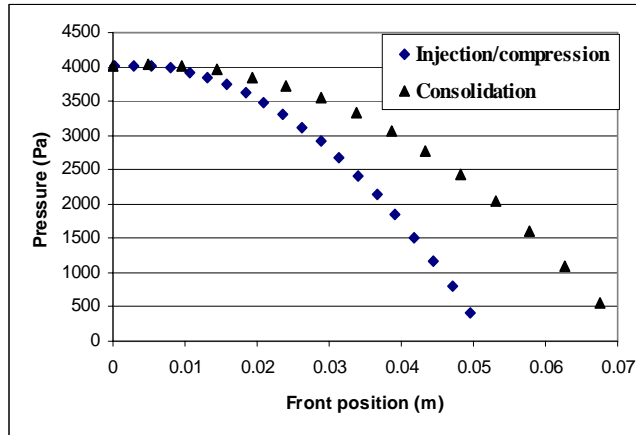
Fig. 4 : Resine pressure profile along the bold at the end of the process
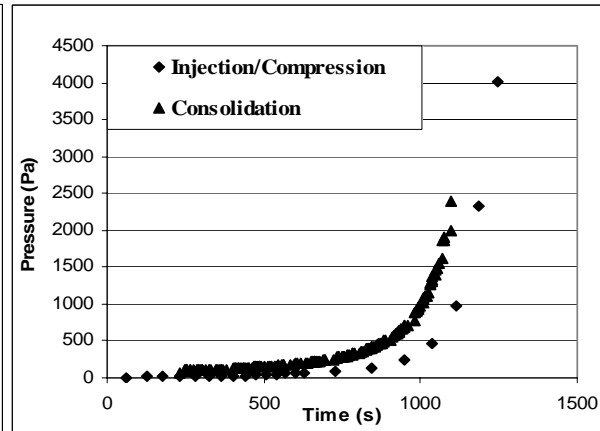
Fig. 5 : Resine pressure profile at the center of the mold during the injection

Even though the mesh geometry is different, the mold dimensions are of the same range for the two presented configurations. The pressure profiles obtained in both cases have the same trend and the pressure levels reached are of the same order of magnitude. As confirmed by Pham et. al., the resin pressure profile along the mold is parabolic [5]. Knowing the pressure inside the mold would help dimensioning the production in terms of press requirements, and maximum compression velocity.

CONCLUSION AND FUTURE DEVELOPMENTS

The present paper shows the possibility to model forced deformation and the compression driven resin flow induced in the I/CM process. Further extension of the code towards other LCM technologies is possible, involving other class of materials such as a gap filled with resin or a sandwich core, provided that the materials behavior (dry and wetted preform, resin, foam core in the case of sandwich materials…) is characterized under a compressive load. Constant pressure compression in Resin Film Infusion (RFI) could then be modeled successfully. The consolidation process simulation can be used to model the mechanical behavior of an impregnated perform and thus determine the contribution of the fluid pressure during the compression. Moreover, the flow induced deformations that occur in some processes such as in sandwich composites molding or in Vacuum Assisted RTM (VARTM) could be simulated [7]. As LIMS can also solves for 3D structures, further developments are currently in progress in order to model a 3D-I/CM process.

REFERENCES

1. K. M. Pillai, C. L. Tucker and F. R. Phelan, "Numerical Simulation of Injection/Compression Liquid Composite Molding. Part 1. Mesh Generation", *Composites Part A: Applied Science and Manufacturing*, Volume 31, Issue 1, Pages 87-94 (2000)

2. K. M. Pillai, C. L. Tucker and F. R. Phelan, "Numerical Simulation of Injection/Compression Liquid Composite Molding. Part 2: Preform Compression", *Composites Part A: Applied Science and Manufacturing*, Volume 32, Issue 2, Pages 207-220 (2001)

3. K. Han, L.J. Lee, M. Liou, "Fiber Mat Deformation in Liquid Composite Molding. II : Modeling", *Polymer Composites*, Volume 14, Issue 2, Pages 151-160 (1993)

4. S. Bickerton and M. Z. Abdullah, "Modeling and Evaluation of the Filling Stage of Injection/Compression Molding", *Composites Science and Technology*, Volume 63, Issue 10, Pages 1359-1375 (2003)

5. X.T. Pham, F. Trochu and R. Gauvin, "Simulation of Compression Resin Transfer Molding with Displacement Control", *Journal of Reinforced Plastics and Composites*, Volume 17, Issue 17, Pages 1525-1556 (1998)

6. M. Bruschke, S. G. Advani, "A Finite Element/Control Volume Approach to Mold Filling in Anisotropic Porous Media", *Polymer Composites*, Volume 11, Pages 398-405 (1990)

7. C. Binetruy, S.G. Advani, "Foam Core deformation during Liquid Molding of Sandwich Structures : Modeling and Experimental Analysis", *Journal of Sandwich Structures and Materials*, Volume 5, Issue 4, Pages 351-376 (2003)

Numerical Modeling of Underfill Resin Cure Evolution during Chip-Scale-Packaging

Rajesh R. Gomatam[1], and John P. Coulter[2]

Department of Mechanical Engineering and Mechanics, Lehigh University, Bethlehem, PA 18015, E-mail: raga@lehigh.edu[1] and jc0i@lehigh.edu[2]

SUMMARY: In flip-chip packages the chip is mounted directly on to a substrate using a grid-array of solder bumps. In order to minimize the thermal stress, it is necessary to use glass-filled epoxy encapsulant, traditionally known as 'Underfill', to improve the reliability of flip-chip solder joint interconnections. By applying an underfill encapsulant into the gap between the IC chip and the substrate, the thermal stress on the solder joints during each temperature excursion can be uniformly dispersed throughout the encapsulated structure, leading to an enhanced improvement o the fatigue durability. In an actual manufacturing process establishing efficient curing of the underfill resin in the solder-reflow oven is of paramount importance, as it is directly linked to the fatigue reliability of the part. Unfortunately, there are a number of parameters, such as, curing kinetics of underfill resin, temperature profile in the reflow oven, solder bump temperature, and solder bump patterns that interact with each other in determining the degree of cue. The current work addresses the aspect of predicting the underfill resin cure during an actual manufacturing process, taking into account all the process variables that influence the underfill resin cure.

KEYWORDS: Underfill Resin Cure, Chip-Scale-Packaging, Degree of Cure, Curing Kinetics, Solder Temperature, Reflow Oven Temperature Profile

INTRODUCTION

Over the last few decades, the microelectronics industry, in the form of computer and communication devices for the fast treatment of huge amounts of data has grown rapidly in size. Thus, integrated circuits (ICs) with high performance are in demand [1 - 3].

Flip chip assembly technology was originally developed in the early 1960s with IBM's Controlled Collapse Chip Connection process also known as C4. An integrated circuit chip is placed with its active face down onto a ceramic substrate, and electrical/mechanical connections are made with both the topside metallurgy (TSM), and ball limiting metallurgy (BLM). In recent years, flip chip assembly has evolved quite rapidly.

In contrast to the classic C4 process, state-of-the-art flip-chip assembly uses organic substrates in what is known as Flip Chip on Board (FCOB) or Direct Chip Attach (DCA) technology. In general, the assembly processes for these technologies are both costly and time consuming.

The direct attachment of a solder-bumped flip chip to an organic substrate requires the use of an underfill encapsulant to enhance the reliability of the flip-chip assembly.

An underfill with a high modulus, a coefficient of thermal expansion (CTE) matching that of the organic substrate, and with good adhesion to both the substrate (with and without solder mask) and the outermost passivation layer of the silicon die are required [4, 5]. By applying an underfill encapsulant into the gap between the IC chip and the substrate, the stress on the solder joints during each temperature excursion can be uniformly dispersed throughout the encapsulated module, leading to an enhanced improvement in the reliability.

Unfortunately, flip chip on board processing has yet to become a low cost, high throughput process compatible with high volume surface mount processing. Due to the advent of numerous classes of underfill material, varying in flow, curing characteristics, and also different manufacturing processes, it is essential to develop a design tool to facilitate prediction of cure behavior during an actual manufacturing process.

The current work addresses the aspect of underfill resin cure during an actual manufacturing process, taking into account all the process variable, such as underfill cure kinetics, solder bump temperature, temperature in reflow oven, and solder bump configurations, that influence the resin cure. The numerical tool developed gives an easy to use tool for process engineers to control and fine-tune the multiple, interacting process variables for efficient manufacturing of reliable packages.

RESULTS AND DISCUSSIONS

The manufacture of Chip-Scale packages takes place in 4 distinct steps:
1. Alignment and placement of the IC chip to the substrate;
2. Solder reflow cycling and flux residue cleaning
3. Dispensing underfill encapsulant on one or two edges of the assembly followed by capillary flow to fill the gap between the chip and the substrate;

4. Cure reaction of the underfill encapsulant in a solder reflow oven.

Theoretical Background

For the purpose of analyzing the cure process during manufacture, we consider the case of a completely filled underfill condition, which is passed through a reflow oven with a programmed heating profile. Fig. 1 shows the pictorial representation of the physics of the problem.
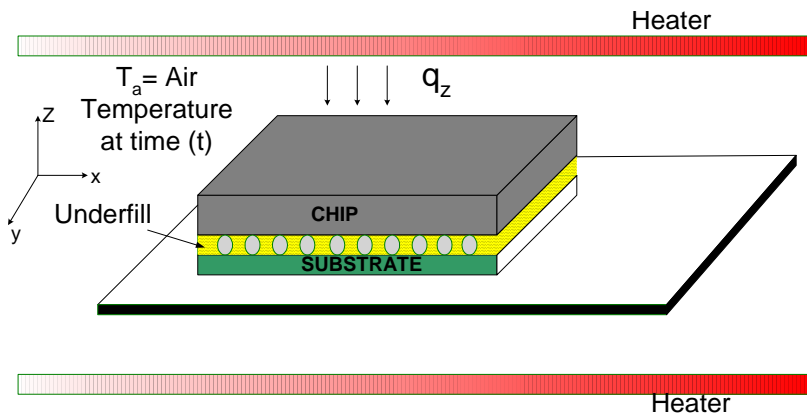
Fig. 1 Pictorial representation of the physics of the problem in reflow-oven

The temperature distribution, the degree of cure of the resin inside the flip-chip depends on the rate at which heat is transmitted from the environment into the material. The temperature inside the resin can be calculated using the law of conservation of energy together with an appropriate expression for the cure kinetics. The individual governing equations within the substrate, chip, and underfill resin are given below:

(a) Internal governing equations

$$\rho C_p \left[\frac{\partial T(x,y,z)}{\partial t} \right] = k\nabla^2 T(x,y,z) \tag{1}$$

(b) In the resin

$$\rho C_p \left[\frac{\partial T(x,y,z)}{\partial t} \right] = k\nabla^2 T(x,y,z) + \dot{H}_r \tag{2}$$

where H_r is the rate of heat of reaction, C_p is the specific heat, ρ is the density, and k is the thermal conductivity of the material.

The rate of heat of reaction is given by the expression

$$\dot{H}_r = \rho \Delta H_r \frac{\partial \alpha}{\partial t} \tag{3}$$

where α denotes the degree of cure, and the rate of cure is given by the expression:

$$\frac{d\alpha}{dt} = k\alpha^m (1-\alpha)^n \tag{4}$$

Furthermore, the boundary condition between chip top surface and air is evaluated by Eqn. 5, indicated below.

$$q_z'' = h(T_s - T_\infty) \tag{5}$$

where h is the convention heat transfer coefficient, T_s is the temperature on top of the chip, and T_∞ is the temperature of the air.

In the current paper, 'Dexter 4531' was utilized as the model underfill. From the kinetic experiments, the following kinetic constants were obtained, which were applied in Eqn. 3, which are indicated in Table 1. Furthermore the total heat of reaction was found to be 109 J/g at 170°C.

For the purpose of our simulation a 'Finite Difference' numerical scheme was employed. The whole chip was discretized into a small mesh pattern, and the nodal values for temperature, and degree of cure were evaluated over the time period of 4 minutes following the programmed heater profile in the reflow oven. Furthermore, the solder geometry was approximated from a cylindrical geometry to a square block based on equivalent volume.

Table 1. Kinetic Constants for Dexter 4531 Underfill

Temperature (°C)	k	m	n
130	0.0674	0.7	0.64
150	1.16	0.586	1.49
170	1.21	0.629	3.13

Case Study

This simulation results presented in this paper was done to predict the degree of cure during the actual CSP manufacturing process implemented in a manufacturing process. For this case study, the dimensions of the CSP used are: chip = 10 mm x 12 mm, pitch of solder bumps = 0.94 mm, bump diameter = 0.38 mm, gap height = 0.25 mm, thickness of chip = 0.38 mm and thickness of substrate = 0.6 mm. In this case, the Dexter 4531 underfill resin was utilized, for which the kinetic rate constants are indicated in Table 1. Furthermore, in this the solder bump temperature was kept at 25°C, and the curing was done in the solder reflow oven according to the prescribed reflow oven heating temperature profile.

First, the value of the convection heat transfer coefficient was ascertained to be 1018 W/m^{2}K, which was obtained by matching the simulated chip surface temperature close to that obtained from experiments. Fig. 2 shows the graphical representation of the % degree of cure at the end of 4 minutes. We first note that for all time periods the curing behavior is symmetric. Our results also show that the degree of cure is found to be maximum at the edges, and minimum at the center. Fig. 3 shows the plot of % degree of cure at 3 locations, namely inner, middle, and outer nodal locations. From Fig. 3, we note that after a period of 4 minutes we have a 70% cure near the edges, which gradually reduces to less than 30% at the center of the chip. Furthermore, in the center we observe that the cure is less than 10% for the first 3 minutes, and later during the last 1 minute the cure reaches to 23%. From this simulation, we clearly infer that in the current process implemented in this case study; underfill cure is either incomplete or insufficient.
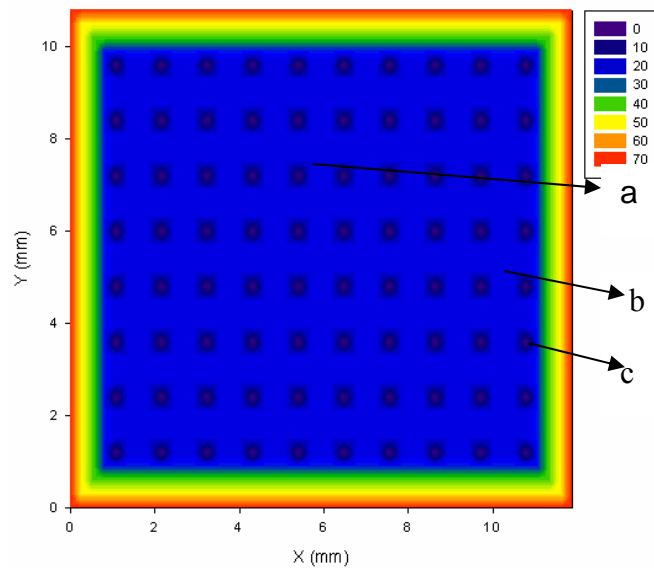
Fig. 2 Chip Surface Temperature Profile
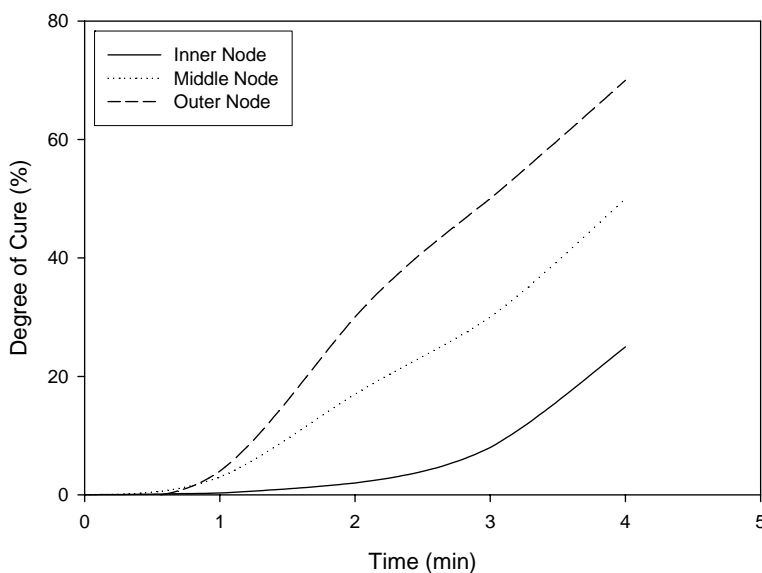
Fig. 10 % Degree of Cure at Outer, Middle and Inner Nodes for Case # 1

CONCLUSIONS

During the present study, an effort was undertaken to develop science-based numerical model to enhance the understanding of the underfill resin cure process that occur during microelectronics manufacturing. Models were developed to simulate the underfill curing process during CSP manufacturing process, which would facilitate efficient evaluation of a manufacturing process, and identify potential manufacturing processes relevant to chip-scale packaging process. This numerical scheme takes into account the heat conduction, and convection process in the actual manufacturing process, making the model more useful as an evaluation tool to assess part durability through process changes. Also, in this paper a case study was presented to illustrate the usefulness on this design tool.

REFERENCES

1. W. J. McClean, "A report of the integrated circuit industry"; Integrated Circuit Engineering Corporation: Scottsdale, AZ (1986).
2. C. P Wong, *Adv. Polym. Sci.*, Volume 84, Pages 65-72 (1988).
3. M. L. Mings, *Electronic Materials Handbook*, ASM International, Metals Park, OH (1989).
4. S. Machuga, S. Lindsey, K. Moore, and A. Skipor, "Encapsulant for Flip Chip Structures", *Proc. Of The Thirteenth IEEE/CHMT International Electronics Manufacturing Technology*, Pages 53-58 (1992).
5. G. Suranarayana, "Flip Chip Solder Bump Fatigue Life Enhanced by Polymer Encapsulation", *Proc. of The 40th Electronics Components and Technology Conference*, 1990, Pages 1338-1344 (1990).

PREFORM MODELING AND EFFECTS:
I. MICROMODELING OF FABRIC PERMEABILITY

Computer Modeling for the Prediction of the In-Plane Permeability of Non-Crimp Stitch Bonded Fabrics

C.Lekakou, S.Edwards, G.Bell and S.C.Amico

School of Engineering, University of Surrey, Guildford, Surrey GU2 7XH, UK

SUMMARY: The purpose of this paper is to present and validate a model for the prediction of in-plane permeability in non-crimp stitch bonded fabrics. The model is based on the combined flow through the multi-layer assembly in each non-crimp fabric. The permeability of each layer of the assembly is predicted on the basis of a meso-/micro-flow computer model. In this the meso-flow between fiber tows is considered as Stokes's flow and it generally progresses ahead the micro-flow. Darcy's law is employed to model micro-flow through each fiber tow, taking into account injection and capillary pressures in both types of flow. Transverse mass transfer is considered from the advancing meso-flow to the micro-flow through the permeable boundaries of fiber tows. The model is tested in biaxial non-crimp stitch bonded fabrics with either chain or tricot stitch. Excellent agreement exists between predictions and experiment when the meso-channels are straight of homogeneous cross-section. The permeability predictions are very sensitive to the dimensions of the meso-channel cross-section and require input data from a detailed microstructural analysis for meso-channels with varying cross-section.

KEYWORDS: Permeability, modeling, non-crimp, stitch-bonded, fabrics.

INTRODUCTION

Non-crimp stitch-bonded fabrics are a later class of fabrics with some advantages over existing unidirectional prepregs and other fabrics, such as woven fabrics. The presence of stitch allows for multi-layer assemblies of unidirectional fibers, where each layer may be in a different specified orientation and where the stitched assembly is easy to handle. Hence, the purpose of the non-crimp stitch bonded fabrics has been to replace unidirectional prepregs aiming at costs reductions by shortening and automating the lay-up time. On the other hand, they have the benefit of reduced through-thickness crimp in comparison to woven fabrics leading to improvements in mechanical properties [1] although some in-plane crimp is present.

The stitch, and more specifically the type and tightness of stitch affect the drapeability/formability of the fabric. Two common types of stitch are the chain stitch and the tricot stitch, where the former is generally tight and restrictive in forming, whereas the latter is much more favoured for the manufacturing of formed products.

Regarding the prediction of the permeability of fabrics, the non-crimp fabrics have the advantage to have a simple design, where each layer may be possibly assumed as a unidirectional fiber layer.

Amico and Lekakou [2] developed a permeability model, implemented in a computer code, which allows the prediction of in-plane permeability parallel to the fibers for assemblies of fiber tows characterized by meso-channels, between the fiber tows, and micro-channels between the fibers within each tow. This computer model has been successfully validated with respect to both, advancing meso-flow and micro-flow. The computer model for the prediction of the in-plane permeability of non-crimp stitch bonded fabrics presented in this study is based on this meso-/micro-flow model.

PERMEABILITY MODEL

Each layer in the non-crimp stitch bonded fabric was considered as an array of parallel fiber tows with meso-channels between the tows, where the meso-channels and the tows were assumed to be of rectangular and elliptical cross-section, respectively [2]. Axial Stokes's flow was considered in the meso-channels and Darcy's law was applied within the porous fiber tows, taking into account injection pressure and capillary pressure in both types of flow. Transverse flow transfer was modeled from the leading flow front to the lagging flow and a partial-slip boundary condition was applied at the permeable boundaries of meso-channels.

The flow through the multi-layer assembly was modeled as the total of parallel flows through each layer [3], in the direction of the total flow, so that the total permeability, K_{tot}, was given by the average of permeabilities if all layers were assumed to be of the same thickness:

$$K_{tot} = \frac{\Sigma K_{Li} H_{Li}}{\Sigma H_{Li}} \tag{1}$$

where K_{Li} and H_{Li} are the permeability and thickness of layer i.

If the fiber direction in layer i was parallel to the total flow direction, the permeability K_{Li} was calculated on the basis of the computer model by Amico and Lekakou [2]. If the fiber direction in layer i was at 90° with respect to the total flow direction, the permeability $K_{Li,T}$ is given by the relation

$$K_{Li,T} = \left[\frac{1}{L_{Tot}} \left(\Sigma \frac{L_{mes,i}}{K_{mes,i}} + \Sigma \frac{L_{micro,i}}{K_{micro,T}} \right) \right]^{-1} \tag{2}$$

where L_{Tot} is the total flow length, $L_{Tot} = \Sigma L_{mes,i} + \Sigma L_{micro,i}$, $K_{micro,T}$ is the transverse permeability of fiber tow and

$$K_{mes,i} = \frac{H^2_{mes,i}}{12} \tag{3}$$

where $H_{mes,I}$ is the height of the rectangular meso-channel in layer i.

EXPERIMENTS

The experiments included in-plane permeability measurements in an RTM mold with central injection (radial outward flow). Six layers of non-crimp stitch bonded fabrics were used in each permeability experiment and no central hole was cut for the injection. Silicone oil was used as the infiltrating liquid in each permeability experiment. After the permeability experiment, a curing Araldite epoxy was injected to make an RTM laminate which was used to measure total thickness, H, and fiber volume fraction, V_f, and geometrical parameters of the fibers, fiber tows and meso-channels in microstructural analyses of mosaics of micrographs.

Three types of non-crimp stitch bonded glass fiber fabrics were used as presented in Table 1. EBX936 and EBXhd936 were $\pm 45^o$ biaxial fabrics whereas ELT850 was a $0^o/90^o$ biaxial fabric. EBX936 had chain stitch whereas the other two fabrics had tricot stitch.

Table 1: Non-crimp stitch bonded fabrics used in this study

Fabric Code	Fibre Type	Percentage of Each Ply				Stitch Type
		0°	90°	+45°	-45°	
EBX936	Glass	---	---	50_1	50_2	Chain
EBXhd936	Glass	---	---	50_1	50_2	Tricot
ELT850	Glass	50_2	50_1	---	---	Tricot

RESULTS AND DISCUSSION

Table 2 presents the results of the predicted and measured permeabilities, where all results have been extrapolated to the permeability corresponding to $V_f = 0.55$, using the Carman-Kozeny relationship. Parametric studies showed that the predicted permeabilities were very sensitive to the value of meso-channel width. Starting with the $0^o/90^o$ biaxial fabric ELT850, one of the two layer directions (90°) proved most appropriate for validating the permeability model, since it had regular and straight meso-channels (see Fig.1). Using an average meso-channel width, $w = 3.8 \times 10^{-4}$ m, the predicted permeability agreed exactly with the measured permeability value.

However, the meso-channels of EBX936 and EBXhd936 were not at all straight, as shown in Fig.2 and Fig.3. When the maximum values of the measured meso-channel widths were used for EBX936, $w_{-45,max}=2.37 \times 10^{-4}$ m and $w_{+45,max}=3.34 \times 10^{-4}$ m, the predicted permeabilities varied significantly from the measured values, as presented in Table 2. By using the average measured values, $w_{-45,ave}=1.52 \times 10^{-4}$ m and $w_{+45,ave}=1.68 \times 10^{-4}$ m, excellent agreement was reached between predictions and experiment. The same occurred with EBXhd936, where
$w_{-45,max}=2.37 \times 10^{-4}$ m and $w_{+45,max}=1.53 \times 10^{-4}$ m and
$w_{-45,ave}=2.15 \times 10^{-4}$ m and $w_{+45,max}=1.85 \times 10^{-4}$ m.

Table 2: Results of the predicted and measured permeabilities of the tested non-crimp stitch bonded fabrics.

Fabric code	Predicted Permeability (m²)		Measured Permeability (m²)		Predicted Permeability (m²)	Measured Permeability (m²)
ELT850	K_{90} = 1.48x10⁻¹¹		K_{90} = 1.48x10⁻¹¹			
EBX936, $w_{meso,max}$	K_{-45} = 1.14x10⁻¹¹		K_{-45} = 5.42x10⁻¹²		K_{+45} =2.41x10⁻¹¹	K_{+45} =6.54x10⁻¹²
EBX936, $w_{meso,ave}$	K_{-45} = 5.38x10⁻¹²		K_{-45} = 5.42x10⁻¹²		K_{+45} =6.54x10⁻¹²	K_{+45} =6.54x10⁻¹²
EBXhd936 $W_{meso,max}$	K_{-45} = 6.62x10⁻¹²		K_{-45} = 5.52x10⁻¹²		K_{+45} =6.54x10⁻¹²	K_{+45} =3.02x10⁻¹²
EBXhd936 $W_{meso,ave}$	K_{-45} = 5.51x10⁻¹²		K_{-45} = 5.52x10⁻¹²		K_{+45} =3.02x10⁻¹²	K_{+45} =3.00x10⁻¹²
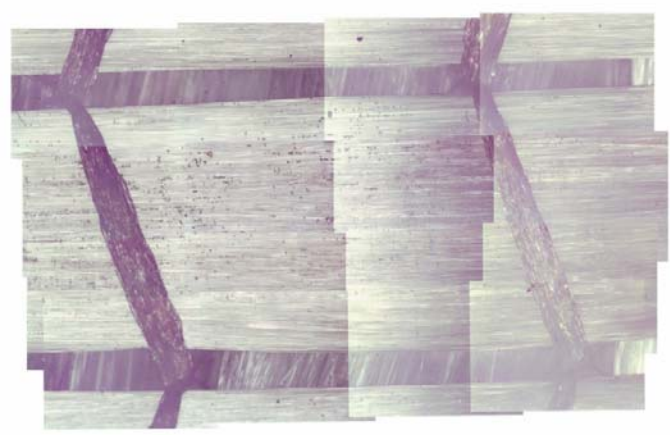
Fig.1. The 90° layer of ELT850.
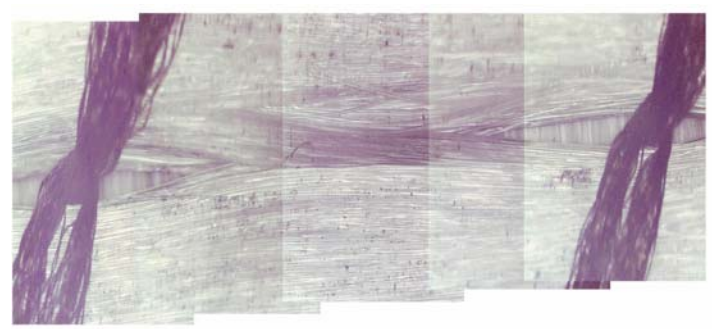
Fig.2. Fabric structure of EBX936.

Fig.3. Fabric structure of EBXhd936.

CONCLUSIONS

A model has been presented for the prediction of the in-plane permeability of biaxial non-crimp stitch bonded fabrics based on the assembly of flow units in parallel (for different layers) or in series, whereas the prediction of the permeability of each layer along the fiber direction is based on a meso-/micro-flow model [2]. Successful permeability predictions in comparison with experimental data were achieved for straight meso-channels as in fabric ELT850. However, several stitched fabrics display a large extent of in-plane waviness and the width of their meso-channel has a large effect on their permeability. As a result, detailed microstructural analysis is required to determine average meso-channel dimensions, which when inputted in the computer model yielded in-plane permeability predictions in excellent agreement with experimental data.

REFERENCES

1. P.J.Hogg, G.A.Bibo and M.Kemp, "Mechanical characterization of glass- and carbon-fiber reinforced composites made woth non-crimp fabrics", *Composites Science and Technology,* Vol.57, no.9-19, 1997 pp.1221-1241.

2. S.Amico and C.Lekakou, "Flow through a two-scale porosity, oriented fiber porous medium", *Transport in Porous Media*, Vol.54, no.1, 2004 pp.35-53.

3. E.Heardman, C.Lekakou and M.G.Bader, "In-plane permeability of sheared fabrics", *Composites A*, Vol.32, 2001, pp.933-940.

A Permeability Prediction for (Un)Sheared Non-Crimp Fabrics

R. Loendersloot [1], R. Akkerman [1] and S.V. Lomov [2]

[1] *Department of Engineering Technology, Composites Group, University of Twente,P.O. Box 217, 7500AE Enschede, The Netherlands: r.loendersloot@ctw.utwente.nl*
[2] *Department of Metallurgy and Material Engineering, Composites Group, Katholieke Universiteit Leuven, Kasteelpark Arenberg 44, B3001 Leuven, Belgium*

SUMMARY: A permeability prediction model for relaxed and sheared Non-Crimp Fabrics is proposed. The model is based on geometrical features of the fabric. The stitches penetrating the uni-directional plies of the NCF induce distortions of the fibers in the plane of the fabric. These Stitch Yarn induced fiber Distortions (SYD) form flow channels, which determine the permeability of the NCF. The channels are connected to each other in overlap regions, allowing the fluid to flow from one channel to another and finally to impregnate the entire preform. A network of SYD flow channels is created to account for the statistical variations in the dimensions of the SYDs. The system of flow resistances is solved analogously to the solution of the effective resistance of an electrical circuit with parallel and serial resistances. The flow in each of the SYD domains is calculated employing an energy minimisation method. Analysis of different networks, with varying spatial distribution of the dimensions of the flow channels, allows the prediction of the variation in the permeability of an NCF.

INTRODUCTION

Resin Transfer Molding (RTM) has proven to be a cost effective production method for near-net shaped products with a high accuracy and a high reproducibility. The application of Non-Crimp Fabrics (NCF) in RTM combines improved properties with relatively low production costs. The absence of undulation (or crimp) of the fiber bundles of an NCF improves the in-plane properties relative to woven fabric composites, whereas the stitches in the material prevent a significant drop of the through thickness properties. The growing application of NCFs in complex shaped structural components increases the urge for models predicting the drape properties of the material and the resulting impregnation behavior.

Accurate flow simulations, which require detailed knowledge on the impregnation behavior, are an essential tool in finding the optimal RTM process parameters. One of the most critical parameters in the mold filling simulations is the permeability of the fibrous preform, which is in essence a geometric quantity.

This research aims to predict the permeability of NCFs based on a network of flow channels, which dimensions depend on geometrical features of the fabric and the fabric deformation. The analysis of a network of flow channels allows the incorporation of statistical variations of the channel dimensions, in the permeability prediction. These variations were observed during analysis of different types of NCFs [1-4].

GEOMETRY OF A NON-CRIMP FABRIC

A single layer of a Non-Crimp Fabric (NCF) consists of a stack of uni-directional plies of fibers. The stack of plies is stitched by the warp knitting process, according to a certain pattern (e.g. chain or tricot). A more detailed description of the stitching process is found in Lomov *et al.* [1]. The stitches induce fiber distortions in the plane of the fabric when penetrating the NCF, as clearly shown in Fig. 1.

| (a) | (b) |
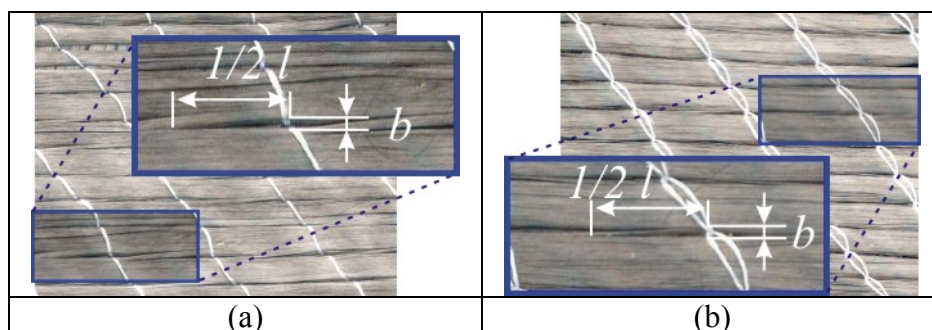
Fig. 1. Stitch Yarn induced fiber Distortions on the top and the bottom face of a ±45° biaxial Non-Crimp Fabric, with a chain knit pattern. *b* is the width and *l* the length of the SYD.

The dimensions of the Stitch Yarn induced fiber Distortions (SYD) and the effects of shear are discussed in [2-4]. A distribution of the dimensions of the SYDs is found. This distribution is explicitly incorporated in the permeability prediction model.

PERMEABILITY NETWORK MODEL

Unit Cell and Interaction Regions

The proposed permeability model is based on a unit cell approach. The unit cell is the flow domain formed by the SYD. In- and outflow regions of the SYD unit cells, which connect the unit cells and allow the fluid to flow through the reinforcement, are found in overlapping regions as depicted in Fig. 2. The amount of these regions and their locations depend on the dimensions of the SYDs, the needle spacing, the stitch distance in machine direction and the orientation of the fibers with respect to the machine direction. Note that they are affected on a local level by the distribution of the dimensions of the SYDs.

Possible locations of the overlapping regions are limited to integer multiplications of the projected distances d_p of the needle spacing D_n and stitch distance D_s in the fiber direction (Fig. 2).

It can be derived that:

$$
\begin{aligned}
d_p^n &= \frac{D_n}{\cos\theta_1 \left(\tan\theta_1 + \tan\theta_2 \right)} \\[2ex]
d_p^s &= \frac{D_s \sin\theta_1 \tan\theta_1 \tan\theta_2}{\tan\theta_1 + \tan\theta_1}
\end{aligned}
\tag{1}
$$

with θ_1 and θ_2 as defined in Fig. 2. Note that the fiber angles may be different from 45° (in triaxial and quadriaxial NCFs), but shear does not affect the distances d_p, provided a trellis frame shear is assumed.
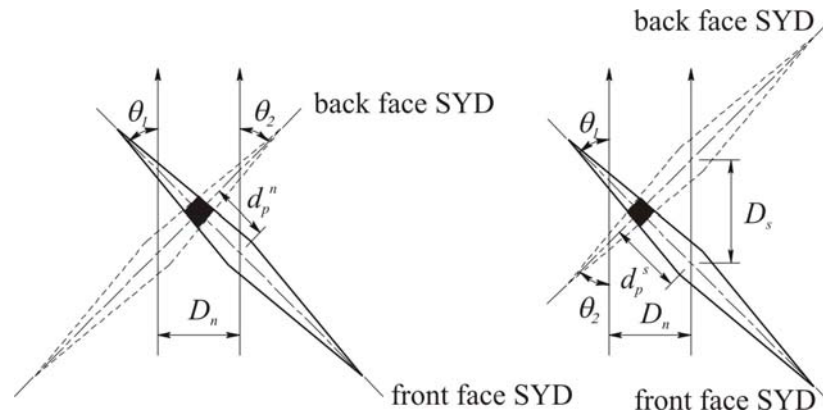
Fig. 2 Locations of overlap regions (dark areas) depend on integer multiplications of the projected distance d_p^n and d_p^s on the SYD. θ_1 is the fiber angle of the upper layer, θ_2 the fiber angle of the bottom layer.

Unit Cell Flow Solution

The flow resistance of the each of the unit cells is computed with a multigrid flow solver [5]. A 3D Stokes' flow is assumed in the unit cell:

$$
\nabla p - \mu \nabla^2 \cdot \underline{u} = \underline{0}
\tag{2}
$$

The solution is obtained by solving Eqn. 2 on a staggered grid and using a bipolar mapping routine. The shape of a single SYD is assumed to be perfectly bipolar.
The fiber bundles, forming the boundaries of the SYD unit cell, can either be assumed to be solid or to be permeable. In the latter case, Brinkmans' equation is solved in the fiber bundle:

$$
\mu \nabla^2 \cdot \underline{u} - \mu \underline{\underline{K}}_{tow}^{-1} \nabla \cdot \underline{u} = \nabla p
\tag{3}
$$

with $\underline{\underline{K}}_{tow}$ the intra-bundle permeability. The permeability of the fabric will be overestimated in case the yarns are assumed to be solid, especially for reinforcements with a high fiber content [6]. However, incorporation of Eqn. 3 in the computations may increase the required CPU time to calculate the flow drastically.

SYD Network Solution

A network of flow resistances is constructed using the coordinates of the interaction regions and the calculated unit cell flow resistances between the interaction regions. The network domain has to be large enough to represent a continuous, possibly deformed reinforcement. The dimensions of the flow domains, and as a consequent those of the interaction regions, are assigned randomly, but in correspondence with the averaged value and distribution determined from the geometrical analysis of the preform. The system of flow resistances is solved analogously to the solution of the effective resistance of an electrical circuit with parallel and serial resistances, with the pressure gradient ∇p and the voltage drop V and secondly the fluid velocity $\underline{u}$ and the current I as congruent variables. The ratio of the permeability $\underline{\underline{K}}$ and the viscosity μ is congruent with the inverse of the electrical resistance R:

$$u = \frac{\underline{\underline{K}}}{\mu} \cdot \nabla p \leftrightarrow I = \frac{1}{R} V \qquad (4)$$

The principle permeabilities and the orientation of the principle axes are found iteratively. The principle of minimised work in the system is employed to solve the flows in each of the domains for given boundary conditions. The work $W^{(i)}$ in SYD domain i is defined as the product of the pressure gradient and the fluid velocity:

$$W^{(i)} = \nabla p^{(i)} \cdot \underline{u}^{(i)} = \mu \left(\underline{\underline{K}}^{-1} \cdot \underline{u}^{(i)} \right) \cdot \underline{u}^{(i)} \qquad (5)$$
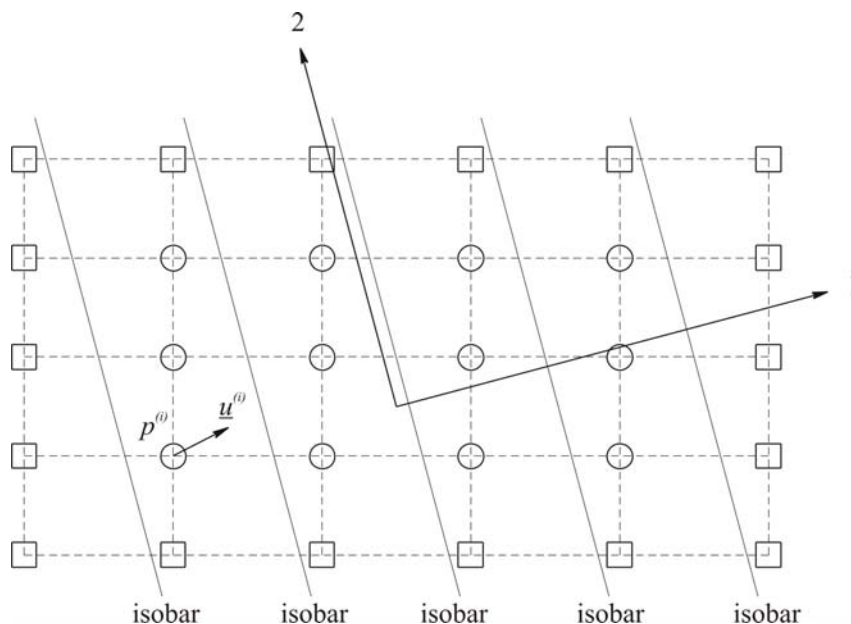
Fig. 3. Grid of interaction points (circles: inner points, squares: outer points at which the boundary conditions are applied). 1 and 2 refer to the principal directions, the pressure p and fluid velocity $\underline{u}$ at point i are indicated. Isobars visualise the assumed linear pressure gradient.

Subsequently, an initial guess of the principal directions is made and a linear pressure gradient in one of the principal directions is applied on the boundaries of the network domain (Fig. 5):

$$\underline{\nabla} p^{(i)}_{BC} = \mu \underline{\underline{K}}^{-1} \cdot \underline{u}^{(i)} \qquad (6)$$

with $\underline{\nabla} p^{(i)}_{BC}$ the pressure gradient on boundary point i and $\underline{u}^{(i)}$ the corresponding fluid velocity. The work W and the boundary conditions are combined in the objective function Φ:

$$\Phi = \sum_{i=1}^{N} \left(\mu \left(\underline{\underline{K}}^{-1} \cdot \underline{u}^{(i)} \right) \cdot \underline{u}^{(i)} \right)^2 + \psi \sum_{i=1}^{M} \left(\underline{\nabla} p^{(i)}_{BC} - \mu \underline{\underline{K}}^{-1} \cdot \underline{u}^{(i)} \right)^2 \qquad (7)$$

with N the number of interaction points in the network, M the number of boundary points and ψ a weight factor for the boundary conditions: the higher its value, the better the boundary conditions are satisfied. Minimisation of the objective function Φ yields the fluid velocities in the SYD unit cell. The direction of the average fluid velocity should correspond with the principal direction in which the pressure gradient is applied. The initial guess of the principal directions is updated and the system is solved again. This procedure is repeated until convergence is reached. The effective permeability of the system can be calculated, once the local fluid velocities are determined. The effective permeability corresponds with the principal permeability in the direction in which the pressure gradient is applied.

CONCLUSIONS

A permeability prediction model for Non-Crimp Fabrics is proposed. The model is based on the geometry of the fabric. The distortions induced by the stitching form a network of flow channels. Statistical distributions in the dimensions of the flow channels is accounted for by analysis of a network of these flow channels. The model will require more CPU time than the currently available purely uni-directional models, but, in contrast to those models, the network model is able to quantify the statistical distribution observed in experiments.

FUTURE WORK

Experiments are being analysed currently to validate the model. The experiments are performed on single layer undeformed and sheared Non-Crimp Fabrics of different manufacturers.
Secondly, the model does not yet account for the interaction occuring between different layers of NCF. This has to be addressed in order to analyse realistic preforms.

ACKNOWLEDGEMENTS

REFERENCES

1.	S.V. Lomov, E.B. Belov, T. Bischoff, S.B. Ghosh, T. Chi Truong and I. Verpoest, "Carbon Composites Based on Multiaxial Multiply Stitched Preforms. Part 1: Geometry of the Preform", *Composites Part A,* Vol.32, 2001, pp. 1379-1394.

2	R. Loendersloot, S.V. Lomov, R. Akkerman and I. Verpoest, "Architecture and Permeability of Sheared Carbon Fiber Non-Crimp Fabrics", *Proceedings of SAMPE Europe*, Vol. 24, 2003, pp. 141-148.

3.	R. Loendersloot, R.H.W. ten Thije, S.V. Lomov, R. Akkerman and I. Verpoest, "Geometry, Compressibility and Porosity of Sheared Non-Crimp Fabrics", *Proceedings of SiComp*, Vol. 14, CD-edition.

4.	R. Loendersloot, R.H.W. ten Thije, R. Akkerman and S.V. Lomov, "Permeability Prediction of Non-Crimp Fabrics Based on a Geometric Model", *Proceedings of ECCM-11*, accepted.

5.	C.H. Venner and, A.A. Lubrecht, "Multi-Level Methods in Lubrication", *Tribology Series*, Vol. 37, Elsevier, 2000, ISBN 0-444-50503-2.

6.	E.B. Belov, S.V. Lomov, I. Verpoest, T. Peeters, D. Roose, R.S. Parnas, K. Hoes and H. Sol, "Modeling of Permeability to Textile Reinformcements: Lattice Boltzmann Method", *Composites Science and Technology*, Vol. 64, 2004, pp. 1069-1080.

Permeability Network Model of Non-Crimp Fabrics

M. Nordlund[1], T.S. Lundström[1], V. Frishfelds[2], A. Jakovics[2]

[1]*Division of Fluid Mechanics, Luleå University of Technology,*
SE-971 87 Luleå, Sweden: markus.nordlund@ltu.se
[2]*University of Latvia, Zellu 8, LV-1002, Riga, Latvia*

SUMMARY: We will here combine previous studies to yield a model that can predict the true permeability of NCFs. The model includes the geometrical features from the stitching process as well as statistical variations. A correlated randomisation is performed by the use of Monte Carlo simulations in order to mimic the global geometry of the fabric. The permeability for the unit cells, which describes the local geometry of the fabric, are thereafter determined by CFD-simulations. The permeability model for a biaxial fabric including the features from the stitching process proves that the correlation distance together with the amount of irregularity have only slight influences on the global permeability, while the presence of crossings and the average channel width are extremely important for the total permeability.

KEYWORDS: Permability, Network model, Unit cell, Monte Carlo, CFD, Stitch, Crossing.

INTRODUCTION

In previous work we have developed a general statistical permeability network model [1,2] and a CFD-unit cell model for the permeability of Non-Crimp Fabrics, NCFs [3]. We will here combine these studies to yield a model that can predict the true permeability of NCFs.

The NCFs consists of layers of parallel fiber bundles stitched to other layers preferable laid in other directions. This results in formation of channels between the bundles which consists of a large amount of fibers. The two scale porosity implies that there will be two types of flow during impregnation i.e. within and between the bundles where the second kind is likely to be of highest importance for the overall flow rate and thus the permeability [4]. The possible location of the bundles is limited to a certain volume but their actual position within this volume can vary [1]. The stitching and fibers going from one bundle to another add to the complexity. The implication of this is that there will be easy and less easy paths for the fluid to penetrate the fiber network. The flow through fabrics used in composite manufacturing is usually modeled with Darcy's law, which in its general form is written as:

$$v_i = -\frac{\mathbf{K}_{ij}}{\mu} p_{,j},$$ (1)

where v is the superficial velocity, $\mathbf{K}$ the permeability tensor μ the dynamic viscosity and p the pressure. On the first hand, the permeability of perfect geometries of different types is well known, see for instance: [5] regular packing of cylinders.

On the second hand there is a lack of knowledge of systems having detailed geometrical description of the features from the stitching process and irregularities in the geometry. Alterations to perfect geometries have been considered in a few cases. It has, for instance, been shown that perturbations to the fiber pattern and radii can give remarkable changes to the permeability [6].

BASIC APPROACH

The bundles and the inter-bundle channels are direct consequences of the stitching. The stitching process also gives rise to two other major geometrical features of the fabric, namely the penetration of the channels by the thread where the fabric is stitched, Fig. 1a, and the crossing of fibers between two neighbouring fiber bundles, Fig. 1b.
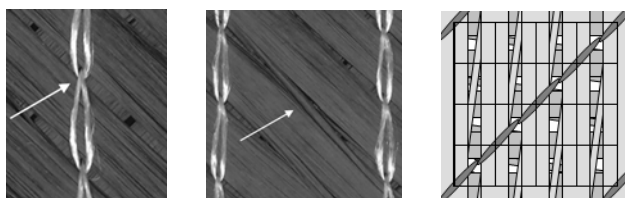
Fig. 1. Top view of a biaxial NCF showing a) the thread and b) the crossings. c) Typical distribution of the different features from the stitching process in a biaxial NCF and its unit cell distribution.

Due to the periodicity of the stitching process, the geometrical features are repeatable in a fabric and their distributions are hence dependent on the stitching pattern. Profound CFD-simulations of the whole fabric are to date impossible due to the enormous amount of volume elements required to fully resolve the geometry and flow. The fabric can instead be divided in unit cells, cf. Fig. 1c, which facilitates the simulations.

In order to develop a global permeability model for a biaxial fabric, which takes into account the effects from the stitching process and statistical variations, the work in three previous studies [1,2,3] will be combined. The global permeability of a fabric can be calculated by the use of a network model as was done in [1,2]. The tactic with the network model is to connect a number of unit cells with different permeability and thereafter calculate the overall permeability of the fabric. The unit cells in the network are connected to each other by the fluxes through the cell faces, see Fig. 2a.
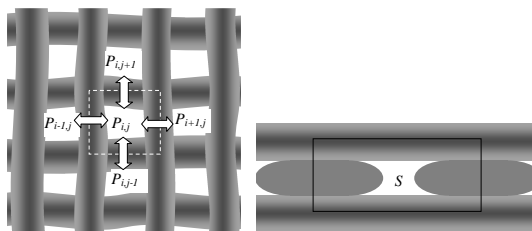
Fig. 2. a) Placement of bundles in layers for biaxial fabric building a framework for network model. b) Side view of a unit cell in one layer.

The total fluxes through the unit cell faces are obliged to satisfy mass conservation for incompressible fluid [2]:

$$\int v^x_{i-\frac{1}{2},j} dS + \int v^y_{i,j-\frac{1}{2}} dS + \int v^x_{i+\frac{1}{2},j} dS + \int v^y_{i,j+\frac{1}{2}} dS = 0. \qquad (2)$$

The boundaries parallel to the pressure gradient are set to be periodic, while pressure boundary conditions are set on the boundaries perpendicular to the pressure gradient. In real fabrics there will also be alterations of the geometry along the inter-bundle channels which is implemented in the network model so that the geometry and consequently the permeability can vary freely with spatial coordinate. The randomisation of the geometry is correlated i.e. adjacent unit cells are coupled to each other and their geometry and spatial coordinate can be determined by the use of a Monte Carlo method as in [1]. The two global parameters used in the Monte Carlo method are: the amount of irregularity in the system, τ, and what kind of irregularities that dominates, shift or inclination, γ [1]. Application of the network model and generation of channel gap distribution by the Monte Carlo method is performed on a biaxial fabric with a structure as the one in Fig. 1c, where every fourth cell contains the thread and the middle cell between these thread cells contains a crossing. Having the network, it must be filled with permeability values. This is done by usage of CFD-simulations on three types of cells: *the plain unit cell*, *the thread unit cell* and *the crossing unit cell* [3]. The discrete permeability values from the CFD-simulations, from variations of the geometries of the three cells, are fitted to analytical functions in order to obtain a permeability function for an arbitrary unit cell:

$$K_{cell}(b,h,c,t) = T(b,h,t) \cdot C(b,h,c) \cdot K_{plain}(b,h), \qquad (3)$$

where the function $T(b,h,t)$ is the contribution from the thread, $C(b,h,c)$ from the crossings, K_{plain} is the permeability for a plain unit cell and c and t determines the extent of the crossings and thread in the channels with width, b, and height, h, respectively. As indicated in Fig. 1c, the thread and the crossing cannot exist in the same unit cell.

RESULTS

The permeability of the unit cells is strongly dependent of the channel width and the size of the crossing, see Fig. 3a,c. It is also obvious that a thread unit cell has a lower permeability than a plain unit cell, see Fig. 3b. When the unit cell permeability data are put into the network model the influence from the global parameters may be studied.
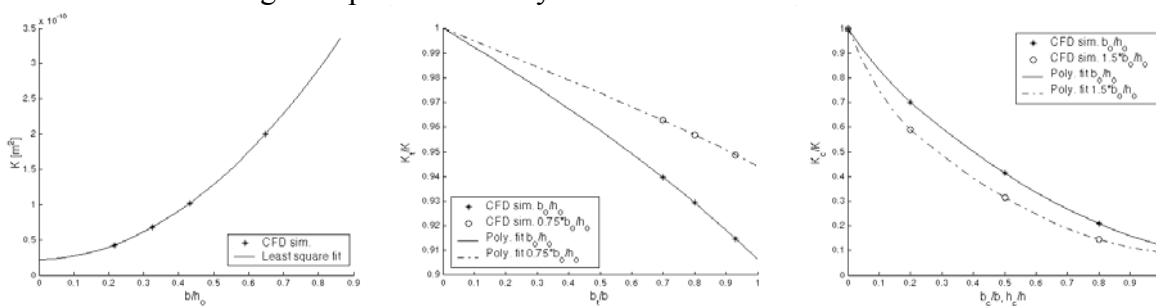
Fig. 3. a) Permeability for variation of the channel width. Influence of b) the thread, T(b,h,t), c) the crossings, C(b,h,c), on the permeability for two channel shapes, b/h.

At a given γ, the total permeability of a system with the size of 100×100 cells first increases with the irregularity τ, but afterwards it decreases as described in [1], see Fig. 4a. The change of the global permeability is smaller than for a structure without the thread or crossings [1], since the local permeability for the unit cells including the thread or the crossings have weaker dependence on the channel parameter, b/h, than the plain unit cell. Naturally, the standard deviation of the channel width increases monotonously with τ since an increased irregularity results in greater variations of the channel width, cf. Fig. 4a. Fig. 4b shows that the permeability increases with the characteristic correlation distance, l_0, along the bundles as the wide gaps gets longer. This is especially true for higher standard deviations, σ. In comparison, the permeability for a regular structure without the thread and the crossings is $1.0224 \cdot 10^{-10}$ m^2, which indicates that the thread and crossings are very important for the permeability.
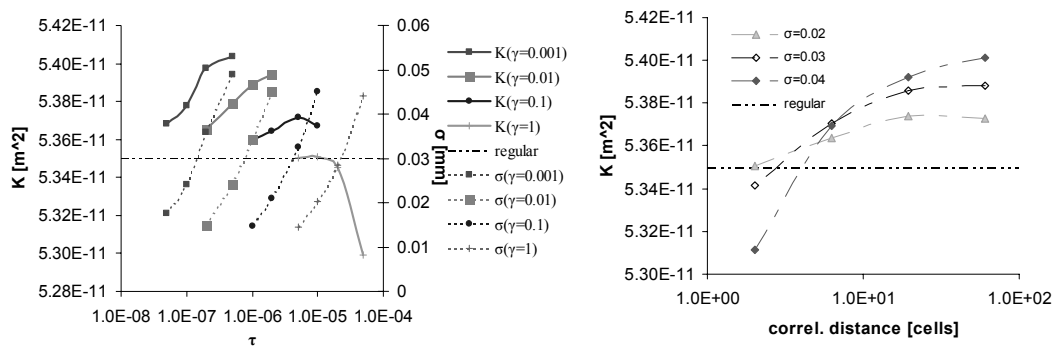
Fig. 4. The influence of a) the Monte Carlo parameters τ (bottom axis), γ (in legend) and b) the correlation distance on the global permeability for different standard deviations for a network structure including the thread and the crossings as in Fig. 1c.

Fig. 5a shows that the average channel width also considerably influences the global permeability, while the standard deviation of the channel width at the same Monte Carlo parameters $\tau=10^{-6}$, $\gamma=10^{-2}$ only changes slightly. Fig. 5b shows that the influence of the crossing width is extremely important, while there is only a weak dependence of the global permeability on the size of the thread. Thus all the deviations from regular structures involving changes of c or changes in spatial placement of the crossings in the structure leads to significant changes of the total permeability.
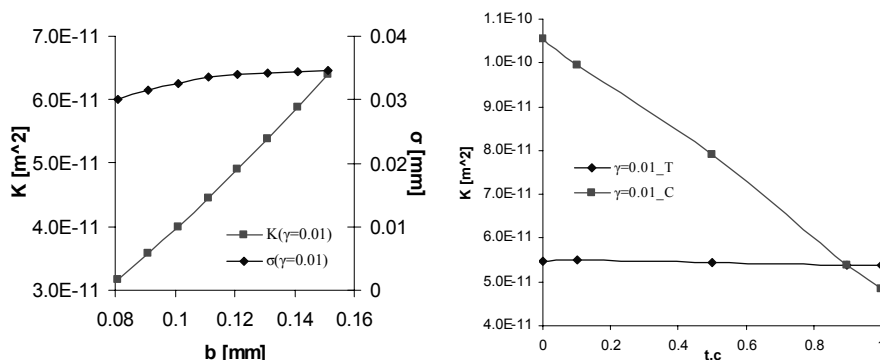
Fig. 5. The influence of a) average channel width and standard deviations and b) the sizes of the thread and the crossings on the permeability for $\gamma=0.01$.

The permeability from the global network model can be validated to experimental data on the permeability for a real fabric with similar geometrical dimensions. The measurements provided by SICOMP AB give permeability data between $2.49 \cdot 10^{-11}$ and $4.82 \cdot 10^{-11}$ m^2. The inclusion of the thread and crossings greatly improve the prediction of the permeability, about $1 \cdot 10^{-10}$ m^2 without to about $4\text{-}5 \cdot 10^{-11}$ m^2 with thread and crossings.

CONCLUSIONS

A global permeability network model for real NCFs has been developed. The model is based on a network of unit cells including the features from the stitching process as well as statistical variations of the geometry. The model shows that the global permeability only varies slightly with the Monte Carlo parameters, which set the irregularity of the network of unit cells. The global permeability also shows a weak dependence on the correlation distance between adjacent cells. The largest influences on the global permeability are from the presence of fibers crossing the inter-bundle channels and the average channel gap width. The standard deviation of the gap width and the presence of the thread have less effect on the global permeability. Validation shows that the model is greatly improved when including effects from the stitching process.

ACKNOWLEDGEMENTS

REFERENCES

1. Lundström, T.S. and Frishfelds, V. and Jakovics, A. (2003). A Statistical Approach to the Permeability of Clustered Fiber Reinforcements, Composites: Accepted for publication.
2. Frishfelds V., Lundström, T.S., Jakovics, A. (2003). Permeability of clustered fiber networks: modeling of unit cell. *Mechanics of Composite Materials*, N2-3. **In print**.
3. Nordlund, M. and Lundström T.S. (2004). Numerical Study of Different Features of Non-Crimp Fabrics and Their Influence on the Permeability, *Submitted to Journal of Composite Materials*.
4. Binétruy, C. and Hilaire, B. and Pabiot J. (1997). The interactions between flows occurring inside and outside fabric tows during RTM, *Composite Science and Technology*, **57**: 587-596.
5. Gebart, B.R. (1992). Permeability of unidirectional reinforcements for RTM. *Journal of Composite Materials*, **26**: 1100-1133.
6. Lundström, T.S., Gebart, B.R. (1995). Effect of perturbation of fiber architecture on permeability inside fiber tows. *Journal of Composite Materials*, **29**: 424-443.

Interpretation of Permeability in a Unidirectional Non-Crimp Stitched Preform by Geometrical Description of the Porosity

L. Bizet [1], J. Bréard [1], G. Bouquet [1], J.P. Jernot [2], and M. Gomina [2]

[1] *Laboratoire de Mécanique, Physique et Géosciences,*
Université du Havre, BP540, 76058 Le Havre Cedex, France.
laurent.bizet@univ-lehavre.fr, joel.breard@univ-lehavre.fr, guy.bouquet@univ-lehavre.fr,
[2] *ESCTM du CRISMAT, ENSICAEN,*
6, Boulevard du Maréchal Juin, 14050 Caen Cedex, France.
jernot@ismra.fr, gomina@ismra.fr

SUMMARY: For a unidirectional non-crimp stitched glass fabric (also called quasi-UD), we present experimental results of permeability (saturated and unsaturated values) and a description of the pore structure using stereology. It is shown that for real fibrous media, the permeability can be related to the experimentally measured porosity by the well-known Kozeny-Carman equation in terms of the mean free path through the porous phase within and around the fiber bundles.

KEYWORDS: unidirectional composites, non-crimp stitched fibrous preform, permeability, stereology.

INTRODUCTION

In the modeling of resin transfer molding process, an abundant literature exists which assimilates the structure of fibrous preforms with an ideal geometrical arrangement [1,2]. Thus numerical studies are facilitated and qualitative indications are obtained on the influence of the fibrous architecture on the macroscopic resin flow. But this kind of approach does not rely on the microstructural parameters which really characterize the porosity.

The objective of this study is to demonstrate that flow properties within a real fibrous media can be assessed by mean of microstructural parameters of the porous phase directly attainable from stereology. The porosity of a unidirectional composite material is first investigated using image analysis. The permeability for the resin flow parallel to the fibers is then expressed as a function of porosity and in terms of the characteristics of the porous phase. Finally, a comparison between the experimentally measured permeability on real fibrous composites and the prediction from the microstructural characteristics of the porous phase is presented.

MICROSTRUCTURE ASSESSMENT

Influence of the Stitching

Even for the simple fabric used in this work (UD glass fiber-reinforced polyester), primary investigations had shown a complex relationship between the geometrical parameters and the volume fraction of fibers [3]. As can be seen on Figs. 1 and 2, a two-scale microstructure is observed : the microscale, inside the yarns and the macroscale, between the yarns. That defines a microporosity and a macroporosity respectively denoted further as μ and M. Moreover, the dispersion of the fibers is not the same near and far away from the stitching yarns. Consequently, in order to describe the microstructure, a simple geometric model using a regular array of fibers and/or yarns is unrealistic : a more general microstructural description must be used.

Z = 2.20 mm	*Z = 5.20 mm*
Z = 3.20 mm	*Z = 6.20 mm*
Z = 4.20 mm	*Z = 7.28 mm*
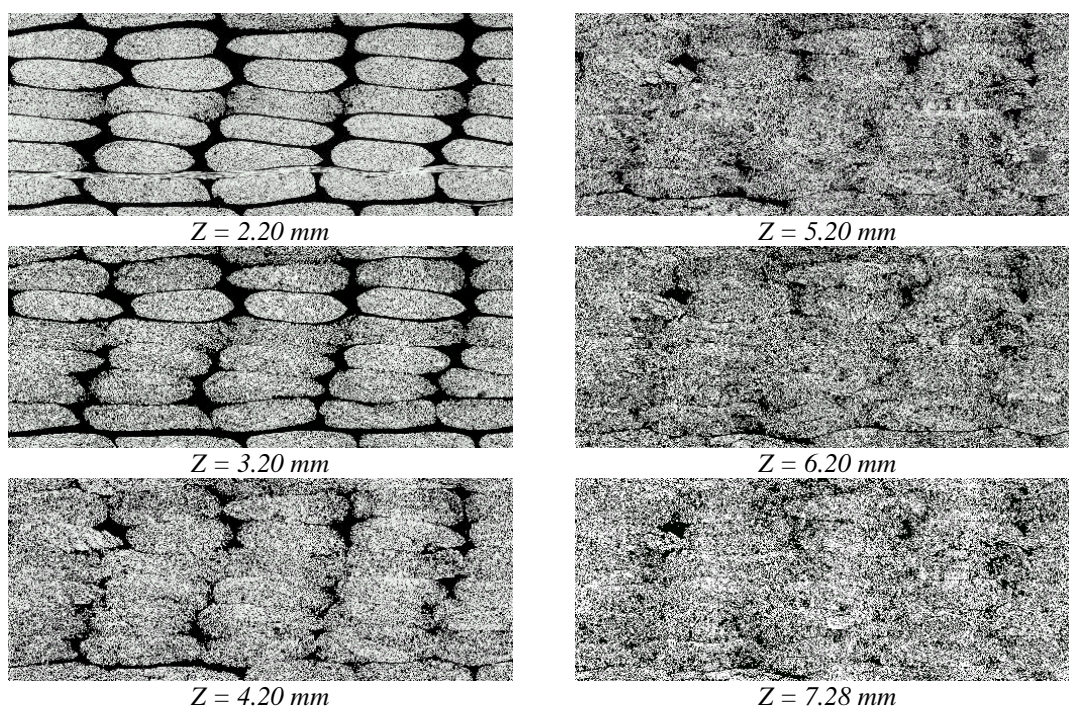
Fig. 1 : Serial sections through a RTM sample along the direction of fibers (the volume fraction of glass fibers is 0.55 and the thickness of one layer is approximately 0.45 mm)

(a)   *(b)*
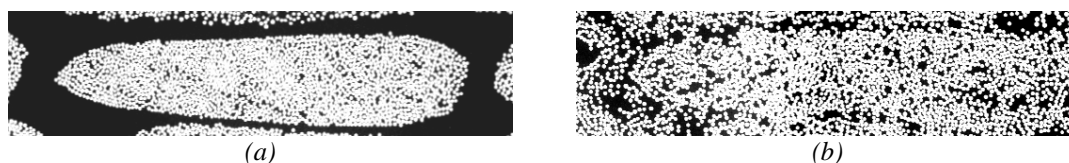
Fig. 2 : Two sections through the same yarn : (a) near the stitching, (b) far away from the stitching.

Mean Free Path through the Porous Phase versus Porosity

For a two-phase material, a general stereological relationship exists between the mean free paths through each of the two phases [4]. It can be written as $\overline{L(F)} + \overline{L(P)} = 1/N_L$ where $\overline{L(F)}$ and $\overline{L(P)}$ are respectively the mean free paths through the fibers and through the pores and N_L is the number of intersections, per unit length, between the fiber/pore interface and a random line of analysis. Moreover, as the composite is unidirectional, the microstructure observed on a plane cut perpendicular to the yarns can be analyzed as if it was defined in 2D space : for a random dispersion of non-overlapping discs of radius r, it can be demonstrated, from geometrical probabilities, that $N_L = 2r\,N_A$, where N_A is the number of discs per unit area. It follows that $\overline{L(F)} = (\pi/2)r$ and the mean free path through the porous phase is expressed as a function of the areal fraction of porosity, $A_A(P)$, by

$$\overline{L(P)} = \frac{\pi\,r}{2}\frac{A_A(P)}{1 - A_A(P)} \qquad (1)$$

This equation is valid, whatever the dispersion of the discs, under the hypothesis that they possess the same size. It can be extended to non-overlapping ellipses with the same orientation if r is replaced by the semiaxis, a, of the ellipse (the choice of the semiaxis depends on the direction of analysis). The application of formula (1) to the microstructure of our UD composite allows to define mean free paths through the microporosity and through the macroporosity (the yarns are then modelized as ellipses). The theoretical results are compared, in Figs. 3 and 4, with the experimental ones measured by image analysis.
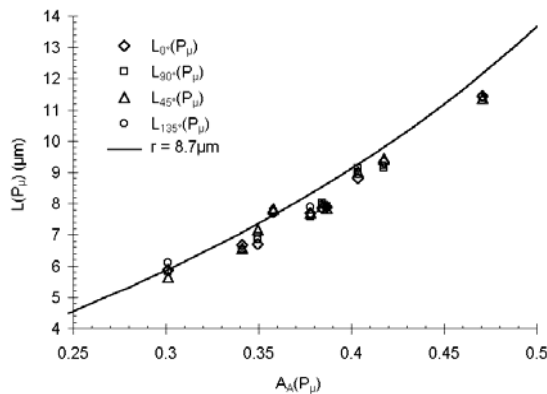
Fig. 3 : Mean free path through the microporosity (same radius r for all fibers).
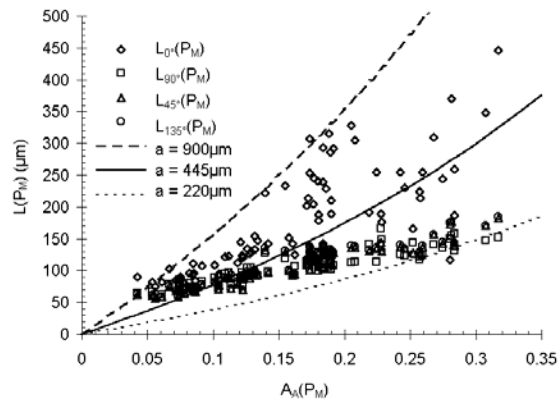
Fig. 4 : Mean free path through the macroporosity (around the yarns)

PERMEABILITY ASSESSMENT

Permeability versus Mean Free Path through the Porous Phase

For a 3D porous material, the permeability, K, can be expressed as a function of the porosity, $V_V(P)$, by the classical Kozeny-Carman equation [5] : $K = c_0 \left[V_V(P)\right]^3 / \left[S_V\right]^2$ in which c_0 is a constant and S_V the specific surface of the solid/pore interface (per unit volume of material). But there is a stereological relationship [4] between the mean free path through the porous phase, the porosity content and the specific interface area : $\overline{L(P)} = 4\,V_V(P)/S_V$. The Kozeny-Carman equation can then be written :

$$K = \frac{c_0}{16}\,\overline{L(P)}^2\,V_V(P) \tag{2}$$

In this equation, the permeability is simply expressed as the product of the volume fraction of the material accessible to the flow by the square of a characteristic length.

Permeability versus porosity

For the UD composite under consideration, on a plane cut perpendicular to the yarns the areal fraction of porosity, $A_A(P)$, is nothing else but its volume fraction, $V_V(P)$. Combining equations (1) and (2), the permeability can then be expressed by

$$K = \frac{c_0 \pi^2}{64}\,r^2\,\frac{A_A(P)^3}{\left[1 - A_A(P)\right]^2} \tag{3}$$

This equation can be found in the literature [5] but it is classically obtained via the introduction of an hydraulic radius. Only stereological relationships have been used here and applied to the particular case of the UD composite.

RESULTS AND DISCUSSION

Equation (3) can be applied to any homogeneous medium i.e. with a uniform distribution of the porous phase. But this is not the case for the UD composite under consideration (cf. Fig. 1) hence the global porosity cannot be used to compute the permeability. Consequently, the contributions of the microporosity, $A_A(P_\mu)$, and the macroporosity, $A_A(P_M)$, must be calculated separately. They are related to the global porosity, $A_A(P)$, by

$$A_A(P) = A_A(P_M) + \left[1 - A_A(P_M)\right]A_A(P_\mu) \tag{4}$$

and thus the macroporosity P_M can be derived from the measures of the total porosity, P, and the microporosity P_μ. The evolutions of $A_A(P_\mu)$ and $A_A(P_M)$ are reported in Figs. 5 and 6 for measurements performed near and far away from the stitching yarn. One can observe that, when the total porosity increases (i.e. the fiber volume fraction decreases) the mean microporosity remains roughly the same while the mean macroporosity increases.
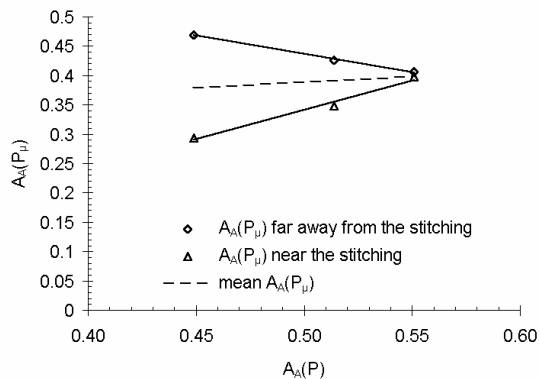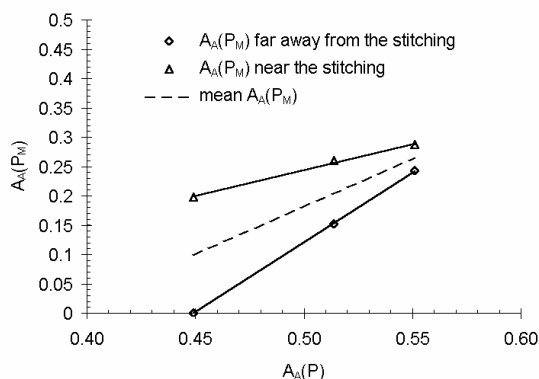
Fig. 5 : P_μ versus global porosity.   Fig. 6 : P_M versus global porosity.

The permeability K_μ corresponding to P_μ is calculated using the areal fraction $A_A(P_\mu)$ and the fiber radius r : $K_\mu = \left(c_0\pi^2/64\right) r^2 A_A\left(P_\mu\right)^3 / \left[1 - A_A\left(P_\mu\right)\right]^2$. The permeability K_M corresponding to P_M is calculated using the areal fraction $A_A(P_M)$ and the semiaxis, a, of the ellipse-shape yarn : $K_M = \left(c_0\pi^2/64\right) a^2 A_A\left(P_M\right)^3 / \left[1 - A_A\left(P_M\right)\right]^2$. For a direction of macroscopic flow parallel to the fiber bundles, the global permeability of the composite may be expressed as the sum of the micro and the macro permeabilities weighed by their respective areal fractions :

$$K = A_A\left(P_\mu\right)K_\mu + A_A\left(P_M\right)K_M \tag{5}$$

The theoretical values calculated from equation (5) are reported in Fig. 7 and compared with the experimental measurements. The best fit to the experimental results is obtained with $A_A(P_M)$ and $A_A(P_\mu)$ determined near the stitching yarns, for r=8.7 μm and a=445 μm. This last value corresponds to the radius of a disc with an area equivalent to the one of the yarns.
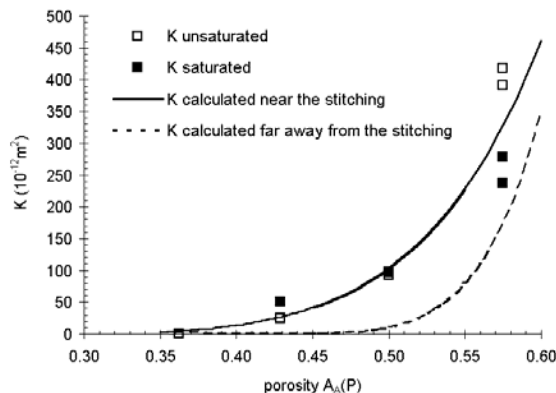
Fig. 7 : Experimental and calculated results of permeability.

CONCLUSIONS

The permeability of a stacking of unidirectional glass-fiber fabrics was assessed using microstructural parameters of the porous phase determined by stereology, and compared with experimental measurements. The free mean path through the porous phase and fractions of micro and macroporosity are shown to be the relevant microstructural parameters needed for an intrinsic determination of the permeability. Such an approach, which might be applied to any fibrous media, may provide useful information for the numerical simulations of the permeability and for the analysis of the unsaturated-saturated transition.

ACKNOWLEDGEMENTS

REFERENCES

1   B.R. Gebart "Permeability of unidirectional reinforcements for RTM", *Journal of Composite Materials*, Volume 26, Issue 8, Pages 1100-1133 (1992).
2   T.D. Papathanasiou "Flow across structured fiber bundles: a dimensionless correlation", international Journal of Multiphase Flow, Volume 27, Issue 8, Pages 1451-1461 (2001).
3   L. Bizet, J. Bréard, G. Bouquet, J.-P. Jernot, M. Gomina "Influence des fils de trame sur la structure de matériaux composites unidirectionnels", Comptes-Rendus des JNC13, Strasbourg, France (2003).
4   R.T. DeHoff and F.N. Rhines "Quantitative Microscopy", Mc Graw Hill, New York (1968).
5   J. Bear "Dynamics of fluids in porous media", Dover Publications, New York (1972).

PREFORM MODELING AND EFFECTS
II. GLOBAL EFFECTS OF PERMEABILITY

Development of Permeability Models for Saturated Fluid Flow across Random and Aggregated Fiber Arrays

T.D. Papathanasiou[1] and Xiaoming Chen
Department of Chemical Engineering
University of South Carolina
Columbia, SC 29208, USA

[1] *Corresponding Author's e-mail: papathan@engr.sc.edu*

SUMMARY We investigate computationally the effect of randomness as well as the effect of fiber aggregation on the hydraulic permeability (K_{eff}) of unidirectional fiber arrays. For this we carry out extensive viscous flow computations in various structured and unstructured fiber arrays using the Boundary Element Method (BEM) implemented on a 256-node Beowulf Intel cluster. Geometries are generated through a Monte-Carlo process, starting from uniform square arrays or from regular arrays of fiber clusters. Up to 196 individual fibers are included in each simulation Results demonstrate that at high values of (ϕ), deviations from the uniform array result in a decrease of K_{eff}. At lower porosity levels, the permeability shows a maximum at some intermediate value of the mean Nearest Neighbor Distance ($\bar{d}_{nnd}$). Finally, it is shown that fully clustered fiber arrays have higher K_{eff} than randomized ones; it is shown that for these systems (K_{eff}) scales with the deviation of Ripley's K-function for the given microstructure from that of the Poisson distribution.

KEYWORDS: permeability, fibrous media, liquid molding, composites manufacturing

BACKGROUND

Fibrous media are usually idealized as consisting of periodic or random arrays of fibers, which are typically represented as cylinders of circular cross section and constant radii [1,2]. In such representations, a unit cell can be identified; solution of the governing flow equations in this unit cell yields the flow rate (Q) and pressure drop (ΔP) from which the hydraulic permeability can be found using Darcy's law, $K_{eff} \approx \dfrac{Q}{\Delta P}$. However, regular fiber arrays are rarely encountered in real applications. Instead, fibers are either used in the form of bundles or in the form of preforms in which individual filaments assume random positions (Fig. 1). The permeability of structured arrays of fiber bundles was studied by Papathanasiou and co-workers [3-5] as well as by Advani and co-workers [6-8]. The permeability in random or quasi-random fiber arrays was also studied [9-10]. However, little work has been done to distinguish between random fiber distributions and correlate them with permeability data.
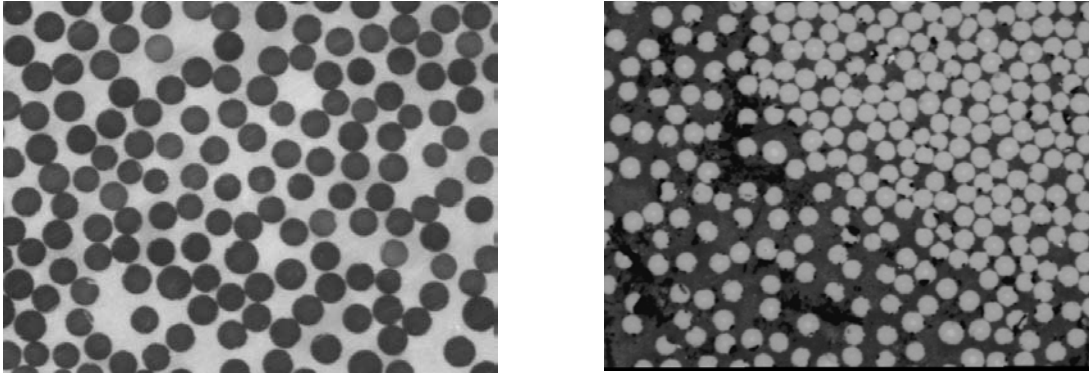
Fig. 1: Typical microstructures of unidirectional laminates. The image to the left is a technically flawless micrograph. The image to the right (showing the transition from a cluster to a resin-rich region) illustrates some problems commonly found in micrographs obtained from polished cross-sections. Both images obtained in our Laboratory using a BX50 Olympus microscope at 200x magnification.

MODEL SYSTEMS

Microstructures such as those of Fig. 1 can undoubtedly be used in a computational study. However, use of micrographs in computational work poses certain practical difficulties, such as fluctuation of fiber volume fraction in different image frames, existence of damaged (Fig. 1, right) or mis-oriented fibers or other 'edge' effects. As an alternative, computer simulation allows both, flexibility and exact control of the generated microstructures. In this work, fiber distributions were generated using a Monte Carlo perturbation method. This is a variant of the method described by Torquato [11] the difference being that the acceptance or rejection of a microstructural configuration is governed by a 'non-overlap' rule. To generate a fiber distribution, the model requires inputs such as the porosity (ϕ), the number of fibers (N_f), a minimum allowable inter-fiber distance (d_{min}), the number of perturbation steps (N_p), the maximum displacement of fiber during a move (δ) and an initial fiber distribution. Given a sufficient number of randomizing steps, this model produces fiber distributions possessing similar spatial characteristics (as evidenced by the corresponding pair-correlation function); additionally, these distributions are independent of the initial configuration. Due to the finite fiber size and the imposition of d_{min}, the simulated fiber distribution can never be completely random (that is, Poisson). Actually, the model employed in this study may be viewed as one of the self-inhibiting (or hard-core) models [12]. The minimum inter-fiber distance (d_{min}) is a key parameter affecting the spatial statistics of the generated microstructures. Fig. 2 shows two fiber distributions generated with different minimum inter-fiber distances and ϕ=0.7. It is clear that small values of d_{min} result in microstructures characterized by small fiber aggregates randomly placed throughout the domain. As d_{min} increases, the pattern becomes more regular. Additionally, the patterns generated through the MC process become more regular as the porosity gets smaller. It is known that the K(r) of patterns generated by a self-inhibiting model will fall below that corresponding to a Poisson pattern.

It is also known that, in the absence of strong clustering, K(r) is not a sensitive measure at longer length scales. In this situation, it is meaningful to use the Nearest Neighbor Distance (NND) as the measure to characterize the microstructure. For each fiber, one nearest neighbor distance can be found. While in a regular pattern the NNDs take the same value, a distribution of NNDs exists in a random pattern. Apparently, the distribution of NNDs corresponds to the distribution of narrowest pore spacing in the studied fibrous porous media and the allowable minimum value of NND is just the minimum inter-fiber distance specified by the model. The histograms of distributions of NNDs for the selected patterns in Fig.2a-b are plotted in Fig.2c. The skewed and steep shape of the distribution of NNDs is typical for the hard-core model [13].
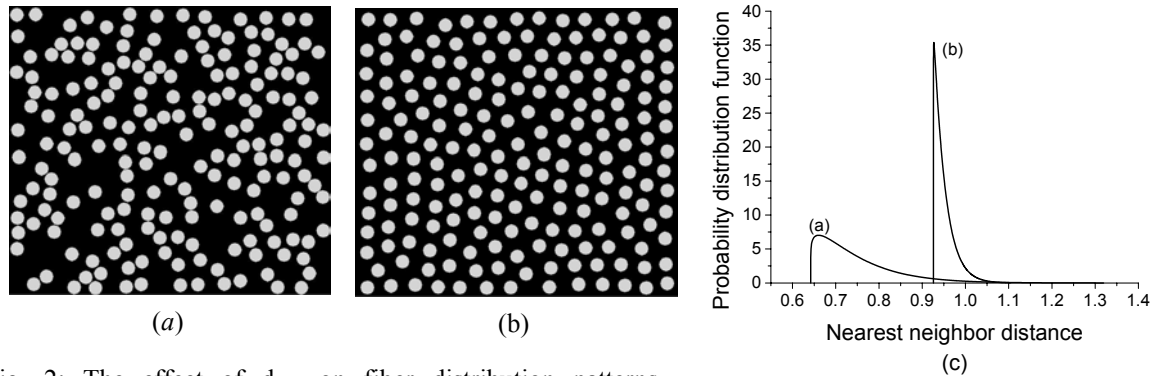
Fig. 2: The effect of d_{min} on fiber distribution patterns generated through a Monte-Carlo algorithm, starting from a square array. $\phi = 0.7$, $N_f = 196$. (a): d_{min} =0.05D; (b): d_{min} =0.5D. (D) is the fiber diameter

RESULTS AND DISCUSSION

Simulations were carried out using a parallel BEM code developed in-house, in microstructures generated at four different porosities ($\phi = 0.7, 0.6, 0.5, 0.45$) and with different minimum inter-fiber distances. In all models, N_f =196. There is a small but measurable size effect that is currently being investigated in detail. However, this does not change the trends discovered in this study. The mean nearest neighbor distance is used to correlate the microstructure to the dimensionless permeability K_{eff}/R^2. Lower values of $\bar{d}_{nnd}$ correspond to fiber arrays that deviate the most from the uniform square array. The results of a large number of simulations are plotted in Fig.3. Open symbols represent the corresponding permeability data for regular square packing arrangements at ϕ=0.7, 0.6, 0.5 and 0.45 respectively, as obtained by numerical simulation. The permeability of different microstructural realizations (at the same level of porosity) can vary significantly, particularly at relatively low porosity. For this reason several realizations are studied at each level of (ϕ, $\bar{d}_{nnd}$) and averages along with the corresponding error bars are shown in Fig. 3. For low porosities, the computational results show that K_{eff} decreases as the extent of randomness of the fiber distribution (manifested by lower $\bar{d}_{nnd}$) increases.

This behavior is much more pronounced at lower porosities and suggests that extensive deviation from the uniform array results in the formation of many narrow gaps which effectively block the flow while not forming any easy flow path. This observation agrees with the recent finding by Bechtold et al.[10]. It does not contradict the common view that clustering will increase the permeability, since there is no significant clustering observed in such random microstructures. At high porosity (ϕ=0.7), there is a trend for the permeability to increase as $\overline{d}_{nnd}$ decreases further down to less than about half the fiber radius. This is likely due to the fact that the chance to form easy flow path is bigger in random structure of high porosities. It is also noticed that permeability in a fiber array with large $\overline{d}_{nnd}$ actually exceeds that of the square array. This is because the model tends to form a hexagonal array which has a larger permeability than that of a square array when the porosity is smaller than a certain value.
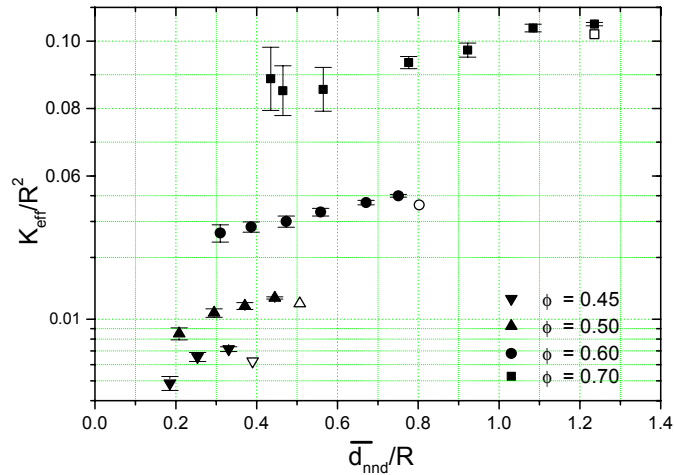
Fig. 3. Correlation of permeability with the mean nearest neighbor distance. Each filled data point represents the average of 10 simulations. The size of the error bars is 2σ, (σ) being the standard deviation.

To verify that clustering results in increased K_{eff}, we carried out simulations in clustered microstructures. The models used in this were generated by the same Monte Carlo method, starting from a regular pattern containing four clusters. To quantify the deviation of the clustered pattern from randomness, the following statistic measure was used:

$$L = \frac{1}{N}\sum_i K(r_i)/\pi r_i^2 \qquad r_i \leq r_0 \qquad (1)$$

where r_i is the distance at which K(r) is evaluated and πr^2 is the theoretical value for the Poisson distribution. If the pattern is clustered, L is larger than one. If the pattern is regular, L is less than one. Fig. 4 shows the correlation between L and K_{eff}. It is evident that clustering does increase the permeability dramatically because of the formation of wide flow path. As the fiber distribution becomes randomized, it is expected that the constriction effect by the narrow pore spacing will again become the dominant factor. It is noted that L fails to correlate with K_{eff} when there is no strong clustering.

CONCLUSIONS

We have shown that deviation of the microstructure of a fibrous medium from the uniform square array results in permeability changes that can be correlated to the mean Nearest Neighbor Distance ($\bar{d}_{nnd}$) of the random microstructure. It is also shown that fully clustered fiber arrays have higher permeability than random ones; for such clustered systems it is shown that permeability scales with the deviation of Ripley's K-function from the Poisson distribution.

REFERENCES

1 Bruschke, M. V. and Advani, S. G., 1993, "Flow of Generalized Newtonian Fluids across a Periodic Array of Cylinders", *J.Rheol.*, Vol. **37**, pp. 479-498.

2 Gebart, B. R., 1992, "Permeability of Unidirectional Reinforcements for RTM", *J. Comp. Mat.,*, Vol. **26**, pp. 1100-1133.

3 Papathanasiou, T.D., 1997, "On the Effective Permeability of Square Arrays of Permeable Fiber Tows", *Int. J. Multiphase Flow*, Vol. **23**, pp. 81-92.

4 B. Markicevic and T.D. Papathanasiou, "A model for the transverse permeability of bi-material layered fibrous preforms", Polymer Composites, **24**(1), 68-82, 2003

5 T.D. Papathanasiou, E. Gravel, S.C. Barwick and E.D. Dendy, "Non-isotropic structured fibrous media: The permeability of regular arrays of fiber bundles of elliptical cross-section", Polymer Composites, **23**(4), 520-529, 2002

6 Sadiq, T. A .K., Advani, S. G. and Parnas, R. S., 1995, "Experimental Investigation of Transverse Flow through Aligned Cylinders", *Int. J. Multiphase Flow*, Vol. **21**, pp755-774.

7 Pillai, K. M. and Advani, S. G., 1995, "Numerical and Analytical Study to Estimate the Effect of Two Lengths Scales upon the Permeability of a Fibrous Porous Medium", *Transport in Porous Media*, Vol. **21**, pp. 1-17.

8 Ranganathan, S., Phelan, F. R. Jr. and Advani, S. G., 1996, "A Generalized Model for the Transverse Fluid Permeability in Unidirectional Fibrous Media", *Polymer Composites*, Vol. **17**, pp. 222-231.

9 Ghaddar C. K., 1995, "On the permeability of unidirectional fibrous media: A parallel computational approach", Phys. Fluids, Vol. **7**, pp. 2563-2585.

10   Bechtold G. and Ye Lin, 2003, "Influence of fiber distribution on the transverse permeability in fiber bundles", *Comp. Sci. and Technol.*, Vol. **63**, pp. 2069-2079.

11 Torquato S., 2001, Chapt. 12 in : Random Heterogeneous Material, Springer-Verlag.

12 Ripley B. D., 1977, "Modeling Spatial Patterns", *Journal of Royal Statistical Society, Series B*, Vol.**39**, pp. 172-212.

13   Pyrz R., 1994, "Quantitative Description of the Microstructure of Composites. Part I: Morphology of Unidirectional Composite Systems", *Comp. Sci. and Technol.*, Vol. **50**, pp. 197-208.
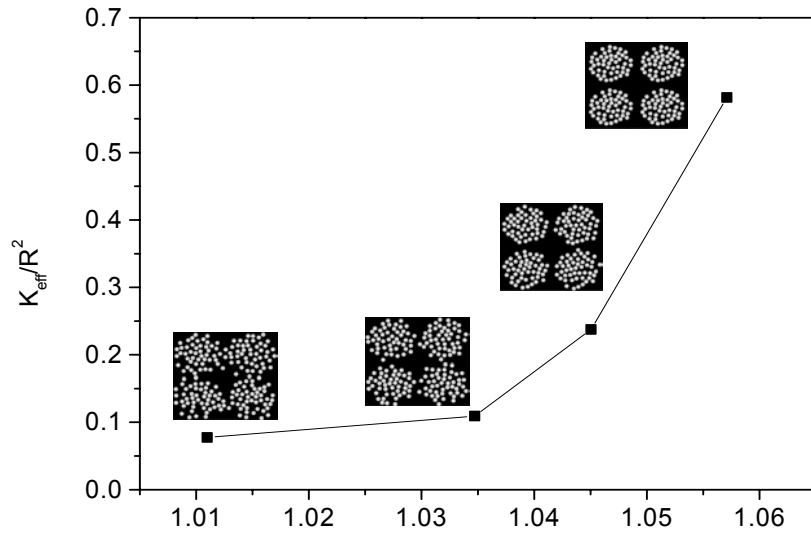
Fig. 4: Correlation of permeability in clustered patterns with L (Eqn. 1). $\phi = 0.7$, $N_f = 196$.

Prediction of the Effects of Fiber Architecture on Permeability Using the Stream-Surface Method

Chee Chiew Wong, Francois Robitaille, Andrew C Long*, and Christopher D Rudd

School of Mechanical, Materials, Manufacturing Engineering & Management
University of Nottingham, University Park, Nottingham NG7 2RD, UK.
* Corresponding author's email: Andrew.Long@nottingham.ac.uk

SUMMARY: Accurate permeability data is critical to successful mold filling simulations for processes such as resin transfer molding (RTM). While permeability measurement techniques are technically mature, full characterization of any particular textile is impractical due to the stochastic nature of the textile. As such, permeability models based on the architecture of the fabric are desirable for process design and analysis. This paper describes the 'Stream-Surface' method to predict permeability based on the fabric structure, modeled using a generic textile model, TexGen, developed at the University of Nottingham. The initial systematic validation of the method, which also looked at effects such as tow shape and fiber volume fraction on permeability, is presented here. The method was also applied to cross sections of a twill weave model. Comparisons between the Stream-Surface results and the more computational intensive CFD calculations are promising, whereby the 'Stream-Surface' method predicts values and trends very similar to the CFD method. The significant potential of the 'Stream-Surface' method is in its calculation speed, at least 300 times faster than the CFD method.

KEYWORDS: permeability, permeability prediction, Stream-Surface, textile model.

I. INTRODUCTION

Mold filling codes for processes such as resin transfer molding (RTM) almost exclusively use Darcy's law to describe flow through the porous textile. Darcy's law gives the average velocity of the fluid as a function of the pressure gradient, fluid viscosity and permeability of the porous medium. As such these simulations are only as good as the supplied permeability data. Permeability is normally measured experimentally and while measurement techniques continue to improve, published data continually reports a large permeability distribution.

Permeability is very sensitive to the architecture of the preform, as seen by variations with fiber volume fraction, fiber reorientation and fiber compaction. Additionally, textile reinforcements have an inherent statistical nature. Such complications make a full experimental characterization of any particular reinforcement a time consuming and expensive task.

Permeability prediction models based on the fabric architecture would be valuable to process design and analysis. Early analytical models for unidirectional textiles [1,2] and later, numerical models for more specific types of textiles [3], offer a good insight into the capability of such models. A general model based on structural model of textiles would be more advantageous, as proposed by Lomov et al [4] and the present authors. The former uses Lattice-

Bolztmann to predict permeability and while it can be accurate, it can also be time-consuming, which can be problematic where a large number of simulations are needed.

The 'Stream-Surface' method [5] is a generalized method for predicting permeability developed by the authors. This method has been constructed to be efficient without sacrificing the details. A generic textile model, TexGen, also developed by the authors [6], is used to create the data files for this method automatically. The work on 'Stream-Surface' is still ongoing. The first part of this paper describes the initial results from a systematic study to validate the method. In the second part, the method is applied to a more realistic textile model.

II. MODELING METHODS

TexGen is a textile modeler which can be used to create virtually any description of a textile. It starts of with vectors defining the textile's interlacing pattern, which are smoothed out and volumes created around them to represent the tows. Additional features applicable to the model include in-plane shearing, statistical variation and interference correction algorithms. A specific flow domain can be specified and exported in a variety of formats for further processing, including the output for the Stream-Surface method. Cross sections can also be extracted automatically for analysis.

The Stream-Surface method reduces the complexity of a flow problem by using a network of interconnected planes bisecting basic volumes representing free and porous channels of flow. Flow is assumed to follow Darcy's law, whereby the free channels with height h have a permeability of $h^2/12$ according to the Hagen-Poiseulle relation for flow between two stationary plaques. Tow permeability can be specified using simple analytical model such as Gebart [1]. By solving the flow for these stream-surfaces with known individual permeability values, an effective permeability can be calculated for the domain. While the Stream-Surface was developed for 3D models and further development is needed before this can be implemented, this paper describes its applications in 2D cross-sections.

III. VARIATIONS OF A SINGLE POROUS TOW

A study, as described in [7], has been undertaken which aims to document the effects of the various factors that affect permeability of a textile and also to provide validation for the Stream-Surface method. The systematic way of achieving this is to begin with a simple 2D single tow geometry, progressing to multiple-tows and multi-layers, before going on to 3D structures. In this section, a 2D cross section of a single porous tow is analyzed.

Calculation methods

Figure 1 shows the 2D single tow flow domain and the steps in generating the 1.5D Stream-Surface mesh. Each of the nodes in the 1.5D mesh has an associated height corresponding to the volume (or area) it represents. This is used to calculate the 'permeability' of the free channels and also ensures that continuity is satisfied. The Stream-Surface flow is solved using a finite difference solver while flow in the 2D mesh was solved using a commercial CFD package, FLUENT™.

The permeability of the cell can then be calculated from the resultant pressure distribution using Darcy's law. Results obtained using the Stream-Surface method are compared to that obtained from the more computationally intensive CFD method.
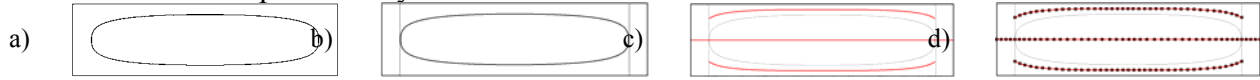
Figure 1 – Schematic of the 2D single tow case and the steps in generating the Stream-Surface mesh: a) initial domain, b) identification of basic flow volumes, c) identification of bisecting curves and d) the final Stream-Surface mesh.

Permeable boundary

The Stream-Surface method assumes that flow in the free channel is similar to that between two stationary solid boundaries. However, this assumption is flawed in the presence of a porous tow, whereby one (or more) of the boundaries surrounding the free channel is permeable [8]. An effective height is recalculated for the free channel using the following equation, which ensures the continuity of flow at the permeable boundary:

$$h_{effective} = h_i \left(1 + \frac{3}{\sigma} \left(\frac{\sigma + 2\alpha}{1 + \alpha\sigma} \right) \right)^{1/3} \text{ with } \sigma = \frac{h_i}{\sqrt{k}} \tag{1}$$

h_i is the original height of the free channel, k is the permeability of the bounding porous material and α is a dimensionless quantity dependant on the structure of the bounding porous material. At the moment, α is used as a fitting parameter. This issue will be studied in more detail to find a more intelligent way to account for the permeable boundaries.

2D CFD vs 1.5D Stream-Surface

The shape of the tow is defined using the following generalised ellipse equation:

$$y = \pm \left(1 - \frac{x^2}{a_t^2} \right)^n \tag{2}$$

The effects of four geometrical parameters have been studied. The first (P1) is the tow aspect ratio, a_t (width/height). The second (P2) is the power n, which defines the shape of the tow. The third parameter (P3) is the cell fiber volume fraction. Values chosen for this are in multiples of the maximum cell fiber volume fraction for the nominal case (when the cell's height and width is equivalent to that of the tow). The last parameter (P4) is the cell aspect ratio. 17 combinations of the four parameters were simulated. The tow permeability is calculated using Gebart's model [1] for tows perpendicular to flow with quadratic fiber arrangement and fiber diameter of 15.8 μm (8.065×10^{-13} – 2.132×10^{-12} m^2 for tow fiber volume range of 0.416 – 0.500). α has a value of 0.15, from fitting the Stream-Surface result of nominal case 1 to the CFD calculation.

The predicted effects of parameters P1, P2, P3 and P4 on permeability obtained using the Stream-Surface and CFD methods are compared in Figures 2a to 2d respectively. A drop of permeability with increasing tow aspect ratio is observed in Figure 2a. This is because the free channels on top and below the tow are becoming narrower and longer, constricting the flow of resin which primarily flows around the tow. Figure 2b shows an increase in permeability as the tow shape changes from a rectangular-like shape to an ellipse.

Again, the main factor is the change of the resistance in the free channels which open up as the tow becomes more elliptical. Figures 2c and 2d predict a drastic drop in permeability with increasing cell fiber volume fraction and aspect ratio respectively. Change in these two parameters has a direct impact on the geometry of the free channels which become very narrow at either a high cell fiber volume fraction or aspect ratio. More importantly, the Stream-Surface and CFD results show a very good agreement, quantitatively and qualitatively.
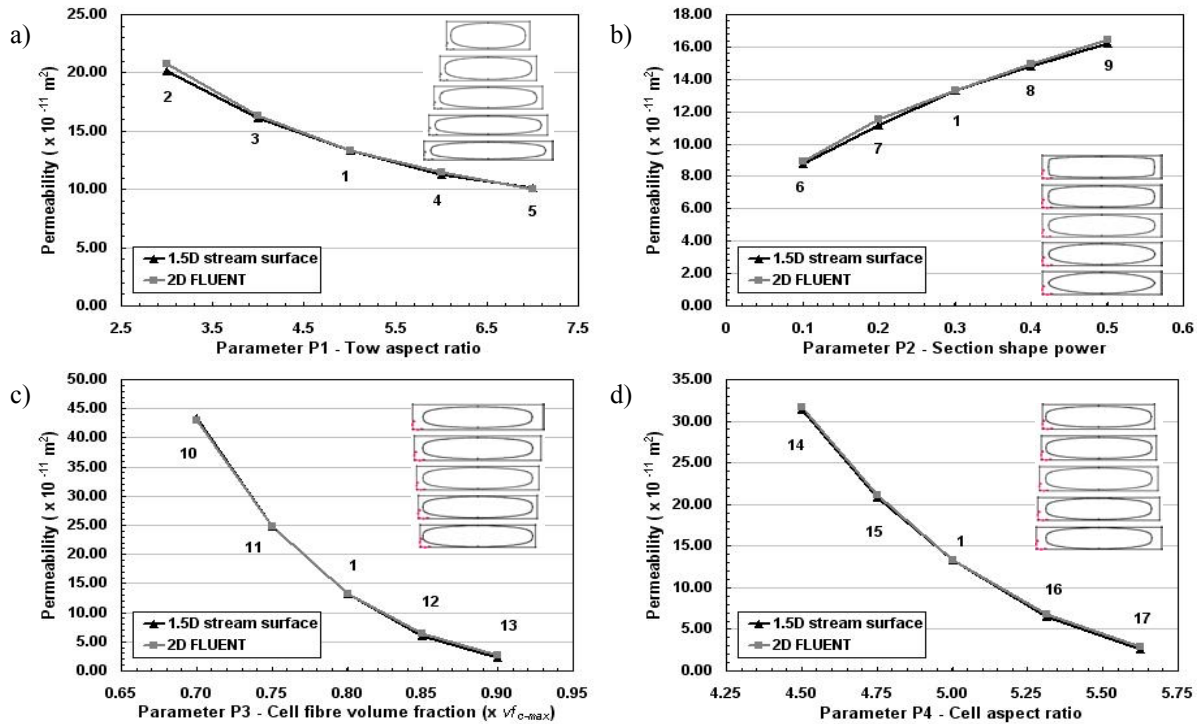
Figure 2 – The effects of: a) tow aspect ratio, b) section shape power, c) cell fiber volume fraction, and d) cell aspect ratio, on the cell permeability.

IV. SHEAR IN 2:2 TWILL WEAVE

A study using the unit cell of a 2:2 twill weave was performed in [9] to demonstrate the generic permeability modeling approach for 3D models. In this section, 2D cross sections of the same textile model were analysed using Stream-Surface and compared to CFD calculations. Figure 3 shows the textile models considered with tows at the nominal ply angles of ±45° and sheared by 30° in two directions. Sections taken at tow crossovers and between crossovers were analysed for both flow along the x and y-axes. Isotropic tow permeability was assumed (4.38 x 10^{-12} m^2 with 50% V_f based on Gebart [1]). The height of the free channels has not been modified to account for permeable boundaries as the fitting method is not sufficient to cover the complicated flow in these cases.

Results are shown in Figure 4. Some of the CFD simulation did not converge and were generally limited by difficulty in mesh generation. As most of the resin flowed around the tows, the geometries of the free channels are the main factor in determining the permeability of the cells. More encouraging perhaps is that the two methods predicted very similar permeability trends, even though the permeable boundary conditions were ignored in Stream-Surface.

This further strengthens the applicability of the stream-surface method for predicting permeability, demonstrating the fact that it can model a more complex case than a single tow.
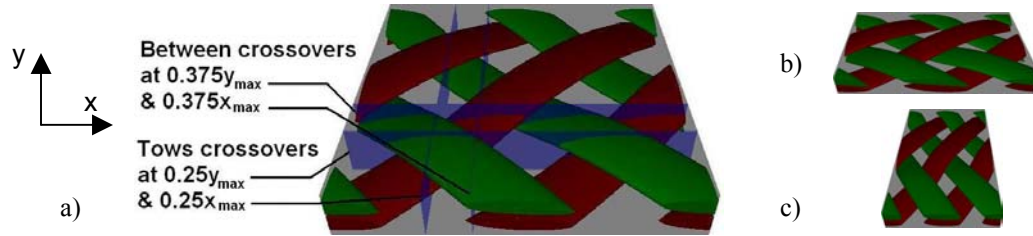
Figure 3 – 2:2 twill weave fabric models. a) Nominal ±45° case with cross sections taken as shown. Model sheared to ply angles of (b)±30° and (c)±60° with respect to x-axis.
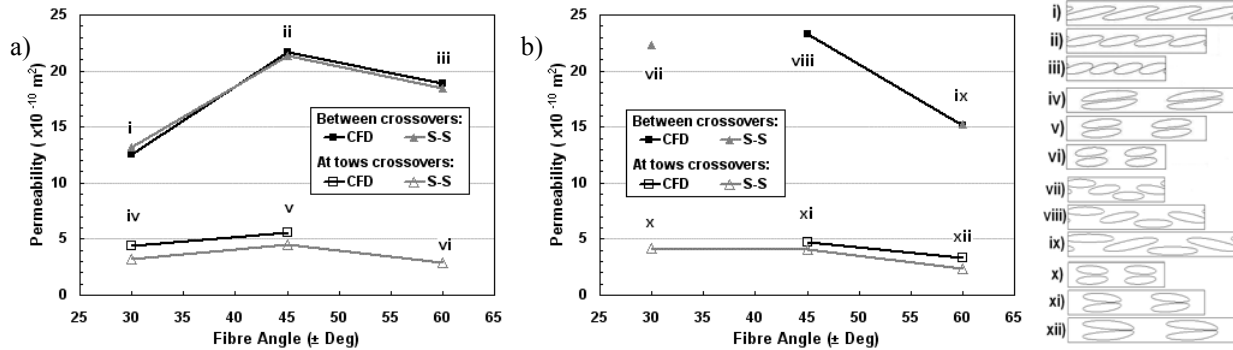
Figure 4 – Predicted permeability of the cross sections for flow along (a) x and (b) y-axes.

IV. CONCLUSIONS

The Stream-Surface results compared extremely well with the CFD calculations for both sets of analyses: single tow and twill weave. While these 2D calculations are of limited use in predicting the permeability of actual preforms, it is an integral part in the development of the Stream-Surface method, further strengthened by the good agreement of the results.

The overall execution time including mesh generation and flow simulation for the two methods in both set of analyses are approximately:

- Single tow analyses: CFD vs. Stream-Surface – 6 minutes vs. 1 seconds
- Twill weave analyses: CFD vs. Stream-Surface – 30 minutes vs. 5 seconds

All analyses were performed on a standard PC (P4 1.7GHz). Whilst one might use the CFD method to get a more accurate solution, the Stream-Surface method may be more efficient when a large number of predictions are needed.

Future work will proceed with further validation of the Stream-Surface method with expansion to include 3D models. Several issues such as isotropic tow permeability in the current analyses and also permeable boundary conditions need to be studied in detail.

REFERENCES

1. B.R. Gebart, *J.Composite Materials*, **26** (1992) 1100.
2. B.T. Astrom, R.B. Pipes, S.G. Advani, *J. Composite Materials*, **26** (1992) 1351.
3. P. Simacek, S.G. Advani, *Polymer Composites*, **17** (1996) 887.
4. S.V. Lomov, G. Huysmans, Y. Luo, R.S. Parnas, A. Prodromou, I. Verpoest, F.R. Phelan, *Composites A*, **32** (2001), 1379.
5. F. Robitaille, A.C. Long, C.D. Rudd, *Plastics, Rubbers and Composites*, **31** (2002) 238.
6. F. Robitaille, A.C. Long, I.A. Jones, C.D. Rudd, *Composites A*, **34** (2003) 303.
7. F. Robitaille, C.C. Wong, A.C. Long, C.D. Rudd, *Proc. ICCM-14, San Diego, California,* July 2003.
8. G.S. Beavers, D.D. Joseph, *J. Fluid Mechanics*, **30** (1967) 197.
9. A.C. Long, C.C. Wong, M. Sherburn, F. Robitaille, *Proc. 25th Int. SAMPE Europe Conference, Paris,* March 2004, 325.

Robust Design of RTM Process with Statistical Characterization of Permeability and Flow Simulation

Jing Li, Chuck Zhang, Richard Liang and Ben Wang
Department of Industrial Engineering
Florida A&M University-Florida State University College of Engineering
2525 Pottsdamer Street, Tallahassee, FL 32310-6046

ABSTRACT

The resin transfer molding (RTM) process has gained extensive attention for its capability of producing complex structural parts, which has resulted in a rapid growth in RTM applications. However, this process is still underutilized relative to its potential. One major barrier is that the reproducibility of the finished parts is often lower than expected, which increases the cost for RTM components. In the RTM process, major quality problems come from unbalanced resin flow in the mold filling process. Fiber preform permeability is a key parameter that influences resin flow behavior. However, due to variations existing in raw materials and processing, the preform permeability varies across regions within a part or from part to part. This variability results in reduced reproducibility of the finished RTM components. This research studied the statistical properties of the typical race-tracking permeability in RTM processes. Based on this statistical characterization, a robust design approach was developed to help design RTM processes to be insensitive to preform permeability variations coming from materials and processing, thereby consistently manufacturing higher quality composite components.

Keywords: **Resin Transfer Molding (RTM), Process simulation; Flow-modeling**

1. INTRODUCTION

In the RTM process, resin flow is governed by a number of process parameters, such as fiber reinforcement permeability, resin chemistry, rheology, injection pressure/flow rate, mold complexity and human factors. Among these parameters, preform permeability, which can be described by Darcy's law, plays a crucial role in the RTM mold filling process. The primary sources of quality and reproducibility problems in resin flow are induced defects, voids and dry spots. These defects are often caused by unbalanced resin flows, which are directly related to fiber preform permeability variations. Improper fiber preform preparation/loading and fiber deformation are leading causes for permeability variations [1]. Therefore, precise characterization of preform permeability is key to the success for both flow simulation and actual manufacturing processes. RTM manufacturers require a process that is insensitive to the material variations to achieve robust design.

During the past decade, many studies have reported on permeability characterization and RTM process design optimization [1-4]. These research studies have provided a fundamental understanding and some experimental results for fiber permeability and optimum design of the RTM process.

However, these permeability studies only investigated bulk/average permeability of fabrics in RTM processes. Quantitative and statistical analyses of local permeability variations, such as race-tracking effects, are lacking in current RTM literature. In addition, most current RTM process design optimization studies did not consider the effects of local permeability variations. In this research, a comprehensive study investigated the statistical properties of typical race-tracking permeability in RTM processes. With the statistical analysis results, a robust RTM process design method was introduced and illustrated.

2. METHODOLOGY

2.1 Statistical Characterization of Race-Tracking Permeability In RTM manufacturing, since the injection gates are often positioned at the edges of the mold, edge effect or race-tracking may be encountered. Characterizing the permeability in the race-tracking areas in imperative so that the RTM process can be designed and controlled properly. This research establishes a correlation between race-tracking permeability and average permeability with the assistance of RTMSim, a flow simulation software developed by the authors based on a control volume/finite element method (CV/FEM). In experiments, no special care was exercised in transporting, cutting or laying up fabrics in order to make the experimental environment as close as possible to actual manufacturing process, and inevitably produce race-tracking. Repeated experiments were performed under the same circumstances. To obtain race-tracking permeability, an inverse approach was employed. Simulation results were used to infer the race-tracking permeability. With different distribution assumptions (gamma distribution, Weibull distribution and lognormal distribution), ratios indicating the severity levels of race-tracking permeability were fitted by statistical models. Then a goodness-of-test was employed to compare the fitting performance of different distributions to find the best statistical model that describes the statistical properties of race-tracking permeability data.

2.1.1 Determination of Race-Tracking Permeability In this study, one-dimensional permeability measurement experiments were designed to study the statistical properties of permeability. WR24-5X4 woven fabrics (surface density = $810g/m^2$ and solid density = $2500kg/m^3$) from Owens Corning Company were used as the test material for these experiments. In repeated experiments, the average permeability values of fiber preforms at the regions in the whole mold cavity where the test liquid flowed slowest were calculated using Darcy's Law. With the assistance of flow simulation, race-tracking permeability was obtained by several trial runs through an inverse approach. The permeability for the central region and estimated rack-tracking permeabilities were input into the RTMSim software to obtain a flow pattern. Simulated results were compared with the flow processes recorded by a digital camcorder. Both filling times and flow patterns located in a similar range of the actual race-tracking permeabilities for both edges were acquired. Comparing the experimental flow process with simulation results, a pair of race-tracking permeabilities was obtained. This procedure was repeated 46 times, resulting in 46 pairs of permeability values.

2.1.2 Statistical Analysis Results To obtain more precise analysis results by avoiding truncation or rounding errors, the following ratio was defined for quantifying a severe level of race-tracking permeability:

$$Ratio = \frac{race - tracking\ permeability}{average\ permeability} = k_r/k_a$$

The ratio data were calculated from the 46 experiments. These ratio data were analyzed instead of original race-tracking permeability values. To obtain the statistical properties of the permeability ratios, hypothesizing a distribution family for observation data was structured and the results were compared to determine the best model. Three continuous distributions were selected to fit the k_r/k_a values: Gamma distribution (*gamma(..)*); Weibull distribution (*Weibull(..)*) and Lognormal distribution (*LN(,)*).

In this study, the maximum-likelihood estimation (MLE) method was selected to derive the distribution parameters. The candidate distributions were estimated as *Gamma(2.48, 2.759); Weibull(1.638, 7.6829) and LN(1.71, 0.6869)*. Since none of these three distributions perfectly fit the data, the authors closely examined the distributions to determine the one that best represented the true underlying distribution for the k_r/k_a values. The goodness-of-fit is an effective method for evaluating the fitting of a distribution to the data. In this study, the Chi-Square test was performed as goodness-of-fit hypothesis test [5]. From the hypothesis test, the Weibull distribution was found to perform the best. Therefore, the Weibull distribution was determined the best for representing the k_r/k_a values. It should be noted that the assessment was case specific (for woven fiber, one dimensional experiment setup), and the k_r/k_a values for other fabrics may not necessarily be represented by Weibull distributed variables.

2.2 Robust Design of RTM Processes Locations of gates and vents play a crucial role in RTM process/tooling design. Many studies regarding RTM process design and optimization have been conducted [6-8]. In most of these studies, researchers assumed that permeability of the preform was either uniform/isotropic across the part or deterministic, i.e. no consideration of stochastic nature of permeability. These assumptions are invalid in many actual RTM production conditions, particularly when race-tracking is present. This paper introduces a new concept of optimum RTM process design. This method minimizes the sensitivity of the mold design to uncertain material properties by choosing the appropriate locations of gates and vents, improving the robustness of RTM tooling and processes design.

2.2.1 Robust RTM Process Design Methodology In the RTM process, the major factors that determine the resin flow behavior and final part quality can be grouped into two classes: deterministic factors and stochastic factors. Injection pressure, flow rate, mold temperature, etc. are the deterministic factors, which means they can be measured or controlled as desired. The primary sources of uncertainty include the preform permeability dominated by its microstructure and the variability of rheological and kinetic properties of the resin. Those uncertainties presented by the above factors occur at different magnitudes. Only race-tracking permeability was considered as a stochastic factor in this study.

The same material described in Section 2.1 was used for the robust RTM process design so as to utilize the conclusion that the k_r/k_a values were distributed as Weibull random variables (*Weibull(1.638, 7.6829)*). With the assistance of computer simulation, different combinations of statistically generated input and deterministic parameters can be used as inputs for the flow simulation software to assess tooling designs with well-defined objectives. Therefore, the robust design approach involves two components: a virtual experiment and a Monte-Carlo simulation. Figure 1 illustrates the robust process design approach.

Dry spots create major defects in RTM process. Usually, the vent is positioned at the location where the flow entraps the air. Once the tooling design is completed, the vent location cannot be changed during the course of manufacturing. However, for most fiber preforms, permeability variations, especially the variation of race-tracking permeability, vary at the ending locations of the flow. Because of variations in process parameters, the flow does not end where desired. Therefore, to obtain a robust tooling design, the vent should be placed at the location that minimizes the ending locations variations due to uncertainties in process parameters.
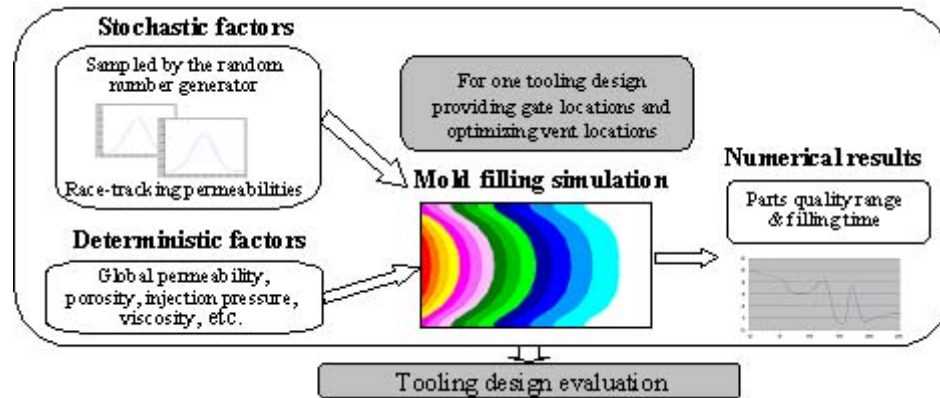
Figure 1: Illustration of the robust process design approach

A vent location dispersion value was defined to quantify the ending locations variation. Using this dispersion value, part quality can be quantified. Usually, the process design with a comparatively smaller dispersion value is preferable. This can be generalized for multi-vent cases.

To illustrate this method, a rear car door was designed and tested, as shown in Figure 2(a). For this case study, it was assumed that the average permeability was constant and the ratios of race-tracking permeability over average value were statistically distributed variables (*Weibull(1.638, 7.6829)*).

(a) Part geometry   (b) Tooling design #1   (c) Tooling design #2
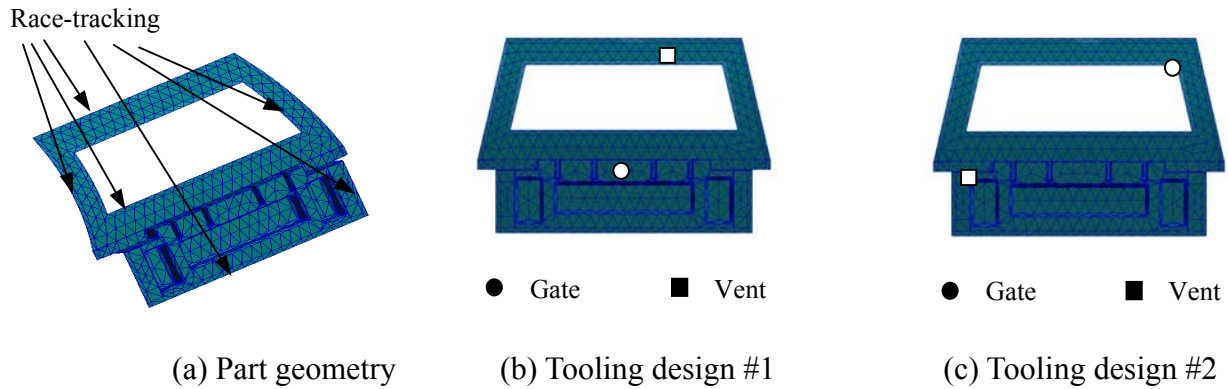
Figure 2: Car door example

A typical tooling design for this part is to position the gate at the center of the main region, as shown in Figure 2(b). However, after evaluating other locations of the gate, a smaller vent location dispersion value was found, which indicated a better gate/vent design. For one gate and one vent tooling design scenario, it was determined that they should be located along the length direction of the part (Figure 2(c)). The vent location dispersion value was reduced from 15.64 to 6.06.

3. CONCLUSIONS

This paper reported on two studies: statistical characterization of race-tracking permeability in RTM process and robust design of RTM process. In the first study, sources of variations in RTM processes were analyzed and the most important source of variability – preform race-tracking permeability – was investigated. By repeating one-dimensional permeability measurement experiments and corresponding simulations, race-tracking permeability data were acquired via an inverse method. A ratio of permeability in the race-tracking area to the average permeability of the preform, k_r/k_a, was defined to indicate the severity level of race-tracking permeability. The ratio data were characterized statistically with different distribution assumptions. The Weibull distribution was found best suited for representing the values. The second study involved the optimum design of the RTM process based on the statistical characterization of race-tracking permeability of fiber preform. The optimization objective was to realize robust process design, which makes the process insensitive to the preform material variations. The process design approach was illustrated through an example of RTM processing a rear car door. The result from the example indicated that the robust process design approach was effective in reducing the process sensitivity to preform permeability, as well as the mold filling time.

4. REFERENCES

1. C.L. Lai and W.B. Young, "Model Resin Permeation of Fiber Reinforcements After Shear Deformation," *Polymer Composites*, Vol.18, No.5, 1997, 642-648.
2. R. Gauvin, F. Trochu and M.L. Diallo, "Permeability Measurement and flow simulation through fiber reinforcement," *Proceedings of the Workshop on Manufacturing Polymer Composites by Liquid Molding*, NIST, 1993, 131-163.
3. V.M.A. Calado and S.G. Advani, "Effective Average Permeability of Multi-layer Preforms in Resin Transfer Molding," *Composite Science and Technology*, Vol.56, 1996, 519-531.
4. Y. De Parseval, K.M. Pillai and S.G. Advani, "A Simple Model for the Variation of Permeability Due to Partial Saturation in Dual Scale Porous Media," *Transport in Porous Media*, Vol.27, 1997, 243-264.
5. A.M. Law and W.D. Kelton, *Simulation Modeling &Analysis Second Edition*, McGraw-Hill International Editions, 1991.
6. W.B. Young, "Gate Location Optimization in Liquid Composite Molding Using Genetic Algorithms," *Journal of Composite Materials*, 1994, 28 (12).
7. R. Mathur, B.K. Fink, S.G. Advani, "Use of Genetic Algorithm to Optimize Gate and Vent Locations for the Molding Process," *Polymer Composites*, 1999, 20 (2).
8. S. Jiang, C. Zhang, B. Wang, "Optimum Arrangement of Gate and Vent Locations for RTM Process Design Using a Mesh Distance-based Approach," *Composites Part A*, 33 (2002).

Mold Filling Simulations for RTM:
Influence of the Scatter of Preform Permeability

F. Desplentere [1], S.V. Lomov [1], I. Verpoest [1]

[1] *Metallurgy and Materials Engeneering Departement, Katholieke Universiteit Leuven*
Kasteelpark Arenberg 44, B-3001 Leuven Belgium Frederik.desplentere@mtm.kuleuven.ac.be

SUMMARY: This paper describes the incorporation of variability of preform permeability data into a mold filling simulation software (PAM-RTM from ESI-group).
The input for the statistical parameters of the local permeability scatter can be obtained from a large number of permeability measurements [1] or by simulation based on textiles modeled with WiseTex software [2,3]. Internal textile geometry, needed for these models, can be obtained by using micro CT measurements [4].
Assigning permeability values to each element in a finite element model can be done in a totally random way [5] or in a correlated way. In this paper, the interaction of the correlation function, the assigned local permeability scatter and the resulting global permeability scatter is discussed based on Monte-Carlo simulations. This information can then be used to simulate a distribution of permeability over a 3D shaped preform for a part under consideration to prevent poor gate and vent locations.

KEYWORDS: Permeability scatter, correlated distribution, mold filling simulation

INTRODUCTION

As the RTM technique is still gaining lot of interest to produce textile composite parts using thermoset and thermoplastic materials, simulations for this kind of process are also important to lower the amount of inferior parts. A common important parameter for both material families is the permeability of the textile preform. Measurements on undeformed preforms, in a flat mold geometry with dimensions 0,3 by 0,3 meter resulted in a standard deviation of 22% for the permeability of the textile [1]. This permeability is valid for the whole preform and will be called global permeability from now on. This is the first important reference value.
Second source of information can be data obtained on the internal geometry of a textile. Using X-ray microcomputer tomography, a scatter for the spacing between yarns in a 3D textile preform of 6% has been found [4]. Dimensions of the yarns of the same kind of textile resulted a scatter of 16%. With this information, a textile internal geometry model can be built within the textile modeling software WiseTex. Models built with this software can serve to calculate mechanical properties and also local permeability of fabrics [3]. Within this investigation, additional scatter due to mold shapes is not considered.

AIM OF THIS PAPER

In this paper, the main scope is to look for the correlation between the scatter of the local permeability value and the scatter of the global permeability value. The local permeability can be defined in two ways.

- First of all, a totally random normal distribution for the permeability along the longitudinal direction can be used with a coefficient of variation of 20%.
- A second possibility is assigning the local permeability values in a correlated way. In these cases, permeability changes between neighboring zones are limited through a correlation function. Also for this case, only scatter for permeability is implemented for the longitudinal direction. Within this investigation, this function is an exponential function taking into account the distance between the centers of gravity of the two considered zones, namely $\text{maximum deviation} = e^{-A \cdot \text{distance}}$. This function is characterized by a correlation value A [1/m], which is an unknown parameter. Increasing A, increases the permeability change between the considered zones.

IMPLEMENTATION
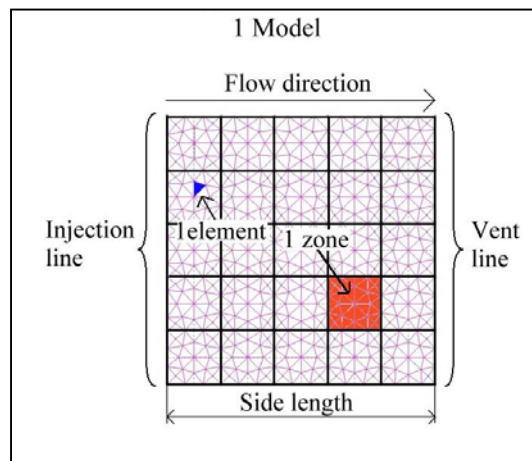
Fig. 1 Important terms for this investigation

In order to assign different permeabilities to a textile to be simulated using PAM-RTM, it is necessary to divide the textile preform model in zones (see Figure 1). In this investigation, only square mold models are considered. The meshing program subdivides each zone in a number of elements. This subdivision is characterized by the mesh density, this is the amount of elements /m². To each zone, the permeability in flow direction can be assigned in a totally random way. The permeability along the transverse direction is kept constant and equal to the average permeability of the longitudinal direction. All elements in one zone have the same permeability vector.

To obtain scatter for the global permeability, the Monte-Carlo technique is used. A certain amount of input files, each describing one model for the mold filling simulation software, is generated and solved by a pre-processing program. To be able to run these Monte Carlo simulations with PAM-RTM in an automatic way, batch programming was used. While PAM-RTM is solving the model, it generates a set of output files. The global permeability for each model is calculated from the corresponding output file (= filling as function of time) generated by PAM-RTM. This is done using the solution for Darcy's law in the one-dimensional case $K = \dfrac{0,5.L^2.\mu.\phi}{\Delta p.t}$ where K = global permeability [m²], L = side length [m], μ = resin viscosity [Pa.s], ϕ = porosity [ ], Δp= pressure drop [Pa] and t = filling time [s].

As performing a mold filling simulation with PAM-RTM is still taking some time, the amount of simulations for the Monte Carlo implementation is limited to 1000. With this amount, it is already possible to draw some conclusions. Influences of different parameters will be checked on the correlation between the average standard deviation for the local and global permeability. Those parameters are (see also Figure 1):

- The number of zones considered along 1 side
- The side length of the mold cavity
- The mesh density
- The correlation value A (only in the correlated cases)

The scatter for the local permeability will be characterized as follows: first of all, the standard deviation of all the permeability values assigned to the different zones within one model is calculated. This is done for all the models and in this way, an average standard deviation for the local permeability can be calculated.

The scatter for the global permeability is obtained from the length of the 95% probability interval of the global permeability distribution. Out of the length of this interval, a standard deviation for the global permeability can be obtained.

IMPLEMENTATION OF RANDOM PERMEABILITY DISTRIBUTION
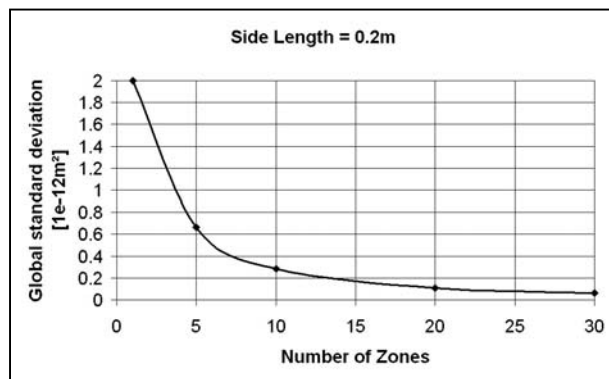
Fig. 2 Influence of number of zones

As the distribution of the permeability values with average value 10.10^{-12} m² and standard deviation 2.10^{-12}m² to the different zones is done in a totally random way, the average local standard deviation is always around 2.10^{-12}m². Analyzing different inputs for the parameters resulted in Fig. 2. The side length of the model is 0.2 meter. Out of Fig. 2, one can conclude that the number of zones along a side plays an important role. The standard deviation for the global permeability is smaller if more zones along a side are considered. For infinite number of zones, the standard deviation for the global permeability will be zero. This can be explained by the fact that the smaller the zones are, the smaller the region to have the average permeability value and the smaller the influence on the global permeability. In the mold filling, the small low permeable zone will be surrounded by resin and will not affect the flow front, as it would be the case for a large area with a low permeability. The situation as discussed above (random distribution of permeability values) is not realistic, because in nature, there doesn't exist parameters, which have infinite gradients as function of position. To have realistic models, a correlation function have been implemented in the preprocessing software of PAM-RTM to assign the permeability values to the different zones.

IMPLEMENTATION OF CORRELATED PERMEABILITY

To define the permeability in a correlated way, the following technique is applied. First of all, a correlation matrix is calculated between all the zones present in the model by applying the correlation function between the two considered zones. This matrix has to be multiplied by the variance to obtain the covariance matrix V. This matrix is a symmetric, positive definite matrix, which can be Cholesky decomposed. This mathematical decomposition method is applied to obtain a lower triangular matrix L and its transpose which results in $V = L.L^T$. Next to this, a column vector Z has to be generated, which is a Gaussian vector with zero mean and covariance matrix I, with I the identity matrix. Since all the values in the matrix Z are mutually uncorrelated, a Gaussian random number generator can be used to sample the values making up the vector Z. Consider now the vector Y defined as follows: Y = L.Z. Applying the expectation operator yields:

$$E(Y) = L.E(Z) = 0 \quad E(YY^T) = L.E(Z.Z^T)L^T = L.I.L^T = L.L^T = V \tag{1}$$

Eqn. 1 proves that this technique can be used to define the permeability in a correlated way, if the average value for the permeability is added to each element of the matrix Y, these values can be assigned to the corresponding zone in the considered model.

PRE- AND POSTPROCESSING RESULTS

Fig. 3 shows the preprocessing results for different parameters. The number of zones along the length of the model is kept constant and equal to 5. Out of this figure, one can conclude

Fig. 3 Pre-processing results

- The larger the correlation value, the smaller the standard deviation for the local permeability.
- For the same correlation value, the standard deviation for the local permeability is larger for larger models. This is due to the fact permeability can change more if larger distances are possible within the model. If the distance between two points is equal to the correlation value, the maximum change in local permeability value is 63% of the reference standard deviation.
- The smaller the correlation coefficient, the more random the model becomes. For correlation value = 0, there is no correlation (= random distribution).
- The local standard deviation changes linearly with the applied reference standard deviation
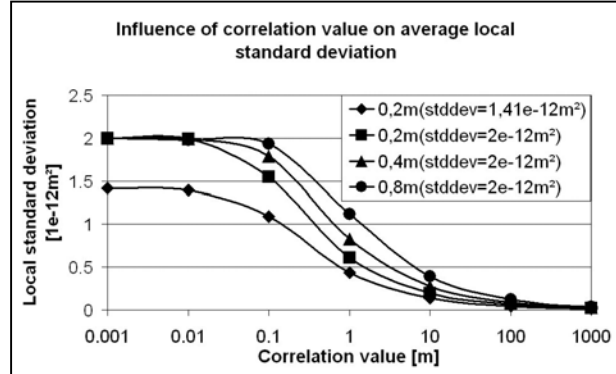
After generation of 1000 files with locally distributed permeability values according to the reference distribution and using the correlation value, one obtains a distribution for the filling times of the model and hence also a distribution for the global permeability. From this distribution, the standard deviation is calculated and displayed in Fig. 4 in case of 5 zones and a side length of 0.2m. As conclusion, one can say the larger the correlation value, the smaller the standard deviation for the local permeability. All the values all over the model are almost the same. Of course, these values are chosen out of the reference distribution. For this reason, the global permeability distribution has a standard deviation, which is equal to the standard deviation of the reference distribution. This investigation shows that the standard deviation for the global permeability is allows equal or lower than the reference standard deviation.
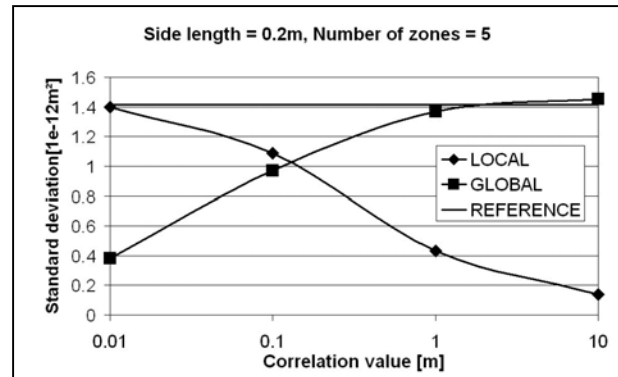
Fig. 4 Global versus Local standard deviation

CONCLUSIONS

For this investigation, still a lot of influences can be examined. Out of a large amount of simulation cases and investigation of the local permeability, it should be possible to define the correlation value. Together with the reference distribution for the local permeability, a general idea of the scatter on the global permeability will be possible to obtain. In future, implementing the scatter in the transverse direction has to be done. Next step in this investigation is to implement this scatter for arbitrary pieces and to allow a viscosity change.

REFERENCES

1.   K. Hoes, M. Vanheule, H. Sol, "Statistical distribution of permeability values of different porous materials", *Proc. of The Tenth European Conference on Composite Materials (ECCM-10), 2002*
2.   E. Belov, S.V. Lomov, I. Verpoest, T. Peters, D. Roose, K. Hoes, H. Sol, R.S. Parnas, "Modeling of permeability of Textile Reinforcements – Lattice Boltzmann method ", *Proc. of the Society for the Advancement of Material and Process Engineering EUROPE (SAMPE EUROPE 2004),2004*
3.   S.V. Lomov, I. Verpoest, "Modeling of permeability of Textile Reinforcements – Lattice Boltzmann Method", *Proc. of the Society for the Advancement of Material and Process Engineering EUROPE (SAMPE EUROPE 2004),2004*

4.   F. Desplentere, S.V. Lomov, D.L. Woerdeman, I. Verpoest, M. Wevers, P. Szucs, A. Bogdanovich, " Geometrical characterization of 3-D warp-interlaced fabrics", *Proc. of the Society for the Advancement of Material and Process Engineering USA (SAMPE USA 2003),2003*

5.   A. Long, F. Robitaille, C.D. Rudd, I.A. Jones, "Modeling strategies for Textile Composites," *Proc. of the Internatial Conference on Composite Materials (ICCM 14), 2004*

---

1.   Hoes K. , D.D., M. Vanheule, H. Sol. *Statistical distribution of permeability values of different porous materials*. in *ECCM10*. 2002.

PREFORM MODELING AND EFFECTS: III. COMPRESSIBILITY

Non-Elastic Effects during Compression of Fiber Reinforcements

A. A. Somashekar, S. Bickerton, and D. Bhattacharyya

Center for Advanced Composite Materials, Department of Mechanical Engineering
The University of Auckland, Private Bag 92019, Auckland, New Zealand
Corresponding Author's email: s.bickerton@auckland.ac.nz

SUMMARY: Many techniques used for the production of fiber-reinforced polymer composite articles require compression of the reinforcement to achieve desired material composition and properties. A common approach in the literature has been to assume non-linear elastic deformation of the reinforcement when modeling composites manufacturing processes. However, previous research has demonstrated viscoelastic behavior, as well as permanent deformation. These fibrous materials also respond differently if a liquid resin is introduced within the reinforcement structure, which is significant to a range of composites manufacturing processes. A series of experiments were designed and carried out to further investigate these non-elastic effects, and to establish their relative importance. Specifically, the aim has been to determine the proportion of each type of deformation and its variation with respect to time. Material behavior during and following cyclic loading and unloading has also been studied.

KEYWORDS: viscoelastic recovery, permanent deformation, elastic springback.

INTRODUCTION

A wide variety of manufacturing processes have been developed to produce fiber-reinforced polymer composite articles. Such articles find application in industries as diverse as marine, automotive and space, to name a few. Of particular concern to this research are the Liquid Composite Manufacturing (LCM) group of processes, wherein a resin is injected into the mold containing the reinforcement. These techniques require compression of the fibrous reinforcement to achieve the desired material composition and properties. To include compression deformation in LCM process simulations, a standard technique has been to assume that the reinforcement deformation is non-linear elastic [1,2]. However, previous research has demonstrated viscoelastic behavior, as well as permanent deformation [3][4]. These materials also respond differently if a thermo-set (low viscosity) polymeric resin is introduced within the reinforcement structure, which is of particular significance to LCM processes [5].

A series of experiments were designed and carried out to further investigate these non-elastic effects, and to establish their relative importance. Specifically, the aim has been to determine the proportion of each type of deformation and its variation with respect to time. Material behavior during and following cyclic loading and unloading has been studied.

This research will help in further understanding the forces required for molding, and the distribution of stresses acting on the mold. The long-term goal of this work is the development of a comprehensive reinforcement deformation model, incorporating the different kinds of deformation observed. This will be important for improving simulation of composites manufacturing processes in general.

EXPERIMENTAL WORK

Dry reinforcement samples comprising 10 layers each (200 mm x 200 mm) were cut from Continuous Filament Mat (CFM, 450g/m^2) and Plain Weave Fabric (PWF, 600 g/m^2) E-glass material. The glass fiber preforms were compacted to a target final fiber volume fraction (V_f) on an 'Instron' 1176 Universal Testing Machine with a 200 kN auto-ranging load cell. Following compaction, the strain was held constant for varying periods of time. The testing machine crosshead was then returned rapidly to its initial (un-compacted) position, thus enabling the reinforcements to recover thickness. A rectangular aluminium plate was placed on the reinforcements, and two laser displacement gauges mounted on the crosshead measured the recovery of the preforms by reading the position of the plate. Fig. 1 shows this arrangement. The constant stress on the preforms as a result of the plate was 120 Pa. The presence of the plate not only facilitated the measurement of the preform height at any given time (by allowing the laser displacement gauges to be focussed on it), but also provided a constant stress on the preforms to clearly define the initial height/volume fraction. The mounting of the laser gauges on the moving crosshead enabled the direct measurement of the preform height at any given time. The final V_f was chosen considering the type of reinforcement material, and typical values used in composites manufacturing. The compaction load was also monitored throughout the experiments.
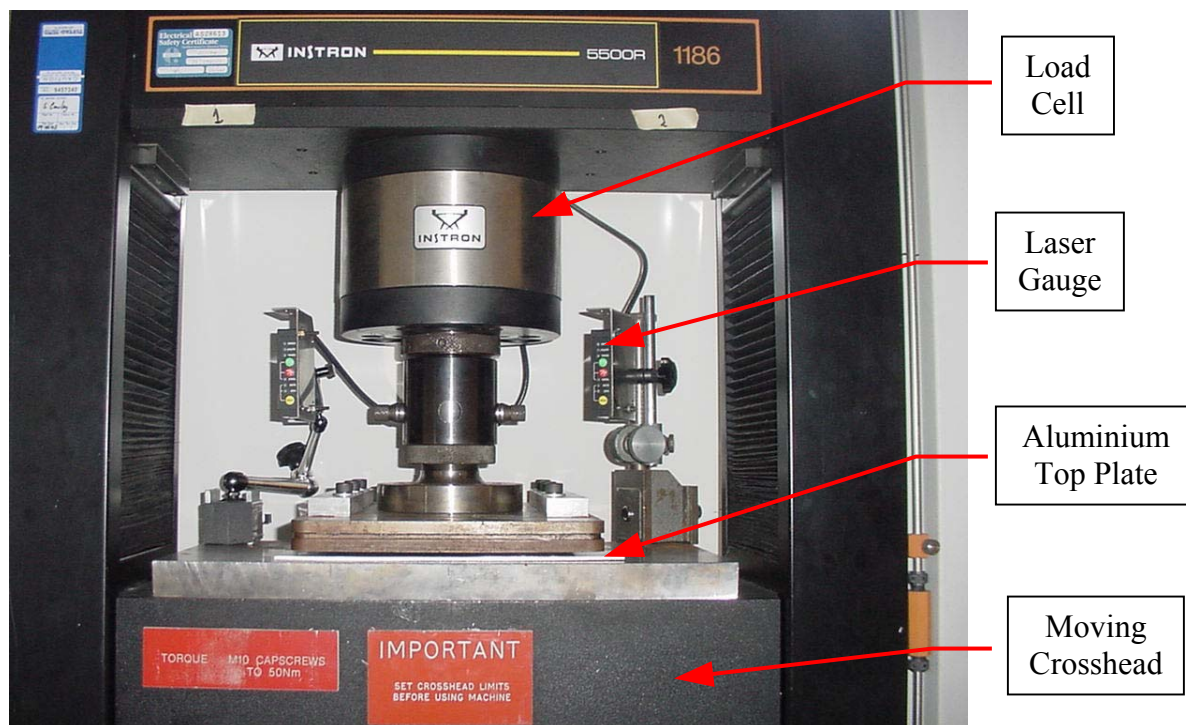

Fig. 1 Experimental set-up

Three CFM specimens were compacted to a target final V_f of 40% at a compaction speed of 5 mm/min. The strain was held at the final V_f for a time period of 6 sec, 10 min and 100 min respectively. At the end of this holding period, the testing machine crosshead was rapidly (at 100 mm/min) returned to its initial (un-compacted) position, thus enabling the preforms to recover height. Readings were taken for a period of 25 minutes following the start of preform recovery.

In a separate experiment, a sample was subjected to 20 cycles of loading and unloading to the same final and initial V_f as above, and at the same compaction and return speed (5 mm/min). Following the last cycle, readings were taken for 25 min to record the recovery of the pre-form.

For PWF, the testing programme was the same as that given above for CFM, except that the target final V_f was 60%.

RESULTS AND DISCUSSION

Continuous Filament Mat (CFM) Glass Fiber Reinforcements

Fig. 2 (a) and Table 1 show the results obtained for the CFM material where the strain was held constant for varying periods of time at the final V_f. It is interesting to note that the time intervals of constant strain used had no impact on the various quantities shown in the table, and that they are almost identical in all three cases. (The constant strain period is not included in the plots for ease of comparison).

From the experimental data it was found that it took about 2.5 sec for the load to substantially diminish from the start of rapid return of the crosshead [from the compacted to its initial (un-compacted) position]. From this point of negligible load, the preforms recovered height rapidly for about 8 sec. This period of rapid recovery represents the elastic springback of the reinforcements. Recovery was recorded for a further 25 minutes. During this period slow but steady increase in the height of the preforms continued to take place. This prolonged recovery is the viscoelastic or time-dependent recovery of the preform. The un-recovered deformation at this stage was treated as permanent deformation. In reality, viscoelastic recovery does not actually cease at that stage, but continues at a very slow rate. Displacement gauge readings were noted about 16 hours later, and increase in preform height of about 0.2 mm was found to have occurred during that time.

From Table 1 it can also be seen that elastic springback and permanent deformation are significant components, while viscoelastic recovery is a small proportion of the total deformation of the preform. This could be due to the nature and structure of CFM glass fiber reinforcements. The layers of material sit loosely on one another, and a considerable proportion of the bulk volume of the reinforcements is empty, enabling significant elastic and permanent deformation to take place.

The compaction load data was also recorded in all tests, but is not presented here.

A direct comparison of the stress on the preform can be made for the tests where the strain was held constant for 10 min and 100 min. Stress relaxation occurs during this time, and the longer the duration of constant strain, the greater is the stress relaxation.

Table 1 CFM and PWF Glass Fiber Preforms: Components of Deformation

	CFM (V_f = 40%) Compaction Speed = 5mm/min				PWF (V_f = 60%) Compaction Speed = 5 mm/min			
Strain held for	6 sec	10 min	100 min	20 cycles load/unload	6 sec	10 min	100 min	20 cycles load/unload
Height								
Initial, mm	33.7	34.5	34.4	34.6	7.1	7.5	7.6	8.0
Compacted, %	12.0	11.4	11.7	11.6(last)	42.5	39.9	41.5	43.6(last)
After elastic spring-back,%	60.6	60.6	60.1	42.4(last)	71.2	70.1	70.0	62.9(last)
Final, %	64.5	64.7	64.0	44.2(last)	81.7	79.8	80.0	67.6(last)
Deformation, mm	29.7	30.6	30.3	30.6	4.1	4.5	4.5	4.5
Elastic spring-back, %	55.2	56.0	54.8	34.9(last)	49.6	48.1	46.7	34.4(last)
Visco-elastic recovery,%	4.5	4.1	4.4	2.0(last)	18.4	18.4	19.0	8.0(last)
Permanent deform, %	40.3	39.9	40.8	63.1(last)	32.0	33.5	34.3	57.6(last)

The preform subjected to 20 cycles of loading and unloading showed a steady decline in un-stressed thickness as the test progressed, and this tended to a constant value towards the end of the test. A plot of stress vs V_f, Fig. 3 (top), also shows a shift of curves towards the right, which becomes diminished as the experiment progresses, and is almost negligible towards the end. There is little change in stress vs V_f from cycle-to-cycle at that stage. This shows that the reinforcement reached a steady state and no further permanent deformation was taking place.

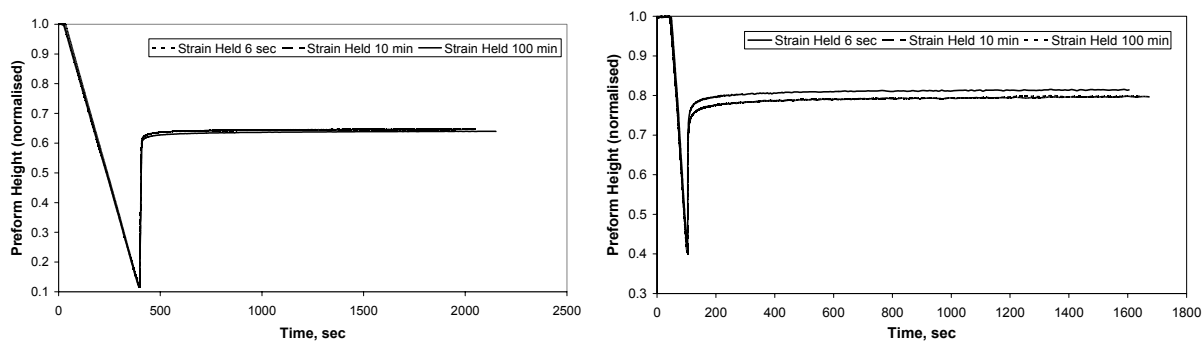Fig. 2 (a) CFM and (b) PWF: Preform Height vs Time
(Note: Constant strain period has not been shown for ease of comparison).

There is however a difference between the target V_f (as set by pre-determining the motion of the machine crosshead) and the actual V_f achieved (as calculated from the displacement gauge readings). The actual V_f is around 42.5%. This difference of about 0.25 mm between the

machine and gauge readings is consistent throughout the experiment. A better method for the future would be to set the crosshead movement required based on the gauge readings.

Plain Weave Fabric (PWF) Glass Fiber Reinforcements

Fig. 2 (b) and Table 1 highlight the results of the constant strain tests on PWF reinforcements. As in the case of CFM reinforcements, the time durations of constant strain have not had any effect on the different components of deformation, and the plots of preform height vs time are almost identical. However, there is more significant viscoelastic recovery, which is comparable to the elastic springback and permanent deformation. Once again, this phenomenon could be attributed to the architecture of PWF glass fiber reinforcements. Woven materials fit naturally and efficiently into compact volumes, unlike CFM. There are also two other factors that come into play when woven reinforcing fabrics are compacted – stacking and nesting. Stacking refers to the manner in which consecutive layers of material are stacked to form the reinforcement. During compaction, layers naturally try to fit into grooves that exist between consecutive tows, and this is referred to as nesting. These issues may account for the fact that both elastic and permanent deformation are less compared to those of CFM, while the time-dependent viscoelastic recovery is comparable to both those quantities. Other issues discussed earlier with regard to CFM (time taken for the load to be released after compaction and constant strain period, rapid elastic springback, slow viscoelastic recovery and very small viscoelastic recovery after many hours) also apply to this material; however, the values computed are different. Again, as in the case of CFM, stress relaxation occurs when the strain is held constant, and longer the time period, greater is the reduction in stress.
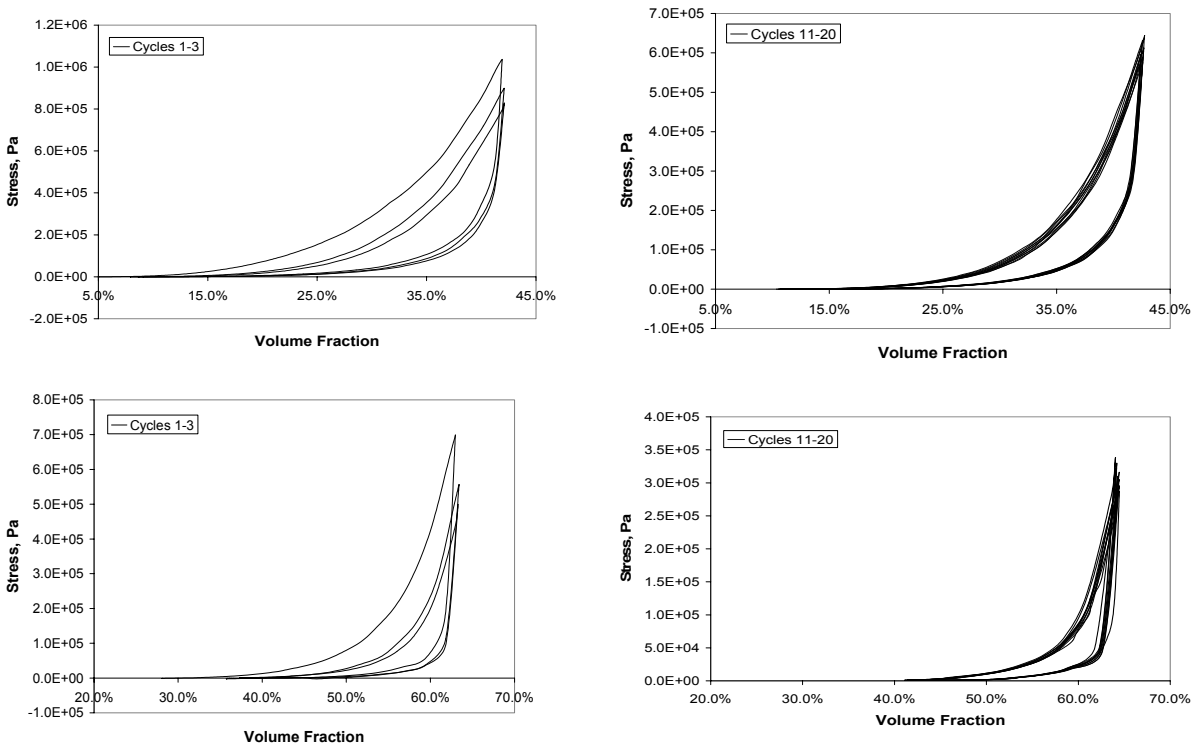

Fig. 3 Stress vs V_f - Cyclic Loading and Unloading: a) and b) CFM cycles 1-3 and cycles 11-20. c) and d) PWF cycles 1-3 and cycles 11-20.

The results for the cyclic loading and unloading test qualitatively mirror those for the CFM. As in the earlier case, as the test progressed, the reinforcement tended to reach a steady state, Fig. 3 (bottom). The elastic springback and viscoelastic recovery components tended to diminish, while the permanent deformation increased. The earlier comment regarding the target and actual V_f applies here also, with the actual V_f being around 62.5%.

CONCLUSIONS

1. The existence of viscoelastic recovery and permanent deformation has been clearly demonstrated. This highlights the complex non-elastic behavior that occurs during compression of fiber reinforcements.
2. The elastic spring-back, viscoelastic recovery and permanent deformation of CFM and PWF glass fiber reinforcements are not affected by the time durations of constant strain used.
2. Viscoelastic recovery in CFM is almost an order of magnitude less than elastic springback and permanent deformation, while this was significant in PWF.
4. The cyclic loading and unloading experiments show that the reinforcements reach a steady-state, and no further permanent deformation takes place. There is little change in stress vs V_f towards the end.

ACKNOWLEDGEMENTS

REFERENCES

1.   T. G. Gutowski, Z. Cai, S. Bauer, D. Boucher, J. Kingery and S. Wineman, "Consolidation Experiments for Laminate Composites", *Journal of Composite Materials*, Vol. 21, July 1987, Pages 650-669.
2   X.-T. Pham, F. Trochu and R. Gauvin, "Simulation of Compression Resin Transfer Molding with Displacement Control", *Journal of Reinforced Plastics and Composites*, Vol. 17, no. 17, 1998, Pages 1525-1556.
3.   N. Pearce and J. Summerscales, "The Compressibility of a Reinforcement Fabric", *Composites Manufacturing*, Vol. 6, no. 1, 1995, Pages 15-21
4.   S. Bickerton, M. J. Buntain and A. A. Somashekar, "The Viscoelastic Compression Behavior of Liquid Composite Molding Preforms", *Composites Part A: Applied Science and Manufacturing*, Volume 34, 2003, Pages 431-444.
5.   R. A. Saunders, C. Lekakou and M. G. Bader, "Compression in the Processing of Polymer Composites 2. Modeling of the Viscoelastic Compression of Resin-Impregnated Fiber Networks", *Composites Science and Technology*, Volume 59, 1999, Pages 1483-1494.

Influences of the Sewing Process on the Compaction Behavior of Fibrous Preforms

Ogale, A.[1], Floeck, M.[1], Stadtfeld, H. C.[1], Mitschang, P.[1] and Bickerton, S.[2]

[1] *Institut fuer Verbundwerkstoffe GmbH, Erwin-Schroedinger-Strasse 58, 67663 Kaiserslautern, Germany: amol.ogale@ivw.uni-kl.de*

[2] *Center for Advanced Composites Materials, University of Auckland, Private Bag 92019, Auckland, New Zealand: s.bickerton@auckland.ac.nz*

SUMMARY: The compression behavior of textile fabrics and the preforms made from them significantly influences the subsequent process steps, i.e. liquid composite molding (LCM). These influences can range from a mere advantage in handling of assembled preforms to local changes of fiber volume content (F_v) with their respective change in local permeability. The phenomenon of preform structural compaction depends on the geometry of the particular preform, i.e. fabric type, fabric geometry, tailored reinforcements, preforming procedures, parameters, etc. Out-of-plane compaction of fibrous preforms can result in possible in-plane extensions. While a stack of fabric layers is able to extend within its in-plane directions, a debulked preform utilizing appropriate sewing patterns is limited in this respect. This paper presents preliminary results of studies performed at Auckland and Kaiserslautern concerning preform compaction behavior of stitched and unstitched fibrous reinforcements. Initial investigations are presented into the effect of preform assembly sewing techniques on the compaction behavior of these structure.

KEYWORDS: Preform, compaction, fiber reinforced polymer composite, sewing, liquid composite molding

INTRODUCTION

In the LCM processes, particularly, resin transfer molding (RTM), preform placement and its near net shape is of primary importance [i]. Composite manufacturing by means of RTM is a widespread technology and has high scope to develop in order to obtain high quality products. The interrelation between the manufactured preform and final fiber reinforced plastic (FRP) characteristics is linked by means of the RTM process. Since preforms are the latest sub- product before the LCM process, they need to be manufactured considering all the RTM related aspects: mold placement, compaction behavior, probable hindrances for resin transfer, etc. Preforms can be manufactured in various ways according to their end applications. Tailored reinforcements or sewn multi-textile-preforms have remarkable advantages in terms of their near-net-shape and ready-to-impregnate features. Sewn assembly can hold two or more layers of mono- or multi-structural reinforcing materials. Different sub-preforms can be sewn with varied pre-compaction level according to the tooling need.

Preform pre-compaction during stitching and compaction during the RTM process influence the preform permeability. Compaction behavior of sewn preform is influenced by the sewing thread tension, stitching pattern, and presser-foot pressure (compression of reinforcing material during stitching) [i].

Many researchers have made attempts to examine compaction of fibrous lay-up [ii,iii,iv]. Grimsley et. al. explained the compaction behavior of stitched multi-axial non-crimp fabric (NCF) material in dry and wet condition during vacuum assisted resin transfer molding (VARTM) [iv]. The time-dependent tooling forces acting on the unstitched preforms during the RTM process are also of great importance relating to preform properties and injection technique [v].

Some studies regarding compaction behavior of differently stitched NCFs have been found in the literature and the influence of stitch density is explained [vi]. Influence of garment based sewing technology on the preform compaction was not well exploited before; therefore, it is a topic of discussion within the scope of this paper. In the current work, influence of sewing thread tension and stitch density on the preform compaction behavior is examined. The relationship between applied compaction stress and corresponding fiber volume content has been evaluated.

EXPERIMENTATION

Preform Manufacturing

Preforms were manufactured according to a set design of experiment, so that the influence of sewing parameters is clearly visible. Three different types of textile fabric systems made up of glass fibers were used for the experimentation: plain woven fabric (821 g/m^2), biaxial NCF, (1200 g/m^2) and triaxial NCF (1200 g/m^2). The sewing thread used was a standard polyester thread from Amann & Söhne GmbH & Co.KG. (No. 50). An automatic sewing machine (from KSL Keilmann Sondermaschinenbau GmbH) was used for preform stitching and the stitching speed was 1,000 stitches/min. The applied thread tension for preform manufacturing was set to two extreme levels. Low needle thread tension was 68 cN, corresponding bobbin thread tension was 144 cN, high needle thread tension was 500 cN, and the corresponding bobbin thread tension was 250 cN. Two different stitch densities were achieved by using different stitch patterns. Stitching patterns were designed using CAD software and fed to the sewing machine. Table 1 shows the experimental design.

Table 1: Design of experiment: preform panel manufacturing

Fabric Type		Stitch pattern			
		5 mm x 5 mm (13.33 stitches/cm^2)		20 mm x 20 mm (3.33 stitches/cm^2)	
		Low thread tension (300 cN)	High thread tension (500 cN)	Low thread tension (300 cN)	High thread tension (500 cN)
Plain woven		X	X	X	X
Non-crimp fabric	Biaxial	X	**X**	X	X
	Triaxial	X	**X**	X	X

Sewn preforms were then punched to the exact size of the testing rig (180 x 220 mm). To investigate the reproducibility and homogeneity of the recorded data, three specimens were stitched for every set of preforming variables.

Testing

Preforms were tested for dry compaction behavior in terms of stress required to compress the particular stitched lay-up and corresponding reduction in the thickness. An Instron testing machine was used at constant speed mode. First the specimen was loosely inserted between the two parallel plates of the test rig, as the test proceeded; the plates were driven together at a constant speed compressing the lay-up. The Instron records the applied load and corresponding preform thickness. The thickness data can then be converted into fiber volume content, thus it is possible to plot a graph of F_v obtained against the applied load on the lay-up. All of the stitched preforms were tested and compared with the results of unstitched fabric lay-up.

RESULTS AND DISCUSSION

Time Dependent Compaction

Preforms were tested for dry compaction behavior in terms of stress needed to compress the particular stitched and unstitched lay-up to obtain required fiber volume content. The results of progressive preform compaction were classified according to the stages of fiber volume content (from 55 to 65% fiber volume content). Fig. 2a shows the time dependent compaction behavior of biaxial NCF, triaxial NCF, and woven fabric. Fig. 2b shows a plot of compaction stress vs. change in the preform thickness. The triaxial fabric preform has high initial thickness thus it starts compacting earlier than the other types of preforms and needs high compaction stress to achieve the required preform thickness.
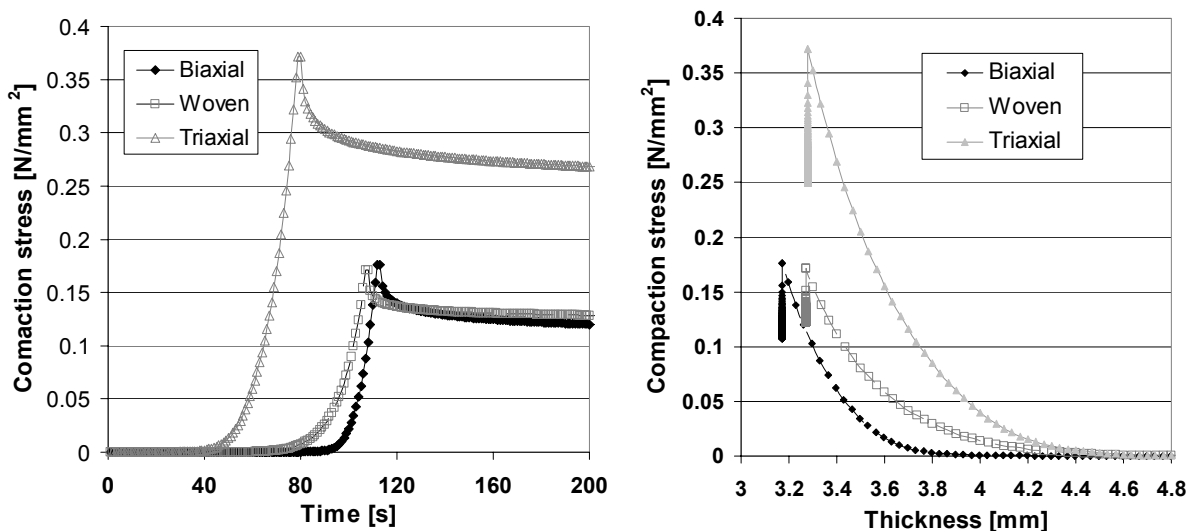
g. 2: Compaction behavior of 20 x 20 stitched preforms for achieving 60% fiber volume
a) Plot of compaction stress vs. time b) Plot of compaction stress vs. preform thickness

On the other hand, biaxial fabric has less preform thickness so the required compaction stress is also lower than the triaxial fabric lay-up. Because of the wavy structure of woven fabric, the lay-up thickness is higher compared to the well oriented biaxial fabric, thus more compaction stress is needed to achieve 65% fiber volume.

Fiber Volume Content a Function of Compaction Stress

A plot of the peak applied compaction stress required to achieve corresponding fiber volume content is shown in Fig. 3. The maximum stress required to compact a preform was 38 KN (in case of preform with 5 x 5 stitching pattern and high thread tension). Thread tension applied during the preforming is a vital parameter in case of preforms stitched with a high stitch density. In the category of stitched preforms, a 20 x 20 stitched preform requires the smallest compaction stress to achieve the required fiber volume content. Preforms stitched with low stitch density are not affected by the applied thread tension. The same trend was observed for triaxial and woven fabrics but with the different intensities.
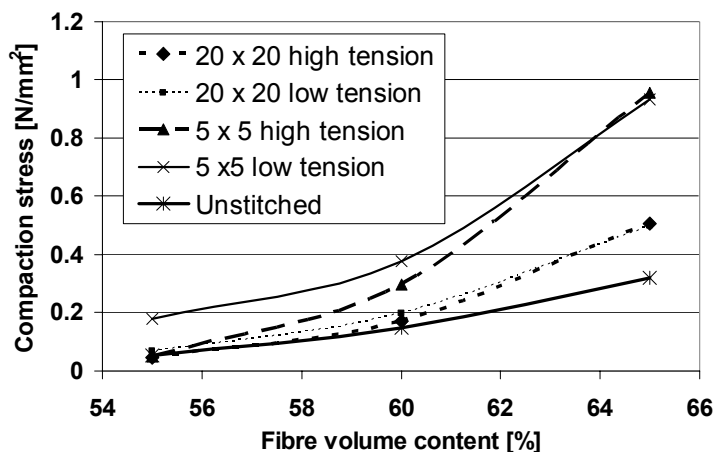
Fig. 3: Compaction behavior of biaxial NCF lay-up

Fig. 4 shows the combined data of compaction stress required for all the various stitched preforms and unstitched lay-ups. In general, achieving high F_v%, stitched preforms require more compaction stress than the unstitched lay-ups. On the contrary in the case of stitched preforms with low stitch density, the initial compaction stress needed was lower compared to the unstitched preform.
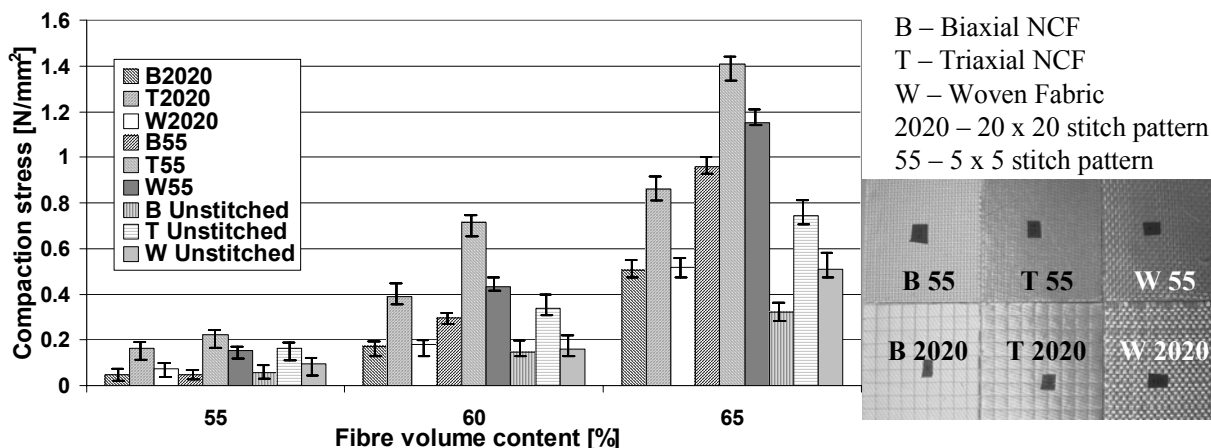
Fig. 4: Steps of F_v % with respect to compaction stress for different textile preforms

The preforms stitched with the high stitch density are blocked to further free movement of reinforcing fibers, thus the phenomenon of fibrous compaction [iii] is more complex. Therefore, this type of preform requires higher compaction stress to achieve the desired preform thickness. Preforms stitched with the low stitch density allow further rearrangement of the reinforcing structure which facilitates easier fibrous compaction. Therefore, up to a certain level, these require low compaction stress to compress the complete structure compared to the preforms with densely stitched preforms, and unstitched fabric lay-up. As the preform compaction proceeds, the reinforced fibers may get repositioned which causes the linear deformation of a preform. Due to the stitches, fiber reorientation becomes difficult and it does not allow the linear deformation of a stitched structure. Thus, the higher compaction stress is required to obtain desired preform thickness. Only in the case of unstitched lay-up, unhindered linear deformation is allowed. This phenomenon keeps the lay-up compacted and causes easy deformation of the lay-up, thus it requires less compaction stress to reach the required preform thickness.

CONCLUSION

According to the basic textile structure, sewn preforms show different compaction behavior than the unstitched lay-up. The lay-up structure and sewing parameters influence the final preform fiber volume content, thus for particular preform application it is possible to use specified sewing variables. Intensity of applied thread tension and stitch density are the parameters of preform engineering and can be optimized for different sub-preforms. Sewing operation supports the pre-compaction of fibrous lay-up to a certain extent of fiber volume content. Pre-compacted preforms with high stitch density can be suitable in the process stage of net shape preforming which again reduce the tool loading time.

REFERENCES

[i]   P. Mitschang, A. Ogale, J. Schlimbach, F. Weyrauch, C. Weimer, "Preform Technology: a Necessary Requirement for Quality Controlled LCM-Processes", Polymers & Polymer Composites Vol. 11, No. 8, Pages 605-622 (2003).

[ii]   B. Chen and T.-W. Chou, "Compaction of woven fabric preforms in liquid composite molding process: Nesting and multiplayer deformation", *Compos Science and Technology, Volume 60,* Pages 2223-2231 (2000).

[iii]   B. Chen, A. H.-D. Cheng, and T. -W. Chou, "A nonlinear compaction model for fibrous preforms", *Composites Part A: Applied Science and Manufacturing, Volume 32,* Pages 701-707 (2001).

[iv]   B. W. Grimsley, P. Hubert, X. Song, R. J. Cano, A. C. Loos and R. B. Pipes, "Flow and compaction during the vacuum assisted resin transfer molding process". Internet address: http://techreports.larc.nasa.gov/ltrs/PDF/2001/mtg/NASA-2001-33sampe-bwg2.pdf

[v]   S. Bickerton, H.C. Stadtfeld, and P. Mitschang, "Modelling tooling forces generated during the resin transfer molding process", *Proc. 24th International SAMPE Europe conference*, Paris, April 1-3, Pages 693-701 (2003).

[vi]   S. V. Lomov, E. B. Belov, T. Bischoff, S. B. Ghosh, T. Truong Chi, and I. Verpoest, "Carbon composites based on multiaxial multiply stitched preforms. Part 1. geometry of the preform", *Composites Part A: Applied Science and Manufacturing, Volume 33,* Pages 1171-1183 (2002).

Compaction of Dry and Lubricated Reinforcements

Teresa Kruckenberg [1] and Rowan Paton [2]

[1] *Center for Advanced Materials Technology, School of Aerospace, Mechanical and Mechatronic Engineering, University of Sydney, Sydney, NSW, 2006, Australia*
[2] *Cooperative Research Center for Advanced Composite Structures (CRC-ACS), 506 Lorimer St., Fishermens Bend, Victoria, 3207, Australia*

SUMMARY: This paper presents an experimental investigation into the quasi-static compaction behavior of carbon fiber reinforcement fabrics. The reinforcements tested included several non-crimp fabrics, a five-harness satin-weave fabric and a plain-weave fabric. Stacks with from two to ten layers, both dry and lubricated with water-diluted glycerine, were tested. The compaction tests were conducted on an MTS machine, using crosshead movement to measure compaction, with careful correction for machine compliance. Power model curves were able to fit the compaction data reasonably well. The non-crimp fabrics and five-harness satin fabric compacted more easily than the plain-weave fabric. Thicker stacks were found to compact more easily than thinner stacks. Lubricated stacks compacted more easily than dry stacks. It was found that the carbon fiber reinforcements tested have similar compaction behavior. A procedure to predict the compaction thickness under higher pressures by using the thickness measured at 100 kPa, such as under a vacuum bag, is also presented.

KEYWORDS: Carbon fiber fabrics, reinforcement fabrics, compaction, volume fraction.

Introduction

The compaction of stacks of dry reinforcement to a desired thickness (and perhaps a desired permeability) is an important aspect of many composite manufacturing processes, especially liquid molding processes. Therefore, measurement or prediction of the compaction behavior of reinforcement stacks provides important processing data.

This paper describes a procedure for conducting quasi-static compaction tests first devised by Liu and Triantafillou [1]. This procedure has been progressively modified to minimise any errors from machine compliance. The procedure has been used as described here to measure quasi-static compaction behavior of carbon fiber reinforcements, including non-crimp, satin-weave and plain-weave fabrics. The reinforcements were tested in the usual dry condition, and a "lubricated" condition, partially impregnated with water-diluted glycerine.

Experimentation

Materials

Details of the fabrics tested are given in Table 1. The fabrics were cut to either 200×200 mm squares or 175 mm diameter rounds using templates. Stacks of 2 plies, 4 plies, 6 plies and 10 plies were made up. Some stacks were lubricated with water-diluted glycerine (1 part water to 3 part glycerine by weight, with a viscosity of approximately 50 cPs at room temperature). The lubricant was poured onto each layer of fabric and carefully brushed across the surface until the fabric was saturated. A summary of the test matrix is given in Table 2.

Table 1: Details of carbon fiber fabrics tested
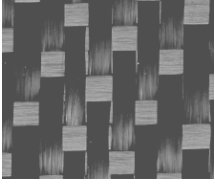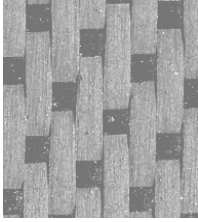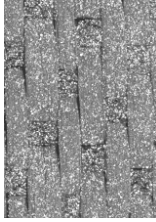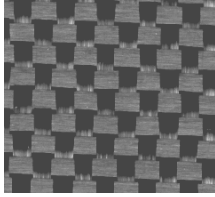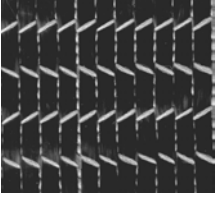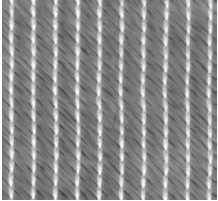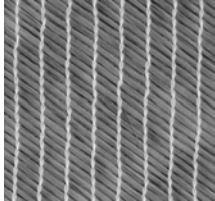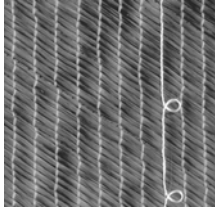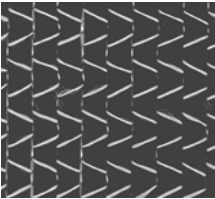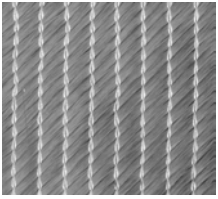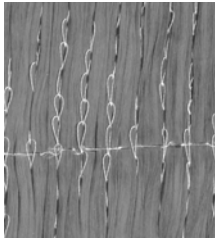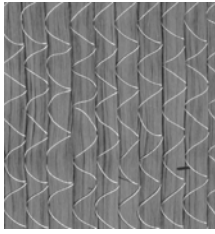
Fabric	Supplier	Fabric Style	Areal Weight (g/m^2)	Fiber Orientation
G926	Hexcel	6K 5H satin weave (no binder)	370	0/90
RC200P	SP Systems	3K plain weave	195	0/90
FCIM156	Formax	T700 12K-FOE quadraxial NCF	1068	0/-45/90/+45 (even dist'n)
XC411	SP Systems	12K biaxial (double bias) NCF	408	+45/-45
SQ1091R	Saertex	12K quadraxial NCF (right hand version)	1091	0/+45/90/-45 (even dist'n)
SQ1090L	Saertex	12K quadraxial NCF (left hand version)	1091	0/-45/90/+45 (even dist'n)
NC2	Hexcel	12/24K biaxial NCF	930	0/90/0 (83.9% in 0 dir'n)

Table 2: Summary of test matrix

Fabric	Ply Number	Lay-up	Specimen Number	
			Dry	Wet
G926 (no binder)	2	$[0]_2$	2	1
	4	$[0]_4$	1	1
	10	$[0]_{10}$	2	1
RC200P	4	$[0]_4$	2	2
	10	$[0]_{10}$	2	2
FCIM156	4	$[0,0_F,0,0_F]^*$	2	2
XC411	2	$[0]_2$	2	4
	10	$[0]_{10}$	2	2
SQ1091R + SQ1090L	4	$[0_R,0_{LF},0_R,0_{LF}]^*$	2	1
NC2	2	$[0]_2$	3	2
	6	$[0]_6$	2	1

* R = right hand, L = left hand, and F = ply flipped over

Table 3: Photographs of reinforcements

G926 (no binder)	G926 (P03 binder)	G926 (HP09 binder)	RC200P
FCIM156 upper surface	FCIM156 lower surface	XC411 upper surface	XC411 lower surface
SQ1091 upper surface	SQ1091 lower surface	NC2 upper surface	NC2 lower surface

Areal Weight of Reinforcements

The nominal areal weight is specified in each case by the material supplier. It was found that the areal weight of the non-crimp fabric specimens differed significantly from the supplier's value, and for these fabrics the measured areal weight was used in calculations.

Experimental Apparatus

The compaction tests were conducted on a 250 kN MTS machine. The reinforcements were compacted between an upper circular steel platen 150 mm in diameter and a lower circular steel platen 200 mm in diameter.

Thickness reduction measurements were obtained using cross-head displacement. These measurements were carefully corrected for machine compliance as described below.

Compliance of Experimental Apparatus

Test machine compliance was measured by running the test (carefully) without a reinforcement stack. A typical load-displacement curve from the machine compliance tests is shown Figure 1. It can be seen that there is an initial non-linear curve "foot", followed by a linear compliance. The non-linear initial stage is believed to be caused by slight departures from parallelism of the two platens. Some force must be applied before full contact: thereafter, the apparatus deforms elastically. It was found that machine compliance could be easily varied by common setup operations such as releasing and reapplying hydraulic pressure to the grips, or releasing and reapplying the cross-head lock to the top platen. The test system was also found to sometimes exhibit a slight amount of slip during the day. Therefore, a compliance test was run at the start of the day, and at the end of the day, as a minimum.

Difficulty was encountered in establishing a clear zero-load reference point for use in correcting the crosshead displacement measurements for machine compliance. Therefore the test crosshead displacement measurements were corrected by the machine compliance curve using a common reference point corresponding to a load such as 3 kN clearly within the linear portion of the compliance curve.

Although the machine compliance was found to be non-linear at low loads, it was found that ignoring the non-linearity at low loads caused less than 1% error in specimen thickness calculations, even for thin specimens, and only at low loads. Therefore the machine compliance was treated as being fully linear for the purposes of establishing the "zero-load" displacement and correcting the crosshead displacements.
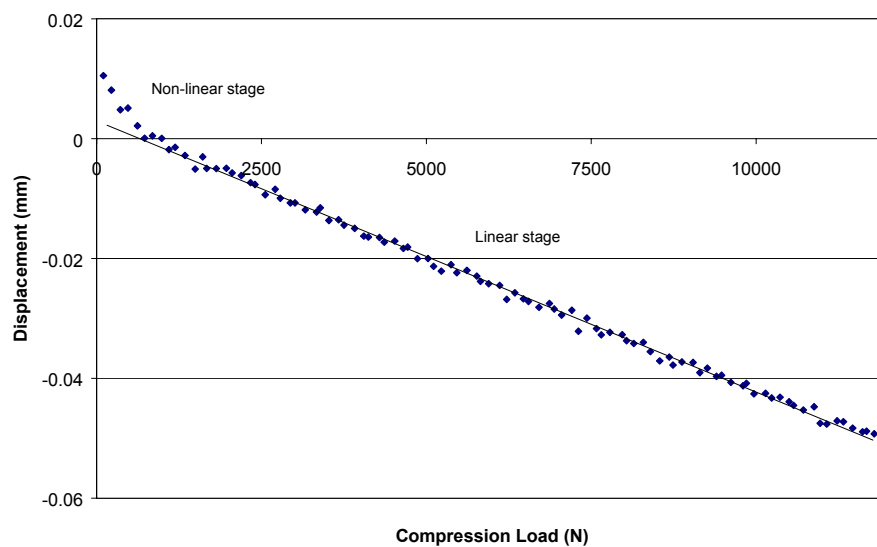
Figure 1: Typical machine compliance curve

Procedure

All compaction tests were conducted at room temperature. A machine compliance test was first conducted. The bottom platen was then lowered to form a 9 mm gap for insertion of the compaction specimen. The compaction specimen was placed centrally on the lower platen. It is known from previous testing at CRC-ACS and elsewhere that compaction behavior of the stack is "viscoelastic" [2,4]. This is believed to be caused by the time-dependant rearrangement of the fibers and fiber bundles under compaction. This work was intended to produce compaction data for use in liquid molding processes where the compaction loads are applied well before the resin is injected. Therefore loads were held at 50, 100, 200, 300, 400, 500, 600, and 700 kPa for 5 minutes [2,4] to allow for the relaxation of the fabric stack [2] and generate "equilibrium" compaction curves.

Fiber Volume Fraction (V_f) was calculated using Eqn 1 below [3]. N = number of layers, A = fabric areal weight, ρ = carbon fiber density (1780 g/m^3), and t = thickness of specimen:

$$V_f = \frac{AN}{\rho t} \tag{1}$$

RESULTS AND DISCUSSION

Compaction Curves

The V_f achieved by compaction for five minutes at the nominated pressures is shown in Figures 2 to 8. The compaction response can be expressed by the following two-parameter power model, where K is the "initial" V_f (V_f achieved at P_0) and m the stiffening index [2]. In this work, P_0 is defined as 100 kPa, so that when $P = 100$ kPa, $K = V_f$.

$$V_f = K\left(\frac{P}{P_0}\right)^m \tag{2}$$

This simplifies the analysis of the compaction data, and allows easier prediction of compaction behavior as explained later. Regression analysis was conducted to fit power model curves to the experimental compaction results. The power model parameters obtained are listed in
Table 4, with σ being the standard deviation of the fitted parameter. The power models curves appear to fit the compaction responses of the reinforcements quite well, although it can be seen that the Power Law fit is slightly low at around 200 kPa and slightly high at 700 kPa.
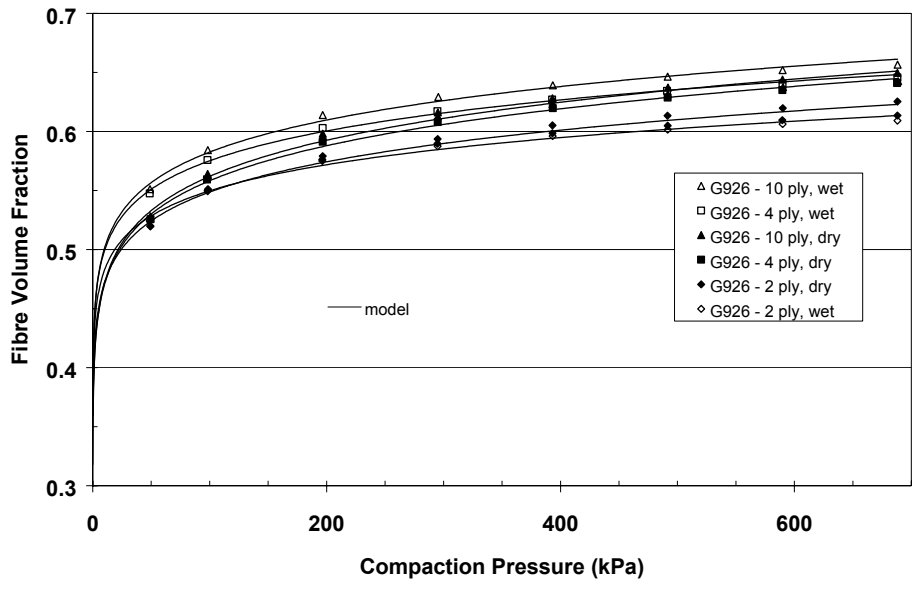
Figure 2: G926, experimental data and Power Law fit
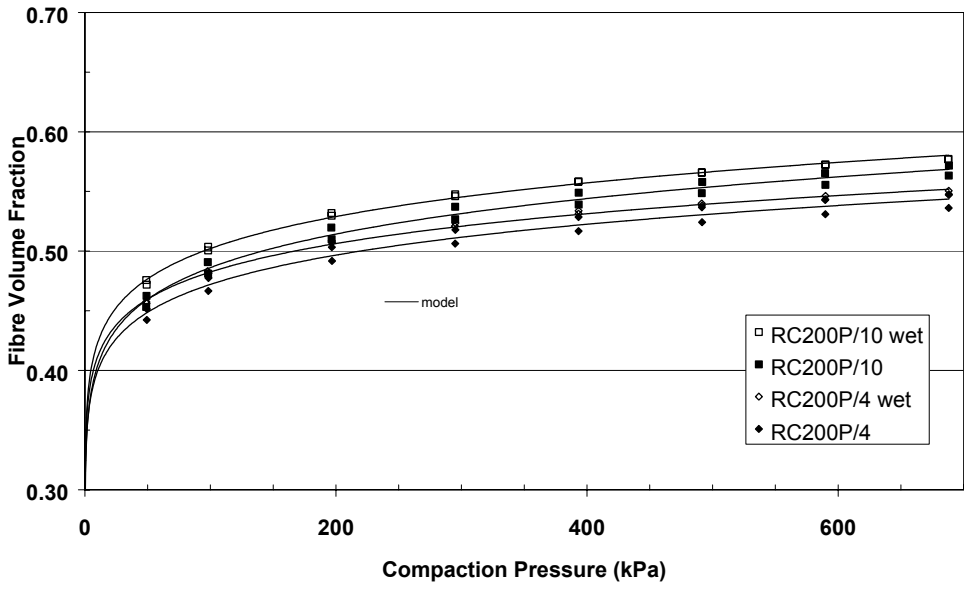
Figure 3: RC200P, experimental data and Power Law fit
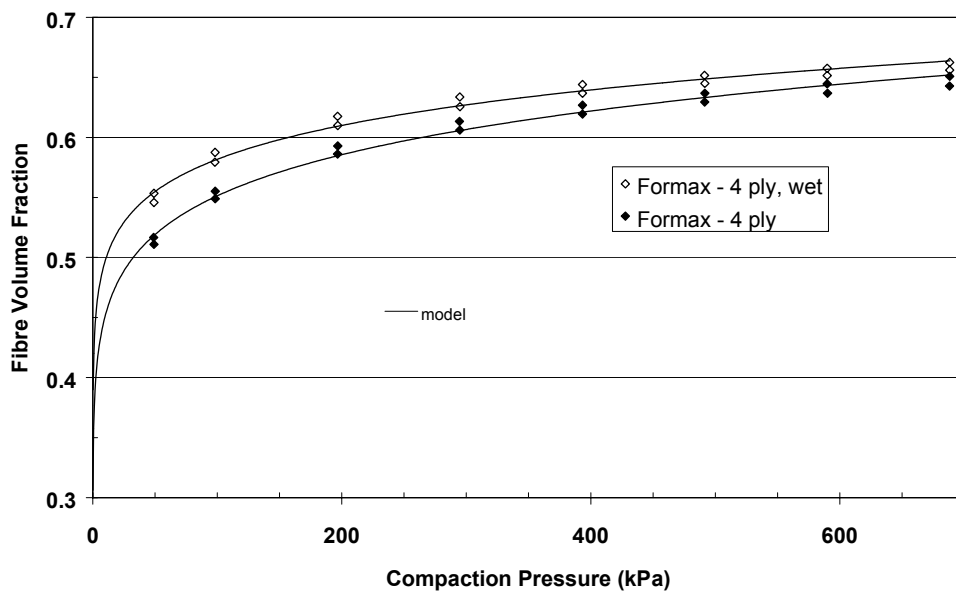
Figure 4: FCIM156, experimental data and Power Law fit
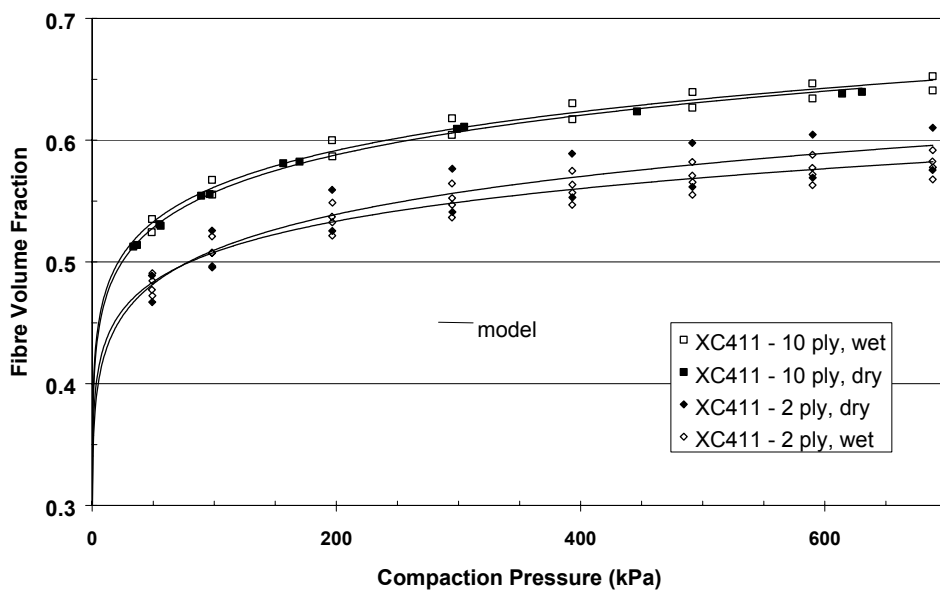
Figure 5: XC411, experimental data and Power Law fit
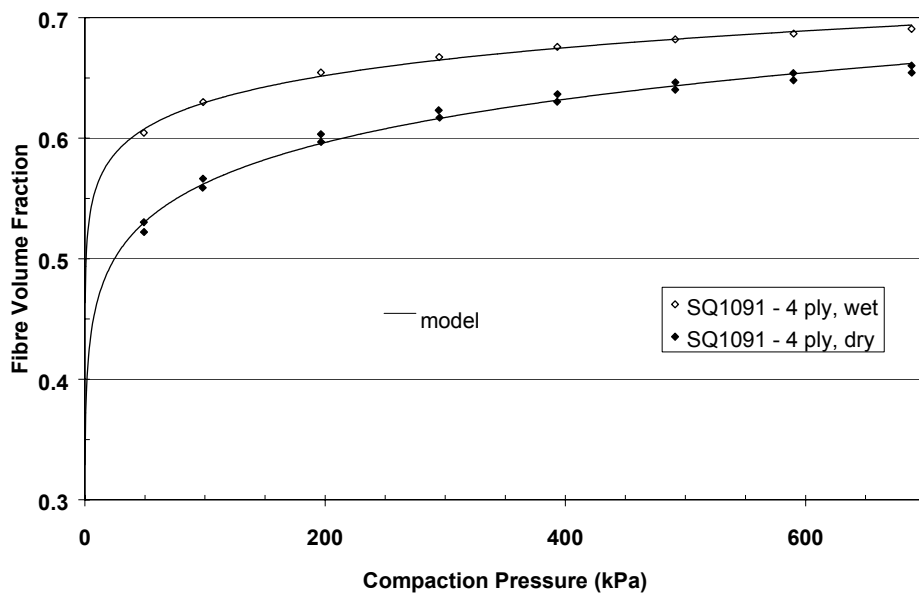
Figure 6: SQ1091R + SQ1090L, experimental data and Power Law fit
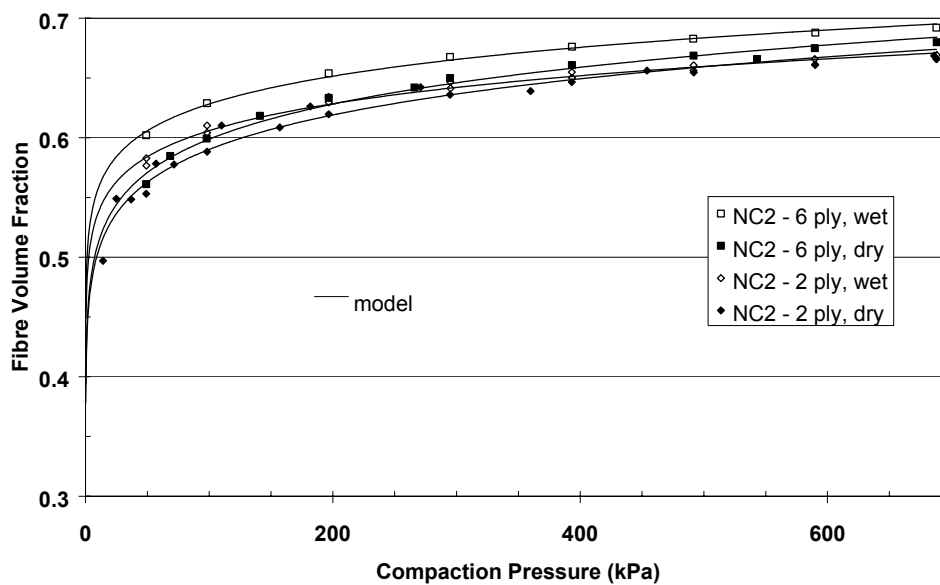
Figure 7: NC2, experimental data and Power Law fit

433
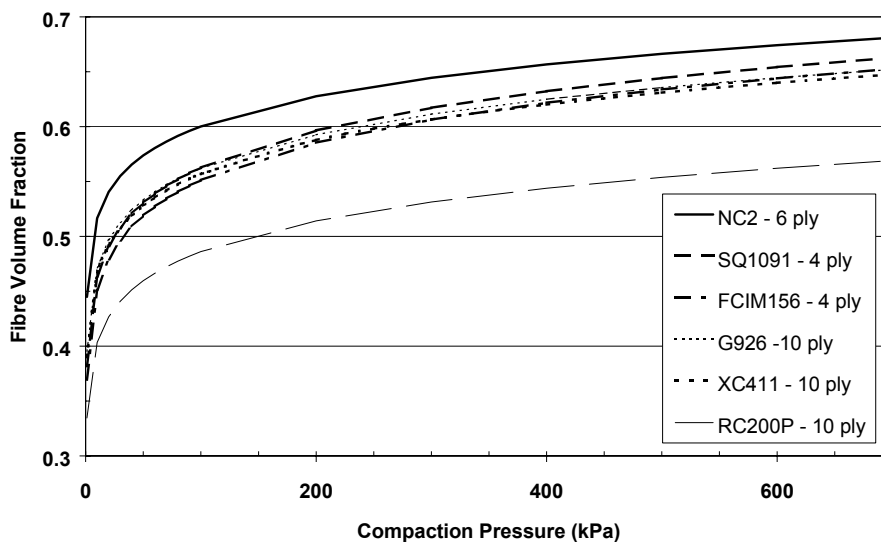
Figure 8: Comparison of all reinforcements (thickest stacks)

Table 4: Power Law parameters, P_0 = 100 kPa

Reinforcement	Number of layers	K	σ for K	m	σ for m
G926 (no binder) dry	10	0.5621	0.0034	0.0764	0.0023
	4	0.5583	N/A	0.0747	N/A
	2	0.5488	0.0095	0.0658	0.0054
G926 (no binder) wet	10	0.5825	N/A	0.0656	N/A
	4	0.5752	N/A	0.0619	N/A
	2	0.5497	N/A	0.0568	N/A
RC200P dry	10	0.4861	0.0063	0.0811	0.0011
	4	0.4721	0.0048	0.0732	0.0003
RC200P wet	10	0.5022	0.0059	0.075	0.0027
	4	0.4824	0.0001	0.0696	0.0006
FCIM156 dry	4	0.5512	0.0026	0.0869	0.0002
FCIM156 wet	4	0.5818	0.0065	0.0683	0.0013
XC411 dry	10	0.5570	0.0019	0.0775	0.0009
	2	0.5096	0.0089	0.0809	0.0029
XC411 wet	10	0.5615	0.0068	0.0754	0.0004
	2	0.5092	0.0088	0.0707	0.0035
SQ1091R + SQ1090L dry	4	0.5626	0.0068	0.0843	0.0018
SQ1091R + SQ1090L wet	4	0.6297	N/A	0.0504	N/A
NC2 dry	6	0.6002	0.0222	0.0650	0.0095
	2	0.5899	0.0169	0.0666	0.0048
NC2 wet	6	0.6283	N/A	0.0525	N/A
	2	0.6059	0.0059	0.0528	0.0013

Table 5: Relaxation factors

Reinforcement	Number of layers	Relaxation factor	
		Dry	Wet
G926 (no binder)	10	0.0280	0.0400
	4	0.0260	0.0340
	2	0.0210	0.0380
RC200P	4	0.0265	0.0345
	10	0.0285	0.0385
FCIM156	4	0.0200	0.0370
XC411	2	0.0180	0.0255
	10	N/A	0.0360
SQ1091R + SQ1090L	4	0.0175	0.0250
NC2	2	0.0290	0.0380
	6	0.0310	0.0330

For all fabrics tested, K was higher with an increased number of layers in the stack: this is expected because of the greater opportunities for nesting with more layers. Other testing by Kruckenberg [5] has indicated that, for fiberglass plain-weave fabrics using this test technique, the V_f is also higher as the number of layers in the stack is increased. The stiffening index m was more often slightly higher with an increased number of layers: compaction at the later stage became easier. If the reinforcement was lubricated, K was higher with a thicker stack, but the stiffening index m decreased: further compaction became harder.

The curves for the thickest stacks for each reinforcement are shown in Figure 8. The NC2 fabric was the easiest to compact: the RC200P was the most difficult. The remaining non-crimp fabrics and the G926 had similar compaction behavior.

Relaxation of Reinforcements

The amount of relaxation during the five-minute hold was also of interest. A "relaxation factor" was measured at 100 kPa. This was defined as below, where t_i is the initial thickness, and t_f is the final thickness after 5 minutes at 100 kPa. As shown in
Table 5, the relaxation factor was found to increase with more layers in the stack, and with lubrication. The SQ1091 showed the least relaxation, and the G926 the most. Non-crimp fabrics would be expected to have less relaxation than woven fabrics because there is less bending of fibers, and less possibilities for the fiber network to reorganize.

$$\frac{t_i - t_f}{t_i} \qquad (3)$$

Prediction of Compaction Curves

The reader will have noticed the similarity in the shape of the compaction curves presented. This suggests that a good working prediction of the compaction curve could be made by measuring only the thickness under a compaction pressure of 100 kPa (this could be a simple compaction test under a vacuum bag), and predicting the shape of the compaction curve using typical values of *m*. To investigate the usefulness of this proposal, Figure 9 below shows all the dry compaction curves measured in this work, plotted with a normalised *K* of 0.6.
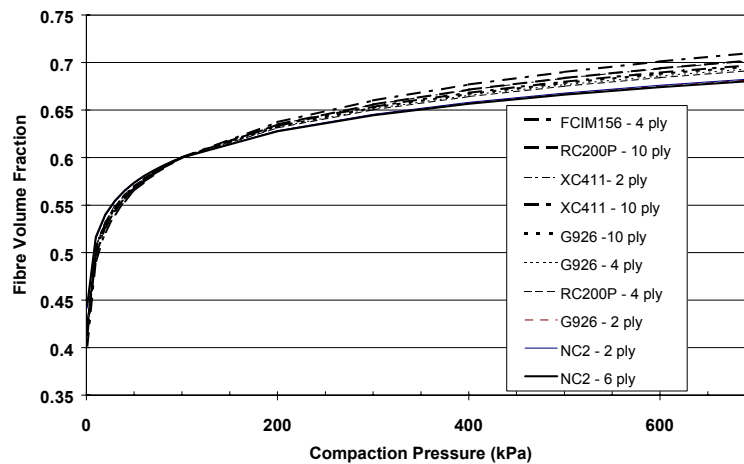
Figure 9: Compaction curves plotted with $K = 0.6$ in all cases.
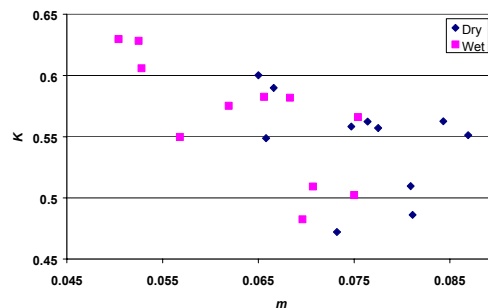
Figure 10: Values of *m* for dry and wet fabrics

It can be seen that the spread is low, (<3% at 700 kPa), especially if thicker stacks are considered (and NC2, which has a low *m*, is left out). Typical values of *m* can be chosen for groups of fabrics: Figure 10 shows that the spread of *m* is different for dry and wet fabrics.

Conclusion

The compaction test procedure described here appears to work well, if carefully applied, with frequent calibration of the machine compliance.

Thicker stacks are easier to compact, as are lubricated stacks. The similarity of compaction curves shown here suggests that a useful prediction of the compaction curve could be made on the basis of a single compaction test under a vacuum bag.

Acknowledgements

References

1. Liu, X. L., and Triantafillou J., "Compaction of non-crimp fiberglass reinforcements", CRC-ACS internal technical memorandum TM 01007, Melbourne, 2001.

2. Robitaille, F and Gauvin, R, "Compaction of textile reinforcements for composites manufacturing I: review of experimental results", *Polymer Composites*, 1998, **19**, 198-216.

3. Saunders, R.A., Lekakou, C. and Bader, M.G., "Compression in the processing of polymer composites 1. A mechanical and microstructural study for different glass fabrics and resins", *Composites Science and Technology*, 1999, **59**, 983-993.

4. Kim, Y.R., McCarthy, S.P. and Fanucci, J.P., "Compressibility and relaxation of fiber reinforcements during composite processing", *Polymer Composites*, 1991, **12**, 13-19.

5. Kruckenberg, T., "The use of vibration for resin infiltration and compaction of composites", *PhD Thesis*, University of Sydney, to be published 2004.

Unsaturated Flow in Compressible Fiber Preforms

J. Wolfrath [1], V. Michaud [1], A. Modaressi [2], and J.-A. E. Månson[1]

[1] *Ecole polytechnique fédérale de Lausanne, Laboratoire de Technologie des Composites et Polymères, CH-1015 Lausanne, Switzerland*
[2] *Ecole Centrale Paris, Laboratoire de Mécanique des Sols, Structures et Matériaux, 92 295 Châtenay-Malabry Cedex, France*
Corresponding Author's e-mail: jan-anders.manson@epfl.ch

SUMMARY:

In many cases of composite processing by liquid matrix infiltration, the reinforcement is compressed when it comes in contact with the liquid and relaxes as the matrix flows within its pores. In parallel, as the reinforcement is generally made of fiber tows, these become gradually saturated. Modeling of the process hence requires solving the coupled equations of multi-phase flow in a compressible medium. For isothermal infiltration, the physics of the process are similar to imbibition/drainage phenomena encountered in soil mechanics. Using this similarity, a finite-element code originally developed for soil mechanics is adapted to simulate the multiphase flow of polymer in a compressible porous preform. The dual scale of the porous medium is accounted for by introducing an additional sink term. The chosen case study is polypropylene transversally infiltrating glass fiber mats as used in the production of Glass Mat Thermoplastic blanks. The progression of the flow front, the fiber volume fraction and local preform stress profiles, as well as the saturation and local matrix pressure profiles are obtained. The influence of processing and materials parameters is discussed in light of the experimentally observed phenomena, pointing out the advantages and limitations of the approach.

KEYWORDS: non-saturated flow, compressible preform, dual-scale, finite element.

INTRODUCTION

In many cases of composite processing by liquid matrix infiltration under externally applied pressure, the reinforcement is progressively compressed when it comes in contact with the liquid under increasing pressure and relaxes as the matrix flows within its pores. In parallel, as the reinforcement is generally made of fiber tows, hence presenting a two-level structure, the fiber tows become gradually saturated.

This coupled process is schematically represented in Figure 1:
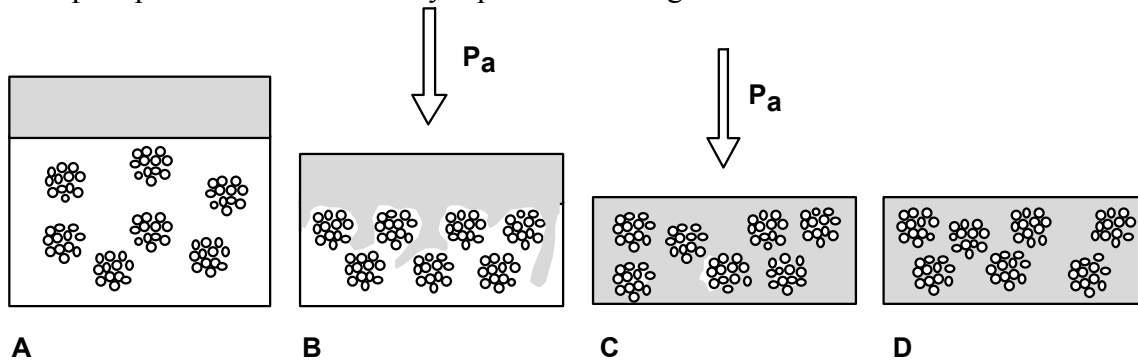
Figure 2: Infiltration of a compressible dual-scale preform by a fluid taking into account mutli-phase flow. A: intial state of a dry preform and separated fluid. B: pressure is applied, infiltration and compression of the preform start. C: macro-impregnation completed, micro-impregnation on the way. D: preform completely impregnated.

Modeling of the process hence requires solving the coupled equations of multi-phase flow and mechanical equilibrium. For isothermal infiltration, the physics of the process are similar to imbition/drainage phenomena encountered in soil mechanics. Using this similarity, a finite-element code originally developed for soil mechanics is adapted to simulate the multiphase flow of polymer in a compressible porous preform. The case study presented here is polypropylene transversally infiltrating glass fiber mats as used in the production of Glass Mat Thermoplastic blanks. The dual scale of the porous medium is accounted for by introducing an additional sink term based on the solution of radial flow into an elliptical glass fiber tow, as experimentally observed [1].

THEORY

General equations & numerical solution

The governing equations are written in one dimension over a representative volume element ΔV, following reference [2]. These equations consist in Darcy's law, mass conservation in the liquid and solid phase and stress equilibrium, all equations accounting for the saturation S. This set of non linear differential equation is solved with the finite element code GEFDYN. The formulation applies a Galerkin procedure for space discretization and a modified Newton method for the iterative solution [3].

Macro-Saturation

The saturation S is defined as the local ratio of resin volume fraction V_m over $(1-V_f)$, where V_f is the fiber volume fraction. It is generally expressed in soil mechanics as a function of pressure. The relationship is given by the drainage or imbition curve for the considered system. The obtained curves can be fitted to phenomenological equations introducing a threshold pressure (p_0), which must be overcome to initiate infiltration, and a shape parameter (α).

As long as the pressure remains below p_0, saturation is equal to zero. For $p \geq p_0$, S increases, and a potential law to describe this is the Van Genuchten law [4]:

$$S = 1 - \frac{1}{\sqrt{1 + \alpha^2 (p - p_0)^2}} \text{ valid for } p > p_0. \tag{1}$$

The curve shape is described by α and varies with the pore size distribution, with the size and type of reinforcement and with the wetting behavior of the matrix on the reinforcement. This value is empirically estimated for a given system or obtained by fitting experimental drainage/imbibition curves [5]. The threshold pressure p_0 corresponds to the capillary pressure differential to infiltrate the largest of the accessible pores. It may be negative for a wetting system. In composite processing, however, contrary to soil science, the saturation, in addition to being a function of the pressure, is also a function of time owing to the dual-scale of the reinforcement, and the high viscosity of the infiltrant. Indeed, infiltration is often reported to take place in two steps [6], representing the macro-impregnation, in the large pores between the fiber bundles, and the micro-impregnation, within the fiber bundles. Depending on wetting properties and kinetics of the infiltration, the saturation of the macro-pores can be accomplished prior to the impregnation of individual fiber bundles.

Micro-Saturation

To account for this, a sink-term is added in the code, assuming that infiltration first takes place gradually in a macroscopic scale as represented by the Van Genuchten law. Then, as soon as the bundles are surrounded by matrix, the micro-impregnation consists in the radial infiltration of matrix in the bundles. The pressure differential driving the micro-impregnation is the difference between the local pressure in the preform around the bundle and the pressure in the entrapped gas within the bundle plus the capillary pressure. The cross section of a fiber bundle and its dimensions are represented in Figure 2:
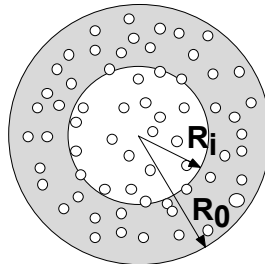
Figure 3: Schematic of a representative GMT bundle cross section. R_i is the internal and non-impregnated radius and R_0 is the intial radius of the bundle.

One fiber bundle contains an average of 100 fibers (N=100). The fiber radius r_f is about 5 μm. The fiber volume fraction in the compressed bundle is assumed to remain constant and equals 0.7 ($V_{f,b}$).

The micro-impregnation in the fiber bundle is carried out in the direction orthogonal to the fibers of an initially dry cylindrical fiber bundle, of initial radius r_0, under constant applied pressure P_a. The equations are written in cylindrical coordinates. We assume saturated flow and Newtonian behavior of the matrix.

Integration of Darcy's law and mass conservation equations over radial distance yields to [1]:

$$r_i \ln\left(\frac{r_i}{r_0}\right)\dot{r_i} = \frac{-K_p}{\eta(1-V_{f,b})}(P_g(r_i) - P_c - P_a) \qquad (2)$$

where r_i is the unimpregnated bundle radius, r_0 the initial bundle radius, $\dot{r_i}$ the derivative of r_i over time, K_p the fiber bundle permeability, η the matrix viscosity, $V_{f,b}$ the fiber volume fraction in the bundle, P_g the gas pressure, P_a the applied pressure and P_c the capillary pressure, which is the pressure difference existing across the air-liquid interface.

Furthermore, the fiber bundle transverse permeability tensor K_p is determined by Gebart's formulation [7] based on fiber arrangement parameters. If we consider air entrapment during impregnation in the bundle and no dissolution in the polymer matrix, this will lead to a void pressure increase within the reinforcement, which can be evaluated using the ideal gas law. The analytical calculation of the evolution of the micro-saturation with time, assuming gas entrappment for constant pressures of 2, 3 and 5 bars is given in Figure 3 A.

A)   **B)**
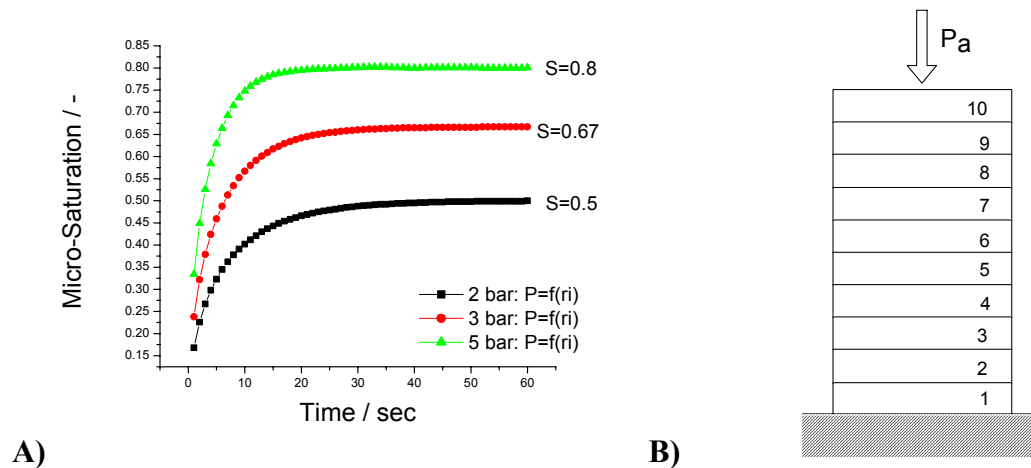
Figure 4: A) Analytical micro-Saturation curve of a glass fiber bundle impregnated by polypropylene at a pressure of 2, 3 and 5 bars. Accounting for gas pressure function of $r_1{}^2$. B) Grid of 10 elements used for numerical model.

The void pressure increase leads to a decrease of the final saturation value: for an applied pressure of 2 bars and after 50 seconds of impregnation, the micro-saturation reaches 0.5 instead of 1 for the case of constant void pressure. These non-negligible micro-impregnation times, between 15 and 60 seconds, confirm the need to introduce this effect in the complete model.

RESULTS

Isothermal unidirectional transverse infiltration of polypropylene at 200°C into glass mats is modeled using the modified Gefdyn program. The compressive behavior of the fiber preform, as well as the variation of permeability with volume fraction fibers are experimentally determined [8], and bi-linear fit curves are introduced into the code.

The Van genuchten parameters values are $\alpha = 2 \cdot 10^{-8}$ and $p_0 = 1$ bar. In this case study, a pressure of 2 bars is applied with a ramp of 1bar per second to an initially dry preform of 4mm thickness. The dry preform is represented by a grid of 10 elements and 63 nodes. The first element is placed at the bottom and the 10th element at the top of the preform, where the polymers enters under applied pressure (Figure 3B). In the following figure, the positions in the preform are referred to as 1, 5, 8, and 10, each value corresponding the referred element. Once the pressure applied, the evolution of the macro-saturation and micro-saturation are calculated and given in Figure 4A and B respectively. It is observed that the time necessary for the fluid to reach the bottom side of the mold is about 6.5 seconds since the macro-saturation of the element 1 is observed to increase suddenly after 6.5 seconds. Then, once the flow front has reached one given element, the impregnation of the bundle at this level can start (Figure 4A). It is to notice that the time to impregnate a bundle is about 30 seconds and is then much longer than the time to macroscopically fill the preform. This information is of interest because it shows that an apparently well-impregnated part may contain residual air entrapped in the fiber bundles. Furthermore, the micro-saturation reaches a plateau at $S_{micro}=0.5$, so a full impregnation of the bundle is not accomplished for an applied pressure of 2 bars,. This result is in accordance with the value obtained analytically (Figure 3A). It can then be concluded that for this material system, a higher pressure is necessary to complete bundles impregnation: 5 bars, for instance would provide a $S_{micro}=0.8$. Evolution of the preform height, local resin pressure and effective stress on the preform are also obtained, indicating a global preform compression followed by relaxation of the preform, as expected.
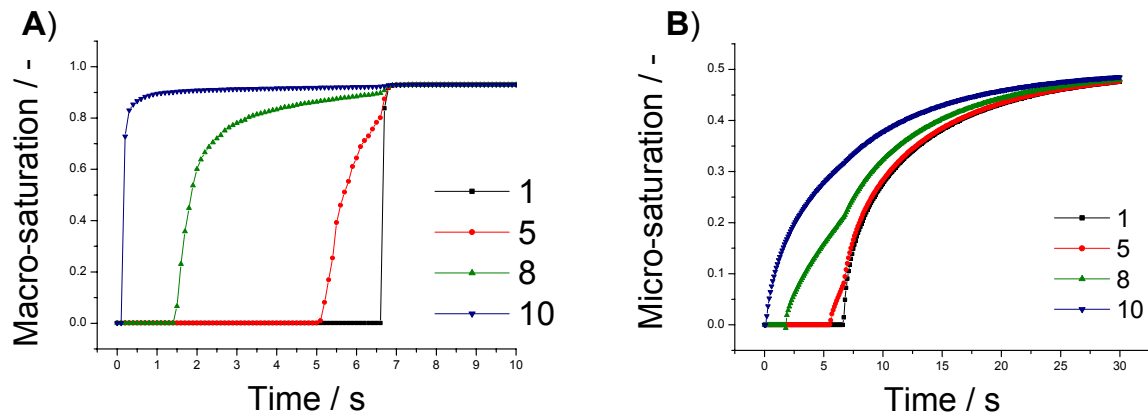
Figure 5: Evolution of the macro-saturation (A) and the micro-saturation (B) at different position in the mold: from element 1 (bottom) to element 10 (top).

CONCLUSIONS

This paper presented a Finite Element tool to model the unsaturated flow of polymer in a compressible dual-scale preform. Micro-impregnation is taken into account by the introduction of a sink term, based on the practical observation of delayed micro-impregnation in GMT materials. The progression of the flow front, the local pressure and stress values as well as the macro-saturation and micro-saturation profiles are predicted. The main issue remaining is the accurate description of the material and process parameters used in the model, such as the parameters of the Van Genuchten law, the amount of gas entrapped, the variation of permeability with saturation. Careful validation with model experiments are thus a remaining step.

REFERENCES

1.	BERNET, N., et al., *An impregnation model for the consolidation of thermoplastic composites made from commingled yarns.* Journal of composite materials, 1999. **33**: p. 751.
2.	MICHAUD, V., R. TORNQVIST, and J.-A. MANSON, *Impregnation of compressible fiber mats with a thermoplastic resin. Part I: Theory.* Journal of composite materials, 2000: p. 1150-1173.
3.	AUBRY, D. and A. MODARESSI, *Manuel scientifique GEFDYN.* Ecole Centrale Paris, 1996: p. Châtenay-malabry.
4.	VANGENUCHTEN, M.T., *A closed form for predicting the hydraulic conductivity of unsaturated soils.* Soil Sci. Am. Soc., 1980: p. 892-898.
5.	DOPLER, T., A. MODARESSI, and V. MICHAUD, *Simulation of metal-matrix composite isothermal infiltration processing.* Metallurgical and materials transactions B, 2000. **31B**: p. 225-234.
6.	PARNAS, R.S. and F.R.P. Jr., *The effect of heterogeneous porous media on mold filling in Resin Transfer Molding.* SAMPE QUARTERLY, 1991: p. 53-60.
7.	GEBART, B.R., *Permeability of unidirectional reinforcement for RTM.* Journal of composite materials, 1992. **26**(8): p. 1100-1133.
8.	MICHAUD, V., R. TORNQVIST, and J.-A. MANSON, *Impregnation of compressible fiber mats with a thermoplastic resin. Part II: Experiments.* Journal of composite materials, 2000: p. 1174-1200.

Modeling the Viscoelastic Behavior of Fiber Reinforcing Fabrics

Piaras A. Kelly[1] and Rehan Umer[2]

[1] *Department of Engineering Science, School of Engineering,*
University of Auckland, Auckland, New Zealand,
and Corresponding Author's e-mail: pa.kelly@auckland.ac.nz
[2] *Center for Advanced Composite Materials, Department of Mechanical Engineering, School of*
Engineering, University of Auckland, Auckland, New Zealand: rume001@ec.auckland.ac.nz

SUMMARY: The deformation of fibrous materials plays an important role in the Liquid Composite Molding (LCM) processes. These materials display markedly non-linear viscoelastic characteristics. A model of fibrous material deformation is developed, incorporating this non-linear viscoelastic response, with a view to being used in simulations of LCM processes. The model is one-dimensional and is appropriate for the simple fiber compaction deformation which occurs during LCM processes. A limited number of compaction experiments were carried out to determine the model parameters for a continuous filament mat. These included a rapid compaction (100mm/min), a number of slower compactions to the same final volume fraction, and then a number of tests at a constant compaction speed to different final volume fractions. The model gives reasonably good results over a range of compaction speeds and volume fractions.

KEYWORDS: Viscoelastic, Fibers, Reinforcements, Relaxation, Modeling, Compaction, Process Modeling.

INTRODUCTION

The Liquid Composite Molding (LCM) processes, such as Resin Transfer Molding (RTM), Injection/Compression Molding (I/CM) and Vacuum Assisted Resin Transfer Molding (VARTM) are popular processes for the manufacture of fiber-reinforced composite materials. All these LCM processes involve placement of a reinforcing fibrous material within some form of closed mold. The fibrous material is then compacted, before being impregnated with a polymer resin. The response of the fibrous material to compaction, and its subsequent response right throughout the manufacturing process, is of some importance in these processes, as it directly influences the required tooling forces, process times and other important manufacturing parameters. This paper is concerned with modeling the deformation of fibrous materials as occurs during these LCM processes.

Models of reinforcement deformation generally account for non-linear elastic deformations (e.g. [1]). The viscoelastic response of these materials has been noted many times (e.g. [2]), but the modeling of this response has been reported less often.

Earlier work has pointed to the importance of accounting for the viscoelastic response [3], particularly for processes in which the mold cavity thickness might change (e.g. in I/CM or VARTM).

The objective of this paper is to produce a simple working model of the deformation of fibrous materials, which incorporates their non-linear elastic and viscoelastic characteristics, and which can be used in simulations of the LCM processes.

MODEL AND EXPERIMENTS

A Model of the Compaction Tests

During preform compaction, not only are the deformations large, but the viscous effects are markedly non-linear, indicating fairly large energy changes in the material. In what follows, a model is developed which allows for this complex constitutive behavior, for the simple deformation which occurs during preform compaction. The model introduced is purely mechanical, not accounting for temperature variations; it is essentially a one-dimensional version of a finite–strain, linear viscoelastic, thermomechanical model (see, for example, [4]), only with a non-linear viscous response. First, introduce the free energy function

$$\Psi(e,\xi_i) = \Psi_\infty(e) + \sum_{i=1}^{N} \Gamma_i(e,\xi_i) \tag{1}$$

Here, e is the external (observable) strain variable, and ξ_i are $i = 1,\ldots,N$ internal kinematic variables, describing the viscous effects in the material. $\Psi_\infty(e)$ is the free energy at equilibrium, that is, the energy stored after all viscous effects have terminated, whereas the second term is the so-called configurational free-energy, which characterizes the non-equilibrium state. The free energy is chosen to be of the form

$$\Psi(e,\xi_i) = \Psi_\infty(e) + \sum_{i=1}^{N} \frac{E_i}{n_i + 1}(e - \xi_i)^{n_i + 1} \tag{3}$$

This reduces to the linear, so-called generalized Maxwell, model (a free spring in parallel with N Maxwell units) when $n_i = 1$. By taking $n_i \geq 1$ one obtains a model incorporating non-linear viscous effects. Following standard thermodynamics arguments, the stress is now obtained through a differentiation:

$$\sigma = \frac{\partial \Psi(e,\xi_i)}{\partial e} = \frac{\partial \Psi_\infty(e)}{\partial e} + \sum_{i=1}^{N} E_i(e - \xi_i)^{n_i} \equiv \sigma_\infty + \sum_{i=1}^{N} q_i \tag{4}$$

The total stress is thus the equilibrium stress σ_∞ together with N viscous stresses; note that q_i can be interpreted as the viscous forces/stresses, and ξ_i the strain, acting in a dashpot attached to a non-linear spring.

The thermodynamic force is

$$f_{\xi_i} = -\frac{\partial \Gamma_i(e,\xi_i)}{\partial \xi_i} = E_i(e-\xi_i)^{n_i} \tag{5}$$

which can be seen to be equal to the q_i, so the mechanical dissipation (the rate of working of the internal stresses which lead to an energy loss) is, by definition,

$$\Phi(e,\xi,\dot\xi) = -\frac{\partial \Psi(e,\xi)}{\partial \xi}\dot\xi = \sum_{i=1}^{N} f_{\xi_i}\dot\xi_i = \sum_{i=1}^{n} q_i\dot\xi_i \tag{6}$$

Take now a viscosity law of the form

$$q_i = \eta_i(e_{max} - e)^{-m}\dot\xi_i \tag{7}$$

Here, η is the viscosity, m is a material parameter, and e_{max} is the maximum theoretical strain possible in the material. It can be seen that this implies that the greater the strain (volume fraction), the more rapid the rise in stress for a given strain-rate. The idea here is that the more tightly packed are the fibers, the less room there is for fiber slippage, and hence viscous effects [2]. In the limit, of course, no slippage should be possible. Eqns. 6 and 7 imply that $\Phi = \sum \eta_i(e_{max} - e)^{-m}\dot\xi_i^2$, which is positive, as required by the second law, provided $m \geq 0$.

It remains to write down the evolution (first order differential) equations for the viscous forces, which follow from $q_i = \eta_i(e_{max} - e)^m\dot\xi_i = E_i(e-\xi_i)^{n_i}$:

$$\dot q_i = -\frac{n_i E_i^{1/n_i}}{\eta_i}\left[(e_{max} - e)^m q_i^{2-1/n_i} - \eta_i \dot e q_i^{1-1/n_i}\right] \tag{8}$$

In Eqn. 8, the strain measure e employed is the true (logarithmic) strain and $\dot e$ is the rate of deformation. In terms of volume fractions, these are ($\dot V_f$ is the rate of change of V_f)

$$e = \ln\frac{V_f}{V_{f0}}, \qquad \dot e = \frac{\dot V_f}{V_f} \tag{9}$$

Experimental Procedure

A study has been undertaken into the deformation characteristics of a glass-fiber continuous filament mat (CFM, 450 g/m^2). Each preform sample consisted of 8 layers, cut into 0.2 m squares. The samples were placed between a set of rigid, parallel plates set up in an Instron 1186 testing machine, the upper plate fixed with the cross-head moving up.

Initially, each sample was compacted with a constant force of 200 N (stress $\sigma = 5\,\text{kPa}$) and allowed to compact until an equilibrium position was reached and no further deformation occurred. This low level of stress and associated viscoelastic response were deemed not to affect the viscoelastic response of the material at the much higher loads encountered during full compaction, but allowed one to define an initial volume fraction V_{f0} (≈ 0.1), which is needed to define the practical measure of strain (Eqn. 9).

Once the initialization was complete, a constant velocity compressive strain history was applied, and the compaction force applied to the sample was recorded. This constant velocity compaction was then followed by a period in which the sample was held at constant thickness.

Samples were compacted to a volume fraction $V_f = 0.35$ at speeds of 0.035, 0.5, 2, 10 and 100 mm per minute. This final, rapid, test was conducted to determine the instantaneous response of the material, for which it was assumed that viscous effects were negligible. After compaction, the samples were held at $V_f = 0.35$ until the stress relaxation curves leveled out into a constant equilibrium stress, which occurs when all viscous effects have terminated. A further series of tests were carried out at 2 mm/min to final volume fractions of $V_f = 0.25$ and 0.45. A number of the tests were repeated to ensure the reliability of the experimental procedure.

RESULTS AND DISCUSSION

Figures 1 and 2 show the results for a model with $N = 2$ and the data in Table 1.

E_1	n_1	E_2	n_2	η_1	η_2	m
20	8	260	1	1e5	1e3	1

Table 1 Model parameters (see Eqns. 3 and 7)

The model gives reasonable results over a range of compaction speeds and volume fractions.

The model does not match the data perfectly. One important reason for this is that there are permanent deformations occurring in the material, which are not accounted for in the model. For example, on a micromechanical level, fibers may well nest between other fibers during loading, and might not tend to return to their original positions within the perform after removal of the load, no matter how much time has elapsed.
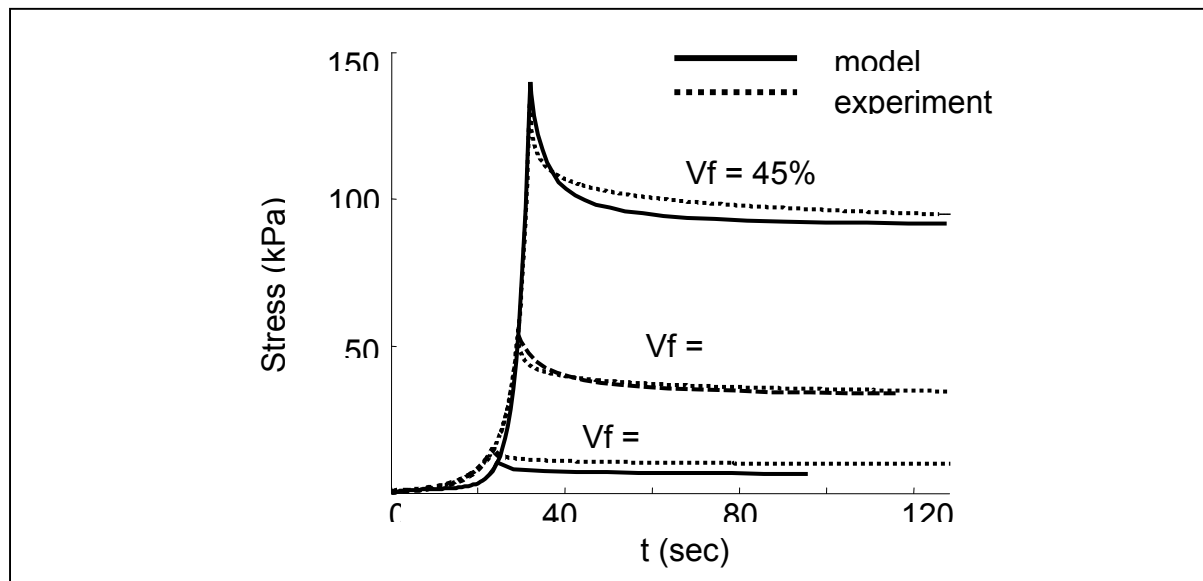
Fig. 1 Results for compaction at 2 mm/min to $V_f = 0.25$, 0.35 and 0.45
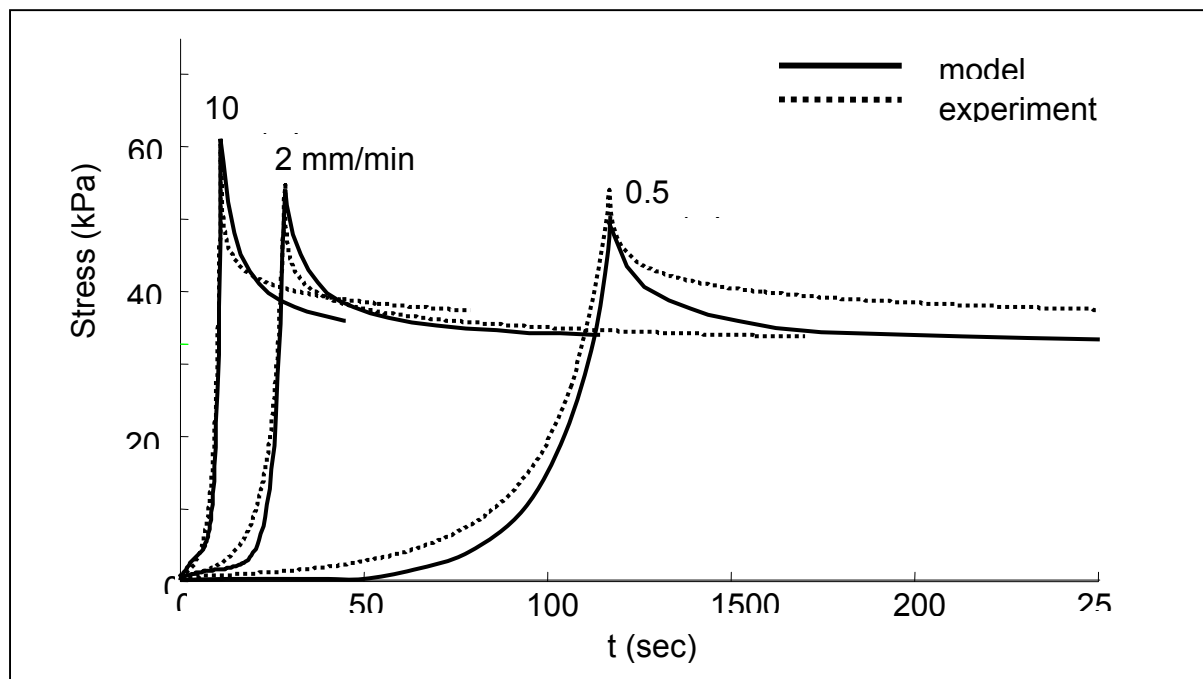
Fig. 2 Results for compaction to $V_f = 0.35$ at different speeds

CONCLUSIONS

A simple one-dimensional model of fiber compaction has been developed for use in simulations of Liquid Composite Molding processes. The model requires a number of parameters, and these were obtained for a CFM mat by carrying out a limited number of tests (including a rapid compaction test, a number of compactions at different, slower, compaction speeds, and a number of compaction tests to different volume fractions). The model gives reasonable results over a range of compaction speeds and volume fractions.

REFERENCES

1.   M. Li and C.L. Tucker III, "Modeling and simulation of two-dimensional consolidation for thermoset matrix composites", *Composites: Part A*, Volume 33, Pages 877-892 (2002).

2.   N. Pearce and J. Summerscales, "The compressibility of reinforcement fabric", *Composites Manufacturing*, Volume 6, Pages 15-21 (1995).

3.   S. Bickerton, M.J. Buntain and A.A. Somashekar, "The viscoelastic compression behavior of liquid composite molding preforms", *Composites Part A*, Volume 34, Pages 431-444 (2003).

4.   M. Kaliske, "A formulation of elasticity and viscoelasticity for fiber reinforced material at small and finite strains", *Comput. Methods Appl. Mech Engrg.*, Volume 185, Pages 225-243 (2000).

5.   Z. Cai, "A Nonlinear Viscoelastic Model for describing the deformation behavior of braided fiber seals", *Textile Res. J.*, Volume 65, Pages 461-470 (1995).

PREFORM MODELING AND EFFECTS: IV. PERMEABILITY MEASUREMENTS

New Set-Up for Permeability Measurement

Qiang Liu and Richard Parnas

Institute of Materials Science, Univ. of Connecticut, Storrs, CT, 06269 USA:
rparnas@ims.uconn.edu

SUMMARY: The determination of accurate permeability values is critical to process simulations for liquid composite molding. And due to the statistical nature of the permeability[1], set-ups are needed to measure them accurately and quickly. Based on the different available set-ups, especially the one developed by Hoes[1], two new developments will be presented in this paper, one for in-plane permeability and the other for through-thickness permeability measurement. Specifically, a new sensor design is developed for the in-plane set-up to permit the use of electrically conductive reinforcement (carbon fabric), and to check the correctness of the in-plane assumption; and a new design for a through-thickness set-up is offered to permit high-speed data acquisition and reduce the race-tracking error.

KEYWORDS: Permeability; Process simulation; Liquid Composite Molding (LCM); Data Acquisition; Labview; Race-tracking; etc…

I. INTRODUCTION TO HIGH-THROUGHPUT PERMEABILITY MEASUREMENT

Composite materials are used in many kinds of applications. Among composite processing techniques[1, 2], RTM (Resin transfer molding) is one that has recently gained rapid acceptance[3]. RTM allows the molding of large complex shaped composite parts with a good surface finish and little pollution. This process consists of filling a closed mold cavity with reinforcements and injecting a resin through one, or several points. A unique feature of the RTM processing technique is that liquid resin has to flow a long distance to impregnate the dry fibers. The measure for the ease of the resin flow in the fiber preform is the permeability of the preform. Accurate permeability values are extremely important for the resin flow simulation and mold design due to the often encountered problems of non-uniform impregnation, void and dry spot formation[4], lengthy impregnation cycles, etc… With known permeability one can compute flow behavior in large complex molds, the pressure distributions in the mold, the required clamping pressure to hold the mold closed, and the required strength of the mold to retain its shape during the molding operation[5].

Permeability is a pore-structure parameter which depends only on the pore geometry of the porous media[6] but is complex and even changes during the preform manufacture. Rudd, et al. reviewed the deformation behavior of some mats and fabrics and made fiber architecture predictions, and then they applied models to estimate the in-plane permeabilities of those performs[7]. The usual way of getting permeability values is by experiments. Two kinds of experimental methods for permeability measurement are distinguished: unidirectional flow methods[8-14] and radial flow methods[8, 10, 11, 19-21]. In addition, unidirectional (1D) flow methods can also be distinguished by saturated and unsaturated flow methods.

In the saturated 1D method, experiments are conducted by forcing a test fluid through the whole mold in which the fabric is preplaced and compressed, and measuring the steady-state relationship between the flow and the pressure drop across the length of the mold[8]. Usually a linear relationship is obtained between the steady-state flows of a Newtonian fluid and its pressure drops. And in the unsaturated 1D test, the fluid flows through the dry fiber bed, replacing the air present in the material. Although the 1D test is the most straightforward set-up, there are a number of errors associated with it. The first is the "race tracking", or "edge effect" error, which means the preferential flow of the fluid along the mold walls when there is a small gap between the edges of the preform and the mold wall. According to Neale[15] and Parnas[16], the sensitivity of the 1D test to the edge effect is a function of the mold width. Many have made efforts to minimize the error due to the edge effect in their measurement. Diallo[14] et al. and Binetruy[17] et al. used silicone sealant; Parnas[18] et al. and Lekakou[19] et al. stuck a tape on the material edge. Another disadvantage of the 1D test is that at least three measurements have to be done to fully characterize the in-plane permeability tensor: one for the permeability values in two perpendicular axes and one to derive the angle with respect to the reference axis. In addition, mold deflection problems (especially associated with transparent plastic mold lids) and the problems due to incomplete saturation also exist[7].

The radial test (or 2D test) can only be used in unsaturated flow methods. The set-ups consist of a lower metallic mold-half with an injection hole in the middle, and a transparent top. Inside the mold, the fluid flows through the fabric from the central injection port. One uses constant injection flow rate or injection pressure. The transparent top-half allows one to record the flow front progression by means of a video camera for later derivation of fluid superficial velocity. The main advantage of the 2D test is that it allows the determination of both in-plane permeability components and the angle of them with respect to the reference axes all in one single experiment[1]. So it is much less time-consuming than 1D test. However, the data reduction procedure which converts the pictures of flow front positions to usable digital values is still time-consuming. In addition, the material and the flow front have to be visible throughout the experiment for people to use the camera. But there is always mold deflection problems[11] associated with the transparent plastic top of the mold. To counter the problem the transparent top plate is often covered with a steel frame to enhance bending stiffness[11], while this method reduces the visibility.

To counter the problems associated with the 2D tests, Hoes[22] et al built a new set-up, in which both the top-half and the bottom-half were made of stiff metals which solved the mold deflection problem quite well (see figure 1 below). The bottom-half includes 43 sensors located on straight lines at 0, 22.5, 45, 67.5, 90, 180, 270^0, and the injection hole can be seen in the middle. An epoxy seal provides electrical insulation between the sensor wire and the metal mold plate as well as preventing fluid leakage. This sensor design is limited to electrically nonconductive fabric and electrically conductive fluid. When fluid flows over the sensor, the circuit is closed, providing a signal to the computer indicating the time of arrival of fluid at each sensor location. The whole set-up sits in a Carver Press. The data acquisition and analysis are automated so the permeability is known within a few seconds after the experiment. The connection of the instruments with the computer and the use of the software in this set-up greatly saved time compared to the usual 2D tests.

Example permeability values for Syncoglass R420 woven fabric are shown in figure 1[1] below. From this figure, one can see that permeability is a statistically distributed parameter and can not be characterized by only a few experiments[1].
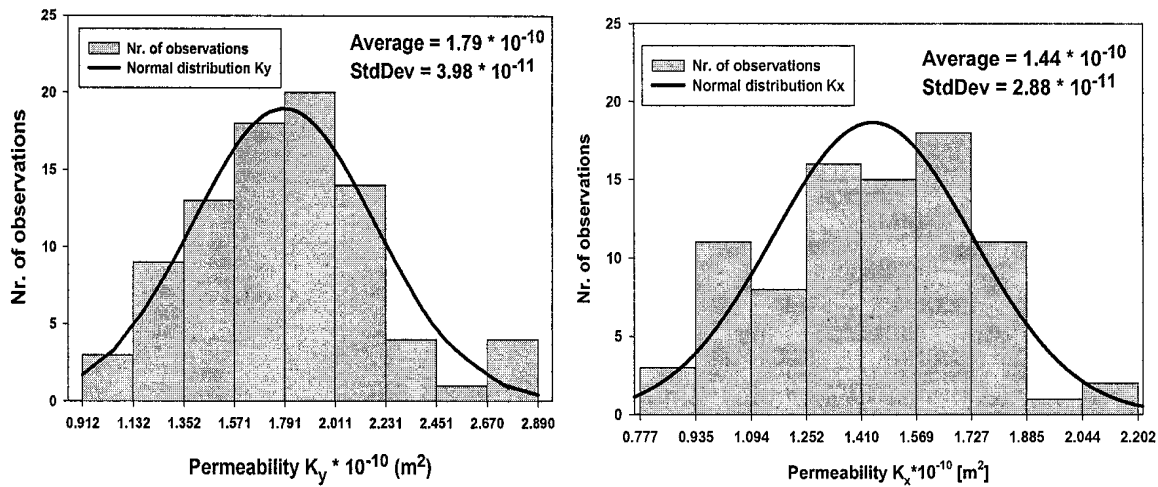
(a) In the warp[4] direction   (b) In the weft[5] direction
Figure 1. Syncoglass R420 permeability distribution at 41.7% fiber volume fraction

2. NEW SENSOR DESIGN FOR IN-PLANE PERMEABILITY MEASUREMENT FOR CARBON FABRIC

The sensor plate used earlier contained 43 sensors in one quadrant. While good enough to illustrate the statistical distribution of permeability data, a sensor plate with sensors in all four quadrants around the injection hole will provide several advantages. Figure 2 shows a new sensor plate with 105 sensors.
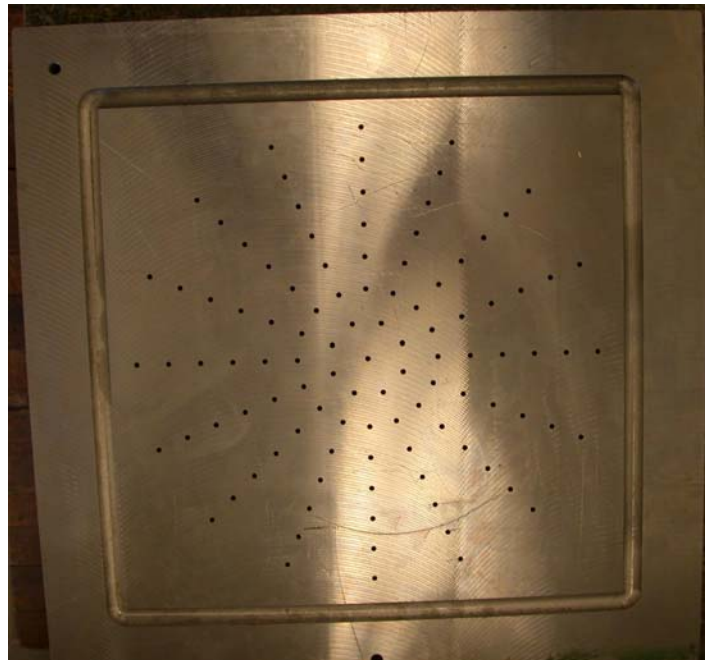
Fig 2. Top Sensor Plate

The new sensor plate also uses a modified sensor, in which the sensor is slightly recessed below the plate level, to prevent compressed electrically conductive fabric from touching and shorting out the sensors (See figure 3 below), while still permitting the injected conductive fluid to produce a response in the computer. In this way one can also measure the in-plane permeability values for electrically conductive fabric such as carbon.
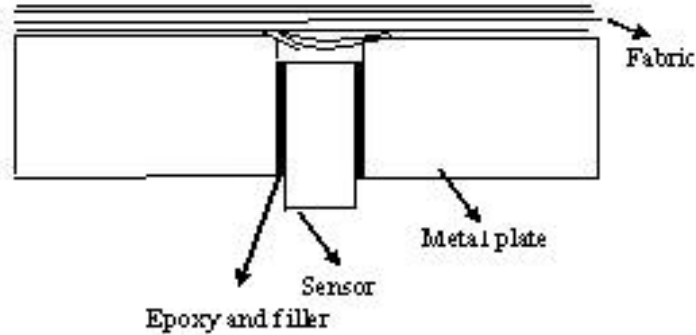
Figure 3. Recessed sensor.

Experiments prove the applicability of this idea. A small rectangular metal plate is used with six sensors inserted in and distributed evenly (See figure 4 below). The sensor is an electrically conductive copper wire with PVC insulation coating. The sensor is inserted through a hollow copper screw. An O-ring seals and fixes the sensor position when compressed by tightening the screw into the plate (See figure 4 (c) below).
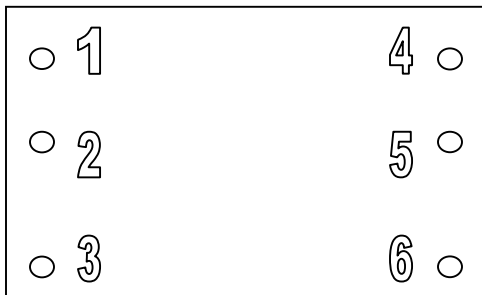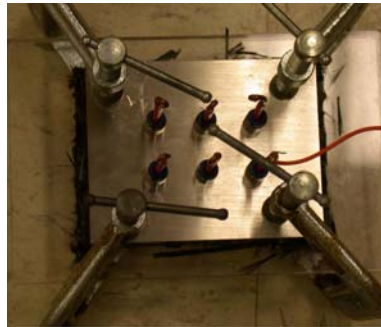
(a) Front view　　　　　　　　(b) Back view　　　　　(c) Sensor Design

Figure 4. The sensor plate used in our experiment.

Each sensor is recessed a small distance d, which can be quantitatively measured by a Digimatic Depth Gauge (Mitutoyo 700-105). Carbon fabric is placed on the top of the sensor plate, covered with a transparent top plate, and everything is compressed. Next, the voltage across an electrical resistance (in such a circuit as shown in figure 5(a) below) is measured, before and after fluid injection through a central hole drilled through the transparent top. Here the results are shown for one sensor in Figure 5(b) in which the voltage values are shown with the corresponding recess distances d. In figure 5, one can see that d=0.4~0.5 mm is the distance range for good sensor performance. This circuit design also permits sensor I/O through the digital channel on the interface card for high efficiency.
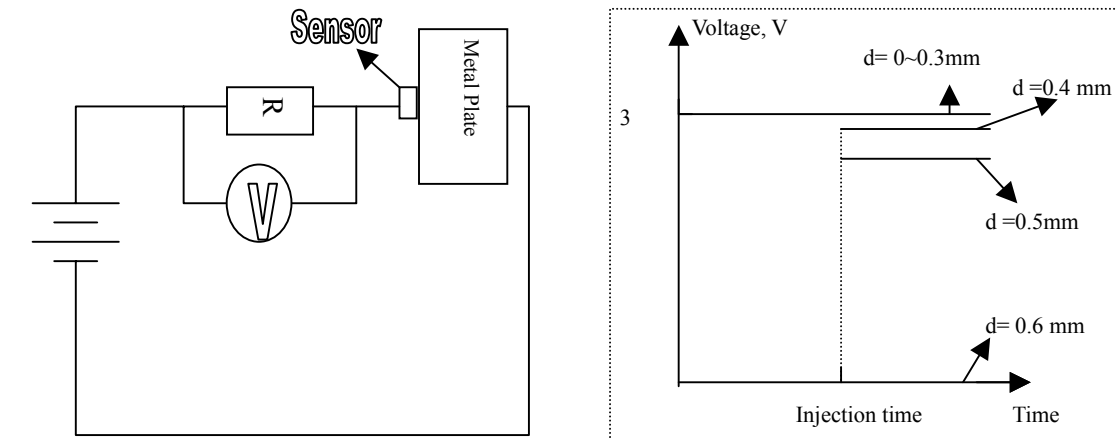
(a) Electrical circuit used in the experiment.   (b). Experimental results of one sensor.

Figure 5

3. HIGH SPEED DATA COLLECTION

With this new set-up, the authors plan to measure the statistical distribution of in-plane permeability values for electrically conductive fabric. A number of preforms will be used to collect permeability data at one fiber volume fraction to generate a distribution, and then another set of data can be collected at another fiber volume fraction. A through-the thickness permeability rig is also being developed to rapidly collect necessary to characterize 3-dimensional flow behavior (see figure 6 below).

1. Elastic bladder

2. Filter (Sample filled between the two filters)

3. Metal support

4. Metal frame

5. Guide

6. Stop

7. Air hose

8. Fluid entrance

9. Fluid exit
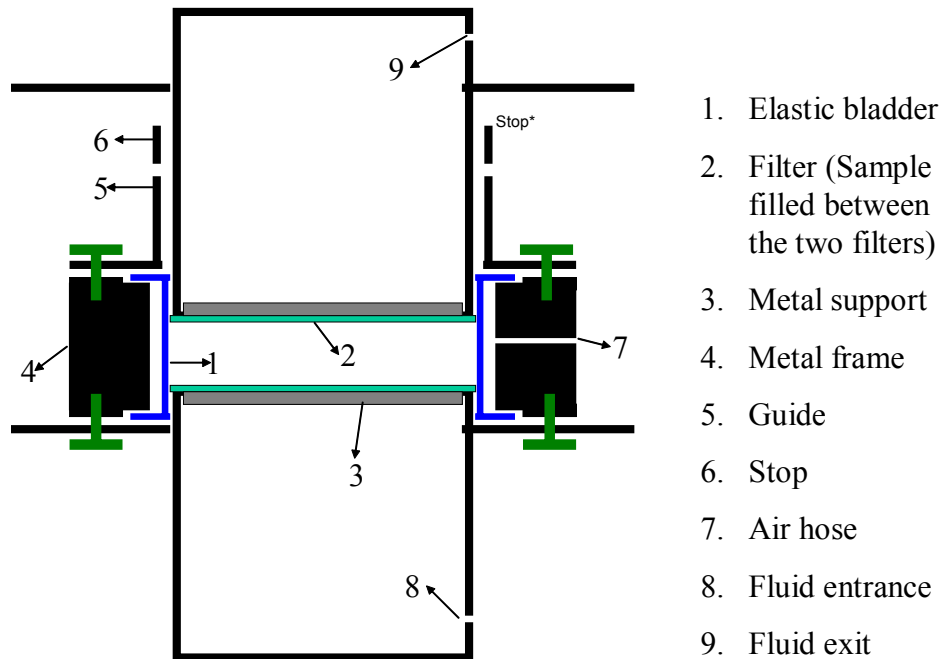
Figure 6. The set-up being built for through-thickness permeability measurement

An inflatable elastic bladder will seal the edges of the fabric so as to reduce race-tracking errors. Fluid is pumped from bottom to top by a constant flow rate pump and pressure differences are measured by a differential pressure transducer (Dwyer 645-15). Stops of calibrated thickness are used to control the thickness and so the fiber volume fraction of the sample. Then, one can obtain through-the-thickness permeability values at several fiber volume fractions using one sample by replacing the stops.

4. ACKNOWLEDGEMENT

5. REFERENCES

[1]. Kris Hoes, PhD Thesis, University of Brussels, Brussels, 2003
[2]. Vetrotex – Saint Gobain, Brochure: Memento 2001
[3]. Jingyi Xu and Yulu Ma, The Technology and Applications of Resin Transfer Molding (RTM), China Plastics, 6(1), 9-16 (1992).
[4]. L. Baichen, S. Bickerton and S. G. Advani, Modeling and simulation of resin transfer molding (RTM) – gate control, venting and dry spot prediction, Composites, 27A, (2), 135-141 (1996).
[5] Richard. S. Parnas, Liquid Composite Molding, Carl Hanser Verlag, Munchen, 2000.
[6]. F. A. L. Dullien, Porous Media - Fluid Transport and Pore Structure, Academic Press, INC. 1992
[7]. Kruckenberg, T. and Paton, R., Resin transfer molding for Aerospace Structures, Kluwer Academic Publishers, Dordrecht, The Netherlands, 1998.
[8]. R. S. Parnas and A. J. Salem, A comparison of the unidirectional and radial in-plane flow of fluids through woven composite reinforcements, Polymer Composites, 14(5), 383-394 (1993)
[9]. P. Ferland, D. Guittard and F. Trochu, Concurrent Methods for permeability measurement in resin transfer molding, Polymer Composites, 17(1), 149-158, (1996).
[10]. R. Gauvin, et. al., Permeability measurement and flow simulation through fiber reinforcement, Polymer Composites, 17(1) 34-42, (1996).
[11]. R. B. Gebart and P. Linström, Measurement of In-plane permeability of fiber reinforcements, Polymer Composites, 17(1) 43-51, (1996).
[12]. T. S. Lundström, et. al., In-plane permeability measurements: a Nordic round-robin study, Composites, 31A(1) 29-43, (2000).
[13]. S. Amico and C. Lekakou, An experimental study of the permeability and capillary pressure in resin-transfer molding, Composites science and Technology, 61, 1945-1959, (2001).
[14]. M. L. Diallo, R. Gauvin and F. Trochu, Key factors affecting the permeability measurement in continuous fiber reinforcements, Proceedings of ICCM, 11, 441-451, (1997).
[15]. G. Neale and W. Nader, Practical significance of Brinkman's extension of Darcy's law: coupled parallel flows within a channel and a bounding porous medium, Canadian Journal of Chemical Engineering, 52, 475-478, (1974)

[16]. R. S. Parnas and Y. Cohen, Coupled parallel flows of power-law fluids in a channel and a bounding porous media, Chemical engineering communications, 53, 3-22, (1987)

[17]. C. Binetruy, B. Hilaire and J. Pabiot, The interaction between flows occurring inside and outside fabric tows during RTM, Composites Science and Technology, 57, 587-596, (1997).

[18]. Parnas, R. S. et al., Permeability Characterization. Part 1: A Proposed Standard Reference Fabric for Permeability, Polymer Composites, 16, (6), 429-445, (1995).

[19]. C. Lekakou, et. al., Measurement Techniques and effects on in-plane permeability of woven cloths in resin transfer molding, Composites, 27A, 401-408, (1996)

[20]. K. L. Adams and L. Rebenfeld, In-plane Flow of Fluids in Fabrics: Structure/Flow Characterization, Textile Research Journal, 57, 647-654, (1987).

[21]. B. N. Greve and S. K. Soh, Directional Permeability Measurement of Fiberglass Reinforcements, SAE Transactions, 99, 331-343, (1990).

[22]. Kris Hoes, et. al., New set-up for measurement of permeability properties of fibrous reinforcements for RTM, Composites, 33A, 959-969, (2002).

Standardizeable Permeability Work Cell for Fibrous Reinforcements

Stadtfeld, H.C.; Weyrauch, F.; Mitschang, P.

Institut fuer Verbundwerkstoffe GmbH,
Erwin-Schroedinger-Strasse 58, 67663 Kaiserslautern, Germany
hubert.stadtfeld@ivw.uni-kl.de

SUMMARY: A permeability measurement work cell was developed at the Institut fuer Verbundwerkstoffe GmbH. It consists of an aluminum mold with integrated dielectric sensors and a LabVIEW-based control software. These sensors allow to monitor the progression of the flow front at any point in time. Consequently, the 2D permeability of any given fabric can be determined within minutes. This paper introduces the set-up, the software, and the capabilities of a standardized approach to measuring the 2D permeability of fibrous reinforcements in an easy and efficient manner.

KEYWORDS: permeability, 2D measurement, dielectric sensors, automated set-up, RTM.

INTRODUCTION

Liquid composite molding technologies such as RTM have established themselves in the industry. In the case of RTM the potential of this process encompasses short cycle times, high fiber volume fractions, high surface quality, and the possibility of implementing complex geometries. With growing popularity of this manufacturing technique, process simulations like LIMS [1] have become important since they enable engineers to predetermine the precise location of injection gates and vents in RTM molds according to the properties of the fibrous reinforcement to be used. To use these process simulation tools, engineers are required to know the components of the permeability tensor of the reinforcing material as a function of the degree of compaction, i.e. fiber volume fraction. There are two ways of determining the required permeability values, i.e. either to measure it experimentally or to rely on the use of software that will provide the permeability based on the assumption of representing a reinforcement structure by means of idealized unit cells.

Permeability measurement

The first approach, i.e. experimental determination, provides well-established and verified methods of obtaining the in-plane permeability values and is the subject of this paper.

Experimental methods of measuring the in-plane permeability of a porous media can be differentiated by the characteristics of the injection gate. Hence, one can differentiate between 1D injection methods (line gates) and 2D injection methods (point gates).

While the mathematical evaluation of the permeability within the 1D method is very straight forward, the experimental set-up itself provides challenges. The race-tracking phenomenon [2], preform slippage inside the mold, and the requirement to know the major flow directions of the material under investigation prior to the experimental investigation are just a few of the problems to be mentioned. The result of a successful 1D measurement is *one* permeability value for *one* of the main axes of flow at a specific fiber volume fraction.

Performing a 2D measurement is rather simple but the mathematical procedure to calculate the permeability is more demanding. With the 2D method neither edges need to be sealed off, nor does the preform tend to slip inside the mold. With one experiment one generates a complete set of permeability values for a given fiber volume fraction.

The usage of metal molds generates the need to use sensor systems to determine the flow front position inside the closed mold. Researchers [3], [4] found different approaches to meet these challenges. A more recent approach [5] suggests to use an array of mold-embedded, resistance-based point sensors to obtain the time the flow front reaches each of the positions of the sensors inside the array. Ideally, an analogue lineal sensor system should be introduced into the mold since this allows to obtain the desired flow front position at any instant of time.

Permeability measurement work cell

Such a lineal sensor system has been developed, and patented [6], [7] by the Institut fuer Verbundwerkstoffe GmbH. The permeability measurement work cell is formed by a permeability measurement tool, mounted on a RTM-Press, a computer which runs the measurement and data acquisition software LabVIEW®, and an injection unit.

The permeability tool shown in Figure 1a) has a mold cavity area of 640 mm by 420 mm and consists of two 80 mm thick aluminum plates. By means of spacer plates virtually any fiber volume fraction can be achieved. Temperature control of the tool up to a maximum temperature of 160 °C allows using reactive resin systems.

The upper mold provides three possible injection locations (1 gate, 2 vents) and contains six dielectric lineal sensors, as it can be seen in Figure 1a). The sensor system implemented in the permeability measurement work cell depends on the change of the dielectrical properties of the materials inside the cavity due to a fluid which gradually saturates the porous media. In general, dielectrical sensors can not be used with conductive reinforcing materials such as carbon fibers. The system developed at IVW prevents the sensors from generating short circuits through a surface treatment, thus eliminating this limitation.

During an experiment, the test fluid enters the mold cavity through the center gate and starts to saturate the preform inside the mold. As the flow front reaches the first horizontal sensors, the previously constant sensor outputs continuously start to rise over time (ellipse 1 in Figure 1a). As the experiment progresses, the next ellipsoidal flow fronts are obtained (2, 3 in Figure 1a). These ellipsoidal flow fronts generate the respective sensor output levels documented in Figure 1b). Whenever a sensor is completely wetted, the output voltage remains constant over time and forms a plateau. With the knowledge of the actual sensor length and the plateau voltage, a relation between voltage and length scale can be determined for each lineal sensor, which allows to transform the sensor signal into the desired flow front position.

Finally, after all sensors have been wetted completely, the injection is stopped and the experimental part is concluded.

a)

b)
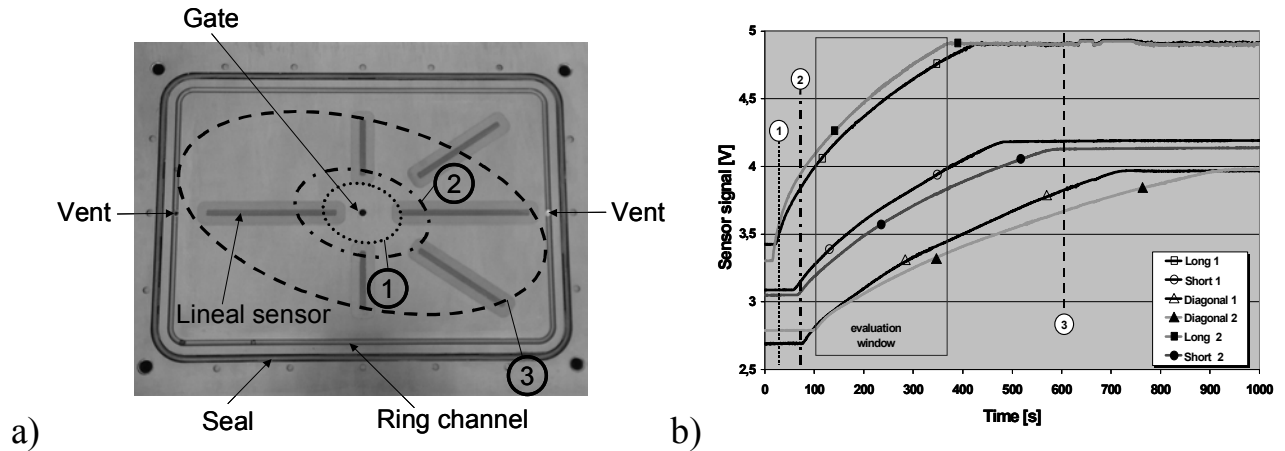
Figure 1a) IVW-permeameter with integrated dielectrical lineal sensors. Schematics of typical flow front ellipses during a permeability experiment are provided in 1a) with their corresponding sensor output voltages displayed in 1b)

Now the permeability can be calculated from pressure, fiber volume fraction and flow front position over time. Figure 2 shows the interface created to provide injection control and to perform a variety of permeability evaluations.

a)

b)

c)
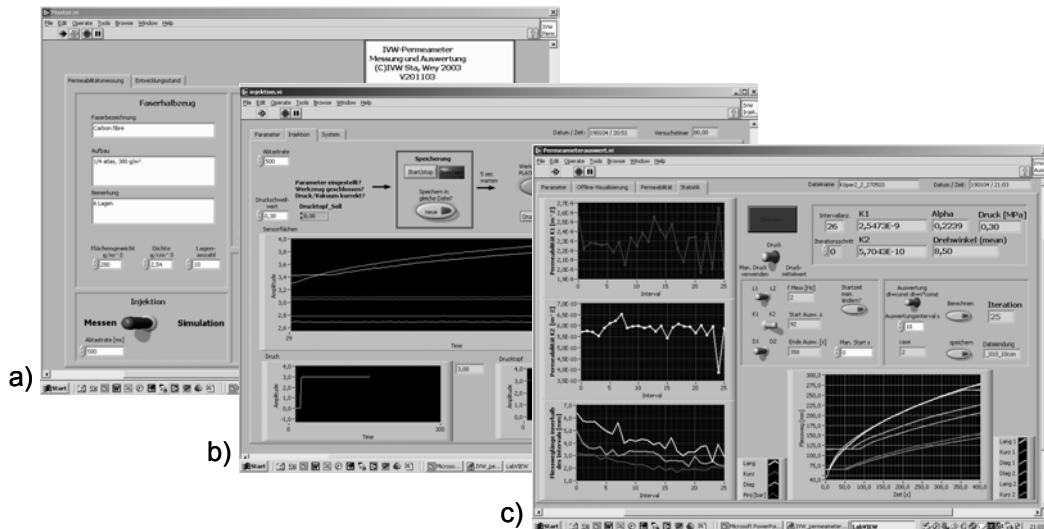
Figure 2: Front panels of permeability measurement and injection control software programmed with National Instruments LabVIEW®. a) Input of experimental parameters b) Injection control with on-line sensor output and c) Permeability evaluation front end

The actual computation of the permeability values requires to read the flow front positions of three sensors, to generate a suitable elliptical equation, to determine the respective angle of rotation, to transform the ellipse into the mold coordinate system, and finally to determine the permeability values K1 and K2 according to [8]. Since only three of the six sensors are used for a permeability evaluation, varying the sensor triplets for each calculation allows to cross-check and compare permeability values obtained for the experiment.

This feature can prevent local inconsistencies to affect one sensor, therefore, completely misleading the results of the measurement. It also allows to interpret the homogeneity of the preform under investigation.

Generally, the values determined with different sensor triplets do not differ significantly. Nevertheless, Figure 3 shows that it can be advantageous to obtain a mean value for K1 and K2 by running all possible sensor combinations.

The difference between the respective K1 and K2 values of a single experiment using different sensor triplets in Figure 3 demonstrates one shortcoming of the currently used numerical evaluation procedure. The displayed experimental result shows that generating a flow front ellipse from just three values is not enough. To address this issue, non-linear curve fitting procedures such as the Levenberg-Marquard approach are under current investigation.
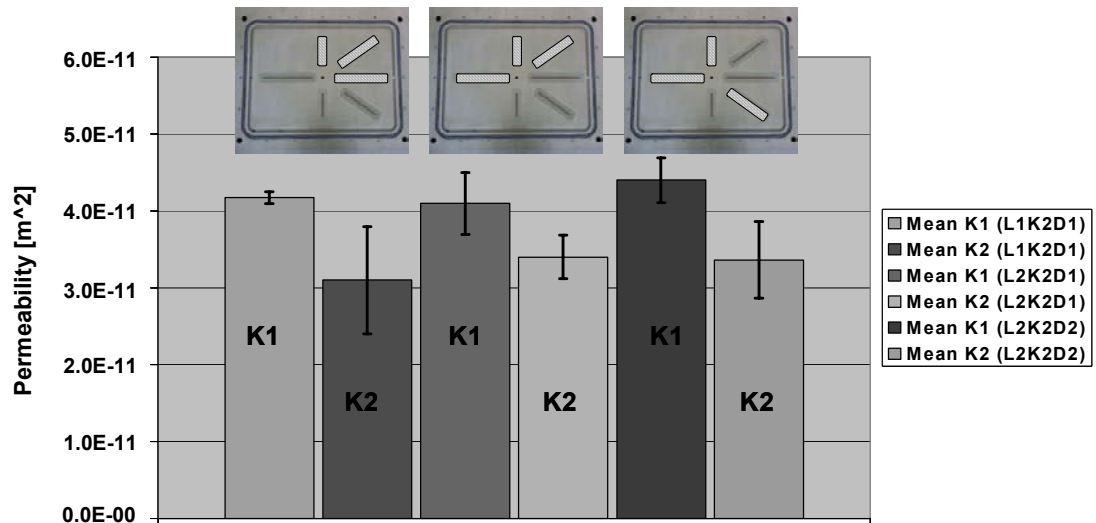
Figure 3: Example of experimentally determined permeabilities using different sensor triplets of the work cell

The data file of each experiment is recorded to the hard disk of the computer, allowing to come back and repeat the permeability calculation or even to replay the actual injection of each experiment performed. Since the set-up and the evaluation of the in-plane permeability values are almost completely automated, a multitude of measurements can be performed within one day. Therefore, this work cell represents a tool to easily obtain the permeability of a preform which is to be used in mold filling simulations.

Conclusion

In this paper a new permeability work cell has been introduced. This work cell enables the determination of the permeability of electrically conductive and non-conductive reinforcing materials due to a dielectric sensor with a special surface treatment. Since the mold as well as the sensors are manufactured from aluminum, the possibility of mold deflections, which are a possible source of error, are minimized. The metal mold allows the use of any kind of curing resin system as test fluid while also providing temperature control up to 160 °C.

This measuring equipment in combination with the software developed for the process control and permeability calculation enables the time-efficient determination of the in-plane permeability values of a fibrous reinforcing structure. Shortcomings in existing evaluation routines have been detected and will be addressed by means of non-linear curve fitting routines.

Acknowledgements

References

[1] Simácek, P., Sozer, E.M., Advani, S. G.: User Manual for DRAPE 1.1 and LIMS 4.0 (Liquid Injection Molding Simulation). Technical Report Center for Composite Materials 98-01, Delaware, 1998.

[2] Hammami; R. Gauvin F. Trochu: Modeling the edge effect in liquid composites molding. Composites Part A. 29 (1998), 603-609.

[3] Wang, X.M., Ehlers, C., Kissinger, C., Neitzel, M.: Experimental investigation of piezo-electric wafers in monitoring the resin transfer molding process. Smart Materials and Structures. 7(1), 121-127.

[4] Barooah, P., Sun, J.Q.: Lineal sensors for flow sensing in liquid injection molding of composites. Journal of Materials Processing and Manufacturing science. 7(4) (1999), 416-427.

[5] Hoes, K., Dinescu, D., Sol, H., Vanheule, M., Parnas, R., Luo, Y., Verpoest, I.: New Set-up for measurement of permeability properties of fibrous reinforcements for RTM. Composites Part A. 33 (2002), 959-969.

[6] Deutsches Patent DE 10004146: Anordnung zur Vermessung der Ausbreitung eines Matrixmaterials in elektrisch leitfähigen Verstärkungsstrukturen, München, 2000.

[7] Kissinger, C.: Ganzheitliche Betrachtung der Harzinjektionstechnik – Messsystem zur durchgängigen Fertigungskontrolle, IVW- Schriftenreihe, Band 28, Dissertation Universität Kaiserlautern, 2001.

[8] Shafi, V.: Beitrag zur Charakterisierung der Permeabilität flächiger Verstärkungsmaterialien. Dissertation Universität Kaiserlautern, 1996.

Measuring the Permeability of Preform Packages

H. Talvensaari[1], E. Ladstätter [2], R.W. Lang[3], and W. Billinger[4]

[1,2,3]Polymer Competence Center, Leoben, Austria
[4]Fischer Advanced Composite Components AG, Austria
Corresponding Author's e-mail: talvensaari@pccl.at

SUMMARY: To obtain useful flow simulations to support mold design, it is necessary to use accurate permeability values. In the work described here, the permeability of carbon fiber preforms with and without stitches was measured. A perform is a multilayer package of material ready to be impregnated using liquid transfer molding technology. The main parameters which vary in the preforms are the stitching pattern, meaning the distance between the stitch rows through the preform, the stitching thread tension and the stacking sequence of the layers. The permeability measurements were carried out using a continuous, two-dimensional radial-flow measurement technique. The measuring device consists of an aluminium mold with integrated dielectric sensors (surface treated to prevent short circuit). The sensor system relies on the change in the dielectric properties of the material as saturation takes place. The results showed that stitching has a positive influence on the permeability. The stacking sequence was found to be the most effective way to influence permeability.

KEYWORDS: preform, resin transfer molding, stitching pattern, thread tension level, stacking sequence.

INTRODUCTION

Resin transfer molding (RTM) is having increasing success in the composite manufacturing industry. In the RTM process, the reinforcement is placed into a mold, resin is injected to impregnate the fibers and the finished part can be demolded after the resin has cured and cooled down. Since resin transfer molding is often used to produce large, structural parts [1], the resin must flow long distances in the fiber reinforcement. This creates a demanding task for the tool makers, who must decide on the number and placement of the injection ports and vents. To be able to predict the flow of the resin through the fiber reinforcement, it is necessary to use accurate permeability values in the computer simulations. The resistance of the reinforcing material to the liquid flow is called permeability. The basic equation [1] generally accepted to describe flow in a porous medium is known as Darcy's law (Eqn.1).

$$Q = \frac{K}{\mu} \frac{\Delta P}{L} \qquad\qquad (1)$$

where Q = flow rate (m/s), K = permeability (m²), μ = viscosity of the fluid (Pa s), ΔP = pressure difference (Pa) and L = flow length (m).
Preforms made from woven fabric show an interlaminar pore structure between the layers [2].

Preforms with stitches exhibit this phenomenon even more distinctly due to the distortion of the fibers caused by the needle and the stitching thread. A fiber-free zone is created which provides an easy pathway for the distribution of liquid.

EXPERIMENTAL

The device used to measure permeability with electrical sensors was developed by the Institute for Composite Materials GmbH (IVW), Germany. The permeameter consists of an upper mold in which the sensors are embedded, the electrical circuit, a pressure vessel and software for the permeability calculation written at the institute.

Materials and Sample Preparation

A 5-harness satin weave, manufactured by Hexcel Fabrics, France, was used in this study. This carbon fabric has a surface density of 370 g/m². Fig. 1 shows the stitch types created at the two thread-tension levels selected for this work. At 480 cN (Newton), the upper thread and the bobbin thread interlock beneath the specimen. At the thread tension level >500 cN the knot is placed between the upper and lower layers of the preform. The exact location of the knot is not known. As can be seen in Fig. 1, when the knot is somewhere between the layers, double the number of resin-rich areas are created. A polyester thread No. 220 – dtex 150(2) from Gütermann, Germany, was used as the stitching thread. The specimens were sewn and cut using an automated sewing machine. All of the permeability measurements were performed on preforms with six layers. At a cavity height of 2 mm, the nominal fiber volume fraction was 62%. Two different stacking sequences were generated in the following way (Fig. 1). For the 2x3 lay up, two layers of fabric were sewn together and three of these two-layer packages were laid in the mold. For the 1x6 preform, six layers of fabric were sewn together forming one package. For comparison purposes, permeability of an unstitched preform was also measured.
The preforms were stitched using two different stitching patterns. Stitch rows cross the whole length and width of the preform with a row spacing of 10 mm or 20 mm. The stitching was at an angle of ±45° to both warp and weft. After sewing, the machine automatically cut the performs out. A circular hole with a diameter of 8 mm, was punched in the middle of the preform specimen to avoid transverse flow through the sample during injection.

Permeability Measurements

Preforms were manually laid inside the mold cavity and the hole in the middle was aligned with the pressure sensor. The upper mold, embedded with 6 sensors, was then clamped on to the lower mold. To obtain the necessary equation for the permeability calculation, the flow front position was needed from 3 sensors. The flow front positions were determined by the relationship between the voltage and the wetted length of the sensors [3]. The values of K1 and K2, the main axis of the flow, and the angle of the maximum flow front (K1) with respect to the mold coordinate system, were given by the software. Since the K2 values were relatively precisely 2/3 of the K1 values, and K1 is considered more important for this study, only the K1 values are presented here. In this study the average angle of the maximum flow front was 58° for the unstitched preform and 62° for the stitched preforms.
The angle is measured moving away from the positive x-axis towards the positive y-axis. The results given here are the average of 3 measurements.

A vegetable oil with a viscosity of 0.006 Pa s (Pascal seconds) was used as the test fluid.
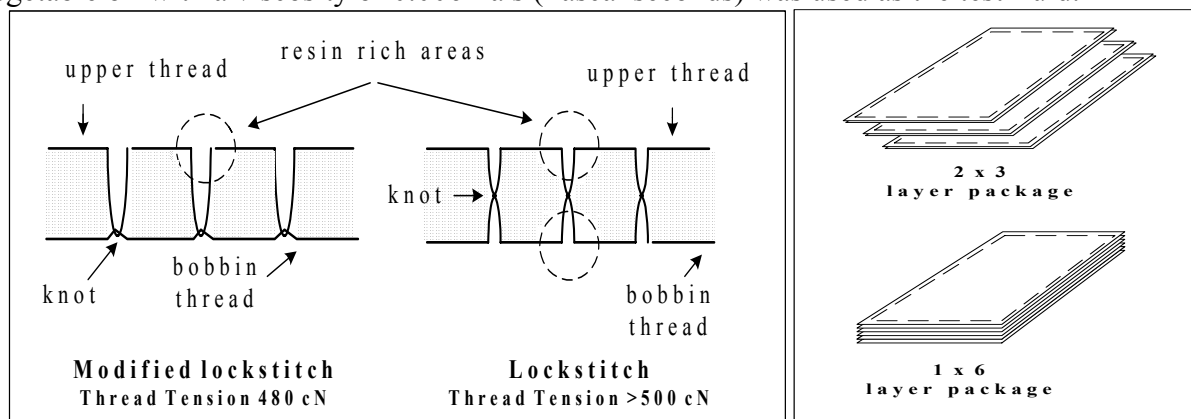
Fig. 1 Modified lockstitch, lockstitch and resin rich areas presented on the left side. Stacking sequences of the preforms presented on a right side

RESULTS AND DISCUSSION

Comparing the results between stitched and unstitched (0) preforms at the first row (A), it can be seen that stitches are influencing the permeability. Values increase as the number of stitches increases. This results from the fact that the stitch holes create high-permeability channels throughout the preform in which the liquid is able propagate easily.

The influence of the stitches is also seen in the tables in the second row (B). The 10x10 stitching pattern exhibits higher permeability than the 20x20 stitching pattern because of the greater number of flow paths for the resin. The first set of columns is an exception to this pattern. It is assumed that the lower thread tension level (Fig. 1) gives enough space for the fiber tows to move and nest in such a way that the fiber-free area created by the stitch decreases and no longer provides an easy pathway for the liquid.

The 2x3 stacking sequence has a higher permeability in all cases (Row C). An easy flow passage between the interfaces is created by laying three packages, each having two layers of fabric stitched together, into the mold. It is assumed that the flow penetrates the packages through the stitch holes and simultaneously increases the flow in the adjacent interface. The 1x6 package is a tight structure of fiber tows and the flow through the whole preform is therefore much more complex than that through the 2x3 stacking sequence preform.

Looking purely at thread tension (Row D), no clear trend can been seen. If however only 10x10 stitching pattern is considered, the higher thread tension level is found to yield higher permeability in both stacking cases. This could be a result of larger stitch holes created by the tauter stitching thread. As explained above, the lower thread tension level allows the fibers to reorganise around the stitching thread and diminish the gap area. It is possible that the number of stitches present in the stitching pattern 20x20, is not enough to demonstrate the same behavior.

Table 1 Permeability results
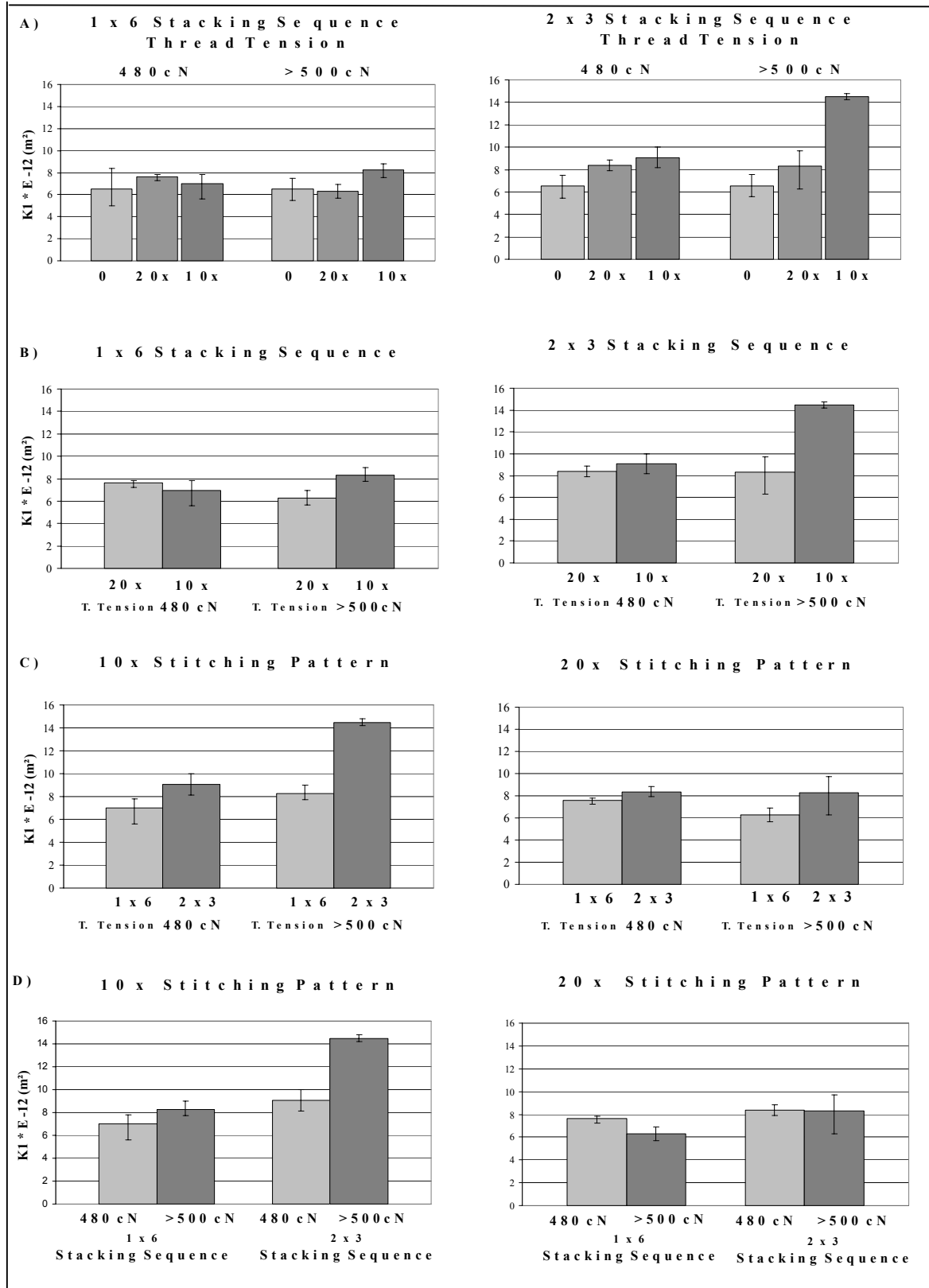
* The error bar shows the minimum and maximum measured values

CONCLUSION

In this work the permeability of preforms made of woven carbon fiber fabric was measured. The preforms had a number of different characteristics whose influence on the permeability have been discussed. The main variables of the preforms were the stitching pattern, stacking sequence and stitching thread tension. The tests have shown that the stitches have a positive influence on the permeability if compared to the perform without stitches. The stitching style, in this case a stitch row distance across the whole preform of 10x10 mm or 20x20 mm, made a difference. The 10x10 mm stitching pattern resulted in a higher permeability due to the larger number of stitches. Thread tension levels (480 cN and >500 cN), did not seem to show any common trend when comparing the results. However, when the 10x10 mm stitching pattern alone was examined, it was found that the higher thread tension level resulted in higher permeability. Stacking sequence was however discovered to be the most effective way to influence permeability. Stacking three preform packages into the mold yields higher permeability results than one preform package, where both constructions have the same total number of layers.

REFERENCES

1.   T. M. Kruckenberg and R. Paton. (1998). Resin Transfer Molding for Aerospace Structures. Kluwer Academic Publishers, Dordecht.

2.   K. L. Adams and L. Rebenfeld, "Permeability Characteristics of Multilayer Fiber Reinforcement. Part 1: Experimental Observation", *Polymer Composites, Vol. 12, no 3. 1991, p. 791-85.*

3.   H. C. Stadtfeld, P. Mitschang, C. Weimer and F. Weyrauch, "Standardizeable 2D-Permeability Measurement Work Cell for Fibrous Materials", *Manual of The 6th International AVK-TV Conference Baden-Baden, Germany, October 2003, p. C13-8 – C13-11.*

The Effect of Permeant on the
Measured Permeability of a Reinforcement

John Summerscales

Advanced Composites Manufacturing Center
School of Engineering,   Reynolds Building
University of Plymouth
Plymouth,   Devon,   PL4 8AA,   United Kingdom.

SUMMARY: Darcy's Law did not initially contain a term for the viscosity as the value for water could be taken as one.   Further the equation does not include a term for contact angle as the model assumes flow in wetted media.   In order to model Liquid Composite Molding processes, it was necessary to add a viscosity term to account for the range of fluids used.   For unsaturated (wetting) flow, the conditions at the flow front will be different to the wetted flow behind the flow front.   The wetting flow permeability may vary with the fluid.   Steenkamer *et al* (1995) concluded that "fabrics should be characterized with the actual liquid molding resin selected for a given application".   This paper will review the literature and discuss the need to introduce a further term to Darcy's Law to account for the different surface energies/contact angles at the flow front in the determination of reinforcement permeabilities using model fluids.

KEYWORDS: permeability, permeant, test fluid.

INTRODUCTION

The manufacture of continuous fiber-reinforced thermosetting matrix composites in closed molds often employs the techniques usually referred to by the generic names Liquid Molding Technologies (LMT) or Liquid Composite Molding (LCM), and more specifically known as Resin Transfer Molding (RTM) [1-6].   For larger structures, Resin Infusion under Flexible Tooling (RIFT) [7-9] is becoming increasingly important.   A variety of other acronyms have been used for these processes [10].

RTM and RIFT processes are normally modeled using Darcy's equation [11].   The one-dimensional form of this equation relates volumetric flow rate (Q) to the process parameters:

$$Q = \frac{KA.\Delta P}{\mu L} \qquad (1)$$

where K is a constant of proportionality known as the permeability, A is the cross sectional area of the porous medium normal to the flow direction, $\Delta P/L$ is the pressure gradient driving the flow and μ is the fluid viscosity.

For simulation of the process, modeling should use the tensor form of Darcy's equation.

Kozeny [12] and Carman [13] developed an expression to relate the volumetric flow rate of fluid to the microstructural features of the porous bed:

$$Q = \frac{\varepsilon A m^2 \Delta P}{k \mu L}$$
(2)

where ε is the porosity (one minus volume fraction of fibers), m is the hydraulic radius, and k is the Kozeny constant. Blake [14] defined the hydraulic radius as the volume in which fluid actually flows, εV (where $V = AL$), divided by the wetted surface area (S). Substituting $m = \varepsilon V/S$ into equation 2 yields:

$$Q = \frac{\varepsilon^3 A V^2 \Delta P}{k \mu S^2 L}$$
(3)

The measurement of the permeability of the laminate stack is clearly a function of a number of parameters as indicated above. Darcy's equation, as originally proposed to model the flow of water in the aquifers at Dijon, did not include a viscosity term as water has a notionally constant viscosity over the temperature range considered (1.792 mPas at 0°C; 0.8902 mPas at 25°C). A viscosity term has now been introduced into the equation which permits modeling of a variety of resin systems. The equation as originally proposed was for saturated (*i.e.* fully wetted porous medium) flow. It is now generally accepted that the equation can be used for unsaturated (wetting) flow and hence it finds application in modeling the processes under consideration here. However, there is evidence that the measured permeability is a function of the test fluid used.

Griffin *et al* [15, 16] reported permeability (units x 10^{-12} m^2) variation in radial flow experiments between 165-208 for glycerol and 1288 for polyester resin for the impregnation of the same twill weave carbon fiber fabric.

Steenkamer *et al* [17] reported experiments to compare motor oil, diluted corn syrup and vinyl ester resin, and state that "the motor oil showed little affinity for the fiberglass reinforcements, while the vinyl ester resin and the diluted corn syrup wet out the fiber quite well". In a more complete report of this work [18] they claimed that "fabric permeability is dependent on the type of test fluid used". They also stated that "surface tension and contact angle measurements indicate that interactions at the microscopic level between the fiber and the test fluid account for these differences in permeability". They noted that "since sizings/binders are usually soluble in the resin, the chemical composition of the resin may … change during infusion, in addition to gel-induced changes". They conducted unsaturated radial flow in-plane permeability experiments at a constant flow rate of 16.2 cm^3 s^{-1}. The mold was 250 mm square with a 3.175 mm cavity between two 25.4 mm acrylic face sheets. The tests were conducted on two fabrics each at two volume fractions using three fluids under identical experimental conditions. The summary results are presented in Table 1.

**Table 1: Mean values of permeability for three fluids and two fabrics
under identical conditions (data derived from Steenkamer et al, references 17/18)**

	A_f (gsm) V_f (%)	Diluted corn syrup/ deionised water	Motor oil SAE 10W-30	Vinyl ester resin Derakane 411-C50
Certain Teed 816 continuous strand mat	450 16.9	$K_{11} = 5.5 \times 10^{-9}$ m^2 $K_{22} = 6.1 \times 10^{-9}$ m^2	$K_{11} = 10.0 \times 10^{-9}$ m^2 $K_{22} = 10.5 \times 10^{-9}$ m^2	$K_{11} = 7.3 \times 10^{-9}$ m^2 $K_{22} = 8.2 \times 10^{-9}$ m^2
Certain Teed 816 continuous strand mat	450 22.6	$K_{11} = 3.2 \times 10^{-9}$ m^2 $K_{22} = 3.6 \times 10^{-9}$ m^2	$K_{11} = 7.1 \times 10^{-9}$ m^2 $K_{22} = 7.2 \times 10^{-9}$ m^2	$K_{11} = 5.7 \times 10^{-9}$ m^2 $K_{22} = 6.4 \times 10^{-9}$ m^2
Hexcel DB170 biaxial ±45° knit	595 43.9	$K_{11} = 0.93 \times 10^{-9}$ m^2 $K_{22} = 0.77 \times 10^{-9}$ m^2	$K_{11} = 2.52 \times 10^{-9}$ m^2 $K_{22} = 1.50 \times 10^{-9}$ m^2	$K_{11} = 1.55 \times 10^{-9}$ m^2 $K_{22} = 1.22 \times 10^{-9}$ m^2
Hexcel DB170 biaxial ±45° knit	595 58.6	$K_{11} = 0.70 \times 10^{-9}$ m^2 $K_{22} = 0.56 \times 10^{-9}$ m^2	$K_{11} = 1.74 \times 10^{-9}$ m^2 $K_{22} = 1.32 \times 10^{-9}$ m^2	$K_{11} = 1.23 \times 10^{-9}$ m^2 $K_{22} = 0.87 \times 10^{-9}$ m^2
Viscosity:		190 mPa s	155 mPa s	135 mPa s
Work of adhesion:		1125 µN cm^{-1}	658 µN cm^{-1}	634 µN cm^{-1}
Work of spreading:		-189 µN cm^{-1}	16 µN cm^{-1}	-74 µN cm^{-1}
Contact angle:		44.6°	spreads	37.7°

These data show the highest value of permeability when the flow fluid is motor oil and the lowest value of permeability when the flow fluid is corn syrup. The viscosities of the fluids increase in the sequence resin, oil then corn syrup. Micro-Wilhemy dynamic contact angle measurements were performed on single fibers extracted from the continuous strand mat with three test liquids (deionised water, glycerol and formamide analyser, each with contact angles greater than zero). This was used to inform the calculation of the work of adhesion, work of spreading and contact angles (Table 1). Both the principal in-plane permeabilities and the work of spreading increased as the test fluid was changed from diluted corn syrup to vinyl ester to motor oil. The work of spreading is negative for the first two of these liquids indicating that pressure must be applied to achieve wetting of the fiber surfaces. They conclude that "until a more complete understanding of fluid-fiber interactions is developed, it appears that fabrics should be characterized with the actual [liquid molding] resin selected for a given application, since permeability measurements made with other idealized fluids yield only apparent permeabilities".

Karbhari and Palmese [19] investigated four different sizings on S2-glass fibers used in preforms for resin transfer molding (Table 2). They state that "fiber-sizing-resin interactions occurring during the infusion stage affect wet out and local flow behavior through the development of stoichiometric imbalances in local regions.

**Table 2:   Surface free energies (SFE), flow rates and capillary pressures
for different surface coatings on S2-glass fibers wetted with vinyl ester resin
(data derived from Karbhari and Palmese, reference 19)**

Materials	Sized for	polar SFE dyne cm^{-2}	dispersive SFE dyne cm^{-2}	total SFE dyne cm^{-2}	transient flow g min^{-1}	steady flow g min^{-1}	capillary pressure x 10^4 dyne cm^{-2}
449 sizing	Epoxy	10.88±2.51	44.44±4.52	55.33±5.17	20.1	0.4	99.6
463 sizing	Epoxy	6.94±1.40	45.07±2.80	52.00±3.13	14.1	1.1	97.8
933 sizing	BMI/PEEK	12.60±3.02	32.50±3.95	45.10±4.97	21.6	0.5	78.1
365 sizing	UPE/VE	8.6±1.18	33.09±1.0	41.69±2.25	20.9	1.9	76.6
Note that the fiber diameters were 13 µm for 365 sized fiber and 9 µm for the other three							
411-C50 VE		1.2±1.0	34.2±1.0	35.4±0.7	-	-	-

In the context of a European-funded project (BE5477), the permeability was measured for a series of reinforcement fabrics. The Plymouth data from wetting radial flow experiments was used to inform an isothermal VIp/SEPRAN simulation of rectilinear experiments where race-tracking had been eliminated conducted by Brochier in France. For Brochier E3795 (290 gsm 5-harness satin weave with flow enhancing tows) Injectex 6K carbon fiber fabric, the simulation modeled the experimental curves well. For Brochier E3833 (290 gsm 5-harness satin weave with no flow enhancing tows) 6K carbon fiber fabric, the results were more variable. The permeability reported by another partner, measured in saturated rectilinear flow using a glycerol/water mixture was consistently higher than permeabilities measured at Plymouth [20] and hence over-predicted the flow distance at any time during the simulated experiment [21].

Fell *et al* [12] conducted wetting radial flow experiments on 13 layers of 7781 satin-weave glass fiber fabric with the warp fibers aligned using LY564-1 epoxy resin in a 3 mm mold cavity (notional fiber volume fraction of 51%). The variable process parameters are given in Table 3. The driving pressure was 1.70×10^5 Pa in all experiments.

Table 3: Permeability experiments on 7781 satin weave glass fabric.

Expt	T (°C)	μ (Pa s)	V_f (%)	Hole (mm)	K_1 (x 10^{-12} m^2)	K_2 (x 10^{-12} m^2)
1	30	0.437	48.6	0	8.75	9.22
2	35	0.296	48.3	0	8.54	8.39
3	30	0.437	49.2	8	10.31	9.25

Parallel experiments on the same batch of reinforcement were conducted at two other laboratories using wetted uniaxial flow in a rectilinear mold with a glycerol/water mixture as the permeant and using a multiple cavity rectilinear experiment with corn syrup. The reported permeabilities were in the approximate ratio 1:2:3 for resin:glycerol:corn syrup experiments. Bréard [23] measured permeabilities in one-dimensional flows and found ratios ranging from 0.4 for unidirectional reinforcements to 0.8 for fiber mats between unsaturated and saturated preforms. Bréard *et al* [24] have compared unsaturated and saturated dynamic flows through porous media and propose to introduce the degree of saturation into the equations that govern the flow in order to increase the accuracy of numerical predictions. They state that, "except at very low injection velocity for which capillary effects may come into play, there is more resistance to the flow in a dry preform than when the fabric or mat has already been wetted and has become saturated". For three types of reinforcement (random, bidirectional and unidirectional) they clearly showed that the permeability in unsaturated flow (i.e. before the flow front has moved to fill the cavity) is lower than for saturated flow. After the apparent mold fill, the permeability rose from the unsaturated to the saturated flow value with a small delay attributed to the time required for complete saturation of the tow.

CONCLUSION

There is a growing body of evidence to indicate that the measured permeability in unsaturated (wetting) flow differs from that in saturated (wetted) flow. This may be a function of contact angles and/or surface energies. It would be useful if this situation could be resolved so that permeabilities could be translated between fluids in order to permit quantitative modeling of Liquid Composite Molding processes using permeabilities measured with non-curing Newtonian fluids.

REFERENCES

1. K van Harten, 'Production by resin transfer molding', in R A Shenoi and J F Wellicome (editors): *Composite Materials in Maritime Structures,* Cambridge University Press, Cambridge, 1993, Chapter 4, 86-126.

2. K Potter, *Resin Transfer Molding*, Chapman & Hall, London, 1997, ISBN 0-412-72570-3.

3. CD Rudd, AC Long, KN Kendall and CGE Mangin, *Liquid Molding Technologies*, Woodhead Publishing, Cambridge, 1997, ISBN 1-85573-242-4.

4. TM Kruckenberg and R Paton (editors*)*, *Resin Transfer Molding for Aerospace Structures*, Kluwer Academic Publishers, Dordrecht NL, 1998, ISBN 0-412-73150-9.

5. W P Benjamin and S W Beckwith, *Resin Transfer Molding*, SAMPE Monograph 3, Covina CA, 1999. ISBN 0-938-99483-2.

6. R S Parnas, *Liquid Composite Molding*, Hanser Gardner Publications, 2000. ISBN 1-569-90287-9.

7. CD Williams, SM Grove and J Summerscales, *Resin infusion under flexible tooling (RIFT): a review*, Composites Part A: Applied Science and Manufacturing, 1996, A27(7), 517-524.

8. D Abraham and R McIlhagger, A review of liquid injection techniques for the manufacture of aerospace composite structures, Polymers and Polymer Composites, 1996, 4(6), 437-444.

9. D Cripps, TJ Searle and J Summerscales, Chapter 21: Open Mold Techniques for Thermoset Composites, In R Talreja and J-A Månson (editors): *Comprehensive Composite Materials Encyclopædia, volume 2: Polymer Matrix Composites,* Elsevier Science, Oxford, July 2000, pp 737-761. Set ISBN: 0-08-043720-6.

10. SW Beckwith and CR Hyland, *Resin Transfer Molding: a decade of technology advances*, SAMPE Journal, November/December 1998, 34(6), 7-19.

11. HPG Darcy, "Les fontaines publiques de la ville de Dijon", Dalmont, Paris, 1856.

12. J Kozeny, Uber die kapillare Leitung des Wassers in Boden, Sitzungsberichte Akademie der Wissenschaft Wien Math-naturw, 1927, 139(Kl.abt.IIa), 271-306.

13. PC Carman, Fluid flow through a granular bed, Transactions of the Institute of Chemical Engineers (London), 1937, 15, 150-166.

14. FC Blake, The resistance of packing to fluid flow, Transactions of the American Institute of Chemical Engineers 1922, 14, 415-421.

15. PR Griffin, The flow of liquid polymers through fibrous reinforcements, PhD thesis, University of Plymouth, September 1995.

16. J Summerscales, PR Griffin, SM Grove and FJ Guild, Quantitative microstructural examination of RTM fabrics designed for enhanced flow, Composite Structures, 1995, 32(1-4), 519-529.

17. DA Steenkamer, DJ Wilkins and VM Karbhari, Influence of test fluid on fabric permeability measurements and implications for processing of liquid molded composites, Journal of Materials Science Letters, 1 July 1993, 12(13), 971-973.

18. DA Steenkamer, SH McKnight, DJ Wilkins and VM Karbhari, Experimental characterization of permeability and fiber wetting for liquid molding, Journal of Materials Science, 15 June 1995, 30(12), 3207-3215.

19. VM Karbhari and GR Palmese, Sizing related kinetic and flow considerations in the resin infusion of composites, Journal of Materials Science, 1 November 1997, 32(21), 5761-5774.

20. EJ Carter, AW Fell and J Summerscales, Final Report on University of Plymouth work in Task 2: SIMULATION, University of Plymouth report BE5477/UoP/FR/2/A/CC/1.0, February 1996.

21. EJ Carter, AW Fell and J Summerscales, Validation of the simulation software for two-dimensional isothermal moldings using Brochier validation experimental data., University of Plymouth report BE5477/UoP/IR/2.1/D/CC/3.0, February 1995.

22. AW Fell, EJ Carter, PR Griffin and J Summerscales, The principal permeabilities of 7781 glass fabric and some discussion of the discrepancies in values reported by the three test houses, University of Plymouth report BE5477/UoP/IR/1.2/D/CC/15.0, November 1995.

23. J Bréard, Materiaux composites a matrice polymère: modelisation numerique de la phase de remplissage du procède RTM et determination expérimentale de la pérmeabilité d'un renfort fiberux, PhD thesis, Université du Havre - France, 1997.

24. J Bréard, Y Henzel, F Trochu and R Gauvin, Analysis of dynamic flows through porous media, part I: comparison between saturated and unsaturated flows in fibrous reinforcements, Polymer Composites, June 2003, 24(3), 391-408.

Permeability Measurements:
In Plane and through the Thickness

Maarten Labordus

Center of Lightweight Structures TUD-TNO
Kluyverweg1, 2629 HS Delft, The Netherlands
Corresponding Author's e-mail: M.Labordus@ind.tno.nl

SUMMARY: Liquid molding processes like RTM and vacuum infusion are becoming more and more state-of-the-art in the composite industry. Resin flow simulation software for these processes has also been around for many years. One of the key input parameters required for a good flow simulation is the permeability of the fiber reinforcement. No standard, general accepted permeability test has been established yet. Currently, most composite research institutes have developed their own permeability test set-up. Methods based on visual tracking of the resin flow front with circular or even spherical are notoriously inaccurate and sensitive to small variations in preform dimensions. The Center of Lightweight Structures TUD-TNO has developed permeability measuring devices for accurate in-plane and through-the-thickness permeability measurements following the conditions for Darcy's Law as close as possible. This paper describes the experimental set-up and gives some results.

KEYWORDS: Permeability, in-plane, through-the-thickness, liquid molding, vacuum infusion, RTM, permeameter, flow simulation

INTRODUCTION

The filling stage of the resin transfer molding process is considered to be an analogy of ground water flow though soil. A mathematical relation to describe this process, the (viscous) flow through porous media, was formulated by Darcy in 1856. Darcy's law is now generally applied to model RTM. Applied to a one-dimensional flow Darcy's law is:

$$Q(t) = \frac{k(x)A(x)}{\eta(t)} \frac{dp(x,t)}{dx}$$

with:
Q(t): the time-dependent volumetric flow rate (m^3/s)
η(t): the time-dependent fluid viscosity (Pa.s)
A(x): the surface area of the cross section of the mold (m^2);
  A(x) can depend on the position x in the mold
dp(x,t)/dx: the pressure gradient in the flowing resin (Pa/m)
k(x): the apparent reinforcement permeability (m^2)

During mold filling, when a resin is injected with a constant pressure in an isotropic reinforcement, the flow direction is constant; the flow velocity decreases in time. In a steady state fluid flow, the flow rate is constant with respect to the magnitude and direction.

In a rectangular mold cavity (A(x)=A) containing a reinforcement material with a permeability independent from x, the pressure gradient dp(x,t)/dx equals the linear pressure drop Δp/Δx. With a model viscous fluid, the viscosity is η(t)=η. Based on this equation a method is developed to determine the permeability of reinforcement materials, under the assumptions that a steady state flow method is adequate to model a (non-steady state) filling process, thus neglecting interfacial phenomena (e.g. fiber wetting, impregnation) and that the reinforcements are isotropic, or, in case of woven (orthotropic) fabrics, the reinforcements are characterized in the principal directions. An apparatus is developed in which the permeability of a (preformed) reinforcement material is measured in a steady state flow of a model fluid instead of a (curing) resin. The cavity of this apparatus contains an adjustable top side so the cavity can be adjusted to the thickness h of the preform. Also, the permeability of a non-preformed reinforcement can be determined as a function of the fiber volume fraction by repeatedly varying the cavity thickness h, thus compressing the reinforcement, and measuring the permeability. The volumetric flow rate Q of the model fluid is determined by measuring the mass of the fluid flown through the mold during a given time interval divided by the density of the model viscous fluid. With assumptions described, the permeability is calculated by:

$$k = \frac{\eta}{bh} \frac{\Delta m}{\Delta t} \frac{1}{\rho} \frac{\Delta x}{\Delta P}$$

EXPERIMENTAL SET-UP

The experimental set-up consists of the CLS permeameter, a plastic fluid container, an electronic scale and a personal computer with a data-acquisition system. It is placed in a laboratory with a temperature control (22±0.5°C). The reinforcements are placed in the permeameter cavity. The cavity height is adjusted to the desired level, in order to obtain the correct fiber volume content in the preform. The container with the glycerol-water mixture is pressurised to a pressure of 0.4 bar. After opening the valve at the fluid inlet, the fluid flows through the reinforcement and fills the container on the scale.
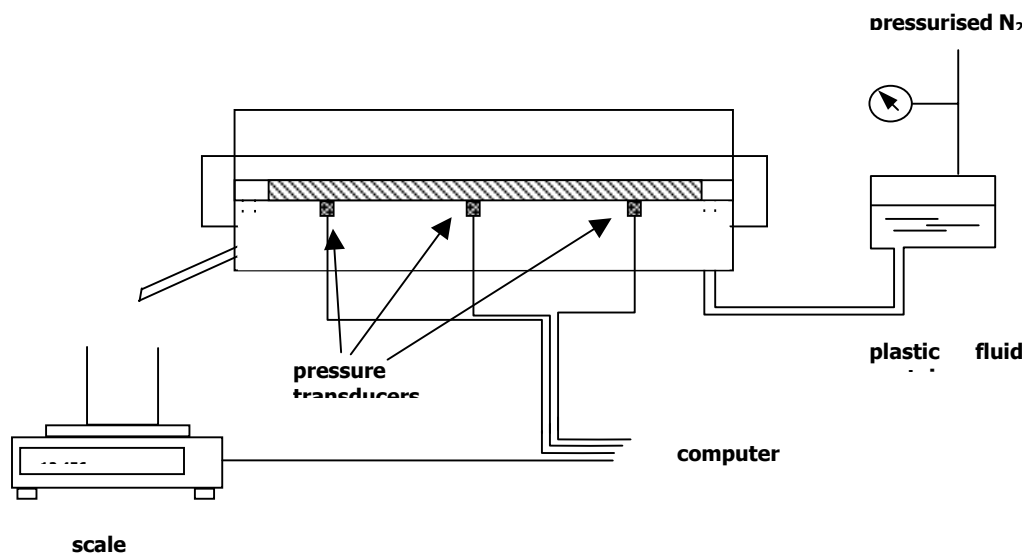
Figure 1: In-plane permeameter

A custom made LabView data acquisition program processes the output signal from the scale, the time interval Δt (s) (read from the PC clock) and the output signals from the pressure transducers. The program automatically determines when the flow has stabilised by analysing the statistical properties of the pressures and mass flow in time. From the data acquired during a period of stable flow, the mass flow $\Delta m/\Delta t$ (g/s) and pressure gradient $\Delta p/\Delta x$ are calculated with a best-fit method. From given values of accuracy and the statistical properties of the stable flow, an estimated error for the permeability is calculated as well. If the operator desires so, the height of the mold cavity can be changed and a new test run is started.

For permeability tests through the thickness, a similar approach was followed. From literature, it was known that the through the thickness permeability could be 5 to 10 times lower than the in plane permeability. The effect of short-cut flows around the perform would therefore also be 5 to 10 times more significant. It was decided to build a set-up with two separate regions. A central measuring region and a circumferential region where the flow was discarded. The layers of reinforcements were placed in an aluminium casing were they were clamped between two aluminium honeycomb layers, supported by two sheets of metal mesh. This configuration allowed for an almost undisturbed uniform feeding of the complete surface of the reinforcement. The pressure was measured in the cavity in the casing just above and below the reinforcement in the central measuring region. The height of the casing could be adjusted to be able to measure permeability's for a range of fiber volume contents.
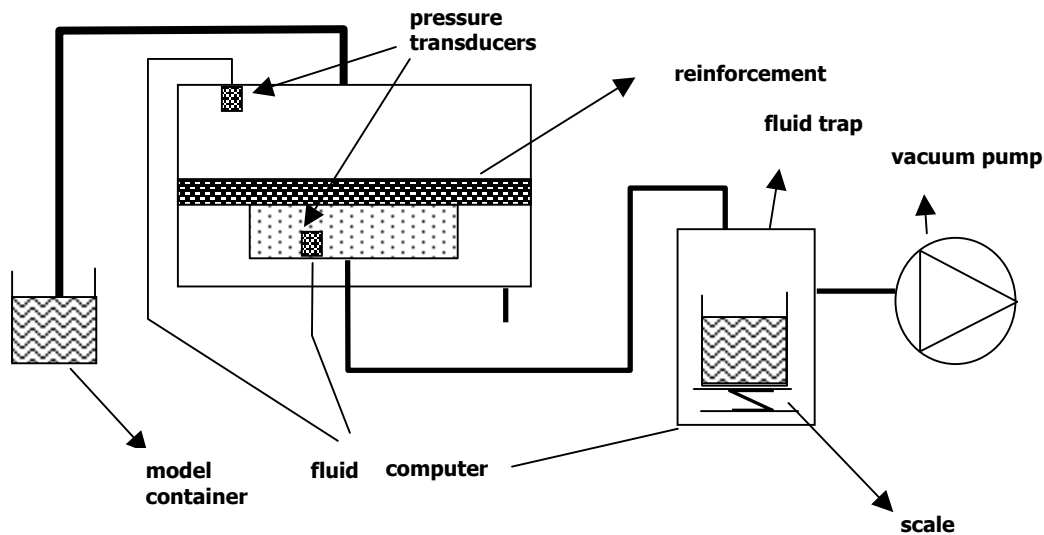
Figure 2: Through-the-thickness permeameter

RESULTS

The results of the permeability measurements are listed in table 1. In the third column the direction of cutting from the fabric is listed; $(0)_{10}$ indicates that 10 layers, cut lengthwise from the fabric (0° direction), are stacked. As can be seen, the results vary greatly for different types of fiber reinforcements. Materials like Unifilo or Injectex have relatively high permeabilities and allow for fast fill times when used in infusion processes.

Other materials like normal fabrics or non-crimp fabric show a much lower permeability. To be able to use these materials in an infusion process, they need to be combined with materials with a higher permeability like Injectex fabric or Unifilo. Another common procedure is to use a sacrificial flow enhancing material like a Newbury infusion membrane or Airtech flownet placed on top of the laminate in combination with a peelply. When a laminate is infused in such a way, the resin actually flows over the laminate and then impregnates it through the thickness. As can be seen from the permeability test results, the through thickness permeability for non-crimp fabrics is indeed much lower than the in plane permeability. This causes problems when infusing thick laminates.

Table 1: Test data

#	Material	Lay-up	Vf	Direction	Permeability (m2)	Standard deviation (m2)
1	Unifilo 750	--	29	In-plane	6.9 10-10	3 10-12
2	Injectex EF630	$(0)_{10}$	42	In-plane	2.3 10-10	7 10-13
3	G947 E3910	$(0)_{25}$	60	In-plane	2.1 10-11	2 10-13
4	E3836	$(0)_{28}$	61	In-plane	1.3 10-11	1 10-13
5	G904	$(0)_{13}$	44	In-plane	1.1 10-10	2 10-12
6	E3833	$(0)_{13}$	55	In-plane	5.6 10-11	1 10-12
7	Injectex E3795	$(0)_{13}$	55	In-plane	9.7 10-11	5 10-13
8	Injectex EF630	$(90)_{12}$	50	In-plane	2.6 10-10	2 10-12
9	6K T700 600	$(+45)_5$	60	In-plane	1.8 10-11	2 10-13
10	6K T700 600	$(+45)_5$	60	Through-the-thickness	3.2 10-12	3 10-13
11	12K T700 603	$(0)_5$	60	In-plane	4.8 10-11	3 10-13
12	12K T700 603	$(90)_5$	60	In-plane	2.1 10-11	4 10-13
13	12K T700 603	$(90)_5$	60	Through-the-thickness	6.8 10-12	5 10-13

CONCLUSIONS

The following is concluded:

- The measurement of the permeability of a reinforcement sample in the permeameters is a simple and fast routine. The permeameters have turned out to be adequate apparatus for measuring permeability's of reinforcement materials.
- The precision of the permeameter method is at minimum 1% during an experiment. The precision decreases to at least 6% by repeating measurements on the same preform. If the permeability of several identical preforms of an equal number of layers of the same fabric is measured, the precision will further decrease due to unknown variations in the fabric samples and the unknown influence of the preforming stage.
- The assumption is correct that a steady state flow method with which the permeability is measured is adequate to model a (non-steady state) filling process. The adequacy is proved by the agreement between the calculation of the propagation of errors and the relative standard deviation (coefficient of variation) of the within-experiment results (both 1%)
- It is recommended that, additionally, the permeability of the fabrics should be measured over a wide range of fiber volume fractions using the adjustability of the permeameter. By curve-fitting with the (modified) Kozeny-Carman equation the permeability data are more conclusive and applicable than the discrete data from the measurements of this work.

481

REFERENCES

1. R.S. Parnas et al., "Report on Manufacturing Polymer Composites by Liquid Molding", NISTIR 5373, September 20-22, 1993, N.I.S.T., Gaithersbrug
2. J.C. Miller, J.N. Miller, "Statistics for analytical chemistry", Ellis Horwood Ltd., Chichester, 3rd edition, 1993
3. A.E. Schedegger "The physics of flow through porous media", University of Toronto Press, 1957, p.104-105

POST-PROCESS PROPERTIES AND CHARACTERIZATION

Multi-Criteria Thermal Optimization by Evolutionary Algorithms of Resin Cure, Processing Stresses and Cycle Time in Liquid Composite Molding

Edu Ruiz and F. Trochu

Center de Recherches Appliquées Sur les Polymères (CRASP)
Département de Génie Mécanique,
École Polytechnique de l'Université de Montréal, H3C 3A7, Canada
e-mails: eduardo.ruiz@polymtl.ca, francois.trochu@polymtl.ca

SUMMARY: *Liquid Composite Molding* (LCM) regroups a number of increasingly used composite manufacturing processes. A proper selection of process parameters is crucial to yield successful molding results and obtain an appropriately cured part with minimum defects. In the case of thermosetting resins, the polymerization shrinkage increases the complexity of the thermo-mechanical problem. Numerical analysis of the internal stresses developed during resin cure and subsequent part cooling does not only help to understand the process, but it is also necessary to make thermal optimization reliable. The scope of this work concerns the optimization of resin cure, cycle time and residual stresses during LCM composite processing. A multi-criteria optimization algorithm called *LeCoq* (Logical Evolutionary Curing Optimization and Quenching) based on evolutionary algorithms was developed to optimize a multi-dimensional objective function that incorporates the following conflicting goals: minimization of residual stresses, maximization of the final degree of cure and reduction of cycle time. An optimized temperature profile obtained with this approach minimizes cycle time and processing stresses while avoiding thermal degradation of the matrix and composite delamination. Process optimization with two different objective functions is conducted for a thick composite part. Two optimized temperature cycles are obtained and the results are compared and discussed.

KEYWORDS: Liquid Composite Molding, thermal analysis, residual stress, optimization.

INTRODUCTION

In LCM fabrication, a number of process parameters such as mold temperature and inlet pressure have a great impact on part performance. Adequate process parameters are critical to ensure successful molding conditions and reduce cycle time, heating sources, mold deformation, etc. Minimization of the mold filling and curing time diminish energy consumption during the molding cycle. Finally, and maybe this is the most important point to consider in the case of thick composites, an optimum choice of process parameters results in minimum number of defects, such as micro-cracks, delamination, warpage, spring-in, etc. The work on LCM curing optimization reported in the literature can be divided as follows: (1) reduction of cycle time; (2) reduction of cure gradients; (3) reduction of thermal gradients; and (4) reduction of cooling stresses.

This investigation aims at developing a comprehensive thermal optimization methodology that considers simultaneously each of the above mentioned effects. The optimization algorithm must be based on the physics of the curing process in order to provide meaningful results. The study focuses on the minimization of the internal stresses that appear during *cure* and *cooling* of the thermosetting matrix as a result of temperature and cure gradients. The objective function to be minimized is constructed from physical information on the cure and temperature gradients, cure and cooling stresses, cycle time and maximum allowed exothermic temperature. An evolutionary strategy based on Genetic Algorithms (GA) is implemented for the minimization of the objective function. Optimization studies are carried out for a thick glass/polyester laminate to demonstrate the advantages of the proposed methodology.

PROCESSING STRESS ANALYSIS

In the present work, the composite cure is analyzed through the thickness of the part by a one-dimensional Crank-Nicolson finite difference formulation to solve the energy equation [1]. An adaptative time step control based on Fourier's number and on the reaction rate was implemented to avoid computational inconsistencies. In this approach, different thermal boundary conditions can be set at the mold surface or at the positions of the heating/cooling system inside the mold wall. To properly simulate the heat exchanges across the mold cavity, thermal and kinetic properties of the composite (and mold) must be appropriately characterized. The thermo-chemical and viscoelastic models for a glass/polyester composite are taken from [2]. It was experimentally found that long after the gel point the resin elastic modulus is still very low, for a polymerization degree less than 40%. This degree of polymerization, called *After Gel Point* (AGP) [2], was then taken as base line to analyze the evolution of mechanical properties. Properties and durability of composite parts are strongly affected by processing stresses. Excessive stress levels may lead to important defects during cure or after processing, when the part is cooled to room temperature. A comprehensive curing optimization algorithm should account for the internal stresses that appear during composite processing and aim at reducing these stresses. Processing stresses can be calculated by the Classical Laminate Theory (CLT) in a one-dimensional analysis. In this investigation, the one-dimensional energy equation was coupled to the CLT equations to evaluate the internal stresses developed during part processing [3].

Evolutionary algorithms

During the last years, Evolutionary Algorithms (EA) have received increasing attention in numerous research and industrial applications. Generally, EA outperform conventional optimization algorithms for problems which are discontinuous, non-differential, include multi-modal noise and are not well defined [4]. In the applications to LCM optimization, EA are often coupled to numerical process simulation. In order to evaluate the objective function (or *fitness* function) for a given set of process parameters (called *design variables*), numerical simulation of the process must be carried out for these design variables. In the case of curing optimization, the energy and kinetic equations must be computed for a set of thermal boundary conditions selected by the optimization algorithm. This means that optimization may become infeasible if the numerical evaluation of the fitness function requires large computational efforts.

The use of one-dimensional process modeling presents the advantage of being not too time consuming compared to two or three-dimensional finite element simulations. This allows performing a large number of evaluations (such as required by the EA optimization) in a relatively short computer time.

Problem identification

In this investigation, seven functions have been identified to describe the competing objectives of process efficiency versus part quality. The final fitness function to be minimized is a weighted combination of these partial objectives. The seven sub-objective functions proposed can be summarized as follows:

1) Maximum final extent of cure (J_{fc}).
2) Minimum processing time (J_{time}).
3) Minimum exothermic peak temperature ($J_{T_{max}}$).
4) Minimum curing internal stresses (J_{stress}).
5) Minimum cooling stresses ($J_{cooling}$).
6) Constant trough-thickness degree of cure at AGP level (J_{AGP}).
7) Minimum through-thickness cure gradients after AGP level (J_{cure}).

Optimization procedures based on EA usually exhibit low convergence rates, requiring sometimes an exorbitant number of evaluations of the fitness function. It has been shown that the use of Gauss-Sigmoid fitness functions strongly increases the learning speed of EA [5]. In this work, the sub-objective functions were written in the form of unitary sigmoids (varying from 0 to 1) to increase the convergence rate of the optimization algorithm [3]. Considering that an improved LCM mold contains heating/cooling elements, a desired (i.e., optimized) temperature profile can be imposed during processing. In this investigation, the mold temperature profile is discretized in a series of heating and cooling ramps Q_i and dwell times dt_i (i.e., design variables to be optimized). The degree of success of a set of design variables (Vd) can then be quantified by a weighted combination of the sub-objective functions. The cure-cycle optimization in LCM can thus be stated as follows:

$$\text{Minimize the sigmoid:} \qquad F_f(Vd) = \frac{A_f}{B_f + e^{-F_\omega C_f}} + D_f \qquad (1)$$

$$\text{subject to:} \qquad Vd \in Cs \qquad (2)$$

$$\text{with:} \qquad Vd = [Q_1, dt_1, Q_2, dt_2, ..., Q_n, dt_n]; \qquad Cs = [Q_{max}^+, Q_{max}^-] \qquad (3)$$

$$F_\omega = \omega_{fc} J_{fc} + \omega_{T_{max}} J_{T_{max}} + \omega_{AGP} J_{AGP} + \omega_{cure} J_{cure} + \omega_{stress} J_{stress} + \omega_{cooling} J_{cooling} + \omega_{time} J_{time}$$

where $F_f(Vd)$ is the fitness function to be optimized, and A_f, B_f, C_f and D_f are the coefficients of the sigmoid. Parameter Cs represents the constraints of the design vector Vd (i.e., the maximum mold heating/cooling ramps). Parameters ω are the weighting coefficients for each sub-objective function implemented to take into account a particular concern in the optimization procedure.

Note that the use of sigmoid sub-functions scaled between 0 and 1 simplifies the setting of the weighting coefficients. In fact, the default value of the weighting coefficients is 1, which indicates that the minimization of the fitness function considers proportionally the effects of each sub-objective function. Finally, an optimization algorithm called *LeCoq* (Logical Evolutionary Curing Optimization and Quenching) based on EA was developed to minimize the fitness function $F_f(Vd)$ [3].

RESULTS AND DISCUSSION

A simple curing cycle is now studied for a 20 *mm* thick glass/polyester composite [3]. The selected two heating ramps curing cycle (see fig. 1) has two variables: the first heating ramp Q_1 and the first dwell time dt_2, while the other parameters are fixed. By changing Q_1 and dt_2, a two-dimensional search space can be defined. The goal of this optimization is to minimize curing stresses and processing time. Because the curing temperature (T_3) is fixed, function J_{fc} can be neglected. Note that function $J_{cooling}$ is also be neglected in this example. Two different optimization strategies are tested for this thick part. In the first case, it is assumed that residual stresses can be minimized directly by minimization of the cure gradients. This means that only J_{AGP} and J_{cure} sub-objective functions need to be used to reduce curing stresses. To account for processing time and matrix degradation, the sub-objective functions J_{time} and J_{Tmax} are included in the fitness function. The weighting coefficients of such optimization become:

$T_{init} = 30\ ^{\circ}C$
$T_3 = 130\ ^{\circ}C$
$Q_3 = 9\ ^{\circ}C/min$
$Q_2 = Q_4 = 0.$

$dt_1 = 41\ min.$
$dt_4 = 60\ min.$

$T_2 = T_{init} + Q_1\ dt_1$
$dt_3 = (T_3 - T_2)/Q_3$

$$\omega_{AGP} = 1 \qquad \omega_{cure} = 1$$

$$\omega_{time} = 0.75 \qquad \omega_{T_{max}} = 0.75 \qquad (4)$$

$$\omega_{stress} = 0 \qquad \omega_{cooling} = 0 \quad \omega_{fc} = 0$$

$$0 < Q_1 < 1.5\ ^{\circ}C/min \qquad (5)$$

$$0 < dt_2 < 85\ min$$
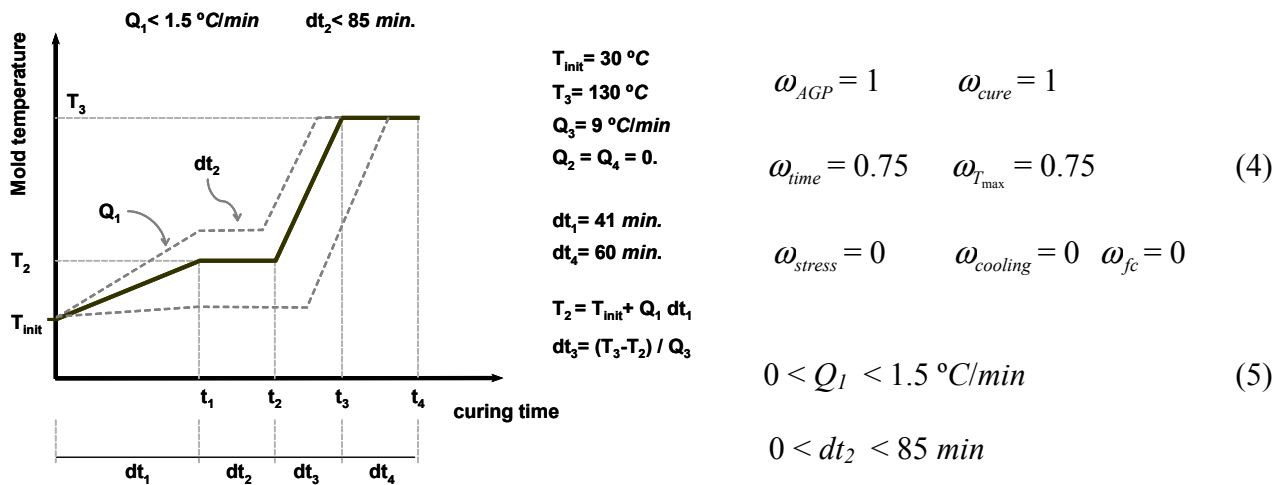
Fig. 1 Curing cycle used for the optimization of the 20 *mm* thick composite.

The two design variables were progressively increased, which resulted in the functional space drawn in the contour plot of fig. 2.a. A ditch of near optimum values vertically divides the fitness representation into two zones. At low values of Q_1 (zone 1), excessive processing times dominate the fitness function (i.e., $J_{time}=1$). Increasing Q_1 (zone 2), the processing time decreases, but an *outside-to-inside* cure appears resulting in high cure restrictions, although the contour plot is lighter than in zone 1. Between these two regions, the minimum (dark vertical ditch) can be found at the limit where the *inside-to-outside* cure changes to an *outside-to-inside* cure.

This temperature profile was then optimized using the *LeCoq* code, which found the optimum value shown in fig. 2.a. The second case consists of a full optimization, in which curing stresses are added to the previous optimization (i.e., in this case J_{stress}=1). Fig. 2 shows contour plots of the fitness function. Note that in this case, curing stresses are high and transform zone 2 of the previous case into a dark region, thus reducing the near optimum space into a thin knife-shaped region. Moreover, in this full optimization, the optimum value changes considerably from the previous solution (i.e., the solution without stress analysis).
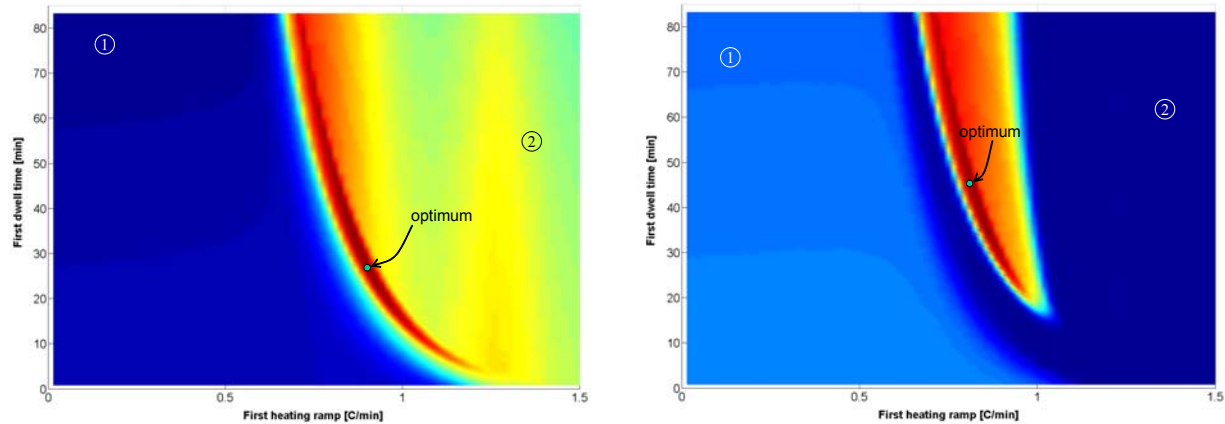
Fig. 2. Contour plots of the fitness function for the two heating ramps curing cycle: (left) without considering internal stresses; (right) considering internal stresses (full optimization).

CONCLUSION

In this investigation, a methodology is proposed for the optimization of the curing cycle in LCM manufacturing. Seven optimization criteria are presented to account for the minimum cycle time, maximum extent of cure, minimum exothermic temperature, minimum cure gradients and minimum curing and cooling stresses. The temperature profile to be optimized is discretized in a series of heating/cooling ramps and dwell times. An evolutionary algorithm was implemented to minimize the fitness function. The proposed methodology, used to minimize the cycle time and residual stresses in a 20 *mm* thick composite, was found to be a useful tool to improve composite cure while reducing processing stresses (i.e., part defects) for a minimum cycle time.

REFERENCES

1   Edu Ruiz, "De la Caractérisation des Matériaux et Simulation du procédé à l'Optimisation de la Fabrication des Composites par Injection sur Renfort", *PhD. Thesis*, *École Polytechnique de Montréal*, 2004, pp. 500.

2   Edu Ruiz, and F. Trochu, "Thermo-Mechanical Properties during Cure of Glass-Polyester RTM Composites: Elastic and Viscoelastic Modeling", submitted to *J. Composite Materials*, Oct. 2003.

3   Edu Ruiz, F. Trochu, and R. Gauvin, "Internal Stresses and Warpage of Thin Composite Parts Manufactured by RTM", accepted in *Advanced Composite Letters*, Sept. 2003.

4   H.-P. Schwefel, *Evolution and Optimum Seeking*, Wiley ed., 1995, pp. 456.

5   K. Shibata, and K. Ito, "Gauss-Sigmoid Neural Network", *Proceedings of Int. Joint Conference on Neural Networks IJCNN'99*, Washington, DC, USA, 1999.

6   Edu Ruiz, and F. Trochu, "Comprehensive Thermal Optimization of Liquid Composite Molding to Reduce Cycle Time and Processing Stresses", submitted to *Polymer Composites*, Dec. 2003.

Characterization of Defects in
Low-Cost Resin-Infused Aeronautical Structures

L. Petrescue[1], P. Hubert[2], S. Gordon[3], A Johnston[1], and M. Munro[4]

[1]*Institute for Aerospace Research, National Research Council Canada, Ottawa, ON, Canada K1A 0R6 Corresponding Author's e-mail: laura.petrescue@nrc-cnrc.gc.ca*
[2]*Dept. of Mechanical Engineering, McGill University, Montreal, QC, Canada H3A 2K6: pascal.hubert@mcgill.ca*
[3]*Flight Dynamics Corp., Saint-Jean-sur-Richelieu, QC, Canada J3B 7B5: gordons@flightdyn.com*
[4]*Dept. of Mechanical Engineering, University of Ottawa, Ottawa, ON, Canada K1N 6N5: munro@eng.uottawa.ca*

SUMMARY: Mechanical tests have shown that vacuum assisted resin transfer molding (VARTM) produces consistent, high quality solid laminates made with E-glass/epoxy vinyl ester. However, these laminates have never been employed in certified aeronautical structures and the process for certification of sandwich structures is even more complex. The objective of this work was to develop an understanding of process-induced defects in E-glass/epoxy vinyl ester sandwich panels with a PVC closed cell foam core, fabricated using VARTM. A variety of non-destructive evaluation (NDE) techniques were used to establish their potential for identifying these defects and to correlate the results with visual observations. It was found that thermography and bondline analysis were effective at detecting and characterizing defects such as dry spots and incomplete resin infiltration. Preliminary evaluations of the flow rate under the influence of processing excursions showed that even a small air leak could increase infiltration time by as much as 25%.

KEYWORDS: VARTM, defects, sandwich structure, closed-cell foam core, fiberglass, non-destructive evaluation

INTRODUCTION AND BACKGROUND

E-glass/epoxy vinyl ester composites fabricated by the vacuum assisted resin transfer molding (VARTM) process have shown excellent potential in a range of applications, including kit aircraft, but have never been employed in certified aeronautical structures. Certification-related mechanical tests have shown that VARTM produces consistent, high quality solid laminates [1]; however, the more complex certification of sandwich structures has yet to be addressed. To support this certification process, an understanding of process-induced defects is critical. Previous work in the area of the effect of defects on composite structural performance has shown that tensile, flexural and shear strengths were reduced in the presence of defects such as dry fibers, interfacial cracks, or inclusions in the skin [2].

For example, studies have shown that interfacial cracks artificially induced by Teflon inserts can have an adverse effect on shear strength after they reach a critical length between 25 and 30 mm [3]. However, only limited work has been performed specifically on the evaluation of process-induced defects [4]. The aim of this work was to gain a better understanding of the flow patterns and process-induced defect development in a particular VARTM process variant. An analysis of the flow through the fiber preform was carried out and an assessment of the commonly occurring defects, along with the NDE techniques to detect them, was performed.

EXPERIMENTAL APPROACH

Specimen Fabrication

Trials were performed on 7781 E-glass and PVC closed cell foam core sandwich structures with Derakane Momentum 411-350 epoxy vinyl ester resin (Fig. 1). The core material had a density of 86.5 kg/m^3 and a thickness of 6.4 mm. Three plies of 0.5 mm thick glass fabric were used for the sandwich panel skins. One layer of distribution medium was placed on the top skin. Infiltration of the bottom skin was accomplished by an array of small holes drilled in the foam core. The hole spacing was set to 25.4 mm and 30 mm in the panel width and flow directions, respectively. Specimens were fabricated in an instrumented VARTM test cell where the flow front evolution was recorded by two digital cameras mounted above and below a glass tool plate. Prior to the infusion, the resin viscosity was adjusted to 275 cP by adding monomeric styrene. The vacuum pressure was adjusted to 96.5 kPa and the infusion was performed at room temperature (20 °C).

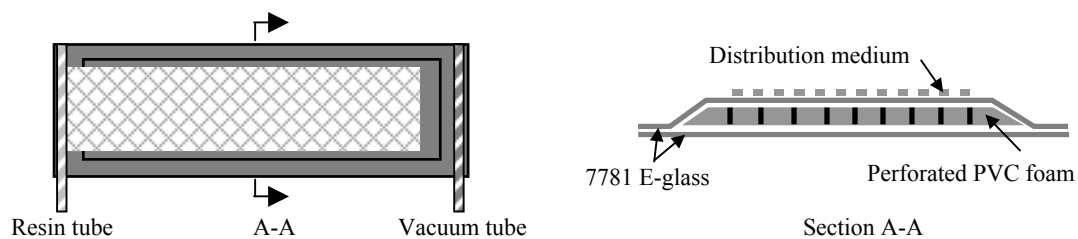Fig. 1 Schematic of sandwich panel specimen

Non-Destructive Evalutaion

A series of non-destructive evaluation techniques were used to examine two representative specimens containing a dry spot and exhibiting incomplete resin infiltration. These specimens were examined using image analysis, edge of light (EOL), thermography, ultrasonic (UT) C-scan, X-radiography, and bondline testing [5,6].

RESULTS AND DISCUSSION

Identification of Defects

A trial and error approach was used to fabricate specimens containing process-induced defects and resulted in the identification of three types of defects: bubbles, dry spots, and incomplete resin infiltration. Bubbles were categorized as air that infiltrated the resin during infusion because of vacuum bag leakage. Two common sources of leaks appeared to be poor vacuum bag integrity caused by damage or aging, and degradation of the seal between the bag and the tool. These problems were easy to rectify prior to infusion by monitoring the pressure of the bag after the vacuum pump was turned off. The flow disturbances resulting from an undetected leak were analyzed using a flow rate image analysis program and are reported in Fig. 2. It was clear that even a small leak could significantly affect the specimen infiltration time, since the presence of such a leak increased the specimen total infiltration time by 25%, from 16 minutes to 20 minutes.
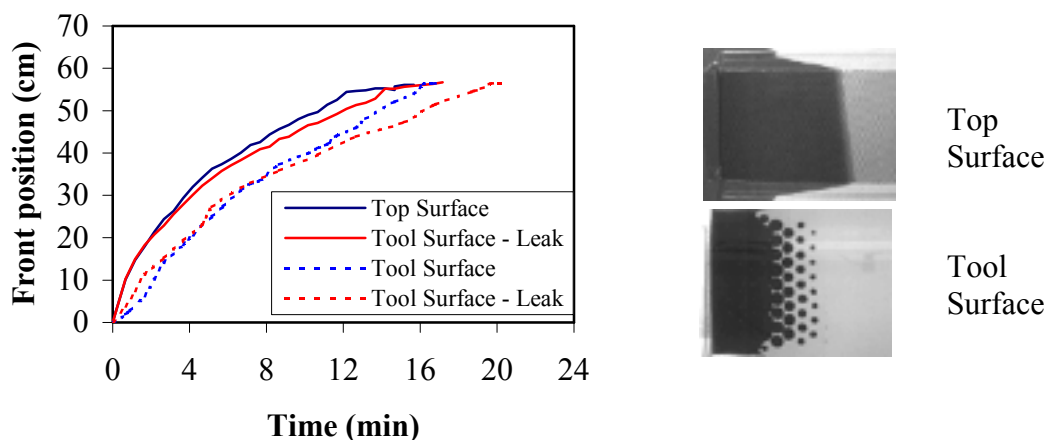

Fig. 2 Effect of vacuum bag leak on top and tool side flow front position and typical specimen infiltration pattern.

Two other defects, dry spots and incomplete resin infiltration, were examined by a number of non-destructive inspection (NDE) techniques. Dry spots occurred where resin did not saturate the preform due to race-tracking on an alternate flow path. It was observed that depending on the location of the dry spot, if the gel time was sufficiently long and the resin viscosity remained sufficiently low, then any dry spots would eventually become saturated with resin unless the resin reached the vacuum port first. Incomplete resin infiltration was related to the flow of the resin through the infiltration holes in the foam core. In some cases, the resin did not fully coalesce on the tool side of the part so the resin flow pattern could be detected.

Summary of NDE results

One specimen with a visually evident dry spot and one specimen with incomplete resin infiltration were analyzed with the NDE techniques identified previously. With the exception of bondline analysis and X-radiography, images from each NDE method are included in this paper. Although newer bond-testing equipment has a recorded output, the bondline analysis equipment available at NRC does not have this capability.

However, manual results indicated that this method was very effective for detection of most of the visible defects. The X-radiography results provided visual analysis of the defects, but only very large defects were apparent, even with the aid of high intensity light and magnification. Therefore, this technique is not recommended for these types of specimens with similar defects. The NDE images acquired for a specimen with a dry spot are summarized in Fig. 3.
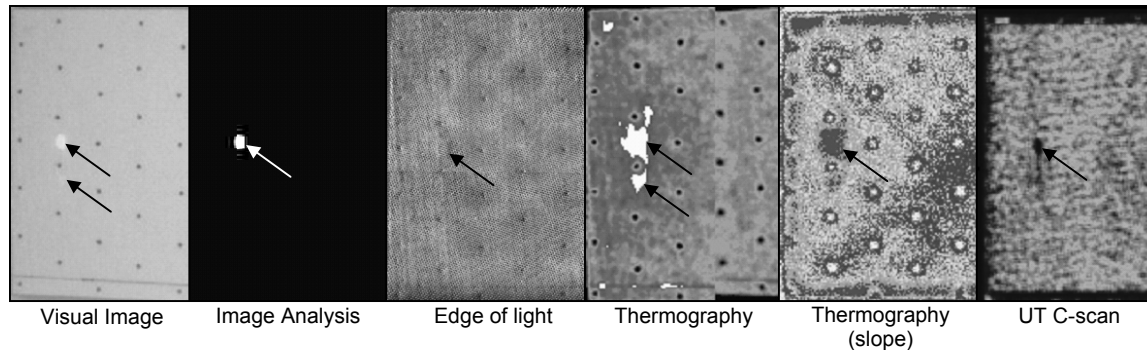

Fig. 3 Results of NDE of specimen containing a dry spot

The first image on the left shows the extent of the defect apparent to the naked eye, including a very obvious dry spot with a smaller spot beneath. The larger dry spot was detectable by all of the NDE techniques shown; however, the smaller spot could only be identified in the thermography images. It should be noted that the results from the UT C-scan image were not conclusive since similar signals that did not correspond to dry spots appeared elsewhere on the specimens. It is obvious that thermography provided a clear image of the defects and the most conservative estimate of the extent of the defect. It will be necessary to perform destructive inspection to determine if the extent of the defect is more closely represented by the infrared image or the slope of the infrared image. Similar NDE analysis was performed on a specimen that experienced incomplete resin saturation, as shown in Fig. 4
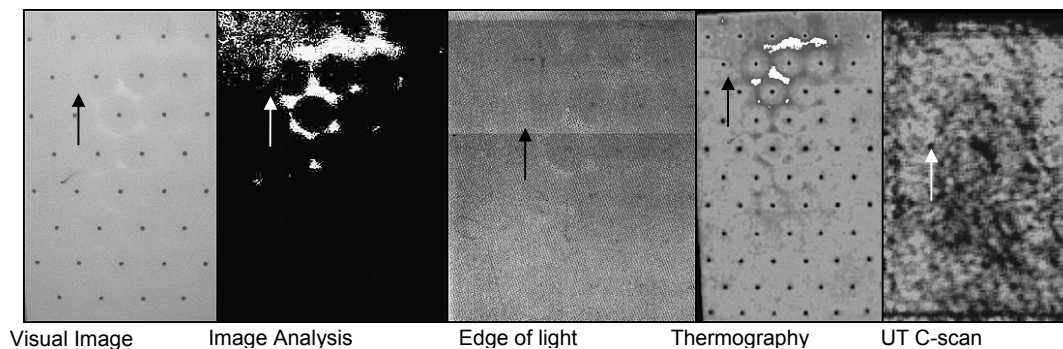

Fig. 4 Results of NDE of specimen containing incomplete resin infiltration

The image on the left again shows the extent of the defect that was visually evident. With the exception of the UT C-scan image, each technique was able to identify the defect. In fact, with thermography and image analysis, the extent of the defect is apparently larger than in the visual image.

The UT C-scan did not provide a clear representation of the defect and therefore, was not used for further investigations. While EOL was capable of detecting the defects, it was more time consuming and would only detect the defect if there were associated surface anomalies.

CONCLUSIONS

Several NDE techniques were evaluated for their ability to characterize process-induced defects. This work showed that thermography was a very effective method. There is also potential in bondline analysis provided that it includes a recorded output. Further work must evaluate the defects to develop a system of defect metrics that could be used for modeling applications. Preliminary studies on the effects of process parameters on part quality showed that there was a significant effect of vacuum pressure loss on both the development of defects and the resin flow rate.

ACKNOWLEDGEMENTS

REFERENCES

[1] R. Boukhili, et al., Mechanical Properties for Low Pressure Resin Infusion Processed Vinyl-Ester/Glass Composites, *Final Report prepared for Flight Dynamics Corporation, CDT project 2731,* École Polytechnique de Montréal, QC (2002).
[2] A.P. Mouritz and R.S. Thomson, Compression, flexure and shear properties of a sandwich composite containing defects, *Composite Structures*, **44**, 263-278 (1999).
[3] R.S. Thomson, et al., Shear properties of a sandwich composite containing defects, *Composite Structures*, **42**, 107-118 (1998).
[4] P. Majumdar, et al., Effect of processing conditions and material properties on the debond fracture toughness of foam-core sandwich composites: experimental optimization, *Composites Part A: applied science and manufacturing*, **34**, 1097-1104, (2003).
[5] G. M. Light and H. Kwun, Review of NDE Methodology of Adhesive Bond Strength Determination, NDE of Adhesive Bonds and Bondlines ASNT Fall Conference: Topical Proceedings, Valley Forge, PA, Oct 9-13, 1989.
[6] C.C.H. Guyott, et al., The non-destructive Testing of adhesively bonded structure: A review, *J. Adhesion*, **20**, 129-159 (1986).

Characterization of Random Long Fiber Composites and Prediction of the Local Stiffness Properties

E. Jao Jules [1], S. Lomov [1], I. Verpoest [1]

[1] *Department of Metallurgy and Material Science (MTM), Katholieke Universiteit Leuven, Kasteelpark Arenberg, 44 B-3001 Heverlee, BELGIUM: Ericka.JaoJules@mtm.kuleuven.ac.be*

SUMMARY: Long glass fiber polypropylene (LGFPP) composites become more and more attractive because they enable easy, low cost part production and good mechanical properties for stiffness, durability and impact. Fiber breakage and local change in orientation occur during the processing of those composites, especially in injection-molding. Fiber length and fiber orientation distributions were measured experimentally and were then used as one of the inputs in the elastic model to get the stiffness properties of the composite, taking into account the local microstructure of the material. The model is based on the inclusion model approach, namely Mori and Tanaka model, and can predict all the engineering constants. A comparison of the results of this model with other models from literature shows good agreement for elastic moduli. In this work the effects of fiber length distribution and fiber orientation distribution on final elastic properties of LGFPP composites were investigated. The length and orientation of the fibers play an important role in the determination of final mechanical properties of LGFPP composites.

KEYWORDS: random, discontinuous long-fiber composites, fiber-length distribution, fiber-orientation distribution, stiffness properties, Mori and Tanaka method.

INTRODUCTION

The use of glass fiber reinforced polypropylene composites in engineering applications increases more and more these last years. Especially, long glass fiber polypropylene (LGFPP) composites offer specific advantages over classical laminates such as higher production rates at lower costs, improved thermal and mechanical properties. However during injection molding of the part fiber breakage occurs, leading to a distribution of fiber lengths inside the material. Moreover a change in orientation of the fibers also takes place during injection process, leading to micro-structural variations that affect the overall mechanical properties of the composite. Hence, the final properties of LGFPP composite are highly dependent on the processing conditions of the part. Therefore the effect of fiber length on the mechanical properties of injection molded LGFPP composites must be combined with the effect of fiber orientation changes because the two effects would determine the final mechanical properties of these composite materials [1].

First, microstructural characterization of LGFPP was performed, using the resin burnout technique to get the fiber length distribution and optical microscopy method (applied to a polished cross-section) to obtain the fiber orientation distribution. Fiber and matrix properties and experimental data on fiber length and orientation distributions were used as input in a software based on Mori and Tanaka method. This was coupled with a Monte-Carlo simulation, which was developed to predict local mechanical properties of LGFPP composites, taking into account the real microstructure in the part.

EXPERIMENTAL

Materials

This work was conducted in collaboration with DOW Automotive, which provides all the materials employed in this investigation in addition to material, CAE, process, testing and application knowledge. The composite material for the study, produced by injection molding, is made of polypropylene reinforced with long glass fibers. The initial length of the fibers was 11 mm and the fiber content was 20% fibers by weight.

Fiber length measurement

To measure the fiber length distribution first the composite material is burnt out in a classical oven. After burning, entangled fibers remain, and some fibers are extracted from the sample and dispersed in a glass dish filled with liquid and stirred carefully to detach the fibers. The liquid is removed and the dish is heated in an oven until vaporised. The dish is then placed under the microscope. Magnified images of fibers are digitised by image analysis software and fiber length distribution is thus determined.

Fiber orientation measurement

Optical microscopy on polished cross-sections was used to measure orientation. This method is based on the fact that individual fibers are assumed to have a circular cross-section, which is the case for the glass fibers [2]. As the intersection of a straight circular cylinder and a plane gives an ellipse, by determining the principal axes of the ellipse, (Fig. 1), the out of plane orientation (θ) is computed from Eqn. 1 [3], exactly valid for an infinite fiber but the difference counts only for an out of plane angle bigger than 89.95°, which is assumed equal to 90°. The in-plane orientation of the fiber (φ) is given directly by the image analysis software.

$$\theta = \cos^{-1}(b/a) \tag{1}$$
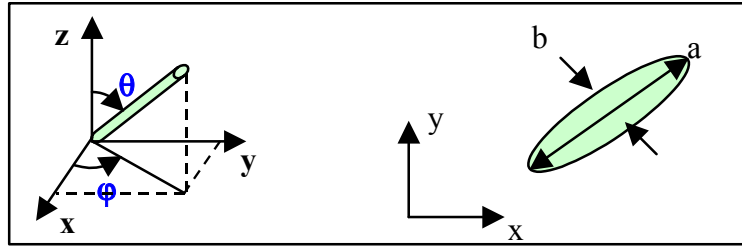
Fig. 1 Elliptical cross-section of a cylindrical fiber cut by a plane

RESULTS AND DISCUSSION

Fiber length

The fiber length distribution obtained for a LGFPP composite is shown Fig. 2. The maximum fiber length is 10.75 mm and the minimum fiber length: 0.5 mm. The mean value, calculated from those experimental data, is: 5.3 mm and the standard deviation is: 2.4.
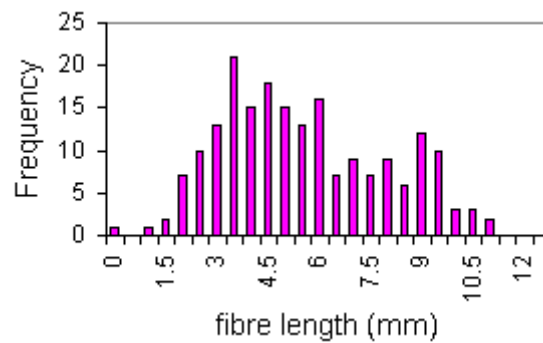
Fig. 2 Fiber length distribution

Fiber orientation

In-plane orientation

Fig. 3 presents the result of the in-plane orientation distribution obtained for the upper surface of the material. We notice that most of the fibers are oriented between 80 and 100°, which corresponds to the flow direction of the injection molding process.

Fig. 3 In-plane orientation distribution

Fig. 4 Out of plane orientation distribution

Out of plane orientation

The distribution of the out of plane orientation (Fig. 4) shows that majority of fibers are oriented between 80 and 90°, which means that the fibers are mainly in plane. The histogram bin closest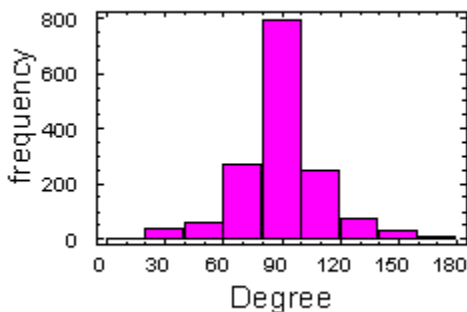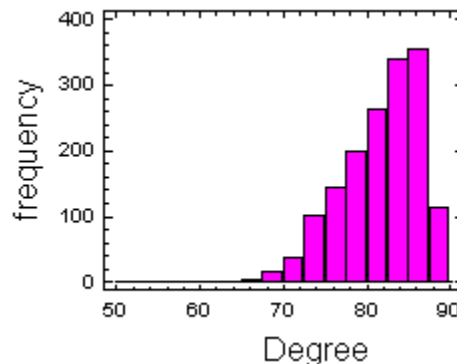 to 90° is determined with large inaccuracy. Fibers oriented at out of plane angle close to 90° have less probability to be cut by a cross-section at a fixed depth than the fibers with lower out of plane angles.

Mechanical properties

A software programme based on the Mori and Tanaka model was developed to predict local mechanical properties of LGFPP [4]. The fibers in the unit cell are modeled by inclusions of an ellipsoid shape. The length and orientation of each inclusion is determined individually by sampling the experimental distribution for length, in-plane and out of plane orientations respectively, using a Monte Carlo simulation. In this way, each inclusion is assigned a unique, independent value for length, in plane orientation and out of plane orientation. Knowing the materials properties, listed in Table 1, the elastic micro-mechanical calculation can then be performed giving the total stiffness tensor of the composite material.

	Matrix	Fibers
Density : ro (g/cm^3)	0.9	2.54
Young's moduli: E = Et (MPa)	1000	70 000
Poisson's ratios: Po = Pot	0.33	0.23
Shear moduli: G = Gt (MPa)	588	29 268
Fiber diameter : d (mm)		0.017

Table 1 Materials properties used in the micro-macro calculation

Fiber length effect

Elastic properties of unidirectional (UD) LGFPP composites were calculated for different constant fiber length values with 10% fibers in volume (24.6% by weight).

According to the results, longitudinal Young's modulus increases with fiber length until a limit length value of 4 mm where the modulus approaches an asymptote equal to the modulus of UD glass polypropylene composite laminate. To validate the modeling results, a comparison was done with UD models such as empirical models (Cox and Tsai-Halpin) and three Finite Element models performed by DOW Automotive (Fig. 5). Different geometries of the composite cell were simulated in FEA models: a single cylindrical fiber embedded in a square matrix cell (FEA1), a single fiber embedded in a circular matrix cell (FEA2), and a cylindrical cell containing more fibers (FEA3).
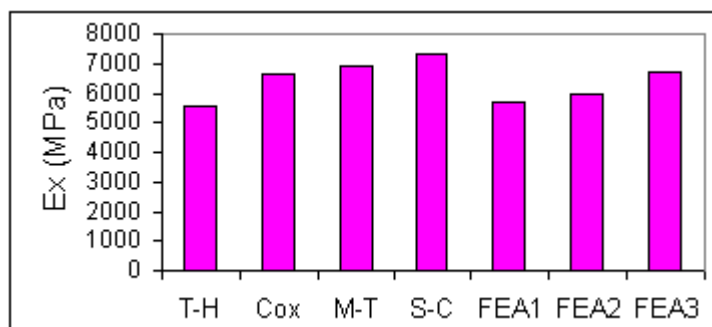

Fig. 5 Longitudinal modulus obtained from different models: Mori and Tanaka (M-T), self-consistent (S-C), Tsai-Halpin (T-H), Cox, Finite Element Analysis (FEA) with l = 3 mm

The Tsai-Halpin model gives the lowest modulus whereas the Cox model and FEA3 give equivalent result. The reason is that in a Cox model, other fibers surround the fiber so the effect of those fibers is taken into account, as is the case in the finite element model with multiple fibers. As the Mori and Tanaka model also takes into account the other fibers, its predicted modulus value is close to the one of Cox. FEA1 and FEA2 have different composite moduli, which means that the geometry of the composite cell can affect the stiffness of the composite material. Finally as usual, the self-consistent model predicts a higher modulus compared to the Mori and Tanaka model because in the first model the fiber is embedded in a matrix with properties of the composite material and not the properties of the matrix like in the second one.

Fiber orientation effect

To understand the effect of the fiber orientations on the final mechanical properties of LGFPP composites, calculations were done for composite material with all fibers aligned in y direction (UD: Table 2, column 2), composite material with in-plane experimental orientation distribution and an out of plane angle equal to 90° for all the fibers (Table 2, column 3). Finally, experimental distribution of in-plane orientation was combined with out of plane orientation distribution to take into account the effect of out of plane orientation (Table 2, column 4). In the three cases, a fiber content of 20% by weight was considered and the experimental fiber length distribution (Fig. 2) was used.

	UD ($\varphi = 90$, $\theta = 90°$)	$\{\varphi_i\}$ and $\theta = 90°$	$\{\varphi_i\}$ and $\{\theta_i\}$
E_x (MPa)	1246 ($\pm$ 5)	1670 ($\pm$ 92)	1629 ($\pm$ 78)
E_y (MPa)	6564 ($\pm$ 179)	5027 ($\pm$ 185)	4614 ($\pm$ 164)
E_z (MPa)	1246 ($\pm$ 5)	1341 ($\pm$ 12)	1309 ($\pm$ 11)

ν_{yz}	0.32	0.25	0.33
ν_{zx}	0.46	0.33	0.33
ν_{xy}	0.06	0.15	0.15
G_{yz} (MPa)	441 ($\pm$ 2)	438 ($\pm$ 2)	533 ($\pm$ 11)
G_{zx} (MPa)	428 ($\pm$ 2)	430 ($\pm$ 2)	451 ($\pm$ 5)
G_{xy} (MPa)	441 ($\pm$ 2)	863 ($\pm$ 43)	835 ($\pm$ 44)

Table 2 Comparison of mechanical properties for a composite material with 20% fibers by weight, with experimental fiber length distribution for different orientations

By taking into account the experimental distribution of out of plane orientation Ey decreases by 8%; the transversal shear moduli increase whereas G_{xy} decreases, which is normal since the fibers are not totally in-plane like when $\theta = 90°$.

CONCLUSION

The length and orientation of the fibers play an important role on the final elastic properties of LGFPP composites, so their local distributions must be known. Elastic modeling results are satisfactory and showed the anisotropy of LGFPP composites. In the future, the model will be extended to include damage development in the fibers and the fiber/matrix interface.

REFERENCES

1.   W. Chin, H. Lui, Y. Lee, "Effects of fiber length and orientation distribution on the elastic modulus of short fiber reinforced thermoplastics", *Polymer. Composites*, Vol.9, no 1, 1988, pp. 27

2.   G. Fischer, P. Eyerer, "Measuring spatial orientation of short fiber reinforced thermoplastics by image analysis", *Polymer Composites*, 1988, pp.9

3.   C. L. Tucker III, S. G. Advani, "Flow and Rheology in Polymer Composites Manufacturing", *Processing of Short-Fiber Systems*, 1994, Chapter 6

4.   G. Huysmans, "Unified micromechanical models for textile composites", *Ph.D*. KU Leuven, 2000

Influence of Stamp Forming Parameters on Final Part Properties of Hydroxyapatite Filled Ethylene Vinyl Acetate Co-Polymer Composites

Shiny Velayudhan[1, 2], P. Ramesh[2], H. K. Varma[2], S. Schmitt[1], and K. Friedrich[1]

[1]Institute for Composite Materials (IVW GmbH), University of Kaiserslautern, Germany.
[2]Sree Chitra Tirunal Institute for Medical Sciences & Technology, Trivandrum, India.
Corresponding Author's e-mail: rameshsct@yahoo.com

SUMMARY: Hydroxyapatite (HAP) filled ethylene vinyl acetate co-polymer (EVA) composites are potential candidates for craniofacial applications. A cost effective technique for obtaining these composites in the clinically significant forms would indeed be a landmark accomplishment. Stamp forming is one of such processes where the cost as well as the performance of the product strikes the right balance. This study was carried out prior to the stamp forming process optimization of the composites into 3-D contours, essential for applications like cranioplasty. In particular, experiments with regard to the development of a two-dimensional stamping method for processing of HAP filled EVA composites using an angle mold (90°) were carried out. The processing conditions like the stamping temperature, time, and stamping rate required to give high-quality right angle bends were established. The quality of stamped forms was gauged in terms of physical appearance, shape conformance and variation in wall thickness. It was found that the stamping temperature and velocity were the key factors, which determined the quality of the stamped part. Too high temperatures, and stamping rates led to severe thinning and degradation of the formed parts, while too low temperatures and stamping rates did not conform the composite to the mold contour. A processing window in terms of stamping velocity and stamping temperature was also established.

KEYWORDS: composite; hydroxyapatite; part quality; polymer; stamp forming, two-dimensional.

INTRODUCTION

Hydroxyapatite (HAP) filled ethylene vinyl acetate co-polymer (EVA) composites are developed in an attempt to formulate "surgeon friendly" material for renovating impaired skull contours. The bone-bonding ability of HAP and pliability of EVA makes the composite ideal for this purpose. In cranioplasty, pre-fabrication of cranioplastic implants using computerized 3-D imaging and automated milling are employed to reduce the operating time and to obtain excellent cosmesis. These techniques, however, are expensive and require a long manufacturing time. Stamp forming has proved to be very cost effective method that improves the performance/cost balance of reinforced polymeric composites via high-speed manufacturing and shaping process [1]. In the current study, we report about the influence of stamp forming parameters on final part properties of HAP-EVA composite forms fabricated using an angle mold (90°).

MATERIALS AND METHODS

Composite sheets having 40 vol.% HAP were used for the study. HAP for the preparation of the composite was synthesized by precipitation route involving ammoniated calcium nitrate and dihydrogen ammonium phosphate. The precipitated HAP was then converted into powder form by spray drying in a laboratory size mini spray drier (Buchi Mini Spray drier, B-181, Switzerland). Cryogenically ground EVA powder (Shriswasan Chemical (M) Pvt. Ltd., Mumbai, India) with particle size less than 300 μm. The polymer matrix contained 28 wt.% vinyl acetate content and a melt flow index (MFI) of 25. The melting temperature of the matrix was determined by differential scanning calorimetry as 68°C. Rectangular composite strips of dimensions (130 x 30) mm^2 were cut from the 2.3 mm thick composite plates, heated above the softening temperatures in a hot air oven and stamp formed using a right angle tool fitted in the 80 kN stamp forming press (HY-Power OP 2MI-TR8-115/30, Italy). The forming technique is schematically represented in Fig. 1 and the variables used for forming are given in table 1.
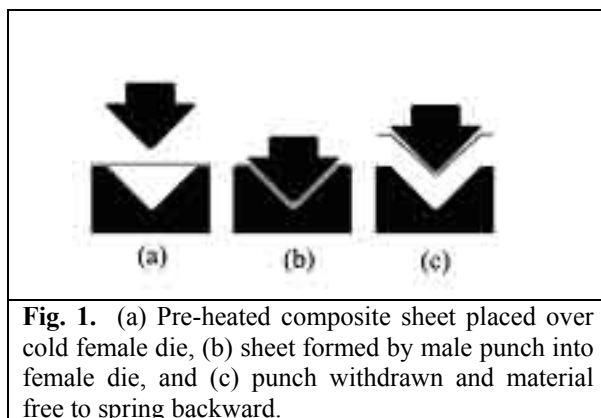

Fig. 1. (a) Pre-heated composite sheet placed over cold female die, (b) sheet formed by male punch into female die, and (c) punch withdrawn and material free to spring backward.

Table 1. Processing variables for forming	
Tool temperature, °C	25
Pre-heat temperature, °C	80-120
Pressure, MPa	6
Forming velocity, (mm/s)	80-250
Time at pressure, (sec)	60

The quality of stamped forms was gauged in terms of physical appearance, shape conformance and variation in wall thickness.

RESULTS AND DISCUSSION

Uniform thickness distribution, optimum average thickness and shape conformance are important properties for manufacturing high quality stamped parts economically. One of the key parameters to obtain a part of a good quality is the selection of the pre-heating conditions [2]. The material has to be heated to a point where it is pliable enough to be shaped while supporting its own weight during the heating/transporting process [3]. Since the hot laminate is exposed to a lower environmental temperature before mold contact and deformation take place, the use of a sufficiently high closing speed also plays an important role in successful forming. In this investigation, two pre-heating temperatures, i.e. 80, and 100 °C were employed. Heating the composite sheets above 100 °C led to excessive sagging and difficulty in handling of the sheet. A series of trial runs were performed in which the stamp velocity was varied in the range 80-250 mm/s. The stamped composite bends thus obtained were examined for the uniformity in part thickness and part angle formed.

For measuring the variation in the thickness of the formed bend, different positions were marked along the longitudinal axis of the bend (Fig.2 a & b) and the thickness at these positions were measured with the aid of a micrometer. As an example, the thickness variation as a function of position for stamp formed bend at 100°C pre-heating temperature and various stamping velocities is given in Fig. 3.

Fig. 2. (a) Schematic diagram of the bend with the longitudinal axis marked (b) the various positions on the bend at which the thickness was measured.

Fig. 3. Variation of wall thickness as the function of position of composite bends formed at 100°C.
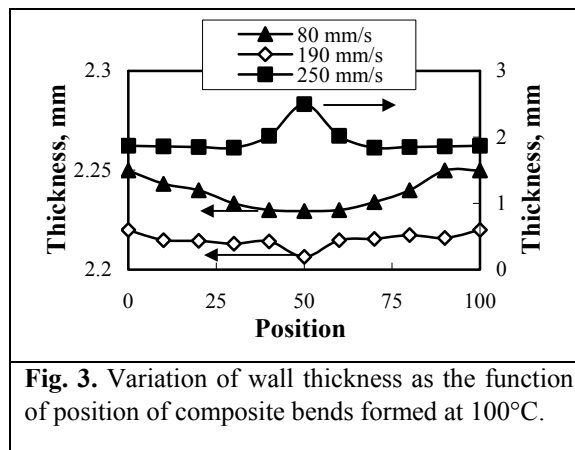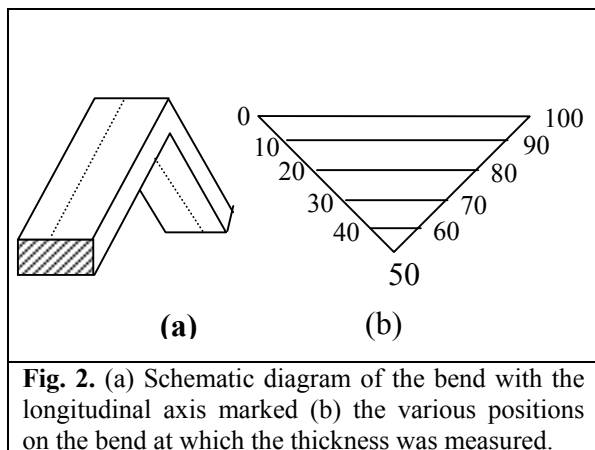
It is apparent from the figure that the quality of the formed bend is influenced by the variation of both the stamping temperature and stamping velocity. The thickness of the bends decreased with increase in stamping velocity. The nature of the thickness distribution curve for the bends formed at 80 mm/s and 190 mm/s stamping velocity was found to be similar. The formed parts had thinner walls at the bend and thicker at the sides of the V-bend. The average thickness of the part formed at 80 mm/s was, however, slightly higher than that formed at 190 mm/s. The thickness distribution of the composite formed at 250 mm/s had thicker walls at the bends and thinner towards the sides.

Stamp forming involves a complex mixture of material deformation processes and most forming processes do not yield parts having uniform wall thickness [4]. The variations in wall thickness of the formed contours have been found to be dependent on temperature and mode of deformation [5]. The observed variation in the wall thickness of the formed bend in the present study is the consequence of progressive draw down of the flat composite sheet into the mold (Fig. 4a).

Fig.4. (a) Schematic of progressive draw down of the composite sheet into the V-mold, (b) reduction in sheet thickness at the bends due to the progressive draw down.
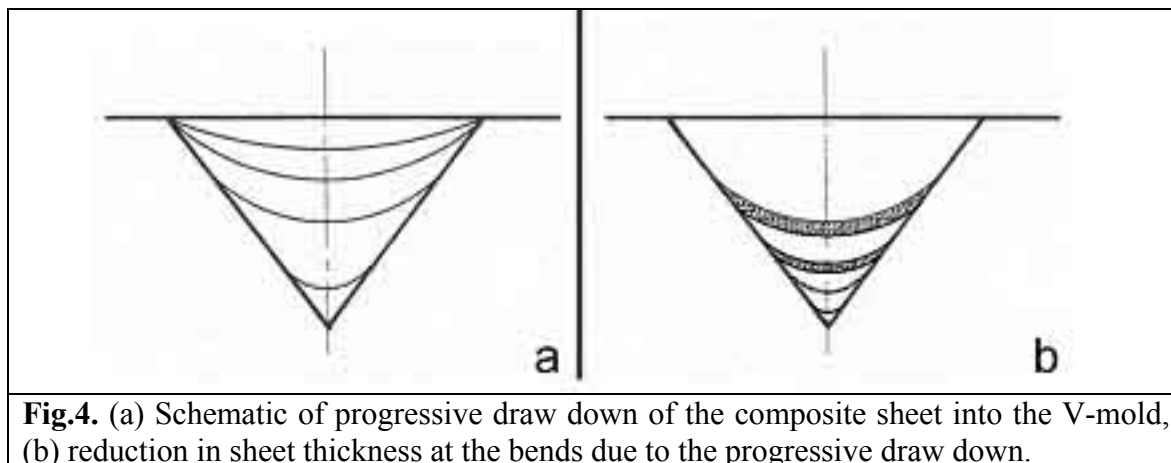
During the initial stages of stretching, the sheet contacts the closest flat surface of the mold while other areas of the sheet continues to stretch. The part of the sheet that touches the cold mold in the initial stages of forming cools down while the other areas of sheet that has yet to touch the mold is still hot. This leads to a non-uniform temperature distribution over the sheet under deformation, resulting in dissimilar material deformation histories. At the bends the sheet contacts the mold during the remote stages of forming operation. The sheet, in this area, thus undergoes biggest stretching and/or largest deformation resulting in the smallest wall thickness at the bends (Fig.4b). At 250 mm/s, the temperature of the sheet at the time of stamping is quite high. The high sheet temperature leads to the material stretching more, enabling more material to be pulled further down the mold resulting in incidence of a web formation at the bends.

The variation of part angle of the composite with respect to the stamping velocity and temperature is given in the Fig. 5.
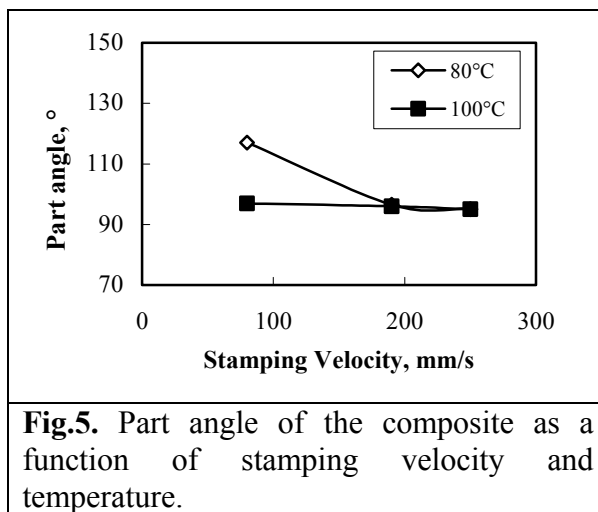

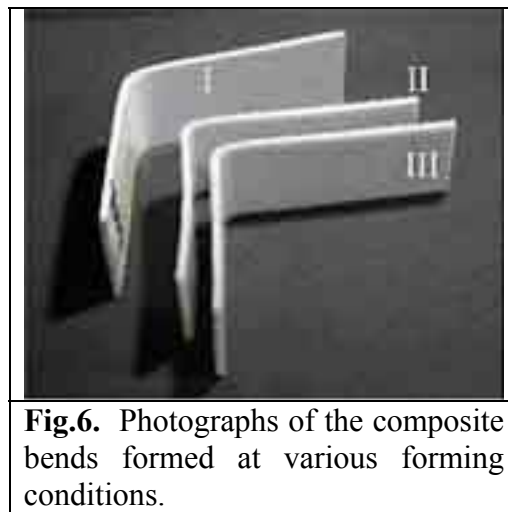**Fig.5.** Part angle of the composite as a function of stamping velocity and temperature.

Fig.6. Photographs of the composite bends formed at various forming conditions.

It is apparent from the figure that the measured angles of the formed bends are greater than 90°. This phenomenon is referred to as 'spring back' effect and results from the anisotropy of thermal properties of composite materials [6]. When the composite cools from the processing temperature to ambient temperature, the polymer matrix would contract more than the reinforcement HAP [α_{EVA} = 160 - 200 x10^{-6}/°C, α_{HAP} = 13 x10^{-6}/°C]. This leads to the development of residual thermal stresses within the composite bend. The stresses distort elastically, thus resulting in some degree of spring back. The formed angle is also influenced by the processing parameters employed. For example, severe distortion of the angle was observed when E28H40 was formed at 80mm/s stamping velocity and 80°C pre-heating temperature (I in Fig.6). The measured angle in this case was found to be 117°. Too low temperature and stamping velocity cools down the composite sheet making it stiff. As a result the sheet does not stretch easily and does not faithfully replicate the mold details. The formed angle decreased to 96° (II and III in Fig. 6) when formed at 100°C and 190 mm/s stamping velocity. This may be attributed to the more sufficient resin flow and the wider melted range at high working temperature.

CONCLUSIONS

HAP filled EVA composites could be successfully formed into two-dimensional contours with the aid of stamp forming technique. From the trials performed a schematic diagram of the processing window for 2-D forming of HAP-EVA composites could be evolved (Fig.6).
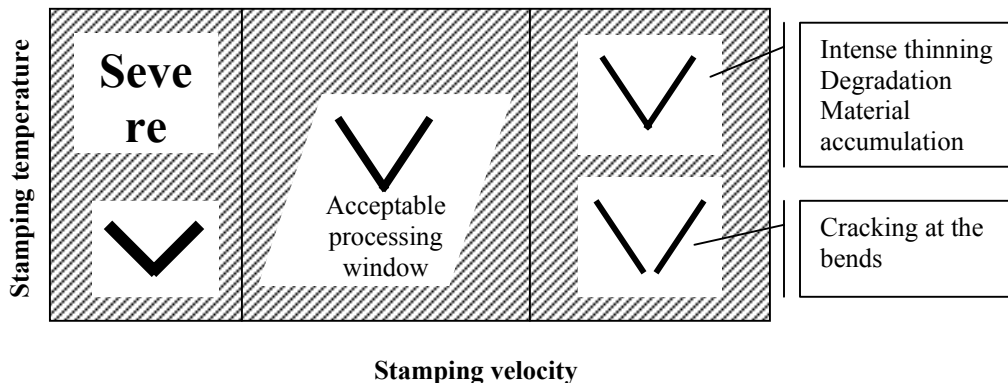

Stamping velocity

Fig. 7. Schematic representation of processing window for
2-D stamp forming of HAP-EVA composites

The experimental studies showed that for successful forming, the temperature of the sheets has to be maintained in the range 90-100°C. This requires the composite to be heated to at least 20°C above the melting point of the polymer matrix. The forming velocity could vary between 190-250 mm/s depending on pre-heating temperature set. Too high temperatures (>100°C) led to severe sagging of the composite sheet, making it difficult to handle and transport. When stamped at high velocities this resulted in intense thinning of the walls and web formation at the bends due to accumulation of the material. Too low temperature and stamping velocity on the other hand cools down the composite leading to the formation of distorted forms.

REFERENCES

1. U. Breuer and M. Neitzel, "High speed stamp forming of thermoplastic composite sheets" *Polymer & Polymer Composites*, Vol. 4, 1996, pp.117.
2. K. Friedrich and M. Hou, "On stamp forming of curved and flexible geometry components from continuous glass fiber polypropylene composites" *Composites Part A*, Vol. 29A, 1998, pp. 217.
3. R. T. Young, M. A. Mcleaod, and D. G. Baird, "Extensional processing behavior of thermoplastics reinforced with a melt processable glass" *Polymer Composites*, Vol. 21, 2000, pp. 900.
4. J. L. Throne. "Thermoforming". Hanser Publishers, Munich, 1987.
5. R. K Okine. "Analysis of forming parts from advanced thermoplastic composite sheet materials". *Journal of Thermoplastic Composite Materials*, Vol. 2, 1989, pp. 50.
6. M. Hou and K. Friedrich, "Stamp forming of continuous carbon fiber/polypropylene composites" *Composites Manufacturing*, Vol. 2, No. 1, 1991, pp. 3.

Structural Analysis of Commingled Yarns

Vinayak Ogale and Ramasamy Alagirusamy
Department of textile technology, Indian Institute of Technology,
Delhi110016, India

ABSTRACT

The commingled yarns are mainly characterized by having nips at very regular intervals in the longitudinal direction. Nips act as the binding points between open portions. In this paper nips of different class are classified into different categories based on their structure. The causes for occurrence and their effect on commingled yarn properties are identified. The degree of interlacing also studied in relation to the process parameters. The results show that commingling process parameters as well as the type of matrix forming fibers significantly affects the structure and properties of commingled yarns.

Keywords: commingled yarns, nip structure, thermoplastic prepregs,

INTRODUCTION

Thermoplastic composites offer new opportunities for fast, efficient processing technology. However, along with their advantages, thermoplastic composites also have introduced new problems into processing. Commingling of the matrix forming fibers and high performance fibers has the potential to achieve high levels of composite properties. However, it is reported that commingled towpregs tend to de-mingle due to non-uniform stretching of commingled yarns during textile and other preform making processes [1]. This would lead migration of the stiffer reinforcing fibers from matrix forming fibers.

Furthermore this will result in non-uniform distribution of fibers in final composite part and lead insufficient impregnation. Consequently, insufficient impregnation affects the mechanical properties of composites [2]. Hence, in order to obtain best composite properties with less severe consolidation conditions, there is a clear requirement for detailed study on the commingling behavior of the fiberglass filaments, which have high modulus and strength, with other matrix forming filaments which will have only moderate modulus and strength.

The structure of nips in commingled yarn is of prime importance because variations in mingled yarn properties are reported mainly due to variations in yarn structure. Structure and properties of commingled yarns mainly depend on type of supply yarn material, mingling process parameters and jet design [3-5]. Although high levels of composite properties are attained with this technique, there is no work reported on the structure of commingled yarns. Hence, there is a clear requirement for detailed study on the structure of commingled yarns with the high performance filaments like glass, which has high modulus and strength with low modulus matrix forming filaments like polypropylene, nylon and polyester. In the present work, an attempt has been made to study the effect of air pressure on structure of GF/Nylon, GF/PP and GF/PET commingled yarns.

EXPERIMENTAL

Design of Commingling Nozzle

The structure of the flow inside the yarn chamber depends on the number of jets, relative location of the jets from each other and from the both open ends of the chamber, angle at which air enters in the chamber and the pressure of the air at entry to the yarn chamber. Since it is very difficult to change these parameters practically, therefore to choose the best commingling configuration CFD analysis of configurations has been done. The commercial CFD package FLUENT 6.1 is used for this study.

Development of commingled yarn samples

A laboratory model of commingling equipment has been developed for the present study. The Glass and matrix forming multifilament yarns from separate packages are combined and fed to a pair of feed roller. After passing the yarn through supporting guides and an air nozzle, the commingled yarn is wound onto a package. Wide range of feed ratios, take up speeds and air pressures could be selected to produce commingled yarns at different processing conditions. The ratio of glass and other matrix forming filaments in commingled yarn is adjusted to get different volume fractions. Total 9 commingled yarn samples from GF/PP, GF/PET and GF/Nylon are developed at air following air pressures: 6, 7 and 8 bar. All other process parameters are kept constant.

TEST PLAN

Nip structure and degree of interlacing
The prepared yarn samples are visually examined form each commingled yarn sample ten specimens of length one meter were selected form different parts of package. The nips have been classified into five different groups according to their structure, namely, braid, entanglement, combination of braid & entanglement, wrap and others (consisting of core, braided core and side by side). The degree of interlacing is also obtained.

$$\text{The degree of interlacing (\%)} = \frac{\text{Total length of nips in the yarn}}{\text{Length of yarn specimen}} \times 100$$

RESULTS AN D DISCUSSION

Structure of nips in commingled yarns
From the microscopic observations nips found in commingled yarns can be classified as braids, entanglements, entangled braids, wraps and others which are shown in *Figure 1*. The occurrence of particular type of nip in a jet depends on the condition of filaments when they are acted upon by the jet.

Braided nips are composed of intertwined filament bundles of glass and matrix forming fibers. It has been observed that, glass filaments split into three or more groups and braiding with matrix forming filaments.
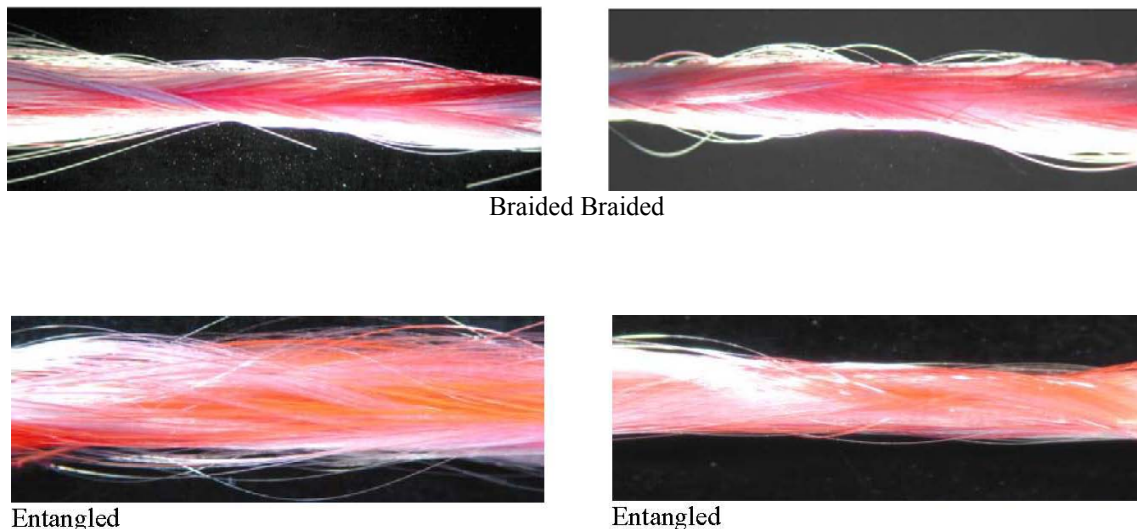

Braided Braided

Entangled   Entangled

Figure 1.Diffrent type of nips formed in commingled yarns
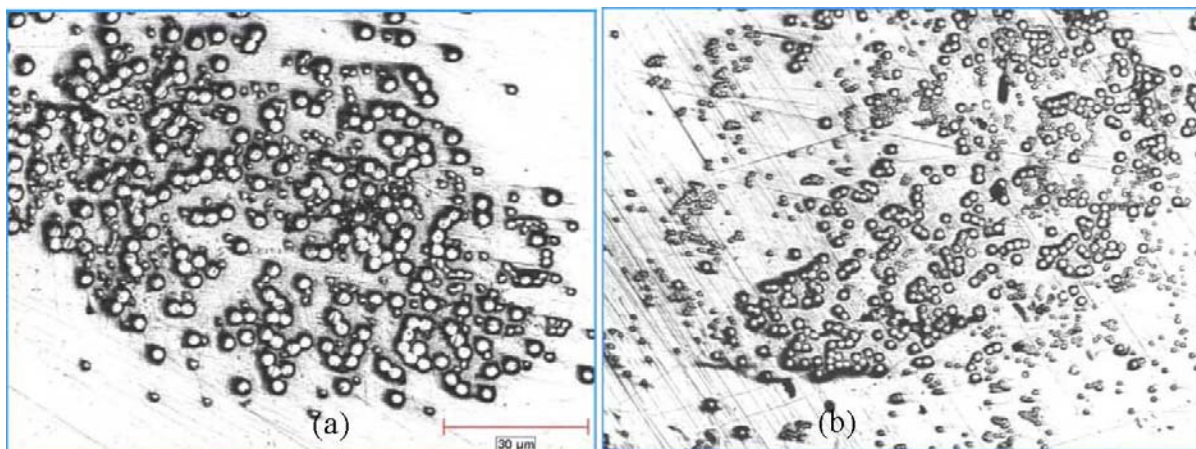
Figure 2 Micrographs of GF/PET and GF/Nylon commingled yarns.

Entanglement nips are formed due to initial opening of matrix forming fibers and Glass fibers; initial opening of filaments would disorganize the filament spatial positions. Further action of air jet would enhance the possibility of random intermingling of the small groups of opened bundles of Glass and matrix forming filaments together. Entangled braid type of nips are similar to braided nips, however sudden change in the direction of strong jets acting on filaments of the small and disorganized bundles of matrix forming filaments and glass filaments which are already built into partial braids would get entangled each other.

Wrap nips in commingled yarns are formed due to improper opening of glass filaments and therefore matrix forming filaments just wrap around un-opened bundles of glass filaments. This type of nip occurs when the formation of nip happens at a location in the nozzle where the air forces are weak. *Figure 2* shows micrograph of GF/PET and GF/Nylon commingled yarns.

Figure 3 shows that with increase in air pressure degree of interlacing increases continuously. With increase in air pressure average nip length increases therefore with increase in air pressure degree of interlacing increases irrespective of nip frequency. At higher air pressures, as velocity of filament rotation inside the nozzle increases, the momentum of the filament movement also increases. This causes the nip length to increase as the air pressure is increased. This trend has been observed for all type of nip structures. Although longer lengths of entangled nips where two types of fibers are intimately mixed are preferable, increase in nip length of other types of nip structures should also result in better resin distribution in the resultant composites. and nip formation.
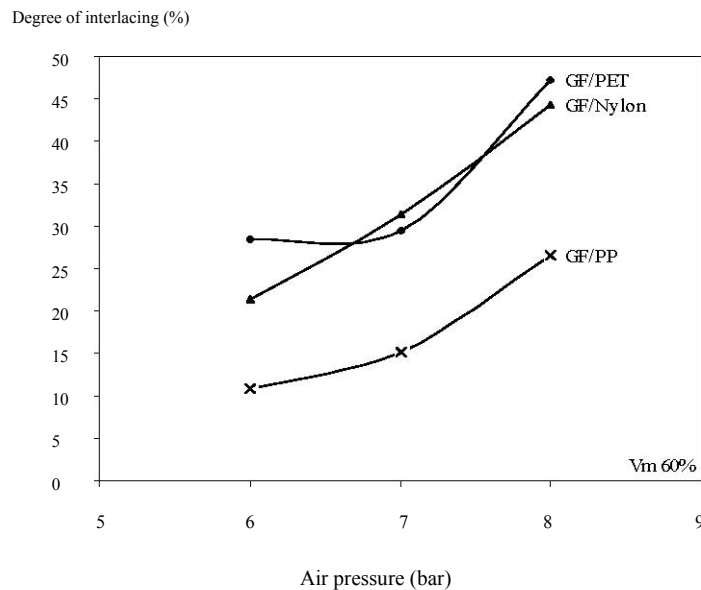
Degree of interlacing (%)

Figure 3 Effect of air pressure on degree of interlacing

Longer nips also provide better stability to commingled yarn structure. GF/PET and GF/Nylon shows higher degree of interlacing than GF/PP yarns poor the same reason explained for nip frequency. These studies clearly indicate that in the case of polypropylene the filament movement inside the nozzle is not quite conducive for commingling

CONCLUSIONS

The structure of Glass/PP, Glass/Nylon and Glass/PET commingled yarns has been characterized. The nip structures are classified into entanglement, braids, entanglement braids and others. The influence of air pressure on degree of interlacing of nips formed is studied. It has been found that Glass/PP yarns have lowest degree of interlacement and generally increase with increase in air pressure. It has also observed that entanglement type of nip structures preferentially form at higher air pressure where as braid type nips form at lower air pressure.

The present work shows that the matrix forming fibers influences of interlacing of commingled yarns.

ACKNOWLEDGEMENT

REFERENCES

1. Ye, L. Friedrich, K. Kastel, J. and. Mai, Y. M. (1995). Consolidation of unidirectional CF/PEEK composites from commingled yarn prepreg, *Compos sci technol*, 54(4):349-358.
2. Long, A.C. Wilks, C.E. and Rudd, C.D. (1995). Experimental Characterization of Consolidation of Commingled Glass and Polypropylene Composite, *Compos Sci Technol,* 61(11): 1591-1603.
3. Versteeg, H.K. Acar, M. and Bilgin, S (1999). Effect of Geometry on the Performance of Intermingling Nozzles*, Text Res J*, 69(8): 545-551.
4. Lazauskas, V. Lukosaitis, A. and Matukonis, A. (1987). Effect of the Design Parameters of the Aerodynamic Device on the Tanglelacing Intensity of Filament Yarns, *Tekhnologiya-Tekstil'noi-Promyshlennosti*, 177(3): 27-30.
5. Imeto, Y. and Chono, S., (1987). Study on Interlaced Yarn. III. Air Flow in Yarn Path, Journal of the Textle Machineary Socity of Japan, 40(5): T47-56**.**

In-Plane Shear Stress Relaxation Modulus of a Carbon-Epoxy Composite

Z.Q. Zhou[1], X.L. Liu[2] and W.K. Chiu[1]

[1]*Department of Mechanical Engineering, Monash University*
Wellington Road, Clayton, Victoria, 3800, Australia
zhong.zhou@eng.monash.edu.au
[2]*Cooperative Research Center for Advanced Composite Structures*
506 Lorimer Street, Fishermans Bend, Victoria, 3207, Australia
x.liu@crc-acs.com.au

SUMMARY: In this paper, a model for the in-plane shear stress relaxation modulus of a carbon-epoxy prepreg composite material is developed. Due to their simplicity, creep tests are used to determine the creep compliances of the material at various temperatures, which are transformed to the stress relaxation moduli through the Hopkins-Hamming method. The results are then fitted into a time shift function and a Prony series. It is shown that the material behaves linear viscoelastically and significant creep/stress relaxation occurs at temperatures higher than 120°C. The model developed is validated through test simulation.

KEYWORDS: Stress relaxation modulus, Viscoelastic material model, Creep test, Carbon-epoxy composites.

INTRODUCTION

Advanced polymer composites are made by reinforcing polymer matrices with fibrous reinforcements. The resulting behavior of the composites then depends upon the property and orientation of the fiber, and the property of the matrix. It is well known that the polymer matrix exhibits viscoelasticity, especially when it is not fully cross-linked, or is loaded at a high temperature or in a humid environment. The viscoelasticity of polymer composites may have significant impact on the design, manufacture and service life of composite structures. For example, the mechanical response of a composite part can be significantly viscoelastic during the later stage of the curing process or when it is reheated to a high temperature for assembly by bonding. Models for stress relaxation modulus need to be established to correctly predict the part distortion during these processes using a viscoelastic stress analysis.

There is relatively a large amount of reported work on viscoelastic analysis of polymer composites; see for example [1-4]. As a result, anisotropic viscoelastic analysis of composite materials is now supported by some commercial finite element packages, such as MSC.MARC. Considerable attempts have also been made to determine the viscoelastic composite material models to be used for the analysis both analytically and experimentally.

For example, White and Hartman conducted experiments to determine the stress relaxation modulus of 3501-6 epoxy resin during cure using DMA (Dynamic Mechanical Analyser) [5]. Also using DMA, Nam and Seferis investigated the viscoelastic behavior of a phenolic-carbon composite material through glass transition and degradation reaction processes in temperature up to 400°C [6]. A comprehensive review on micromechanics models for evaluating viscoelastic properties of composite materials can be found in Reference [7].

In the present work, in-plane shear viscoelastic response of a carbon-epoxy composite material is investigated by isothermal tensile creep tests. The results are processed to fit into a time shift function and a master Prony series representing the in-plane shear stress relaxation moduli of the composites at temperatures up to 150°C. It is shown that the model developed can be used as an input to MSC.MARC to predict the in-plane shear viscoelastic behavior of the composite laminates investigated with reasonably good accuracy.

EXPERIMENTAL WORK

Ideally stress relaxation tests should be used to measure the stress relaxation moduli. However, a stress relaxation test may be more difficult to conduct than a creep test. Therefore, creep tests were used in the present work. The creep compliances determined were then transferred to the relaxation moduli using the Hopkins-Hamming method [8].

Material and Test Apparatus

The material tested was Hexel F593-18 plain weave pre-preg laminates laid-up as $[(45/-45)_6]_S$ with each ply being 0.208mm thick. The laminate was cut into 250mm long and 25mm wide test specimens. Two $90°$ rosette strain gauges were bonded to each specimen to measure the longitudinal and transverse strains during the creep test and a thermocouple was placed next to the strain gages to record the temperature history that the specimen experienced. Uniaxial tension was applied by dead weights using the apparatus described below.
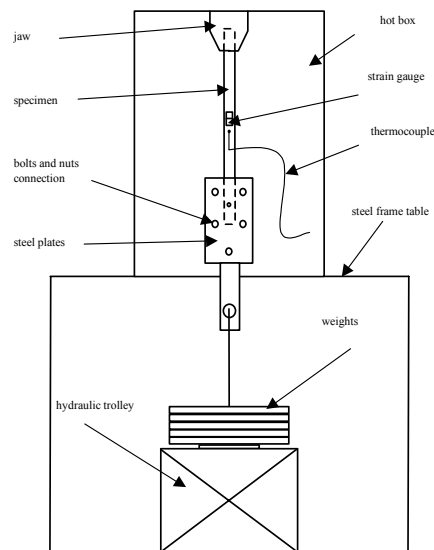

Fig. 1 Schematic diagram of creep test set-up

The creep tests were conducted in a hot box sitting on a steel frame table with a setup sketched in Fig. 1. A mechanical jaw attached to a universal joint fixed to the top of the hot box was used to hold the top end of the specimen. To avoid applying a concentrated load on the specimen, a pair of steel plates connected by five bolts and nuts was clamped on the bottom end of the specimen. Weights were then hung onto the clamping plates to create a uniformly distributed loading along the width of the specimen during test. A hydraulic trolley was placed under the weights to allow almost instantaneous loading when the hydraulic oil pressure was suddenly released.

Experimental Procedure

Since the tests were conducted at relatively high temperatures, a high temperature adhesive for installing strain gauges to the specimen was used. This adhesive is required to cure at three temperature stages (80°C for one hour, 130°C and 150°C for two hours respectively) under 0.2MPa pressure. Such a curing process produced an internal residual stress in the adhesive, and consequently an unwanted adhesive creep during the test. To eliminate the adhesive creep, an annealing process was introduced into the experimental procedure after the strain gauge curing process.

Table 1 Temperature, loading and time of tests

Process		Number of tests	Temperature (°C)	Keeping time (hour)	Applied stress (MPa)	Loading time (hour)
Annealing		all	150	2	0	NA
Creep test	Adhesive	2	150	4	0	NA
	Various temperature	2-3	100	1	10	2
		2-3	120	1	10	2
		2-3	130	1	10	2
		2-3	140	1	10	2
		2-3	150	1	10	2
	Various load	2-3	140	1	6.5	2
		2-3	140	1	10	2
		2-3	140	1	13.8	2

To perform an isothermal creep test, the specimen was preheated by the hot box to the desired temperatures (Table 1) without any loading, and then kept at this temperature for an hour to allow the heat to be transferred to the center of the specimen and to achieve an even temperature distribution in the specimen. Without changing the temperature, the hydraulic trolley was suddenly released and a constant load was then applied onto the specimen for 2 hours and the creep strains were recorded. Details of each of the tests conducted are listed in Table 1.

RESULTS AND DISCUSSION

Creep of Adhesive

Two unloaded tests were conducted to verify the effectiveness of the annealing process in eliminating the adhesive creep during experiment. The specimens were hung in the hot box and heated to 150°C without any loading and kept at this temperature for 4 hours.
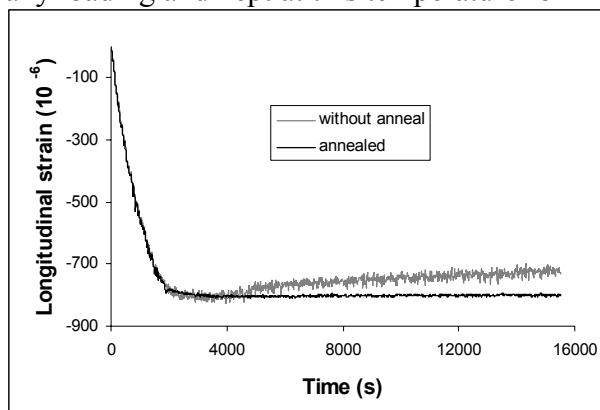

Fig. 2 Adhesive creep strains

Fig. 2 shows the transient strains of the annealed and unannealed specimens respectively. The strain signals were zeroed at room temperature. Due to thermal straining, the longitudinal strain signals shown in Fig. 2 decrease rapidly at the beginning. Once the temperature in the specimen reaches and remains at 150°, the strains are expected to remain unchanged with time if the adhesive does not creep. Such a result is only observed for the curve in dark color in Fig. 2, which represents the creep strain of the annealed specimen. However, the creep strain of the unannealed specimen increases with time, indicating that the adhesive creep occurred during the test. Therefore in subsequent tests the specimen was always annealed after curing the strain gauge.

Creep under Different Loading Levels

A group of tests was conducted to determine if the viscoelasticity of the material was linear within the temperature range considered. The temperature used for these tests was 140°C and the applied tensile stress levels were set to about 6.5MPa, 10MPa and 13.8MPa respectively.

Shear strain curves obtained at the three different stress levels are plotted in Fig. 3. The level of strain increases with the applied stress. Strains measured at the beginning (time = 0 sec) are the elastic strains representing the instantaneous response of the specimens to the applied stresses. Strains after the initial point are the creep strains and are shown to increase with time under all the three loading levels tested.
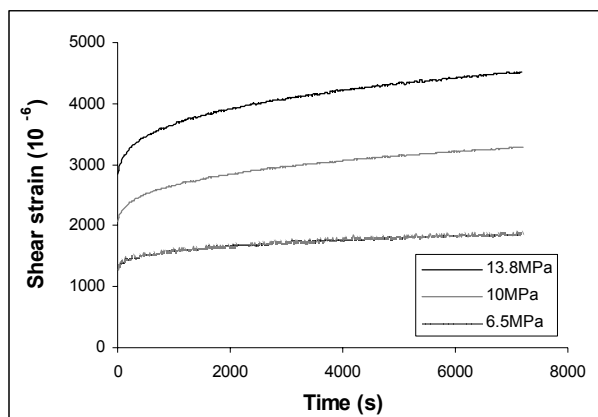
Fig. 3 Strains for laminates under various loads at 140°C

Fig. 4 shows the isochronal stress-strain curves for t=0, 1 hour and two hours respectively. The strains are approximately linearly related to the applied stresses as the isochronal stress-strain curves are almost straight. Therefore the material investigated can be assumed to be linear viscoelastic.
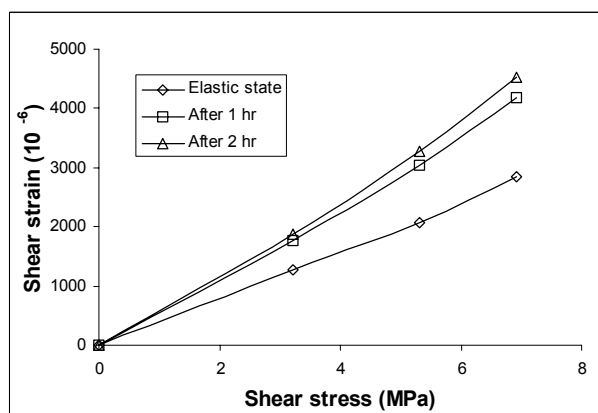

Fig. 4 Isochronal stress-strain curves for laminates loaded at 140°C

Creep at Various Temperatures

More creep tests were then conducted under a tensile stress of 10MPa at five different temperatures: 100°C, 120°C, 130°C, 140°C and 150°C respectively. The longitudinal and transverse strains recorded during the tests were converted to the in-plane shear strain using the procedure documented in ASTM-D3518. The results are shown in Fig. 5 and are averaged over the two or three tests conducted for each test condition. Both the instantaneous elastic shear strain and creep shear strain increase with temperature. Within a time span of about two hours, the material exhibits less than 20% creep strain when the temperature is lower than 120°C and the creep rate gradually increases with the temperature.

Very significant creep (creep strain is 110% of elastic strain) occurs when temperature goes up to 150°C.

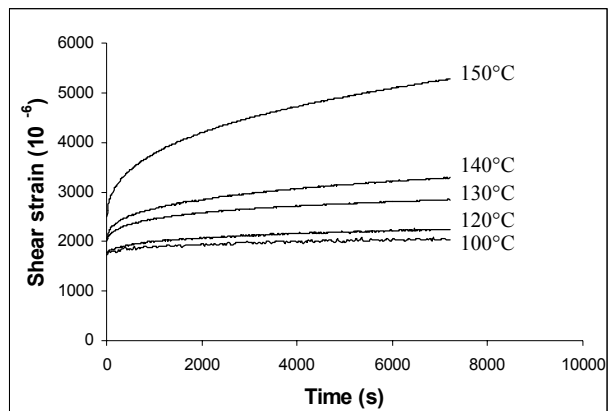
Fig. 5 Transient shear strains at various temperatures

It is straightforward to calculate the creep compliance C(t) from the experimentally determined transient strains γ(t) using the following equation:

$$C(t) = \frac{\gamma(t)}{\tau} \qquad (1)$$

where τ is the shear stress applied.

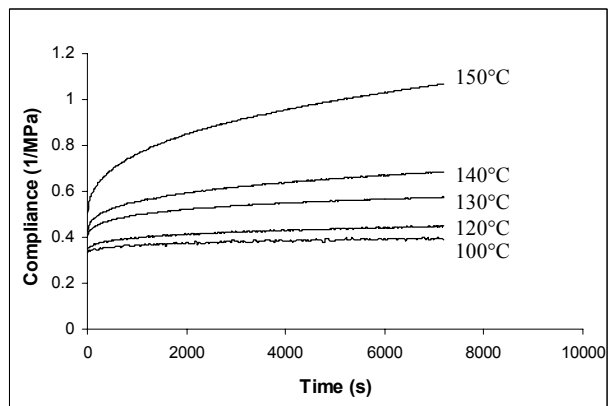The creep compliances obtained are shown in Fig. 6.

Fig. 6 Creep compliance for various temperatures

MODEL FOR STRESS RELAXATION MODULUS

Theoretical Background

For a linear viscoelastic material subject to both thermal and mechanical loads, the stress relaxation modulus can be described by the hereditary integral model, which is an integral expression of generalized forms of the Maxwell and Kelvin model [9]. It defines the time dependant material behavior in a relative simple form, which is often referred as the Prony series:

$$G(t) = G_0 + \sum_{n=1}^{N} G_n [\exp(-t/\lambda_n)] \qquad (2)$$

where, $G(t)$ is the time dependant stress relaxation moduli, G_0 is long term stress relaxation moduli, G_n and λ_n are the amplitudes and time constants for the Prony series respectively.

For a thermal-rheologically simple material, the effect of temperature on the relaxation moduli can be introduced through the following the time transformation:

$$\xi = \int_0^t \frac{dt'}{\alpha(T,t')} \qquad (3)$$

where, t is time, ξ is the reduced time, and α is the shift function which is a function of temperature T.

Model for In-plane Shear Stress Relaxation Modulus

In the present work, the above in-plane shear creep compliance was transformed to the stress relaxation modulus $G(t)$, through the following transformation:

$$\int_0^t G(\tau)\, C(t-\tau)\, d\tau = t \qquad (4)$$

A numerical solution of Eqn. 4 for tabular data was given by Hopkins and Hamming as:

$$G(t_{n+1/2}) = \frac{t_{n+1} - \sum_{i=0}^{n-1} G(t_{i+1/2})[f(t_{n+1}-t_i) - f(t_{n+1}-t_{i+1})}{f(t_{n+1}-t_n)} \qquad (5)$$

in which

$$f(t) = \int_0^t C(\tau)d\tau \qquad (6)$$

A FORTRAN program was written to read the compliance data from the experimental results and then to solve Eqn. 5 to transform the compliances into the stress relaxation moduli. The results are plotted in Fig. 7.
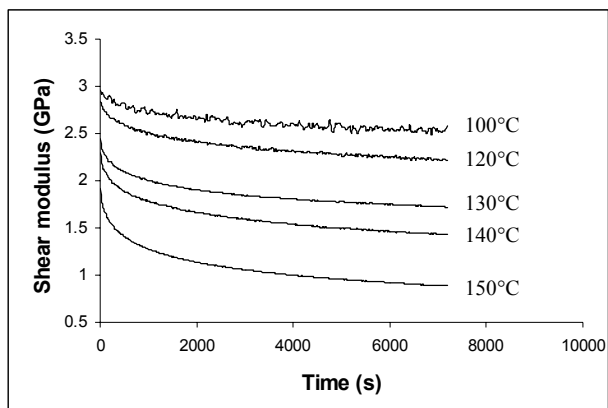
Fig. 7 Stress relaxation moduli for various temperatures
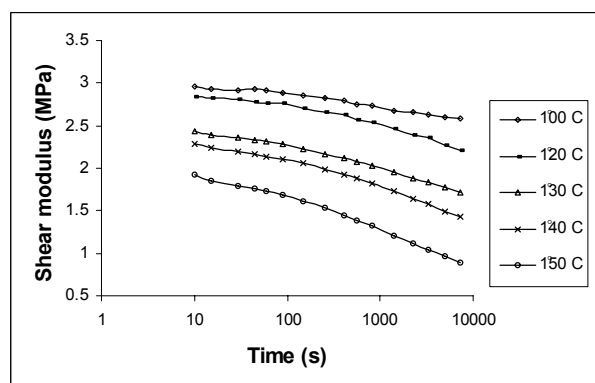
Fig. 8 Stress relaxation moduli in logarithmic time scale

Assuming the material to be thermal-rheologically simple, the stress relaxation curves at various temperatures exhibit an approximate translation shift along a logarithmic time axis. The individual stress relaxation modulus at each temperature (Fig. 7) was then re-plotted in a logarithmic time scale in Fig. 8. Using the shear modulus curve of 100°C as a reference, the other curves were shifted manually along the time axis to the right to form a continuous master curve shown in Fig. 9. The relationship between temperature and the time shifting factor was plotted in Fig. 10 and the shift function α was determined by fitting the points into the following equation:

$$\alpha = 11.672 \, x^2 - 19.652x + 7.786 \tag{7}$$

where, $x = T/100$ and T is temperature.

A nonlinear regression analysis was then conducted to fit the master curve into a five-term Prony series as shown in Fig. 9. Model constants obtained by the fitting are listed in Table 2.

Fig. 9 Master curve of stress relaxation moduli
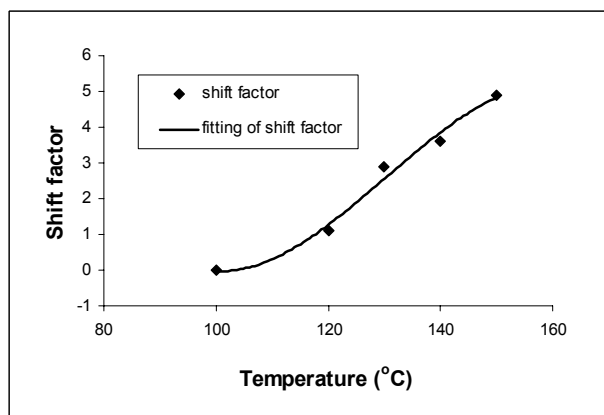
Fig. 10 Time shift factor

Table 2 Relaxation data for the Prony series
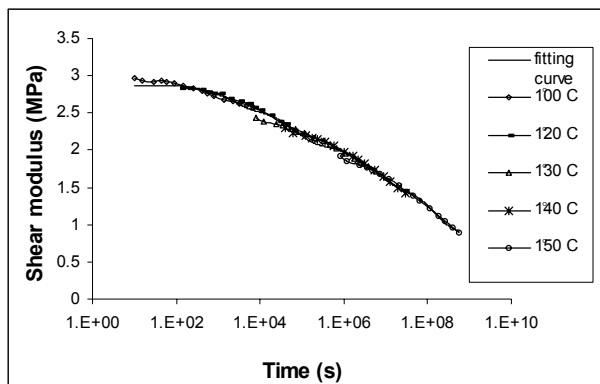
n	G_n (GPa)	λ_n (s)
0	0.89592	
1	0.30402	2050.22008
2	0.49028	73252.7885
3	0.50648	4.90159591×10^6
4	0.67819	1.55861669×10^8

A non-isothermal creep test was conducted to validate the stress relaxation modulus model developed. The specimen used for the validation test was similar to those used for the tests to develop the model, except that a thermocouple was embedded in the middle layer of the composite laminate. Two specimens were used for the test: one was for creep test under an applied stress of 10MPa and the other was hung next to the creep specimen in the hot box for recording the thermal strain which was later deducted from the creep strain recorded. The temperature program applied in the creep test was a hold at 100°C for half an hour, a ramp up to 140°C, and a hold for another half an hour.
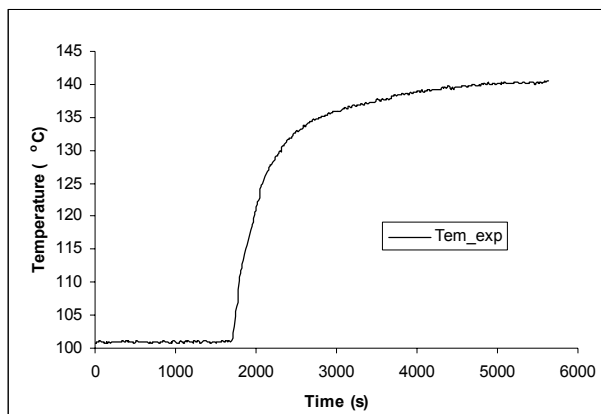
Fig. 11 Temperature program during validation creep test
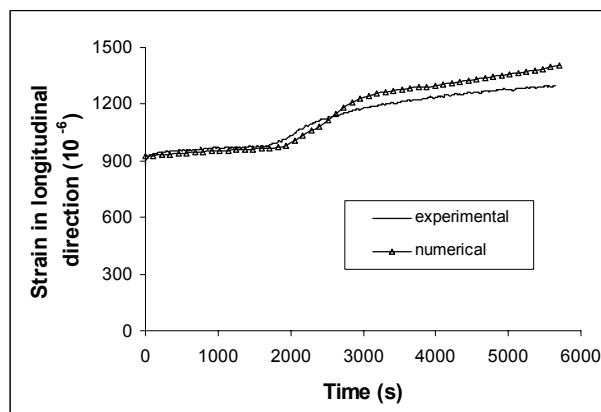
Fig. 12 Comparison of numerical and experimental results

MSC.MARC was used to perform the finite element modeling of the creep test. Due to symmetry, only a quarter of the specimen was included in the model with 20 and 200 elements along its width and length respectively. The temperature applied in the simulation was taken from the readings of the thermocouple embedded in the specimen (see Fig. 11) and a uniformly distributed load was applied instantly to the model and kept constant thereafter.

Fig. 12 compares the numerically predicted and experimentally measured transient strains during the non-isothermal creep test. It shows that there exists a reasonably good agreement between the predicted and experimental strains. The predicted strains are slightly higher than those experimentally measured at 140°C, because the time shift function fitted at 140°C is higher than measured. (see Fig. 10).

CONCLUSION

The in-plane shear relaxation modulus of polymer composites can be measured in a tensile creep test using a simple set-up with reasonable accuracy and consistence. However, attention has to be paid to creep of the adhesive used to bond the strain gauges onto the specimen. Creep was found in the adhesive during initial creep tests. Hence, an annealing process needs to be introduced into the experiment.

The in-plane shear response of ±45° Hexcel F593-18 prepreg laminates at temperatures up to 150°C is found to be linear viscoelastic. The creep rate is relatively low for temperatures below 120°C and becomes more significant at higher temperatures. At 150°C, the creep strain after two hours exceeds the elastic strain.

The in-plane shear viscoelastic behavior of the material investigated can be expressed by a time shift function and a Prony series with four exponential terms. Numerical simulation of the non-isothermal validation creep test confirms that the material model established in this study predicts a viscoelastic response which is in reasonably good agreement with the experimental one. The model also demonstrates the ability to describe creep behavior under non-isothermal temperature history.

ACKNOWLEDGEMENTS

REFERENCES

1. K.Y. Lin and I.H. Hwang, "Thermo-viscoelastic analysis of composite materials", *Journal of Composite Materials*, Vol. 23, 1989 pp. 554.
2. D.C. Hammerand and R.K. Kapania, "Thermoviscoelastic analysis of composite structures using a triangular flat shell element", *AIAA Journal*, Vol. 37, No. 2, 1999 pp. 238.
3. S. Yi, K.S. Chian and H.H. Hilton, "Nonlinear viscoelastic finite element analyses of thermosetting polymeric composites during cool-down after curing", *Journal of Composite Materials*, Vol. 36, 2002 pp. 3.
4. L. Nallainathan, X.L. Liu, W.K. Chiu and R. Jones, "Modeling orthotropic viscoelastic behavior of composite laminates using a coincident element method", Accepted for publication in *Polymers and Polymer Composites*.

5. S.R.White, and A. B Hartman, "Effect of cure state on stress relaxation in 3501-6 Epoxy resin", *Transaction of the ASME: Journal of Engineering Materials and Technology*, Vol. 119, 1997 pp. 262.

6. J.D. Nam and J.C. Seferis, "Viscoelastic characterization of phenolic-carbon fiber composites degradation process", *Journal of Polymer Science: B: Polymer Physics*, Vol. 37, 1999 pp. 907.

7. L.C. Brinson and W.S. Lin, "Comparison of micromechanics methods for effective properties of multiphase viscoelastic composites", *Composite Structures*, Vol. 41, 1998 pp. 353.

8. I. L. Hopkins and R. W. Hamming, "On creep and relaxation", *Journal of Applied Physics*, Vol. 28, 1957 pp. 906-909.

9. Y.M. Haddad, *Viscoelasticity of Engineering Materials*, 1st Edition, Chapman and Hall, London, 1995.

NANOCOMPOSITES

Influence of the Nanoscale Morphology on the Micro- and Macromechanical Behavior of Composites

Jan K.W. Sandler [1], Volker Altstädt [1]

[1] *Polymer Engineering, University of Bayreuth*
95447 Bayreuth, Germany: altstaedt@uni-bayreuth.de
And Corresponding Author's e-mail: jan.sandler@uni-bayreuth.de

SUMMARY: The development of polymer nanocomposites with enhanced physical and mechanical properties also allows an evaluation of the intrinsic properties of the nanoscale constituent. However, as the absolute size of the reinforcement decreases, the particle surface area increases and particle-particle as well as particle-matrix interactions during processing become more prominent. These interactions can induce significant variations in the microstructure of the composite matrix which need to be considered when evaluating the composite performance. Rheological studies can highlight the complex interactions between the nanoscale reinforcements and the polymer molecules. Not only the degree of dispersion and the alignment of the filler within a given system are important factors governing the resulting properties of the composite. Elongational flows during processing for example can lead to a significant load transfer from the melt to reinforcements with a high aspect ratio which can dramatically alter the microstructure of a semicrystalline thermoplastic matrix. Such variations in the microstructure are reflected in an altered micromechanical deformation behavior of the composite. In order to correctly interpret the properties of a given nanocomposite and to be able to predict the behavior of a system as a function of filler type and content these interactions need to be understood.

KEYWORDS: nanocomposites, processing, rheology, structure-property relationships

INTRODUCTION

Although the terms *nanomaterial* and *nanocomposite* represent a fairly new and exiting field in materials science, such materials have already existed for a century in the polymer industry and have always existed in nature. A nanocomposite is defined as a composite material with at least one of the dimensions of one of the constituents on the nanometer scale. Carbon black (CB)-filled rubber for automotive applications is an excellent example for the established implementation of this concept in technical products. The recent drive behind the development of nanocomposites is based on the fact that the properties of a material become increasingly insensitive to flaws at the nanoscale, enabling the exploitation of the unique physical and mechanical properties of very small objects in large-scale components.

Natural materials such as bone, tooth, and nacre are very good examples of the successful implementation of this concept. Such composites exhibit many levels of hierarchical structures from macroscopic to microscopic length scales. Despite these complicated structures, the smallest building blocks in such materials are generally on the nanometer scale and, more importantly, it is a nanoscale reinforcement embedded in a matrix. The concept of creating both structural and functional multi-phase nanocomposites with an improved performance is currently exploited in all types of matrices such as metals, ceramics and polymers. The same accounts for the filler particles, which can be organic or inorganic, and cover a wide range of materials. The resulting composites exhibit a multitude of enhanced properties, both physical (for example, electrical and thermal conductivity) and mechanical (stiffness and strength), so that the material cannot easily be classified as a structural or functional composite. The terms *reinforcement*, as opposed to plain *filler*, are equally frequently used for the nanoscale component without a clear distinction.

Although significant advances have been made in recent years to overcome the problems associated with the manufacture of polymer nanocomposites, processing remains a key challenge to utilize the properties of the nanoscale reinforcement. A primary difficulty is the achievement of a good dispersion and distribution of the filler in the composite, independent of filler type and aspect (length-to-diameter) ratio. Without a proper dispersion, filler aggregates can act as defects, which limit the mechanical performance, and these agglomerates can also adversely influence the physical properties such as optical transmissivity of the matrix.

When dispersing particles with diameters below 1 μm in a medium of low viscosity, diffusion processes, particle-particle as well as particle-matrix interaction forces play an important role in the dispersion process. It is not only the absolute filler size but rather the specific surface area (hundreds of m^2/g) and the resulting interfacial area which significantly influence the filler-matrix interactions during processing. In turn, one would expect these interactions to induce variations in the microstructure of the polymer matrix, which, in the case of semicrystalline matrices for example, have significant implications on the resulting mechanical behavior of the composite in themselves. Therefore, the matrix microstructure must be critically assessed when evaluating the performance of polymer nanocomposites.

OUTLINE

The Polymer Engineering group at the University of Bayreuth is actively pursuing the development of polymer nanocomposites. The aim is not only to produce novel materials with enhanced properties but also to establish the structure-property relationships of these materials for applications ranging from the electronic to the automotive and aerospace sector. It is important to understand the interactions between the various types of nanoscale fillers with a given matrix under given processing conditions to be able to predict the resulting composite behavior. In addition, only a complete evaluation of the composite microstructure allows a determination and evaluation of the intrinsic properties of the nanoscale constituent.

Given the multitude of different nanoscale fillers (carbon black, carbon nanofibers and nanotubes, layered nanoclays, silicate nanotubes, …) with vastly different properties which are theoretically predicted and, in many cases, experimentally verified, the selection of a suitable

material for a given application is crucial. For example, the potential of carbon-based nanomaterials for components requiring the achievement of sufficient electrical conductivity for anti-static applications has been established. On the other hand, layered silicate nanoclays are suited for the development of polymer nanocomposites with improved barrier properties. In contrast, phosphorus-containing molecular additives can be used to produce effective and environmentally friendly flame-retardant polymers.

Independent of the type, shape and aspect ratio of a given nanoscale filler, composite processing leading to a good dispersion and alignment of the filler in a polymer is crucial. For example, the direct physical mixing of a given polymer and nanoscale reinforcement may not form a nanocomposite. This situation is analogous to a polymer blend, and in most cases, separation into discrete phases takes place. In immiscible systems, the limited physical interactions between the two components lead to poor mechanical and physical properties of the final composite. However, the surface chemistry of commonly used layered silicate nanoclays for example can be modified to allow strong interactions of the clay with a given polymer matrix during processing, which can lead to the desired dispersion of individual nanoscale layers.

In this presentation, a variety of different polymer nanocomposites for both structural as well as functional applications will be discussed. It is demonstrated that the processing behavior of such systems has a pronounced influence on the resulting morphology and properties of the final product. Furthermore, the processing parameters can be optimized to further enhance the desired properties of the composites, an approach that can lead to very specialized products.

Structural nanocomposites:

- Carbon nanofiber-and silicate nanoclay-reinforced thermoplastic nanocomposites (standard extrusion and injection molding techniques)
- Carbon-nanofiber/nanotube-reinforced thermoplastic composite fibers (melt-spinning)

Functional nanocomposites:

- Carbon nanotube-filled thermosets for anti-static applications
- Phosphorus-containing molecular additives for flame retardant thermosets

INJECTION-MOLDED THERMOPLASTIC NANOCOMPOSITES

There are at least three general experimental methods to produce polymer nanocomposites: mixing in the liquid state, solution-mediated processes and in-situ polymerization techniques. The direct melt blending approach is much more commercially attractive than the latter two methods, as both solvent processing and in-situ polymerization are less versatile and more environmentally contentious.

A number of thermoplastic nanocomposites have been prepared by twin-screw extrusion compounding and subsequent injection-molding of the prepared masterbatches.

The semicrystalline thermoplastic matrices range from commodity polymers such as polypropylene (PP) to technical thermoplastics such as polyamide (PA) and, finally, to high-performance thermoplastics such as poly(ether ether ketone) (PEEK). In addition, a range of commercially available nanoscale reinforcements have been evaluated, layered silicates (LS), silicate nanotubes (SN) as well as carbon nanofibers (CNF). Depending on the surface area of the nanoscale material, filler loading fractions of up to 15 wt% have been realized using standard processing machines up to the kilogram scale.

The processing behavior of these masterbatches for future large-scale production has been investigated by shear rheological experiments, both with a stress rheometer at low shear rates and with the extruder at high shear rates, respectively. As Fig. 1 highlights, the addition of up to 15 wt% of carbon nanofibers to a PEEK matrix does not significantly alter the processing behavior of this composite system. The nanocomposites show a similar shear thinning as the pure matrix in the shear rate regime typically encountered during extrusion and injection-molding. This behavior also reflects the good degree of dispersion achieved during the twin-screw extrusion process for this material combination.
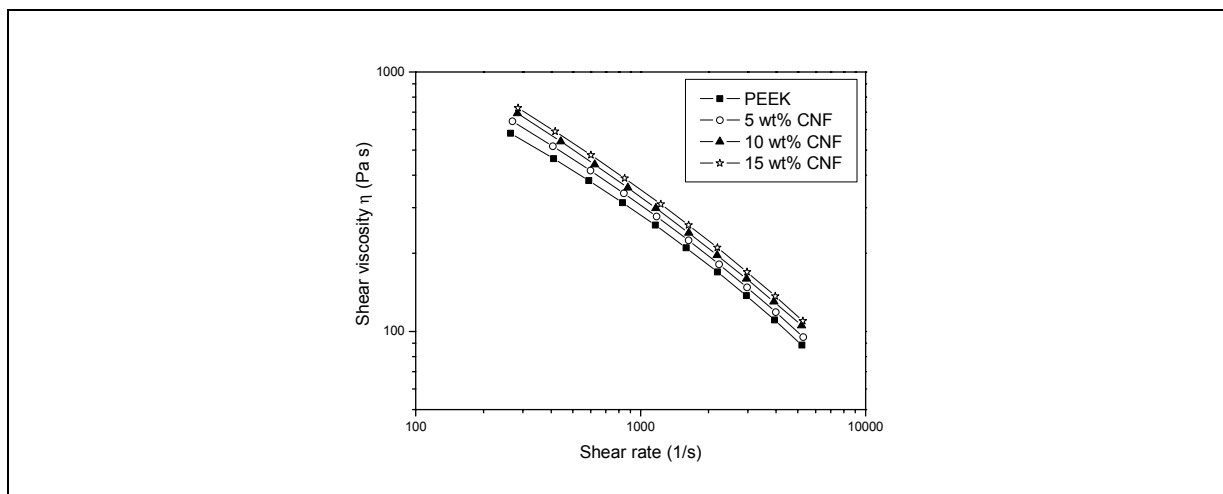
Fig. 1 Shear viscosity of PEEK-CNF masterbatches as a function of the shear rate

In all cases, a good dispersion of the nanoscale reinforcement in the thermoplastics has been achieved. However, in the case of most layered silicate nanoclays an intercalated structure appears to dominate, only seldom a certain degree of exfoliation is observed in the final products. Moreover, the shear-intensive processing has led to a partial orientation of the filler particles with a high aspect ratio. This alignment is a result of the interactions between the reinforcement and the polymer molecules during processing and reflects the typical molecular orientation in injection-molded samples. The scanning electron micrograph in Fig. 2 a) verifies the good dispersion and partial alignment of carbon nanofibers in a PEEK matrix at a loading fraction as high as 10 wt%.[1] Similarly, layered silicate nanoclay PA-6 composites also exhibit a good dispersion and preferential orientation with the direction of flow during processing, Fig. 2 b).[2]

Furthermore, the transmission electron micrograph highlights the dominating appearance of intercalated stacks of silicate nanoclays, although individual fully exfoliated layers can be seen. The orientation of the nanoclay corresponds to the molecular orientation as a function of the processing conditions. For example, in these PA-6 nanocomposites there exists a clear dependence of the mechanical properties on the specimen thickness.[2] This skin-core dependence in turn is reflected in the micromechanical deformation behavior which depends on the orientation of the nanoclays.

In addition to the morphology of the nanoscale reinforcement the matrix microstructure must be assessed in order to fully understand the micromechanical deformation behavior of the nanocomposite. For example, under standard injection-molding conditions, the carbon nanofibers do not induce a variation in the crystalline morphology of the PEEK matrix [1], whereas they act as heterogeneous nucleation sites in a semicrystalline polyproplyene.[3]
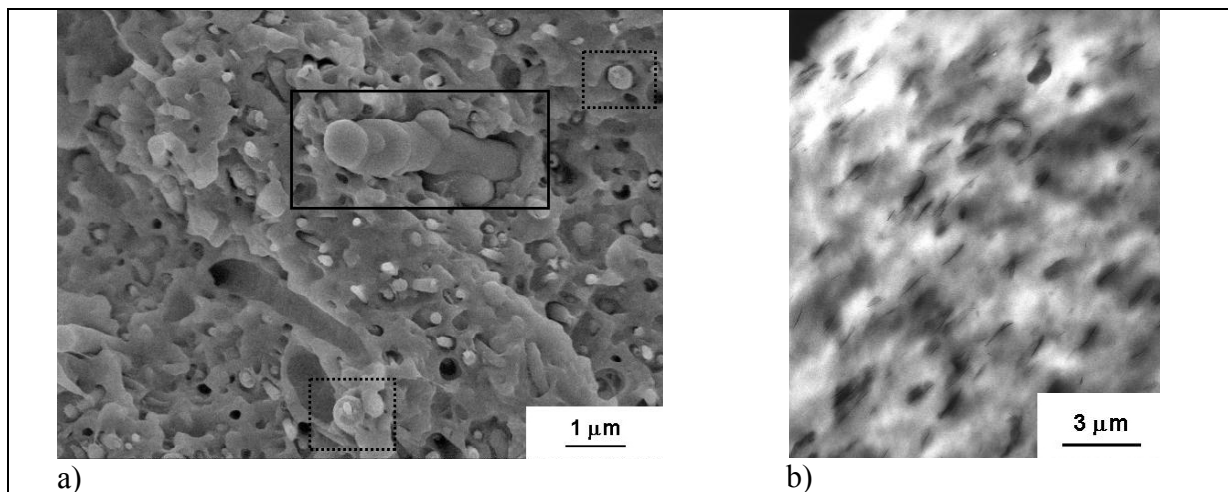

Fig. 2 a) Scanning electron micrograph of fracture surface of PEEK nanocomposites containing 15 wt% CNF and b) transmission electron micrograph of PA6 nanocomposite containing 5 wt% LS

Only a fundamental characterization of the composite microstructure allows an evaluation of the composite properties such as stiffness and yield stress as a function of filler type and loading fraction with regard to the intrinsic properties of the nanoscale phase. This is especially important when attempting to compare the effective reinforcement capability of different nanoscale fillers and to understand complex composite properties such as the tribological wear behavior. [4]

MELT-SPUN NANOCOMPOSITE FIBERS

The most promising current approaches towards increasing the orientation of nanoscale reinforcements within a matrix include the optimization of the extrusion die and stretching the composite melt to form films and fibers. The enhancement of the mechanical performance of thin polymer fibers for example is considered as one key application for the use of nanoscale fillers since the small size of the final composite inhibits the use of conventional reinforcements.

However, the influence of the nanoscale phase on the microstructure of the matrix can become even more pronounced when the composite melt is subjected to elongational flows.

An example of the strong interaction between carbon nanofibers and the PEEK matrix melt during elongational deformation experiments is shown in Fig. 3). As can be seen, there is a significant increase in the force required to draw a composite melt strand as it exits a die with increasing nanofiber content.[5] The load transfer from the melt to the aligned reinforcement during processing alters the spinning behavior of this composite system and can induce significant variations in the resulting matrix microstructure as the system cools down.

Fig. 3 b) highlights the local variations in the matrix microstructure of a melt-drawn PP film containing 0.5 wt% of carbon nanofibers.[3] X-ray diffraction methods especially are suited to characterize both the microstructure of the spun product as well as the in-situ deformation behavior of such nanocomposites.

A range of thermoplastic polymer composite fibers containing carbon nanofibers as well as different carbon nanotubes has been melt-spun and analyzed with regard to the resulting microstructure and mechanical deformation behavior.[6,7] The results presented for these different systems highlight the importance not only to characterize the microstructure of the final composite but also to study the in-situ micromechanical deformation behavior as a function of reinforcement type and content. Again, only a complete understanding of the complex interactions between a given reinforcement and matrix and the chosen processing conditions allows the evaluation of the intrinsic properties of the nanoscale phase and, even more importantly, the desired prediction of nanocomposite properties for technical applications.
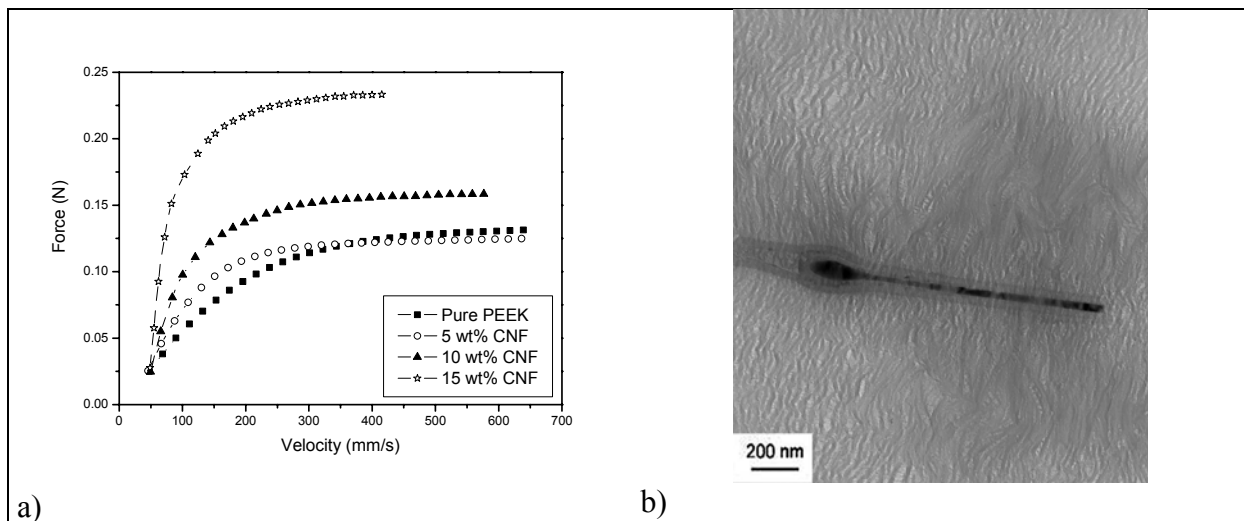

a)   b)

Fig. 3 a) Draw-down force as a function of draw-down velocity of PEEK-CNF masterbatches and b) TEM image of highly-oriented PP film containing CNF

THERMOSET FUNCTIONAL NANOCOMPOSITES

Multi-wall carbon nanotubes have been exploited as electrically conductive fillers in an epoxy matrix.[8-11] The degree of nanotube entanglement and agglomeration and, therefore, the resulting composite microstructure and conductivity can be tailored by adjusting the processing conditions. Here, only a complete evaluation of the kinetics of the phase separation process allows a subsequent optimization of the final composite properties. For example, the agglomeration process of initially well-dispersed CNT can be controlled by the application of electric fields during curing[11], an approach that enables the formation of oriented nanotubes networks which maintain an increased degree of transmissivity of the matrix.

As shown in Fig. 4 a), the CNT network formation in epoxy composites can be monitored by in-situ experiments during curing. The current density of the composite can be measured between two electrodes dipped into the dispersion. The application of both DC and AC electric fields during curing induces the formation of oriented nanotube networks. On the other hand, in-situ rheological experiments can highlight the influence of molecular additives on the processing behavior of epoxy composites and can be used to define critical additive concentrations which will limit the application of such systems in liquid resin technologies such as resin transfer molding or resin infusion. An example of this approach is shown in Fig. 4 b), where the viscosity of an epoxy system with different molecular additives (leading to 3 wt% of phosphorus in the composite) during curing is shown. Such experiments can clearly distinguish between the different chemical reactivity of the additives in this case. In turn, these variations in the curing behavior are reflected in the degree of cross-linking in the final product and the resulting mechanical properties.
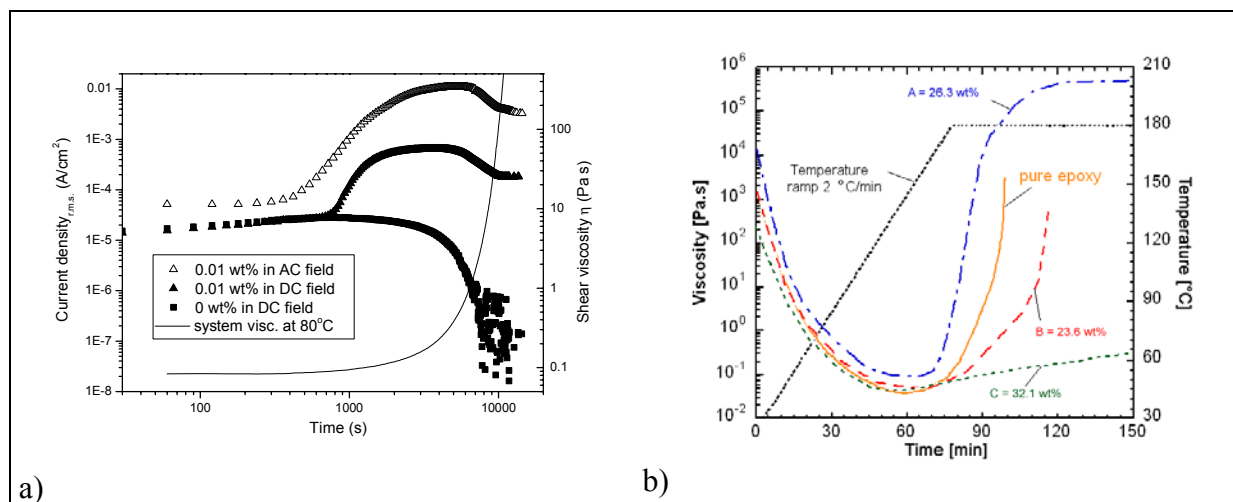

Fig. 4 a) In-situ current density measurements of carbon nanotubes-epoxy composites and b) viscosity of epoxy composites as a function of different molecular additives

CONCLUSIONS

In order to correctly interpret the properties of polymer nanocomposites a detailed investigation of the composite microstructure is necessary. Standard polymer processing techniques can induce a partial orientation of the nanoscale phase which, in turn, can have a significant influence on the matrix microstructure. Such variations in the composite microstructure can lead to an altered micromechanical deformation behavior. It is therefore crucial to understand the complex interactions between the filler particles and the polymer matrix during processing in order to be able to predict the properties of a given nanocomposite system for a given processing technology.

ACKNOWLEDGEMENTS

REFERENCES

1.   J. Sandler, P. Werner, M.S.P. Shaffer, V. Demchuk, V. Altstädt and A.H. Windle, "Carbon-nanofiber-reinforced poly(ether ether ketone) composites", *Composites: Part A,* Vol. 33, no. 8, 2002 pp. 1033.

2.   P. Uribe-Arocha, C. Mehler, J.E. Puskas, V. Altstädt, "Effect of sample thickness on the mechanical properties of injection-molded polyamide-6 and polyamide-66 clay nanocomposites", *Polymer*, Vol. 44, no. 8, 2003 pp. 2441.

3.   J. Sandler, G. Broza, M. Nolte, K. Schulte, Y.-M. Lam and M.S.P. Shaffer, "Crystallization of carbon nanotubes and nanofiber polypropylene composites", *Journal of Macromolecular Science: Part B – Physics*, Vol. 42, no. 3-4, 2003 pp. 479.

4.   P. Werner, O. Jacobs, R. Jaskulka, V. Altstädt, J.K.W. Sandler, A.H. Windle and M.S.P. Shaffer, "Tribological behavior of carbon-nanofiber-reinforced poly(ether ether ketone)", *Wear,* submitted 2004.

5.   P. Werner, F. Wöllecke, V. Altstädt, J.K.W. Sandler, A.H. Windle and M.S.P. Shaffer, "Rheological behavior of carbon-nanofiber-reinforced poly(ether ether ketone)", *Journal of Applied Polymer Science*, in preparation 2004.

6.   J. Sandler, A.H. Windle, P. Werner, V. Altstädt, M. van Es and M.S.P. Shaffer, "Carbon-nanofiber-reinforced poly(ether ether ketone) fibers", *Journal of Materials Science*, Vol. 38, no. 10, 2003 pp. 2135.

7.   J.K.W. Sandler, S. Pegel, M. Cadek, F. Gojny, M. van Es, J. Lohmar, W.J. Blau, K. Schulte, A.H. Windle and M.S.P. Shaffer, "A comparative study of melt-spun polyamide-12 fibers reinforced with carbon nanotubes and nanofibers", *Polymer*, Vol. 45, no. 6, 2004 pp. 2001.

8.   J. Sandler, M.S.P. Shaffer, T. Prasse, W. Bauhofer, K. Schulte and A.H. Windle, "Development of a dispersion process for carbon nanotubes in an epoxy matrix and the resulting electrical properties", *Polymer*, Vol. 40, no. 21, 1999 pp. 5971.

9.   J.K.W. Sandler, J.E. Kirk, I.A. Kinloch, M.S.P. Shaffer and A.H. Windle, "Ultra-low electrical percolation threshold in carbon-nanotube-epoxy composites", *Polymer*, Vol. 44, no. 19, 2003 pp. 5893.

10.   C.A. Martin, M.-K. Schwarz, W. Bauhofer, J.K.W. Sandler, A.H. Windle and M.S.P. Shaffer, "Percolation mechanism in multi-wall carbon-nanotube-epoxy composites", *Composites Science & Technology*, in press, 2003.

11.   C.A. Martin, J.K.W. Sandler, A.H. Windle, M.S.P. Shaffer,K. Schulte, M.-K. Schwarz and W. Bauhofer, "electric field-induced aligned multi-wall carbon nanotubes networks in epoxy composites" *Polymer*, submitted 2004.

Effects of Nanoclays and Carbon Nanotubes on the Flow of Epoxy in Resin Transfer Molding: An Overview

Ayca Ertekin [1], R. Byron Pipes [2*], Lloyd A. Goettler [3]

[1, 2, 3] *Department of Polymer Engineering, College of Polymer Science and Polymer Engineering, University of Akron, Akron, OH, 44325*
Ayca Ertekin: email: ae6@uakron.edu
Lloyd Goettler: email: lagoett@uakron.edu
* Corresponding Author: R. Byron Pipes: email: bpipes@uakron.edu

SUMMARY: A concise overview of the state of the art of carbon nanotubes, nanoclays, their composites and resin transfer molding (RTM), with a particular emphasis on unsaturated flow in woven performs is presented. Experiments are proposed to develop understanding of the basics of the flow of epoxy resins, enriched with layered silicates and/or single wall carbon nanotubes (SWNT), through a porous media via RTM process.

KEY WORDS: Carbon nanotubes, nanoclays, resin transfer molding (RTM), unsaturated flow.

INTRODUCTION

The challenging advances in science and technology during the past few decades have led to a continuous demand for new, easy to manufacture, low-cost, and high performance materials and processes meeting increasingly stringent conditions of advanced technology applications. Due to the promising potential of nanoscale materials and composites, numerous studies have been conducted in nanotechnology research during the last two decades. Among many, two forms of polymer reinforcements in the nanometer range are nanoclays and carbon nanotubes. These nanoreinforcements have different geometric forms such that the clays are in platelet form with nano dimensions in thickness, while carbon nanotubes have diameters on the order of nanometers. Nanocomposites, made of nanoclays or so-called layered silicates as reinforcement, are reported to exhibit noticeably improved mechanical, thermal, optical and physico-chemical properties as compared to the pristine polymers or conventional composites. Other attractive features of nanoclay-based nanocomposites are increased modulus, strength, solvent and heat resistance, decreased gas permeability and improved flame retardancy [1-5]. Although the majority of the published studies have focused on nanocomposite property evaluation and synthesis [1-5], complete dispersion of nanoscale reinforcements in the polymer is still one of the most important and incompletely resolved issues in the manufacturing of nanocomposites [2-3]. Hence, the need for significant energy density to accomplish mixing suggests that chemical potential combined with mechanical mixing will be necessary for the dispersion of nanoreinforcements in polymers.

Likewise, several research groups [8-9] have indicated that carbon nanotubes (CNTs) possess outstanding thermal and electrical properties, low density, and small size with extraordinary resilience. The combination of remarkably high-aspect ratio, exceptional specific stiffness, strength, and high conductivity makes CNTs excellent candidates as fillers in polymer composites, especially for high technology applications, such as; data storage technology, electronic devices and sensors. Nonetheless, several studies [9] have emphasized the opportunity and challenge of controlling aspect ratio, polymer crystallinity, and dispersion [11, 13] in polymers at reasonable costs, to employ them or nanocomposites in commercial applications.

Resin transfer molding (RTM) is a versatile process capable of low cost, high volume and net shape manufacturing of polymer composites. During RTM, impregnation of a polymeric resin through a porous preform, generally in the form of carbon, glass or kevlar textile forms, is followed by a curing reaction either during the mold filling or after the injection is complete and the final product is removed from the mold after the cure cycle is completed. In some cases, postcuring is required to relieve residual stresses and to achieve the desired degree of cure. Numerous studies have been conducted on several aspects of RTM ranging from permeability predictions and measurements [17-20], optimization of heat transfer and cure [23-25], analysis of mold filling [21-22] to void formation during the past few decades. Currently, many research studies on RTM are focused on the development of process models and computer simulation tools for prediction of the flow and curing kinetics in the process.

In this overview, characteristic features of carbon nanotubes, nanoclays, and their nanocomposites will be summarized with a particular emphasis on the most critical issues observed in these nanoscale materials. Then, the basic concepts of polymeric flow in RTM will be discussed with a special attention on the "unsaturated flow" in the woven preforms. Finally, a set of experiments, enabling a combination of macroscopic length scale RTM process with nanometer length scale single walled carbon nanotubes or nanoclays will be discussed so as to explore the feasibility of using nanoreinforced-modified resin systems in RTM.

THEORETICAL BACKGROUND

Nanoclays and Polymer Nanocomposites

Polymer layered silicate nanocomposites (PLSN) can be considered as hybrid structures combining an organic phase (the polymer) with an inorganic phase (the silicate). The most widely used layered silicate, montmorillonite, is a crystalline, 2:1 layered clay mineral in which a central alumina octahedral sheet is sandwiched between two silica tetrahedral sheets. The characteristic features of clays are their high aspect ratio (≥ 1000) and capability to swell and exchange cations into their galleries. There are four processes to synthesize polymer-clay nanocomposites, namely, the solution approach; in-situ polymerization; melt intercalation and the sol-gel technique. Several researchers [1-5] have reported that three basic types of PLSN structures can be obtained depending on the method of preparation and the nature of components (i.e., type of layered silicate, type of organic cations and type of polymer matrix) employed. When the polymer chains enter between the silicate layers, intercalated structures in which a well ordered multilayer morphology such as polymeric and inorganic layers are observed.

If the silicate layers are completely and uniformly dispersed in a polymer matrix, exfoliated (delaminated) structures are observed. It is also indicated that both intercalated and exfoliated structures sometimes coexist in a polymer matrix, forming hybrid structures. XRD and TEM are the most commonly used characterization techniques for identifying the PLSN structures [1-4]. The intercalation of the polymer chains generally increases the interlayer spacing, causing a shift of the diffraction peak towards lower angle values. While XRD provides reliable information only for the intercalated structures, it can be deficient most of the times in differentiating exfoliated structures from disordered, agglomerated structures. TEM and atomic force microscopy (AFM) are also frequently used to characterize nanoparticle dispersion. The former requires meticulous sample preparation whereas the latter needs correct etching or cutting line free flat surfaces.

Carbon Nanotubes and Polymer Carbon Nanotube Composites

Carbon nanotubes (CNTs) are generally described as long and cylindrical fullerenes where the walls of the tubes are mono-atomic in thickness and have hexagonal graphitic structure. The atomic structure of CNTs is generally expressed by means of tube chirality, which is defined by chiral vector and chiral angle. The properties of CNTs strongly rely on the atomic arrangement of the graphine-like structure. The diameter of single-walled CNTs is determined by the chiral vector whereas the length results from a sustained growth process, generally 400-1000 nanometers for SWCN. [9]. CNTs can exist either in single-walled (SWNT) or in multi-walled (MWNT) forms. Detailed information about the structure, properties and processing of CNTs can be found in elsewhere [8, 9]. Terrones [9] emphasized that certain properties of CNTs are strongly dependent on crystalline structure and the number of defects. Thostenson et al. [8] stated that the most critical issue in the processing of CNT polymer composites is uniform dispersion in   the polymer [11, 13, 16], the potential for nanotube/matrix interfacial bonding through functionalization of the CNT [13], wetting and alignment of the carbon nanotubes [14, 15] by the polymer matrix. While Wagner et al. [10] has shown that MWNTs embedded in a polymer matrix exhibit superior stress transfer efficiency of one order of magnitude larger than that of carbon fiber-polymer composites, Salvetat et al. [12] measured the axial and shear moduli of SWNTs by AFM and concluded that the slippage of the CNTs within the bundles caused a decrease in the moduli as the diameter of the tube bundles increased. Sandler et al. [16] showed that the electrical properties of nanocomposites are also strongly affected by CNTs such that only a modest volume fraction of CNTs produced conductivity in the polymers.

Unsaturated Flow Phenomenon in Resin Transfer Molding (RTM)

In conventional RTM studies, the flow of "unmodified" polymeric systems through the preforms has been analyzed by several mass, momentum and energy balance equations based on different strategies [23-25].

General approaches to describe the physics of the flow through porous media in LCM literature are based on global form of Darcy's Law, which describes macroscopic flow through porous media such as homogenous fibrous materials, as follows:

$$\mathbf{u} = -\frac{\mathbf{K}}{\mu}\nabla\mathbf{P} \qquad (1)$$

where $\mathbf{u}$ is the volume-averaged velocity of resin in fibrous porous medium, $\mathbf{P}$ is the volume averaged pressure, $\mathbf{K}$ is the permeability tensor of the fibrous preform, and μ is resin viscosity. The flow of resin through a fibrous medium is typically treated as a single-phase flow in the existing RTM literature since the region behind the flow front is considered to be "fully saturated". Hence, the general trend in modeling the RTM flows is to use the macroscopic equation of continuity [23]:

$$\nabla \cdot \mathbf{u} = 0 \qquad (2)$$

Nonetheless, Advani et al. [17], Pillai [24] and Lee et al. [18] reported that there often are obvious indications of incomplete saturation in woven, stitched or braided fibrous mats behind the resin front in RTM. In the same work, Pillai modeled the flow of resin through woven fiber mats in LCM as a dual-scale porous media where gap regions (~ 1 *mm*) and fiber tow regions (~ 10 *μm*) are treated as different phases. The volume averaging techniques have been adapted to derive the mass and momentum balance equations for the flow of resin in dual-scale porous media by many researchers [18, 23]. Pillai [24, 25] also proposed the idea of a sink term in the equation of continuity in the dual scale porous media. The sink term, S, refers to the rate of resin absorbed by fiber tows per unit volume owing to the delayed impregnation of fiber tows, as follows:

$$\nabla \cdot \mathbf{u} = -\mathbf{S} \qquad (3)$$

It was argued that application of this equation along with Darcy's law successfully predicts the reduction of inlet pressure history observed in woven fiber preforms and explains the partial saturation behind the flow front and the degree of impregnation of fiber tows.

RESEARCH REQUIRED

Only a limited number of studies in the literature have investigated the unsaturated flow in dual-scale porous medium and there is a need for dimensionless parameters that quantify the degree of saturation in Darcy flow. Further, this need is particularly pronounced for multi-scale interactions of flows in dual-scale porous medium for nanoreinforced-modified resin systems. Thus, a fundamental understanding of how the presence of SWNTs or nanoclays influences the flow in dual-scale porous medium is mandatory. The first step in accomplishing this task is to study the changes in the thermoset polymer viscosity and cure kinetics that result from various degrees of dispersion of nanoreinforcements in epoxy composites.

Rheological, thermal, XRD and morphological (TEM) characterizations are required to assess polymer properties in both the liquid and solid phases. Moreover, development of chemorheological models will be essential to describe the simultaneous curing kinetics and viscosity changes with time.

CONCLUSIONS

Dual scale phenomena must be considered when nano-phase reinforcements are added to the low viscosity thermoset polymers employed in RTM. The enhanced physical properties of the polymeric matrix phase of the molded product in the presence of nanoreinforcements may be achieved at the expense of the flow characteristics of polymer. Yet, the understanding developed by research in this important field may well provide an opportunity to achieve multifunctionality of the composite matrix phase such as reduced permeability or enhanced thermal or electrical conductivity and thereby open many new opportunities for RTM in advanced products.

REFERENCES

[1] Alexandre M. and Dubois P., Polymer Layered Silicate Composites: preparation, properties and uses of a new class of materials. *Materials Sci. and Eng.*, 28: 1-63, 2000.

[2] Advani S. G. and Shonaike G. O., *Advanced Polymeric Materials: Structure Property Relationships*, CRC Press, 2003.

[3] Pinnavaia T.J. and Beall G.W., *Polymer-Clay Nanocomposites*, Wiley Series in Polymer Sci., 2000.

[4] LeBaron P. C., Wang Z., Pinnavaia T. J., Polymer Layered Silicate Nanocomposites: an overview, *Applied Clay Science*, 15: 11-29, 1999.

[5] Giannelis E. P., Review: Polymer Layered Silicate Nanocomposites: Synthesis, Properties and Applications, *Applied Organometallic Chemistry*, 12: 675-680, 1998.

[6] Okada, A., Usuki A., *Mater. Sci. Eng. C*, C3: 109, 1995.

[7] Lan, T., and Pinnavaia, T. J., *Chem. Mater.*, 6 : 573, 1994 and *Chem. Mater.*, 6: 2216, 1994.

[8] Thostenson E. T., Renb Z. and Choua T. W., Advances in the science and technology of carbon nanotubes and their composites: a review, *Composites Sci. & Tech.*, 61: 1899–1912, 2001.

[9] Terrones M., Science and Technology of the Twenty-First Century: Synthesis, Properties, and Applications of Carbon Nanotubes, *Annual Review of Matls. Research* 33: 419–501, 2003.

[10] Wagner H. D., Lourie O., Feldman Y., Tenne R., 1998. *Applied Physical Letters,* 72:188–190

[11] Shaffer M. S. P. and Windle A. H., Analogies between polymer solutions and carbon nanotube dispersions, *Macromolecules*, 32, 6864-6866, 1999.

[12] Salvetat, J. P., Briggs G. A. D., Bonard J. M., Bacsa R.R., Kulik A. J., Stockli T. et al., Elastic and shear moduli of single-walled carbon nanotube ropes. *Physical Review Letters*, 82 (5): 944–947, 1999

[13] Gong X, Liu J, Baskaran S, Voise RD, Young JS. Surfactant assisted processing of carbon nanotube/polymer Composites. *Chem. of Materials*; 12 (4): 1049–1052, 2000.

[14] Jin L, Bower C, Zhou O. Alignment of carbon nanotubes in a polymer matrix by mechanical stretching. *Applied Physics Letters*; 73 (9): 1197–1199, 1998.

[15] Ajayan, P.M., Stephan, O., Colliex C., and Trauth, D., Aligned carbon nanotube arrays formed by cutting a polymer resin-nanotube composite, *Science*, 26, 1212-1214, 1994.

[16] Sandler J., Shaffer MSP, Prasse T, Bauhofer W., Schulte K., Windle A.H., Development of a dispersion process for carbon nanotubes in an epoxy matrix and the resulting electrical properties, *Polymer*, 40, 5967-5971, 1999.

[17] Parseval Y.D., Pillai K.M., and Advani S.G., A simple model for the variation of permeability due to partial saturation in dual scale porous media. *Transport in Porous Media*, 27:243–264, 1997.

[18] Lee S. J., Choi M. A., Lee M. H., and, Chang J., Permeability modeling of fibrous media in composite processing, *J. Non-Newtonian Fluid Mech.*, 79: 585-598, 1998

[19] Verheus A. S. and Peeters J. H. A., The Role of Reinforcement Permeability in RTM, Composites Manufacturing, 4: 33-38, 1993.

[20] Trochu F., Ferland P., and Guittard D., Concurrent Methods for Permeability Measurement in RTM, *Polymer Composites*, 17: 149-158, 1996.

[21] Yalvac S., Calhoun R. D., Wu C. H., Wang J. T., Lee J. L. and Tsai S. J., Mold Filling Analysis in RTM, *Polymer Composites*, 17: 251-264, 1996.

[22] Cai Z., Analysis of Mold Filling in RTM Process, *J. of Composite Materials*, 26:1310-1339, 1992.

[23] Tucker III C. L., and Dessenberger R. B., Governing equations for flow and heat transfer in stationary fiber beds. S. G. Advani: Editor, *Flow and Rheology in Polymer Composites Manufacturing*, 257–323. Elsevier, 1994.

[24] Pillai K. M., Governing equations for unsaturated flow through woven fiber mats. Part 1. Isothermal flows. *Composites, Part A*; 33: 1007–1019, 2002.

[25] Pillai K.M. and M.S. Munagavalasa, Governing equations for unsaturated flow through woven fiber mats. Part 2. Non-isothermal reactive flows. *Composites, Part A*; 35: 403–415, 2004.

[26] Pillai K. M. and Advani S. G., A model for unsaturated flow in woven or stitched fiber mats during mold filling in resin transfer molding. *J. of Comp. Matls.*, 32(19): 1753–1783, 1998.

Nanoscale Resin Flow and Permeability of Preformed Single-Walled Nanotube (SWNT) Networks

Zhiyong (Richard) Liang[1], Zhi Wang[1], K. Ravi Shankar[1],Chuck Zhang[1], Ben Wang[1], and Leslie D. Kramer[2]

[1] *Florida Advanced Center for Composite Technologies (FAC2T), Florida A&M University – Florida State University College of Engineering, 2525 Pottsdamer Street, Tallahassee, FL 32310-6046,Corresponding Author chzhang@eng.fsu.edu*
[2] *Lockheed Martin Missiles and Fire Control – Orlando, 5600 Sand Lake Rd. MP-450, Orlando, FL 32819-8907*

SUMMARY: Unlike current techniques of directly mixing carbon nanotube with polymer resin, we fabricate SWNT nanocomposites by using a novel three-step process: SWNT networks are first preformed; a resin solution is then infiltrated through the preformed SWNT networks to realize tube/resin impregnation; and then the impregnated SWNT networks are hot pressed to produce the final nanocomposites. Using this method, uniform nanostructures, tube alignment and high nanotube loading can be achieved in the resultant nanocomposites. In the preformed SWNT networks, individual tubes form ropes or bundles approximately 30~60 nm in diameter and the open distance between ropes in the pore structures are about 50~200 nm. Therefore, resin flow and infusion will occur at nanoscale. In this study, the through thickness permeability (K_{zz}) of the random SWNT preforms were measured. The influences of molecular interactions on resin flow within preformed SWNT networks were examined using molecular dynamics simulation.

Keywords: Nanocomposites, SWNT, Resin flow, Permeability

INTRODUCTION

The single-walled carbon nanotube (SWNT) has received considerable notice because of its unique and exceptional material properties. SWNTs are considered by many researchers the most promising reinforcement for the next generation high performance composites [1,2]. Unlike conventional fibrous reinforcements, SWNTs interact intensively with resin matrix due to their nanoscale dimension (0.4~18 nm in diameter and up to 1 several μm in length), extra-large surface area (as high as 1500m^2/g) and strong van der Waals forces caused by the sp^2 electronic structure. For example, by adding only 1 or 2% by weight SWNTs to resin, the viscosity of the resin/SWNT mixture could dramatically increase.

Sometimes the mixture becomes a thick paste and loses its flow ability, which will lead to poor tube dispersion in nanocomposites.

The authors developed a new approach to prepare SWNT-reinforced nanocomposites that avoids the drawbacks of directly mixing tubes/resin matrix during nanocomposite processing [3,4]. This new method employs preformed tube networks or nanotube mats called buckypapers and a special resin infiltration method. In this process, SWNTs were first dispersed into water with the aid of the selected surfactant and sonication to form a well-dispersed, stable suspension. The SWNTs suspension was filtrated to form buckypapers, which are composed of uniformly preformed SWNT rope networks. Buckypapers are a macroscale dimension and can be handled as conventional fiber mats to attain controllable reinforcement distribution and volume content. In the preformed SWNT networks, individual tubes form ropes or bundles approximately 30~60 nm in diameter, with openings between the tube ropes in the pore structures about 50~200 nm. Therefore, resin flow and infusion will occur at nanoscale. In this study, the through thickness permeability (K_{zz}) of the random SWNT preforms was measured. The influences of molecular interactions on resin flow within preformed SWNT networks were investigated using molecular dynamics (MD) simulation.

NANOSTRUCTURE OF THE PREFORMED SWNT NETWORK

Fig. 1 shows the produced buckypapers for the study. The buckypapers demonstrate good strength and flexibility to allow for handling similar to traditional glass fiber mats. The nanostructure of the buckypaper can be seen in Fig. 2. The buckypaper images show that the tube networks were composed of continuous SWNT ropes, which was the result of the self-assembly of the nanotubes by van der Waals force during buckypaper filtration [5]. The rope size and porous structure of the buckypapers were uniform, indicating very good tubes dispersion in the suspension. The ropes' diameters were in the range of 30~60 nm. The buckypaper nanoscale structures had pores with openings ranging from 50-200 nm, which are much smaller than those in traditional glass fiber and carbon fiber fabrics or mats.
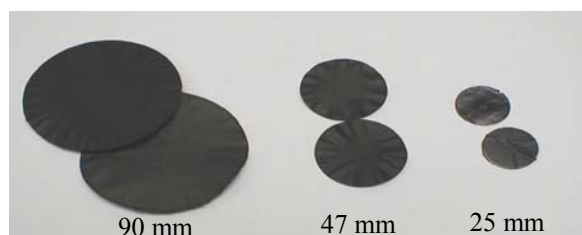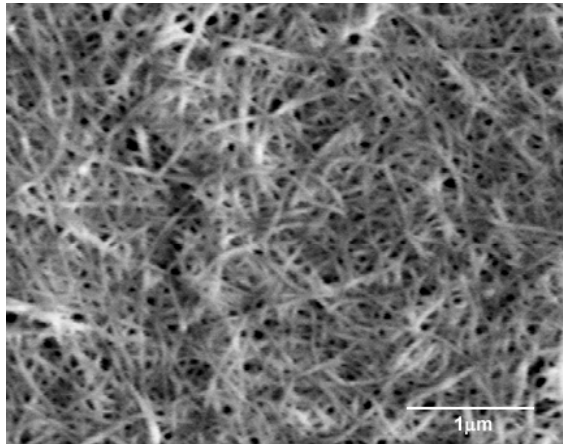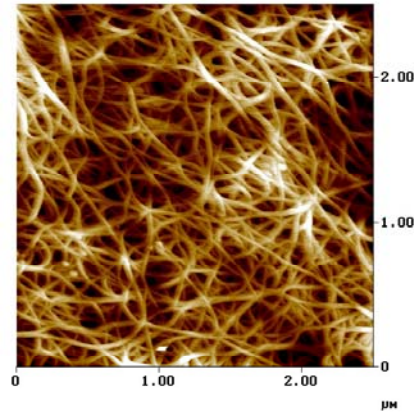

Fig. 1. Single-walled carbon nanotube buckypapers

AFM image   SEM image
Figure 2. Nanostructures of the preformed SWNT network in the buckypapers

COMPARISON OF PORE SIZE AND DIMENSION OF RESIN MOLECULES

Since the buckypaper porous structures were at nanoscale, confirming the comparability between the buckypaper pore size and the dimension of the resin/curing agent molecules in necessary. Under minimum energy conditions, MD simulation revealed that the resin system used in this study, Epon 862 epoxy resin and curing agent molecules (DETDA), have the approximate dimensions of 23 Å × 9 Å × 6 Å and 6.7 Å × 6.5 Å × 1.8 Å, respectively. This is a low viscosity resin system, which is widely used for RTM process. The simulation results indicate that both resin and curing agent molecules could penetrate through the nanostructure and form a 3D cross-link network of resin matrix [6].

PERMEABILITY MEASUREMENT OF SWNT BUCKYPAPER

The through thickness (z-direction) permeability (K_{zz}) of the produced buckypapers was measured for the study. Deioned water was used as the working fluid in the permeability test. The buckypapers acted as filter membranes in the test filter setup. The buckypapers were placed inside a filter and sealed. Under a full vacuum, deionized water was drawn through the buckypaper along the thickness direction. The water flow rate, buckypaper thickness, buckypaper surface area and vacuum pressure were recorded to calculate the K_{zz} of buckypapers with 10-50mm thickness and nanoscale pore structures. The z-direction permeability K_{zz} (saturated permeability) was calculated by the following Darcy's Law [7, 8].

The results of the z-direction permeability tests on the buckypapers are shown in Table 1. The average value of buckypapers' K_{zz} was about $2 \times 10^{-19} m^2$. Compared to conventional glass fiber reinforcement fabrics or mats (V_f=60%), the buckypaper permeability was 8-10 times lower. Therefore, infusing the resin through buckypapers in the in-plane direction, as with conventional RTM and VARTM process of fiber reinforced composites, is almost impossible due to nanoscale pore structure and extremely high flow resistance. The buckypapers had to be infused with resin and impregnated along their thickness direction.

Under this condition, the z-direction permeability is a key parameter for the buckypaper/resin infusion process.

Table 1: K_{zz} of the buckypapers

Buckypaper Thickness (µm)	25.4	31.2	35.7
K_{zz} (m^2)	3.358×10^{-19}	1.105×10^{-19}	1.442×10^{-19}
Average K_{zz} (m^2)	1.968×10^{-19}		

NANOSCALE RESIN FLOW MODELING

Since intensive molecular interactions between nanotubes and resin molecules are expected during nanocomposite processing, MD simulation was used to explore the phenomena of nanoscale resin flow [6]. Assuming the nanotubes were individually dispersed in the buckypaper and the nanotubes' diameters were about 1 nm, a molecular model for illustrating the nanoscale resin flow was developed. The model indicated that the Epon 862 epoxy resin and EPI CURE curing agent molecules are at the same length scale as the pore structure of the (10,10) SWNT networks. In this model, a square nano-pore was constructed with four (10,10) SWNTs 97 Å long. The resulting pore dimensions were 6 nm x 6 nm and the thickness of the model was 3 nm. When processing nanocomposites, the EPON 862 epoxy resin was infused into the buckypaper after mixing with the curing agent. The liquid resin matrix consisted of Shell EPON 862 epoxy resin and EPI-CURE W curing agent (DETDA) with a weight ratio of 100:26.4. The ratio of the resin molecule number to the curing agent molecule number was about 2:1. Finally, 7145 atoms were included in the simulation model. Snapshots of the MD simulations are shown in Fig. 3 and 4. Initially, the epoxy resin and curing agent molecules were placed near the pore opening (some slightly inside the pore, some well outside the pore). During the initial 10 ps of the simulation, the resin molecules were changing their orientations and moving towards the nanotubes. After an equilibration period of 80 ps, the resin molecules close to the nanotube moved closer and wetted the nanotube. However, the resin molecules in the middle of the pore remained in place due to the resin molecules' weak interactions with the nanotubes. This suggests that at nanoscale, strong molecular interactions between SWNTs and resin molecules affect resin flow behavior, possibly because the majority of resin and curing agent molecules interacting with the SWNTs due to their nanoscale dimension and extra-large surface area.
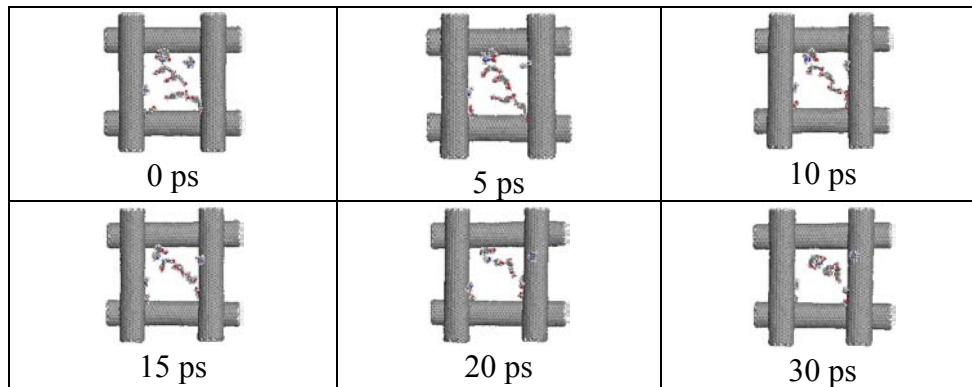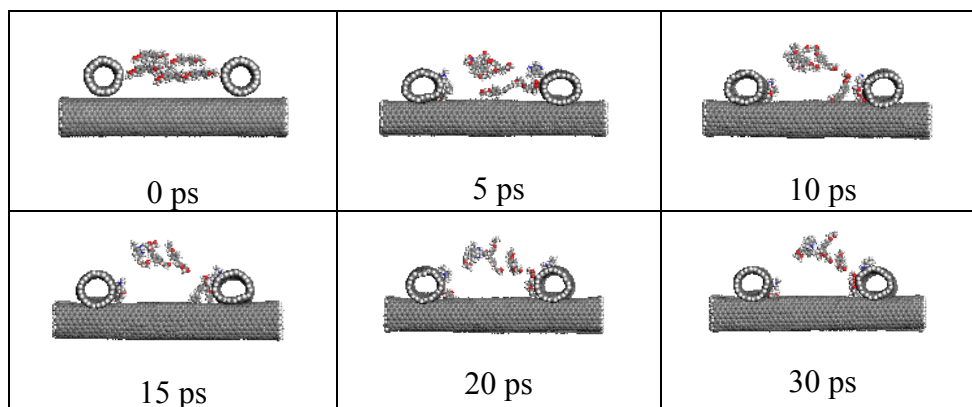
Fig. 3. Top view of the MD simulation results

Fig. 4. Side view of the MD simulation results

This simplified MD simulation clearly indicates the molecular interactions on nanoscale resin flow behavior. The effect of molecular interactions is usually ignored in conventional resin flow models, such as Darcy's Law and Kozeny-Carman (K-C) Equation, used for liquid composite molding processes. For nanocomposite processing, molecular interactions must be considered. New nanoscale resin flow and permeability models require further development.

CONCLUSIONS

In this study, permeability of preformed SWNT networks and nanoscale resin flow behaviors were investigated. Unlike conventional fiber preforms, the pore structure of the preformed SWNT network is at nanoscale and the z-directional permeability of the buckypapers was as low as $2 \times 10^{-19} m^2$. Compared to normal glass fiber reinforcement fabrics or mats (V_f=60%), the buckypapers' permeability is 8-10 times lower. The influences of molecular interactions on the resin flow within the SWNTs' nanoscale pore structure were investigated.

Preliminary MD simulation results show that during nanocomposite processing, strong molecular interactions between SWNTs and resin molecules exist and as a result, resin molecules will likely be attracted to the SWNT surface because of the van der Vaals interactions and extra-large SWNT surface area. The effects of molecular interactions should be considered and new nanoscale resin flow and permeability models require further development for nanocomposite processing.

REFERENCES

1. E.T. Thostenson, Z.F. Ren and T.W. Chou, "Advances in the Science and Technology of Carbon Nanotubes and Their Composites: A Review," Composites Science and Technology, 2001; 61:1899.
2. K.T. Lau and D. Hui, "The Revolutionary Creation of New Advanced Materials-Carbon Nanotube Composites," Composites Part B, 2002;33:263.
3. Z. Liang, K.R. Shankar, K. Barefield, C. Zhang, L. Kramer and B. Wang, "Investigation of Magnetically Aligned Carbon Nanotube Buckypapers/Epoxy Composites," Proceedings of SAMPE 2003 (48th ISSE), Long Beach, CA, May 12-14, 1627-34, 2003.
4. Z. Wang, Z. Liang, B. Wang, C. Zhang and L. Kramer, "Processing and Property Investigation of Single-walled Carbon Nanotube (SWNT) Buckypaper/Epoxy Resin Matrix Nanocomposites," Composite Part A: Applied Science and Manufacturing, (in print).
5. K.D. Ausman, M.J. O'Connell, P.Boul, L.M. Ericson, M.J. Casavant, D.A. Walters, C. Huffman, R. Sanini, Y. Wang, E. Haroz, E.W. Billups and R.E. Smalley, "Roping and Wrapping Carbon Nanotubes," Proceedings of XVth International Winterschool on Electronic Properties of Novel Materials Euroconference, Kirchberg, Tirol, Austria 2001.
6. J. Gou, "Single-walled Carbon Nanotube Buckypaper/Epoxy Composites: Molecular Dynamics Simulation and Process Development," Ph.D. dissertation, Florida State University, 2002.
7. R.S. Parnas, J.G. Howward, T.L. Luce and S.G. Advani, "Permeability Characterization Part I: A Proposed Standard Reference Fabric for Permeability," Polymer Composites, 1995;16(6):430.
8. T.J. Wang, C.H. Wu and L.J. Lee, "In-plane Permeability Measurement and Analysis in Liquid Composite Molding," Polymer Composites, 1994;15(4):278.

The Preparation of Clay/Glass Fiber/Epoxy Hybrid Nanocomposites Using VARTM

Joong Hee Lee[1], Suresh G Advani[2], Liyu Lin[1], and Gye-hyoung Yoo [3]

[1] *Dept of Advanced Materials Engiineering*
Chonbuk National University, Duckjin-dong 1Ga 664-14
Jeonju, Jeonbuk, Korea; *jhl@mail.chonbuk.ac.kr*
[2] *Department of Mechanical Engineering and Center for Composite Materials*
University of Delaware, Newark, DE 19716, USA
[3]*Research and Development Center, Korea Composite Research Co. Ltd.*
Jeonju High Tech Venture Complex Bld#5, Palbokdong 2 Ga, Jeonju, Jounbuk, Korea

SUMMARY: Clay/polymer nanocomposites have received a great deal of attention recently. We prepared clay/glass fiber/epoxy hybrid nanocomposites using a vacuum-assisted resin-transfer molding (VARTM) process. A nanoclay was dispersed in a solvent with vigorous mechanical stirring and then the suspension was mixed with epoxy resin. To study the effects of fiber direction on the clay distribution, unidirectional glass fibers were placed in two directions: parallel and perpendicular to the flow direction. The micro-scale behavior of organophilic montmorillonite in an epoxy resin system was investigated using X-ray diffraction (XRD). The mechanical properties of composites with different clay loadings were measured. The morphology of the nanocomposites was also observed using scanning electron microscopy (SEM) and transmission electron microscopy (TEM). We found that introducing a small amount of nanoclay to the glass fiber-epoxy composites enhanced the mechanical properties. The convection of nanoclay was observed in the fiber-rich region and inside the fiber bundles.

KEYWORDS: clay/glass fiber/epoxy hybrid nanocomposites, vacuum-assisted resin-transfer molding (VARTM), mechanical properties, impact strength

INTRODUCTION

Layered silicates are used as fillers in polymer systems because of the improved mechanical properties [1-4], thermal stability [4-8], gas barrier properties [7, 9], and flame retardant properties of the resulting polymer composites [7,11]. Conventional glass fiber-reinforced polymeric composites are also widely used as structural engineering materials in many industries. One cost-effective processing technique for producing glass fiber-reinforced composites is vacuum-assisted resin transfer molding (VARTM). VARTM is used to manufacture a wide variety of articles, ranging from small armrests for buses to large components for water-treatment plants.

Three different approaches are used to synthesize polymer/clay nanocomposites: the 1) melt intercalation, 2) solution, and 3) in-situ polymerization methods. In the melt intercalation process, a thermoplastic polymer is mixed with organophilic clay mechanically at elevated temperature. The polymer chains are then intercalated directly between layers of the clay [10]. In the solution method [11], the organoclay and polymer are dissolved in a polar organic solvent, allowing the dissolved polymer chains to penetrate the clay layers. After evaporating the solvent, uniform mixing of the polymer and layered clay is achieved. In the *in-situ* method, monomers are intercalated into clay layers directly and then polymerized within the layers. We used the solution method to synthesize epoxy/clay nanocomposites using VARTM. The morphology and mechanical and thermal properties of the nanocomposites were investigated to study the effects of nanoparticles on continuous glass fiber-reinforced polymer composites.

EXPERIMENT

Materials

The epoxy resin used was YD-128 (Kukdo Chemical Co. Ltd.). The epoxide equivalent weight (EEW) of the epoxy resin was 185-190 eq^{-1}. The curing agent was D-230 (New Seoul Chemical Co. Ltd.). The active diluting agent was butyl glycidyl ether (BGE, Kukdo Chemical Co. Ltd.). The organoclay was Cloisite 15A (Southern Clay Products Inc.) and T-800 unidirectional glass fibers (Dong-IL Industrial Co.) were used. All the components of the epoxy system were used as received without purification.

Preparation of nanocomposites

A flat rectangular mold measuring 300×200×3 mm was used to prepare the nanocomposites. A rubber gasket was placed around the perimeter of the mold halves to provide a proper seal. Fig. 1 shows a schematic of the experimental set-up used for the closed-mold VARTM process. Eight grams of organoclay (Cloisite 15A) were dispersed homogeneously in 120 mL of chloroform at room temperature. The suspension was added to epoxy resin. The mixture was stirred vigorously using a mechanical stirrer, and then the chloroform was removed by evaporation. Once the mixture had cooled to room temperature, diluted BGE and the curing agent (D-230) were added and stirred. Finally, the mixture was degassed before injecting it. Five layers of unidirectional glass fiber mat measuring 250×200×3 mm were placed in the longitudinal or transverse directions to investigate the effects of flow direction on nanocomposites. The mold was maintained at a temperature of 50°C during filling. The vacuum was maintained at 75 cm of Hg. The molded nanocomposite was cured at 80°C for 4 h and post-cured at 125°C for 3 h in the oven.
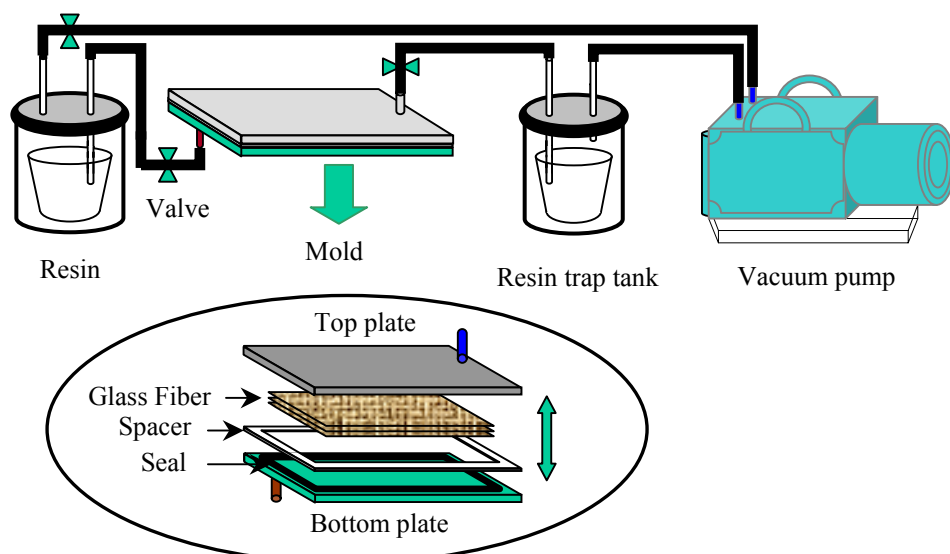
Fig. 1. Schematics of the closed-mold VARTM process

Characterization and testing

X-ray diffraction (XRD) analysis was performed using a Rigaku D/MAX 2500 diffractometer equipped with Cu-*Ka* X-ray and operated at 40 kV and 30 mA. The scanning speed and step size used were 1° min^{-1} and 0.02°, respectively. The diffraction patterns were collected between 1 and 10°. Cured composite samples were prepared by mounting a rectangular flat specimen in an aluminum holder. The powdered clay was compressed and smoothed into a glass holder.

Cross-sections of the composites were examined using a JEOL JSM-6400 scanning electron microscope (SEM) equipped with a PGT EDS (energy dispersive X-ray spectrometer) system. The composition of the composite was analyzed using EDS. SEM samples were cut from the composites, polished, and coated with gold.

Dynamic mechanical analyzer (DMA) tests were performed on a TA DMA-983 in fixed frequency mode at 1 HZ and an amplitude of 0.40 mm. Rectangular DMA specimens measuring 60×10×3 mm were used for the analysis.

The transverse flexural properties of the composites were measured using the three-point bending test according to ASTM D790-97. Rectangular specimens measuring 100×12×3 mm were used. The support span distance was 60 mm and the crosshead speed was 2 mm/min. The impact properties of the composites were also measured using an un-notched Izod impact test according to ASTM D4812. Specimens measuring 64×10×3 mm were used and five tests were performed for each condition.

RESULTS AND DISCUSSION

X-ray diffraction analysis was used to determine the structural characteristics of the clay dispersed in epoxy resin. Fig. 2 shows the XRD patterns of the original organoclay and the epoxy/clay nanocomposites. The basal space of the clays changed from 34.75 to 37.73 Å due to the intercalation of epoxy molecules. The degree of swelling was improved slightly when the solution was used as compared to direct mixing. When the clay content was below 3%, fully exfoliated nanocomposites were obtained. Thermogravimetric analysis (TGA) was performed at a heating rate of 10°C min^{-1} from 50 to 700°C to investigate the thermal stability of the epoxy/clay nanocomposites. The flexural modulus and strength of the nanocomposites were measured using the three-point bending test. Table 1 summarizes the mechanical properties and thermal stabilities of nanocomposites with various clay contents. The flexural strength and modulus generally increased with the clay content. However, the flexural strength of the nanocomposites decreased suddenly above a 3% clay loading. A similar trend was

Table 1. Mechanical and thermal properties of the nanocomposites.

Clay Content (%)	Flexural strength (Mpa)	Flexural modulus (GPa)	**Impact strength** (J/m)	Decomposition temperature (　)
0	70.89	14.63	77.9	251.19
1	70.70	14.94	74.6	256.65
3	85.33	15.20	96.7	274.99
5	58.68	15.49	100.4	286.87

reported previously [3] and it was suspected that there is a critical clay content for improving the flexural strength of a nanocomposite. Surprisingly, the impact strength increased remarkably on introducing a small amount of clay into the glass fiber-reinforced composites. Clay loading improved the thermal stability of the nanocomposites. The decomposition temperature was the temperature at which the weight loss of the nanocomposites was 1% in the TGA curves. Fig. 3 shows the storage modulus (E′) and tan δ of nanocomposites for various clay loadings. The storage modulus increased with the clay content, but no significant changes in the glass transition temperature of the nanocomposites was observed. The SEM images in Fig. 4 show that the nanoclay was distributed uniformly around the glass fiber bundles. The nanoclay particles became less dense downstream in the mold. The nanoclay particles were more uniformly distributed when the resin flows along the fiber direction compared to the flow across the fiber. EDS analysis was used to verify the clay nanoparticles in the nanocomposite.
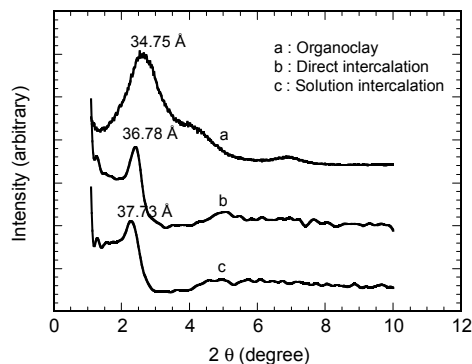
Fig. 2. XRD patterns of organoclay and epoxy/organoclay nanocomposites with 5% clay.
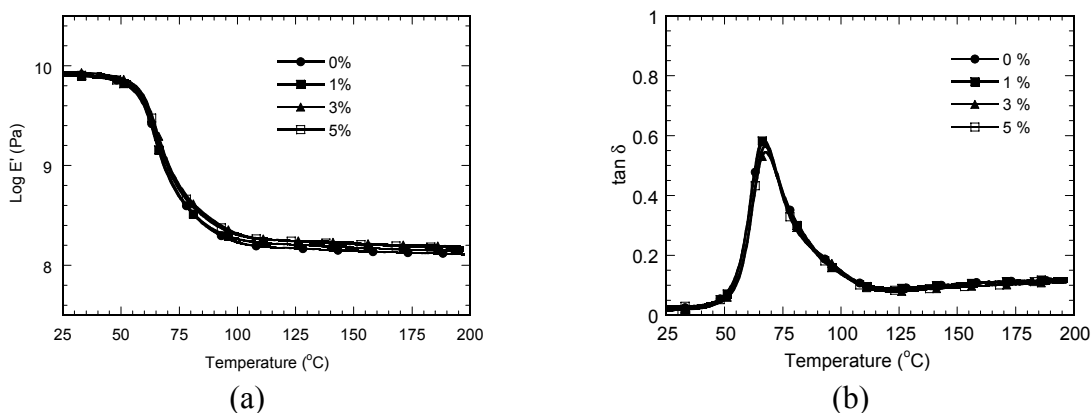

(a)   (b)

Fig. 3. (a) Storage modulus and (b) tan δ of nanocomposites for various clay loadings.

(a)   (b)   (c)
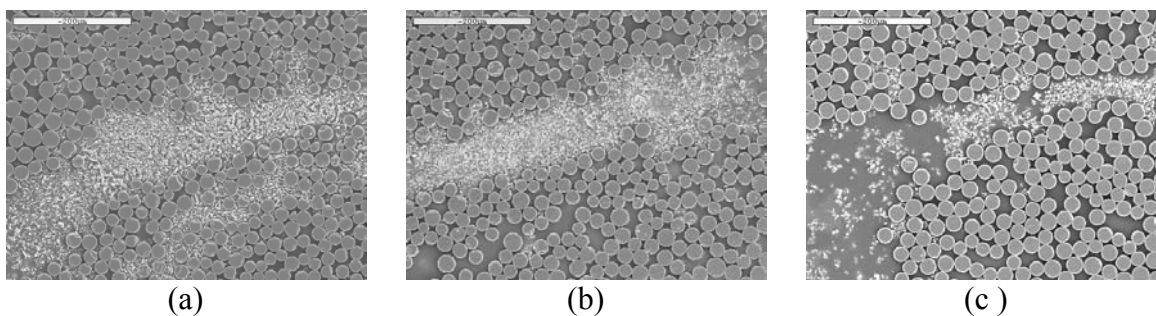
Fig. 4. SEM photographs of cross-sections of the molded part: (a) at the inlet, (b) at the middle, and (c) at the outlet regions

CONCLUSIONS

Clay/glass fiber/epoxy hybrid nanocomposites were prepared using VARTM. The mechanical and thermal properties of the conventional composites improved due to the addition of layered silicates. The impact strength of the nanocomposites was enhanced remarkably by addition of a small amount of clay. The morphology of the hybrid nanocomposites was also observed in two flow directions, parallel to the fibers and perpendicular to the fiber direction.

ACKNOWLEGEMENT

REFERENCES

1. C. Chen and D. Curliss, "Preparation, Characterization, and Nanostructural Evolution of Epoxy Nanocomposites", *Journal of Applied Polymer Science,* Vol 90, pp2276-2287 (2003).
2. A. J. Kinloch and A. C. Taylor, "Mechanical and Fracture Properties of Epoxy/inorganic Micro- and Nano-composites", *Journal of Materials Science Letters,* Vol 22, pp 1439-1441 (2003).
3. A. Haque, M. Shamsuzzoha, F. Hussain, D. Dean, "S2-Glass/Epoxy Polymer Nanocomposites: Manufacturing, Structures, Thermal and Mechanical Properties", *Journal of Composite Materials,* Vol 37, No. 20, pp 1821-1837 (2003).
4. Y. Zhang, J. H. Lee, H. J. Jang, and C. W.Nah, "Preparing PP/clay Nanocomposites Using a Swelling Agent", *Composites: Part B,* Vo. 35 No. 2, pp133-138 (2004).
5. C. Nah, S. H. Han, J. H. Lee, M. H. Lee, S. D. Lim, and J. M. Rhee, "Intercalation Behavior of Polyimide/organoclay Nanocomposites during Thermal Imidization", *Composites: Part B,* Vol. 25, No.3, pp 125-131 (2004).
6. M. Hussain, R. J. Varley, Z. Mathys, Y. B. Cheng, and G. P. Simon, "Effect of Organo-phosphorus and Nano-Clay Materials on the Thermal and Finite Performance of Epoxy Resins", *Journal of Applied Polymer Science,* Vol. 91, pp 1233-1253 (2004).
7. O. Becker, R. J. Varley, and G. P. Simon, "Thermal Stability and Water Uptake of High Performance Epoxy Layered Silicate Nanocomposites", *European Polymer Journal,* Vol 40, pp 187-195 (2004).
8. K. Yano, A. Usuki, and A. Okada, "Synthesis and Properties of Polyimide-Clay Hybrid Films", *J. Polym Sci A: Polym Chem,* Vol. 35, pp 2289-2294 (1997).
9. M. Hussain and G. P. Simon, "Fabrication of Phosphorus-clay Polymer Nanocomposites for Fire Performance", *Journal of Materials Science Letters,* Vol. 23, pp 1471-1475 (2003).
10. S. S. Ray and M Okamoto, "Polymer/layered Silicates Nanocomposites: a Review from Preparation to Processing", *Processing in Polymer Science,* Vol. 28, pp 1539-1641 (2003).
11. L. Jiankun, K. Yucai, Q. Zongneng, Y. Xiao-su, "Study on Intercalation and Exfoliation Behavior of Organoclays in Epoxy Resin", *Journal of Polymer Science: Part B: Polymer Physics,* Vol. 39, pp115-120, (2001).

Manufacturing and Characterization of Experimental Polycarbonate Composites with Reinforced Vapor Grown Carbon Fiber

Young-Kuk CHOI [a], *, Koh-ichi SUGIMOTO [a], Sotaro YAMAUCHI [a], Sung-Moo SONG [b], Morinobu ENDO[c]
[a]Department of Mechanical Systems Engineering, University of Shinshu, 4-17-1 Wakasato, Nagano city 380-8553, Japan: sugi001@gipwc.shinshu-u.ac.jp
[b]Misuzu Industries Co., Shiga, Suwa city 3090, Japan: song001@gipwc.shinshu-u.ac.jp
[c]Department of Electrical and Electronic Engineering, University of Shinshu, 4-17-1 Wakasato, Nagano city 380-8553, Japan: endo@endomoribu.shinshu-u.ac.jp
* Corresponding author's e-mail: sugi004@gipwc.shinshu-u.ac.jp

SUMMARY: Polycarbonate composites based on vapor grown carbon fiber (VGCF) were successfully fabricated by solution-evaporation and rolling methods. Microscopic analysis has shown that the fibers were well dispersed in a polycarbonate matrix.

Increasing the fiber content resulted in the electrical and tensile strengths decreasing in both materials. The accumulation of voids increased in the nanocomposites, which influenced a decrease in the mechanical properties of the material.

The VGCFs delayed the thermal decomposition of the PC which is likely a result of absorption, by the carbon surface, of free radicals generated during the polymer decomposition. The twin-rolling process enhanced the degree of fiber orientation and improved its mechanical and electrical properties. Thin composites showed a high Young's modulus due to the surface alignment of the fibers where thin composites were more concentrated.

KEYWORD: Vapor grown carbon fiber, Polycarbonate, Nanocomposit sheets, Electrical resistivity, Mechanical properties, Decomposition

INTRODUCTION

Carbon fiber and carbon fiber reinforced composites have attracted worldwide interest as high performance materials. Not only for their light weight and high mechanical properties but also for their potential of having extraordinary electrical and thermal properties, carbon fibers are being used in the aircraft and antistatic industries as well as computer housings and exterior automotive parts where the reduction of static electrical charge is necessary [1-2].

Because of a small diameter the VGCFs cause various problems such as a difficult incorporation into a highly viscous polymer matrix and a tendency to agglomerate. This agglomeration especially occurs as fiber content increases when dispersed in a matrix during its production: carbon nanofibers are more attracted to each other than to the liquid. Some researches results indicated poor mechanical properties because of poor fiber wetting, poor fiber dispersion and the presence of voids [3-6].

Some investors also obtained well dispersed carbon nanotubes (CNTs) in a polymer by high energy sonication of a solution of polymers containing dispersed CNTs. This was followed by a solvent-evaporation method, which successfully achieved homogeneous composites [7-12]. The main objective of this study is to investigate precisely the influence of dispersion processing conditions and the analysis of the mechanical, electrical properties using a scanning electron microscopy (SEM) and a wide angle X-ray diffraction (WAXD) on the nanocomposite sheets. We have also corroborated on the mechanical and electrical properties that were a result of the thickness.

EXPERIMENTATION

The matrix used in this study is the polycarbonate (NOVAREX 7020A grade, M_w of 19000g/mol) in pellet form, which were purchased from Mitsubishi Engineering plastics. Vapor grown carbon nanofibers (VGCFs) are VGCF^{TM} from the Showa Denko K.K Company of Japan with diameters of 100-200nm and length of 10-20μm. PC pellets and VGCFs were dried at 120°C in a vacuum for 6hours and 24hours, respectively to remove the water. Because VGCFs are tightly compacted they can only be infiltrated if they are precisely prepared before mixing them with the polymer matrix. We performed a sieving process at 106μm followed 53μm in order to reduce the diameter of clumps.

To obtain uniform dispersion of VGCFs, PC pellets were completely dissolved in the tetrahydrofuran (THF) for about 2hours and the VGCFs were dispersed in a separate THF beaker by sonification and the stirring process for 15minutes. Then the mixture of PC solution was added to the mixture. Sonification and stirring processes were continued for another 15minutes. Next, the solution-evaporation method and rolling processes were performed, respectively, to fabricate the nanocomposite sheets. The thickness constant was about 0.12mm using a twin-roller at 150°C for 20minutes. The nanocomposite sheets's dispersion state was examined using a SEM. X-ray diffraction pattern collected from both the cast and rolling composite sheets at room temperature. The WAXD measurement used CuKα X-ray source radiation at 40kV and 140mA to examine the orientation of VGCFs in the nanocomposite sheets. The degree of the VGCF orientation (f_o) were then obtained using the following equation:

$$f_o = \frac{3 < \cos^2 \Phi > -1}{2}$$

where $< \cos^2 \Phi > = \dfrac{\displaystyle\int_0^{\pi/2} I_{(\Phi)} \cos^2 \Phi \sin \Phi d\Phi}{\displaystyle\int_0^{\pi/2} I_{(\Phi)} \sin \Phi d\Phi}$

where $I(\Phi)$ is the azimuthal intensity distribution. Curves derived from the azimuth scans were fitted to the profiles of the mathematical model investigated with a Pearson VII functions [13].
The volumes of electrical resistivities were measured at room temperature by a standard four-point probe method on a digital high tester.

The tensile tests were carried out with a minimum of 10 samples. The tensile strength and the Young's modulus were obtained from the tensile test, which was carried out at room temperature, according to ISO 527-3 and performed using a Shimadzu tensile tester (AGS-J) at a cross-head speed of 1mm/min.

In order to investigate the effects of the VGCFs on the thermal properties of the matrix, thermogravimetric analysis (TGA) measurements were performed on composite sheets at all concentrations of VGCF. We used the DTG-50 DTA-TGA instruments simultaneously under a nitrogen atmosphere. 10mg of either pure PC and nanocomposite sheets were used for these measurements. The heating rate was 10°C/min at a temperature range of room temperature to 600°C.

RESULTS AND DISCUSSIONS

In order to determine the quality of the structure, Fig.1 shows the micrographs of the PC/VGCF nanocomposite sheets with VGCF loading of 10wt% for the cast and rolling nanocomposites, respectively. In the samples examined, the VGCFs were found to be evenly well dispersed and the fibers were enough to create the strong network. Voids were observed when VGCF content increases i.e. in the 25wt% composites. We concluded that the Voids diminished on the nanocomposite rolling sheet because of the rolling process. The voids could be under the influence of mechanical properties [5].
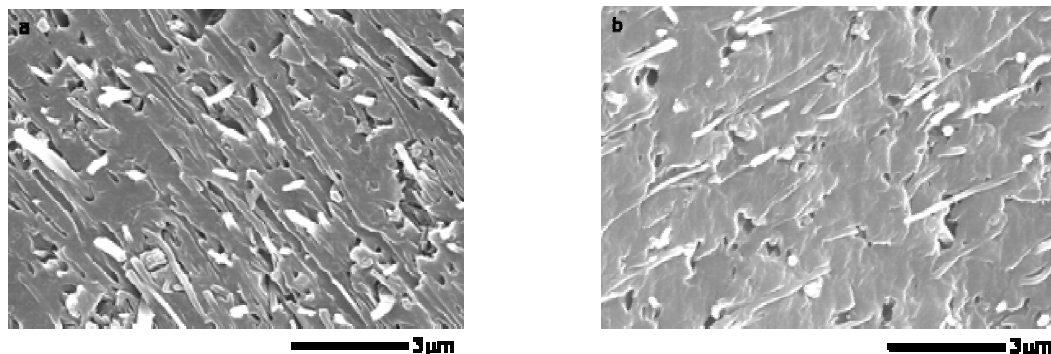

Fig.1 Dispersion of VGCF in a PC matrix; a: 10wt% cast and b:10wt% rolling nanocomposite sheets

The orientation of VGCF was analyzed using the X-ray for the cast and rolling nanocomposite sheets which were reinforced by 10wt% VGCF. The orientation was calculated to be 0.6 and 0.8 for the cast and the rolling nanocomposite sheets, respectively. We estimated from these results that the VGCFs are randomly oriented in the PC matrix and the rolling process enhanced the orientation of the VGCFs.

Fig.2 shows the TGA curves of PC and various filler contents for the nanocomposite rolling sheets. All samples started to decompose above the melting point and the masses remaining at 600°C are due to the remaining VGCFs. Comparing with the TG curves of pure PC and PC/VGCF blending are that the decomposition of materials shifted to a high temperature when increasing VGCF content. This retarding effect is likely to be a result of absorption, by the carbon surface, of free radicals generated during the polymer decomposition [14-15].
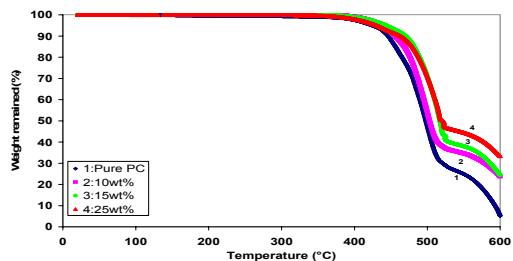
Fig.2 TGA curves of pure PC and various nanocomposite sheets

The influence of VGCF content and thickness on volume electrical resistivity was measured for the casting and the rolling composite sheets. The electrical resistivity decreases with loading. For rolling composite sheets, the high resistivity was measured only at 25wt% not 10 and 15wt%. It is estimated that the VGCF's networks were not well in a wet mixing process because of the high viscosity of the polymer unlike the cast polymer (Fig.3a).
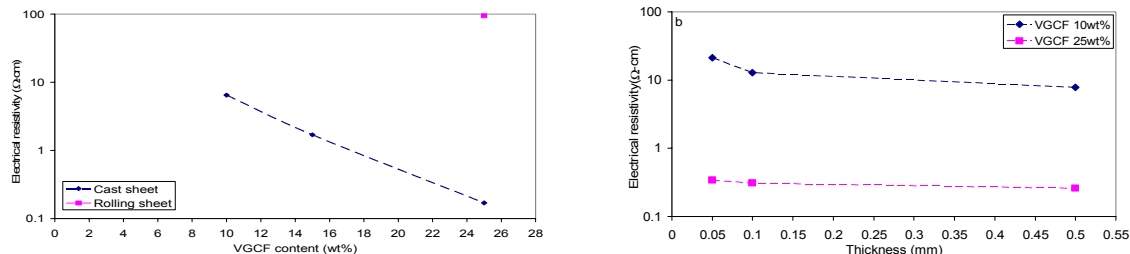

Fig.3 Electrical resistivity of PC/VGCF as a function of the fiber loading and thickness; a: casting and rolling composite sheets, b: cast composite sheets with various thicknesses.

Similar influences of the electrical resistivity are shown at various thicknesses in that the resistivity decreased with an increase of thickness in the cast nanocomposite sheets (Fig.3b). The dependence of the tensile strength and Young's modulus on fiber content for the cast and rolling composite sheets are shown in Figs.4a and b. In Fig.4a, both the maximum tensile strength of the cast and rolling composites resulted in 10wt% of VGCF. For comparison, the tensile strength of the rolling sheets was higher than the casting sheets method. There are two main reasons for this. First, the degree of orientation of VGCF for the rolling sample is higher than that of the cast sheets, determined by using WAXD. In general, the rolling procedure enhances the orientation of VGCFs and polymer chains.
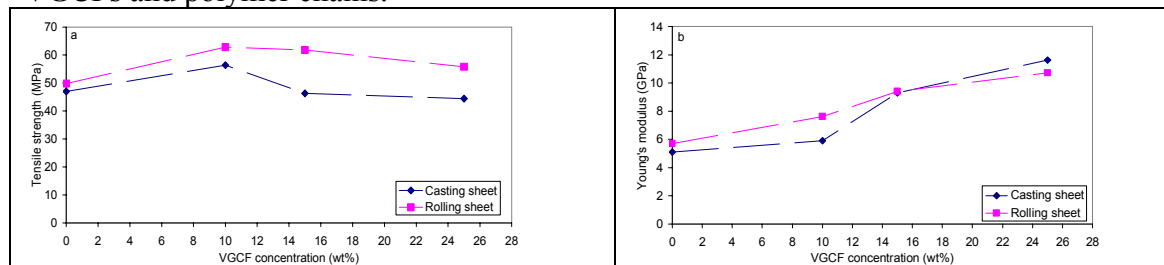

Fig.4. Mechanical properties of PC/VGCF cast and rolling composites reinforced with various amount of VGCF; a: Tensile strength; b: Young's modulus

Second, the rolling process reduces the voids. When the voids decrease, the mechanical properties should be increase. However, there is a major decrease in tensile strength with the incorporation of VGCFs. This suggests that there is a presence of voids in the PC matrix. But the Young's modulus appears largely unaffected by the addition of the
VGCFs, which results in an increases of the tensile modulus (Fig.4b).

We observed on the SEM that there were fractured surfaces on both materials, content of 25wt% of VGCF, and that the majority of the fibers were well coated by the polymer. This indicates that the load transfer from the polymer to VGCF was sufficient to fracture the VGCFs. Fig.5 illustrates the dependence of tensile strength and modulus on thickness for the 10wt% and 25wt% nanocomposite sheets. The tensile strength increases with increasing thickness. We estimated that the reinforcement fibers are probably more uniformly dispersed when the thickness or the number of stacks increases.
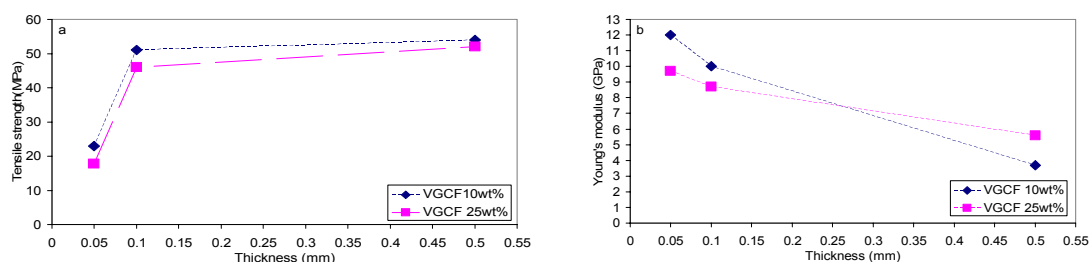

Fig.5 Mechanical properties of PC/VGCF cast composites reinforced with 10 and 25wt% of VGCF; a: Tensile strength; b: Young's modulus.

We noted that the thickness of 0.1mm is the critical point of the tensile strength. Young's modulus decreases with increasing thickness on both the composites. This decreasing is due to the surface effect of the composites. This means that the surface alignment of the fibers is higher where thin composites are more concentrated than the thick composites surfaces. This was confirmed by using a SEM of the surfaces of thin and thick composites at VGCF 25wt%.

CONCLUSION

This research work describes a successful route of the fabrication of the nanocomposite sheets containing VGCF with a homogenous dispersion in a polycarbonate matrix.

The electrical resistivity decreased with increasing VGCF loading because of a good fiber network. However, the voids were increased in the nanocomposites, which influenced a decrease in the mechanical properties of the materials.

The VGCFs delayed the thermal decomposition of PC since it is likely to a result from absorption, by the carbon surface, of free radicals generated during the polymer decomposition. The high orientation of the rolling composites fibers were recorded because the rolling process enhanced the fiber orientation and decreased the voids, suggesting the mechanical properties of the VGCF/PC composite greatly improved, especially in rolling direction. The tensile strength was increased with increasing thickness, while the Young's modulus was decreased with increasing thickness on both the composites due to the surface alignment of the fibers where thin composites were more concentrated.

562

ACKNOWLEDGEMENTS

The authors are grateful to Dr. Yutaka Ohkoshi and Dr.Yasuo Gotoh of the faculty of textile at Shinshu University for their hospitality regarding the facilities at X-ray diffraction pattern and WAXD equipments. The authors also wish to thank to Mr. Asahiko

REFERENCES

1. Barrera, E.V "Key methods for developing single wall nanotube composites", Journal of Materials, Volume 52(11), Pages 38-42 (2000).
2. Sandler.J, Shaffer. M.S.P, Prasse.T, Bauhofer.W, Schulte.K, Windle.A.H "Development of a dispersion process for carbon nanotubes in an epoxy matrix and the resulting electrical properties", Polymer, Volume 40, Pages 5967-5971 (1999).
3. VanHattum FWJ, Serp P, Figueiredo JL, Bernardo CA "The effect of morphology on the properties of vapor grown carbon fiber", Carbon, Volume 35(6), Pages 860-863 (1997).
4. Ciminelli DL, Kearns KM, Ragland WR "Vapor grown carbon fiber (VGCF) composites", Proceedings of the 41st International SAMPE Symposium, Covina, CA, Pages 495-501, March 24-28 (1996).
5. Chellappa V, Chiu ZW, Jang BZ "Electrical behavior of carbon whisker reinforced elastomer matrix composites", Proceedings of the 26th International SAMPE Technical conference, 26, Pages 112-118, Oct.17-20 (1994).
6. Shui X, Chung DDL "Conducting polymer-matrix composites containing carbon filaments of submicron diameter", Proceedings of the 38th International SAMPE Symposium, Pages 1869-1875, May 10-13 (1993).
7. C Bower, R Rosen, L Jin, J Han, O Zhou "Deformation of carbon nanotubes in nanotube-polymer composites", Applied Physics Letter, Volume74, Issue22, Pages 3317-3319 (1999).
8. ZJ Jia, ZY Want, CL XU, J Ling, BQ Wei, DH Wu, SW Zhui "Study on poly(methyl methacrylate)/carbon nanotube composites", Materials Science and Engineering A, Volume 271, Issues 1-2, Pages 395-400 (1999).
9. Qian D, Dickey EC, R .Andrews and T .Rantell "Load transfer and deformation mechanisms in carbon nanotube-polystyrene composites", Applied Physics Letters;Volume76, Issue20, Pages 2868-2870 (2000).
10. Carole A.Cooper, Diana Ravich, David Lips, Joerg Mayer, H.Daniel Wagner "Distribution and alignment of carbon nanotubes and nanofibrils in a polymer matrix", Composites Science and Technology, Volume 62, Pages 1105-1112 (2002).
11. Haggenmueller R, Gommans H.H, Rinzler A.G, Fischer J.E, Winey K.I "Aligned single-wall carbon nanotubes in composites by melt processing methods", Chemical Physics Letter, Volume 330, Pages 219-225 (2000).
12. L.S.Schadler, S.C.Giannaris, P.M.Ajayan "Load transfer in carbon nanotube epoxy composites", Applied Physics Letters, Volume73, Issue 26, Pages 3842-3844 (1998).
13. Heuvel H.M, Huisman R and Lind KCJB "Quantitative information from x-ray diffraction of nylon-6 yarns. I. Development of a model for the analytical description of equatorial x-ray profiles", Polymer Physics Edition, Volume 14, Pages 921-940 (1976).
14. T. Kelen. Polymer degradation, Van Nostrand Reinhold Co., New York, (1983).
15. B.B.Troitskii, L.S.Troitskaya, A.S.Yakhnov, M.A.Lopatin and M.A.Novikova "Retardation of thermal degradation of PMMA and PVC by C_{60}", Eur.Polym.J., Volume 33, No.10-12, Pages 1587-1590 (1997).

Manufacturing and Performance of Carbon Nanotube/High Density Polyethylene Composites

Brian B. Johnson, Michael H. Santare, John E. Novotny, Suresh G. Advani

Department of Mechanical Engineering and Center for Composite Materials
University of Delaware, Newark, DE 19716
Corresponding Author's e-mail: santare@me.udel.edu

SUMMARY: This study describes the manufacturing of Carbon Nanotube/High Density Polyethylene composites (CNT/HDPE) and the testing of these materials to determine several key material characteristics (i.e. stiffness, tensile strength, work-to-failure and wear resistance). These nanocomposites are made from untreated, multiwalled carbon nanotubes and HDPE through a process of mixing and extruding. Materials were created with varying weight percentages of nanotubes (0%, 1%, 3%, and 5%) and then molded and machined to form standard test specimens for small punch testing and block-on-ring wear testing. Mechanical tests were then conducted for the various volume percentages of nanotube content with pure HDPE as the control. It was found that each of the measured mechanical properties of the composite increased as a function of increased nanotube content in the range studied.

KEYWORDS: carbon nanotubes, high density polyethylene, wear resistance,

INTRODUCTION

There has been a recent surge of interest in the use of nanotubes as a reinforcing phase in composite materials, in an attempt to improve the electrical and/or mechanical properties of the unreinforced materials. Of specific interest in certain cases is the improvement of the wear behavior. For example, a significant contributing factor to artificial hip implant failure is loosening of the femoral stem due to osteolysis, which is often caused by polyethylene wear debris [1]. Therefore, it is commonly believed that improving the wear resistance of the polyethylene used in these implants would reduce the failure rate. It has been shown that the addition of CNTs can improve the tribological performance of Ni-P coatings, copper, and carbon/carbon composites [2, 3, 4]. The purpose of this study is to examine the effect of the addition of carbon nanotubes (CNT) to high-density polyethylene (HDPE). Specifically, the material and tribological properties of this new nanocomposite are of interest for a variety of possible applications that require high wear resistance.

MATERIALS AND METHODS

Nanotube Composites

Test samples were made with varying weight percentages of carbon nanotubes in high-density polyethylene. The initial preparation provided enough material for all samples, at each CNT weight percentage, to ensure uniformity of material throughout testing. Multi-walled carbon nanotubes (MWNT) produced by a thermal CVD (chemical vapor deposition) process and virgin HDPE (Marlex® 5502) were used. Appropriate quantities of polyethylene and nanotubes were carefully measured and combined into beakers to produce mixtures of 0%, 1%, 3% and 5% CNT by weight. The beakers were placed in an oven at 200°C for ten minutes to melt the HDPE and then taken out and mixed with a glass rod. The mixtures were pressed into flat wafers, which were then cut into pellets to prepare them for further mixing in a twin-screw small batch extruder (DACA Micro Compounder). The pellets of composite material were then mixed in the extruder at 175°C for 10 minutes, extruded, cut again into pellets and put back into the extruder for 10 more minutes. After the 20 minutes of mixing in the extruder the material was extruded again. Some of the extruded composite was directly formed into small punch samples while the rest was cut into small enough pieces to be compression-molded into wear test samples.

In order to compare mechanical properties of the extruded precursor material, a small punch test [5] was performed as described in Tang et al. [6]. This test gives relative measures of the stiffness, maximum strength, and work to failure for each material. Figure 1 shows a typical Load vs. Displacement graph from the small punch test as well as a comparison of the resulting properties for HDPE with 0%, 1%, 3%, and 5% CNT (normalized to 0% results).
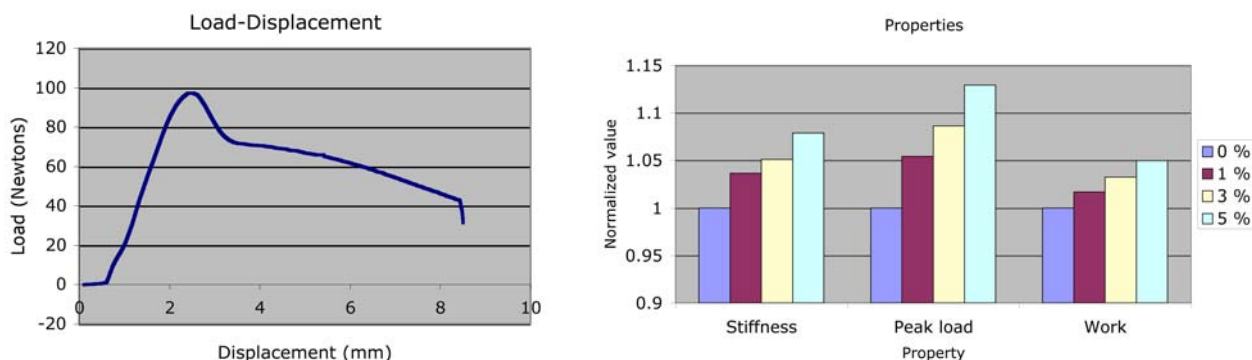

Fig. 1 Typical Load vs. Displacement curve and material property comparison data.

Wear Samples

The various percentages of CNT/HDPE composite materials, prepared as described above, were used to make wear test specimens. Contoured wear samples were produced in accordance to the geometric specifications for use with Falex Block-on-ring wear and friction tester. The samples made of CNT/HDPE material only used a small amount of composite on the wear test surface, with the rest being pure HDPE.

This minimized the amount of composite material used. First a "loaf" of samples was made using a simple compression molding technique. The mold was preheated in a 225°C oven for 20 minutes. A layer of approximately 4g of test material pellets was placed in the mold, covered with 7g of HDPE pellets. This was put back into the oven for 20 minutes with the mold top on and weight applied. The mold was then removed and additional HDPE material was added and placed in the oven for another 20 minutes. Finally, the mold was removed from the oven and allowed to cool prior to removal of the material. The "loaf" was then machining into individual samples (slices).

Wear Testing

Wear testing was performed using a Falex block-on-ring wear and friction tester. A diagram of the test configuration and a photo of the chamber are shown in Figure 2. The experimental procedures were adapted from ASTM G 77 and D 2714 test methods [7]. A load of 200 lbs weight was used and the ring was set to run at a rate of 200 rpm. De-ionized water was used in the chamber for lubrication and to allow for dissipation of heat produced from friction between the wear ring and test sample. Labview software was the acquisition interface used to collect data for friction, displacement, number of cycles, and the temperatures of the test chamber and the wear sample. Data was recorded each minute, over a period encompassing 500,000 cycles. After a test was completed, the water was drained from the chamber and any out-of-the-ordinary aspects were noted such as cloudy or oily water or extensive wear debris.
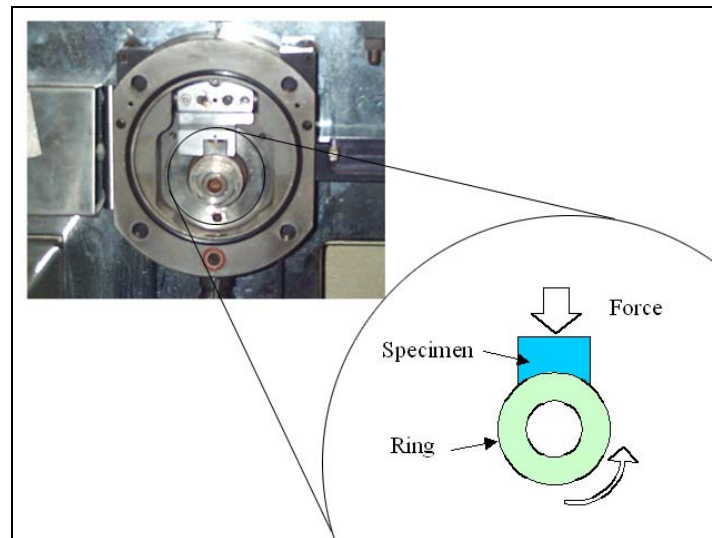

Fig. 2 Test chamber of Falex Wear Tester and diagram of ring and block with rotation and force directions.

RESULTS AND DISCUSSION

As found by Tang et al. [6] material properties determined using the small punch test changed as a function of CNT percentage. As the weight percentages of CNTs were increased the stiffness, maximum strength, and work to failure all increased. Comparing the 0% to the 5% CNT samples the stiffness, maximum strength, and work to failure showed improvements of approximately 8%, 13%, and 5% respectively. In addition to showing that the CNTs improve material properties of HDPE this also confirmed that the materials produced were acceptable for use in further testing to determine tribological properties.

The wear data collected was approximated by a logarithmic curve-fit which gave a value for the wear rate (mm) vs. log-cycles. For each sample, the logarithmic curve was required to meet a minimum correlation (R-squared) value of 90%. The standard deviations of each sample grouping were also calculated. It is apparent from the data that wear decreases with increased weight percentage of CNTs. An improvement of 26% decrease in wear was seen from 0% to 1% samples and an improvement of nearly 40% was seen between the 0% and 5% samples. Figure 3 shows two different plots of the comparison of wear rates for the different samples. It was determined that standard deviations present within each sample group are primarily caused by variation of sample manufacturing processes. Manufacturing steps were strictly followed, however at the micro level there are still deviations in material structure such as polymer chain alignment, branching, and crosslinking. Also, as discussed in Tang et al., the dispersion of the CNTs becomes an important issue both on micro and nanoscale levels, which causes variation of material structure throughout the sample's volume. However, even with these small deviations, the overall trends of the data show that there is improved wear characteristics with increasing weight percentages of nanotubes. Wear tests are currently being run for the 3% samples and data will be reported in the near future.
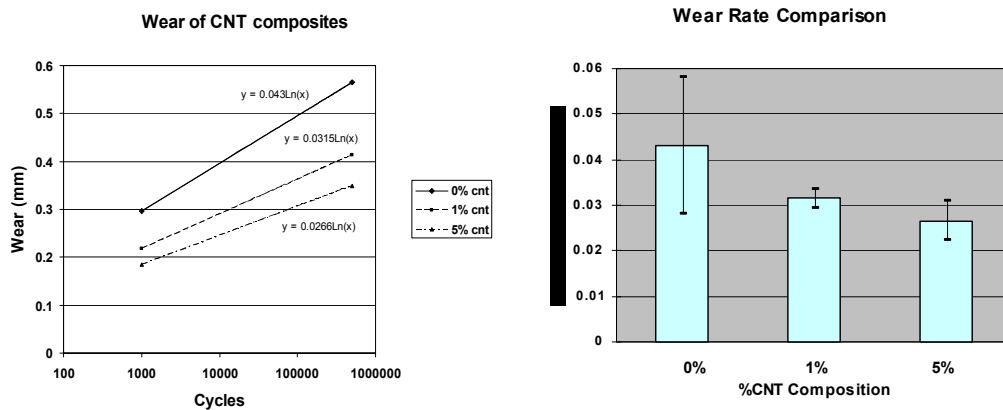

Fig. 3 Wear Rate Comparison for varying CNT%

In some cases after a test was run the water from the test chamber was cloudy due to contamination from a small amount of oil, these occurrences were attributed to small amounts of oil leaking from the spindle housing into the test chamber and were corrected by checking the oil level in the spindle housing and changing it to the appropriate level. In some other instances, samples wore at an extremely high rate and large amounts of shredded polymer material were present in the water and the test chamber. These results were thrown out based on the assumption that there was some type of material defect in the sample that caused it to rapidly fall apart.

CONCLUSIONS

Varying weight percentages of CNTs were added to HDPE in an attempt to improve material properties of HDPE including the wear resistance. As measured by the small punch test, the addition of CNTs improves the material properties compared to the virgin HDPE material. The addition of CNTs to HDPE also decreases the wear rate of the material and this value decreases as the percentage of CNTs is increased. In addition to improvements in stiffness, tensile strength, work to failure and the tribological properties, the addition of CNTs is also likely to change other material properties such as fracture strength and fatigue crack resistance. The authors are currently conducting a series of fracture tests to evaluate these effects as well as additional wear tests on different %CNT samples and hope to report on these in the near future.

ACKNOWLEDGEMENTS

REFERENCES

1.   H.C. Amstutz, M.D., P. Campbell, B.Sc., N. Kossovsky, M.D., and I.C. Clarke, Ph.D., "Mechanism and Clinical Significance of Wear Debris-Induced Osteolysis", *Clinical Orthopaedics and Related Research*, Vol. 276 (1992) 7-18.
2.   W.X. Chen, J.P. Tu, Z.D. Xu, W.L. Chen, X.B. Zhang, D.H. Cheng, "Tribological properties of Ni-P-multi-walled carbon nanotubes electroless composite coating", *Materials Letters*, Vol. 57 (2003) 1256-1260.
3.   S.R. Dong, J.P. Tu, X.B. Zhang, "An investigation of the sliding wear behavior of Cu-matrix composite reinforced by carbon nanotubes", *Materials Science & Engineering A*, Vol. 313 (2001) 83-87.
4.   D.S. Lim, J.W. An, H.J. Lee, "Effect of carbon nanotube addition on the tribological behavior of carbon/carbon composites", *Wear*, Vol. 252 (2002) 512-517
5.   S.M. Kurtz, J.R. Foulds, C.W. Jewett, S. Srivastav, A.A. Edidin, "Validation of a small punch testing technique to characterize the mechanical behavior of ultra-high-molecular-weight-polyethylene", *Biomaterials* Vol. 18(24) (1997) 1659-63.
6.   W. Tang, M.H. Santare, S.G. Advani, "Melt processing and mechanical property characterization of multi-walled carbon nanotube/high density polyethylene (MWNT/HDPE) composite films", *Carbon*, Vol. 41 (2003) 2779-2785.
7.   *ASTM Standards* G77-98 "Standard Test Method for Ranking Resistance of Materials to Sliding Wear Using Block-on-Ring Wear Test

A Study of a Novel Test Method for Self-Healing Techniques Using Microcapsules

Boyoung Jeong [1], Youngki Yoon [2], Kiseok Moon [1*], HiSeak Yoon [3]

[1] *Graduate Student, Department of Mechanical Engineering, Chonnam National Univ.*
300, Yongbong-dong, Buk-gu, Kwangju 500-757, KOREA: jby@chonnam.ac.kr
[2] *Senior Researcher, Institute of Advanced Machinery and Design, Seoul National Univ.*
San 56-1, Shinlim-dong, Kwanak-gu, Seoul 151-742, KOREA: youngki@snu.ac.kr
[1*] *Speaker Graduate Student, Department of Mechanical Eng., Chonnam National Univ.*
300, Yongbong-dong, Buk-gu, Kwangju 500-757, KOREA: ksmoon @chonnam.ac.kr
[3] *Professor, Department of Mechanical Engineering, Chonnam National Univ.*
300, Yongbong-dong, Buk-gu, Kwangju 500-757, KOREA: hsyoon@chonnam.ac.kr

SUMMARY: Recently, self-healing methods of the cracked matrix, especially from polymeric composite materials, became the center of engineering researchers. In this paper, we summarized the self-healing concept for polymeric composite materials and investigated the effect of microcapsule on the crack growth behavior in colorless and transparent matrix, by experimental observation to describe the crack propagation around the microcapsules inside epoxy matrix composite. Compression splitting test for the specimen involving microcapsules was conducted using DCDC (Double Cleavage Drilled Compression) specimen. Through the experiments, we found that the size, relative position, bonding condition and relative stiffness of microcapsules are important parameters to decide the direction of crack propagation, which is related to the rupture of microcapsule for the self-healing.

KEYWORDS: Double Cleavage Drilled Compression (DCDC) specimen, Self-healing techniques, Microcapsules, Crack propagation

INTRODUCTION

The delayed failure in a material with the cracks or the voids is very interesting research topic due to the possibility of observing the crack propagations and the crack growth behavior [1,2]. Especially for in-suit observation of recent self-healing material, the crawling crack propagation technique is very useful. In the previous researches related with a self-healing polymer composite, the research workers [3-5] inspected the fracture plane of the experimental specimen to identify the broken microcapsules in the matrix and the healing efficiency. Some investigators [6, 7] pursued to find a new method to achieve the slow crack growth in kind of brittle materials, like glasses or ceramics.

They suggested a double-cleavage-drilled compression (DCDC) specimen chosen in order to have a slow matrix crack growth and to enable direct observation of the crack front shape.

In this paper, attention has been focused on the possibility of in-suit observations which show the fracture of microcapsules in self-healing structures using DCDC specimen.

Table 1 Material Properties of MS-200 and CZC

MS-200	
Elastic Modulus (GPa)	2
Tensile Strength (kg_f/mm^2)	60
CZC(ZrO_2)	
Elastic Modulus (GPa)	110
Tensile Strength (kg_f/mm^2)	35

EXPERIMENTAL METHODS

Preparation of test samples

Commercially available micro-particles (Young's Co., Korea) were used as microcapsules in self-healing structures because the purpose of this research is in-suit observation of the crack propagation near microcapsules in the matrix. And commercially available transparent epoxy (MS-200) was used as matrix. Materials properties of MS-200 epoxy (Nippon Steel Chemical Co., Japan) and CZC (ZrO_2) micro-particles are listed in Table 1. Figure 1 shows the photos of CZC particles and MS-200.

The DCDC specimens are prepared using hot plate compression method under the commercially recommended condition from the manufacturer. The shape and the dimensions of the DCDC specimen are 40x40x10mm with an 8mm center hole and 2mm pre-cracks from the edge of the hole. All the surfaces of the specimen were mechanically ground and polished even inside of the center crack. Figure 2 shows the schema of DCDC specimen and mold.

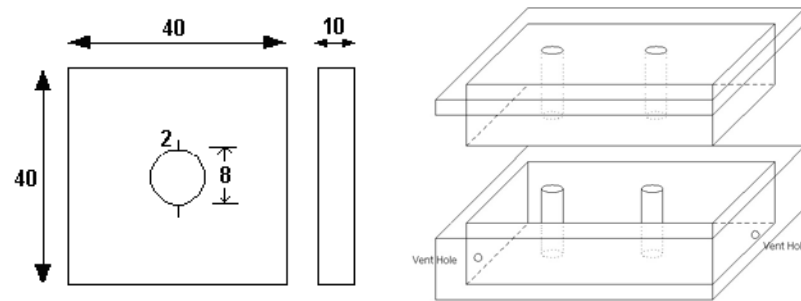Fig. 1 The photos of CZC particles (left) and MS-200 (right)

Fig. 2 The shape of DCDC and the schematic diagram of hot plate mold.

Experimental procedures

Figure 3 shows the experimental set-up of the in-suit compression splitting test. The compression test machine is Instron 8872. A digital CCD video microscope camera is used to observe the crack propagations, and the images with 100 magnifications are acquired in each 10 seconds. The load head speed is 0.01 mm/s by the displacement control.
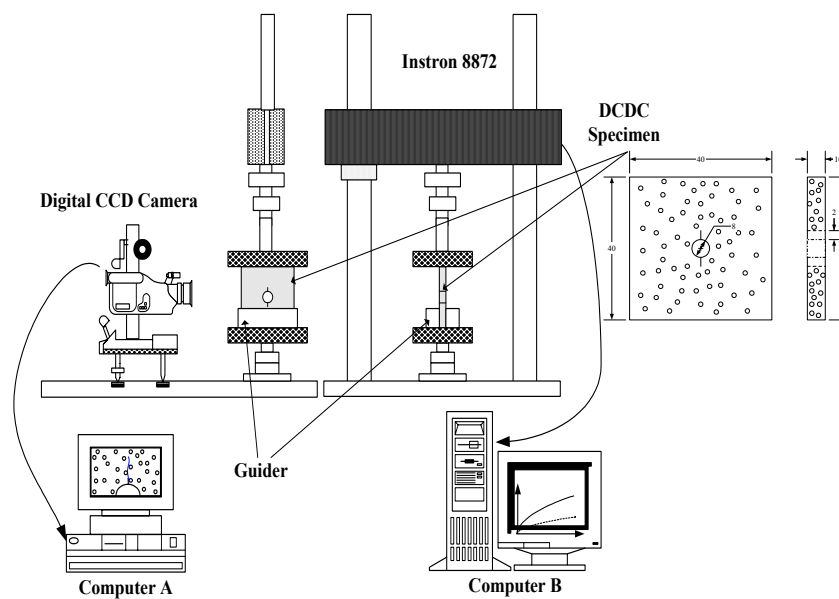

Fig. 3 Experimental set-up for in-suit observation around the microcapsule in a self-healing structure.

RESULTS AND DISCUSSIONS

Compression results

Figure 4 shows the compression test results for the microparticle inserted DCDC specimens. The specimens are in two forms; one is that the microparticle is located on the same direction of crack propagation and the other is that the microparticle is off the direction about 10° degree of an oblique angle. The purpose of the specimens is the embodiment of the similar shelf-healing matrix which has the microcapsules inside to show the effects of the crack near the microcapsules. The microparticles are inserted in the matrix with the microcapsules with healing agent for the experimental convenience. Figure 4(a) shows the debonding on the boundary between the microparticle and the matrix when the crack arrived at the particle. From the experiments, it is expected that the microcapsules will be ruptured and the healing agents will be out from the capsules when the capsules are broken by the propagating crack in the matrix. Figure 4(b) shows that the crack propagation direction can be changed toward the particle in matrix. However, if the gap between the microparticle and the crack is longer than 2mm, the crack just propagates toward its direction independently of the microparticle in the matrix.
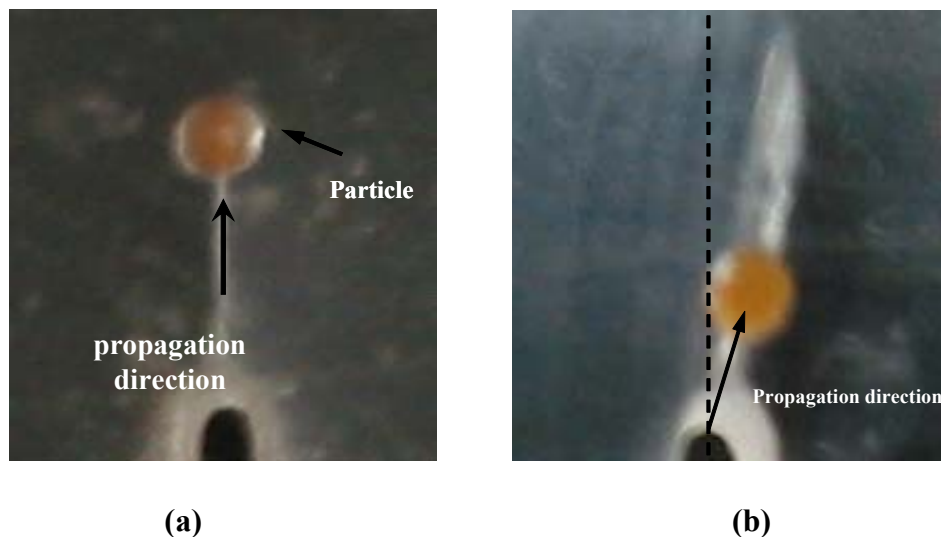

(a)   (b)

Fig. 4 Two geometries of micro-particles in the matrix: (a) on the line of the crack tip (b) on the incline line of the crack tip.

Compression results

Figure 5 shows log-linear scale load-displacement curves of typical DCB specimen and DCDC specimen trough the experiment. DCB specimen's case shows that the displacement rate is high under the low load. However, in DCDC specimen's case, crack propagation is started at a high load condition. It means DCDC is more stable and has lower stress concentration near the crack tip when compared to DCB specimen. In the same load on the specimens, the displacement of DCDC specimen is within the low range and it needs large load to start the crack propagation from crack tip. And after the crack start, the displacement of the crack is in the low range.
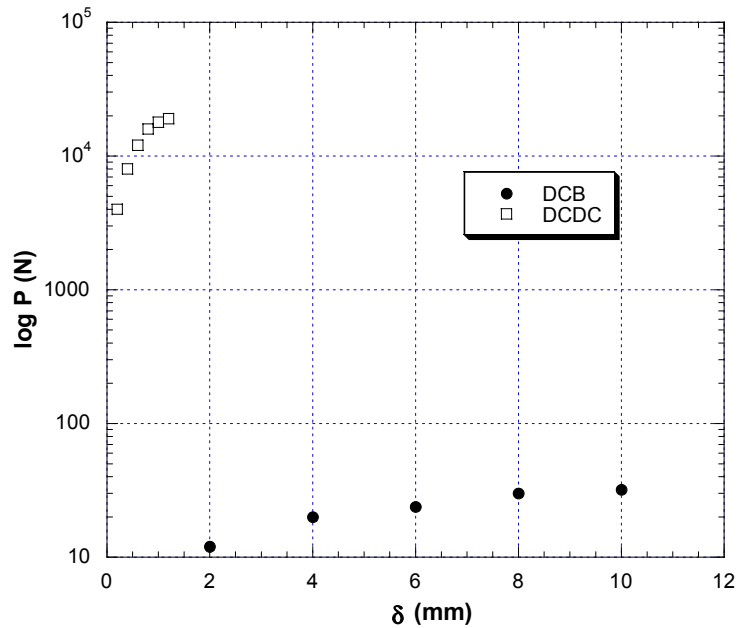
Fig. 5 Log and linear scale load-displacement curves of typical DCB and DCDC specimens

CONCLUSIONS

The most effective mechanism for fracture resistance of the matrix within this experiment is the elastic constraint effect by microparicles. The crack propagations in a microparticle-reinforced brittle matrix were observed and discussed. From the in-situ observation results, the possibilities of the application to the self-healing materials to observe the rupture of the microcapsules which heal the matrix automatically are presented.

ACKNOWLEDGEMENT

REFERENCES

1   Satoshi Yoshida, Jun Matsuoka, Naohiro Soga, "Crack growth behavior of zinc tellurite glass with or without sodium oxide," J. Non-Crystalline Solids, Vol. 279, pp.44~50, 2001.

2.   Y.-K. Lee, M.Tomozawa, "Effect of water content in phosphate glasses on slow crack growth rate," J. Non-Crystalline Solids, Vol.248, pp.203~210, 1999.

3.   S.R.White, N.R.Sottos, P.H.Geubelle, J.S.Moore, M.R.Kessler, S.R.Sriram, E.N.Brown, and S.Viswanathan, "Autonomic healing of polymer composite," NATURE, Vol.409, pp.794~797, 2001.

4.   M.R.Kessler, S.R.White, "Self-activated healing of delamination damage in woven composites," Composites Part A, Vol.32, pp.683~699, 2001.

5.   Eric N. Brown, Nancy R. Sottos, and Scott R. White, "Microcapsule Induced Toughening in a Self-Healing Polymer Composite,"

6.   Yutaka Kagawa, Ken Goto, "Direct observation and modeling of the crack-fiber interaction process in continuous fiber-reinforce ceramics: model experiments," Materials Science and Engineering, A250, pp.285~290, 1998.

7.   K.Goto, Y.Kagawa, K.Nojima, and H.Iba, "Effects of crack-fiber interactions on crack growth rate in fiber-reinforced brittle matrix composite under cyclic loading: model experiment," Materials Science and Engineering, A212, pp.69~74, 1996.

Effect of Gypsum Content on the Properties of PVC/Gypsum Polymer Blend Material: Physico-Mechanical Properties, Thermal Properties and Morphology Development

Nguyen Vu Giang and Kim Myung Yul

Department of Polymer Science & Engineering, Sunchon National University, 315 Meagok, Sunchon, Jeonnam, 540-742 KOREA. And Corresponding Author's e-mail: mykim@sunchon.ac.kr

SUMMARY: Polyvinyl chloride (PVC)/gypsum polymer blend materials were prepared by melt blending of PVC with gypsum and additives. Effect of gypsum content on the properties of PVC/gypsum polymer blend material was studied by investigating physico-mechanical properties, thermal properties and morphology development. It was found that the replacement of gypsum for methylene-butadiene-styrene (MBS) component in PVC/gypsum polymer blend material enhanced the tensile strength, but gradually decreased its impact strength. Besides, with the increase of gypsum content, the elongation at break of material gradually decreased. The presence of the different gypsum contents made a shift of glass transition temperature and increased the thermal stability as well as the processing temperature range of polymer blend materials. The observation of morphology, the results of the physico-mechanical properties and thermal properties proved simultaneously that PVC/gypsum polymer blend material with the gypsum content of 22.56 wt.% reached the optimum results among five kinds of PVC/gypsum polymer blend materials investigated.

KEYWORDS: Gypsum, PVC, blend.

INTRODUCTION

Polyvinyl chloride (PVC), as an important commercial polymer, has been studied and used widely in industrial fields for many years. However, due to its inherent disadvantages, such as low thermal stability and brittleness, PVC and its blend are subjected to some limitations in certain applications [1]. The wet phosphoric acid has obtained by dissolving phosphate ore into sulfuric acid in a artificial way, Namhae Chemical Company has been obtained the wet phosphoric acid according to this way to produce phosphatic fertilizers. A lot of obsolete gypsum produced in this process have been buried. Gypsum consists of a dihydrate sulphate calcite ($CaSO_4.2H_2O$), anhydrate sulphate calcite ($CaSO_4.H_2O$), calcite oxide (CaO), phosphate, and with particle size less than 200 nm. Though a lot of researches on recycling the abandoned gypsum in advanced countries, for example Germany and Japan etc. are being conducted, actually, a small amount of gypsum are used for plaster boards but most are buried in the sea wasting tremendous amount of expenses [1]. Especially, there is no example so far that has researched the mechanical and physical properties of a product by using the gypsum onto PVC resins.

Hence, in polyvinyl chloride (PVC)/gypsum polymer blend research, the primary goal is to enhance the strength end toughness of polymer component using nanoscale reinforcement gypsum. Therefore, in this paper, we mainly investigated the effect of gypsum content with and without the presence of MBS content on the physico-mechanical properties, thermal properties of the PVC/gypsum polymer blend material. Five kinds of rigid PVC/gypsum polymer blend with different gypsum contents were prepared by melt blending method. The morphology development of the PVC/gypsum polymer blend samples is also discussed in this paper.

EXPERIMENTAL

Materials

Suspension polymerization PVC (PVC LS-100, DP = 1000) was provided by Lucky Co. LTD, Korea. Gypsum was produced with particle size less than 200 nm by Namhae Chemical Co, Korea; the composition of gypsum was shown in Table 1. The component ratios of PVC/gypsum and additives used to observe the change of dynamic properties base on the difference of gypsum content was shown on Table 2.

Preparation of PVC/gypsum Polymer Blend Materials

PVC/gypsum polymer blend samples were prepared by melt mixing PVC, gypsum, and processing additives in the roll-mill (Nishimura, KR-250, Japan) at 175°C for 5 minutes. After that, the polymer blend samples were quickly molded into sheets of 3mm in thickness by hot pressing machine (Wabash, G302-BCLX, USA) at 175°C and 20 MPa for 5 minutes, followed by cooling to room temperature at 5 MPa. The sheets were prepared for the structure characterization and the property measurements.

Table 1   Chemical composition of Gypsum (wt.%)

	COM	AVG	STD	MIN	MAX
D-Gypsum	TP-	1.30	0.79	0.32	3.89
	WSP-	0.93	0.68	0.19	3.01
	CaO	33.7	10.37	29.00	36.30
	F-H_2O	23.00	5.76	10.90	36.70
	C- H_2O	17.60	2.65	9.60	20.40

Where:
D : Dry; TP- : Total Phosphate; WSP- : Water Soluble Phosphate; F-H_2O: Free - H_2O;
C- H_2O : Combined - H_2O; COM : Composition; AVG : Average; STD: Standard;
MIN: minimum; MAX : Maximum

Table 2. Sample code and composition of polymer blend material

	PVC (g)	Lubricant (g)	Stabilizer (g)	MBS (g)	Gypsum (g/wt.%)
PVC0	100	0.5	3.0	-	-
PVC1	100	0.5	3.0	7.0	20.0/15.38
PVC2	100	0.5	3.0	-	20.0/16.26
PVC3	100	0.5	3.0	-	30.0/22.56
PVC4	100	0.5	3.0	-	40.0/27.97
PVC5	100	0.5	3.0	-	50.0/32.67

RESULTS AND DISCUSSION

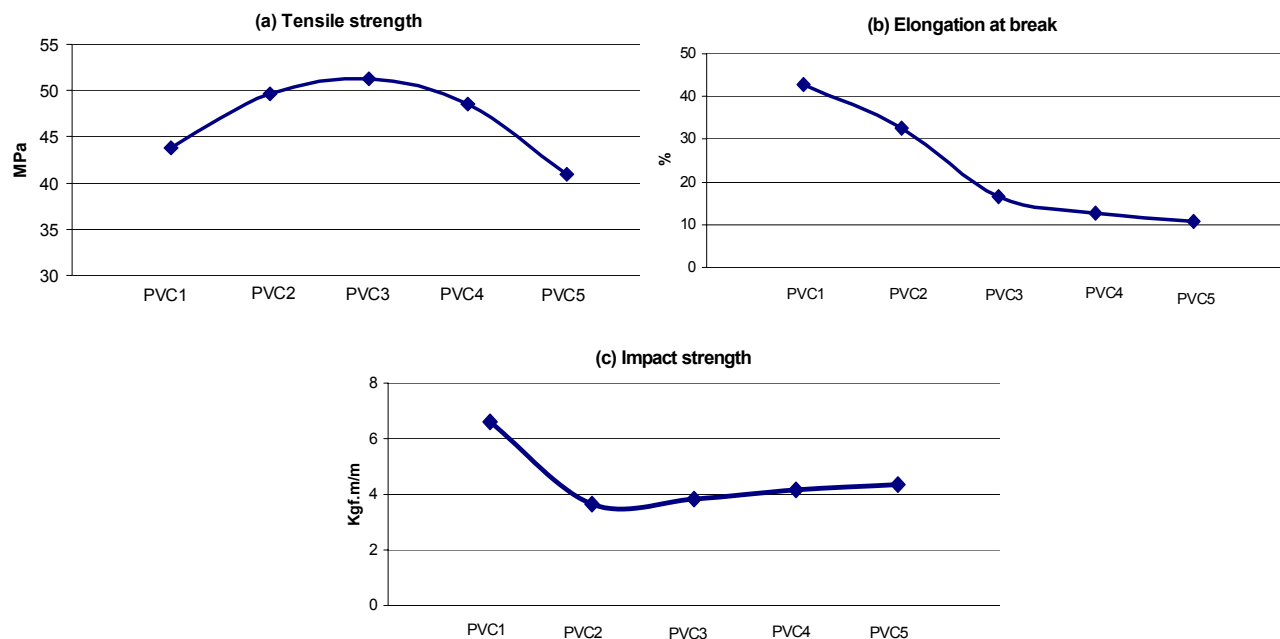**Physico-Mechanical Properties:**

Fig.1 Physico-mechanical properties of PVC complexes containing various amounts of gypsum.
(a: Tensile strength, b: Elongation at break, c: Impact strength)
Upon adding of gypsum to the PVC compound replacing the MBS on PVC2 sample with the content of gypsum of 16.26 wt%., the tensile strength of PVC compound was increased from 43.8 MPa up to 49.6 Mpa (Fig. 1a). The highest tensile strength among five samples was measured on PVC3 sample with the gypsum content of 22.56 wt%, reached a value of 51.3 MPa, then which gradually decreases to 48.5 MPa and 40.9 MPa as the amount of gypsum phase increases at PVC4 and PVC5 samples, respectively. On observation of the elongation at break of PVC compound samples, when MBS, as a reinforcement agent, was rejected from PVC compound, the elongation at break drop drastically from 42.9 % (PVC1, 15.38 wt% gypsum) to 32.7 % (PVC2, 16.26 wt% gypsum) , then 16.5 % (PVC3, 22.56 wt% gypsum), and then gradually decrease to 12.7 % (PVC4, 27.97 wt% gypsum), to 10.85 % (PVC5, 32.67 wt% gypsum). It was revealed that the gypsum phase plays a role as an inorganic distributed phase, which causes a decrease of the flexibility of PVC matrix phase because of the small particle side of gypsum (around 200 nm), which easily intercalated into the vacancy of the bulk polymer [2]. From the impact strength observed, Fig. 1c, comparing between the samples with and without of the presence of the MBS phase the impact strength of PVC compound sample dramatically decreases from 6.61 Kgf.m/m to 3.65 kgf.m/m. It revealed that the gypsum phase not only plays a role as good filler, but also is a good interactive inorganic material with PVC matrix phase, which was well dispersed in the polymer system, and hence good impact strength..

Thermal Properties:

On the observation of glass transition temperature of five samples (Fig. 2), it was obvious that had existentially a limitation of the distribution of the gypsum phase over PVC matrix phase at which made a highest shift of the glass transition temperature. It should be noted that highly electronegative chloride atoms of PVC chains endow PVC with strong polarity. At the same time, large quantities of polar hydroxyl group of gypsum (as showed in Table 1) and calcium (Ca$^+$) layers existing on the surface of gypsum particles make the layer surface polar too. In this case, the dipole-dipole interaction between PVC matrix phase and gypsum dispersed phase may act as driving force for gypsum phase to intercalate into PVC phase. Fig 3 shows the TGA curves of the PVC/gypsum blend samples. It was interesting that for the case of without the presence of gypsum, the decomposed temperature of polymer was about 278 ^{o}C, however, for the other later cases, the decomposed temperature of polymer blend was about 285 ^{o}C. This might be expected that calcium oxide (CaO) presented in gypsum composition which played a role as a fire resistance, effectively scavenge HCl gas liberated from burning halogenated polymer (PVC), thereby reducing the corrosiveness of the generated smoke, and improving the thermal stability of PVC/gypsum polymer blend samples [3].
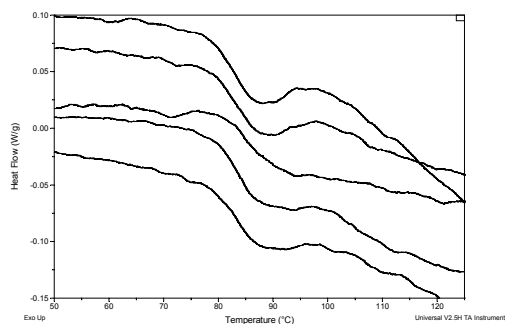
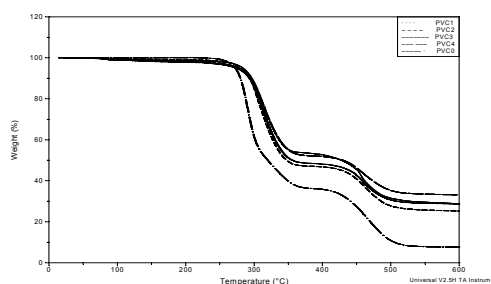Fig. 2 DSC diagram of PVC complexes containing various amounts of gypsum.

Fig. 3 TGA diagram of PVC complexes containing various amounts of gypsum

Morphology of PVC/Gypsum Blend Material
On observation of the distribution of gypsum phase (Fig. 4), it obviously had the change of the morphology of each other. It is clearly realized that for the case PVC3 sample, gypsum phase was best dispersed among the investigation of four given samples, gypsum particles finely intercalated into PVC matrix phase and made significantly a change on morphology of sample. This suggested that the physico-mechanical properties vary in accordance with the morphology changes of the polymer blends. Thus if the gypsum content exceeds 22.56 wt.%, it event will influence no good on the physico-mechanical properties because of the appearance of the coalescence effect.

CONCLUSIONS

The PVC/gypsum blend material was obtained via a melt blending process. The physico-mechanical properties was investigated base on the different gypsum content of the blend samples to establish the mechanical strength of this material. The highest tensile strength of this material was measured at PVC 3 with the content of gypsum component of 22.56 wt.%.

Finally, as a result of adding the gypsum buried in the sea to PVC resin, we cannot only get the polymer blend material that has such superior physico-mechanical properties and thermal stability, but also solves the enviromental problems by using waste matters.
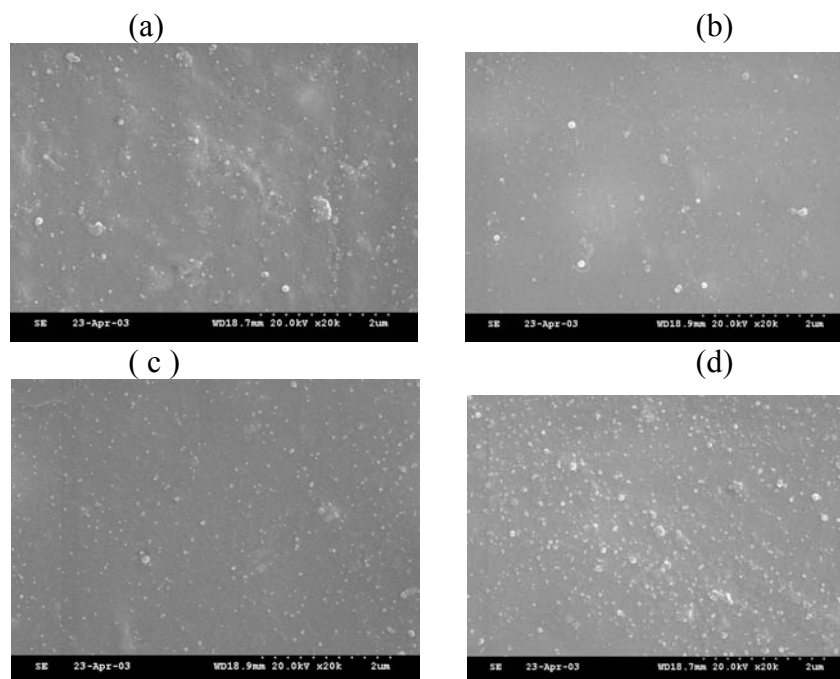
(a)　　　　　(b)

(c)　　　　　(d)

Fig. 4 Micrographs of PVC complexes containing various amounts of gypsum.
(a: PVC1, b: PVC2, c: PVC3 and d: PVC4)

REFERENCES

1. W.H. Starnes Jr., "Structural and mechanistic aspect of the thermal degradation of poly(vinyl chloride)", Progress in Polymer Science, Vol. 27, 2002, Pages 2133-2170.

2. B. Lepittevin, N. Pantoustier, M. Devalckenaere, M. Alexandre, C. Calber, R. Jerome, C. Henrist, A. Rulmont, P, Dubois, "Polymer/layered silicate nanocomposites by combined intercalative polymerization and melt intercalation", Polymer 44, 2003, Pages 2033-2040.

3. J. Wypych, "Polyvinyl chloride degradation", Elsevier Science Publishers B.V., Netherlands, 1985, Pages 59-109